

THREE-DIMENSIONAL ENGINEERED TISSUE MODELS FOR EXPERIMENTAL NANOTHERANOSTICS

By

Anna Guller

A thesis submitted to Macquarie University

For the degree of Doctor of Philosophy

Department of Physics and Astronomy

April 2017



MACQUARIE
University
SYDNEY • AUSTRALIA

Faculty of Science and Engineering

Except where acknowledged in the customary manner, the material presented in this thesis is, to the best of my knowledge, original and has not been submitted in whole or part for a degree in any university. Several parts of this thesis have resulted from collaborative work with my supervisors, other researchers and research institutions. Their contributions are recognised and acknowledged respectively. The studies included into the thesis have been approved by Macquarie University's Animal Ethics Committee (AEC) and Local Ethics Committee of I.M. Sechenov First Moscow State Medical University with the following reference numbers of the approvals ARA2015/006, ARA2015/006-2, ARA2013/007-4 and LEC 11-16/14.12.2016.

Anna Guller

© Anna Guller, Macquarie University, 2017

Dedication

I dedicate this work to Professor Anatoly Shekhter, my lifelong master, maître, colleague and friend. Thank you for teaching me science and art of experimental pathology as a way of the persevering search for the verity. Thank you for encouraging me to keep on in good and bad times. Thank you for the days and years which we spent together looking at the microscopes, talking and mentally sparring not only about the samples. Thank you for sharing with me your attitude to life, and your love to people. I hope to be able to follow your way devotedly.

Acknowledgement

This project, which has been incipient as a series of incredible coincidences in my life, occurred probably, a long time ago, later transformed into intense polemics around pretty vague ideas and risky experiments, and gradually took me completely, becoming my scientific passion. It has been challenging not only for myself, but also required a lot of solidarity and understanding from my beloved family and everyone who shared this tension with us and helped during the years. I understand this very clear and appreciate each minute thing contributed to this work by other people. Now, when the project is at its final stage, my heart is full of gratitude. Probably, the final and the most complex tasks now are to find only a few words to say thank you to everyone who was involved, while not to write a whole new book as it is too hard to put a full stop every time.

My deepest gratitude goes to my supervisor A./Professor **Andrei Zvyagin**, who really has broadened my horizons, opened for me a fascinating world of nanotechnologies and modern bioimaging, and involved me in his amazing dream-team of researchers in Australia and in Russia. I would like to thank you, Andrei, for being persevering in making me to think-out-of-the-box, to leave my stable world of classical pathology and to plunge into the demanding area of modern cross-disciplinary studies, while letting me keep and apply my professional skills and competence in this project. I am very thankful to you for trusting me (sometimes it, probably, was a bit more than I deserved) and for your determination to be brave enough to allow me to do this risky new project on the border between physics, nanotechnologies and medicine under your supervision and under the protection of your name. Thank you for reading my extremely long letters and drafts. Thank you for your strategic thinking, navigating me through the whole project as a voice of reason counsellor and, of course, for your endless kindness, patience and willing to help.

I would like to express my sincere thanks to my co-supervisor, Professor **Yi Qian** (Itsu Sen), a man of a great mind, heart and nobleness, without whose unwavering support this work would not be possible at all. Thank you, Qian, for your credit to me, your everyday support and help in organizing of the major part of tissue engineering experimental work of this project.

I am thankful to Professor **Ewa Goldys**, who always was open to discuss any challenging sides of the project, providing her incredible expertise and experience to help me with the experimental design and the workflow in general. Thank you, Ewa, for many great advises and your readiness to go deep into the details of this tangled research.

My very special and soulful gratitude goes to my collaborators involved into this project and our works in the field of tissue engineering and experimental pathology, who became my dearest friends and vice versa. Several very important names will be kept in my grateful heart forever for being my steadfast shoulders and a reliable team during these challenging times: my dear **Zahra Khabir**, **Annemarie Nadort**, **Liuen Liang** (Olivia), **Inga Kuschnerus**, **Alla Generalova**, **Alfonso Garcia-**

Bennett, Tatiana Rudenko, Evgeniy Khaydukov, Elena Petersen, Denis Butnaru, and Alexander Kurkov. You are amazing. I am also thankful to my colleagues: **Vladimir Semchishen, Inna Kornienko, Andrey Nechaev, Nikolay Landyshev, Ekaterina Grebenik, Paul Grebenyuk, Andrei Vinarov, Leonid Istranov and Elena Istranova, Ruben Aboyants, Alexey Lyundup, Olga Zakharkina, Zoya Milovanova, Olga Dvornikova, Anastasiya Bakastova, Svetlana Kotova, Victor Sokolov, Vladimir Nikolenko, Alexander Luzin and Andrey Zamyatnin** for all kinds of the support, which I had from you. I would like also to thank Professor **Sergey Deyev** for collaboration and for his helpful suggestions with regard to the preparation of the manuscripts.

This work could not be done without the people who always helped me to stay strong and keep above the waterline, shared their thoughts and accepted myself in any state of mind and mood. Thank you so much, dear **Kashif Islam and Sandhya Clement, Wan Aizuddin, Varun Sreenivasan and Ayad Anwer, Meng He, and Yujing Lu, Lianmei Liang, Guozhen Liu and Wei Deng.** Your names always will be very special for me. I am happy to say thank you to the new members of our group, **Vlada Rozova and Dmitriy Polykarpov.** I wish you to be happy and adventurous during your PhD journey. I am also grateful to the members of the Biofocus group and those who was with us in the labs, at the meetings and conferences: **Wenjie Chen, Xianlin Zheng, Saabah Mahbub, Aziz ul Rehman, Zak Wan Ismail, Fei Wang, Andrew Care, Zosia Kautzka, Piotr Wargocki, Abbas Habibalahi, Manoj Kale, Kaixin Zhang, Fei Deng, Fang Gao, Rashmi Pillay, Yan Wang, Ishan Rastogi, Mahdiyeh Dashtbani and Shilun Feng, Martin Ploschner, David Inglis, Lindsay Parker and Nima Sayyadi** for their interest in the subject, understanding and support during my PhD studies.

I am grateful to the laboratory managers **Louise Marr, Tamara Leo and Lucy Lu** for their every-minute and highly professional support of the lab life at the Faculty of Medicine and Health Sciences. Special thanks go to Professor **Mark Connor** for kind permission to use his group's lab space and for abiding our endless background talks, which probably, were a bit distracting. I would like to thank my lab mates at the Faculty of Medicine and Health Sciences for sharing their experience, teaching me a number of new techniques and tricks, while celebrating together the long hours of *in vitro* cell culture on weekdays and weekends. Thank you, **Marina Santiago, Vivien Lee, Shivani Sandchev, Preeti Manandhar, Nitin Chitranshi, Sinduja Subramanian, Sumudu Vindyani-Saubhagya (Simi), Blake Entwisle, Bhooma Venkatraman and Rochelle Boyd.**

I would like to extend my gratitude to our faculty staff members, who helped me in various practical aspects of the PhD life: **Nicole Vella and Debra Birch, Gina Dunford, Liz Bignucolo, Carol McNaught, Lisa Pesavento, and Amit Shrestha.**

Many thanks to **HDR Mentors group** for the great passion to kindness and giving me a way to express myself in a number of new ways. Special thanks to **Mo Hague, Ian Loke, and Kim Tan.**

There were a number of people behind the scientific scene of this project, who hold me up during these years. I am endlessly thankful to **Lana Ghosn and Martin Miles, Yamuna, Ravi and Smithy**

Ravichandran, Larisa and Michael Zolotarev, Tatiana Novikova, Elena Ginzburg, Olga Minaeva and Nikita Minaev, Nelli Govor and Igor Bradis, Irina Zakoshansky, Irina Peskova and Leonid Peskov, Lyudmila Bakunets, Svetlana Pentegova, Sergey Yavorsky, Marina Spirina, and Olga Andreeva.

I would like to express my gratitude to **Vladimir Kleev**, who was my first supervisor in science and taught me the serious attitude to science on the background of his unique sense of humour. Dear Volodya, thank you for everything you had done for me.

I admire Professor **Vasiliy Chirva** from my alma-mater Crimean University, for his devoted attitude to the people and for his decent commitment to the truth even under the enormous pressure of the circumstances.

I am grateful to **Macquarie University** for awarding me the International Macquarie University Research Excellence Scholarship (iMQRes). I would like to thank **ARC Centre for Nanoscale Biophotonics (CNBP)** for financial support of the experimental expenses and the provided possibility to attend the national and international conferences during this project. Special thanks to the staff of the **Department of Physics and Astronomy** (Faculty of Science and Engineering) and **Department of Biomedical Sciences** (Faculty of Medicine and Health Sciences), where my work and myself personally always could find reliable and professional help.

I have to say thank you to **Australia** for giving me hope and faith every morning just by exposing myself to your people, land, sun and sky.

Finally, my amazing, caring, understanding, supporting and unconditionally loving **FAMILY**. I could not survive without you, definitely. And this are you, who make this year-long science journey possible. I am endlessly thankful to my beloved husband and my dearest friend **Konstantin Guller** for his unlimited love and encouragement, his sense of humour, his reasonable thoughts, and his steadfast values. My dear, thank you so much for being with me, and believing in me, despite a number of contraindications. My only son, **Yury Guller (the Junior)**, thank you for being there on the Earth with us, thank you for your ironic smiles, your genius ideas and your crazy ideas as well, for your early birdies and for your lifelong *lemon*. My heart is full of love to my beloved mother **Larisa Grivans** and to the soul of my father **Eugen Grivans**. I feel your selfless love every second of my life. My father and mother-in-law, **Larisa and Yury Guller**, I love you so much... Thank you for your sincere everyday questions: how am I. All my dear **family members**, thank you a lot for supporting me through the years.

List of publications for the period of PhD candidature (2014-2017)

* - publications included into this thesis; # - other publications closely related to the thesis

Papers

1. ***Guller, A.**, A. Generalova, E. Petersen, A. Nechaev, I. Trusova, N. Landyshev, A. Nadort, E. Grebenik, S. Deyev, A. Shekhter and A. Zvyagin (2015). Cytotoxicity and non-specific cellular uptake of bare and surface-modified upconversion nanoparticles in human skin cells. *Nano Research* 8(5): 1546-1562. (IF (2015) – 8.893; 26 citations). Included into the Chapter 4.
2. *Generalova, A., I. Kochneva, E. Khaydukov, V. Semchishen, **A. Guller**, A. Nechaev, A. Shekhter, V. Zubov, A. Zvyagin and S. Deyev (2015). Submicron polyacrolein particles in situ embedded with upconversion nanoparticles for bioassay. *Nanoscale* 7(5): 1709-1717. (IF (2015) – 7.760; 18 citations). Included into the Chapter 5.
3. ***Guller, A.**, I. Kushnerus, Z. Khabir, A. Garcia-Bennett, A. Nadort, L. Liang, E. Goldys and A. Zvyagin (2017). Triple negative breast cancer metastasis to the liver: a tissue engineering model shows the invasion patterns and predicts the effects of free and nanoformulated drugs. *Biomaterials* (to be submitted). Included into the Chapter 7.
4. *Khabir, Z., **A. Guller**, V. Rozova, L. Liang, X. Xu, E. Goldys, H. Hu and A. V. Zvyagin (2016). Skin-nanoparticles interactions: the model study with use of upconversion nanophosphors. To be submitted. A part of this paper included into Addendum to the Chapter 4.

Conference full papers

5. ***Guller, A.**, I. Trusova, E. Petersen, A. Shekhter, A. Kurkov, Y. Qian and A. Zvyagin (2015). Acellular organ scaffolds for tumor tissue engineering. *SPIE Micro+Nano Materials, Devices, and Systems* 9668: 96684G-96684G-96689. (1 citation). Included into the Chapter 6.
6. #**Guller, A.**, A. Nadort, A. Generalova, I. Kornienko, E. Petersen, Q. Yi, A. Shekhter, E. Goldys and A. Zvyagin (2016). Onion-like surface design of upconverting nanophosphors modified with polyethylenimine: shielding toxicity versus keeping brightness? *SPIE Biophotonics Australasia 2016* 10013: 100132Q-100132Q-100135.
7. #Nadort, A., L. Liang, E. Grebenik, **A. Guller**, Y. Lu, Y. Qian, E. Goldys and A. Zvyagin (2015). Systematic assessment of blood circulation time of functionalized upconversion nanoparticles in the chick embryo. *SPIE Micro+ Nano Materials, Devices, and Applications. Sydney, New South Wales, Australia, International Society for Optics and Photonics*. 9668: 96683Y-96683Y-96687. (1 citation).

Conference talks and poster presentations

8. **#Guller, A. E.**, E. V. Petersen, I. A. Trusova, A. B. Shekhter, Q. Yi and A. V. Zvyagin (2015). The seeds and soils: our first results in tumor tissue engineering. *5th Annual Macquarie Biofocus Research Conference, Sydney, Australia. Oral.*
9. **#Guller, A.**, A. Generalova, A. Nadort, E. Grebenik, E. Khaydukov, E. Petersen, I. Trusova, L. Liang, Y. Qian, E. Goldys and A. Zvyagin (2015). Strategies of surface modification of upconversion nanoparticles: towards safe and meaningful applications in vivo. *International Nanomedicine Conference. Sydney. Oral.*
10. **#Guller, A.**, I. Kuschnerus, Z. Khabir, A. Nadort, L. Liang, A. Generalova, E. Petersen, A. Shekhter, E. Goldys, Y. Qian and A. Zvyagin (2016). Putting nanomaterials into the tissue and body context. *HDR Research Showcase: Research by Degrees, Department of Physics and Astronomy, Faculty of Science and Engineering, Macquarie University. Poster.*
11. **#Guller, A.**, A. Nadort, I. Kuschnerus, Z. Khabir, L. Liang, A. Shekhter, E. Goldys and A. Zvyagin (2016). Engineered normal and diseased tissues as ethical, sustainable and reliable alternative models for experimental medicine and nanotechnology research. *CNBP retreat conference-2016, Victor Harbour, South Australia. Poster.*
12. **#Kuschnerus, I.**, A. Nadort, Y. Lu, A. Guller and A. V. Zvyagin (2016). Sensitivity Characterization of an Epifluorescent Microscope for Tracking of Photoluminescent Nanoparticles in Chick Embryo Tumour Models. *5th Student Conference on Medical Engineering Science and in 1st Conference on Medical Informatics. T. Buzug and H. Handels. Lubec, Germany: 27-30. Poster.*

Patent application

13. **#Guller, A.**, A. Zvyagin, A. Shekhter and E. Goldys (2016). Poultry-derived organ specific tissue engineering scaffolds and constructs for regenerative medicine and research applications. *Patent application IES104066. Australia.*

Other important publications

14. **#Guller, A. E.**, P. N. Grebenyuk, A. B. Shekhter, A. V. Zvyagin and S. M. Deyev (2016). Bioreactors in tumor tissue engineering. *Acta Naturae* 8(3 (30)): 44-58. (*IF* (2015/2016) – 1.77).
15. **#Shekhter, A. B.**, T. G. Rudenko, L. P. Istranov, **A. E. Guller**, R. R. Borodulin and A. F. Vanin (2015). Dinitrosyl iron complexes with glutathione incorporated into a collagen matrix as a base for the design of drugs accelerating skin wound healing. *Eur J Pharm Sci* 78: 8-18. (*IF* (2015) – 3.773; 2 citations).
16. **#Rudenko, T. G.**, A. B. Shekhter, **A. E. Guller**, N. A. Aksenova, N. N. Glagolev, A. V. Ivanov, R. K. Aboyants, S. L. Kotova and A. B. Solovieva (2014). Specific features of early stage of the wound healing process occurring against the background of photodynamic therapy using

- fotoditazin photosensitizer-amphiphilic polymer complexes. *Photochem Photobiol* 90(6): 1413-1422. (IF (2015) – 2.008; 8 citations).
17. [#]Kost, O. A., O. V. Beznos, N. G. Davydova, D. S. Manickam, Nikolskaya, I. I., **A. E. Guller**, P. V. Binevski, N. B. Chesnokova, A. B. Shekhter, N. L. Klyachko and A. V. Kabanov (2015). Superoxide Dismutase 1 Nanozyme for Treatment of Eye Inflammation. *Oxid Med Cell Longev* 2015: 5194239. (IF (2015) – 4.492).
 18. [#]Shekhter, A. B., **A. E. Guller**, L. P. Istranov, E. V. Istranova, D. V. Butnaru, A. Z. Vinarov, O. L. Zakharkina, A. V. Kurkov, D. F. Kantimerov, E. N. Antonov, L. V. Marisov and P. V. Glybochko (2015). [Morphology of collagen matrices for tissue engineering (biocompatibility, biodegradation, tissue response)]. *Arkh Patol* 77(6): 29-38.
 19. Vasilets, V. N., A. B. Shekhter, **A. E. Guller** and A. V. Pekshev (2015). Air plasma-generated nitric oxide in treatment of skin scars and articular musculoskeletal disorders: Preliminary review of observations. *Clinical Plasma Medicine* 3(1): 32-39. (IF/SNIP (2015) – 2.423; 4 citations; > 400 reads on ResearchGate).
 20. Kotova, S. L., P. S. Timashev, **A. E. Guller**, A. B. Shekhter, P. I. Misurkin, V. N. Bagratashvili and A. B. Solovieva (2015). Collagen structure deterioration in the skin of patients with pelvic organ prolapse determined by atomic force microscopy. *Microsc Microanal* 21(2): 324-333. (IF (2015) – 1.73; 2 citations).
 21. **Guller, A. E.** and A. B. Shekhter (2015). [Effect of local treatment methods of partial-thickness and deep burns on the structure of postburns skin scars in children]. Chapter 6 /In the monography: [The system of treatment of burn wounds in their own liquid medium]. E. A. Voynovskiy, V. A. Menzul and T. G. Rudenko. Moscow, Russia, Na boyevom postu: 225-246.

Abstract

Nanotechnology is recognized as a powerful tool for investigation and manipulation of a wide range of biological objects and processes in the life sciences and medicine. In particular, nanoscale structures of dual therapeutic and diagnosis modalities are scrutinised in an emerging discipline of nanotheranostics. Nanoparticles, carrying a payload of drugs or coupled with targeting biomolecules and at the same time detectable in living tissues, portray a typical nanotheranostics agent (NTA), which holds promise for advanced medical applications, such as combined visualization of the nanoparticles' transport or biodistribution with controllable drug delivery, or intrasurgical imaging with local treatment of the revealed pathological foci.

The development path of nanotheranostics stems from the existing knowledge base of functional nanomaterial interactions with cells through to their relationship with biological systems at the level of tissues, organs and a whole body, leading to translational clinical research. *In vitro* two-dimensional (2D) cell cultures give overly simplistic biological context, oftentimes providing apocryphal extrapolations of the impact of functional nanocomplexes to the more complex biological systems. On the other hand, laboratory animals represent cumbersome and expensive models for NTA testing. Extension from the existing *in vitro* 2D cell cultures towards the more realistic biomimetic three-dimensional (3D) engineered tissues as testing systems for nanotheranostic particles, while avoiding the limitations of the laboratory animal models, represents the main motivation of this PhD project.

This thesis addresses the development and validation of the novel 3D biomimetic models of living equivalents of human skin epidermis and metastatic breast cancer by using tissue engineering methodology. The feasibility of the developed tissue engineering constructs (TECs) as testbeds for evaluation of transport, cytotoxic and therapeutic effects of nanotheranostics particles was also investigated. Both normal and tumor TEC models were created by using in-house prepared acellular tissue engineering scaffolds, representing substitutes of organ-specific extracellular matrices of skin derma and liver, seeded with linear keratinocytes (HaCaT) and triple negative breast carcinoma cells (MDA-MB-231), respectively. The biological effects and in-tissue behaviour of two types of nanotheranostics agents, upconversion nanoparticles (UCNPs) and mesoporous silica nanoparticles loaded with a fluorescent anti-cancer chemotherapeutic drug doxorubicin, were evaluated in these models.

In a team of my colleagues, I carried out a systematic study of UCNPs, where these nanoparticles were synthesised and surface-modified with the most representative types of moieties and polymers. Comparative study of these surface-modified UCNPs in terms of their safety and biocompatibility were performed using *in vitro* 2D cultures of HaCaT keratinocytes and primary human skin fibroblasts. The results show the significant influence of the cell type, surface coating, concentration and exposure time on the overall toxic effects of UCNPs in 2D cell cultures, while predominantly acceptable levels of the

ABSTRACT

cell tolerance to the tested nanomaterials were demonstrated in the tissue-engineered 3D counterpart model of multilayered epithelium.

I analysed the validity and feasibility of TECs for modelling of early breast carcinoma metastases to secondary organs aiming for development a new testbed for experimental oncology and nanotheranostics. In particular, the specific patterns of cellular kinetics and histological changes associated with the metastatic colonisation of liver acellular scaffolds by aggressive linear breast cancer cells were observed. The rapid proliferation of cells on the scaffold surface at the initial stage of the cell growth, followed by an invasive stage of in-depth cell penetration prefaced by the cell-induced matrix remodelling was noted. In order to validate the model in terms of the ability to show the cancer-specific behaviour in vivo, breast cancer-liver TECs were grafted on chorioallantoic membranes of chick embryos and the significantly enhanced the angiogenic potential in comparison with that of cellular suspensions and acellular matrices, as controls, was demonstrated. Finally, the cytotoxic effects of free doxorubicin and mesoporous silica nanoparticles loaded with doxorubicin were assayed using MDA-MB-231 cells' monolayer culture and the metastatic breast cancer TECs. The TECs appeared to support the greater resilience of cells to doxorubicin, despite its comparable cellular internalisation in both 3D and 2D culture models. Drug-loaded mesoporous silica nanoparticles were predicted to have an improved therapeutic efficacy, as benchmarked against that of free drugs in 3D models.

Thesis structure

The thesis contains eight chapters. The first chapter introduces the main topics and motivation of this study, followed by the thesis outline. Chapters 2 and 3 provide critical reviews of current state of relevant research, including nanotheranostic materials and their biological operational environment. Applications of 3D tissue cultures and tissue engineering models for biomedical and nanotheranostic research are also included. Chapters 4 – 7 report on the results of the project. Summary and future scope are given in Chapter 8.

The results of this work were reported in four peer-reviewed papers and several abstract-refereed conference proceedings.

Contents

Table of Contents

Dedication	V
Acknowledgement	VII
List of publications for the period of PhD candidature (2014-2017)	XI
Papers.....	XI
Conference full papers	XI
Conference talks and poster presentations.....	XII
Patent application	XII
Other important publications	XII
Abstract	XV
Thesis structure.....	XVI
Contents	XVII
Chapter 1. General Introduction and Thesis Outline	1
General Introduction.....	1
Motivation of the Study and the Thesis Outline	3
Chapter 2. Nanomaterials for theranostics.....	5
2.1. Nanomaterials for theranostics: the concept overview of the field	5
2.2. Photoluminescent nanomaterials	9
2.2.1. Upconverting nanoparticles as nanotheranostic agents	11
2.3. Mesoporous silica nanoparticles for nanotheranostics	40
2.3.1. Definitions, synthesis and post-synthetic modifications of mesoporous silica nanoparticles	40
2.3.2. Mesoporous silica nanoparticles as theranostic agents	44
2.4. Conclusion	47
Chapter 3. Three-dimensional in vitro models for nanotheranostics research.....	49
3.1. Biological operational environment of nanotheranostics agents.....	49
3.1.1. Putting nanomaterials into the real tissue and body context: the general scale of the landscape	49
3.1.2. Interaction of nanoparticles with cells.....	51
3.1.3. Beyond the cell: biological barriers of the nanoparticles delivery to the tissues and organs.....	58
3.2. Tissue engineering models of healthy and diseased tissues in nanotechnology research.....	75
3.2.1. Fundamentals of 3D cell culture in vitro and tissue engineering	75
3.2.2. 3D and tissue engineering models of skin in nanotechnology research.....	85

3.2.3. 3D and tissue engineering models of malignant tumors in nanotechnology research.....	90
3.3. Conclusion	96
Chapter 4. Cytotoxicity and non-specific cellular uptake of bare and surface-modified upconversion nanoparticles in human skin cells.....	97
4.1. Introduction	97
4.2. The author's contribution to the paper I.....	98
4.3. Author's contribution to the addendum paper I a	98
4.4. Full paper I "Cytotoxicity and non-specific cellular uptake of bare and surface-modified upconversion nanoparticles in human skin cells"	100
4.4.1. Electronic Supplementary Material.....	124
4.5. Addendum "Cytotoxicity and uptake of upconversion nanophosphors in 3D in vitro model of reconstructed human epidermis"	126
Chapter 5. Submicron polyacrolein particles in situ embedded with upconversion nanoparticles for bioassay	135
5.1. Introduction	135
5.2. The author's contribution to the paper II.....	136
5.3. Full paper II "Submicron polyacrolein particles in situ embedded with upconversion nanoparticles for bioassay"	137
5.4. Supplementary Electronic Information	
Chapter 6. Acellular organ scaffolds for tumor tissue engineering.....	159
6.1. Introduction	159
6.2. The author's contribution to the paper III.....	160
6.3. Full paper III "Acellular organ scaffolds for tumor tissue engineering"	161
Chapter 7. Triple negative breast cancer metastasis to the liver: a tissue engineering model shows the invasion patterns and predicts the effects of free and nanoformulated drugs	175
7.1. Introduction	175
7.2. The author's contribution to the paper IV	176
7.3. Full paper IV "Triple negative breast cancer metastasis to the liver: a tissue engineering model shows the invasion patterns and predicts the effects of free and nanoformulated drugs"	177
7.4. Supplementary information (SI) for the paper IV.....	211
Chapter 8. Conclusions and final remarks	233
8.1. Motivation	233
8.2. Summary and relevance of the study.....	234
8.3. Future perspectives	237
References	i
List of abbreviations	xxiv
Animal ethics approvals.....	xxix

General Introduction and Thesis Outline

General Introduction

Although no generally accepted definition of the nanomaterials exists [1], it is suggested that the engineered particular structures which have at least one dimension of size in the range between 1 to 100 nm [2] are in this category. It includes the structures of the various spatial organization from *zero-dimensional* single nanocrystals and different nanoparticles to one dimensional nanorods and nanowhiskes, following by *two-dimensional (2D)* nanofilms and *three-dimensional (3D)* dendrimers, fullerenes, liposomes, mesoporous particles, nanotubes, nanoclusters etc. [3]. The chemical composition of nanoscale materials broadly varies between single inorganic nanocrystals to the complex structures of organic nature or combinations of organic and inorganic components. However, it is worth to be emphasized that due to the size and very high surface-to-volume ratio the physical, chemical and biological properties of nanostructures are dramatically different from the bulk materials of the same composition [4]. These features are widely employed by nanotechnology as a multidisciplinary field operating with the nanomaterials in terms of their synthesis, fabrication, modification, research and various practical applications. Currently, nanotechnology is the most tightly connected to material science, chemistry, physics, engineering and biomedical research, while the interactions with other spheres are less systematic [5]. However, the emerging discipline of nanomedicine, implying the use of nanomaterials for treatment and diagnosis of various diseases, holds a great promise to improve the quality of life and survival rate for many patients who previously did not have a chance to get any efficient help.

The advantages of the nanostructures, most attractive and appreciated for biological and medical applications, in comparison to more usual molecular compounds, stem from the above mentioned special size and extraordinary high surface area combined with the endless prospects of versatile employment of this surface for various functional tasks. Importantly, these qualities result in the ability of the nanoscale materials to passively accumulate in or to be intentionally targeted to the desired cells and tissues, while delivering the drugs and genes, or serving as contrasting agents for diagnostic purposes. The particular attention now focuses on a novel class of nanomaterials, which include the nanoparticles with dual functionalities, such as therapeutic ability (e.g. drug delivery) and diagnosis potential (e.g. visualization of pathological structures), which are gradually becoming to be recognized as

nanotheranostic agents (NTAs) [6]. Currently, this term pools the radioactive, magnetic, echogenic and luminescent nanomaterials, which can be biofunctionalized as nanodrugs, pro-drugs or drug vehicles and used for image-guided surgery, remote-triggered therapy and precise monitoring of the treatment process *in situ* [7, 8]. These amazing combination of properties of NTAs makes the nanotheranostics one of the most advanced and promising approaches for such challenging applications as treatment of various types of cancer, cardiovascular diseases and AIDS [9], personalized [8] and regenerative [3] medicine.

The main obstacle for wide transfer of nanotheranostic approaches to practical medicine lies in the severe deficiency of reliable preclinical model systems, which could be used to evaluate how safe and how efficient the NTA are in a real living body context [10, 11]. Indeed, the conventional methods to check the biocompatibility of nanomaterials with the use of laboratory animals or 2D *in vitro* cell cultures appear to be neither ethical, not economically reasonable [10] as well as lacking biological relevance [11], respectively, due to the specific conditions and limitations of nanotechnology research.

In fact, testing of the effect of NTA in animals represents definitely a non-optimal choice because of cumbersome experimental design, requiring extensive use of huge numbers of laboratory mammals for fine tuning of the properties of the particles until the anticipated results could be obtained, as even a small change of the material characteristics can induce strikingly different responses in living matter. Other limitations of use of animal models in nanomedical studies, which should be taken into account, are associated with differences between human and animal physiology, metabolic rates and the pathways of processing of xenogeneic materials.

The alternative approach, based on the evaluation of the nanomedicines on cell cultures *in vitro*, is currently the most widely used option. The traditional type of these models implies growing a monolayer of cells on special plastic dishes with periodical changes of liquid culture medium of a defined composition. Nanoparticles are normally added to the culture media, and the effects of the exposure is examined by registering of the biological responses of the cells. However, these plain, 2D models oversimplify the complex 3D biological environment [12] where the nanomaterials should operate. The main shortages of 2D culture include limited cell-cell contacts, sharply flattened morphology of the cells with overexposure of one side of the plasmatic membrane to the culture media and replacement of cell-extracellular matrix interactions by severely corrupted relationship between the cells and the extremely stiff plastic substrate [13]. In addition to the multiple behavioural and metabolic changes resulted from the abnormal mechanical input [11, 14], the equilibrated environment of 2D cell culture with the absence of gradients of soluble factors contributes to progressive loss of phenotypic heterogeneity [15] and selection of fast proliferating and “plastic-adapted” [16] cells.

A nanoparticle in a tissue intervenes with all the tissue components, including cells, extracellular matrix and the interstitial fluids [17]. Considering this, the conditions of testing of the NTAs in

conventional monolayer cell culture remain very far from the reality, and the results of the examination of their toxicity, therapeutic or diagnostic potentials, with a great probability, may be misleading and irrelevant. Following that, a middle way models, benefiting by avoiding testing on animals and utilizing the feasibility of *in vitro* cell culture, which could represent the realistic tissues complexity are in strong demand for efficient development of nanotheranostics [10, 11, 17].

Tissue engineering is well-known as a methodology of recreation of the tissues outside the human body for replacement of irreversibly damaged structures. The basic methodology of tissue engineering relies on combining chosen cells with appropriate 3D substrates, which are playing a role of extracellular matrix and are named as scaffolds, or matrices, in order to create tissue engineering constructs (TECs), as functional fragments of a tissue or even the whole organs. Very recently this approach has been applied for the first time and smoothly become appreciated for construction of healthy and diseased tissues as pharmacological testbeds [18-22]. However, despite the obvious research and practical potential, little emphasis has been placed to date on use of 3D cell cultures created by the methodology of tissue engineering for evaluation of the behaviour and effects of NTAs.

Motivation of the Study and the Thesis Outline

The extension of the existing methodology of studies of the biologically-relevant properties, behaviours and the effects of NTAs, which relies on 2D *in vitro* cell cultures, to the more realistic biomimetic 3D engineered tissues, represents the main motivation of this PhD project. As a first step in accomplishing this goal, in this work, in collaboration with my colleagues, I have demonstrated the significant changes of the effects induced by two types of NTAs, the photoluminescent upconversion nanoparticles (UCNPs) and the mesoporous silica nanoparticles loaded with a fluorescent chemotherapeutic anti-cancer drug doxorubicin, in monolayer cell cultures and 3D engineered models of normal and tumor tissues.

The thesis consists of 8 chapters. Following the current introductory part, the Chapter 2 overviews of the nanotheranostic materials with a special focus on UCNPs and mesoporous silica nanoparticles. Chapter 3 presents a review of biological operation environment of NTAs, as well as application of 3D cell culture and tissue engineering methodology for nanomedical research. In particular, it includes the comparative analysis of 2D and 3D cell and tissue culture conditions and a panorama of the existing *in vitro* 3D systems. Finally, this chapter surveys the existing tissue engineered models of human skin and cancer tumors and the examples of their application for testing of various NTAs. Chapter 4 (paper I, published in *Nano Research* and the Addendum) describes the results obtained in this dissertation study on the effects of bare and surface-modified UCNPs in 2D *in vitro* cultures of human skin cells and in 3D reconstructed viable epidermis. Chapter 5 contains the full paper II, published in *NanoScale* journal and focused on the development and application of a new method of surface modification of UCNPs, the embedding into polymer beads *in situ*. Chapter 6 (paper III, published in *SPIE Proceedings*)

describes the development of the original technique of decellularization of whole organs for creation of acellular organ-specific tissue engineering scaffolds. Chapter 7 (paper IV and comprehensive Supplementary Information, prepared for submission to the *Biomaterials* journal) shows our results in establishment and validation of tissue engineering model of breast cancer metastasis to the liver. In particular, it presents the development of the model as well as the studies of the dynamics and histological patterns of cellular colonization of the organ-specific scaffolds, the angiogenic potential of the engineered tumor grafted in vivo in chick embryos. It also shows the outcomes of the experiments on testing of the cellular uptake and cytostatic action of free doxorubicin (Dox) and mesoporous silica nanoparticles loaded with Dox in the engineered metastatic breast cancer model versus the conventional 2D culture *in vitro*. The final summary and future scope are forming the chapter eight. The list of abbreviations, the ethical approvals can be found in the Appendices.

Nanomaterials for theranostics

In this chapter, the concept of nanotheranostics and the theranostics nanoscale materials is overviewed with a special focus on upconversion nanoparticles (UCNPs) and mesoporous silica nanoparticles (MSNPs) loaded with drugs and contrasting compounds. Synthesis, structure, physicochemical and biological properties of these types of NTA are critically analyzed with regard to their actual and potential biomedical use.

2.1. Nanomaterials for theranostics: the concept overview of the field

The merging of therapeutic and diagnostic capabilities in a single nanoscale particle represents the basic principle of nanotheranostics [8] (Figure 2.1). The treatment potential of an NTA is realized by direct delivery of drug (or gene, peptide, protein, nucleic acid, etc.) payload by the nanoparticle. It also can occur through locally or remotely induced photodynamic effects including hyperthermia and generation of reactive oxygen species, magnetically induced hyperthermia, or therapy may be performed by radioactive emission of the particle [3, 23].

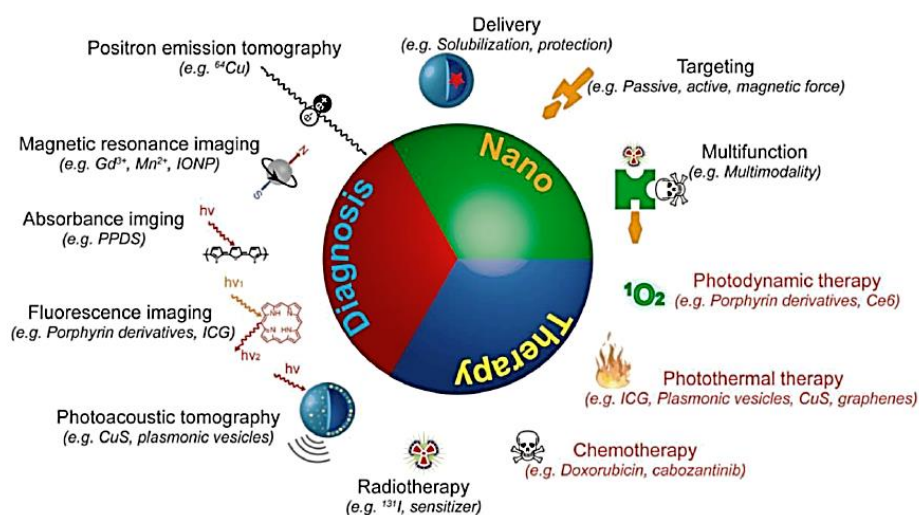


Figure 2.1. Schematic illustration of the concept of nanotheranostics: the combination of nano-size, diagnostic (imaging) and therapeutic (treatment) functions in a single particle. The NTAs can be additionally modified to reach selected molecular targets (targeting). They also can realized the effects triggered by the factors of local environment (pH, heat etc.) or remotely, by physical factors (shown by red font). Finally, some NTAs can perform as multimodal agents, combining several imaging, therapeutic, targeting or triggering keys. Reproduced from [24].

Importantly, even the particles with very inert nature can be transformed into drug nanocarriers and targeted delivery systems [25, 26], thus, the capability to perform as a direct or adapted therapeutic agent can be imparted for all the major classes of the materials used in nanotheranostics (Figure 2.2) by a wide range of methods available for binding of the particles and their cargo [26, 27]. NTAs also can have capabilities of triggered activation of the drug or targeting to specific molecular markers [28] in order to improve efficacy and selectivity of the treatment.

The second principal requirement that any NTAs should met, is the ability to provide imaging contrast. It is worth to note that there is an emerging paradigm shift in understanding of nanotheranostics from very sophisticated but now relatively common applications of multifunctional nanomaterials to the even more complex and demanding field of technology, where it is required that the imaging have to be readily accomplished immediately during the therapeutic action of the particle in addition to the more traditional possibility of visualization of the probe before or after treatment session [29]. Then, these are the imaging functionalities what become the limitation factor for acceptance of the certain nanocompositions as real NTAs.

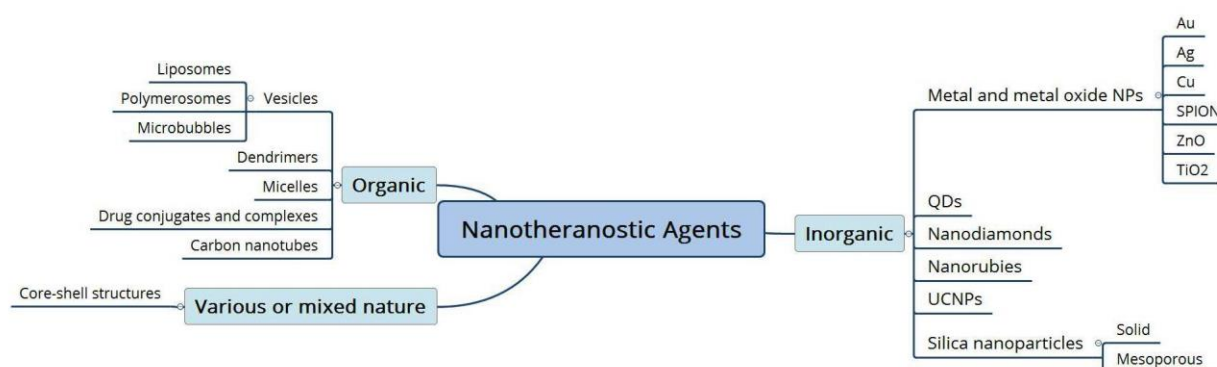


Figure 2.2. Simplified classification of NTAs based on their chemical nature and structural design, accordingly to [28] with minor changes. Only the most widely used nanomaterials are shown. Abbreviations: Au – gold, Ag – silver, Cu – copper nanoparticles; SPION - superparamagnetic iron oxide nanoparticles, ZnO – zinc oxide, TiO₂ – titanium oxide nanoparticles; UCNPs – upconversion nanoparticles.

The imaging modalities most widely used in nanotheranostics differ by their basic physical principles and include optical imaging (as detection and recording of photons emitted by probe), computed tomography, or CT (the selective attenuation of X-rays by different components of tissues and organs), magnetic resonance imaging, or MRI (the parameters of relaxation of water molecules after applied strong magnetic field), ultrasound, or US (the detection of back reflected high frequency sound wave travelling through tissues) and radionuclide-based tomography like positron emission and single photon emission tomography, or PET and SPECT, respectively (detection of γ -emission from the selectively distributed radiotracers introduced into the tissues) [3, 8, 23, 28] (Figure 2.3).

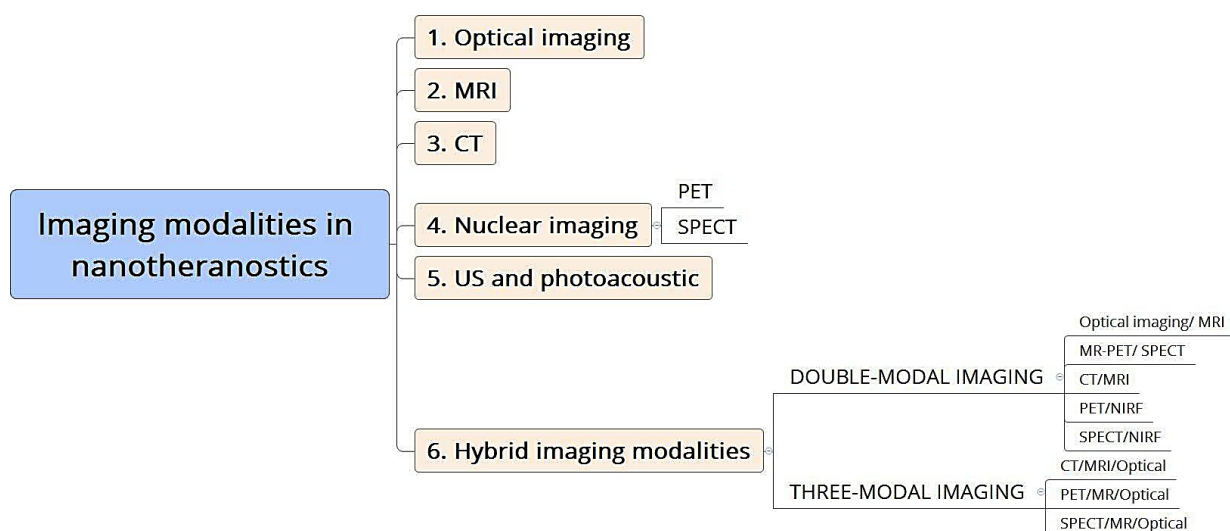


Figure 2.3. Imaging modalities currently used in nanotheranostics, accordingly to the to the recently published comprehensive reviews [3, 8].

Every imaging modality has own advantages and disadvantages, as well as limitations of sensitivity and spatial resolution, which should be taken into account for development of optimal nanotheranostic materials [30]. For example, optical imaging ensures the best molecular sensitivity, in comparison with CT, MRT, nuclear imaging and US, while suffers from the lowest spatial resolution and limited tissue penetration [28].

The ability of nanomaterials to provide and enhance the signal-noise ratio for each imaging approach depend on their chemical and physical properties. In particular, it is expected that the NTAs for optical imaging should be able to absorb light and emit luminescence, while the MRI agents must have paramagnetic properties and the particles for CT should contain electron dense elements. SPECT and PET NTAs must have γ -emitters in their structure and ultrasound contrast materials are usually comprise gas bubbles. The contrasting capability may be inherent to the particles following to their structure and composition, like for example, it happens to superparamagnetic iron oxide nanoparticles (SPION) used for MRI [31, 32]. In addition, there are complex nanoplatforms that allow to combine the materials with proper imaging qualities of different modalities such as, for instance, hybrid magnetic-luminescence particles [33]. Alternatively, the nanostructures, which basically do not have intrinsic imaging contrasting properties, like polymer beads and the majority of organic vesicles, may be also modified by additive engineering with other types of nanoparticles or dyes to create various types of imaging agents, including the multimodal ones [34]. More detailed analysis of the imaging potential of various types of nanomaterials can be found in an excellent review paper [30] and summarized in the Table 2.1.

Table 2.1. Commonly used bioimaging methods and corresponding biomaterials. Adapted from [30] with changes.

Technique	Types of nanomaterials	Signal measured	Resolution	Depth	Sensitivity (moles of label detected)	Throughput
NIRF	QDs, dye-doped NPs, UCNPs, SWNTs and other carbon-based nanomaterials	Light, particularly in the near-infrared	1–3 mm	<1cm	10^{-12}	High
MRI	Iron oxide NPs, Gd(III)-doped NPs, NP-based CEST and hyperpolarized probes (e.g., ^{129}Xe)	Alterations in magnetic fields	50 μm	No limit	10^{-9} – 10^{-6}	Low
PET	NPs incorporating radioisotopes (e.g., ^{18}F , ^{11}C , ^{64}Cu , ^{124}I)	Positron from radionuclides	1–2 mm	No limit	10^{-15}	Low
SPECT	NPs incorporating radioisotopes (e.g., $^{99\text{m}}\text{Tc}$, ^{111}In)	γ -rays	1–2 mm	No limit	10^{-14}	Low
CT	Iodinated NPs, gold NPs, iron oxide-doped nanomaterials	X-rays	50 μm	No limit	10^{-6}	Low
US	Microbubbles, nanoemulsions, silica NPs, polystyrene NPs	Sound	50 μm	Several cm	10^{-8}	High
PAI	Gold nanoshells, gold nanocages, gold nanorods, gold NPs, SWNTs, dye-doped NPs	Sound	50 μm	<5 cm	10^{-12}	High

*Abbreviations: NIRF - near-infrared fluorescence; NPs – nanoparticles; QDs – quantum dots; UCNPs – upconversion nanoparticles; SWNTs - single-walled carbon nanotubes; MRI – magnetic resonance imaging; CEST – chemical exchange saturation transfer; PET - positron emission tomography; SPECT - single photon emission tomography; CT – computer tomography; US – ultrasound imaging; PAI – photoacoustic imaging.

Significant expansion of functional spectra of NTAs can be achieved by employment of a modular principle. Different types of nanomaterials, including metal and metal oxide nanoparticles, fluorescent nanoprobe, silica and polymer compositions, can be combined together to make nanoparticles of a core-shell structure [35-37], dendrimer entrapped particles [38, 39], micelles [40], liposomes [41] etc. As a result, not only optimized imaging [42] and therapeutic modalities may be contributed to the particles, but improved colloidal stability and better biocompatibility may be obtained [43]. Alongside to the putting together various nanomaterials, the fluorescent dyes like conventional fluorescein isothiocyanate (FITC) and its derivatives, the dyes of rhodamine's group, or the substances with the emission peaks shifted towards more preferable for bioimaging near infrared range like indocyanine green (ICG) and cyanines (usually Cy 3.5, 5.5 and 7), also may be included into the complex NTAs structures to enhance their imaging potential. Less often fluorescent proteins, like the most known of them green fluorescent protein (GFP), can be used for modification of NTAs as labelling markers.

The special biologically significant high-affinity ligand such as antibodies, mini-antibodies, peptides, folic acid, hyaluronic acid, carbohydrates, aptamers and oligonucleotides may be included into the NTAs in order to increase specificity of imaging and selectivity of their therapeutic action by binding to specific epitopes with successive inclusion into signalling and metabolic pathways and controlling the cellular fate [9, 44]. This strategy of targeting is based on immune and receptor-mediated interactions between the nanoparticles and cellular membranes and organelles and allow the nanoparticles to exert the desired effects at specific regions of tissues and cells.

Finally, it is reasonable to mention another important trend in nanotheranostics, the use of environment-sensitive and stimuli-responsive reactions to trigger therapeutic effects or to get the nanomaterials visualized at certain time of their exposure to the cells or tissues [45-47]. Various factors may play a role of triggers, from abnormal physicochemical conditions in pathological sites (e.g., pH, temperature, interstitial pressure) or external factors of various physical nature, including light, magnetic and electric fields, ultrasound or thermal effects [44].

2.2. Photoluminescent nanomaterials

Optical imaging, a methodology employing light to visualize structures and processes, plays one of the key roles in nanotheranostics, as, probably, one of the most affordable and versatile approaches [28, 30]. The term "luminescence" describes the phenomena of energy absorption followed by subsequent emission of light [48]. When this definition is narrowed to the absorption and emission of photons (i.e., light-light pairs), it is considered as "photoluminescence" (PL). The PL techniques require combined use of the excitation source, the PL agents (endogenous or exogenous fluorophores) and the detection systems, adapted to the characteristics of the studied fluorophores like spectroscopes, microscopes, tomographs and cameras with certain levels of sensitivity and speed of signal processing. Many naturally occurred compounds are the endogenous fluorophores, including the major components of extracellular

matrix like collagen and elastin and various species related to cellular metabolism such as folate, some vitamins, several amino acids and pigments, cytochromes and nicotinamide adenine dinucleotide (NAD(P)H) [49]. The incomplete list PL materials being used in nanotheranostics to date include semiconductor quantum dots (QDs) [50, 51], nanodiamonds [52, 53], nanorubies [54, 55], carbon nanotubes and other nanocarbons [56, 57], gold and other noble metal nanostructures [58-60], fluorophore-impregnated silica [61] and polymer [62] nanoparticles and upconversion nanophosphors [63]. These materials differ from each other by their photophysical and biological properties. For example, upconversion particles and nanorubies have three times order longer lifetimes of fluorescence, than organic dyes, QDs and nanodiamonds. The photostability, fluorescence intermittency ("photoblinking"), as well as toxic potentials and efficiency of conversion of excitation light into emission are also the parameters making great difference between various PL nanoprobes [64]. However, the main distinction between the mentioned fluorophores displays itself in the mechanism of PL.

There are two mechanisms of PL [65], as it is schematically illustrated on Figure 2.4. The most frequent case is luminescence with a Stokes shift, when the material absorbs the photons of higher energy than lower-energy emission (Fig. 2.4 (a)). The majority of PL fluorophores, like QDs, organic fluorescent molecules, nanodiamonds, nanorubies, gold and carbon nanoparticles exhibit these, conventional luminescence properties. In contrast, the second ladder-like mechanism known as anti-Stokes shift, or upconversion [66] (Fig. 2.4 (b)), is rather extraordinary. In particular, this transformation of near-infrared (NIR) excitation light ($\lambda \approx 980$ nm) into higher energy emission photons, which emerge as narrowband photoluminescence peaks in the visible and NIR spectral range ($\lambda \approx 450 - 850$ nm), takes place in a special class of PL nanomaterials, the upconversion nanoparticles (UCNPs) [66].

The properties of the two types of nanomaterials directly relevant to this thesis are considered in the subsections below. First, the UCNPs will be discussed as a nanoprobes with unique optical properties, which are especially valuable for nanotheranostics, as these particles, ensuring background-free bioimaging, also can be functionalized for therapeutic applications. Next, we will consider mesoporous silica nanoparticles, an excellent example of a highly biocompatible nanostructures, which do not provide an intrinsic optical contrast, but have an incredible versatility in terms of additive engineering and incorporation of contrasting and therapeutic components for creation of NTAs.

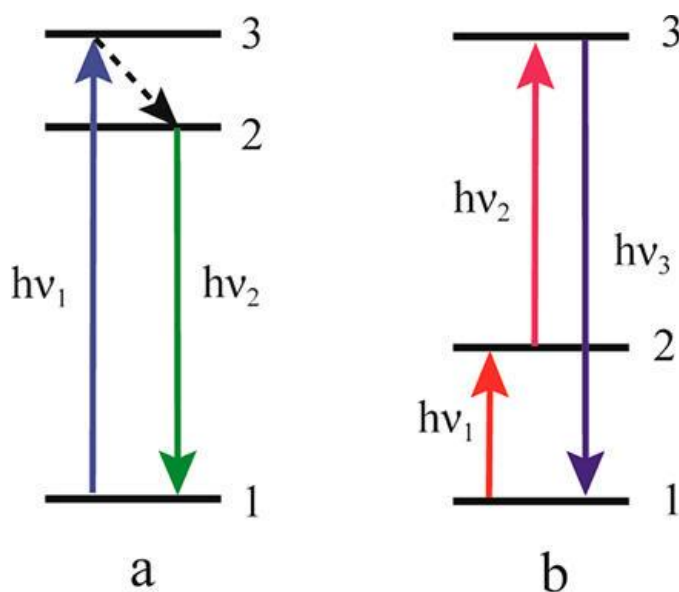


Figure 2.4. Schematic representation of the mechanisms of PL, a simplified energy diagram. (a) Conventional Stokes PL: A luminescent centre in the ground state (1) reaches the excited state (3) by direct absorption of energy from excitation photon of higher energy (blue arrow), and then returns to the ground state through the short-living intermittent excited state (2) and emission of a lower energy photon (green arrow). (b) Upconversion PL: A luminescent centre in the ground state (1) absorbs energy from either an excitation photon or a corresponding energy-transfer to get to the metastable excited state (2), which has relatively long lifetime. Next, another excitation photon or a corresponding energy transfer promotes the luminescent centre to the excited state (3). A radiative transition from this excited state 3 back to the ground state or some other lower-energy state, results in a higher-energy photon emission. Reproduced from [65].

2.2.1. Upconverting nanoparticles as nanotheranostic agents

2.2.1.1. UCNPs as bioimaging agent: the structure and photophysical properties

Upconverting nanoparticles, or nanophosphors (UCNPs), represent the particulate materials of nanoscale able to generate PL by the mechanism of upconversion [65]. There is a growing body of literature on the use of UCNPs in various research and industrial areas (for review, see [65, 67], and references therein) with a notable focus drift towards bioimaging and nanotheranostic UCNPs applications during last two decades [68-71].

Generally, by chemical structure, UCNPs combine an inorganic crystalline matrix (the host) with dopants such as trivalent lanthanide ions (Ln^{3+}), taken at low concentrations [66] (Figure 2.5 (a)). The qualities of the host can contribute a lot to the efficient upconversion PL. The matrices have to possess special asymmetric geometry the a crystal field and wide bandgaps to be transparent for excitation and emission light and effectively transfer the energy [67]. The most popular host materials include Y_2O_3 , $\text{Y}_2\text{O}_2\text{S}$, LaF_3 , NaLuF_4 , NaYbF_4 and NaGdF_4 , TiO_2 and TbF_3 [71, 72], while the dopants are the pairs of different Ln^{3+} , usually the Yb^{3+} , Er^{3+} or Tm^{3+} . Ions of Yb^{3+} play a role of a “sensitizers”, harvesting the photons of excitation light at 970-980 nm and non-radiatively transferring the absorbed energy to the “activator” ions of Er^{3+} or Tm^{3+} . In contrast to erbium and thulium, the ions of ytterbium have only two available energy levels, and absorb near-infrared (NIR) photons with a transition from the $^2\text{F}_{7/2}$ ground state to $^2\text{F}_{5/2}$ relatively long-living excited metastable level (see Figure 2.5 (f)), what makes ytterbium the best choice as a reliable sensitizer. Getting excited under continuous wave NIR irradiation, a pool of the simultaneously excited sensitizers forms throughout the nanocrystal, and the absorbed energy can be transferred to the nearest activators (Er^{3+} or Tm^{3+} ions) bringing them to the higher energy metastable

levels. Next, these activator ions of Er^{3+} or Tm^{3+} emit the photons of shorter wavelengths (upconversion) at several narrow-band PL peaks (see Figure 2.5 (b-e)).

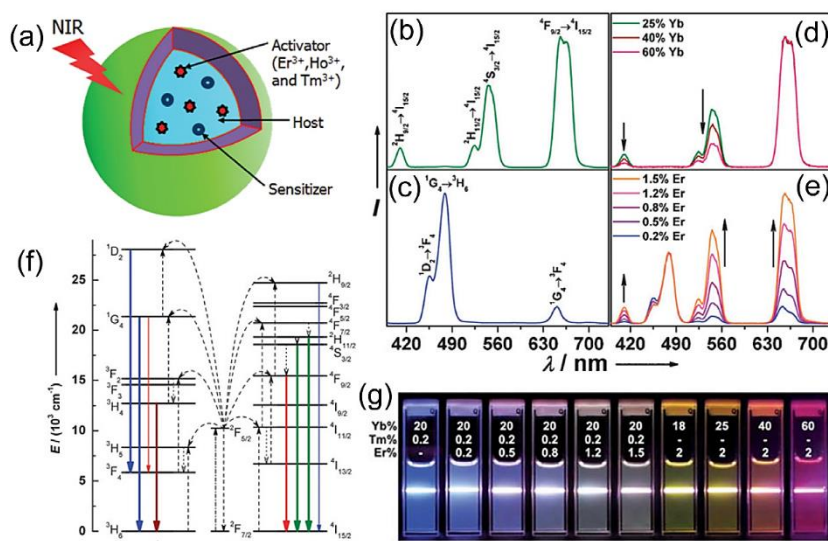


Figure 2.5. The main properties of lanthanide-doped UCNPs. (a) Schematic structure of a UCNP. (b –e) Tuning of room temperature emission spectra of cubic Ln^{3+} -doped UCNPs dispersed in ethanol (10 mM) by changing the combination and the molar ratios of the dopants: (b) Yb/Er, 18/2 mol%; (c) Yb/Tm, 20/0.2 mol%; (d) Yb/Er, 25–60/2 mol%; (e) Yb/Tm/Er, 20/0.2/0.2–1.5 mol%. (d) and (e) show the spectra normalized to Er^{3+} 660 nm and Tm^{3+} 480 nm emissions, respectively. (f) The detailed energy diagram of visible emissions of upconversion PL in Ln^{3+} -doped crystals excited by 980 nm diode laser light

depending on the dopant type. The dashed-dotted, dashed, dotted and full arrows are standing for photon excitation, energy transfer, multiphoton relaxation, and emission processes, respectively. (g) Multicolor emission of UCNPs with fine-tuned dopant ratios added to NaYF_4 nanocrystals host. Reproduced from [73].

An important feature of UCNPs is the tunability of their optical properties such as spectra and brightness. These characteristics may be corrected by three main strategies [67]. The first two ways include changing of the host itself in terms of crystal structure (mainly the crystal symmetry) [66, 74], as well as the size [75] and the shape [76], and the third approach is the modification of the composition and molar ratio of the dopant ions.

Size and shape of UCNPs may influence on the surface radiative and energy transfer processes, resulting, first of all, in changes of brightness and quantum yield (conversion efficiency) [67]. Very roughly, the bigger size is more preferable for obtaining brighter particles due to the higher probability of non-radiative energy loss because of the bigger surface-to-volume ratio in smaller crystals [75–78] and more crystal surface defects in smaller particles [79]. The shape of the nanocrystals also affects the conversion efficiency and brightness of UCNPs both through the contribution of surface-volume ratio and the crystal symmetry to the energy transfer and dissipation [80]. It is generally accepted, that hexagonal phase NaYF_4 ($\beta\text{-NaYF}_4$) is one of the best host matrices to support Ln^{3+} -dependent upconversion process [63, 67, 76, 81], while $\beta\text{-NaYF}_4\text{:Yb}^{3+},\text{Er}^{3+}$ and $\beta\text{-NaYF}_4\text{:Yb}^{3+},\text{Tm}^{3+}$ are currently applied among the most photophysically efficient formulas of UCNPs [82].

The adjustment of the composition and the molar ratio of the dopants can define the emission spectra of UCNPs [67, 71, 72] (see Figure 2.5, (b-e) and (g)), allowing multiplex contrasting techniques to be created [83]. For example, as it is visible from the Figure 2.5 (d), the increasing concentration of the sensitizer, Yb^{3+} , in UCNPs formula $\text{NaYF}_4\text{:Yb, Er, Tm}$ results in a notable growth of the NIR peak. Due to the differences in electronic shells structure between Er^{3+} and Tm^{3+} (see Figure 2.5 (f)), the choice of

the type of activator ion also defines the features of the spectral signature of UCNPs (Figure 2.6), where the increase of a blue peak, and a shift of the energy from green emission to a NIR peak are easily notable. As it is shown below, such a configuration of Tm^{3+} emission also provides some benefits for imaging in biological tissues. Another available strategy of spectral tuning of UCNPs implies the addition of the second activator type and fine adjustment of the emitters concentrations [84, 85] in order to obtain a clear multicolor signal, which can be used for contrasting or employed for light-activated applications and multiplex imaging of the NTA. For example, doping of NaYF_4 host with Ho^{3+} , Er^{3+} and Tm^{3+} as activators and Yb^{3+} as a sensitizer allows achievement of red, green or blue light upconversion PL [86].

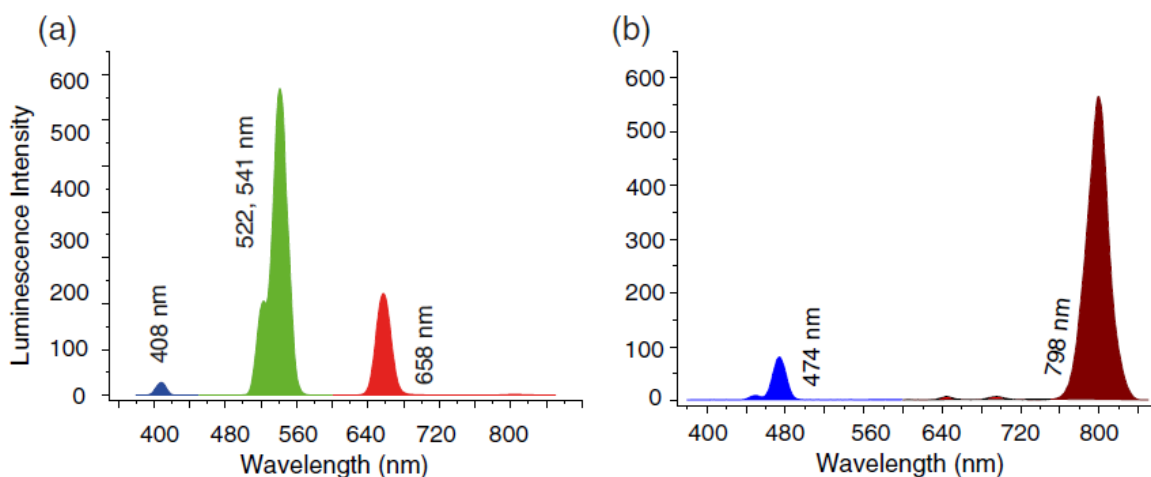


Figure 2.6. Plots of the PL spectra of NaYF_4 : Yb, Er and NaYF_4 :Yb, Tm UCNPs. Reproduced from [87].

NIR excitation and NIR emission peak of UCNPs occur in the “biotissue transparency window” (the wavelength range between 700-1000 nm) [88], providing a possibility of deeper excitation and detection distances in biological matter up to 0.5-1 cm [89], or even up to 2 cm with use of Yb/Tm codoped UCNPs [90, 91], as it is illustrated on Figure 2.7. Excepting the use of X-rays and nuclear imaging like PET and SPECT, these depths of tissues can be imaged only with the US-based techniques and optical methods, which are employing upconversion PL, as the conventional NIRF ensures maximum depth of few millimetres maximum. However, in comparison to US and PAI, upconversion PL bioimaging has much better spatial resolution [30]. The properties of the tissues, in turn, can have some effect on the available depth of imaging, depending on relative concentrations of the main optical absorbers (see Figure 2.7 (a)) [69] and the degree of scattering [92]. Furthermore, as the benefits of NIR excitation, photo-damage of biological samples can be minimized and improvement of signal-to-noise ratio, leading to background-free detection of emission light are achieved [77].

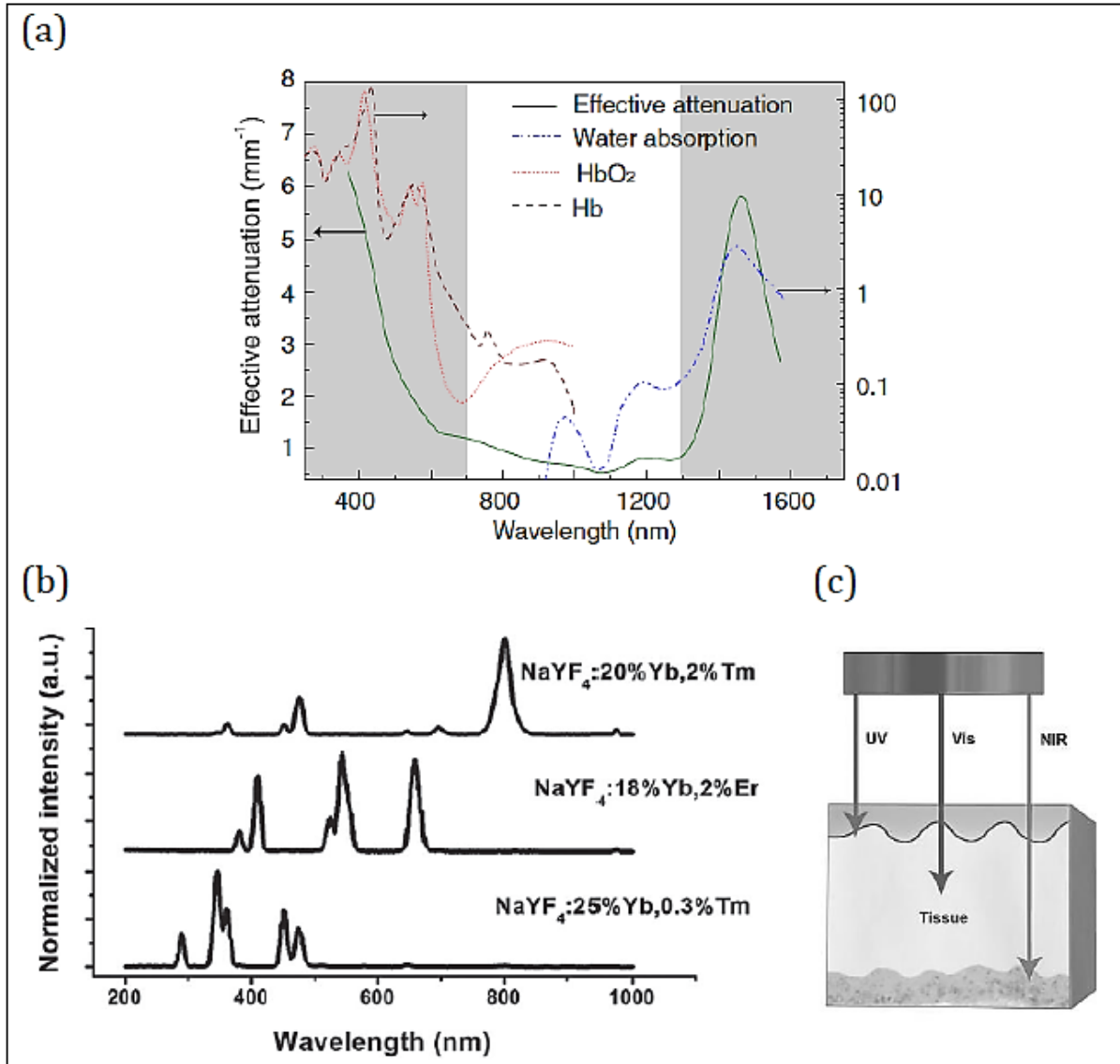


Figure 2.7. Illustration of the advantages of application of UCNP for bioimaging resulting from their excitation and emission spectra. (a) Optical attenuation spectrum mainly originates from absorption and scattering by water (H₂O, blue dashed-dotted line), oxygenated and reduced haemoglobin (HbO₂, red dotted line and Hb, brown dashed line) and results in effective attenuation spectrum of living biotissue (solid green line, calculated for the case of human skin). The white vertical sector on the scheme indicates the approximate range of biotissue NIR optical transparency window. Reproduced from [87]. (b) The emission spectrum of upconversion PL of NaYF₄ host doped with different amounts of Yb³⁺, Er³⁺ and Tm³⁺ and excited of under 980 nm. (c) Schematic representation of the efficiency of bioimaging in terms of the depth of a tissue with using different wavelength of light spanning from UV to NIR spectrum. (b, c) adapted from [93].

Additional privileges of UCNP as bioimaging agents against conventional fluorescent probes rely on non-blinking nature of their PL signal, as well as on absence of photobleaching [63] and the possibility of long-term [77], time-gated [94, 95] and multiplex lifetime-based detection [96] resulting from the long lifetime of photoluminescence of UCNP.

Another important advantage of UCNP is the possibility to use relatively low intensities of excitation light. Upconversion PL is a nonlinear optical process. However, in contrast to two-photon fluorescence and second harmonic generation, it does require only moderate excitation light intensity (1×10^3 W/cm² versus 1×10^6 W/cm², respectively) [63]. In addition, the upconversion PL process can be

excited by affordable continuous-wave light sources instead of femtosecond lasers used for multiphoton microscopy [68], which makes it convenient for wide imaging applications in nanotheranostics. The detectable upconversion process initiates at NIR excitation intensity just below 1 W/cm^2 , which is considered safe for use in live cells and tissues [88, 97].

Taken together, the described structure and the following functional properties of UCNPs define the most important advantages of this nanomaterials as an exceptional bioimaging contrast agents.

The first one can be summarized as the *background-free imaging* [87, 98]. In contrary to conventional organic fluorescent molecules, including tissue endogenic species, which are excited by ultraviolet (UV) or visible light and emitting within the same spectral range with some Stokes shift, the UCNPs absorb the NIR excitation irradiation, which does not induce autofluorescence of the intrinsic tissue fluorophores. This ensures the possibility to easily discern the signal from UCNPs in the living matter. Secondly, following the featured electronic configuration of lanthanide ions, the emission peaks of UCNPs are narrow and well distinguishable [99]. Third, the depth of imaging in tissues can be reliably increased up to 1 cm. Next, the color spectra of the particles as well as their long lifetime of PL can be tuned, providing a possibility for simultaneous detection and activation of several types of structures or molecular species (multiplexing) and time-gated detection. In addition, the PL emission of UCNPs is very stable, what is excepting the common problems of blinking and photobleaching associated with use of conventional fluorescent probes. Finally, the excitation of UCNPs is performed by continuous wave laser sources (as, for example, non-expensive diode lasers) at moderate intensity of irradiation [81]. This makes the biomedical applications of UCNP-based NTAs more safe and affordable.

At the same time, in order to be used in biological environments the additional modifications of as-synthesized UCNPs are needed. The most important approaches of adaptation of UCNPs for biomedical use are considered in the next subsection.

2.2.1.2 Adaptations of UCNPs required for biomedical applications

2.2.1.2.1. Synthesis of UCNPs and their surface passivation for optimization of optical response

As many other nanomaterials, UCNPs may be manufactured in a wide range of shapes and sizes [76, 100, 101] and have an extensive surface area available for further functionalization. In combination with their potential as contrast agents, which stems from the intrinsic properties of the UCNPs nanocrystals as described above, these characteristics make the upconverters particularly attractive for theranostic applications. The range of their possible use includes not only background-free high-contrast and stable visualization of cells and tissues [69, 89, 102-104] or even single-molecules [105], but can be extended to perform various special tasks such as drug delivery [106-109], photodynamic therapy [110-112], immunological and physicochemical sensing [68, 113, 114] etc.

However, the direct use of as-prepared UCNPs in biomedical applications is practically impossible because of capping of the nanocrystals with hydrophobic moieties emerged as a result of almost all

available to date synthetic procedures, which are performed in organic solvents in the presence of surfactants/capping ligands, both used to control growth of the particles and stability of the dispersions. As a result, the as-synthesized particles are lacking the feature of critical biological significance such as water dispersability [115]. In addition, they suffer from absence of functional groups available for the subsequent functionalization [116]. So that, in order to assign the additional functionality to UCNPs the special treatment of the as-synthesized particles' surface, known as functionalization and bioconjugation, should be done (Figure 2.8). The most common approaches to synthesis and post-synthetic modifications of UCNPs are considered below.

To date, four most popular approaches to the synthesis of UCNPs have been reported (Table 2.2), including co-precipitation, thermal decomposition, sol-gel method and a group of methods termed “hydro(solvo)thermal”. The most important differences between these methods consist in the treatment applied to the almost universal set of the precursors, which are used to form the nuclei of the particles, in order to obtain a specific size, shape and crystal structure. It also should be taken into account, that the method of synthesis can affect the degree of aggregation and PL spectra [117]. The comparisons of the advantages and limitations the most common UCNPS synthetic method are presented in Table 2.3.

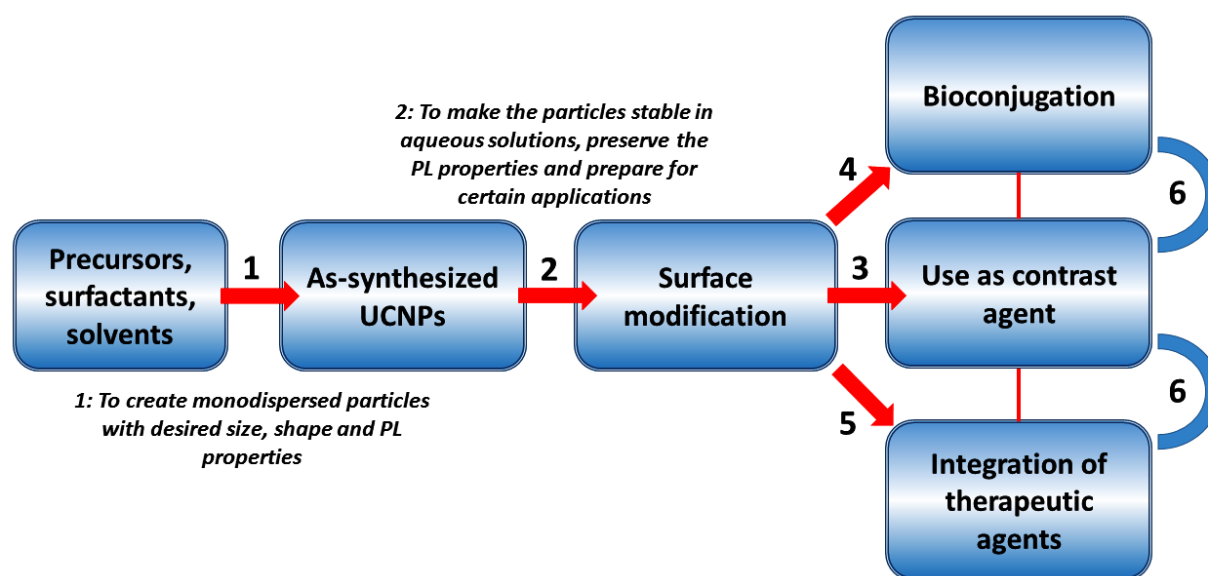


Figure 2.8. Scheme of the processes of adaptation of UCNPs for biomedical applications. (1) Synthesis of UCNPs can be performed by thermal decomposition, solvothermal, sol-gel or co-precipitation methods [118]. The UCNPs resulted from all the synthetic methods cannot form stable dispersions in polar solutions because of presence of hydrophobic ligands on their surfaces. (2) As almost all biomedical applications require transferring UCNPs to aqueous solutions a special step of surface modification should be done. Associated with this quenching of upconversion PL by water may be decreased by formation of core-shell structures, while the hydrophobicity of the particles may be overcome by manipulations with ligands in order to form the hydrophilic interface between the particles and the water-containing environment. (3) Surface-modified hydrophilic UCNPS can be directly applied as contrast agents or additionally functionalized for (4) binding of targeting moieties (bioconjugation) or for (5) inclusion of therapeutic agents. Combined modifications (6) may convert UCNPs into nanotheranostic agents with complex functionalities, including imaging, drug delivery and targeting.

There are several purposes of the post-synthetic treatment of UCNPs on the way to their transformation into NTAs, including 1) preservation of upconversion emission in quenching environment, 2) overcoming the intrinsic hydrophobicity of the particles, 3) conjugation of the particles with targeting biomolecules and 4) integration of therapeutic agents (see Figure 2.8) [77].

Non-linear nature of absorption process defines the limitations of luminescence yield by the power density of the excitation light. On the one hand, the intensity of PL is a critical parameter defining the usability of a UCNP as a contrasting NTA, then, the higher the excitation power, the better. At the same time, the excitation intensity used to get the optical signal from UCNPs must be kept at a moderate level for any biomedical applications [77, 119]. This explains why the attention currently is primarily focused on the sources of potential losses of the upconversion PL emission resulted from the intrinsic properties of the particles. The most notable reason of the possible PL quenching results from the sensitivity of the numerous surface-exposed dopant lanthanide ions in the nanocrystals of UCNPs (Figure 2.9 (a)) to non-radiative energy dissipation resulted from quenching by the ligands and surrounding environment [120, 121]. The main surface-bound compounds, which are able to act as PL quenchers are C–H, O–H or N–H groups of stabilizing ligands (Figure 2.9 (b)) as well as hydroxyl groups in aqueous media [77, 78, 119, 122].

Table 2.2. The methods commonly reported for synthesis of Ln^{3+} -doped upconverting nanomaterials.

Method	The concept, references	Types of nanomaterials (hosts)	Precursors	Solvents, surfacants, capping ligands	Conditions	The examples, references
Co-precipitation	Spontaneous precipitation of the mixed solutions of the dopant source precursor and host material precursor [123]	NaYF_4 ; LuPO_4 ; YF_3 , Y_2O_3 ; $\text{Y}_2\text{O}_2\text{S}$; LaF_3 ; and NaGdF_4	Solutions of lanthanide nitrates or chlorides, solution for the host materials (such as sodium fluoride, phosphoric acid)	Capping ligands (ammonium di-n-octadecyldithiophosphate, polyethylenimine (PEI), polyvinylpyrrolidone (PVP) or chelating agents (EDTA), N-(2-hydroxyethyl)ethylenediamine (HEEDA)	Heat treatment (also referred as 'annealing' or 'calcination') is required in to increase crystallinity of the nanoparticles for the enhanced upconversion PL	[72, 123-125]
Thermal decomposition	Decomposition of trifluoroacetates in presence of oleic acid and octadecene [126-128]	NaYF_4 , LiYF_4 and KGdF_4	Rare-earth trifluoroacetates: $\text{Na}(\text{CF}_3\text{COO})$; $\text{Li}(\text{CF}_3\text{COO})$; $\text{Y}(\text{CF}_3\text{COO})_3$; $\text{Yb}(\text{CF}_3\text{COO})_3$; and $\text{Er}(\text{CF}_3\text{COO})_3/\text{Tm}(\text{CF}_3\text{COO})_3$	High-boiling point solvents (oleic acid, oleylamine, octadecene)	High temperature (250-330 °C), oxygen-free and anhydrous atmosphere	[126, 128-130]

Table 2.2. The methods commonly reported for synthesis of Ln^{3+} -doped upconverting nanomaterials (continue).

Sol-gel processing	The hydrolysis and polycondensation of metal acetate or metal oxide based precursors [131, 132]	BaTiO_3 ; ZrO_2 ; YVO_4 , $\text{Lu}_3\text{Ga}_5\text{O}_{12}$, TiO_2	Metal acetate or metal oxide for the host, and rare-earth acetate	N-propanol, water/oil emulsion of cyclohexane, sorbitan monooleate (Span 80) and nonionic surfactant	Room temperature, sol-gel transitions, drying at 60 °C in air; \pm extra heat treatment for better crystallinity	[131-135]
Hydro(solvo)thermal synthesis	Improved solubilization of the solid reagents and acceleration of the reactions between them under hydro(solvo)thermal conditions (= a pressurized solvent and reaction temperatures above the critical point) [136]	NaYF_4 , YF_3 , LaF_3 and YbF_3 , LuF_3 , Ba_2YF_7 , ZnGa_2O_4 , YVO_4	Host precursors (such as HF, NH_4F , NH_4HF_2 , NaF, and KF) and chloride or nitrite salts or oxides of lanthanides	Alcoholic solution containing the polymer, usually, PEI, PVP, or silica	The reaction mixture (with added ammonium fluoride) is heated to 200 °C in a special heat-resistant Teflon-lined autoclave for 24 h with stirring	[117, 131, 137-147]

Table 2.3. Advantages and disadvantages of typical synthetic routes for UCNPs. Reproduced from with minor changes [118].

Method	Examples (hosts)	Advantages	Disadvantages	References
Co-precipitation	$\text{Y}_3\text{Al}_5\text{O}_{12}$, BaYF_5 , NaYF_4 , LuPO_4 , YbPO_4	Fast synthesis, low cost and simple procedures	Lack of particle size control, considerable aggregation, high temperature calcination typically needed	[117, 148, 149]
Thermal decomposition	LiYF_4 , NaYF_4	High quality, monodispersed nanocrystals	Expensive, air-sensitive metal precursors, toxic by-products	[130, 150-152]
Sol-gel processing	YVO_4 , $\text{Lu}_3\text{Ga}_5\text{O}_{12}$, BaTiO_3 , TiO_2 , ZrO_2	Cheap precursors	High temperature calcination needed, considerable particle aggregation	[131-135]
Combustion synthesis	Y_2O_3 , LaPO_4 , $\text{La}_2\text{O}_2\text{S}$	Fast synthesis, energy saving	Considerable aggregation, lack of particle size control, low purity	[153-155]
Flame synthesis	Y_2O_3 , La_2O_3 , Gd_2O_3	Fast synthesis, large scale	Considerable aggregation, lack of particle size control, low purity	[84, 97]
Hydro(solvo)thermal synthesis	LuF_3 , NaYF_4 , Ba_2YF_7 , ZnGa_2O_4 , YVO_4	High quality crystals with controllable particle size, shape and dopant ion concentrations	Impossibility of observing the nanocrystal growth processes	[140, 142, 156-158]

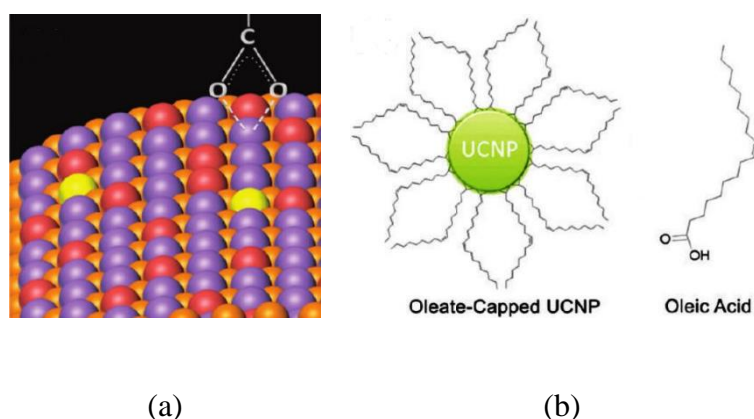


Figure 2.9. Surface properties of Ln³⁺-doped UCNP. (a) Artistic representation of the Ln³⁺-doped UCNPs surface, showing the ions as color-coded spheres: Yb (red), and Er (yellow), Y (purple), F (orange). The coordination of the oleic acid is shown with the Y³⁺ ion; it also can coordinate to other Ln³⁺ ions. The carboxyl ends of the organic ligand conjugate to Ln³⁺ with two C–O bonds. (b) A scheme of oleic-acid capped UCNPs and a structure of oleic acid. Reproduced from [116] with changes.

The efficient methodology to decrease the mentioned PL quenching effects consists in creation of UCNP with core-shell structure, which helps to increase the distance between lanthanide ions and surface ligands of high vibrational states and to reduce the non-radiative energy transfer from the core dopants to the nanoparticle surface [121].

Generally, there are two main types of core-shell structures, termed as “active core/ passive shell” and “active core/active shell” for the involvement of the shell into optical performance of the particles [121]. Another classification indicates also on the method of the shell preparation, discerning the epitaxial particles, where the core is decorated with dense crystalline layers matching the core nanoparticle lattice, and the non-epitaxial nanomaterials, characterized by combination of different materials used for the core and shell, respectively (Figure 2.10).

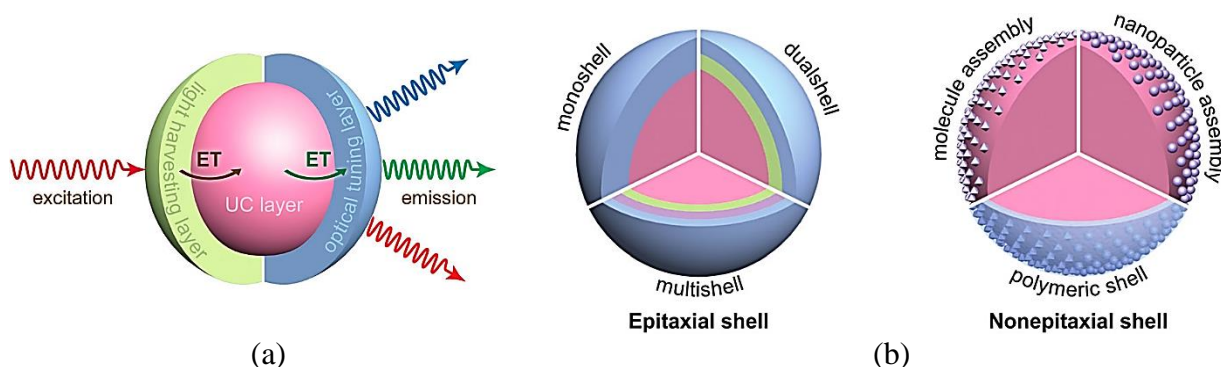


Figure 2.10. Types of core-shell structures of nanoparticles. (a) Schematic view of an active core-shell nanoparticles structure applicable for tuning of the upconversion excitation and emission. ET abbreviation stands for energy transfer. (b) Artistic illustration of the principal architectures of the epitaxial core-shell nanoparticles as uniform structures with single, double or multiple shell layers (on the left) and non-epitaxial core-shell nanoparticles, combining different materials. The epitaxial particles may be also used as cores for non-epitaxial ones. Reproduced from [159] with minor changes.

Initially, the shells were prepared from the same material as a host (or similar ceramic matter, for example NaYF₄, LaF₃ or NaGdF₄) and left undoped (passive shell/active core structure). For example, one of the first studies reported on the preparation of CeF₃:Tb³⁺/LaF₃ (core/shell) nanoparticles, allowed to increase the PL emission intensity and lifetime with respect to these parameters of core-only particles CeF₃:Tb³⁺. This pioneer research confirmed that nonradiative energy losses can be significantly

decreased by shielding effect of LaF_3 shells on centres existing on the surface of $\text{CeF}_3\text{:Tb}^{3+}$ nanoparticles [160]. Next, a series of the various combinations of α - and β -crystals of $\text{NaYF}_4\text{:Yb,Er}$ and NaYF_4 were used as core and shell materials to create cyclohexane dispersions of UCNPs with multicolor (red, yellow and green) luminescence visible by naked eye at natural light. As a result, the core/shell-structured $\alpha\text{-NaYF}_4\text{:Yb,Er@}\alpha\text{-NaYF}_4$ and $\beta\text{-NaYF}_4\text{:Yb,Er@}\alpha\text{-NaYF}_4$ nanocrystals emitted in a green spectral range with enhanced intensity, the ratio of green/red signals intensity shifted significantly towards the green one (Figure 2.11), and saturation power was increased with respect to the particles of shell-less structure [161]. Later, the shells were also doped with lanthanide ions like Yb^{3+} in order to make the active shell/active core structures. It has been rigorously proved that active shell/active core approach helps to increase the upconversion luminescence intensity, in comparison with the core-only and passive shell/active core structures of UCNPs [162, 163].

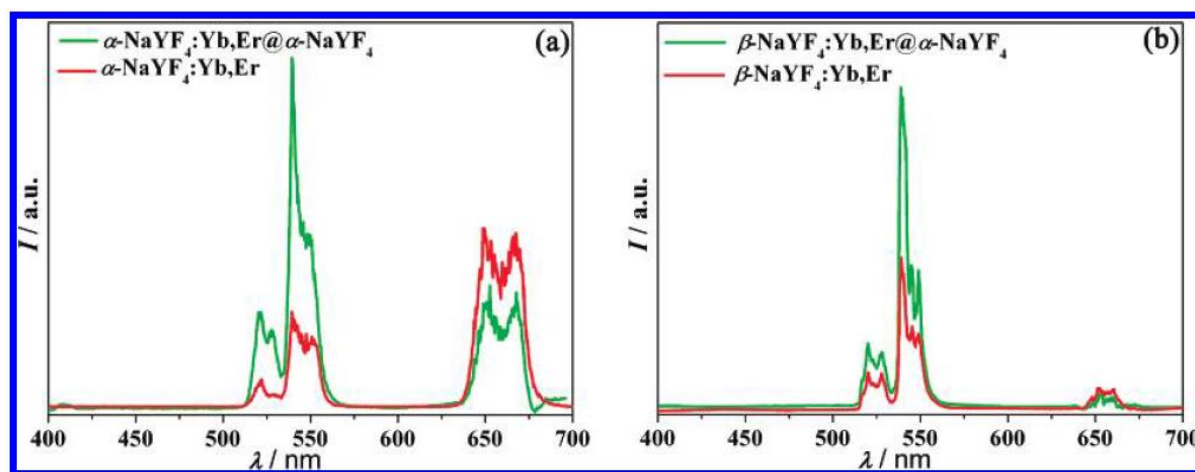


Figure 2.11. The effect of the core-shell structure, crystal phase and shape of UCNPs on upconversion PL spectra of (a) $\alpha\text{-NaYF}_4\text{:Yb,Er@}\alpha\text{-NaYF}_4$ nanopolyhedra, (b) $\beta\text{-NaYF}_4\text{:Yb,Er@}\alpha\text{-NaYF}_4$ nanospheres. Reproduced from [161].

Epitaxial core-shell UCNPs can be prepared by two alternative methods such as the hot-injection and the heat-up strategies (Figure 2.12). The first implies the adding of the precursors for the shell layer (or layers) into the hot reaction mix, where the core particles are forming. The heat-up strategy uses the preformed core particles for subsequent formation of the shell. The notable advantage on the hot injection method is that it allows fast and affordable one-pot scheme, while the heat-up method is useful for creation of more complex and better controlled structures [121].

In order to fabricate the non-epitaxial core-shell UCNPs the layers of the shell can be linked to the surface of the core nanoparticles by chemical bonds or by various polymerization processes [159]. The effectiveness of various molecular species and nanomaterials for surface passivation of UCNPs through core-shell strategy have been demonstrated, as, for example, CdSe quantum dots [164], gold nanoparticles [165], organic NIR dyes as light-harvesting antennas for the $\beta\text{-NaYF}_4\text{:Yb,Er}$ nanoparticles [166]. One of the most popular examples of epitaxial core-shell structure is represented by silica coatings. The solid silica shells are usually prepared by modified Stöber or microemulsion methods, which can be applied for modification of hydrophilic and hydrophobic UCNPs, respectively [167, 168].

In order to create multifunctional and multimodal UCNPs the solid and mesoporous silica shells with embedded functional molecules and nanoparticles can be prepared [108, 168-170].

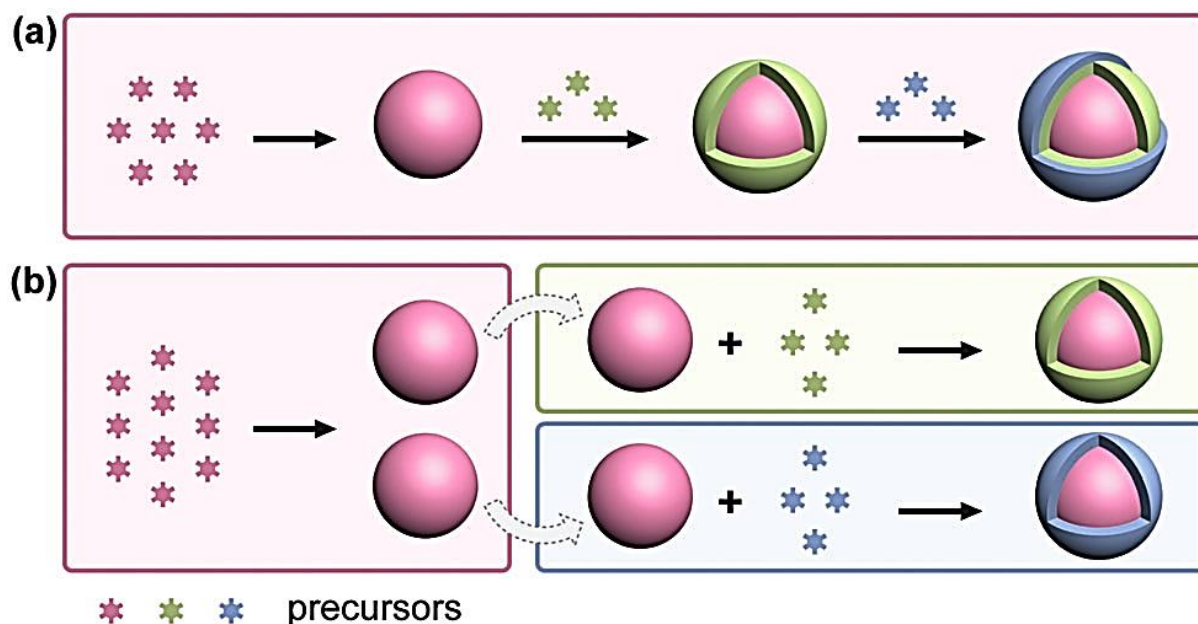


Figure 2.12. The most popular strategies of preparation of epitaxial core-shell UCNPs. (a) The hot-injection strategy: creation of multilayered shell by serial injections of various shell precursors. (b) The heat-up injection strategy. The scheme illustrates one of the advantages of this method such as a possibility to fabricate different shells for the same core nanoparticles in parallel, which is useful for the analysis of the shell functional effectiveness. Reproduced from [159].

The silica shells can help to solve another critical issue regarded to biomedical applications of UCNPs by providing them with the hydrophilic surface. This is a very special feature as the majority of the UCNP core-shell structures preserve hydrophobicity as a result of preparation in organic solvents, while water dispersability is essential for almost all applications of UCNPs, where the interaction between these particles and living matter is expected. The most typical ligands on the surface of the core-only and core-shell UCNPs are oleic acid or oleylamine [78, 121, 162, 171, 172]. Therefore the special treatment to develop UCNPs able to form stable aqueous colloids is in demand.

2.2.1.2.2. Surface functionalization of UCNPs for biomedical applications

While the core-shell technique is primarily focused on preservation and enhancement of PL emission of UCNPs, the complementary methodology of surface modification for water dispersability of the particles, provides “a bridge” between optimized synthesis of UCNPs and their biomedical (including nanotheranostic) applications, which require stability in aqueous biological environments and availability of active functional groups for further conjugation with biologically active molecules [173, 174]. This definition is relatively conditional as the border between some non-epitaxial core-shell formation methods and surface hydrophilization of UCNPs is gradually becomes blurry [175]. The most popular approaches to surface modification of UCNPs include ligand engineering, ligand attraction, layer-by-layer assembly strategy [176] and surface silanization [168] (Figure 2.13). Surface control

during synthesis represent an additional way to stabilize the dispersions of UCNPs in water and provide them with the necessary functionality [72, 173, 177].

The term “ligand engineering” encompasses two types of ligand exchange reactions (such as organic ligand-free scheme and bifunctional molecules ligand exchange method) and a direct oxidation of the oleic acid, which is normally capping the as-synthesized UCNPs [173].

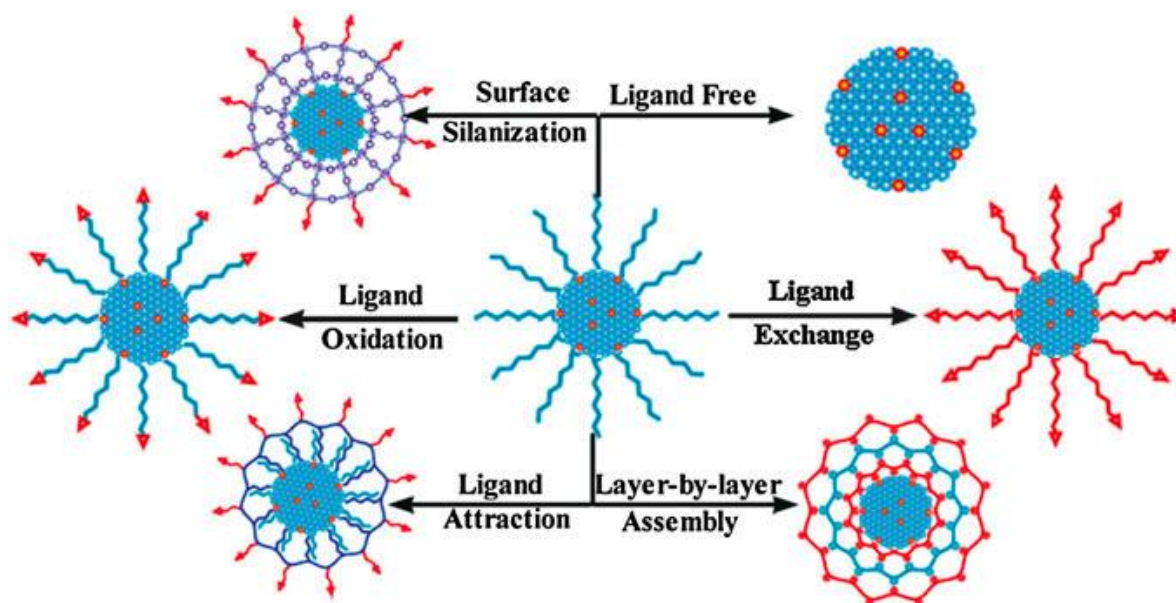


Figure 2.13. The common approaches to the surface modification of UCNPs intended for making hydrophilic particles with pendant functional groups. Reproduced from [177].

The *organic ligand-free* methodology, or *ligand removal*, implies post-synthetic processing of oleate-capped UCNPs under acidic conditions [116], washing in excess of ethanol with subsequent ultrasonic treatment [178] or a ligand exchange with nitrosonium tetrafluoroborate resulting in redispersion of UCNPs in polar solvents such as N,N-dimethylformamide, dimethylsulfoxide or acetonitrile [179]. The method, proposed by the group of J. A. Capobianco [116], allows further conjugations of resulted water-dispersible UCNPs with electronegative groups such as $-\text{SH}$, $-\text{COOH}$, $-\text{NH}_2$, $-\text{OH}$, while the BF_4^- modified UCNPs obtained by the approach realized by C.B. Murrey et al. [179] can also be functionalized with hydrophilic polymers, such as polyvinylpyrrolidone and stay in aqueous media without precipitation for several months.

The bifunctional molecules *ligand exchange* method is based on the replacement of organic ligands residing on the as-synthesized UCNPs' surfaces such as oleate with the bipolar surfactants having functional groups able to make strong bonds to the nanoparticles along with presence of hydrophilic end tails exposed to the water-based environment. This is, probably, one of the most frequently ways of surface modification of UCNPs. A number of various molecules were reported for its successful application, including polyacrylic acid (PAA) [180-182], polyethyleneglycol (PEG)-phosphate [183], PEG-diacid [130], 1,10-decanedicarboxylic and 11-mercaptoundecanoic acids [184], hexanedioic acid

[185], 3-mercaptopropionic acid [186], mercaptosuccinic acid [187], poly(amidoamine) (PAMAM) [188], citric acid [63, 189, 190] and several others.

The *ligand oxidation* method represents direct oxidation of the unsaturated carbon-carbon double bonds of oleic acid (OA) ligands, capping UCNPs as a result of preceding synthetic procedures, into carboxylic acid groups [173] and transforming OA into azaleic acid, the compound readily dispersible in water, dimethylsulfoxide or dimethylformamide. Originally, the Lemieux–von Rudloff reagent ($\text{MnO}_4^-/\text{IO}_4^-$) was used to perform this reaction by Z. Chen and co-authors [191]. Later, a modification of this approach, relying on use of ozone as oxidizing agent was demonstrated [192].

The *ligand attraction* methodology of UCNPs surface modification relies on van der Waals interactions between hydrophobic ligands of as-synthesized particles and hydrophobic tails of amphiphilic polymers (APs), block-co-polymers and surfactants. The hydrophilic portion of an AP faces outwards making the particle water dispersible. Interestingly, in this case the hydrophobic parts of the APs and the UCNPs surfaces do not interact to each other, resulting in better preservation of luminescent properties of the particles [173]. This approach has been successfully applied to prepare stable aqueous colloids of UCNPs with using many various species such as poly(ethylene glycol)-*block*-poly(caprolactone) (PEG-*b*-PCL), poly((ethylene glycol)-*block*-lactic acid) (PEG-*b*-PLA) and poly(ethylene glycol)-*block*-poly(lactic-co-glycolic acid) (PEG-*b*-PLGA) [193], poly(maleic anhydride-*alt*-1-octadecene) (PMAO) [194], PMAO-PEG and octylamine-poly(acrylic acid)-poly(ethylene glycol) (OA-PAA-PEG) [195], sodium dodecyl sulphate, cetyltrimethylammonium bromide (CTAB) and polyethylene glycol *tert*-octylphenyl ether [196], phospholipids [197], poly(L-lysine) [198], 6-aminohexanoic acid [199] and PAA [200].

Layer-by-layer (LbL) assembly strategy is based on electrostatic attraction between the oppositely charged molecules, polyanions and polycations [201], which are alternating on the surface of UCNPs. Technically this method relies on multiple incubations of the particles with chosen compounds and successive washings (to remove the unbind excess of coating molecules). This notably universal approach allows preparation of versatile compositions of the surface coated UCNPs with desired size and charge [173] and may be applied to wide range of materials [121]. It also helpful for fabrication of hybrid composites, containing UCNPs, such as films and fibers [189, 202]. Another advantage of this strategy lies in a possibility to add special functionality such as, for example, light-sensitive molecules [203] to the surface of UCNPs. For the first time, to our knowledge, the method was adapted for UCNPs surface modification by Y. Li and co-authors [176], who sequentially applied polycationic polymer poly(allylamine hydrochloride) (PAH), polyanionic polymer poly(styrene sulfonate) (PSS) and the third layer of PAH coating again. The third layer, having being a polyamine, was used for the next bioconjugation of UCNPs with biotin, demonstrating the possibility of adding a biological functionality.

Surface silanization was briefly discussed with regard to the core-shell methodology as an approach to preserve better PL luminescent properties of UCNPs. In this section it is worth to note that silica coating allows easy carboxyl- or amine- functionalization especially useful for bioconjugation of UCNPs with biological molecules [177].

Finally, in addition to multistep surface modification methods, described above, several attempts to develop a “one-pot” procedure to control the hydrophilicity of UCNPs surface during synthesis were made. This scheme of surface control during synthesis was modified for amine functionalization of UCNPs with polyethylenimine (PEI) [84, 204] or and aminohexanoic acid [205], and introduction of carboxyl groups with small acid molecules [206].

Bioconjugation is the next step to prepare UCNPs for nanotheranostic applications. As the local targeted effects of the particles are desired, the specific recognition elements such as biologically significant molecules should be added to the nanomaterial. Depending on the previous surface modification, two basic approaches of binding the biomolecules to UCNPs can be used, including physical adsorption relying on electrostatic or hydrophobic interactions and covalent chemical binding. The first way is straightforward and simple. For example, folic acid (FA), a popular cancer targeting agent, or streptavidin, a protein of high affinity, both anionic, can be physically adsorbed on the surface of positively charged UCNPs [207, 208]. However, the adsorbed biomolecules can detach from the UCNP in complicated physiological environments. The alternative method is based on the covalent linkage between the functional groups of surface modified UCNPs, from one side, and the active groups of biological compounds, from other side. These linkages are considered very stable even under challenging conditions [88]. In some cases the surface of UCNPs has functional groups as a results of the modification performed to get water dispersability, but more frequently the use of additional treatment or introduction of a linker is preferable [121].

The carboxyl, amine and maleimide (MA) functional groups are commonly used for bioconjugation of UCNPs [209] (Figure 2.14). Carboxyl groups may be available on the of UCNPs, with surface oleate converted to acids such as PAA, azelaic, hexanedioic, citrate, diacid PEG, thioglycolic, several isoforms of mercaptopropionic acid and some other. These groups can react with amine groups of biomolecules with formation of stable amide bonds. The reaction should be facilitated by the intermediate product *O*-acylisourea, which forms as a result of interaction between –COOH terminal groups of surface modified UCNPs and 1-ethyl-3-(3-dimethylaminopropyl) carbodiimide hydrochloride (EDC) and the *N*-hydroxysulfosuccinimide sodium salt (sulfo-NHS). UCNPs terminated with amine groups can be covalently bind to biomolecules with carboxyl, aldehyde (–CHO) or thycyanate (S=C=N) groups. The amine groups are present on the surface of UCNPs modified with PEI [138, 210, 211], PAMAM [188], diamino-PEG [212, 213], (3-aminopropyl) triethoxysilane (APTES) [214, 215] and other molecules. Maleimide (–C(O)NHC(O)–) groups can be provided to UCNPs surface by step-by-step modification with 6-maleimidohehexanoic acid [216] to react with thiol (–SH) groups of cysteines and thiolated

peptides. In particular, very promising for cancer and angiogenesis targeting bioconjugation with modified RGD peptides were proposed by F. Li's [216] and M. Maeda's [217] groups.

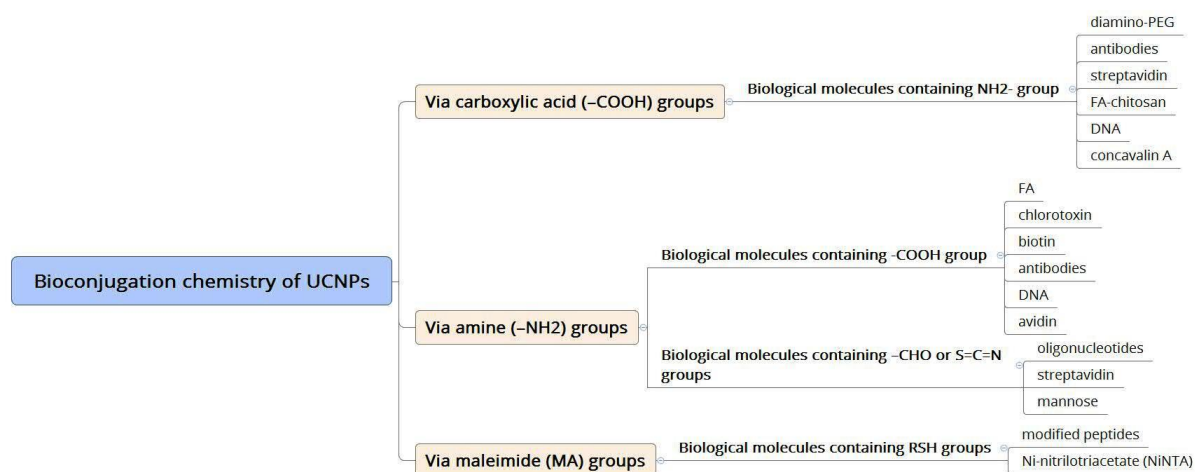


Figure 2.14. The covalent chemical interactions commonly employed for bioconjugation of UCNPs. Based on the internal literature references provided in the comprehensive review [209].

The final step in formation of full-range functional NTA on the base of UCNPs consists in *integration of the particles with therapeutic load (TL)*. In addition to imaging functionalities, UCNPs can serve as delivery agents for drugs, genes, small interfering RNA (siRNA), therapeutic peptides and proteins. They also can deliver the photosensitizers (PS) for photodynamic and photoabsorbers for photodynamic or photothermal therapy (PDT and PTT, respectively). The motivation of the conversion of UCNPs into drug delivery systems is that it can improve the efficacy of the pharmaceutical payloads by influence on solubility, stability, biodistribution (including passive and active targeting), and pharmacokinetics [29]. In particular, the special advantage of UCNPs is the possibility to use light-activated processes for drug release and for PDT/PTT and to apply imaging-guided treatment.

The strategies of incorporation of TLs into UCNPs are partially based on the same principles as bioconjugation methods, described above such as physical adsorption and covalent binding. Another option of introduction of the TLs into UCNPs relies on silica encapsulation (Figure 2.15). Physical adsorption provides more loose connection between the TLs and UCNPs, which is preferable for easy drug release. It is the method of choice for many hydrophobic and or poor water-soluble drugs (for example, the anti-cancer drug doxorubicin). The release of physically adsorbed TLs may be controlled by pH or by NIR light-activated mechanisms, based of transferring of energy of upconversion PL emission to the light-sensitive molecules or composites. In contrast, covalent binding is the best choice for creation of stable nanocomposites such as PS-UCNPs for PDT, where any free leakage of the load is undesirable, but not the optimal strategy for the local drug releasing systems. It also may be a preference for in vivo use of UCNP-drug composites, which are exposed to body defence barriers. The benefit of use of dense silica shells (see Figure 2.15 (a)) is that it can create a storage for water-soluble TLs, which are included into the silica layer the water-in-oil reverse microemulsion technique [218] and then can be released on demand. Mesoporous silica coatings provide an extraordinary high capacity

volume for the drug payloads and may be used for both delivery and release purposes, including NIR light-activated schemes.

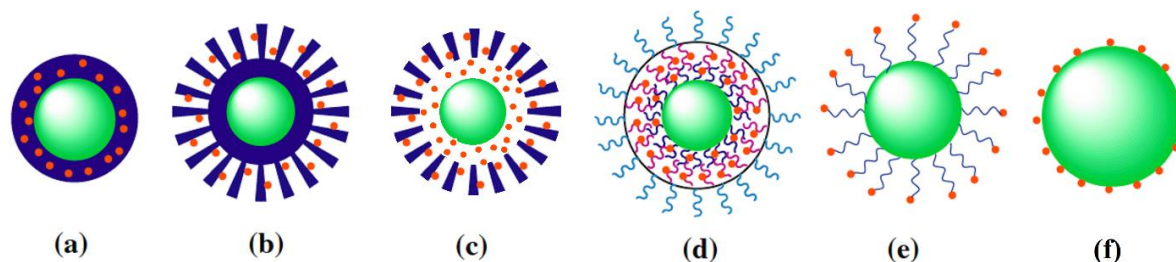


Figure 2.15. The most common strategies for integration of therapeutic load (TL, orange dots) with UCNP (green spheres). (a) Encapsulation of the TL into silica shell (blue circle) coated onto the surface of UCNP; (b) deposition of the TL into the pores of mesoporous silica shell of UCNP via physical adsorption or covalent conjugation; (c) loading of the TL into the pores and cavity of hollow mesoporous silica shell of UCNP; (d) loading of the TL into “hydrophobic pocket” on the UCNP surface, which is formed by ligand attraction method based on interactions between the hydrophobic segments of polymers (pink lines) and UCNP capping ligands (dark blue lines); (e) covalent binding of the TL to the surface of UCNP functionalized with active chemical groups; (f) direct attachment of the TL to the charged surface of UCNP via electrostatic interactions. Not scaled to size. The graphical scheme is reproduced from [173] with changes.

2.2.1.3. Biological effects of UCNP

Biomedical applications of UCNP, including nanotheranostics, require thorough research on the ratio of potential benefits and safety risks associated with use of these particles at different levels of organization of the living matter. Usually, the analysis of the effects of the particles at cellular level can be done by *in vitro* metabolic assays on cell cultures (like MTT, MTS, LDH and CCK-8), exploring the dose- and exposure-dependent effects of UCNP (with regard to the hosts, dopants and surface modification variability) on proliferation and metabolic rates. The *in vivo* tests on animal models may be performed in order to study the behavioural, physiological, histological, haematological and biochemical changes, induced associated with the application of the nanomaterial as well as the effects of their retention and the rates and ways of clearance. At the same time as the mass production of UCNP is rather unlikely, the environmental impact of this materials is mainly outside of the research focus.

The generally held and “transmissive” opinion about UCNP as nontoxic materials is based primarily on the numerous reported results of individual *in vitro* experiments on 2D cell cultures, while the *in vivo* studies are much lesser (for review see [173, 219, 220]). According to these data, the cytotoxicity of various types of UCNP seems to be relatively low: the reported cellular population losses are usually not higher than 10-25% from the control level under the concentrations of UCNP up to 100 or even 1000 $\mu\text{g/mL}$ within the exposure time within 24-72 h. However, more thorough analysis shows that it is a challenging task to make such a definite optimistic conclusion regarding the safety of UCNP as it is almost impossible to compare the observations of different researchers. Indeed, no standard protocols are available and the conditions of the studies (composition, size, surface modifications and charge of the particles, their concentrations, exposure time, cell types etc.) vary very

much. It is also critically important that the absolute majority of the published data have been obtained by experiments on cancer cell lines [209], while it is the viability of the normal cells under exposure to UCNPs what should reasonably be taken into consideration first of all. Surprisingly, only a few studies examine the effects of UCNPs on non-malignant cells instead of the testing on generally less sensitive cancer cell lines [33, 102, 108, 156, 221-233], while also not always were specially focused on the cytotoxicity. Following some of these publications the evidence indicating potential risk of UCNPs application in normal cells has started to come together [221-224].

In particular, W. Kałas et al. [222] demonstrated the significant toxic effects of bare and silica-coated NaGdF₄:Yb³⁺:Er³⁺ nanoparticles on fibroblasts and macrophages *in vitro* under 48 h exposure. It's worth to note that this group provided rigorous evidence of apoptotic death and retarded proliferation rates of the cells, exposed to the silica-coated and bare UCNPs even at the concentrations much lower than 100 ug/mL, while PEG-coating dramatically reduced the cytotoxicity. The second important finding was that the surface modification (PEGylation, dense silica and NH₂-activated dense silica coatings versus bare ligand-free hydrophilized UCNPs) as well as the type of the exposed cells make the main contribution into the outcome effects of the particles under matched conditions of the experiment (Figure 2.16).

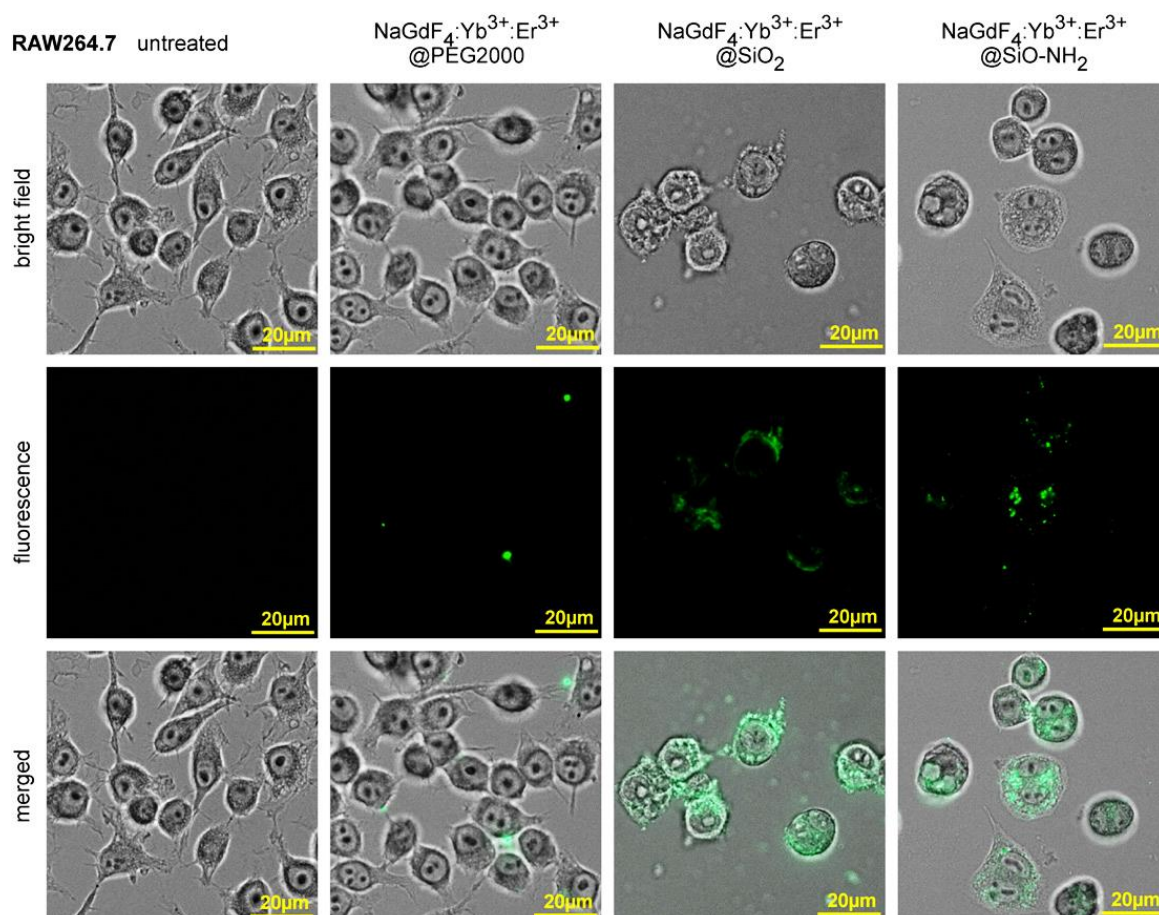


Figure 2.16. Interaction of NaGdF₄:Yb, Er UCNPs with different surface modifications on morphology of RAW264.7 linear macrophages *in vitro*. Note the effect on cellular morphology and the differences in distribution of the nanoparticles with regard to cellular surface and internal volume. Reproduced from [222].

In other study [221], core/shell UCNPs $\text{NaYF}_4\text{:Yb}^{3+}\text{:Tm}^{3+}/\text{NaYF}_4$, in a form of bare particles, hydrophilized with low molecular weight phase transition agent tetramethylammonium hydroxide (TMAH), UCNPs coated with polyethylenimine (PEI) or polymaleic anhydride octadecene (PMAO) also show toxic action on primary hippocampal cell cultures, which was dependent on the method of surface modification of the particles and evidenced as apoptotic death, morphological changes and profound decrease of spontaneous cellular calcium activity. G. Das with co-authors [223] observed strong dependence of biological activity of $\text{NaLnF}_4\text{:Yb,Er}$ ($\text{Ln} = \text{Y, Gd}$) nanoparticles on the method of surface modification with significant toxic effects of the UCNPs with a bilayer of PEG-oleate coating, obtained by intercalation method, on primary human aortic endothelial cells with 50% cell death during the first 24 h of exposure to the particles concentrations up to 75 $\mu\text{g/mL}$. Notable adverse effects of low concentrations of bare spherical $\text{Y}_2\text{O}_3\text{:Eu,Tb}$ UCNPs on murine subcutaneous connective tissue fibroblasts were observed elsewhere [224]. It should be emphasized with regard to the topic of the present thesis, that to the best of our knowledge no any reports on cytotoxicity of UCNPs with use of 3D *in vitro* test systems were published yet.

The information on the behaviour of lanthanide-doped UCNPs at subcellular level is scarce [234, 235]. Specifically, the real-time trafficking of PEG-phospholipid-coated UCNPs in HeLa cells was shown recently, including internalization of the particles through endocytosis, their transport by dyneins (microtubule-dependent motor proteins), accumulation at the perinuclear region, and later release from the cells with the help of kinesins by exocytosis [235]. In addition, the effect of liposomal transfection factor on the redistribution of $\text{NaYF}_4\text{:Yb, Er}$ nanoparticles coated with polyvinylpyrrolidone inside HeLa cells has been observed [234].

As the conventional 2D cell culture experiments cannot reflect the long-time effects of the exposure to UCNPs as well as have the intrinsic limitation for translation of the results to the higher levels of biological organization, the studies on animal models are the only available alternative to date for getting this type of information [220].

The first experiment in worms (*Caenorhabditis elegans*) confirmed that UCNPs do not disturb life span, fertility, egg viability and the animals' growth rate [98, 236, 237] at concentrations up to 10 mg/mL [238]. Later, no any significant adverse effects of lanthanide-doped UCNPs with various types of surface coatings were found by research in mice and in more rarely performed experiments on rats [156]. The animals intravenously injected with UCNPs survived for at least one month without any notable signs of their health impairment [180, 239-243]. In particular, no changes in behaviour, fur condition, haematological parameters and serum biochemistry were detected under observations up to 115 days after introduction of the UCNPs into the animal bodies [180, 240]. However, small decrease of body weight was recorded in long-term study in mice after intravenous injection of 15 mg/kg of body weight UCNPs coated with PAA [180]. The following histopathological examination revealed moderately

increased lymphoid infiltration of white pulp of murine spleen, while other organs did not show any pathological signs [180].

It has been shown that blood circulation time, organ biodistribution, accumulation and excretion of Ln^{3+} -doped UCNP are dependent on the surface modification (in terms of the chemistry and charge) of the particles, and, to some degree, on their size. For example, the PL signal of PAA-coated UCNP injected intravenously in mice rapidly disappeared from blood, and then it emerged mainly in the spleen and liver, less was detectable in the lungs; while in the kidneys and heart only a trace signal was observed. During the first day after injection the signal increased in the spleen and slowly decayed in the liver. The PL of UCNP was detectable in spleen and liver in 2 weeks postinjection, and even after 3 months in intestines [180]. Similar dynamics of organ biodistribution was observed by radioisotope (^{153}Sm) labelled small (8 nm) PEG-coated UCNP with a single exception of greater amount of the particles concentrated in the kidneys and urine, indicating the renal excretion [244]. Very similar data on biodistribution of UCNP in mice was obtained with another study with use of PEGylated $\text{NaYbF}_4\text{:Yb, Tm}$ of less than 20 nm in diameter [242], however the excretion with faeces and urine was observed during 7 days after injection. Rarely small amounts of UCNP were detected also in muscles and heart [245]. PEI-coated UCNP injected in rats accumulated quickly in lungs, later, during the next 24 h, the PL signal maximum shifted to spleen and finally became undetectable after 7 days postinjection [226]. The blood circulation time of UCNP also is strongly influenced by the particles' surface coating. For instance, L. Cheng and co-authors revealed significant increase of two-phase circulation half-times for UCNP coated with PAA and PEG as 0.13/3.5 and 5.1/13.1 minutes, respectively [241]. Intradermally injected $\text{NaLuF}_4\text{:}^{153}\text{Sm}^{3+}, \text{Yb}^{3+}, \text{Tm}^{3+}$ coated with 6-AHA in PBS in a total dose of 4 μg did not induce any histopathological changes in heart, liver, spleen, lungs and kidney of mice after 7 days of exposure as well as no any adverse haematological and biochemical dynamics were found [243], indicating that this route of delivery of UCNP does not lead to any specific reactions.

Some reports indicate on the possibility of long-time storage of UCNP in the body [241], indicating the delayed (more than 3 months) clearance of UCNP coated with PAA and, especially, with PEG, and setting a question about the safety of such deposits and the effects of long-time exposure. It is especially important as there are conflicting data on the presence of the particles in the tissues and organs after several days or months after injection. The majority of the current studies of the pharmacokinetics of UCNP rely on the detection of the particles in the animal body *in vivo* or in organs *ex vivo* by the PL signal and then indicate on the clearance of the particles following the decrease of the PL up to undetectable levels. However, the alternative methods like transmission electron microscopy (TEM) and ion coupled plasma (ICP) measurements. Specifically, the group of Zh. Liu [241] demonstrated that instead of absence of upconversion PL signals from the murine organs 7 days after injection of UCNP, the level of Y^{3+} ions in these organs did not decrease during 3 months, excepting the lungs, where it dropped in 3 first days postinjection. In addition, aggregates of the particles were found by TEM in liver

in 7 days after the exposure to the UCNPs, while the PL signal from the organ was also undetectable. In addition, accordingly to the study referenced above [241], the residues of the UCNPs as approximately 40-50% of the injected doses of UCNP-PAA and UCNP-PEG were observed in liver, spleen and lungs even after 3 months after the experimental challenge, although different types of the particles demonstrated some variations of the clearance dynamics. For example, ultrasmall UCNPs (~ 10 nm) completely excreted with urine in 115 days after injection, while for bigger particles (~ 30 nm) only partial clearance was revealed. The authors of this study, performed in 2011, emphasized the idea that lanthanide-doped UCNPs can be deposited and underwent intracellular decomposition, which, probably, may lead to loss of the upconversion PL. Later, this idea has been proved experimentally. In particular, the decay of the rare-earth oxides nanoparticles with formation of needle-like aggregates in phagosomes was observed recently by T. Xia's group [246]. Finally, although ceramic host-based lanthanide-doped UCNPs are generally considered as low-biodegradable matter [238], the latest results suggest that they are dissolve in aqueous environment with a notable release of Ln^{3+} ions (Figure 2.17) and significant loss of the PL intensities even in presence of surface coatings [247].

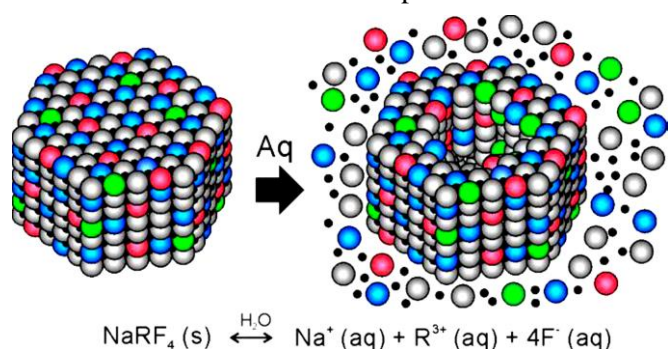


Figure 2.17. The scheme of dissipation of $\text{NaYF}_4:\text{Yb, Er}$ UCNPs in aqueous buffer solution. Reproduced from [247].

Therefore the possible long-time exposure of tissues to the UCNP nanocrystals and the compounds associated with them should be taken into account. The effect of chemical composition of the UCNP is scarcely addressed in the literature. General considerations rely on the idea of relative inert nature of the host crystals, and the possibly biologically significant contributions of the dopant ions and the materials, which are used for surface modification, bioconjugation and TL of the particles. In particular, it is considered that yttrium is generally non-toxic, while some lanthanide ions, especially Gd^{3+} , as well as manganese should be treated with a caution [238]. Although recent *in vivo* studies [238] did not reveal any toxic effects of $\text{Gd}^{3+}/\text{Mn}^{2+}$ contained UCNPs on mice, the authors explain the observation by a possible inhibition of ion leakage because of the inclusion of these ions into a rigid matrix of host crystals and emphasize the limited time of the observation period and the risks of the decomposition of UCNPs at the later stages.

Commonly, lanthanides are referenced as relatively non-toxic elements, as the 50% lethal doses LD_{50} for lanthanide salts vary between 10 and 1100 mg per kg of body weight, for intravenous and per oral administration. The clearance of lanthanides (Ln^{3+} -citrate as an example) from the body is

described as a three-phase model, which includes the first fast stage (from hours to a few days), a slower intermediate phase (from hundreds of hours to several days) and the last, late phase up to 850 days [220, 248]. Nevertheless, it is known that lanthanides can induce inflammatory diseases of lungs in a case of chronic exposure, increase permeability of blood vessels for low molecular weight species and even cause necrotic processes in internal organs such as liver and spleen [220, 249]. Changes in various biochemical parameters of blood (hepatic probes, cholesterol, some enzymes, including $\text{Ca}^{2+}/\text{Mg}^{2+}$ -ATPase and NADH dehydrogenase) were observed after intravenous injections of lanthanide compounds [250, 251]. Ions of lanthanides also can have some negative effects on progeny when administered during lactation or pregnancy, but no any carcinogenic or mutagenic effects were noted [220].

Another interesting property of the lanthanide ions, which should be taken into account with regard to possible biodegradation of Ln^{3+} -doped UNCPs, was discussed by S. Hirano and K.T. Suzuki [248], who indicated on the similarity of ion radiuses of Er^{3+} and Ca^{2+} and discussed a number of potential biological consequences of concurrent/antagonistic action of these species (for the review, see the references therein [248]). Among the mentioned effects, just a few to be nominated, are the modulation of the cellular membrane and cytoskeleton microtubules stability by rare-earth ions [252], inhibition of muscular contractility due to displacement of membrane-bound Ca^{2+} by Ln^{3+} , the strongest inhibition of the calcium channels type T by Er^{3+} and Yb^{3+} . Finally, the lanthanide ions are able to induce so called hormesis effect, which is the ability to stimulate growth of cells at very low doses, becoming inhibitory at higher concentrations. They also were considered as potential drugs [253-257] for at least two relevant areas of nanotheranostics such as therapy of cancer and arthritis (synovitis).

2.2.1.4. Nanotheranostic applications of UCNP

Upconverting nanophosphors, as it follows from the analysis presented in the previous sections, possess unique optical properties that make them the efficient contrast agents. Their functionality can be extended by surface modifications to perform various therapeutic and targeting functions. Taken together, these features allow to consider lanthanide-doped UCNP as the nanomaterials that can perform rather special *nanotheranostic* tasks (see Section 2.1) such as detection the presence if diseased tissue, treatment applied to the pathological structures and monitoring of the treatment outcome [258]. In particular, the list of the available theranostic “duties” of UCNP includes localized drug (or gene) delivery integrated with imaging/ monitoring or/and remote control of the transport and release of the drugs at the desired area, as well as light-activated therapies, including PDT and PTT. This section overviews some representative examples on the use of UCNP as NTAs for the named applications.

2.2.1.4.1. Tracking of drug delivery and release

The first advantage of UCNP as NTAs is very important drug research and for imaging-guided treatment. It stems from the fact that these particles can simultaneously serve as vehicles for various

therapeutic compounds and as background-free (upconversion PL or multimodal) contrast probes. This allows not only the delivery of the drugs, genes or other compounds to the diseased tissues but also provides a way for tracking of the transport of the therapeutic/imaging nanocomplexes as well as the methods to define the intracellular fate of the drugs/genes loaded on UCNPs.

For example, imaging-guided and magnetic targeted drug delivery was demonstrated *in vitro* by applying the $\text{NaYF}_4:\text{Yb}^{3+},\text{Er}^{3+}$ nanocrystals encapsulated into an amphiphilic block copolymer, poly(styrene-block-allyl alcohol), together with iron oxide nanoparticles (IONPs) and anti-cancer drug doxorubicin (Dox) [259]. Up- and down-conversion imaging has been applied to demonstrate internalization of the obtained UCNPs-IONPs@Polymer-Dox multifunctional nanocomposites by HeLa cells and the release of Dox into the cell nuclei in a time-dependent manner. Next, the effectiveness of magnetic targeted drug delivery by the studied nanocomposite into the cancer cells was clearly demonstrated (Figure 2.18). In the same study triple-modal imaging (up- and down-conversion luminescence and MRI) was demonstrated *in vivo*.

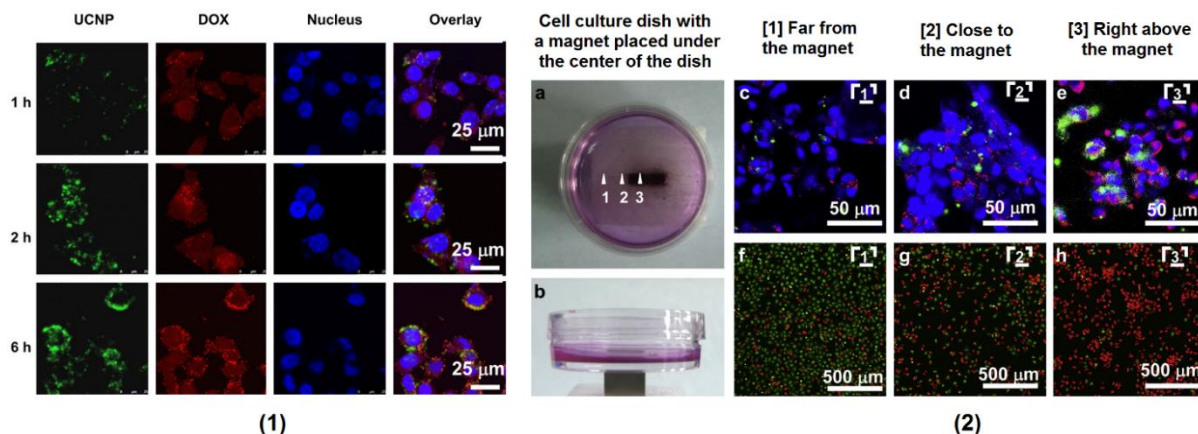


Figure 2.18. In vitro imaging-guided and magnetic targeted drug delivery of UCNPs-IONPs@Polymer-Dox nanocomposite in cultures of HeLa cells. (1) Time-dependent internalization of the nanocomposite in HeLa cells observed by emissions from UCNPs upconversion PL (green) and fluorescence of Dox (red) and DAPI nuclear staining (blue) under the excitation of 980 nm and 488 nm lasers, respectively (confocal microscopy). (2) Demonstration of feasibility of magnetic targeted drug delivery. (a, b) The photos of the experimental setup showing the relative positions for the confocal microscopy images (c-h), indicating increasing ratio of dead cells in the culture. (c-e) Confocal images of HeLa cells after incubation with UCNPs-IONPs@Polymer-Dox in the presence of a magnetic field; color palette is the same as at (1); (f-h) HeLa cells after incubation with UCNPs-IONPs@Polymer-DOX in the presence of a magnetic field, staining with calcein AM (green, for live cells) and propidium iodide (red, dead cells). Reproduced from [259] with changes.

In other *in vitro* study, PEG-coated core-shell UCNPs $\text{NaYF}_4:\text{Yb}^{3+},\text{Er}^{3+}/\text{NaGdF}_4$ bioconjugated with cell-nuclear targeting TAT peptide and loaded with Dox were successfully applied to accelerate the uptake of DOX by nuclei of HeLa cells for 2-6 times in comparison with the untargeted particles. The process was monitored in real time by upconversion PL detection (the signal emitted from the particles core under NIR excitation) and sensitive T_1 -MR imaging (the MRI signal obtained from the shell of the particles) and later confirmed by TEM [260]. The elegant method to control the drug release from the UCNP-based nanocomplexes in living cells employs fluorescence energy transfer mechanism (FRET) [261]. Core-shell UCNPs ($\text{NaYF}_4:\text{Yb},\text{Er}@\text{SiO}_2$) were conjugated with a small interference RNA

(siRNA) stained by fluorescent dye BOBO-3. Having being excited by NIR laser, UCNPs acted as energy donors, when the energy of upconversion PL was nonradiatively transferred to BOBO-3 molecules, which was manifested by decrease of emission intensity of UCNPs and increase of the fluorescence of BOBO-3. As FRET can occur only at tightly positioned species, the effectiveness of this process indicated on the physical distance between the UCNP and BOBO-3 dye, dropping as a result of detachment of the dye-siRNA complex from the nanoparticle up to total disappearance. This allowed to observe gradual release of siRNA into the cells during 24 h and was considered as a very useful tool to examine therapeutic gene silencing in real time. Very recently the similar methodology was successfully applied for quantitative evaluation of release of Dox from the mesoporous silica coating of UCNPs, providing a way to optimize the nanocomplex design for better pharmacokinetics and improved treatment outcome [262].

The principal possibility of in vivo imaging of drug delivery was first confirmed with use of $\text{Gd}_2\text{O}_3\text{:Yb,Er}$ hollow spheres loaded with anti-inflammatory drug ibuprofen. The authors show multimodal (upconversion PL/ MRI) imaging of the UCNPs distribution in mice after subcutaneous injections, while the drug release from analyzed spectroscopically [263]. Later, hollow nanorattles consisted of $\text{NaYF}_4\text{:Yb,Er}$ and containing IONPs were loaded with Dox and injected into tail vein of tumor xenograft bearing nude mice [264]. In this study the delivery of the drug-loaded nanocomplexes to the tumor was confirmed by upconversion PL imaging for the conditions of passive accumulation following the enhanced permeability and retention (EPR) effect and for active targeting by magnetic field. Free Dox injected at the concentrations of 1 and 2 mg/kg of the animal body weight resulted in reduction of the tumor volume for 35 and 53%, respectively. The passively deposited nanocomplexes with Dox, induced 1.4-1.6 time more reduction of the tumor size, while under magnetic targeting their application ended in 96% tumor volume shortage for the lowest loaded dose of Dox (1 mg/kg).

2.2.1.4.2. Light-controlled drug release

Another important strength of UCNPs as drug delivery carriers is the possibility to improve the pharmacokinetics of the drugs by the influence on their biodistribution (and accumulation in the diseased site) and on the drug release parameters. It can be performed by improved passive and active targeting combined with *the light-controlled drug/gene release* employing the UCNP-based *photocaging* or other UV-sensitive systems. Following the featured ability of UCNPs to absorb NIR irradiation and convert the energy into UV light, these nanomaterials can serve for triggering of cleavage of the photoactivable compounds [265, 266] linking the vehicle and the drug/gene loaded into it. Light is easy to manipulate and focus, and NIR triggering avoids the major drawbacks of more conventional light-activated drug releasing systems based on use of ultraviolet (UV) emission because of deeper penetration depth of the NIR light in the body and absence of photodamage of tissues [267, 268] (Figure 2.19).

The original scheme of NIR-triggered release of the caged compounds from UCNP-based nanocomplexes included core-shell $\text{NaYF}_4\text{:Yb,Tm@NaYF}_4$ and 3',5'-di(carboxymethoxy)benzoic

acetate (3,5-DBA), the compound, which possess the absorption spectra partially overlapping with the emission spectra of UCNP ($\lambda=290$ nm). Under UV excitation produced as the emission PL by UCNP, 3',5'-DCMBA converts into 5,7-di(carboxymethoxy)-2-phenylbenzo(*b*)furan (5,7-DCM-2-PBF) and acetic acid. Later other materials to form photo-triggered cages were proposed, for example, poly(ethylene oxide)-block-poly(4,5-dimethoxy-2-nitro-benzyl methacrylate) micelles, absorbing UV light by *o*-nitrobenzyl groups [268] or d-luciferin caged with a 1-(2-nitrophenyl)ethyl group [269].

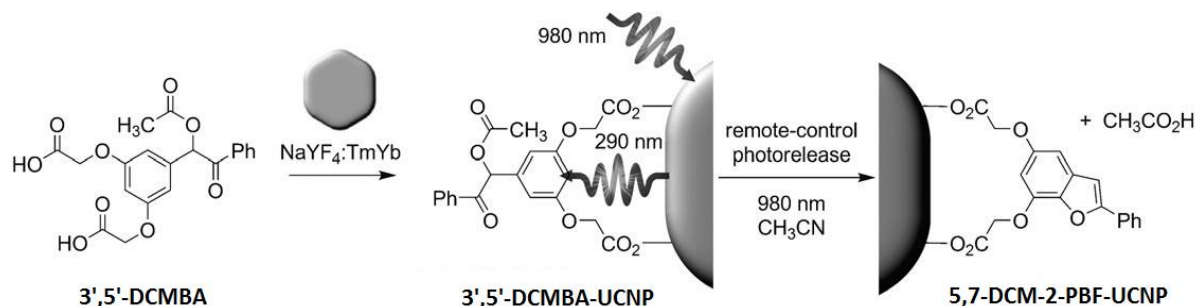


Figure 2.19. Decoration of UCNP with a free benzoin cage, 3',5'-DCMBA results in formation of the remote-control release system 3',5'-DCMBA-UCNP, which can be triggered by NIR light (980 nm) to generate 5,7-DCM-2-PBF-UCNP and release a carboxylic acid. Reproduced from [267] with minor changes.

Next, the cleavage of UV-sensitive covalently bound linkers between the silica-coated UCNP and siRNA under NIR excitation of the nanophosphors was successfully demonstrated by Yang et al. [270] indicating on the possible application of remote light-triggered release for efficient gene silencing in live cells. This method was also used for controlled release of other caged nitric oxide [271] and 2-nitrobenzaldehyde [272]. In order to improve biocompatibility of the nanocomplexes and their TL capacity, the strategy of encapsulation of DNA or siRNA into mesoporous silica shell of NaYF₄:Yb,Tm UCNP with following photoswitchable release of the nucleic acids (NA) from the pore was developed [273]. The effectiveness of the method was confirmed by demonstration of remote control of activation or inhibition of green fluorescent protein (GFP) *in vitro* and in-depth photo-triggered NA release with use of phantom tissue models.

Recently photo-triggered drug release from via upconversion nanocages was shown for the first time in animals [274]. The basic nanostructure was prepared as a core-shell UCNP (NaYF₄:Yb,Tm@NaLuF₄) enclosed into mesoporous silica hollow spheres, and an anticancer drug chlorambucil was caged in the pores and the cavity. To avoid premature release of chlorambucil it was linked to the hydrophobized phototrigger of amino-coumarine derivative. Under NIR laser excitation (980 nm) the phototrigger underwent cleavage, resulting in release of chlorambucil. The nanocomplexes were injected intratumorally into tumor-bearing mice twice, on the 1st and 9th day, and the moderate intensity laser treatment by 980-nm irradiation (50 mW/cm²) has been performed for 20 min each day during 16 days. As a result, the effectiveness of anti-cancer treatment was greatly improved, in comparison to the injections of the free drug in terms of tumor volume reduction. Interestingly, another clinically valuable result was obtained as this method allowed to decrease the frequency of chemotherapeutic injections by the optimized drug delivery kinetics.

Some other promising photo-responsive UCNP-based drug delivery systems are also in the researchers' focus. For example, photosensitive hybrid hydrogel loaded with UCNP can be used for remotely triggered by NIR light release of biomacromolecules, resulting from the photo-induced gel-sol transition [275]. This type of drug delivery devices attracts great attention for local tumor therapy and regenerative medicine purposes.

2.2.1.4.3. Photodynamic therapy

One of the most advanced area of nanotheranostic applications of UNCPs, also based on the mechanisms of energy transfer from the particles to the therapeutic effectors, is the upconversion photodynamic therapy (PDT). Ideally, PDT represents a non-invasive, highly specific and localized treatment option for treatment of cancers of skin, lungs, brain, head and neck, pancreas, intraperitoneal cavity, breast, and prostate [276]. Recently the new options like PDT of recalcitrant wounds and microbial infections were proposed as well [277, 278]. The basic scheme of conventional PDT assumes application of a special light-sensitive compound, the photosensitizer (PS), to the diseased (e.g., tumor) site and activation of the PS by external to the tissues visible or UV light (the most commonly, the red spectra range), which results in generation of reactive oxygen species, able to damage malignant or microbial cells and induce tumor regression or accelerate wound healing. The main mechanism of PDT relying on direct cellular damage by singlet oxygen ($^1\text{O}_2$) is added by vascular shutdown and activation of cellular immune response by attraction of the inflammatory cells [279].

Despite the fact that PDT provides numerous advantages to avoid systemic side effects of conventional chemo- and radiotherapy of cancer, it still has several significant shortages. The first one stems from the unsatisfactory efficiency of PS activation by red light following intensive absorption and scattering of these wavelengths in tissues. This also leads to the limitations of the depth of localizations of the tumors available for the PDT up to several mm. Upconversion nanomaterials are especially useful in overcoming the major limitations of the conventional PDT. UCNP can be loaded with various types of PSs and. At the same time, they can work as transducers converting the energy of deep-penetrating NIR light into visible or UV emission, which can be absorbed by the attached PSs. Tunability of upconversion PL of UCNP allows to create the most efficient combinations of particles and PSs for NIR-triggered PDT.

The pioneering work of Scholfield et al. [280] provided the first proof of the concept of UCNP-based PDT. This group demonstrated effective killing of breast and bladder cancer cells *in vitro* with use of core-shell $\text{NaYF}_4:\text{Yb,Er}@ \text{SiO}_2$ nanoparticles coated with dense silica with incorporated PS merocyanine 540 and bioconjugated with targeting antibodies. Later, PEGylated UCNP loaded with chlorine e6 (Ce6) were successfully applied in animals. Using intratumoral injections of the nanocomplexes, Liu and co-authors [110] verified strong tumor eradication effect and prolonged survival time of mice after PDT treatment (Figure 2.20). They also confirmed the effectiveness of NIR

excitation for increasing of the tissue depths available for the therapy. Next, the first systemic administration of PEGylated NaYF₄:Yb,Er@NaGdF₄ core-shell complexes with Ce6 was shown [281]. In this study a dual-modal imaging (MRI and upconversion PL) was used to confirm the accumulation of the NTA in the tumors, occurred passively following EPR effect. As a result of PDT the tumor growth was dramatically inhibited.

The main trends in development of UCNP-based PDT are centred around the choice of optimal PS or PS combination, the method of integration of the PS with the nanoparticle, and the ways to enhance the therapeutic effects in general [238]. In particular, several PSs attract the major attention of the researchers, including the compounds activated by red light such as zinc (II) phthalocyanine (ZnPc) [282-287], Ce6 [288-291], methylene blue (MB) [292, 293], Rose Bengal (RB) [294-296]. Recently, the PSs excitable by UV light were applied for UCNP-based PDT, like ZnO [297] and TiO₂ [298, 299] as well as the PS with double maximums of absorption like hyaluronated fullerene, activated at wavelengths of 475 and 650 nm [300], or combinations of different PSs, like MC540 and ZnPc [301]. Various approaches were proposed to integrate PSs and UCNPs. The first published schemes relied on inclusion of the PSs into dense silica coatings of UCNPs [280], but this approach suffered from impaired diffusion of oxygen from the environment through of non-porous silica to the PS, decreasing the release of reactive oxygen species (ROS) and the efficiency of PDT as a whole [238]. In order to bypass this limitation, Chatterjee et al. [111] and Lim et al. [302]. used polyethylenimine (PEI) coating of UCNPs to link the ZnPc. However, the PS loading capacity and the stability of the complexes were relatively low, while the potential cytotoxicity of PEI also limited the feasibility of this methodology for PDT [238]. In other work meso-tetraphenylporphine (TPP) photosensitizer was stabilized on the surface of UCNPs by biocompatible PEG-*block*-(DL) lactic acid block copolymers [303] or by covalent bonding [304]. Nevertheless, these approaches do not provide a reliable way to control optimum ratio between PS and UCNP and release kinetics [238]. A growing use of mesoporous silica [301, 305-309] as the optimized material to develop biocompatible and stable nanocomplexes of UCNPs with PSs, probably, indicates on the great potential of this method for upconversion PDT.

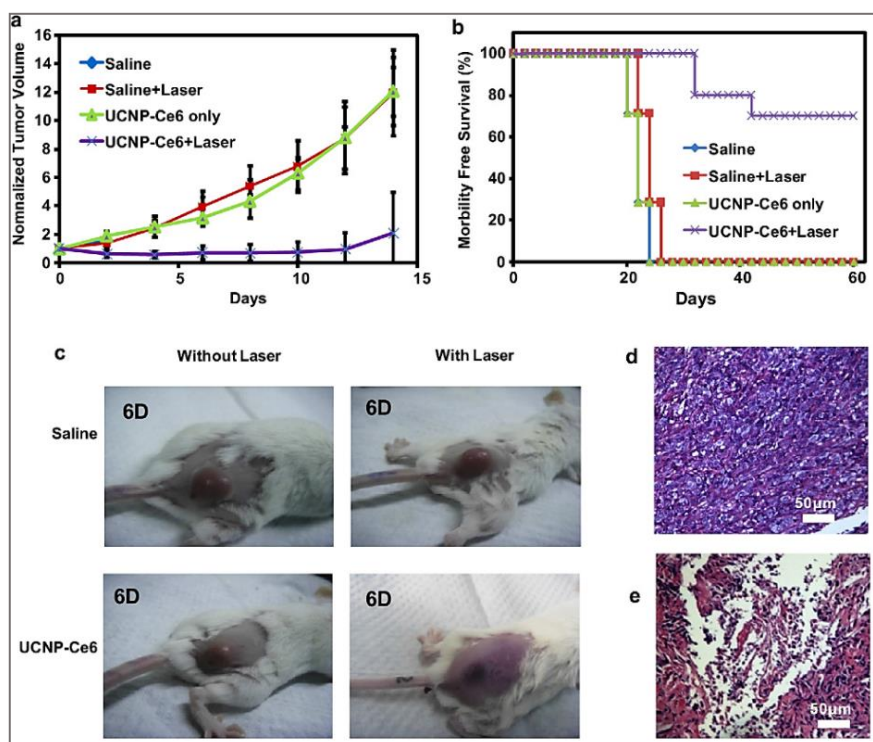


Figure 2.20. The effect of UCNP-based PDT in tumor-bearing mice vivo. (a) The effect of PDT on the tumors' volume, normalized to the initial size of the lesions. (b) The survival curves of mice in 60 days after PDT and control treatments. (c) Photos of mice on the 6th day after various treatments. (d and e) Histological structure of an untreated tumor (d) and a tumor on the 6th day after PDT (e). Note changed cell-matrix ratio, large cell-less necrotic areas and tumor tissue decay in (e). Hematoxylin and eosin staining. (e). Error bars represent variation in 10 mice per group. Reproduced from [110] with minor changes.

Other notable innovations in the field of UCNP-based PDT include development of pH-sensitive NTAs [203] for better cellular uptake under acidic conditions, which are specific for malignancies; co-loading of PS and chemotherapeutic drugs [310] to increase the efficiency of the treatment of chemotherapy-resistant cell populations, and targeting of the nanocomplexes for specific receptors of cancer cells [111, 301, 311] for tumor-specific PDT.

Photothermal therapy represents another direction of the evolution of UCNPs as nanotheranostic systems, employing the ability of several metals and metal oxides like Au, Ag, Pt and CuS nanoparticles and some organic dyes [173], to generate heat following absorption of light. This allows to increase the effectiveness of anti-cancer therapy. One of the most advanced examples of UCNP-based PTT was recently provided by Zhu and co-authors [312]. The nanocomplex was fabricated on the base of core-shell UCNPs, $\text{NaGdF}_4\text{:Yb,Nd@NaGdF}_4\text{:Yb,Er@NaGdF}_4$, covalently bound with RB and a platinum prodrug Pt(IV). Visible light emitted by UCNPs under NIR excitation was absorbed by RB to generate singlet oxygen. At the same time the NTA was able to deliver Pt (IV) into cancer cells (Figure 2.21). The authors rigorously proved all the mentioned principal events and demonstrated significantly enhanced anti-cancer therapeutic efficiency of the proposed nanoplatforms. The results of the study pave the way to obtain better outcomes in treatment of cisplatin-resistant ovarian-cancer.

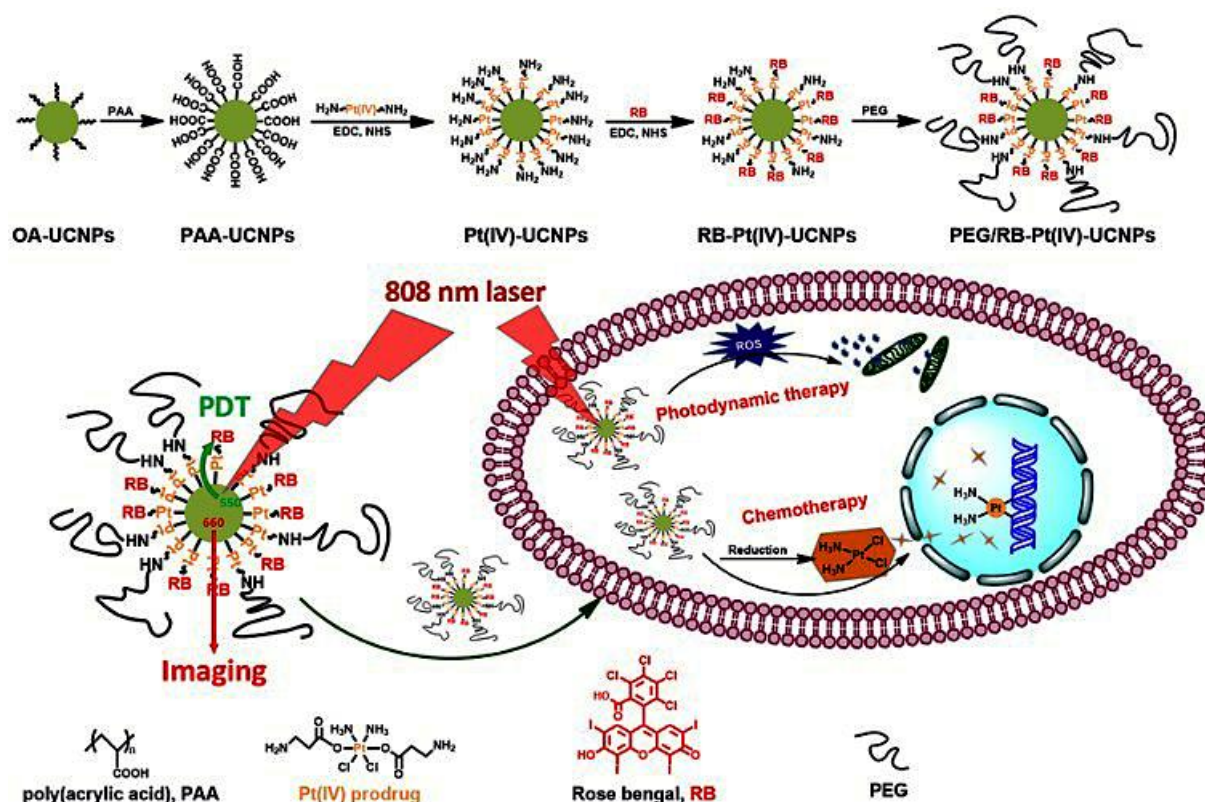


Figure 2.21. Scheme of combined PDT, PTT and upconverting PL imaging with use of UCNP-based nanoplatforms. Such type of NTAs can provide an effective treatment for cisplatin-resistant cancer cells. Reproduced from [312].

2.3. Mesoporous silica nanoparticles for nanotheranostics

2.3.1. Definitions, synthesis and post-synthetic modifications of mesoporous silica nanoparticles

Mesoporous silica nanoparticles (MSNPs) are defined as particulate SiO₂ materials of nanoscale size, having a specific porous structure with the diameter of pores from 2 to 50 nm, corresponding to the term “meso-“, in contrast to the “micro-“ (<2 nm) and the “macroporous” (>50 nm) systems [313]. Despite the fact that MSNPs on their own do not absorb or emit any type of irradiation in the spectral ranges used in biomedicine, these particles represent one of the most promising nanomaterials, in particular useful for theranostic applications as a universal and highly versatile vehicle for drugs, contrast agents, nanostructures and other effectors and sensing probes [61, 314-321]. The most important advantages of MSNPs include huge surface area (~ 700-1500 m²/g), the great loading capacity resulted from the large pore volume (>0.9 cm³/g), tunability of their size (10-1000 nm), shape and pores' diameter (2-30 nm), as well as the flexibility in terms of surface modification of exterior and interior of the particles. In combination with relatively cheap and easy mass production these properties favour biomedical use of MSNPs [314-316, 322, 323].

The first samples of mesoporous silica (mSiO₂) with fully opened pores possessing a specified narrow size distribution between 2 and 10 nm, were synthesized for the catalyst applications by the

researchers from Mobile Oil Corporation [313] and later have become known as a family of Mobile Crystalline Materials, or MCM, including the most investigated 2D hexagonal MCM-41 (Figure 2.22 (a, b)), 3D cubic MCM-48, and lamellar MCM-50. After that a number of other mesoporous silica ($mSiO_2$) materials have been developed by virtue of modifications of the templates and the conditions of the reaction, for example the widely used SBA-15 (Santa Barbara Amorphous-15) [324]. In addition, by the modification of the synthetic methods, other nanomaterials may be introduced into the MSNPs (Figure 2.22 (c, d)) to enhance their functionality.

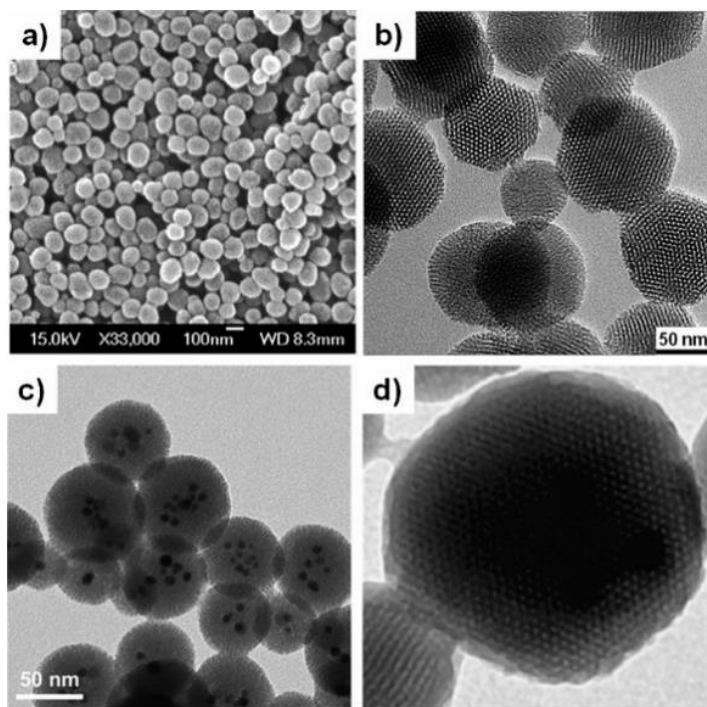


Figure 2.22. SEM and TEM images of MCM-41 nanoparticles. (a) SEM and (b) TEM images of pure MCM-41 nanoparticles. (c) MCM-41 MSNPs with incorporated iron oxide and silver nanoparticles; (d) MCM-41 with encapsulated Zn-doped iron oxide nanoparticles. Reproduced from [325].

The original synthetic procedure for MCM was based on formation of amorphous silica walls around the assemblies of micelles of amphiphilic surfactant such as cetyltrimethylammonium bromide ($C_{16}H_{33}N(CH_3)_3Br$, CTAB), acting as a template, and followed by removal of this template by calcination (high temperature treatment) (Figure 2.23).

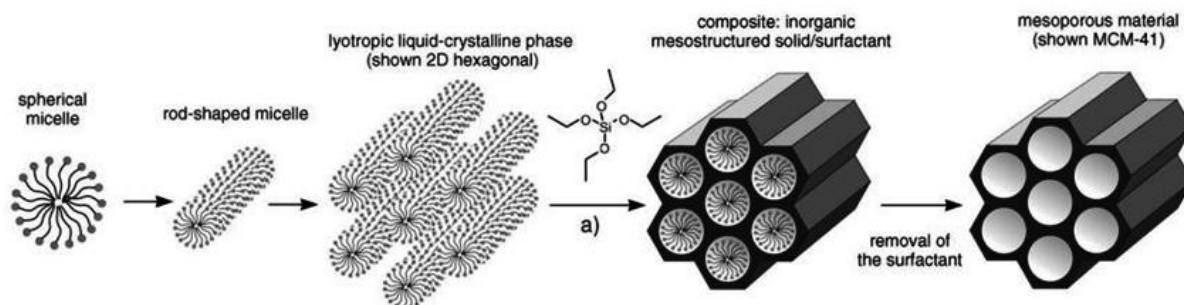
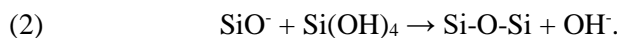
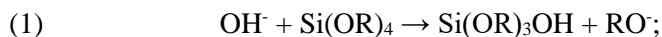


Figure 2.23. The schematic view of the synthetic procedure used for fabrication of MSNPs. Reproduced from [326].

Next, a variety of synthetic approaches was proposed, but essentially all of them require a source of silica, a surfactant, a catalyst of basic or acid nature and a solvent (usually, water or ethanol) and rely on catalyst-mediated consequence of hydrolysis (1) and condensation (2) of the organosilane precursors,

contributing to the formation of a sol phase and subsequent condensation of the small sol particles into a gel [325]:



Several sophisticated approaches have been developed for the control and modification of the size and morphology of the pores [313, 327] and the particles as a whole [316, 328]. For example, the shape of the particles may be regulated by the concentration of the template and by tuning of the so called packing parameter g [323], defined as the ratio of the volume of the hydrophobic part of the surfactant (V) and the product of the effective area of the head group at the micelle surface (A) and the kinetic length of the hydrocarbon tail (l): $g = \frac{V}{A \times l}$. For example, the use of single-chain surfactants with large head groups ($g < 1/3$) results in formation of spherical micelles, single-chain surfactants with small head groups ($1/3 < g < 1/2$) give cylindrical micelles, while single-chain surfactants with small head groups, e.g., CTAB special surfactants with large hydrophobic polar head and double-chain surfactants with large head groups and flexible chains ($1/2 < g < 2/3$) help to produce 3D cylindrical micelles [323] (see Figure 2.22). Besides the conventional MSNPs various special morphologies of the particles also can be developed by the modification of the basic sol-gel surfactant template mechanism. For example, recently the methods to prepare hollow and rattle types of MSNPs were proposed [318] (Figure 2.24). These types of MSNPs allow to obtain the large volume of interstitial hollow space in combination with mesoporous shell, which can be used for highly efficient loading of therapeutic or diagnostic components, including combinations of several kinds, including the normally immiscible, compounds to get extraordinary multifunctional nanotheranostic complexes [318].

In order to introduce functional groups and allow development of the advanced mechanized pore-opening mechanisms, the external and internal surfaces of MSNPs can be functionalized as during the synthetic process (co-condensation method), as after the particles have been formed (post-synthetic modifications) [325]. In co-condensation methods the organic structures are added in the form of silanes, and then covalently bound to the structural framework of the particles [329]. By the post-synthetic treatment, the functional ligands can be added, for example, with use of electrostatic interactions between anionic MSNPs surfaces and cationic molecules like PEI to get the possibility of the delivery of the particles to the cell nuclei [330, 331].

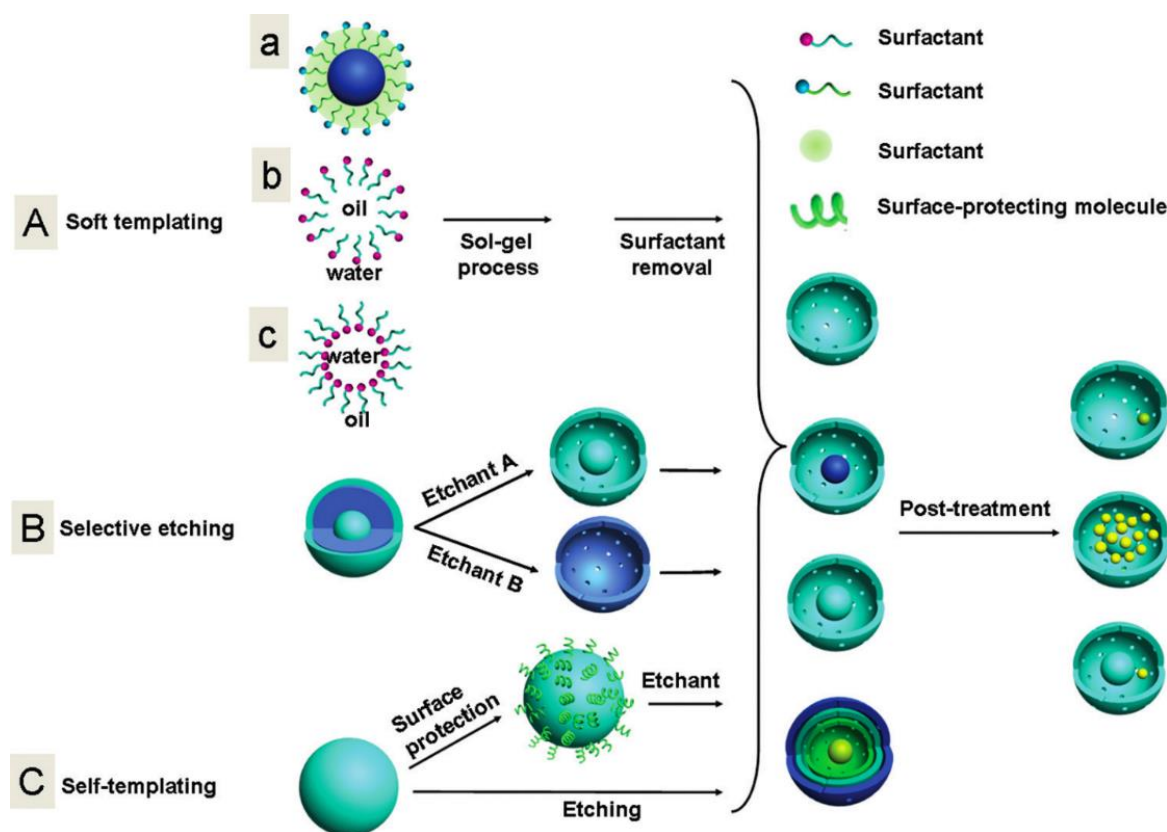


Figure 2.24. The artistic representation of the methods for the synthesis of hollow/rattle-type mesoporous silica nanoparticles. (A) The basic soft templating method with using of different soft templates (a-c); (B) selective etching procedure, and (C) self-templating method. Reproduced from [318].

Loading of the different types of drugs and other molecules into the pores and cavities of the MSNPs may be performed by soaking of the particles in the cargo molecule solutions, resulting in the absorption of the payloads on the particles' surfaces. Because of that the loading capacity of MSNPs is correlated with the available surface areas [332]. In order to facilitate the controllable release of the cargo molecules from MSNPs the modifications, involving electrostatic and hydrogen bonding between the loads and the nanoparticles may be employed [325]. However, the nature of the loaded molecules has own strong effect on release kinetics. Generally, the hydrophilic drugs or other hydrophilic molecules are easily released from MSNPs in water-based solutions, while the hydrophobic loads are escaping the particles in a case of contact with the matter of hydrophobic nature like, for example the lipids of cellular membranes [333]. Then, the additional measures are needed to control the drug release or, in contrast, preservation of the diagnostic probes in the MSNPs to keep the advantages provided by the delivery of the materials by the nanoagents. In particular, a number of MNSP-based mechanical systems to control the pores' opening were suggested as well as the approaches for the triggering of the release by various physical stimuli. For example, the breakability of the covalent bonds between molecules attached within the pore channels, shrinking and swelling of polymer surface coatings, attachment and removal of bulky compounds (including nanocrystals) over the pore openings may be employed as well as a number of

other schemes [325]. Development of various nanomachines (nano-valves, nano-pistons, nano-impellers, nano-lids, snap-top systems etc.) [325, 334, 335] for the pore-gatekeeping purposes on the base of MSNPs is also a very hot research topic [336, 337]. The release of the cargo molecules from MSNPs may be controlled additionally by triggering mechanisms. In particular, the feasibility of light-triggered [338, 339], pH-dependent [334, 335, 340], magnetically-driven [341] MSNP-based drug release systems was demonstrated.

2.3.2. Mesoporous silica nanoparticles as theranostic agents

By virtue of the extraordinarily large active surface area and internal volume, the mSiO₂ structures may be used as almost universal building blocks (both as the core and shell components of the nanocompounds), allowing integration with various functional components like magnetic materials, fluorescent dyes, upconverting nanoparticles, drugs and many others. The resultant nanocomposites then can be applied as theranostic agents, combining the functionality to provide treatment and diagnostics in the same nanoparticle [342]. A wealth of information about the preparation and feasibility validation of MSNP-based NTA is available now [337, 343-346]. In the context of the current work, only a few the examples of the most sophisticated drug-delivery systems and MSNP-UCNPs theranostic composites will be considered below.

A unique complex addressing a number of challenges of modern anti-cancer chemotherapy has been demonstrated recently the group of N. Khashab [347], who not only successfully loaded MSNPs with two drugs, gemcitabine (GEM) and doxorubicin (DOX), taken at unprecedented high therapeutic concentrations, 40wt% and 32wt%, respectively, but also proposed the strategy to control the drug release and to prevent premature burst increase of the drug concentrations. Using the high doses of the drugs with different mechanisms of action in combination with the controllable release, the authors of this study achieved the selective delivery of the cargo to the tumor by the nanoparticles and provided the way to avoid the development of drug resistance usually emerged as a result of single-medicine treatment of tumors. The surfaces of MSNPs were functionalized with positively charged amine groups, and then GEM was loaded into the pores and bound to NH³⁺ ligands. The gold clusters coated with bovine serum albumin (AuNC@BSA) were engineered on the surface of MSNPs to realize pH-sensitive pore gatekeeping mechanism. Finally, DOX was also bound with the AuNC@BSA nanogates. Gold nanoclusters coated with biocompatible proteins are well-known photostable imaging agents with long fluorescence lifetime, having an intense red-NIR emission and two photon excitation. This allowed to detect the accumulation of the theranostic nanocomposites both *in vitro* and *in vivo* (Figure 2.25).

In addition, this work shows the methodology allowing to circumvent the surface-charge related challenges, earlier demonstrated for the loading of DOX into amine-functionalized MSNPs [348].

Mesoporous silica is a popular material for creation of core-shell structures in combination with UCNPs. For example, tri-modal synergetic therapy in one single nanotheranostic system was developed

as Gd-UCNPs core/mesoporous silica shell nanotheranostics (UCMSNs) for the co-delivery of a radio-/photo-sensitizer hematoporphyrin (HP) and a radiosensitizer/chemotherapeutic drug docetaxel (Dtxl) [309]. In this work the synergetic chemo-/radio-/photodynamic tri-modal therapy resulted in complete tumor elimination under near infrared (NIR) and X-ray irradiation. The treatment course was observed with simultaneous bimodal magnetic/upconversion luminescent (MR/UCL) imaging.

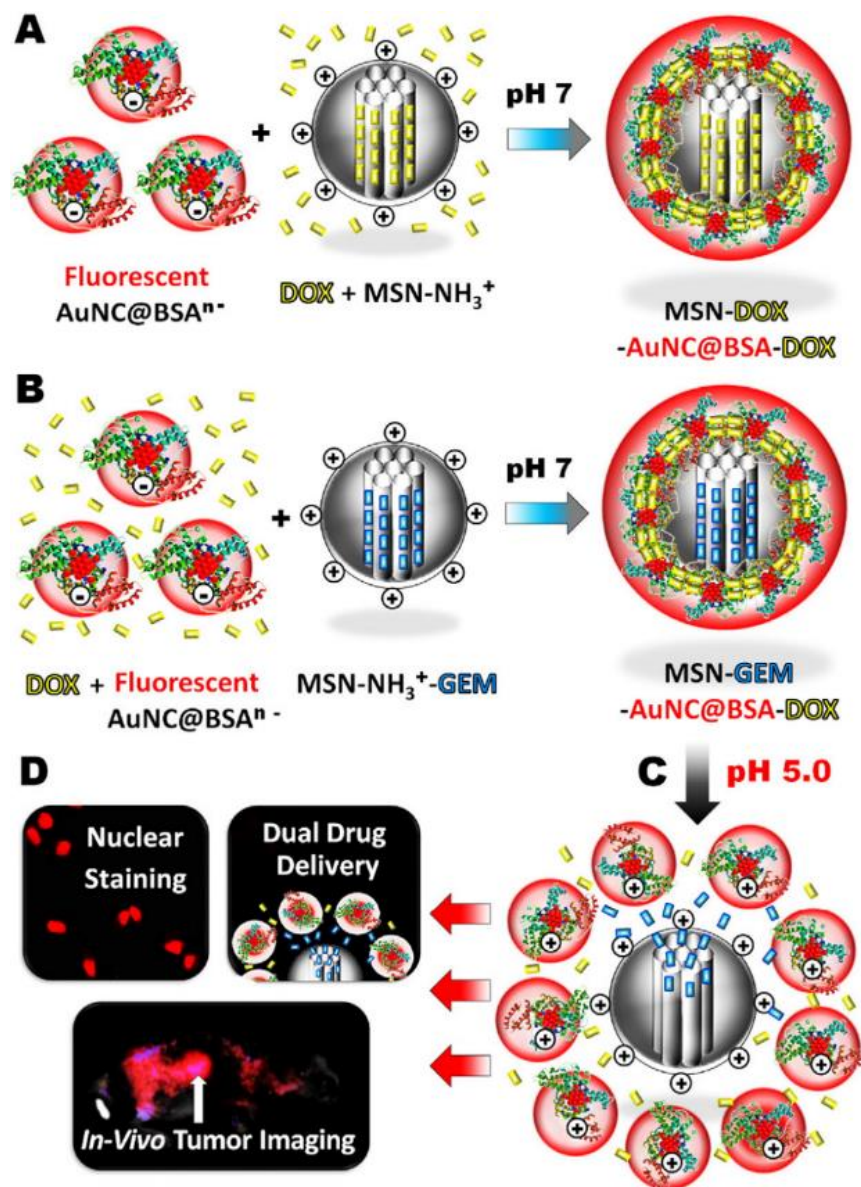


Figure 2.25. The schematic view of the strategies for development of multifunctional dual-drug loaded nanocarriers on the base of MSNPs for cancer treatment and imaging. (A) Single drug loading. Self-assembly of fluorescent anionic AuNC@BSA with positively charged DOX-loaded MSNP-NH₃⁺ results in formation of MSNP-DOX-AuNC@BSA. (B) Dual drug loading. Self-assembly of fluorescent anionic AuNC@BSA and DOX with cationic charged GEM-loaded MSNP-NH₃⁺ results in MSNP-GEM-AuNC@BSA-DOX. (C) This complex can be cleaved under acidic pH environment. (D) Applications of multifunctional dual drug-loaded MSNP-GEM-AuNC@BSA-DOX nanocarriers. Abbreviation: MSN=MSNP. Reproduced from [347].

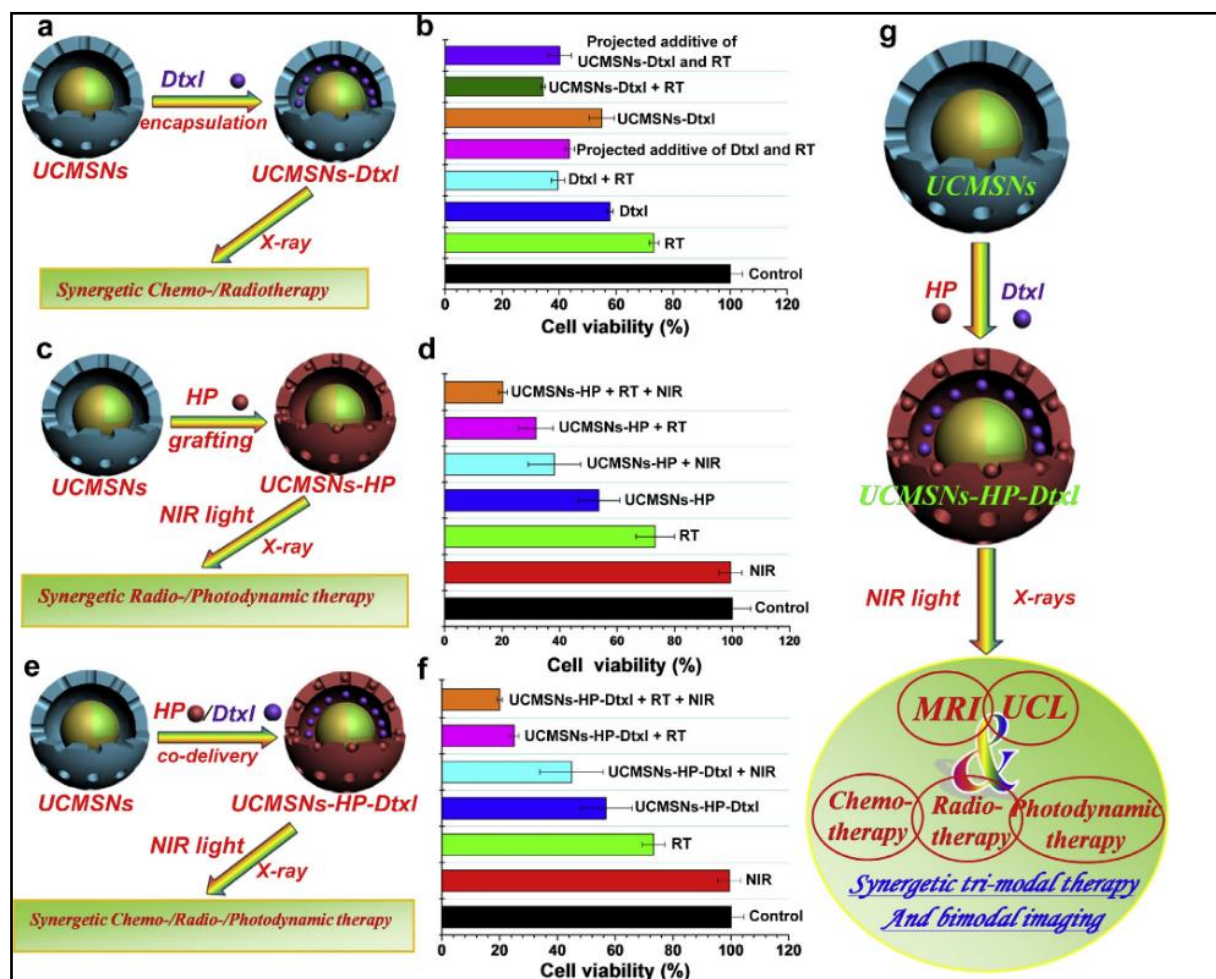


Figure 2.26. Schematic view of the validation of the UCMSN nanotheranostic platform performed on in vitro cultures of HeLa cells. Formation of the particles of different composition (a, c, e, g) and the synergetic effects on viability of cells achieved by (b) chemo/radiotherapy; (d) radio-/photodynamic therapy; (f) chemo-/radio-/photodynamic therapy. The projected additive cell viability of the corresponding synergetic therapy was calculated by multiplying the cell viability of one treatment by the cell viability of the other. (g) Schematic diagram of UCMSNs-HP-Dtxl of formation of the particles, synergetic chemo-/radio-/photodynamic tri-modal therapy and magnetic/upconversion photoluminescence (MR/UCL) bimodal imaging upon NIR excitation (980 nm) and X-ray irradiation.

Tissue engineering is a novel sphere of application of theranostic potential of MSNPs. A concept proof of the idea of smart porous tissue engineering scaffolds, equipped with capped MSNPs was demonstrated by N. Mas and co-authors [349]. Such type of scaffolds may be employed as implantable drug delivery systems for sustainable and controllable drug release and contrasting purposes. In the cited work the pores of MCM-41 were capped with adenosine triphosphate (ATP) mixed with 3-(2-(2-aminoethylamino)ethylamino)propyl-trimethoxy silane. In presence of ATPase the caps can be hydrolysed to release the compounds loaded into the MSNPs. The capped MSNPs were bound to the gelatine matrix to result in biocompatible porous scaffold, supporting the cell growth.

Finally, it should be emphasized that MSNPs are generally considered as bioinert and highly biocompatible particles. However, the detailed studies on this issue with special focus on surface

modifications of the particles are very important as the recent reports indicate potential cyto-, histo- and organ-specific toxicity of these particles [350, 351].

2.4. Conclusion

In this chapter, the principles of nanotheranostics were considered, as well the fundamentals and recent advances in the fields of two major contributors to this emerging discipline, including photoluminescent nanomaterials and mesoporous silica nanoparticles. The development of NTAs is on its way from research laboratories to clinics with strong translational incentives. However, a number of questions are still unaddressed. The better understanding of the interactions of NTAs with biological environment is critically important. In particular, the main body of the data available at the moment has been obtained in the experiments performed on conventional monolayer cell cultures *in vitro*, while the tissue, organ and body levels as the operational fields of the nanomaterials are much less studied. The special attention should be placed on rational design of the nanotheranostic materials for meaningful and safe use of the nanomaterials in the real body context. In the next chapter these challenging questions will be addressed.

Three-dimensional *in vitro* models for nanotheranostics research

This chapter is focused on modern understanding and modelling of the interactions of nanotheranostics materials with biological environment of human or animal organisms, where NTAs are at the core. I begin with a review of nano-bio interfaces from single cells to whole organisms, followed by an overview of major body biological barriers in the transport and biodistribution of nanomaterials. Next, three-dimensional (3D) tissue culture and tissue engineering fundamentals are presented with regard to realistic biomimetic models, where exogenous nanomaterials meet biological systems. Finally, analysis of the state-of-the-art applications of 3D biomimetic *in vitro* models of skin and malignant tumors for nanobiotechnology and nanomedicine are presented.

3.1. Biological operational environment of nanotheranostics agents

As it was discussed in the Chapter 2, nanoscale materials have a number of unique properties, making them especially attractive for biomedical research and clinical applications. However, contacting with the living matter, the artificial nanostructures appear as xenobiotics. As a result of absence of specialized evolutionary developed mechanisms of reaction on this challenge, and in an effort to response, the body should involve a spectra of actions, which finally can facilitate or improve the biological functions or able to initiate various dangerous changes up to fatal damage, sacrificing a certain biological element for the name of more general survival priorities.

3.1.1. Putting nanomaterials into the real tissue and body context: the general scale of the landscape

Any possibility of direct interaction between nanomaterials and biological objects requires matching of their physical scales. Considering the fact that the size of nanomaterials is usually referred as at least one of the dimensions lying in the range between 1 and 100 nm [2], it's worth to mention that this definition is relatively conditional, because of high variation of the properties of the nanoparticles, resulting from intentional changes by synthetic procedures and post-synthetic modifications, agglomeration and sedimentation of the particles in biological liquids and biologically-induced alterations of xenogeneic nanoscale structures such as protein corona formation, phase transitions, restructuring or dissolution [352]. Following this, an “average” nanoparticle can be measured as a structure of subcellular calibre, having a size varying from that comparable with some biological

macromolecules like DNA to the organelles as large as lysosomes. In general, the mean diameter of nanoparticles is similar to the size of viruses (Figure 3.1).

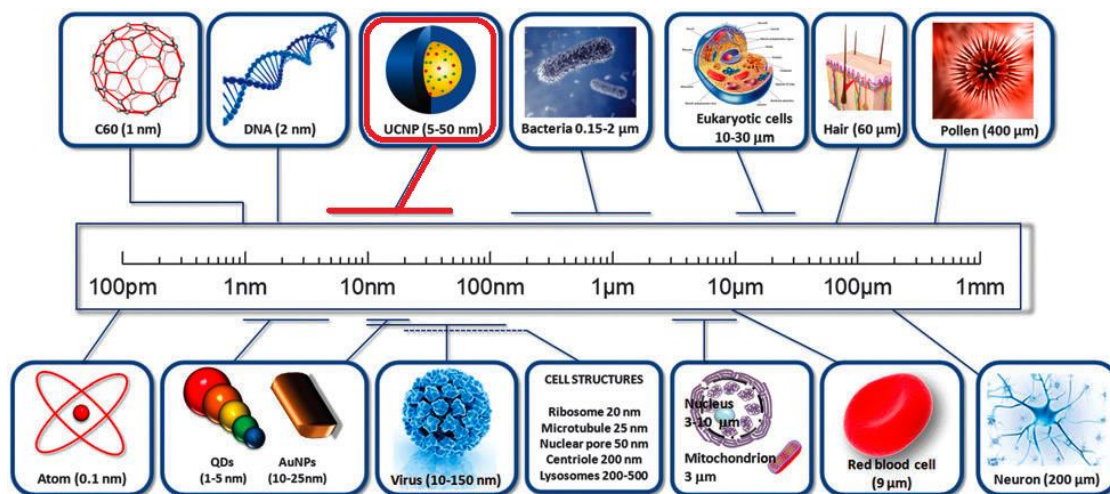
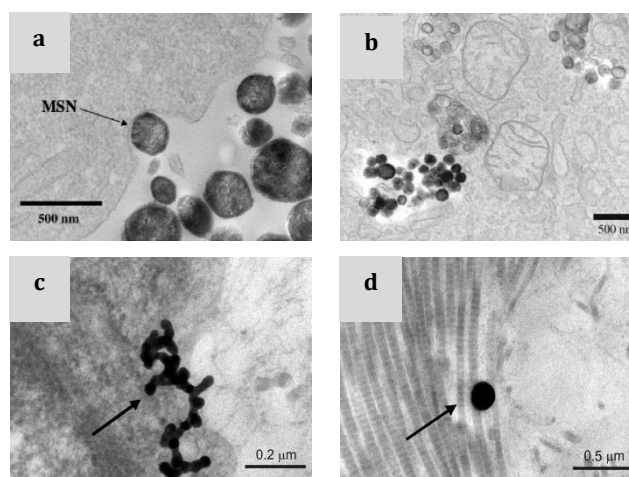


Figure 3.1. Scale considerations for nanoparticles referred to biologically relevant compounds. The average size of lanthanide-doped UCNPs is shown as an example. Reproduced from [220].

Following the indicated interrelationship, the main and the most common contact points, involved into interaction of nanomaterials with cells and subcellular components are the lipid bilayer membranes of the cells and, in a case of permeation into the cells, the membranes of the cytoplasmic organelles (Figure 3.2 (a, b)) [353]. The only exception inside the cells, probably, is presented by cytoskeleton, which can be directly approached by nanomaterials (Figure 3.2 (c)). Outside the cells, nanoparticles can encounter with the components of extracellular matrix (ECM), such as collagen fibres and fibrils, elastic fibres, fibronectin, fibrin, laminin and other glycoproteins, glycosaminoglycans and proteoglycans. For example, the mean average size of a nanoparticle is close to the diameter of fibrils of collagen type I, the most usual constitutional component of ECM of skin, tendons and ligaments, fibrous cartilage etc., ranges between 10 nm to several hundred nm [354] (Figure 3.2 (d)). In addition, depending on the type of tissue and its functional state, the intercellular spaces of different volume can be available for accumulation or permeation of nanoparticles. Nanomaterials also interact with liquid biological mediums like blood, lymph, interstitial and synovial fluid.

Figure 3.2. The interactions between nanoparticles and cells shown by TEM. (a) MSNPs entering a HeLa cell. Note the invagination of the cellular membrane at the site of contact. (b) Accumulation of MSNPs in a cytoplasmic vesicle of a HeLa cell. Two cross-sections of mitochondria are visible on the right. (c) An aggregate of TiO₂ nanoparticles in porcine epidermis is surrounded with fine mesh of cytoskeleton filaments. (d) A gold nanoshells in porcine dermis among collagen fibres. The arrows indicate nanoparticles. (a, b) Reproduced from [314] and (c, d) reproduced from [355] with minor changes.



The interactions at nano-bio interfaces, most significant for biomedical applications of nanomaterials are considered in the next subsections.

3.1.2. Interaction of nanoparticles with cells

3.1.2.1. Internalization, intracellular trafficking and exocytosis of the nanoparticles

The majority of nanotheranostic applications require entering of the nanoparticles into the cell and its certain organelles in order to trigger the expected effects or labelling of a specific target. This process is known as cellular uptake, or internalization of the nanomaterials and always requires the nanoparticle to cross outer plasma membrane of the cell as well as the membranes of the organelles. Plasma membrane is a natural border of mammalian cells, composed by lipid bilayer with the patched inclusions of proteins and sugars. It surrounds the cell as a whole and has a defence and metabolic-regulating function, preserving the homeostasis of the cell by controlling the molecular and ion exchange between the cell and its microenvironment. In addition, the cytoplasmic organelles are pocketed by the membranes of a similar structure. The small molecules like O₂ and some non-polar compounds can permeate the membrane passively, by diffusion. In contrast, if an inorganic nanoparticle encountered the outer cell membrane (the mechanisms responsible for the probability of this event will be discussed below), it can cross this barrier by two alternative strategies, such as the entrance by pore formation and the endocytosis [356]. The first one relies on formation of pores in the lipid bilayers and could be damaging to the cells because of destroying of the intracellular ionic and macromolecular balance. This way is employed by cationic nanoparticles, some needle-shaped material and small metal clusters [356], and usually results in notable cytotoxicity, up to the cellular death [357]. Other types of artificial materials can enter the cells by endocytosis [356], emerging in the forms of phagocytosis or pinocytosis, e.g. clathrin- and caveolin-mediated endocytosis [358] (Figure 3.3) and involving enclosure of the particles into a fold of outer cell membrane with subsequent formation of the vesicles, having their own membranes, and trafficking of these vesicles into the cell [359].

As the nanoparticles become entrapped in these vesicles, they cannot immediately reach the structures in cytosol [356, 358, 360], and this obstacle is still one of the main bottlenecks of the efficient nanodrugs and nanoprobe delivery [356]. Depending on uptake pathway, the endocytic vesicles may evolve into early endosomes to endolysosomes through the harsh acidification of the content, which may result in degradation of the internalized materials, like it happens for clathrin-mediated endocytosis, or avoid acidification and follow trafficking to the Golgi complex or to transcytosis (caveolin-mediated endocytosis). In a case of macropinocytosis the early endosomes may fuse back to the cellular membrane or transform into late endosomes and endolysosomes [359]. The release of the particles from the endosomes may naturally occur following the destabilization of the membranes and pore formation or may be intentionally induced by some fusion factors, like, for example, fusogenic peptides naturally observed in viruses, which can be attached to the surface of the nanomaterial (for the review see [360]).

In turn, the structure and composition of the nanoparticles taken via endocytosis can be changed before their release into the cytosol following the enzymatic activity and decreased pH. This may also lead to various effects, including the unpredictable, outcomes of the action of the products of the nanoparticles degradation on cells.

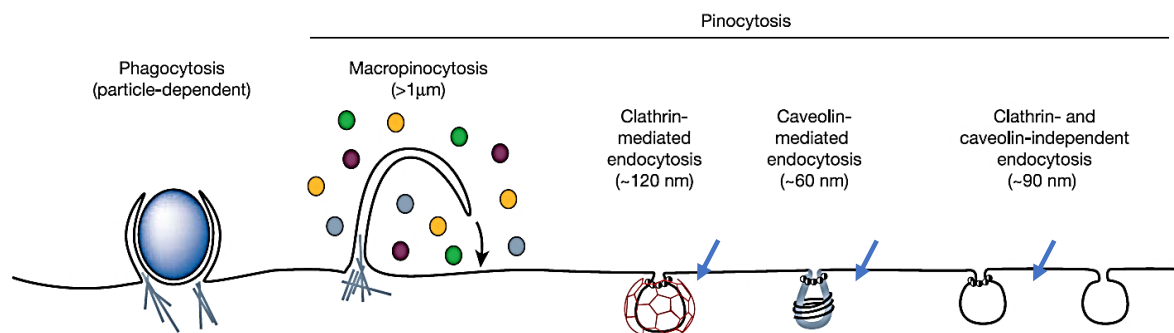


Figure 3.3. The mechanisms of endocytic uptake in mammalian cells. The type of the uptake pathways depends on the nature of cargo (large fragments of solid materials like bacteria, or collagen fibres for phagocytosis and the fluids, possibly containing dispersed material like ligands, lipids and receptors for pinocytosis), the size and mechanism of formation of endosomal vesicle. Phagocytosis is limited to the special cell types only (macrophages and some others). Macropinocytosis is non-selective uptake of large portions of extracellular liquid with the dispersed material by formation of the membrane protrusions. This process is dependent on actin-filaments polymerization. Clathrin-mediated endocytosis is a process of internalization of the receptor-bind ligands, macromolecular and nanosized materials, which relies on formation of a temporary membrane pit (approximately 100 nm in diameter) coated from the internal side of the cell membrane with a framing cytosol lattice-like protein, the clathrin (shown in red). Caveolin-mediated endocytosis is a receptor-independent internalization pathway. Caveolin as a scaffolding protein assembling in the cytoplasm, binding to membrane cholesterol rafts and able to concentrate locally the certain classes of signalling molecules with forming of small concave membrane pits called caveolae ($\approx 60\text{--}80$ nm). Clathrin- and caveolin-independent endocytosis is a common name for a number of the less frequent or the less studied mechanisms of uptake. Detachment of the endocytic vesicles from the membrane under some pathways may be dependent on contraction protein dynamin, the contraction protein (blue arrows) [359]. Reproduced from [358] with minor changes.

The internalization of the nanomaterials is a dynamic process. Following the enclosure into the endocytic vesicles, the particles can be transported by throughout the cell intracellular motor proteins, dyneins (centripetal) or kinesins (centrifugal) alongside the microtubules of cytoskeleton, finally leading to the exocytosis, or elimination of the particles from the cell, as it has been demonstrated by the elegant experiments with UCNP_s, coated with PEG and incubated with HeLa cells [235].

The balance between the internalization of the nanoparticles and their elimination from the cells may vary in a wide time range, from the whole processing taking several hours [235] to the absence of any notable exocytosis during several days [225]. However, the process of exocytosis is significantly less studied, in comparison with the research of endocytosis [361]. Then, last observation and the similar data [102] should be taken with caution as they were not based on single-cell assays and may demonstrate a sort of cumulative result of specific population kinetics and metabolism of stem cells. In addition, other mechanisms of intracellular trafficking and exocytosis are, probably, employed in a case of the submicron particles (≈ 500 nm), as disruption of microtubules have no effect on it [362]. Some other observations indicate that the size [363] and shape (for review see [361]) of the particles has a strong influence on the rate of the exocytosis (Figure 3.4).

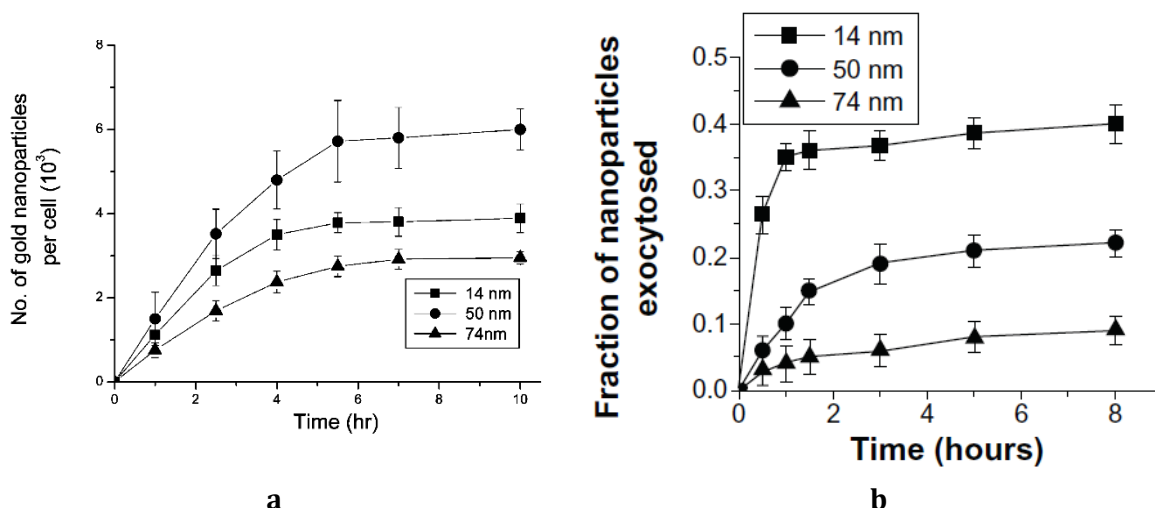


Figure 3.4. Dynamics of endocytosis and exocytosis of gold nanoparticles: the controversial effect of the nanoparticles size. (a) Endocytosis; (b) Exocytosis. The time required for endo- and exocytosis is dependent on competition between the thermodynamic driving force for membrane wrapping and the receptor diffusion kinetics directly (for endocytosis) and inversely (for exocytosis). The 50 nm nanoparticles exhibited the fastest wrapping time, while the smallest nanoparticles had the slowest wrapping time [363]. Reproduced from [364] for (a) and [363] for (b).

The probability, efficiency, the mechanisms and the biological effect of cellular uptake of the nanoagents is strongly influenced by their key physicochemical parameters such as size, shape and the surface properties as well as by the experimental conditions in general, including exposure time, concentration of the particles and the temperature.

3.1.2.2. Effects of the nanoparticles' size

The size of the nanoparticles is one of the most important characteristics, defining their internalization capability, and, as a result, their biological effects. The fundamentals of these significance are originate from the idea of dramatic increase of the particles' surface area, acting as a side in nano-bio interface, along with the reduction of the size. Several concepts were discussed with regard to this. One of the early ideas was that smaller particles can easier enter the cells, retrieved from the comparisons of uptake kinetics of micro- and nanoparticles [365]. Later it became generally accepted that the law linking the size of the particles and the cellular uptake of them is not linear. The data indicating heterogeneity of the cell membrane on the length scale of 10-50 nm as well as its fluidity and the changes of the particles' properties in a case of their agglomeration and formation of the multiparticular rafts in contact with the plasmalemma (for the review see [352]), induced the search of the optimal size of the nanoparticles, allowing the most efficient internalization. Indeed, following a number of reports, the particles with a diameter of approximately 50 nm [364] or as smaller as 20-30 nm [366, 367] accumulated in the cells faster and in bigger amounts, than those of larger sizes. These observations are in accordance with a thermodynamic model, proposed by S. Zhang and co-authors, which predicts that for receptor-mediated endocytosis the optimal radius of the ligand-coated nanoparticles is in the range of 25-30 nm following the best combination of the degree of the membrane tension and the surface concentration of the particles [368]. However, there is also seemingly conflicting

data indicating the successful or even preferential internalization of the nanostructures of a bigger size (in the range of 200-500 nm in diameter) [362, 369] as well as the results demonstrating the preferential uptake of the particles smaller than 20 nm [370, 371], especially ultrasmall ones [371], in comparison to the larger nanomaterials. Therefore, the current understanding of the effect of the nanostructures' size on internalization is more complex, and involves the mechanism of the cellular internalization of the particles. To summarize, very generally, it is currently accepted that the ligand-coated nanoparticles with a diameter <200 nm, most probably, interact with clathrin-coated pits, whereas the particles of bigger size and the particles lacking the targeting ligands undergo caveolin-mediated endocytosis, macropinocytosis and phagocytosis [362, 372]. Aggregation of the nanoparticles is an additional geometry factor affecting the uptake. For example, 25% decrease of internalization of aggregated transferrin-coated gold nanoparticles was observed in HeLa and human lung cancer cells, in comparison to the single nanoparticles, while in the breast cancer linear cells the opposite trend was visible [373].

The size of the nanoparticles is responsible for some aspects of their biological activities. For example, the efficacy of 14 nm NO-releasing silica nanoparticles against microbial biofilms was higher than the bigger particles (50 and 150 nm) with the identical NO-release [374]. Numerous publications also provide evidence for the size-dependent cytotoxicity of various nanostructures. Most commonly, smaller particles induced more potent damage of the cells resulting in decrease of viability and cellular death, while the bigger nanoagents (with a size of 100 nm and more) were less cytotoxic or non-toxic. In particular, this effect was observed in *in vitro* cultures of endothelial cells exposed to the monodisperse amorphous spherical silica particles [375] and in mouse macrophages and human bronchial epithelium interacting with poly (lactic-co-glycolic acid) (PLGA) and titanium dioxide (TiO₂) nanoparticles [376]. The cytotoxic action of the smaller nanoparticles can be attributed to the increased absorption and denaturation of the intracellular proteins on the huge reaction surface of the nanostructures [376], resulting in alteration of multiple cellular functions.

3.1.2.3. Effects of the nanoparticles' shape

Effect of the nanoparticles' shape on the cellular uptake is, probably, mediated individually by some third mechanisms, because, as follows from the literature, the observations on this subject result in conflicting data. For example, the rod-shaped colloidal gold nanoparticles were internalized by HeLa cells less intensively, than the particles of the spherical shape [370]. In contrast, in HepG2 cells, more notable uptake of DNA/PEI-methoxyPEG/cyclodextrin nanorods was demonstrated, in contrast to the nanoparticles of the same composition and spherical shape [377]. The same behaviour was also observed in the experiment with mesoporous silica nanoparticles with different aspect ratios incubated with human melanoma cells [378]. Almost complete inhibition of macrophagal phagocytosis was achieved by the development of polystyrene nanoparticles with extremely high aspect ratio (>20), described as worm-like nanobelts, while the conventional spherical particles of the same composition and the equal volume were intensively phagocytosed. The observed effect was considered as a result of minimizing

the size-normalized curvature of the particles [379]. Indeed, in the recent comprehensive review [380], the importance of the studies of the effects of shape of the nanoparticles for biomedical applications was emphasized. The authors indicated that the most promising advances in nanomedical cancer drug development are connected with the creation of filamentous and worm-like micelles, as well as many other nonspherical shapes of the nanoparticles such as, for example, disks and needles.

3.1.2.4. Effects of the nanoparticles' charge

Surface charge of the nanoparticles may vary from negative to neutral and positive. This parameter is extremely important for stability of the water-based dispersions of the particles as the electrical repulsion can prevent their aggregation and subsequent sedimentation. In a case of the electrically neutral surface like, for example, PEG-coatings, the steric mechanisms are employed to avoid undesirable aggregation of the particles. At the same time, the surface zeta-potential has strong influence on cellular uptake of the nanoparticles (Figure 3.5). For instance, in the study of the same-size carboxymethyl-substituted dextran-coated iron oxide nanoparticles with the surface charge ranged from -50 to 5 mV, the preferential uptake of the particles with the greater negative charge was observed in the culture of human colon cancer cells [381]. The same trend was found in the interaction between the lung cancer cells and cerium oxide nanoparticles [382]. At the same time, coating of the calcium phosphate nanoparticles coated with polyethylenimine (PEI), the polymer with high cationic charge, also resulted in increased uptake in different types of the cells [383, 384]. It was shown that the uptake of positively charged PEI-coated lanthanide-doped UCNPs in HeLa cells relies on clathrin-mediated endocytosis [384]. The enhanced uptake of positively charged nanoparticles is facilitated due to electrical attraction between the negatively charged cell membrane and the cationic nanoparticle [369].

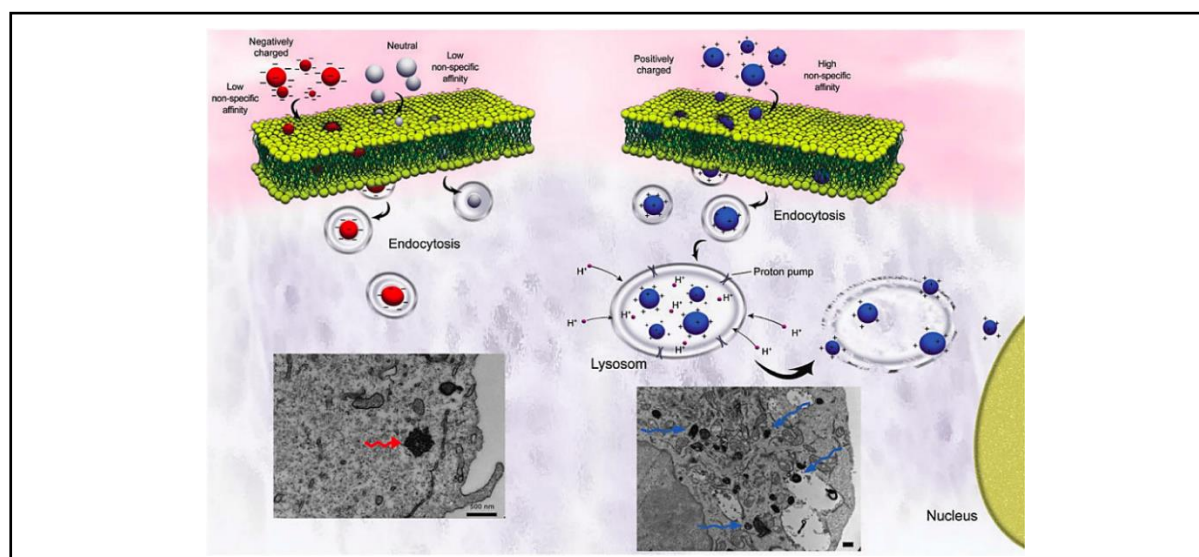


Figure 3.5. The effect of surface charge on cellular uptake of the nanoparticles. The uptake of the cationic nanoparticles is facilitated, in comparison to neutral and negative-charged particles, by non-specific electric attraction to the cellular membrane. Accumulation of positively charged nanoparticles in the lysosomes can induce the “proton sponge” mechanism leading to the lysosome disruption and the particles escape to cytosol. The inserts are TEM images demonstrating accumulation of anionic (left) and cationic (right) iron oxide nanoparticles in HeLa cells. Reproduced from [385].

The possible explanation of the increased internalization of the charged particles in general, in comparison to electrically neutral ones was proposed by K. Lam's group [386]. In their research the nanoparticles with electrically neutral PEG coating was transformed into a series of micellar nanoparticles, which had the PEG termini bound with anionic aspartic acid or cationic lysines and tested on murine macrophages. It was shown that high surface charge, either positive or negative, increases the macrophagal uptake after opsonisation of the particles in fresh mouse serum. In other study, the higher protein absorption on cationic nanoparticles was accompanied with decreased uptake in lung cancer cells [382]. These results indicated that the protein corona formation occurred during the contact of nanomaterials with the biological liquid mediums is involved significantly into the processes of cellular internalization of the nanoparticles. It is also important that the surface charge of the nanoagents is very significant for the biocompatibility characteristics. It is well known, that positively charged particles are more cytotoxic, than their negative or neutral counterparts [387]. This cationic-induced cytotoxicity is explained by the damaging effects of this type of the particles on the membrane structures of the cells [357].

3.1.2.5. Interaction of the particles with different types of cells

One of the most ignored factors in nanomedical and nanotoxicological research is the effect of specific cell type on interactions with nanomaterials [353, 388]. The majority of uptake and viability assays use a few lines of tumor cells, while the number of different normal cell types of human body is evaluated as 120-200 [353, 389]. In fact, the interaction between the cells and nanomaterials can be considered as a sort of foreign body reaction, a series of self-defensive acts, involving inflammation at the level of a tissue [390], but occurred at the cellular level. Then, the structural and functional variability of the cells result in different forms of this reaction on the contact with various nanomaterials. It involves different uptake pathways and timing and different sensitivity to damaging effects of the nanoparticles and different detoxication strategies [353, 388]. For instance, it has been found that redox-active polymer-coated nanoceria was nontoxic for normal cells of stroma, while induced cytotoxic damage in squamous tumor cells [391]. Similar discrimination of cytotoxicity and uptake between normal and various types of cancer cells was shown for hydroxyapatite nanoparticles [392]. Enhanced cancer selectivity of cytotoxic action was shown for ZnO nanoparticles [393]. In other study differential internalization of the same size polystyrene nanoparticles with different surface modifications in normal monocytes and macrophages [394]. Notable variation of uptake and cytotoxicity between a number of different immortalized cell lines was observed also for superparamagnetic iron oxide nanoparticles [353]. In a recent publication different mechanisms of cellular defence employed by keratinocytes and monocytes exposed to silver nanoparticles was demonstrated [395].

The mechanisms responsible for distinctive reactions of various cell types on the nanoparticles exposure are not fully explored. The currently accepted point of view implies that the natural

physiological properties (e.g., capability for phagocytosis), proliferation rates and the antioxidants levels, specific for each cell type, are the most important factors of the influence [396].

3.1.2.6. Targeting of the nanoparticles

In order to improve the uptake of nanoparticles to the cells, the strategies of targeted delivery may be employed. The most known receptors for clathrin-mediated endocytosis include transferrin (widely overexpressed in cancer cells [397] and in endothelial cells, involved in blood-brain barrier structure [398]); receptor tyrosine kinases like the epidermal growth factor receptor (EGFR) and HER2 especially relevant for some types of cancer; lectins, which are usually exist in many types of normal cells [359]; and riboflavin, having the carrying protein overexpressed in breast cancer [399]. Some heterodimer receptors, like integrins may be internalized by mixed clathrin- and caveolin-dependent mechanisms, in a way, when some combinations of the subunits are processed by one pathway, while other employs the other entering [400, 401]. Some types of integrin receptors are overexpressed in tumor vasculature and may be used for targeting of cancer microenvironment. In particular, many ligands of integrin receptors contain an amino acid sequence arginine-glycine-aspartic acid (RGD), which is widely used as a target for precise delivery of nanoparticles into cancer and endothelial cells [402-404]. Cell-penetrating peptides also rely on different endocytosis pathways. For example, TAT peptides are positively charged and employ direct transferring through the membrane by the formation of inverted micelles during contact to the phospholipids of the membrane [405]. In contrast, octaarginine may be internalized by macropinocytosis and avoid lysosomal degradation [406]. Caveolin-mediated endocytosis is thought to be responsible for internalization of receptors of folic acid (FR- α) [359], which can be found in many types of malignant tumors.

3.1.2.7. Signs and mechanisms of cytotoxicity of the nanoparticles

There are a number of signs indicating that the nanomaterial induces a cytotoxic effect on the cells. The simplest approach relies on the testing whether the nanoparticles of certain type induce death of the cells. However, it has been shown, that the majority of eukaryotic cells can survive after short time exposure to the nanomaterials, taken at the low concentrations ($<10 \mu\text{g/mL}$). Next, the damaging action of nanostructures usually increases in dose- and time-dependent manner. More precisely, changes of the cellular or nuclear morphology, alterations of cellular membranes integrity, changes of mitochondrial activity, leaking out of cellular components, release of lactate dehydrogenase, oxidative stress (resulted from generation of reactive oxygen species (ROS) an emerged as the decreased ratio of glutathione/glutathione disulphide) and lipid peroxidation of the plasma membrane can be detected by various methods. In addition, inflammation emerged as increased levels of several signalling molecules such as IL-1b, IL-6, IL-8 and TNF- α , is another manifestation of the adverse effect of the nanoparticles on cells. Genotoxic effects of nanoparticles can be revealed by the assays examining the extent of DNA damage. Finally, the number of cells undergoing apoptosis and necrosis is also the sensitive measure of

cytotoxicity. These signs may be presented in various combinations and intensities, because different nanoparticles can induce distinctive biological responses, including the varying degree of cytotoxicity [407].

Despite the individual character of every cell type-nanomaterial type interactions, some common mechanisms of cytotoxicity can be described. Not universal, but the most frequent of them, as it was proposed by A. Nel, is ROS formation [408]. It can be induced by the interference of nanomaterials with redox active proteins, the interaction with oxidative organelles such as the mitochondria, chemical reactions of the nanoparticle coating, reactive surface groups or ions leached from the NP surface in the acidic environment of endo- or lysosomes and the activation of several signalling pathways through interaction with cell surface receptors [396]. ROS generation can cause secondary effects like protein denaturation, inflammation, damage of mitochondria membranes and damage of DNA and distorting of the signalling pathways, or polymerization of actin stress fibers with following changes of cell morphology [396, 408, 409]. The second common mechanism of cytotoxicity is leaching of free ions and increase of reactive surface groups emerging following the degradation of the nanoparticles in late endosomes and lysosomes under effect of acidic pH [410]. The third most important mechanism of nanotoxicity originates from binding of serum proteins to the surface of the particles and formation of protein corona [396]. Protein corona has strong influence on uptake of the nanoparticles, and it also links the toxicity at the cellular level with the effects of systemic administration of the nanomaterials, defining to significant extent their biodistribution in the body and the immune response [388, 411]. Finally, a number of the observed biological responses on the exposure of the cells to nanomaterials may be corrupted as a result of agglomeration, aggregation and sedimentation of the particles. These processes change the effective dose of the nanoparticles [412] and significantly influence on cellular uptake and, then, on cytotoxicity (for detailed review see [396]).

3.1.3. Beyond the cell: biological barriers of the nanoparticles delivery to the tissues and organs

3.1.3.1. The exposure routes, biodistribution, metabolism and excretion of the nanomaterials

Nanoparticles can enter into the human or animal body as a result of intentional administration or accidental exposure by inhalation, ingestion, dermal application and injections (including intravenous, intramuscular, hypodermal and intradermal ones as the most used ways). After this the nanoparticles can be translocated to the blood and different organs, where they can accumulate and/or undergo different degrees of various metabolic transformations and then be eliminated from the body by the excretion mechanisms (Figure 3.6). As it can be seen from the Figure 3.6, the exposure routes affect the further distribution of the particles. Inhalation of the nanoparticles results in the most extensive exposure of the organs of different physiological systems, while the intravenous injections, providing the direct

access to the blood circulation, allow more precise organs' or pathological structures' targeting by appropriate design of the nanoparticles. As the particles developed for combined diagnostic and therapeutic use are usually should reach specified sites in the body, the injection route is usually preferable for nanotheranostics. However, for skin-related applications, the topical administration of the NTAs may be more efficient. Ingestion route of the body exposure to the nanoparticles may be useful, first of all for drug delivery, but, especially in a case of the medical manipulations on liver, it can allow nanotheranostic applications as well.

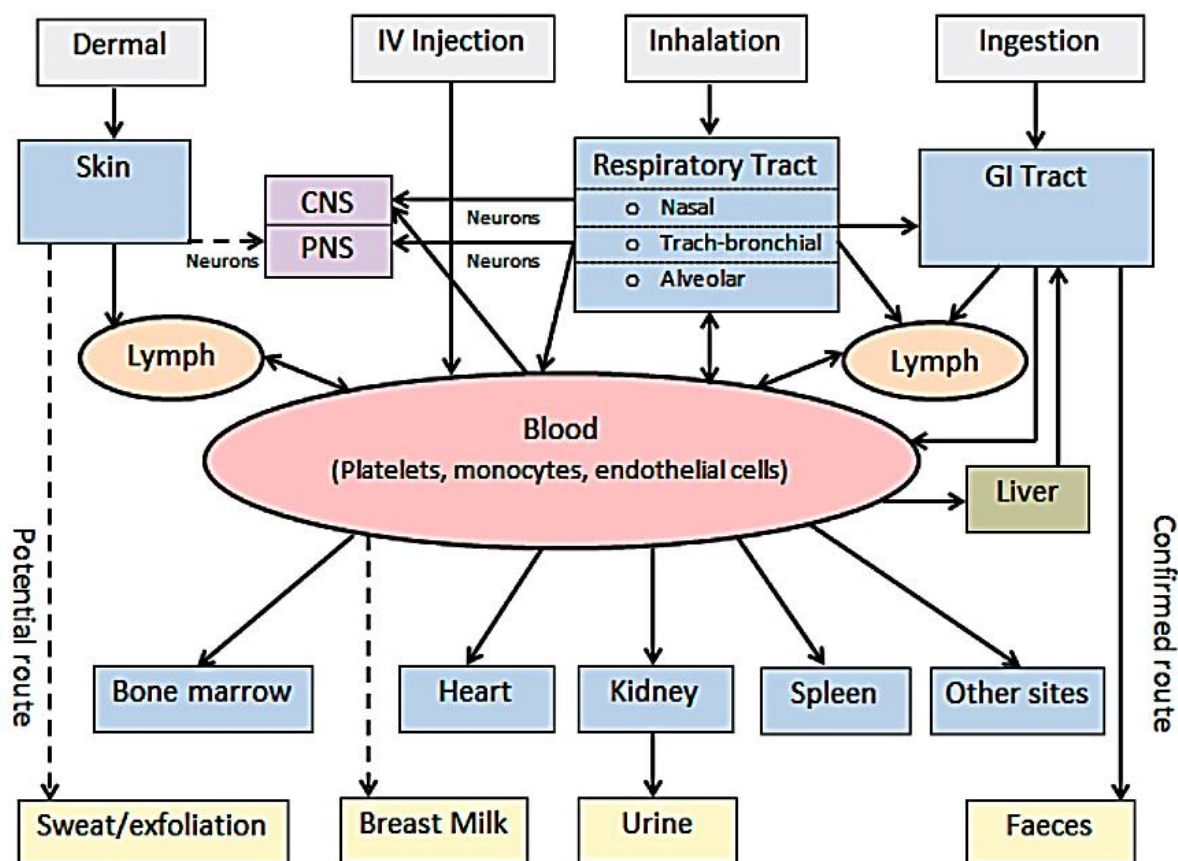


Figure 3.6. Exposure, biodistribution and excretion routes of nanoparticles in human and animal body. Solid arrows indicate the most important and experimentally confirmed routes; and dashed arrows show potential routes. Abbreviations: CNS - Central nervous system; PNS - Peripheral nervous system; GI - Gastrointestinal; IV - Intravenous. The blood circulation ways connecting different organs to each other are not shown. Reproduced from [413].

Biodistribution of the nanoparticles after entering to the blood circulation is strongly influenced by their size, shape, charge and surface chemistries (Figure 3.7). The most notable trends are sequestration of the large nanoparticles (>150-200 nm) by liver, spleen and lungs and kidney filtration of the smallest nanostructures. Positive charge of the particles, resulted from the certain surface chemistries, also contributes into the accumulation of the nanoparticles in the same organs, while neutral and negatively charged particles can escape liver and spleen uptake to a significant degree. Elimination of the particles from the body is mostly performed by liver and kidneys and depends on both exposure routes and biodistribution patterns (see Figure 3.7).

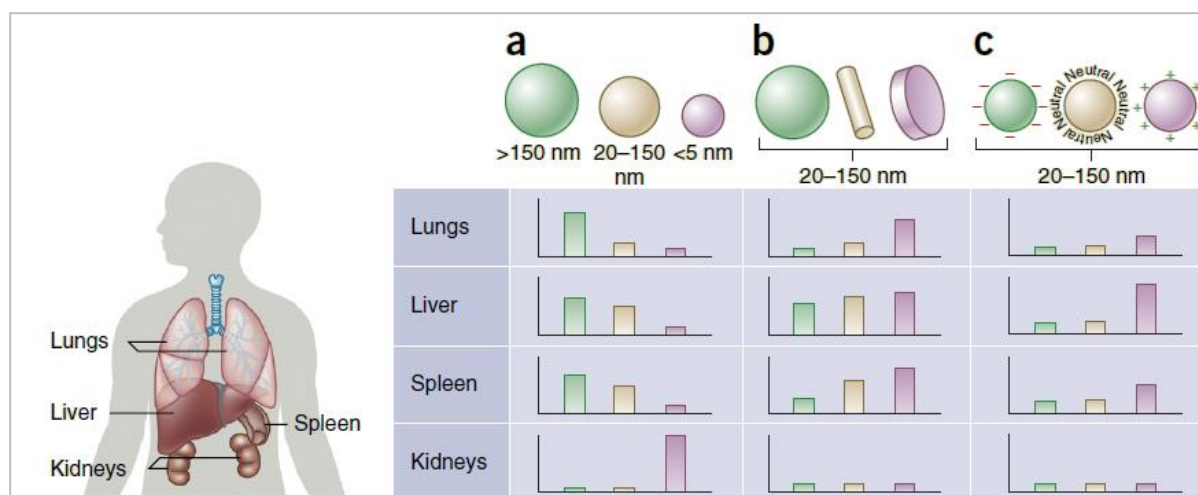


Figure 3.7. Effect of size, shape and surface charge of the nanoparticles on their biodistribution in different organs. Generalized artistic presentation. (a) Size-dependent biodistribution of spherical nanoparticles. The particles of the size range of 100–200 nm have the best chances to escape filtration by liver and spleen and extravasate through vascular fenestrations of tumors (the EPR effect). The large particles (> 150 nm) accumulate mainly in liver, spleen and lungs. The smallest particles (< 5 nm) are filtered by kidneys. (b) Effect of the shape of the nanoparticles on their organ biodistribution. The unique rheological properties of the novel nanoparticles having cylindrical and discoidal shapes, in comparison to spherical particles of the same size and composition, can substantially change of circulating lifetimes, cell membrane interactions and macrophage uptake, and, finally, affect the organ biodistribution. (c) Surface charge of the nanoparticles and their biodistribution. The particles with positive charge induce more intensive opsonization and, following this more efficient uptake by macrophages and sequestration from the blood flow. Negatively charged and neutral particles have longer circulation lifetimes and less accumulation in the organs of MPS. In both b and c, the effects are considered if the size of the nanoparticles is in the range from 20–150 nm. Reproduced from [414].

Despite the fact that the size and surface properties of the nanoparticles make these materials very advantageous as drug or contrast delivery agents, on the other hand, the same features lead to a number of challenges of overcoming of several biological barriers on the way to the desirable destination. The most important benefits of biomedical applications of the nanoagents such as possibility of safe and efficient delivery of drugs and probes to the specific sites of the body, such as site-specific targeting, controllable drug release, reduction of side effects and increased half-life time, stem from special size range and tunability of the surface properties [415]. In particular, nanoparticles can selectively accumulate in tumors and inflammatory focuses due to enhanced permeability and retention (EPR) effect, emerged as a result of increased extravasation of the particles of nanoscale range through pathologically tortured and fenestrated vasculature and limited venous and lymphatic drainage [416]. This strategy of nanoparticles application is known as passive targeting, in contrast to the active targeting, implying biofunctionalization of the particles' surfaces with the biologically significant ligands, which could be recognized and internalized by the certain cellular populations [417]. However, a number of supercellular biological barriers significantly impede the practical achievability of these goals. Some of the most significant barriers, which those the current study deals to certain extent, are discussed below.

3.1.3.2. *The circulation barrier*

First, and, probably, most important, of this barriers is the rapid clearance of the nanoparticles from the blood performed by the combined immune mechanisms of opsonization and subsequent phagocytosis of the xenogeneic material by the macrophages and lymphocytes of mononuclear phagocyte system (MPS) [418]. This results in the particles' deposition, predominantly, in the liver, spleen and lymphatic nodes and follicles, contributing to non-specific accumulation in healthy organs and decreasing the amount of the nanomaterials delivered to the target structures [414]. Such deposits also induce a risk of secondary damage of these healthy organs due to nanotoxicity or release of the cytotoxic compounds loaded into the particles. Following this the circulating pool of the nanoparticles becomes sequestered, the time of their interaction with the target structures like tumors is shortened and the probability of the efficient drug delivery or other expected activity is limited.

The opsonisation (formation of a special type of protein corona composed by serum proteins such as complement compounds, immunoglobulins, fibronectin and apolipoproteins [419]) of the nanoparticles occurred after their contact with blood [418]. Opsonization makes the nanoparticles "visible" to the cells of MPS and leads to rapid phagocytosis. Formation of the nanoparticles' protein corona after contact with serum also can hinder the possibility of receptor-mediated targeted delivery of the nanoparticles, because the opsonins can hide the recognizable molecular moieties [420].

In respond to this challenge different strategies were developed with an intention to prevent serum protein absorption or control the composition of protein corona of the nanoparticles exposed to the blood. The most known approaches include modification of the nanoparticles' surfaces with PEG (PEGylation), and biomimicry strategies such as coating with CD47 peptide, which is recognized by macrophages as a signal of the own body origin, or wrapping of the particles into the coatings resembling the membranes of red blood cells or leucocytes (for the detailed review see [414] and [417]). Another interesting new strategy implies the "hitchhiking" of the nanoparticles incorporated into the membranes of red blood cells, monocytes, macrophages or T-cells [421].

3.1.3.3. *Interaction of the nanoparticles with ECM*

All the tissues of human or animal body are not simple aggregates of cells, as certain amounts of extracellular matrix (ECM), a product of the cells, which has a complex biochemical and structural organization, provides mechanical support to the cells and also plays a number of regulatory and signalling roles both in normal and diseased states [422-428]. The amount, composition, architecture and functions of ECM vary between different types of tissues and change dramatically in pathological conditions. For example, the major difference exists between the tissues of epithelial and mesenchymal origin. In particular, the main matrix structures of epithelial tissues like skin epidermis, linings of the majority of internal organs and endothelial linings of blood vessels are basement membranes, to which the cells attach by their basal poles. These membranes are mainly composed by collagen type IV,

laminin, heparan sulphate proteoglycans, nidogen (entactin) and BM-40 (osteonectin, SPARC) [429], as well as perlecan and minor collagens like collagen XV and XVIII [428]. Functionally in normal state the basement membranes separate epithelial and connective tissue structures and regulate the transport between the mentioned body compartments. They also play a critical role in tumor development, as the ability of the dysplastic epithelial cells to cross the basement membrane is a principal sign of malignization [430, 431]. The intercellular spaces in epithelial tissues are very narrow, and the cell-ECM ratio is shifted towards the cells (Figure 3.8 (a)).

In contrast, ECM of connective tissue is more abundant than the cells, which are separated by large volumes of mixed composition, which contains collagens, glycoproteins, proteoglycans and glycosaminoglycans (Figure 3.8 (b)). Some of this molecules like collagen and fibronectin contribute to the fibrillar structure of the ECM, while other form so called ground substance. The important feature of the connective tissue ECM is high degree of hydrophilicity of ground substance, resulting, first of all, from the great swelling capacity of hyaluronic acid and other glycosaminoglycans. The ground substance of the ECM also contains a mixture of soluble morphogens like growth factors, cytokines and ions. Sometimes the ECM located in vicinity of the epithelial cell sheets is termed “pericellular”, and the ECM of connective tissue type is described as “interstitial” [428], but to our opinion it is fully correct, as like it was explained above, in connective tissues (fibrous connective tissue, fat tissue, bone, cartilage, and blood) the interstitial matrix borders the cells.

Nanoparticles transport across the different types of ECM is a crucial factor of their ability to reach the therapeutic targets. Unfortunately, the scientific information about interactions between ECM and nanomaterials is scarce, probably, because of limited possibilities to model and study these processes. Therefore, the current concept is partially based on the data on the ECM permeability for macromolecules [432]. The first step ECM barrier, which the nanoparticles should cross after entering the blood circulation is the basement membrane of blood and lymphatic capillaries. Next, depending on the site of escape, the structure of the surrounding tissue may be of “epithelial” type or “connective tissue” type in terms of the cells-ECM ratios. The parenchyma of organs like, for example, liver or epithelial linings is formed by relatively densely packed cells. Then, after permeation through the endothelial cells and crossing of the basement membrane the nanoparticles are usually expected to reach the parenchymal cells immediately. However, for instance, in the liver the specialized ECM-filled pericapillary zone exists, which is known as the Disse space, separating the walls of sinusoid capillaries from the hepatocyte trabeculae and serving as a reservoir for the substances escaping the blood flow [433]. The situation appear to be even more complex in tumors, as they have highly heterogeneous structure with uneven distribution of interstitial matrix. Only at very early stages of the cancerogenesis the tumor cells form the dense aggregates lacking ECM. Later, the more proliferation occurs, the more ECM accumulates at the tumor site. Next, the dysregulation of ECM is growing along with the increasing degrees of malignancy and emerges as enhanced resorption or excessive accumulation of

matrix components as well as disbalance of proteolytic enzymes activity [431]. So that, the nanoparticles, which successfully passed through the circulation barrier and reached the tumor, most probably, first would interact with the ECM. In a case of normal connective tissue structures, the chances of the nanoparticle to reach the resident cells directly after escaping the blood vessels are also relatively low following the biological architecture discussed above.

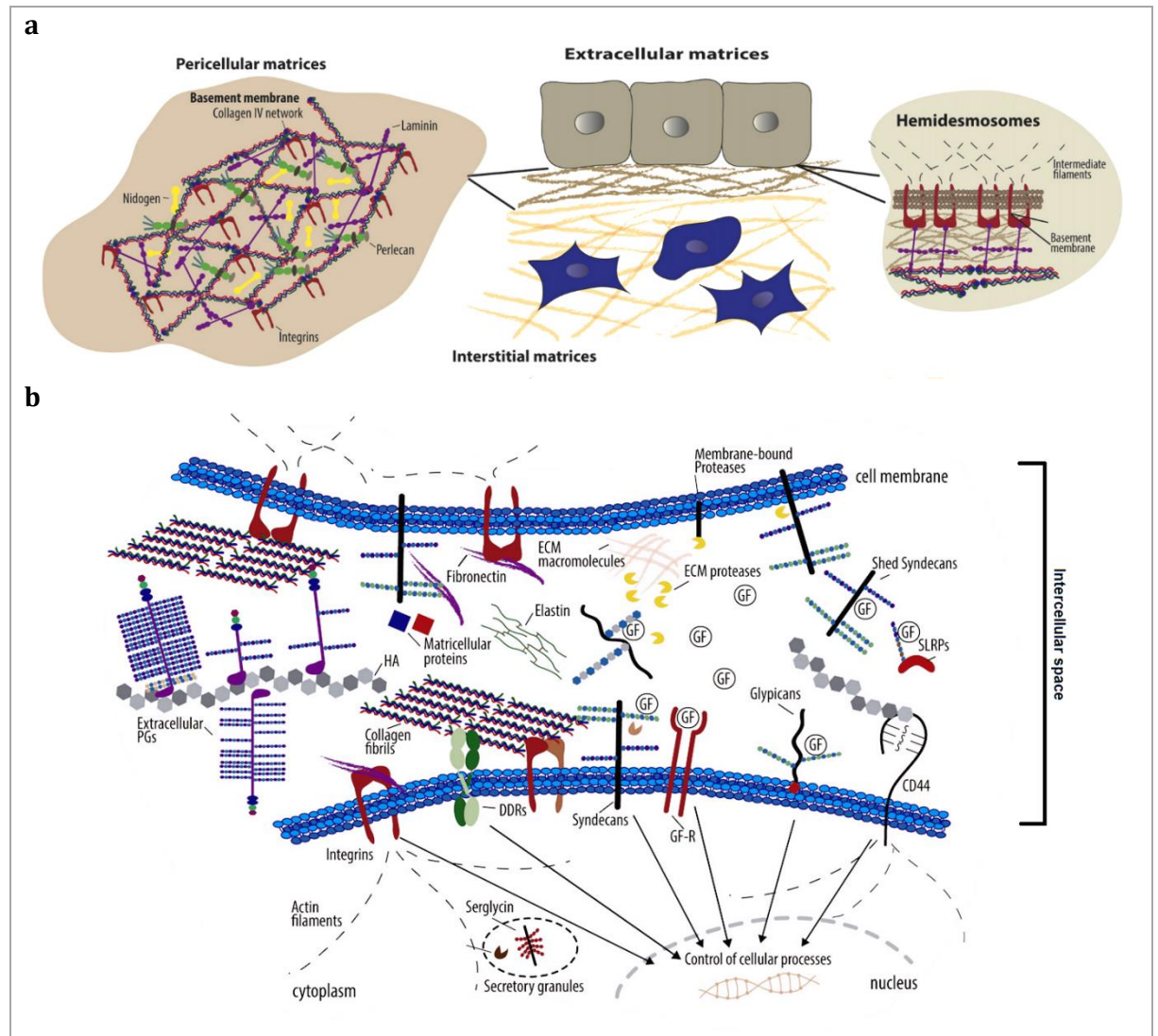


Figure 3.8. Schematic overview of major components of ECM and related cell surface receptors. (a) The relationship between a cell sheet, the underlying basement membrane (pericellular matrix) and the interstitial ECM. The structure of basement membrane is shown on the left. Hemidesmosomes (on the right) anchor the epithelial cells to basement membranes via integrins (the transmembrane receptors of cellular wall, connecting laminins of basement membrane and the intermediate filaments of the cytoskeleton). (b) The ECM of connective tissue type fills the intercellular spaces and forms a dynamic and complex 3D network. The cell-matrix adhesion is mediated by a set of surface receptors, including integrins, cell surface proteoglycans, the hyaluronic acid receptor CD44; and membrane-associated enzymes (DDR, syndecans). Growth factors (GF) are normally bound to the ECM components like proteoglycans and released to be involved in signalling cascades when the matrix is being remodelled or degraded. ECM remodelling is mainly enzymatically driven process relying on various metalloproteinases such as MMPs, ADAMs, ADAMTs, as well as on cathepsins, and plasminogen activators, and GAG-degrading enzymes, such as heparanases and hyaluronidases. ECM remodelling occurs in normal conditions in response to the changed mechanical stresses. In pathological state the extensive remodelling of ECM may result in its partial destruction, degeneration or, oppositely, the excessive accumulation of interstitial matrix components (fibrosis). Reproduced from [428] with changes.

The nanoparticles can be transported across ECM mainly by Brownian motion as it was earlier shown for macromolecules, and the ECM-nanomaterial interactions can be influenced by steric (porosity and fibre size), mechanical (stiffness/ compliance) and adsorption factors [432, 434-437]. The effective pore size of basement membrane is estimated as 0.14 μm [435], indicating the first barrier of size filtering for the particles. In the “connective tissue” type ECM the size of the voids is bigger. The pores in the gel prepared from collagen type I, which is the major constituent of the “connective tissue” ECM, had the diameter of about 0.47 μm . In addition to the direct size filtering effects, the laws of diffusion should be taken into consideration such as decreased motility of the objects with larger hydrodynamic diameter and dependence of the mass transfer rate on the viscosity of the isotropic environment, resulting in inhibited motility of the larger particles and impaired transport in extremely non-homogenous media like ECM [438]. Indeed, it was demonstrated that smaller spherical nanoparticles diffuse faster than larger particles or the nanomaterials with different aspect ratios than 1:1 [439]. However, small spherical particles frequently arrange as chains and travel slowly, like ellipsoids [440] (cited by [438]). In any case all the nanoparticles diffuse much slower than traditional drugs [438]. Critical significance of the nanoparticles’ size in transport through the ECM was also demonstrated in the studies on magnetophoretic guidance of iron oxide nanoparticles [436, 441]. First, the smaller particles achieved higher velocities even under weaker magnetic force. In addition, the average velocity of 275 nm diameter PEGylated nanoparticles was 1.5 mm/h, whereas if the size increased up to 800 nm while maintaining the same per NP magnetic susceptibility the magnetic mobility decreased greater than 1,000-fold to less than 0.01 mm/h. The possibility of the control by of the transport of the nanoparticles through brain ECM was demonstrated in other study [442]. It has been shown that the velocity of the particles for 51-123% may be increase by the means of dilating of the extracellular space with infusions of various buffers and by enzymatic degrading of the matrix constituents. Interestingly, the pre-infusion of the brain tissue with isotonic buffer gave the biggest rise of the nanoparticles’ transportation efficiency.

Another factor affecting the transport of nanoagents through ECM is affinity of the particles to the ECM components resulting from electrostatic interaction [432] and physical absorption. As ECM contains a number of charged macromolecules, it is expected that the permeation of the nanoparticles through it depends on their surface potential. For example, cationic nanoparticles can be attracted by negatively charged polymer molecules, which are abundant in ECM (mainly, glycosaminoglycans). In fact, experimental studies [432] show that charged particles travel through ECM slowly than electrically neutral. However, counterintuitively, another experimental observation, obtained with use of the various size nanoparticles electrostatically shielded by PEG to different degree, demonstrated that in electrically neutral collagen gels the denser PEG coating resulted in improved diffusion of the particles. At the same time, the diffusion through the model basement membrane (Matrigel) was 10 times slower than in collagen gels and did not increase with the better charge shielding. At the same time, in Matrigel the

thresholding zeta-potential, below which the particles were mobile, has been defined at the level of approximately 12-14 mV [435]. In other research both cationic and anionic small (2 and 10 nm) gold nanoparticles were able to bind to self-assembled collagen fibers, and the smallest particles (2 nm) exhibited even mechanical integration with collagen fibers. These results may be explained by the model developed by the group of R. Jain and L. Munn [432]. Accordingly to these model, the electrostatic interactions between ECM fibers and diffusing particles are affected by the diameter of the fibers (as the fibre diameter increases above the size comparable to the Debye length, the repulsive forces become less important).

The interaction of the nanoparticles with ECM is also influenced by the high hydrophilicity of this environment and the presence of a milieu of ions of signalling molecules in it. ECM is responsible for the interstitial hydrostatic pressure and takes part in transcapillary exchange of soluble molecules. The level of the interstitial hydrostatic pressure depends on concentration of ECM molecules with high water binding capacity (first of all, hyaluronan). The increased hydrostatic pressure is a normal sign of edema observed in inflammatory and cancerous tissues [443]. The most obvious result of changes in ECM concentration and swelling is the impaired diffusion, as it was discussed above. In addition, in a case of theranostic agents like UCNPs, the hydrophilicity of the environment may result not only in transport limitations, but also in photoluminescence quenching by water [77, 444] and impaired possibility to deliver optical signals through the highly scattering [445] media. Finally, the interaction with the soluble components of ECM may result in absorption of the macromolecules on the surface of the particles, changing their properties as it was described for protein corona effects [438].

3.1.3.4. Interaction the nanoparticles with the tumor-specific barriers

Although EPR effect allows passive targeting of the nanoparticles to the cancer foci, a special tumor-specific biological barrier to this emerges such as significantly elevated interstitial fluid pressure (IFP) [446] and solid stress [447]. Indeed, a few FDA approved nanotherapeutics demonstrate only modest survival benefits [448]. The mechanism of gaining of the interstitial fluid pressure is linked to the pathological angiogenesis in tumors [449], which results in formation of the leaky and tortures blood vessels, which are inefficient in delivery of oxygen and removal of the metabolic products. Following this the tissue hypoxia is up-regulated, triggering the cancer cells proliferation enhancement and increased ECM production and stiffening [450, 451]. The vicious circle is forming, leading to the tens of times, in contrast to normal tissues, IFP [452], hypoxia and solid stress increase in malignant tumors, and formation of very heterogeneous tumor microenvironment, preventing the efficient drug delivery (Figure 3.9).

A smart approach to alleviate the permeation of the nanoparticles into the tumors experiencing increased IFP/solid stress have been proposed recently [448]. The basic idea of the authors was to employ EPR effect to deliver and accumulate the 100 nm long-circulating nanoparticles to the tumor

through leaky vasculature and then decrease the diameter of the particles, making it possible to diffuse through densified ECM. To do this the gelatine nanoparticles embedded with 10 nm quantum dots (QDs). After extravasation the gelatine core was degraded with local metalloproteinases (which are excessively present in the stressed tumors) and the QDs were successfully released and able to penetrate through dense collagen matrix.

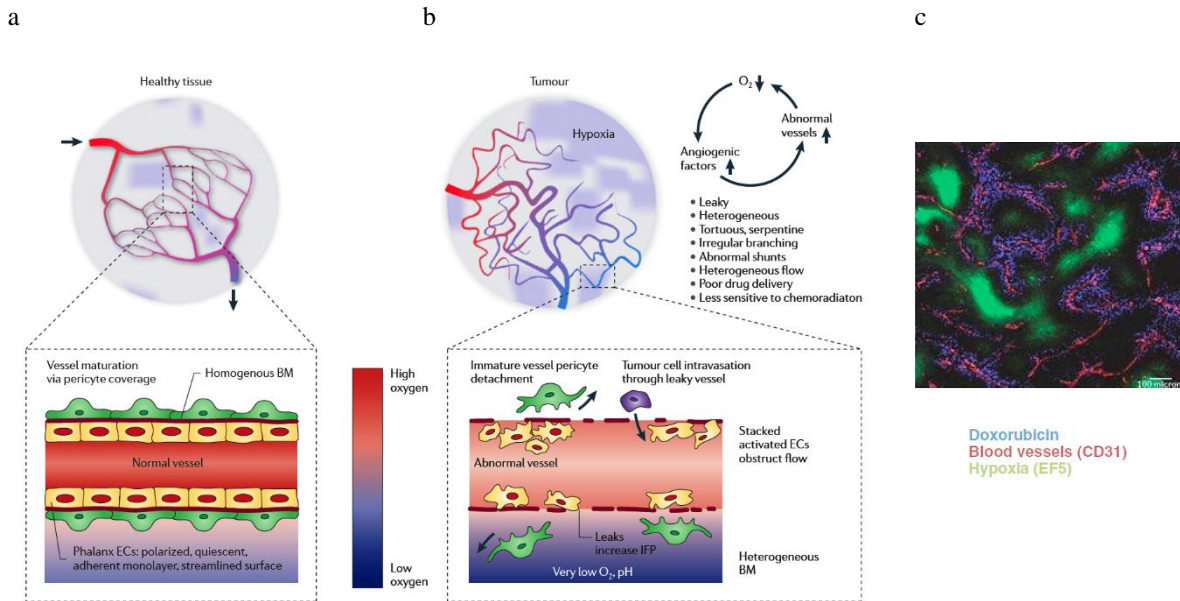


Figure 3.9. The role of structural changes of tumor vasculature in formation of tumor-specific biological barrier for drugs and nanoparticles' transport. (a) The branching pattern (upper panel) and the structure of blood vessels in normal tissue. Note regularity of blood vessels' geometry and the continuous layer of endothelial cells (ECs) on uninterrupted basement membrane (BM). Structural and functional changes in tumor vasculature, including corrupted geometry of blood vessels, disrupted barrier function, and compromised hydrostatic and osmotic gradients. (b) Severe structural and functional abnormalities of tumor vasculature and formation of chronic hypoxic regions. (c) The immunohistochemical labelling illustrates the limited penetration depth of doxorubicin in a solid tumor and demonstrates that the large volumes of hypoxic tissue inside the tumor are unaffected by the drug as a result of compromised transport by aberrant vasculature. (a, b) Reproduced from [453]. (c) Reproduced from [454].

The second major contributor to the formation of tumor-specific biological barrier is abnormal cellular-stromal interactions, giving rise to another vicious circle. In many types of cancer the accelerated metabolism of the matrix constituents has been revealed [455]. It includes both enhanced accumulation of the ECM components combined with increasing stiffness of the tumor tissue, which promotes cancer progression and up-regulated activity or local concentrations of matrix-degrading enzymes [456-458]. These changes are also characteristic for wound healing process, therefore the concept of tumors as non-healing wounds emerged [459, 460]. The next step in development of this idea links the key mechanisms of wound repair and cancer progression such as epithelial-mesenchymal transition (EMT, resulting in acquiring, in particular collagen-synthetic function by cancer cells [461]) and fibrotic transformation of excessive blood vessels [462] under hypoxic conditions and excessive level of metalloproteinases [460, 463, 464]. As it happens during abnormal wound healing and scarring, the cancer progression is associated with a switching on of set of pathways, leading to the up-regulated

proliferation of the cells, increasing hypoxia, EMT, “emergency” type of angiogenesis, accumulation of the ECM and its accelerated turnover. These complex interactions are illustrated by the example of breast cancer at Figure 3.10. All these processes together result in growing solid stress in the tumor, acting as another important obstacle on the way of the therapeutic molecules and nanoagents.

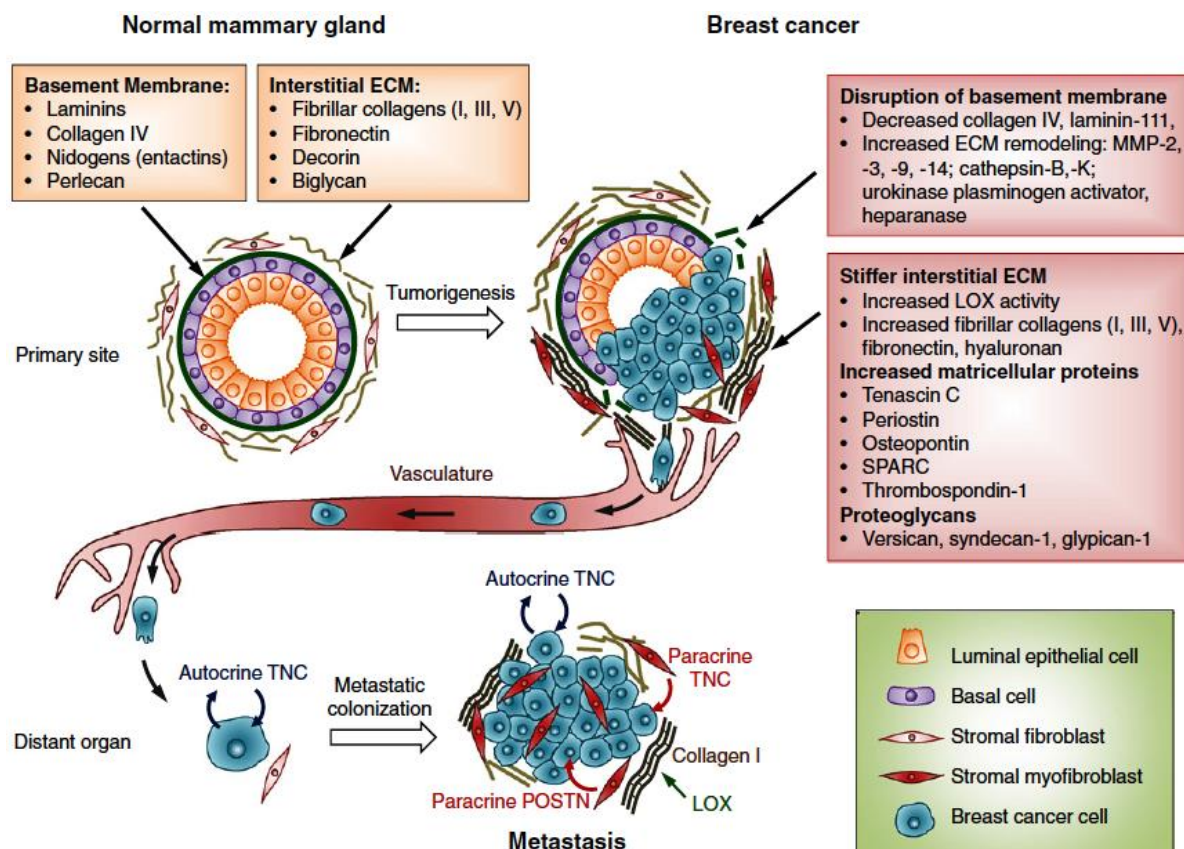


Figure 3.10. The role of ECM changes in breast cancer progression and metastasis. Alteration of normal stroma of mammary gland during cancer transformation and progression. Note emergence of myofibroblasts as a result of EMT, disruption of basement membrane by ECM remodeling enzymes like MMPs, heparanase and others with proliferation and invasion of dysplastic cells of epithelial or basal layers of the gland ducts, and changes in composition and properties of ECM in cancer focus. Cancer associated fibroblasts produce excessive collagen, fibronectin and other matrix components. These proteins become cross-linked because of high levels of lysyl oxidase (LOX), finally resulting in stiffening of the tissue. Matricellular proteins that contribute to the cancer cell plasticity such as tenascin C, periostin, osteopontin, SPARC and thrombospondin-1 are also upregulated. After detachment of metastatic cells from the primary tumor, they initiate the secondary colonies, relying on signals from the ECM such as type I collagen (collagen I), crosslinked by LOX, tenascin C (TNC) and periostin (POSTN). Reproduced from [451].

Considering the data, discussed above, the most promising strategies to improve the results of the efficiency of the nanoagents delivery to the tumors may include decrease of the size of the particles, reasonable surface chemistry for optimization of the zeta-potential for better penetration through ECM and cellular uptake (which are, at the moment appear as opposite tasks) , anti-fouling coatings, and elimination of excessive pressure inside the lesions (cytostatic and cytotoxic reduction of the cell number, antiangiogenic, anti-oedematous and ECM-degrading approaches).

3.1.3.5. Organ-specific barriers (with a special consideration of the skin barrier)

Organ- and tissue specific barriers are another obstacle in delivery of the nanoparticles to the desired sites. Due to the specialized histological structure, consisting, as a rule a combination of cellular layers, basement membranes and loose ECM, the transport of the nanotherapeutics and nanoprobe from the systemic blood flow or from the outer environment is very limited. The most known examples of these type of the barriers are blood-brain, blood-testis and placenta barriers [465]. All of them play a protection function, defending the critically important structures (brain, reproductive apparatus and embryo, respectively) from pathogens and xenobiotics. In broad sense, the epidermis of skin and mucous membranes also represent this type of the barriers [466]. The nanoparticles smaller than 100 nm may utilize some mechanisms to permeate across the organ-specific barriers [465]. The ability of the particles to permeate through the organ-specific barriers is very finely tuned by the size and surface chemistry. The detailed analysis of this features can be found elsewhere [34, 414, 465], but, in general, it can be said that the nanoparticles can cross the lung, gut, skin, and placental barriers [467].

In the context of the current study the penetration of the nanoparticles through *the skin barrier* and their biological effects in the skin are of special interest. The delivery of drugs and nanoagents throughout the skin has a number of advantages. For example, the ease of application of the drugs/nanoparticles and a possibility to improve pharmacokinetics of the drug/ nanoagent with bypassing the absorption in the gastrointestinal tract, which is usual “draining way” in a case of oral administration, are important. In addition, transcutaneous delivery allows to avoid injections and the complications related to them. It’s also pain free and makes it possible to extend the exposure times [468, 469]. At the same time, the effectiveness of the complex structure of the skin barrier against transport of the certain substances and materials of various nature is variable and may be changed to some extent by chemical and physical factors or following a disease [470]. Therefore, the risks associated with intentional or accidental contact between skin and different nanomaterials are also have to be taken into account with regard of the ease of the application.

The mammalian skin consists of 3 main layers such as 1) epidermis (the most external layer), composed by the cells of epithelial origin, 2) dermis, or derma, the connective tissue layer, which stems from the mesenchymal progenitors, and 3) subdermal fat tissue, or hypoderma. Epidermis is exposed to the environment, and interacts with the greatest amounts of the drugs, nanoparticles or other materials applied to the surface of the skin. It consists, predominantly, of 4-5 sublayers of keratinized stratified squamous epithelium. The deepest one, known as basal layer (stratum basale), lies on the basement membrane, located between the epidermis and derma. This is a cambial zone of the epidermis, where the epidermocytes are capable to proliferate. Cells in the epidermis move gradually towards the surface, changing their differentiation state from metabolically active cubic epithelial phenotypes to dead keratinized flattened cells (this process is known as desquamation). Two sublayers, laying above the

stratum basale, stratum spinosum and stratum granulosum, respectively, are composed of the viable epidermocytes (keratinocytes), specialized to synthesise keratins and keratohyalin as well as other proteins and lipids. These lipids (glycoceramides, sphingomyelin and phospholipids) are stored in tubulovesicular organelles referred as the lamellar bodies. These compounds are secreted to intercellular space by exocytosis and gradually moved to the upper layers of epidermis [471]. The cells in stratum spinosum and stratum granulosum also accumulate large amounts of keratin filaments and densely contact each other by desmosomes. The upper two sublayers, stratum lucidum (it exists only in a few body areas with specialized thick skin) and stratum corneum, are formed by dead elongated flattened cornified keratinocytes (corneocytes), arranged in a multilamellar array. All these skin layers as well as skin appendages contribute to the fate of the drugs or nanomaterials applied on the surface of the epidermis, involving different permeation routes (Figure 3.11).

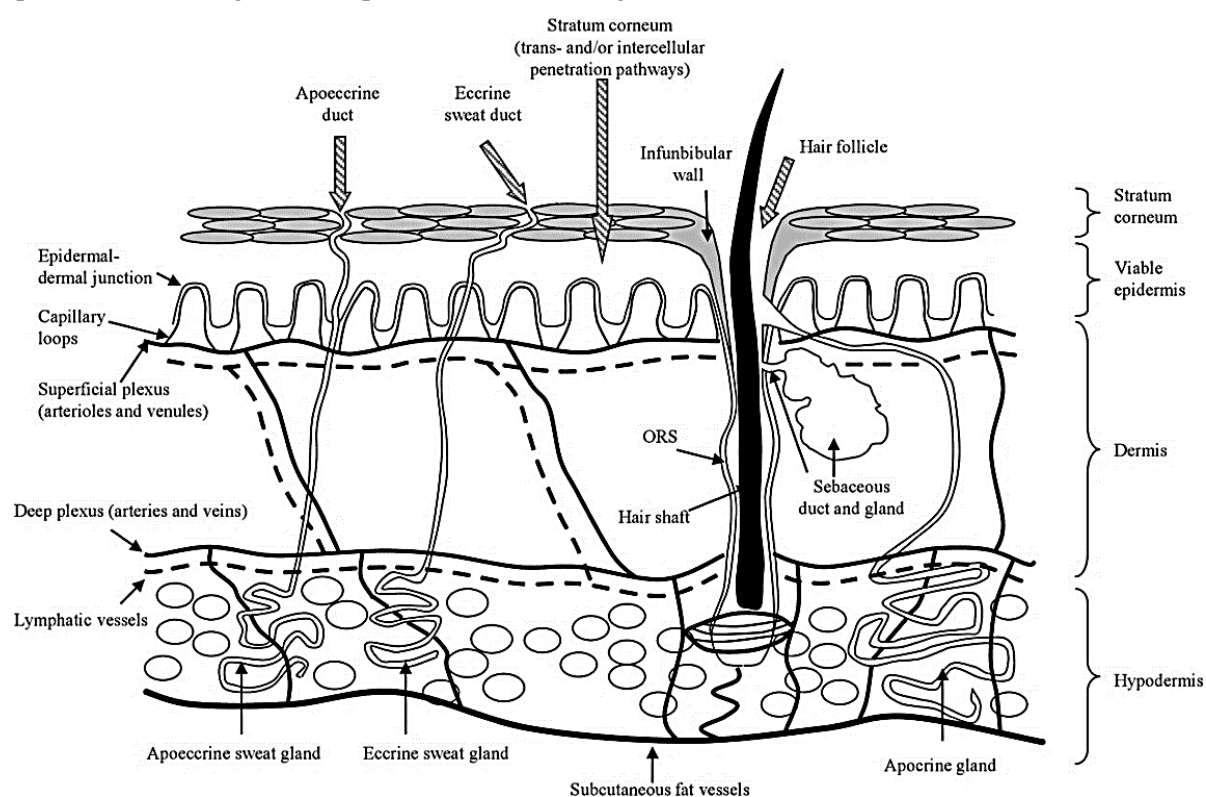


Figure 3.11. The diagram of the structural organization of human skin and the main transcutaneous permeation routes. The epidermis top layer, stratum corneum, is formed by parallel 10-25 layers of densely packed dead keratinocytes (corneocytes) embedded in lipid matrix [471]. It represents the main barrier of the skin. There are viable epidermal layers, basement membrane (epidermal-dermal junction), papillary and reticular layers of dermis and hypodermal fat below it. Epidermis gets O_2 and nutrients from the superficial plexus by diffusion (as the epidermal tissue itself stays avascular), and the dermal and fat layers are supplied by the deep plexus. These two vascular structures are communicate by the vertical capillary loops, passing through the dermis, and also connect to the subcutaneous blood and lymphatic vessels. The appendages of the skin, including hair follicles, sebaceous and sweat glands have their basal parts in hypoderma or derma and penetrate the skin layers reaching the outer surface of epidermis. The striped arrows show the main permeation routes. ORS – outer root sheath of hair follicle, it is lined by the cells of basal epidermis. The scheme is not scaled. The thickness of viable epidermis is 50-100 μm , the thickness of stratum corneum is 10-30 μm (in normal thin skin), and the thickness of dermis is highly variable (500-2000 μm in average). Reproduced from [468].

As it can be seen from Figure 3.11, the main routes of permeation of soluble substances and particular materials across the skin include two pathways through the stratum corneum (transcytosis and permeation by intercellular spaces) and the ways along the skin appendages (hair follicles and the ductal parts of the glands). The size of the openings of the appendages varies between 50 and 150 μm (sometimes hair follicular units reach 700 μm in diameter) [469], providing a kind of “sinkholes” for the permeating materials coming from the skin surface. However, the skin appendages occupy only 0.1% of the total skin area, excepting some special areas, therefore the topmost epidermal sublayer, stratum corneum, functionally comprises the most potent biological defence barrier of the skin [472], preventing both loss of water from inside the skin and entering of various materials and substances from outside. This is ensured by the “bricks” (the corneocytes) and “cement” (lipids) structure of stratum corneum, where the cells are surrounded by multilamellar lipid bilayers. The two major classes of lipids of stratum corneum, ceramides and saturated fatty acids, are the products of enzymatic processing of the excretes of the underlying sublayers. Together with cholesterol and the hygroscopic compounds collectively named natural moisturizing factor, they form the complex material filling the intercellular spaces in the stratum corneum. Interestingly, in this densely packed lamellar structure, cholesterol provides a certain degree of fluidity and flexibility, preventing formation of a fragile system [473]. The corneocytes are surrounded by the cell membrane with highly cross-linked proteins, making it stiff (cornified). About 80-90% of internal volume of corneocytes consists of the keratin filaments aggregated into bundles by matrix protein filaggrin synthesized in the keratinocytes of stratum granulosum (Figure 3.12) [473].

Relative contribution of transappendageal, transcellular and intercellular routes into transport of the substances and particles across the stratum corneum is not equal. In particular, the permeation via skin appendages in general is limited, as it was mentioned above, but it may contribute to the rapid diffusion at the early time periods after application of the compounds [474]. While the transcellular permeation is extremely slow due to the number of involved barriers, the intercellular route is considered as the most efficient, independently on the nature of the applied compounds and despite the fact that the diffusional pathways of the soluble molecules and particles elongates up to 300-900 μm and involves the partition of the transported matter between hydrophilic intracellular proteins and intercellular lipids [475] (see Figure 3.12).

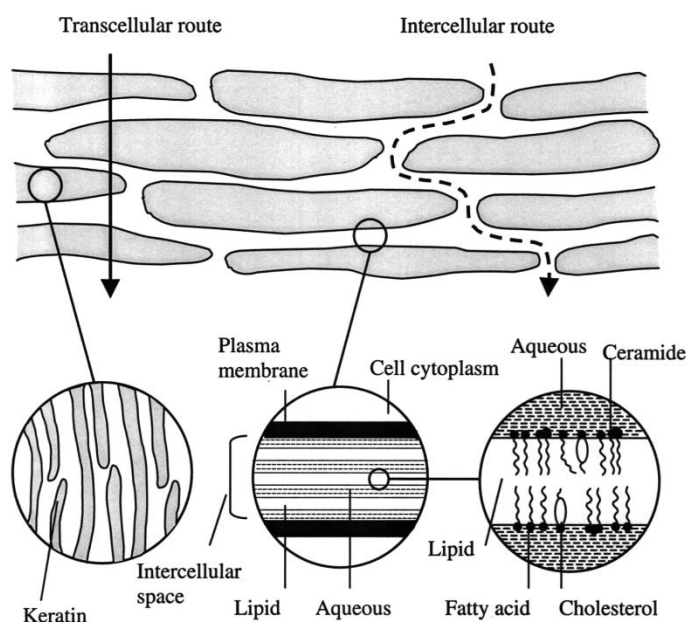


Figure 3.12. The ultrastructure of the stratum corneum and the related permeation routes. A scheme shows the organization of stratum corneum accordingly to generally accepted “bricks-and-cement” model and the suggested permeation routes in the stratum corneum, including the transcellular route pathway via the corneocytes and the intercellular lipid matrix and the intercellular pathway through the lipid matrix between the corneocytes. The inserts schematically demonstrate the ultrastructure of stratum corneum compartments. (Left) The arrangement of aggregated keratin filaments inside the cell envelope, which is composed of hydrophilic cross-linked proteins (cornified envelope proteins) and a covalently bound lipid envelope [468]. The keratin lamellae are separated by lipid-rich material [476]. (Middle and right) The ultrastructure of intercellular spaces of stratum corneum. Reproduced from [472].

The bulk of the stratum corneum intercellular space is filled by lipids, which results in limited permeability of this skin part for the water-soluble and hydrophilic compounds. However, due to the presence of some aqueous component in the lipid lamellae (such as polar head groups) and keratin-rich corneocytes, the hydrophilicity of the stratum corneum may change to some extent, and the barrier for water permeation is not absolute. Certain chemicals, known as chemical penetration enhancers (CPEs), as well as physical damage and some pathological conditions may significantly increase the permeability of stratum corneum.

The methods to control skin permeability is of special importance for biomedical use as they can help to improve the delivery of the drugs and nanomaterials to the target structures. CPEs are among the most used agents to achieve the better permeability. Among the popular formulations of CPEs different classes of chemicals can be found including alcohols (short chain: ethanol, isopropyl alcohol; long chain: hexanol, octanol etc.), cyclic amides (azone), alkyl, benzoic acid and fatty acid esters; ether alcohols (“Transcutol”), fatty acids (oleic acid, linoleic acid, palmitic acid, stearic acid etc.); glycols (dipropylene glycol, propylene glycol etc.); sulfoxides (dimethyl sulphoxide, etc.); surfactants of various nature (sodium lauryl sulphate, Tween 80, etc.) and terpenes (menthol, etc.) [474]. The mechanisms of action of CPEs are based on the effects of their interactions with the components of stratum corneum barrier such as keratins and lipids. The exact mechanisms of action of CPEs are individual and not fully studied, however, in general the majority of them are based on lipid fluidization, lipid extraction and change of the lipid ordering, as well as effects on keratin such as displacement of bound water [472, 474, 477]. The optimal choice of the CPE can help to achieve a special goal of the topical application of the drug or nanoparticles on the skin, as the agents may be deposited in the epidermis or its special sublayers or delivered to the systemic blood circulation through the dermis. The physicochemical

fundamentals for the solutes transport through skin is diffusion-partition-solubility theory, which describes the relationships between distribution of the transported matter in the immiscible phases (such as skin proteins and lipids) and intrinsic solubility of the compound [474, 477].

Summarizing the information of the considered physicochemical defence systems on the transport of drugs and nanomaterials, the skin as a whole can be considered as a combination of complex permeability barriers of various nature. The main massive of the data related to the skin permeability was obtained in the experiments with the soluble materials. Nanoparticles penetration through the skin has been analyzed in several publications [478–485] and summarized in the recent review [486]. The principal message resulting from these papers is that the smaller particles and longer exposure time are the most important factors contributing to the delivery of the nanoparticles across the epidermis. However, there is no final verdict on the ability of nanoparticles to penetrate stratum corneum and translocate to the deeper, epidermal and dermal layers as the results of the studies are conflicting almost like 50/50 ratio even for the cases where various penetration enhancers have been used [486]. The scheme summarizing the current understanding of the factors affecting the penetration and permeation of the nanoparticles through skin is shown at Figure 3.13.

The other side of the problem, such as the effects of the nanomaterials, conventional drugs as well as CPEs and other vehicles, on the components of the skin tissues is also very important. As it has been discussed, the permeation of the macromolecules, drugs and nanomaterials through skin is significantly limited by stratum corneum. However, in a case of crossing of this first-line barrier, the listed materials can be transported to the deeper parts of the skin and cleared by blood and lymphatic circulation as well as they may undergo uptake and biotransformation by the cells. In addition, as the dermis of skin is a fibrous connective tissue, the conditions described for the interactions of the nanomaterials and solutes with ECM are applicable as well (Figure 3.14).

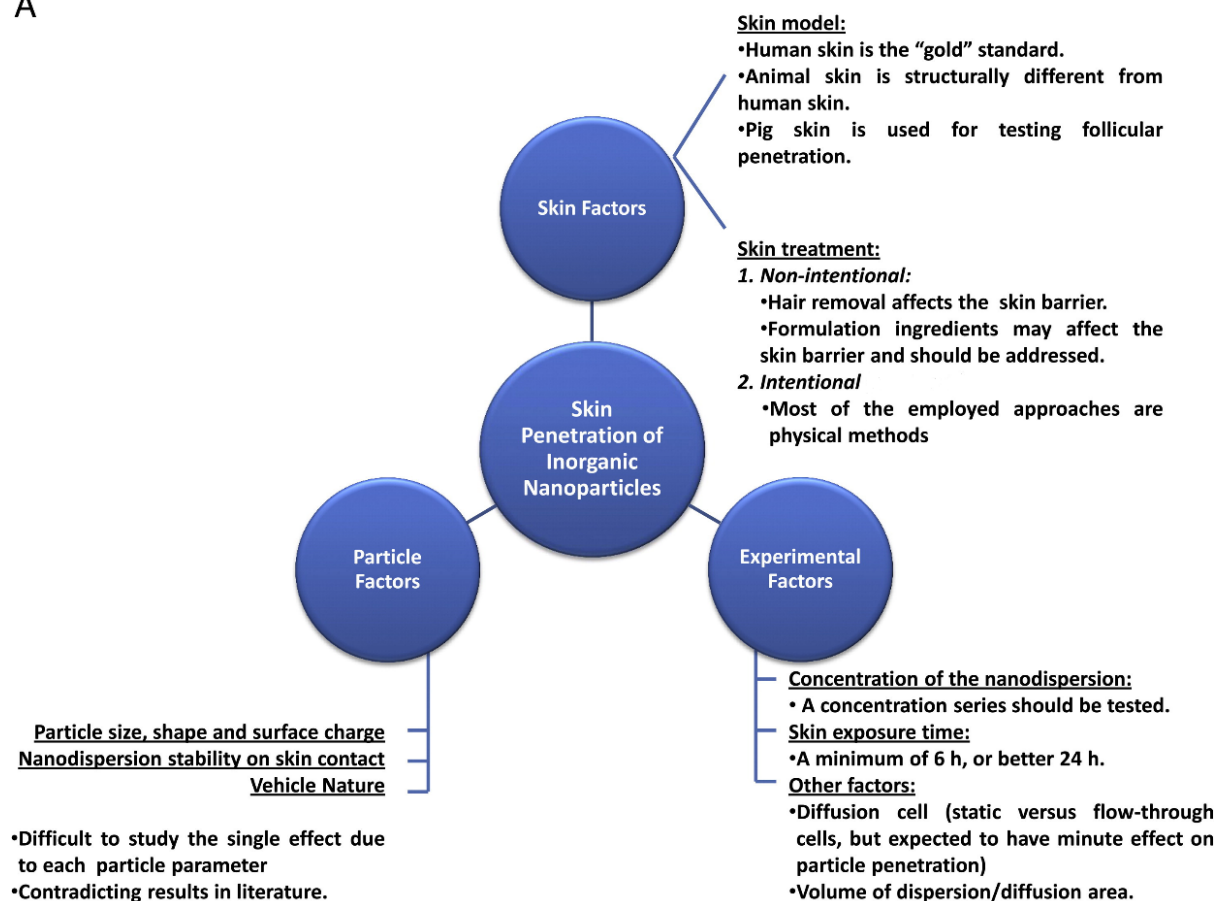
Taking these multiple interactions into account, the safety aspects of application of nanomaterials and associated compounds as CPEs for biomedical use, including theranostics, in the skin is of special importance. Several studies are available on this topic. For example, it has been shown that silver nanoparticles, depending on dose and surface modification, induce inflammatory response and decrease the viability of epidermal keratinocytes *in vitro* and provoke the focal inflammation in skin *in vivo* [487]. Similar results were obtained for Cd/Se quantum dots [488]. In other research, negligible permeation of ZnO nanoparticles into viable layers of skin was found, while the solubilisation of the nano-ZnO resulted in Zn^{2+} ion leakage and increase of zinc level both locally and in the blood [478].

The ability of small gold nanoparticles to embed into collagen fibers was demonstrated in the experimental conditions [437], indicating possible modification of the properties of the dermis ECM in living skin exposed to this type of nanostructures. This interaction potentially may change the stiffness and nanoscale landscape of the ECM, resulting in changes of the cellular behaviour and wellbeing [489,

490]. In addition, CPEs also can have special effects on skin cells and matrix. For example, oleic acid can induce proliferation of keratinocytes, increase the rate of keratinization and intracellular concentration of calcium ions [491].

At the same time, the studies of the nanomaterials' transcutaneous transport and their biological effects on skin encounter a number of methodological and ethical limitations. As the availability of human skin is limited, the most used replacement material is skin of pigs. The majority of skin permeability studies are performed with use of *ex vivo* setups like Franz diffusion cells and Saarbruecken penetration cells [492], where excised skin samples are placed on a special stages and underwent topical application of the studied formulations. These models do not allow to evaluate the biological effects of the nanoparticles, drugs and CPEs as the cells are in non-viable state (usually – frozen and thawed). Animal testing of the toxicity and irritation potential of the materials, which have been a standard for long time, now gradually eliminated from the research toolbox because of ethical considerations, rising costs and legislation [467, 493, 494], while the potentially irrelevant 2D *in vitro* cell culture assays are still in use. The novel approaches utilizing the tissue engineering modelling of skin and its parts can help to overcome this limitations and provide sustainable 3D *in vitro* platforms for testing both permeability and biological responses of skin on applications of the nanoagents.

A



B

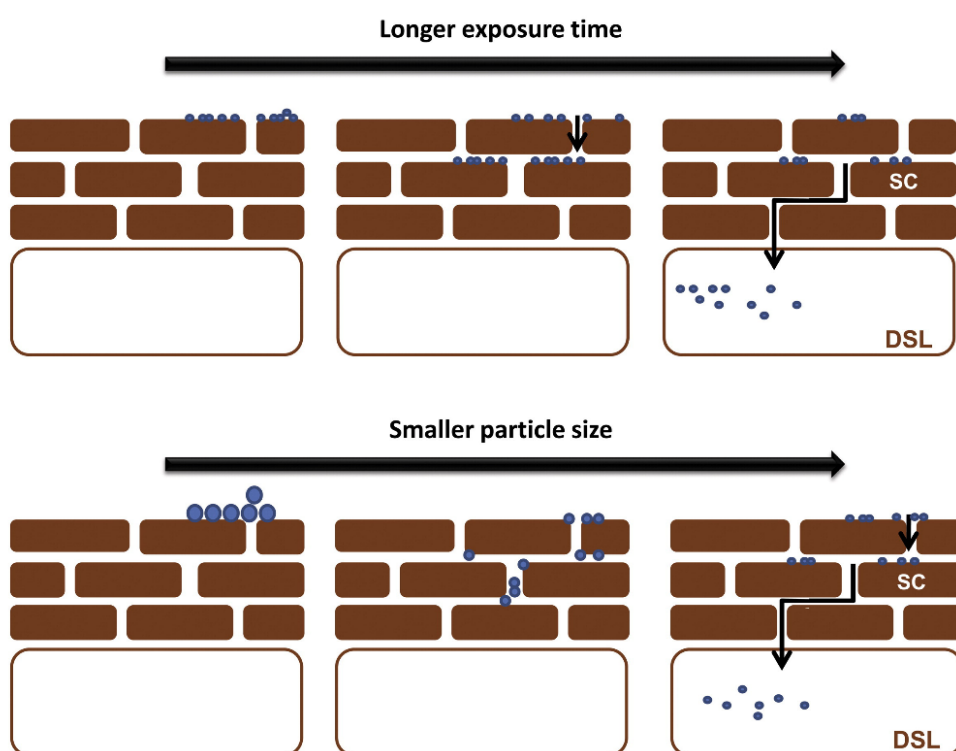


Figure 3.13. Schematic presentation of the factors affecting the ability of the nanoagents to penetrate/permeate the skin barrier. Abbreviations: SC, stratum corneum; DSL, deeper skin layers. Reproduced from [486].

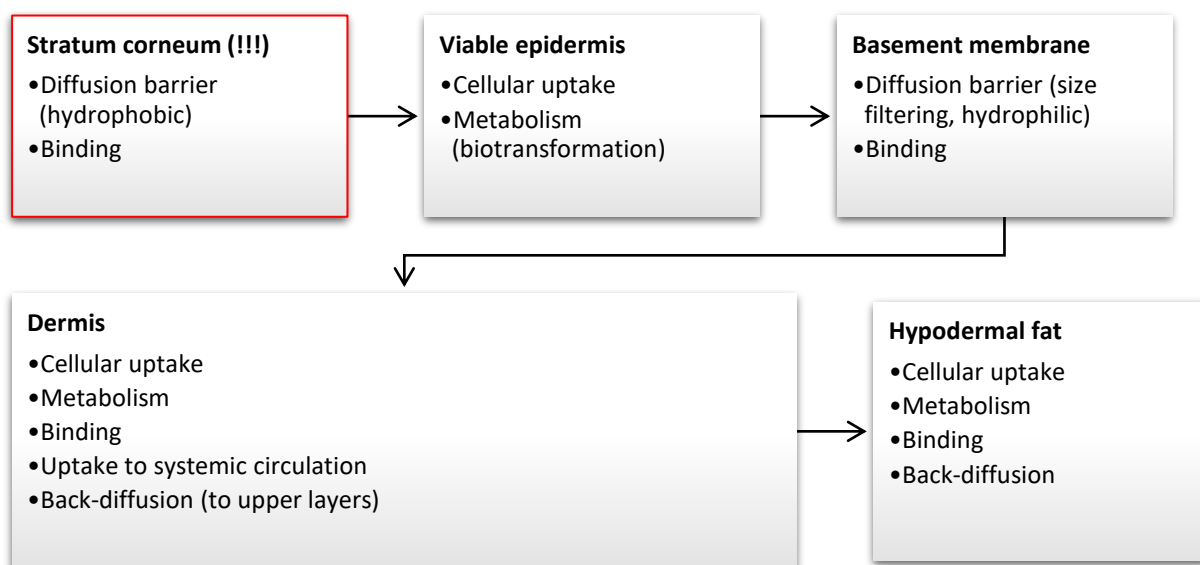


Figure 3.14. The schematic view of the most important processes involved into the transport of the soluble materials and nanoparticles through the skin. The idea of the scheme is taken from [495] and applied with significant changes.

3.2. Tissue engineering models of healthy and diseased tissues in nanotechnology research

The results of recent studies emphasize the advantages of nanotechnology approaches for clinical use and biomedical research. However, the real entry of nanoagents into these practical fields is hindered due to the lack of adequate, ethical and sustainable models, capable to reflect the complexity of the biological environment, where the nanoparticles should operate [496]. There is a growing understanding of the limitations of monolayer conventional 2D *in vitro* cell cultures and animal models with regard to the studies of the safety risks, biological effects and nanotheranostics applications of the materials of nanoscale size [11, 467]. In this subsection the basic methodological and theoretical aspects of 3D *in vitro* tissue culture and experimental tissue engineering will be considered with special emphasis on modelling of normal skin and malignant tumors and their applications in nanotechnology research.

3.2.1. Fundamentals of 3D cell culture *in vitro* and tissue engineering

The principally unavoidable limitations of conventional 2D *in vitro* cell culture is absence of realistic cellular microenvironment, which results in abnormal morphology, gene expression, signalling, behaviour and responses of the cells, grown on the flat and stiff plastic surfaces. This includes artificial character of cell-cell and cell-substrate interactions as well as abnormal metabolism due to the absence of chemical and physical gradients in the culture medium [497, 498]. It is gradually become appreciated that the data obtained with use of monolayer *in vitro* cell cultures should be treated with caution as the complexity of real histology and physiology of normal and pathologically changed tissues and organs is largely ignored in this type of models. It is especially important in the fields of drug research and

nanotheranostics, where the therapeutic responses and diagnostic reliability are highly dependent not only on the reactions of the target cells, but also from the effects of the whole-tissue environment and contributions of various physiological systems, as it was discussed in the previous section of the current chapter. A more appropriate approach allowing to reconstruct *in vitro* much complex structures than cellular monolayers or suspensions *in vitro*, first emerged as a recognized research tool in late 1990s, and now is known as three-dimensional (3D) cell/ tissue culture *in vitro*. This term includes various types of experimental setups, where the cells are placed into the conditions making them to create tissue-like structures of various degree of complexity and heterogeneity [499]. The most important features of the 3D *in vitro* cultures, that can change the biological properties of the cells and their responses on the external challenges like the nanoparticles' application are compared with the conventional 2D cultures at Figure 3.15. The main goal of 3D cell culture us to fill the gap between the experimental use of the monolayer cell cultures *in vitro* and the studies involving animals [497, 499].

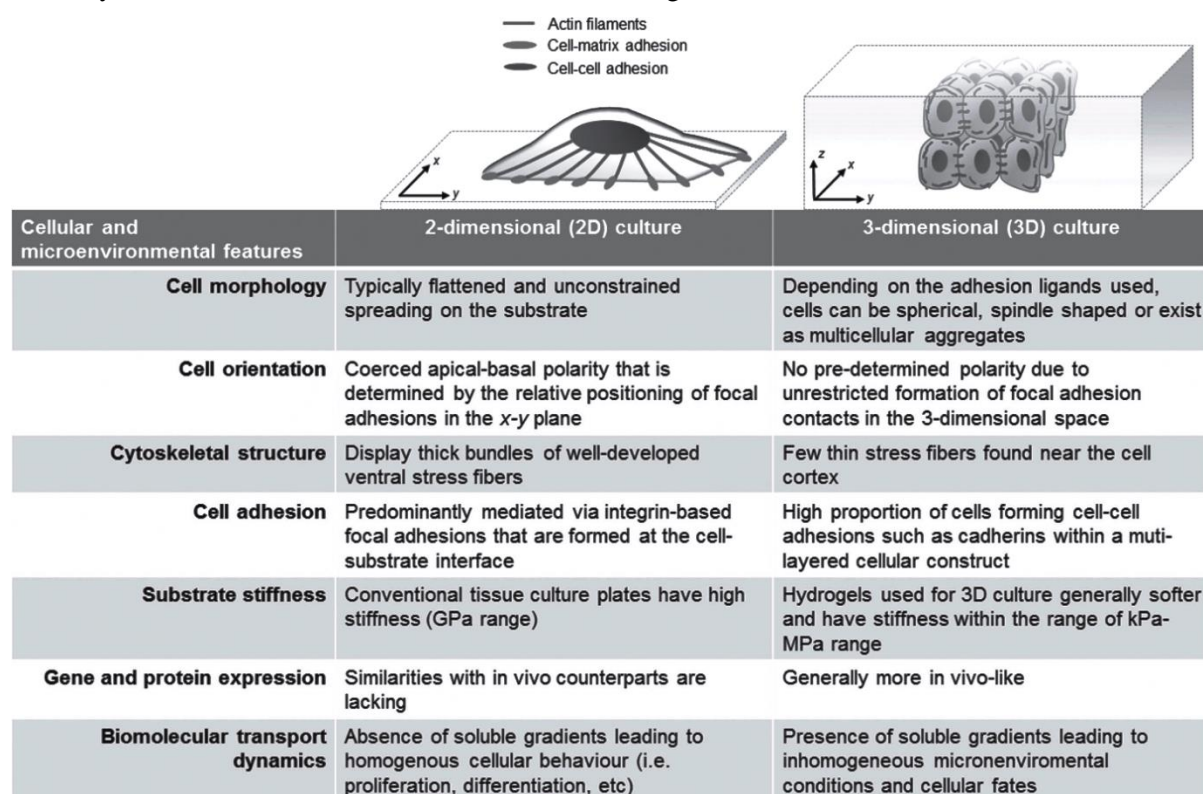


Figure 3.15. Principal differences between 2D and 3D *in vitro* cell culture, which may contribute to the distinctive behaviour of the nanoparticles and cellular responses. Reproduced from [11].

There are 2 main types of 3D *in vitro* cultures such as scaffold-free and scaffold-based systems [498], depending on the presence of supporting and guiding substrate, which plays a role of the natural ECM of the modelled tissue. Scaffold-free cultures are the 3D cellular aggregates like multicellular spheroids, embryoid bodies and multilayer cellular sheets. In fact, all the “scaffold-free” cultures contain some ECM as the cells usually preserve the capability to synthesize the matrix compounds. Scaffold-based cultures may be classified by the physical form (gels and solid scaffolds), origin of the materials used for scaffold production (natural and synthetic), and methods of production (derived from natural

sources or fabricated by engineering methods). A special category of 3D cultures is presented by organotypic models such as organ explants (thin slices of the excised organs as well as small organs) and small animals (zebra fish and mouse embryos, and *drosophila melanogaster*) maintained *ex vivo/ in vitro* [499].

The most advanced 3D *in vitro* systems, the tissue engineering constructs (TECs) [500], are scaffold-based, multicomponent cultures, involving complex combinations of the acting factors and maintenance conditions in order to reconstruct a certain tissue or organ in their normal or diseased state. The terminological border between 3D cell culture *in vitro* and tissue engineering models currently is not very clear. Initially the engineered tissues were purposed for the replacement of the severe damaged human body structures under the framework of regenerative medicine. However, now the tissue engineering methodologies were shared with the field of experimental morphology. In the current study we accepted the work definition of experimental TECs for the complex scaffold-based 3D *in vitro* cell cultures, which model a certain tissue, organ or pathological structure (e.g. a tumor) and also may survive and reproduce the physiological behaviours of the modelled structure if grafted *in vivo* (in animals).

3D cell cultures are maintained in culture mediums, as it normally performed in conventional *in vitro* techniques. However, in addition to static culture conditions, when the growing cells and culture medium are not moving relatively to each other, 3D *in vitro* cultures can be developed as dynamic systems, with flowing culture media or moving cellular constructs. The engineering setups used for the dynamic 3D cell culture are known as bioreactors [501]. The detailed analysis of bioreactor systems in tumor tissue engineering is provided in our recent review [502].

The choice of the cells that can be cultured in 3D conditions is almost the same as for conventional monolayer culture *in vitro*. It includes adhesive primary and linear cell types of different degree of differentiation – from stem cell to the mature, fully differentiated phenotypes. However, the seeding and culturing conditions for the cells in 3D *in vitro* systems may differ from the matching 2D cultures mainly because of limitations of mass transfer in the volume of the modelled tissues [503]. Cell seeding procedures for 3D culture can be the same as in conventional monolayer development, but also can be modified to achieve more specific spatial placement and more efficient distribution. For example, one of the approaches widely used in 3D culture and tissue engineering is high density seeding, when large amounts of cells are delivered in a small volume of culture medium. Cells also may be mixed with the semi-liquid substrates; or cellular suspensions may be perfused through the scaffolds, or other types of fluid flows may be employed with use of bioreactors.

The simplest type of 3D *in vitro* cell cultures is multicellular spheroids. This model was proposed by R. Sutherland [504] more than 40 years ago, and, having being relatively underestimated at the beginning, later, especially during the last two decades, it was recognized as extremely valuable tool to

study the cell-cell interactions, the effects of metabolic gradients on proliferation and apoptosis, transport and biotransformation of the drugs and nanomaterials, drug resistance and methods of bioartificial tissues' formation (more efficient cell delivery for regenerative medicine and 3D printing). The most important benefit of the spheroid 3D culture, making it an especially useful instrument for cancer research, is their ability to recapitulate the structure and physiology of small fragments of solid tumors, including the gene expression, tissue architecture, invasive behaviour and drug responses [505] (Figure 3.16).

The capability to form spheroids was confirmed for many cell lines, as well as various methods of spheroid growth initiation were demonstrated. In addition, these platform allows co-culturing two and more different cell types, for example hepatocytes and mesenchymal stem cells [506] or tumor cells and endothelial cells [507] to develop heterospheroids (histoids). The most popular approaches are hanging drop and liquid overlay method, both based on the assembling of cellular aggregates under gravity force [508, 509]. Modern modifications of these methods allow to get multiple spheroids of uniform size and density, which is very useful for high-throughput pharmacological screenings [510-512]. Another advantage of spheroid 3D culture is availability of the multiple methods for endpoint assays of the structure and functional state of spheroids [513]. Spheroids also may be placed into hydrogels (see Figure 3.16), seeded on scaffolds or implanted in animals.

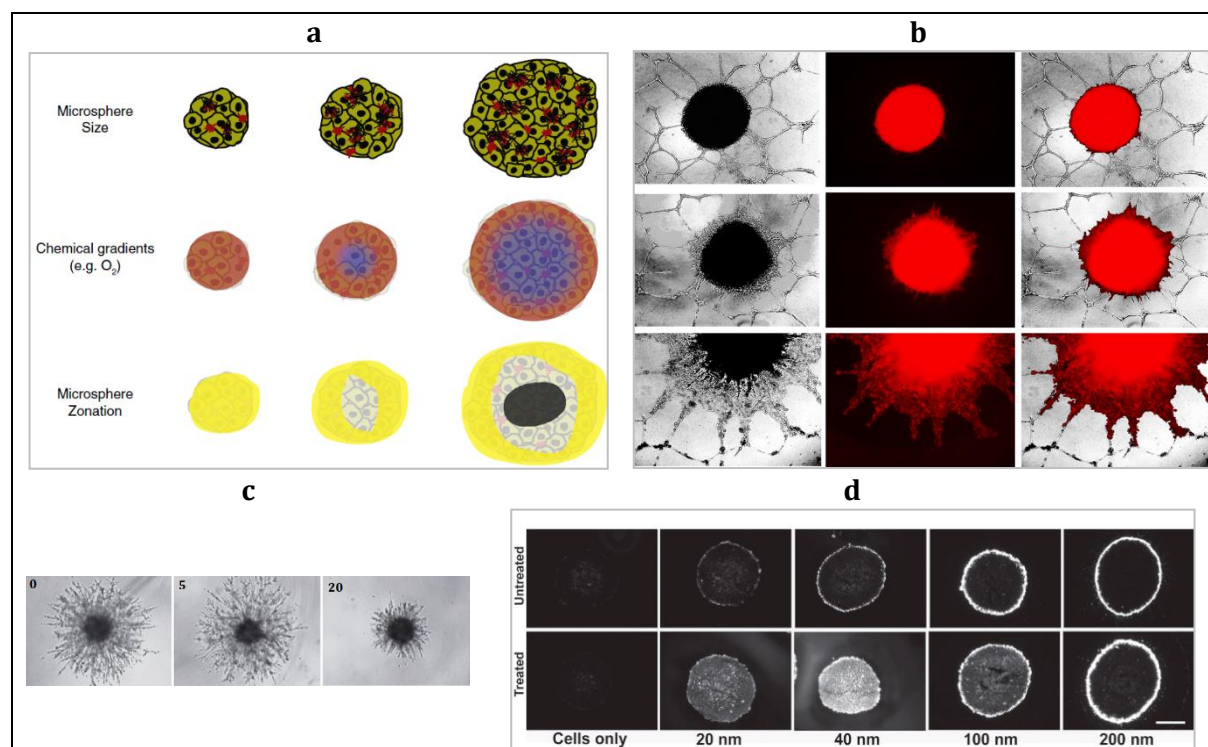


Figure 3.16. Principal features and applications of 3D spheroid cell cultures in vitro. (a) Development of metabolic gradients and matching zonal structure during spheroids' growth (yellow: proliferative zone; black: necrotic zone). Reproduced from [514]. (b, c) Spheroids in Matrigel. (b) Preferential invasion of the MDA-MB-231 cells, labelled with red fluorescent protein (RFP), along the blood capillary tubules grown in Matrigel. The cells seeded as a spheroid (the up row) gradually escape the core On day 3 (middle row) and from metastatic outgrowth protrusions on the day 7 (bottom row). Bright field (left column), fluorescence of RFP (middle column) and overlay (right column). Reproduced from [505]. (c) Effect of anti-cancer drug Sulforaphane on invasiveness of MDA-MB-231

cells. Numbers indicate concentration of the drug in μg . Reproduced from [505] with changes. (d) Intensity and distribution of fluorescence indicate the effect of collagenase (0.1 mg/mL for the “treated” and 0 mg/mL for “untreated”) on permeability of spheroid formed by SiHa (human cervical carcinoma) cells for various sizes of fluorescently-labelled polystyrene nanoparticles. Scale bar is 200 μm . Reproduced from [515] with changes.

Scaffold-based 3D cultures reconstitute not only the cellular complexes, but mimic the simplified tissue structures, where the cells interact with the ECM (or its analogue). So, the scaffolds play a role of the ECM, and then they should not only perform as a passive vehicle, but have to be an active template, guiding the cellular phenotype and behaviour in a manner close to that observed in the modelled tissue [516]. Scaffolds may be selectively prepared from natural and synthetic materials or produced by the combination of the compounds of different origin.

The natural materials usually used for 3D cell culture *in vitro* include individual components of ECM (mainly “connective tissue type”) like collagen, fibrin, fibronectin, hyaluronic acid and others. Some materials can be obtained from plants or animals as well, like seaweed-derived alginates and chitosan or different types of silk, respectively. Scaffolds also may be created as less chemically defined compositions of natural origin, for example, the basement membrane extracts (“Matrigel”, “Cultrex”) [499, 517].

There is an alternative procedure to produce the scaffolds of natural origin, which is known as decellularization (DCL) [518]. It implies a treatment, usually physical or chemical (or combined), of excised animal organs, or less frequently, the discarded donor tissues and organs of human origin, embryonic waste and cadaveric materials [519, 520]. As a result of DCL the cellular membranes are destroyed, including the attachment structures, connecting the cells with the surrounding ECM. Extensive washing with water, buffers and, sometimes, enzymes, helps to remove the cellular debris, including the nuclear residuals. Initially DCL was purposed for removal of immunogenic determinants (which are predominantly of cellular origin) from the materials intended for further use in reconstructive surgery and regenerative medicine [516] (Figure 3.17).

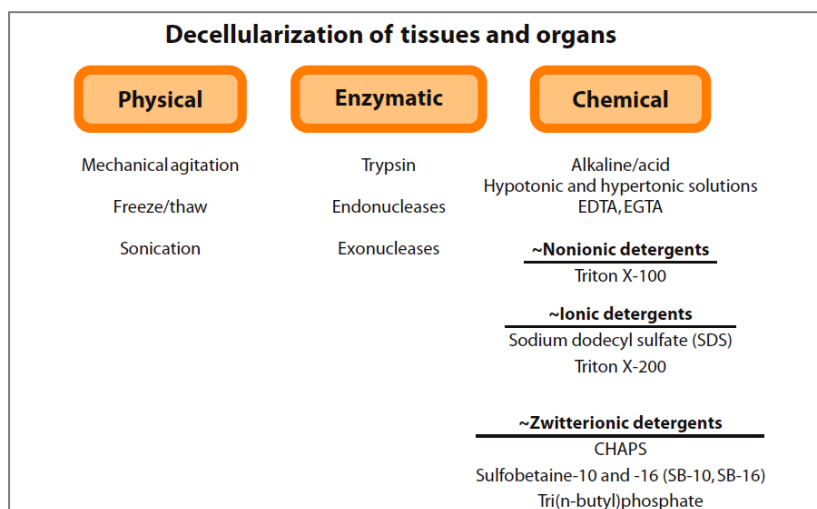


Figure 3.17. Techniques used for DCL of tissues and organs. Physical, chemical and enzymatic treatment may be used individually or in combinations. Abbreviations: CHAPS, 3-((3-chol-amidopropyl)dimethylammonio)-1-propane-sulfonate; EDTA, ethylene diamine tetraacetic acid; EGTA, ethylene glycol tetraacetic acid. Reproduced from [521].

DCL may be carried out by continuous immersion of the tissues in the cell-destroying and washing reagents, or, in some cases, it also can be achieved by perfusion of natural vasculature of the whole organs [522, 523]. The most attractive feature of the scaffolds, obtained by DCL, is the chemical composition close to the natural ECM. Despite the fact that CL changes the ratios of the individual components of the ECM, the principal matrix constituents are preserved as well as ECM-bound signalling molecules [524]. Whole-organ DCL allows to keep not only the chemical contents of ECM, but also the spatial organization of the treated organs and tissues. In particular, the perfusion DCL of whole organs saves the shape of the whole organs and preserves the internal geometry of their compartments, including the vasculature tree. This provides a possibility for further recellularization of the DCL organs and tissues and their clinical and research use [520] (Figure 3.18).

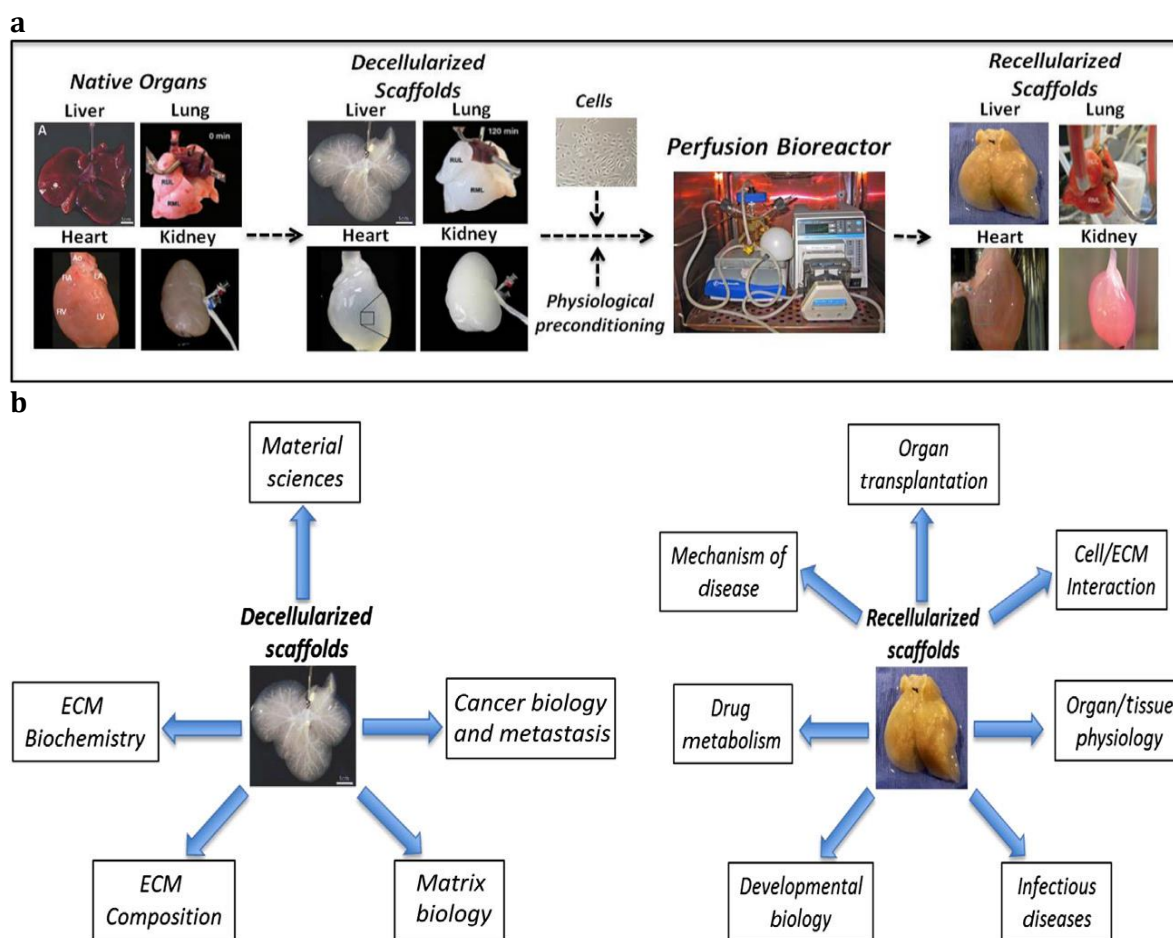


Figure 3.18. The concept of whole-organ tissue engineering. (a) DCL of whole organs by perfusion through natural vasculature allows preservation of the organs shape, internal spatial organization of ECM an its chemical composition. The decellularized organ scaffolds can be repopulated with different types of cells in order to get functional organ-specific TECs. (b) Examples of the applications of whole-organ DCL scaffolds and organ-specific TECs. Reproduced from [525].

The greatest advantages of the naturally-derived scaffolds are biocompatibility and presence of cell-attachment moieties. They are also biodegradable, which is important for creation of the implantable TECs, but may be undesirable for long-time maintenance of the culture system *in vitro*. The most

important drawback of the scaffolds, prepared from natural materials is the batch-to-batch variability of their structure and composition and relatively limited tunability of the mechanical properties, in comparison to the cell culture substrates produced from synthetic substances [498]. In addition, the difficulties of purification of the biologically-derived materials and the risks of pathogen transmission are also should be taken into account [526].

Synthetic scaffolds can be prepared from various polymers, self-assembled peptides, titanium and ceramic materials [498]. The most notable contributions into the field of 3D cell culture based on synthetic scaffolds have been done with use of polyacrylamide (PA) hydrogels, PEG and various polyesters like poly (lactic acid) (PLA), poly(glycolic acid) (PGA), poly(lactic-co-glycolic acid) (PLGA), and poly(ϵ -caprolactone) (PCL) [527, 528]. Synthetic scaffolds, in contrast to the natural ones, provide excellent reproducibility, well defined chemistry and a numerous possibilities for tailored modifications and the mass production [528]. In particular, the mechanical properties of synthetic scaffolds may be tuned by changing of the polymer concentrations and polymerization conditions [527]. The detailed comparison of the advantages and disadvantages of natural and synthetic scaffolds with regard of the key factors of 3D cell culture have been done in the recent comprehensive review papers [527, 528] (Table 3.1).

Two main platforms of scaffold-based 3D cultures such as hydrogel systems and the models created with use of the solid porous and fibrous materials may be classified depending on the physical state and morphology of the matrix [498].

Hydrogels are crosslinked hydrophilic polymers, which can be purely natural or synthetic, or they can combine the materials of different origin [529]. Their stiffness is in the range characteristic for soft tissues (measured in kPa, in contrast to the cultural plastic, which have the values in GPa range [13]), they are widely used to mimic ECM cellular microenvironment. Hydrogels used for 3D culture should have good biocompatibility (or could be modified to achieve it) and, in a case of tissue engineering applications, biodegradability. High water contents, facilitation transport of soluble factors, oxygen, nutrients and wastes. The controllability of the gelation process by the temperature, pH, light stimuli or ion concentrations allows to prepare mixtures of the liquid precursor polymer and cells and later induce solidification of the gel [530].

Table 3.1. Advantages/disadvantages of scaffolds prepared from natural and synthetic materials for 3D cell culture. Based on [527] with changes and added with the data from [528].

Characteristics	Naturally derived matrices	Synthetic & semi-synthetic matrices
Biocompatibility for 3D cell culture	• Very high	• Basically low , but tunable
Bioactivity	<ul style="list-style-type: none"> • Biocompatible and bioactive (ample ligands for cell adhesion and signaling) • Difficult to isolate specific bioactive factor for experimental study 	<ul style="list-style-type: none"> • Bioinert (require passive protein absorption (polyesters) or extra engineering (PEG)) • Greater control over bioactivity with less experimental confounding
Mechanical properties	<ul style="list-style-type: none"> • Tunable via additional crosslinking • Generally alters ligand density • Limited to low-range elasticities 	<ul style="list-style-type: none"> • Tunable with minimal/no bioactivity change • Broad range of physiological elasticities
Matrix degradation	<ul style="list-style-type: none"> • Basically biodegradable • Cell-mediated matrix remodelling • Difficult to control 	<ul style="list-style-type: none"> • Enzymatic or hydrolytic degradation is possible • Predictable degradation of synthetic material • Requires modification for cell-mediated degradation
Growth factor content	• Difficult to completely remove	• Absent
Dynamic study	• Generally short-term studies due to matrix remodelling	• Can be longer term
Advanced manipulations	• Limited due to poor handling properties and non-specific bioactivity	• Available

Natural polymers most frequently used for preparation of hydrogel substrates for 3D cell culture *in vitro* are collagen, fibrin, hyaluronic acid, alginate, chitosan, silk or basement membrane extracts (“Matrigel”, “Cultrex”). Hydrogels also can be produced from decellularized tissues [531-533]. Synthetic gels are prepared from PEG, poly(vinyl alcohol), poly(2-hydroxy ethyl methacrylate) [529]. In general, basic biological activity of the scaffolds is a function of ligand density [499]. Due to the growth factors’ presence and availability of numerous cell-attachment sites, the hydrogel scaffolds prepared from natural materials demonstrate intrinsic biocompatibility and may be considered as the substrates promoting growth of the cells in 3D conditions, while the gel scaffolds produced from synthetic materials are basically only “permissive” and require additional modifications in order to improve the cell attachment and viability [529] (Figure 3.19).

Solid scaffolds for 3D cell culture and tissue engineering has more defined spatial structure and higher stiffness than hydrogels. Their porosity defines the total surface available for the cells and the density of ligands [499], while the geometric organization contributes into formation of special designs of the reconstructed tissues like, for example, layered constructs used for skin, intestines, bladder and blood vessels modelling [498] (Figure 3.20).

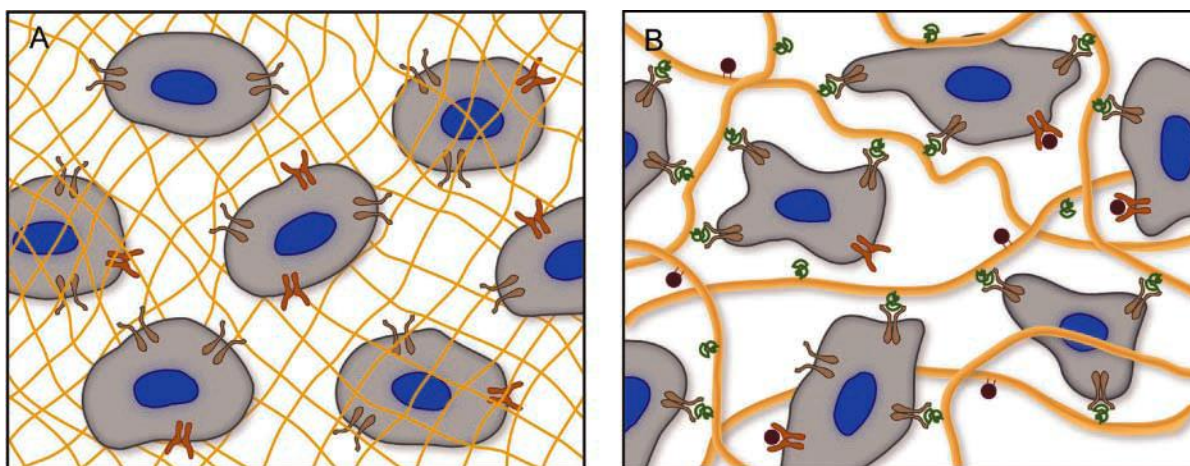


Figure 3.19. Permissive (A) and promoting (B) hydrogels for 3D cell culture. Synthetic polymers (yellow mesh in A) provide a liveable 3D space for the cells; but they don't have signalling moieties to activate integrins (brown) and other surface receptors (orange) of cell-ECM interactions. Naturally derived polymers (yellow mesh in B) present a myriad of integrin-binding sites (green) and growth factors (purple) coordinated to the ECM, initiating multiple signalling cascades. Reproduced from [529].

As well as hydrogel scaffolds, solid matrices may be prepared from natural and synthetic polymers, ceramic materials and decellularized tissues and organs. In addition, various modifications of physicochemical properties and nanotopography of the matrices can be achieved by surface modifications with use of biologically active molecules and nanomaterials [517]. Depending on the morphology, solid scaffolds can be generally classified into two categories such as fibrous and porous [498] (see Figure 3.20), while the decellularized tissues and organs used as scaffolds share the features of both of these categories.

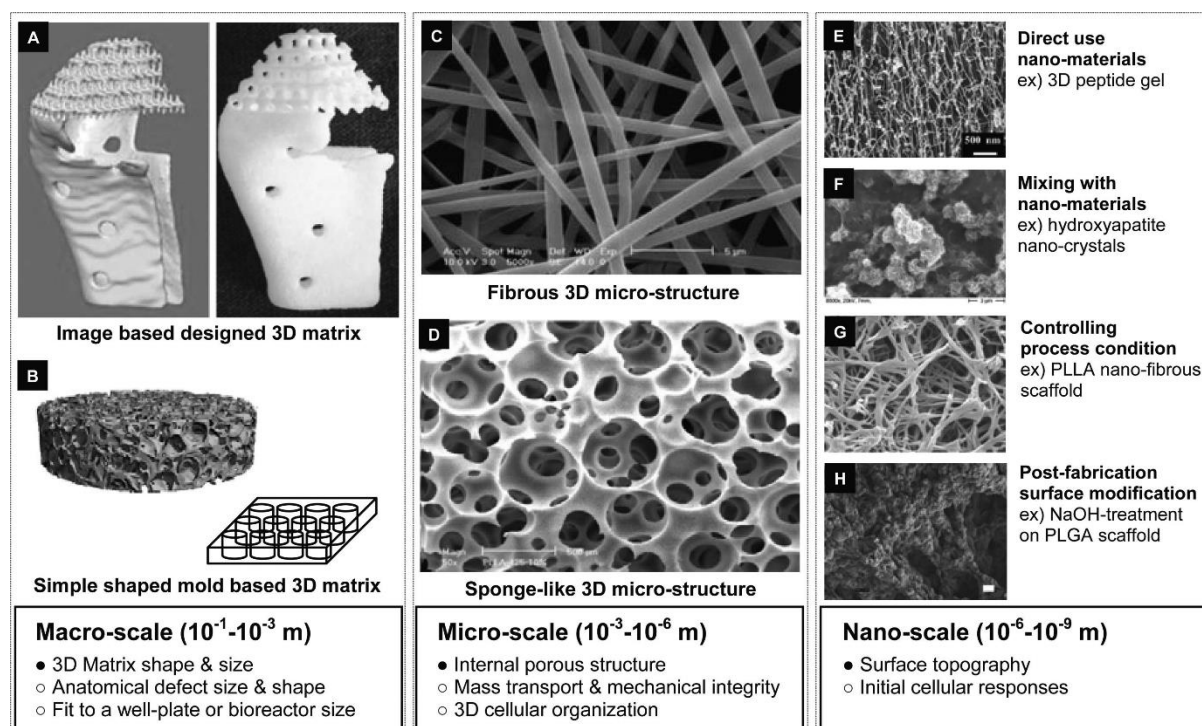


Figure 3.20. Morphological diversity and design criteria of solid scaffolds for 3D cell culture. The desired morphology of the scaffolds may be created at macro- (A, B), micro- (C, D) and nanoscale (E-H), depending on the requirements of the model. Macroscale features are important for the general usability of the devices.

Microscale parameters define mass transport limitations and the initial cellular arrangement. Nanoscale characteristics determine bioactivity of the scaffold such as cell adhesion, motility and phenotype guidance. (A) Implantable scaffold recreated by computer-assisted design on the base of computer tomography image. (B) Development of porous scaffold fitted for the use in multiwell culture plates. Micro-CT image. (C) Fibrous scaffold prepared by electrospinning technology. (D) Pore size, shape and interconnectivity have strong influence on cell adhesion, motility and proliferation as well as on mass transfer of oxygen and nutrients. (E-H) Four methods to achieve nanosized 3D structural features of the scaffold. PLLA: poly-L-lactic acid. Reproduced from [517].

Solid scaffolds may be fabricated by engineering methods or derived immediately from the natural tissues and organs by DCL (see above). The engineering scaffold fabrication methods can be classified for 5 categories such as phase-separation based methods, rapid prototyping, electrospinning and nanotechnology based techniques (for the detailed review see [534-538]). The additional treatment of the materials in order to optimize their characteristics may be done by heat, by use of the adhesives, by light (photopolymerization) [500] and by various approaches of additive engineering [539].

Phase-separation based methods are used for preparation of porous scaffolds and rely on formation of two immiscible phases, where at least one is a polymer and the second one plays a role of porogen and removed as a result of the processing. Depending on the involved phases and the method of their treatment, there are several approaches such as solvent casting/particulate leaching, freeze drying, gas foaming, melt molding and liquid-liquid phase separation. These methods are relatively simple and affordable, some of them allow to control the pore size and connectivity, but the majority of them only result in generation of the macro- and microstructured scaffolds, while the obtaining of nanoscale features is still challenging. Rapid prototyping [540] is a group of manufacturing approaches, which includes stereolithography (SLA), selective laser sintering (SLS), fused deposition modelling (FDM), 3D printing and plotting. Some of these methods operate with solid or powder-form materials only (SLS, FDM, 3D printing), while SLA employs liquid polymers, and 3D plotting is almost universal. Rapid prototyping usually involves computer assisted design of the scaffolds. This allows to get precisely defined spatial structure, including the shape of the scaffold, pores interconnectivity and size [541]. Some of the methods require heating of the compounds to the high temperatures, which excludes a possibility of introduction of biologically active molecules into the scaffold at the time of manufacturing (SLS, FDM), another may use toxic products, which are difficult to remove from the scaffolds (SLA). In general, the rapid prototyping is an excellent approach for the desktop production [542] of the scaffolds for pilot 3D culture experiments purposed, for example, to evaluate the effects of the scaffolds geometry on mass transfer or on the other effects related to the culture conditions, or, in contrast, after finding the optimal configurations, the scaffolds for high-throughput assays may be developed by these approaches. The best combinations of the scaffold-optimization possibilities at the moment, is, probably, provided by 3D plotting, this method may be used for a broad range of the materials and the conditions of the treatment are flexible. However, it may be time-consuming in the process of the scaffold parameters adjustment and the ways to improve the mechanical properties of the matrices are also in demand [534, 543].

Electrospinning allows to produce fibrous scaffolds (see Figure 3.20 (C)) for experimental use and for mass applications with reasonable ease and affordability [534]. This well-established method is based on formation of polymer threads under high voltage [544]. Initially it was mainly applied for manufacturing of the scaffolds from synthetic materials, but now the electrospun matrices also can be prepared from natural polymers like collagen [545] and hyaluronic acid [546], as well as natural-synthetic hybrid fibres [547]. The important advantage of this approach is a possibility to control the diameter of the fibres down to nanoscale, their alignment and the degree of porosity of the scaffold [548]. In addition, it may be combined with various modifiers, including biomolecules [549] and nanomaterials. For example, electrospinning recently was employed in preparation of the nanofibers with embedded UCNPs [202, 550].

Nanotechnology is widely involved in modification of various types of the scaffolds and cell labelling and controlled delivery for the purposes of 3D culture and tissue engineering [551]. For example, introduction of the nanoparticles into the scaffolds were used for control of differentiation of the stem cells [552], cellular adhesion on the matrix [553] or for optimization of the mechanical properties of the scaffolds [554-556] and development of conducting composites [557], local delivery of the signalling molecules and drugs [558-561]. A promising approach based on use of binding of magnetic nanoparticles with cells for assembling of cellular aggregates (such as spheroids) and tissue-like structures under application of external magnetic forces [562-565].

Next subsections are focused on the review of applications of the 3D cell culture and tissue engineering models of normal skin and tumors in nanotechnology research.

3.2.2. 3D and tissue engineering models of skin in nanotechnology research

The studies of penetration, distribution, cytotoxicity and uptake of nanomaterials in skin require special approaches in modelling of the structural and physiological aspects of this organ-specific barrier. The conventional methodology, which was developed in pharmacology for analysis of the mechanisms and the effects of topical applications of the drugs on skin, relies mainly on use of excised samples of human or animal skin (for penetration and permeation assays in diffusion cells), *in vitro* testing on the monolayer cultures of the skin cells (keratinocytes, fibroblast, macrophages, and dendritic cells) and acute and chronic toxicological challenges in live animals. Partially these techniques were transferred to the field of nanotechnology research. However, the specificity of the nanomaterials in terms of the fine tunability of their physicochemical properties, diffusional characteristics and interactions with the tissues' components results in the need of multiple comparisons and precise control of the various combinations of experimental conditions. This reasonably leads to impelled shift towards advanced *in vitro* substitutions of the animal models [11]. In addition, a number of recent legal regulations all over the world ban use of the animals and force the development of the alternative models for the replacement

of animal use in pharmacology and cosmetology [494, 566]. *In vitro* 3D cell culture and tissue engineering methodology not only provide several options in order to meet these requests. Moreover, the *in vitro* skin corrosion and skin irritation tests on reconstructed human epidermis are officially recommended by Organisation for Economic Cooperation and Development (OECD) test guidelines [567]. High-quality *in vitro* reconstructions of viable human skin with use of the cells of human origin also allow to avoid the issues of interspecies extrapolation and study both penetration and irritation effects of the nanomaterials in the same experimental setup.

Generally, 3D *in vitro* cell culture and tissue engineering are used for creation of human skin equivalents (HSE, also referred as living skin equivalents, LSE) models such as reconstructed human epidermis (RHE), consisting of multilayered epidermal cellular construct with stratum corneum, grown on the acellular natural or synthetic scaffolds, and full-thickness models (FT), which include both epidermal and dermal parts, where the dermal part may be presented by various scaffolds (hydrogel and solid), populated with dermal fibroblasts and, more rare, other types of cells. The RHE models mimic the morphology and physiological properties of human epidermis [494]. Depending on the cells used to recreate the epidermal part of HSE (primary keratinocytes or immortalized HaCaT cells), the efficiency or growth and the rate of keratinization varies. As the HaCaT cells are phenotypically limited at not-cornified differentiation state, they may be applied to create large amounts of artificial epidermis, but need a special treatment to induced keratinization [568]. In contrast, primary cells have lower growth potential, but easily develop the stratum corneum *in vitro*. In general, the procedure used to initiate formation of the cornified multilayered epidermis usually includes bringing of the growing epidermal layer to the air-liquid interface (known as “air-lifting”) after a period of normal submerged culture in the media [569]. This exposure to the phase border induce formation of the stratum corneum. Cornification of epidermis may also require change of the culture medium to another type of it, for example, for the serum-free medium [570]. In FT HSE the epidermal and dermal parts may be initially grown in different culture mediums and then combined together. As the keratinocytes are more sensitive to the environmental factors than fibroblasts, the culture medium for the final development of the FT HSE the choice of the culture medium mainly depends on the epidermal cells “preference” (Figure 3.21).

Several protocols for 3D culture and tissue engineering of HSE models suitable for *in vitro* testing and for grafting in animals were reported to date and some of them are now commercially available and well described in the literature [571-582] (Table 3.2). The most popular models have been validated for compliance to the OECD standards with a notification that the possible overpredictability should be taken into account because of increased absorption properties of the HSE. Also it is suggested that the FT models are superior to RHE for the prediction of toxicity and biotransformation of the topically applied compounds [583]. In addition to the reconstruction of normal skin equivalents, the *in vitro* models of some skin diseases like atopic [584] and eczematous [585] dermatitis, psoriasis [586], melanoma [587, 588] and non-melanoma skin cancers [479] were proposed. Various substitutes of FT

skin, epidermis and dermis are also clinically applied as plastic materials for reconstructive surgery purposes [589].

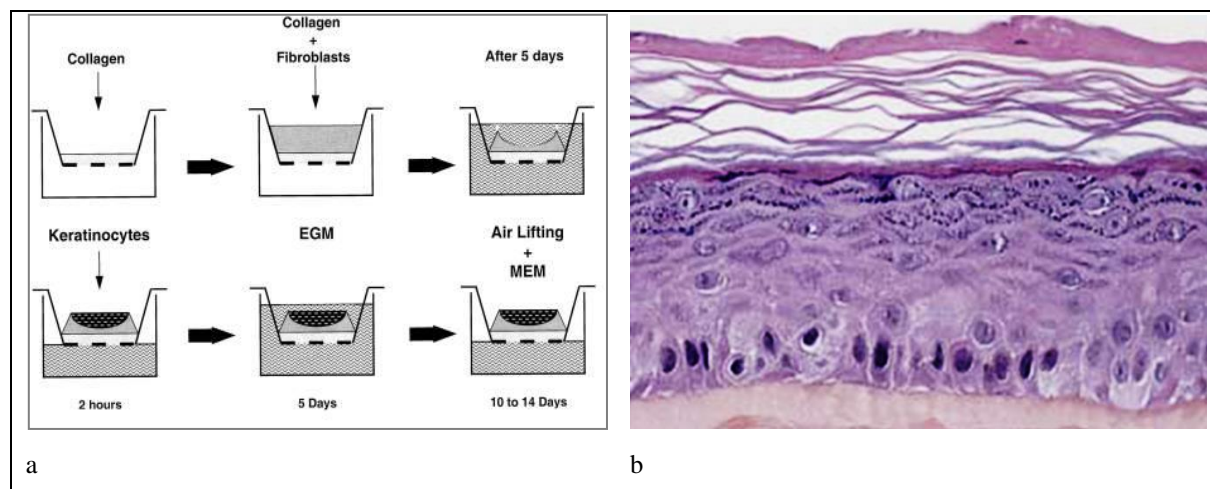


Figure 3.21. The principle of formation of the HSE *in vitro* and the morphological organization of various types of HSE. (a) Step-by-step procedure of development of FT HSE: filling of the cell culture inserts with collagen gel; formation of the next layer of collagen with fibroblasts; contraction of the collagen by fibroblast during 5 days *in vitro*; adding of the keratinocytes or skin cancer cells into the developing nest; submerged culture in epidermal growth medium (EGM) for 5 days and, finally, air lifting and growth in the maintenance medium (MEM). Note the concave surface of collagen gel contracted by fibroblasts. Following this feature the additional control of the area exposed to the tested compounds is needed when using this type of FT HSE [590]. Reproduced from [588]. (b) The histological structure of EpiSkin™ RHE model: note well differentiated layered structure of the reconstructed epidermis. Reproduced from [591].

Analysis of the literature reveals several examples of the use of 3D HSE in nanotechnology research. The studies were focused on: 1) penetration of the nanoparticles through the RSE [592, 593] and FT reconstructed normal skin [479, 590] and *in vitro* modelled skin diseases [479]; 2) cytotoxicity of the nanomaterials in 3D epidermal cultures [594, 595]; 3) effect of morphine-loaded solid lipid nanoparticles on wound healing model created with use of EpiDerm-FT construct [596]; and 4) targeted drug delivery by the NTA on the base of UCNPs into *in vitro* 3D model of epidermis [597] (Table 3.3).

Table 3.2. The most reported in the literature 3D and engineered models of normal skin for experimental use.

Name	Manufacturer	RHE or FT?	Culture area	Cells used in the epidermal substitute	Subepidermal structure (by the manufacturer's or literature descriptions)	Ref.
EpiSkin	Episkin SNC (L'Oréal), France/ Laboratoires SkinEthic, France	RHE	1.1 cm ²	Second passage normal human keratinocytes, 13 days of <i>in vitro</i> growth	Type I bovine collagen matrix, representing the dermis, surfaced with a film of type IV human collagen, representing the basement membrane	[598, 599]
SkinEthic		RHE	0.6 cm ²	Normal human keratinocytes (NHEK), 17 days of <i>in vitro</i> growth	Inert polycarbonate filters	[598, 599]
EpiDerm™	MatTek Corporation, USA	RHE	0.6 cm ²	Normal, human derived epidermal keratinocytes (NHEK)	Tissue culture inserts, specially prepared (agarose gel coating (?))	[598, 599]
EpiDerm-FT™		FT		Normal, human derived epidermal keratinocytes (NHEK), 17 days of <i>in vitro</i> growth	A collagen matrix containing viable normal human dermal fibroblasts (NHDF), a well-developed basement membrane	[583, 600]
Cosmital (in-house model)	Wella/ Cosmital, Germany	FT	0.8 cm ²	Interfollicular epidermal keratinocytes derived from human skin (first or second passage), 14 days of <i>in vitro</i> culture	Cell culture inserts (Snapwell™, Costar) seeded with postmitotic human fibroblasts on the undersurface of their microporous membrane	[598, 601]
Phenion	Henkel/ Phenion, Germany	FT	?	Normal, human derived epidermal keratinocytes (NHEK), passage 3; 6-8 weeks of <i>in vitro</i> growth	Chemically cross-linked lyophilized bovine achilles tendon collagen, and normal human dermal fibroblasts, passage 5	[583, 602]

Table 3.3. Experimental application of 3D *in vitro* culture and tissue engineering models in nanoresearch.

Model	Nanomaterial and experimental conditions	Purpose	Results	Ref.
EpiDerm™ model epidermal membrane placed in a Franz' diffusion cell	Quantum dots (QDs), 24 h exposure <i>in vitro</i> ; 4 h exposure under occlusion <i>in vivo</i>	Comparison of penetration of QDs into human skin <i>in vivo</i> (tape stripping assay in volunteers) and <i>in vitro</i>	Accumulation of the QDs in stratum corneum was revealed both <i>in vitro</i> and <i>in vivo</i> , no penetration and permeation to the deeper layers was found	[592]
EpiDerm™	Silica nanoparticles, positively or negatively charged (20 nm, -13.35 mV and +37.33 mV; 100 µL, 500 µg/mL, 8 h exposure + 6 days of post-exposure observations), <i>in vitro</i> ; sophisticated image analysis	Analysis of the effect of the nanoparticles' surface charge on translocation through the epidermis	Initially the anionic nanoparticles permeate the epidermis more rapidly, than the cationic ones, but finally observed penetration depth after 6 days post-exposure was the same for the both types of the particles	[593]
Excised human skin, EpiDerm-FT™, peeling skin disease (PSD) model, non-melanoma skin cancer (NMSC) and in-house normal FT HSE, prepared with keratinocytes and fibroblasts from the same patients	Flexible dendrimer-type carrier, core-multishell (CMS) nanotransporters, loaded with Nile Red or tagged with indocarbocyanine (ICC); 6 and 24 h exposure	The skin penetration study	Similar patterns of penetration of the CMS nanotransporters in the excised and reconstructed skin. After 6 h exposure – only accumulation in the stratum corneum was notable, and after 24 the particles penetrated into the deeper skin layers. Altered absorption in the diseases' models	[479]
In-house FT HSE: HaCaT keratinocytes grown on collagen type I (from rate tails) with fibroblasts during 7 days in submerged culture and 13 days in air-lifted culture	Au nanoparticles, 15 nm in diameter, hydrophilic, -35.1 mV, citrate stabilized, 2 or 24 h exposure time	Analysis of the effects of exposure time and the tissue fixation of penetration of Au nanoparticles; comparison with the previous tests on human skin with the same particles	After 2 h exposure in FT HSE the particles localized in SC only. This result is equivalent to the 24 h exposure experiment in human skin. After 24 h the nanoparticles penetrated through epidermis to the dermal layer of HSE. Fixation increased localization of the nanoparticles in the stratum corneum the and penetration to the dermal layer after 24 h exposure	[590]
EpiDerm™	Envirox™ fuel additive, containing cerium oxide nanoparticles; compared with non-nano cerium oxide	Skin irritation test and cytotoxicity assay	No adverse effects on 3D HSE, no difference between nanoparticles and non-nano cerium oxide	[594]

Table 3.3. Experimental application of 3D *in vitro* culture and tissue engineering models in nanoresearch.

(Continue).

2D HaCaT keratinocytes <i>in vitro</i> culture, EpiDerm™, and <i>in vivo</i> rabbit skin irritation model	Nanosilica, 7 and 10-20 nm, up to 500 mg/mL	Study of the cytotoxic effects of nanosilica in 2D HaCaT <i>in vitro</i> culture and in the HSE model; the role of the particles' size; the irritation potentials of nanosilicas on rabbit skin	Nanosilicas reduced the cell viability of keratinocytes in 2D culture at concentrations of ≥ 30 -50 $\mu\text{g/mL}$ in a dose-dependent manner. Neither signs of irritation was found in HSE even at the concentration of 500 $\mu\text{g/mL}$ of nanosilica, nor acute cutaneous irritation <i>in vivo</i> .	[595]
EpiDerm-FT™; and laser burn-wound healing model on EpiDerm-FT™	Morphine-loaded solid lipid nanoparticles (SLN), mean size about 180 nm	Study of the effect of morphine-loaded SLN on wound closure in a new HSE-based 3D <i>in vitro</i> wound healing model	Morphine, morphine-loaded and unloaded SLN accelerated reepithelialisation; low cytotoxicity and irritation effect of the tested particles, as well as possible prolonged morphine release	[596]
EpiDerm-FT™	UCNPs, biofunctionalized by anti-CD163 antibody (anti-rosacea) and loaded with topical antibiotic drug doxycycline, an anti-microbial drug Azelaic acid	Evaluation of the transdermal delivery of the nanoemulsion containing UCNPs as a NTA for further use in rosacea treatment	Penetration through the FT HSE, increased uptake of the nanoemulsion by dermal keratinocytes and fibroblasts and deeper penetration into the skin layers, in comparison to the topical application of the antibiotic and/or antimicrobial drug alone	[597]

As it follows from the analysis of the literature reports, the use of 3D *in vitro* culture and tissue engineering models of skin in nanotechnology research is at the early stage, and only a few papers are available to date. However, these publications confirm feasibility of the 3D *in vitro* skin constructs for a spectra of testing purposes, which are of special importance for the future development of safe and meaningful applications of nanotheranostics technologies in biology and medicine.

3.2.3. 3D and tissue engineering models of malignant tumors in nanotechnology research

Cancer biology and oncology applications impose a number of very challenging requirements for the nanomaterials such as combination of the ability to pass through a series of biological barriers, having being functionally efficient at the site of the destination (a tumor) and safe in general (a body). The barriers, which the nanoparticles encounter on their way to the malignant tissue, depend on the exposure route (see Figure 3.6) and the parameters of the nanoparticles (see Figure 3.7), finally defining the biodistribution of the nanomaterials, introduced into the body. Next, if the particles successfully reached the tumor, they enter into extremely tangled microenvironment as it was discussed above in the

subsection 3.1.3.4. In particular, the heterogeneous cellular composition, uneven tissue density and hydrophilicity, non-uniform blood supply and drainage by the abnormal vasculature, as well as hypoxic and acidic conditions, increased interstitial fluid pressure (IFP) and solid stress (due to proliferation of the cancer cells and accumulation of ECM) in combination with abnormal ECM composition and developing drug resistance contribute to the complexity of the operation field of the nanomaterials applied as drug delivery vehicles, nanodrugs, diagnostic or research nanoprobes.

The ability of the nanotheranostics agents (NTAs) to perform functional tasks is strongly dependent on their relationship with the different components of the tumors and generally influenced by the microenvironment conditions in multiple ways. Therefore, it was suggested that conventional 2D monolayer cell cultures *in vitro* are inadequate models for studies on tumor-nanomaterials interactions. In response to this challenge 3D *in vitro* culture and tissue engineering models of malignant tumors have been proposed. In addition to the information discussed in the previous sections of the thesis, the detailed motivation of this methodological change can be found in several recent reviews [17, 21, 603-606].

Analysis of the literature, available by PubMed, Scopus, Web of Science and Google Scholar databases revealed 23 original research reports on testing of the mutual effects of 3D tumor cell cultures and engineering tumors and nanomaterials. As it is shown on the Figure 3.22, the most popular methods in these studies include preparation of multicellular spheroids, hydrogel-based cell cultures and solid scaffold-based models. Two publications were available on the tumor-on-a-chip (microfluidic bioreactor) models, and single reports were found on tumor cells culture on microcarriers (polymer microbeads) exposed to nanoparticles loaded with chemotherapeutic drugs and on the cancer cells invasiveness in Matrigel-coated transwell inserts under the action of gadolinium metallofullerenol nanoparticles.

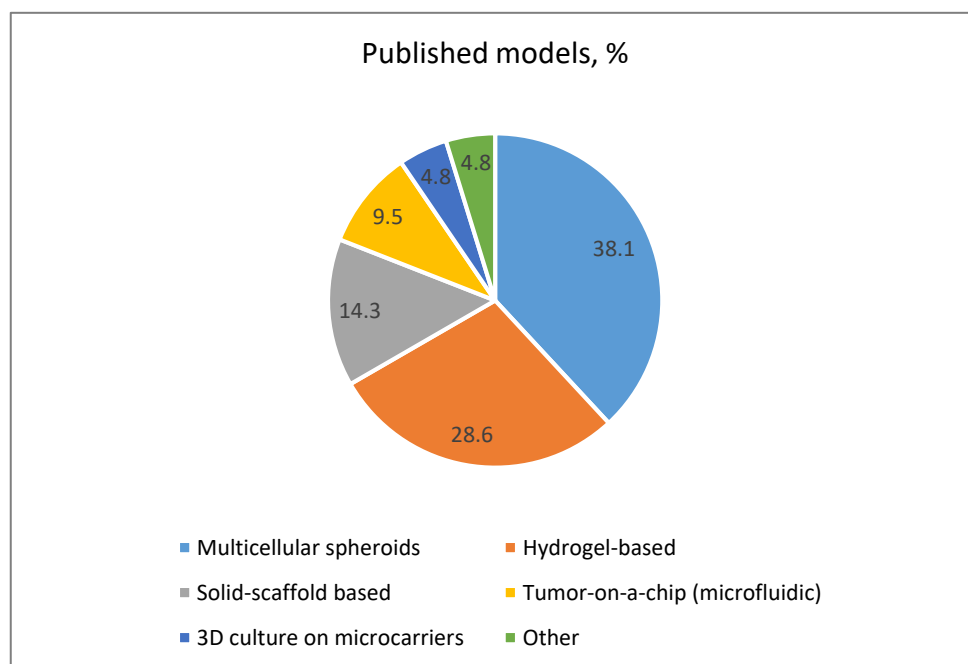


Figure 3.22. Types of the 3D *in vitro* cell culture and tissue engineering models applied in nanoresearch accordingly to the literature data.

Almost all the reported models were created with use of human linear cells, and in the majority of the studies only one cell type was employed in separate experiments, excepting only the study, where the mix of linear breast carcinoma cells (MCF-7) and primary adipose cells was applied to create self-assembling cellular aggregates in a microfluidic chip in order to mimic heterogeneous mammary cancer environment and evaluate the effectiveness of the gold nanoparticles-mediated photodynamic therapy (PDT) [607]. Among the nanomaterials, evaluated with use of 3D *in vitro* culture and tissue engineering tumor systems the nanoparticles prepared from various polymers, quantum dots (QDs), liposomes, micells, gold and metal oxide nanoparticles are most used (Table 3.4).

Table 3.4. The most typical interacting components in the nanoresearch studies performed on 3D *in vitro* cultures of tumor cells and engineered tumors and published to date.

Model type	Cancer types (cell lines)	Nanoparticles (NPs)	Refs.
MULTICELLULAR SPHEROIDS			
Monotype spheroid	Cervical carcinoma (SiHa)	Fluorescently-labelled polystyrene beads coated with collagenase or albumen	[515, 608]
	Breast carcinoma (MCF-7)	Gold NPs	[371]
	Pharinx squamosus carcinoma (FaDu)	Polystyrene beads and liposomes	[609]
	Prostate carcinoma (LNCaP)	Polymer micelles as delivery systems, chemotherapeutics	[610]
	Cervical carcinoma (HeLa)	QDs, polymer NPs, chemotherapeutics	[611]
	Glyoma (U87MG)	Targeted polymer NPs, chemotherapeutics	[403, 612]
	Neuroblastoma (SH-SY5Y)		[613]
Monotype spheroid + grafting in CAM	Breast carcinoma (MCF-7)	Targeted UCNPs	[103]
Monotype spheroids grown on micropatterned agarose gel	Colon adenocarcinoma (SW480)	ZnO NPs	[614]
HYDROGEL-BASED MODELS			
Hydrogel (hyaluronic acid-based)	Prostate carcinoma (LNCaP)	Polymer NPs, chemotherapeutics	[615]
Hydrogel (ICC polyacrylamide)	Hepatocellular carcinoma (HepG2)	QDs	[616]
Hydrogel (collagen)	Breast carcinoma, TNBC (MDA-MB-231)	Polymer NPs, chemotherapeutics	[617]
	Cervical carcinoma (HeLa)		[618]
	Colorectal carcinoma (HCT116), drug resistant and parental type cells		[619]
	Ileocecal colorectal adenocarcinoma (HCT8), drug resistant and parental cell types		[619]
	Osteosarcoma (U2OS)		[617]

Table 3.4. The most typical interacting components in the nanoresearch studies performed on 3D *in vitro* cultures of tumor cells and engineered tumors and published to date (continue).

Model type	Cancer types (cell lines)	Nanoparticles (NPs)	Refs.
SOLID SCAFFOLD-BASED MODELS			
3D chitosan-alginate porous scaffold	Mouse prostate cancer (TC-2)	Iron oxide NPs, modified with PEG-chitosan, PEI, RFP plasmid and chlorotoxin	[620]
AlgiMatrix™	Breast carcinoma, TNBC (MDA-MB-468)	Nanostructured lipid carriers, chemotherapeutics	[621]
	Human Non-Small Cell Lung Cancer (NSCLC) cell lines H460, A549, H1650, and H1650 stem cells		[621, 622]
TUMOR-ON-A-CHIP MODELS			
Microfluidic chip (collagen hydrogel)	Breast carcinoma (MCF-7)	Fluorescent NPs	[623]
Microfluidic chip (self-assembled cellular aggregates in the confined space)	Breast carcinoma (MCF-7) + primary human adipose-derived stromal cells, 1 : 1 mixture	Gold NPs coated with PEI and linked with ALA as a photosensitiser	[607]
OTHERS			
(PLGA)-chitosan-gelatin microcarriers	Retinoblastoma (Y79)	Polymer NPs, chemotherapeutics	[624]
Matrigel coating of Transwell inserts	Breast carcinoma(MCF-7; MDA-MB-231)	Gadolinium metallofullerenol	[625]

To the best of our knowledge, the earliest paper on the subject has been published in 2007 [515]. Since 2010 the notable shift of the research focus has been occurring, when the initially predominant studies of penetration and cytotoxicity of the nanomaterials in 3D cellular environment were added with the complex evaluation of the nanoparticles' uptake, nanoparticles-based therapeutic approaches, targeted drug delivery by the nanoagents and examination of the ways to overcome the drug resistance of the tumor cells with use of various nanoformulations (Figure 3.23).

Most of the data obtained to date on nanomaterial interactions with 3D reconstructed tissues was obtained with use of multicellular spheroids. This is relatively simple model, which currently equipped with the methods of the endpoint analysis much better than other modelling schemes. Spheroids are widely used to analyse the mechanisms of the penetration and translocation of the nanoparticles into the solid tumor masses and testing of the sensitivity of the cancer cells growing in 3D conditions to the chemotherapeutic drugs. For example, T. Goodman and co-authors demonstrated that the carboxyl-functionalized polystyrene nanoparticles bigger than 100 nm cannot penetrate the cervical carcinoma spheroids, but the transport of the particles may be improved by the collagenase coating of the nanoparticles' surfaces [515], indicating the critical role of ECM barrier even in very tightly bound cellular aggregates (see Figure 3.16 (d)). Next, the strong effect of the nanoparticles design and surface coatings on their ability to penetrate the tumor spheroids was shown on cervical carcinoma spheroids [611]. In this study the reduced uptake efficiency of QDs in spheroids, in comparison to 2D monolayers

cultures, was observed, resembling the features of drug resistance phenomenon found in tumors *in vivo*. Surprisingly, negatively charged QDs had revealed better than cationic QDs penetration into the spheroids. Another paper [610] compares the effects of free anti-cancer chemotherapeutic drug, paclitaxel (PTX) with the PTX-loaded poly(ethylene glycol methyl ether acrylate)-*b*-poly(carboxyethyl acrylate) block copolymer self-assembled micellar delivery system (PTX-MS) in 2D monolayer culture and in spheroids of human prostate carcinoma cells. It was found that PTX-MS were more than 10 times less toxic than free drug in 2D cell culture, while in the spheroids the micelles had higher and faster cytotoxicity than free PTX.

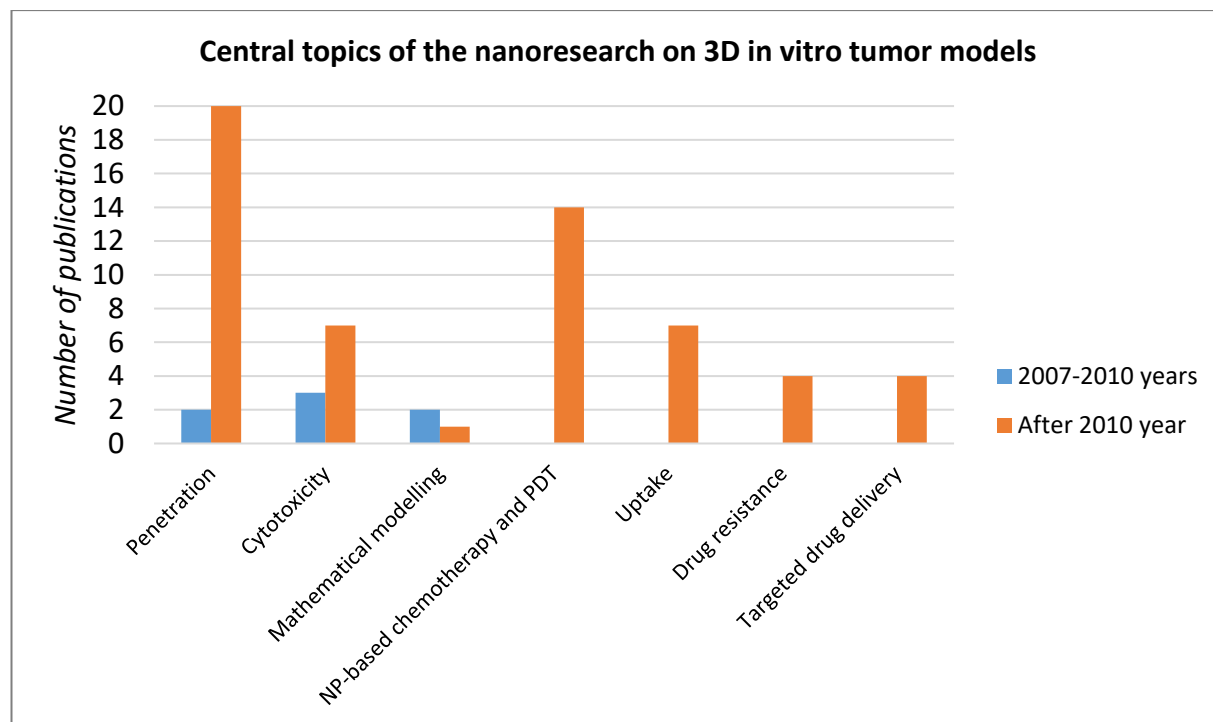


Figure 3.23. The most important research topics in the field of nanoresearch performed with use of 3D *in vitro* tumor cell cultures and engineered tumors in 2007-2000 according to the literature data. Some of the papers combine different topics. NP – nanoparticles, PDT – photodynamic therapy.

In hydrogel-based models the decreased toxicity of QDs, in comparison to 2D cultures, was confirmed [616]. The cells seeded into a hydrogel prepared from modified hyaluronic acid, formed aggregates resembling spheroids and expressed significantly higher levels of multidrug resistance (MDR) proteins, than the same cells (prostate cancer) in monolayers [615]. Doxorubicin-loaded polymer nanoparticles (Dox-NPs), 54 nm in diameter, prepared from amphiphilic block copolymers based on PEG and poly(ϵ -caprolactone) (PCL) penetrated through the hydrogel and were internalized by the cells by caveolin-dependent and macropinocytotic mechanisms and bypassing the drug efflux systems of drug resistance.

The more complex tumor models, involving solid scaffolds, also provide the evidence of increased chemotherapy resistance of cancer cells in 3D culture conditions, in comparison to the monolayers. For

instance, dramatic differences between 50% inhibitory concentrations (IC₅₀) were found for various chemotherapy drugs in 2D and 3D models (Figure 3.24). In addition, the targeted delivery of DNA by PEG-chitosan-PEI-modified iron oxide nanoparticles was demonstrated in the model of prostate cancer on 3D chitosan-alginate porous scaffolds [620] as well as the delivery of various chemotherapeutic drugs into model non-small-cell lung cancer and breast carcinoma self-assembled spheroids in a commercially available solid scaffold (AlgiMatrix™) [621].

Drugs	IC ₅₀ value (μM)							
	H460 Cells		A549 Cells		H1650 Parental Cells		H1650 Stem Cells	
	2D	3D	2D	3D	2D	3D	2D	3D
Cisplatin	3.47±0.45	84.26±5.63 [®]	4.20±0.2 1	75.79±4.52 [®]	2.09±0.98	66.13±7.36 [®]	4.84±0.62	126.14±12.42 [®]
Gemcitabine	2.33±0.16	91.07±7.01 [®]	2.56±0.45	87.31±9.64 [®]	2.68±0.58	103.72±9.68 [®]	6.03±0.84	177.79±14.03 [®]
5-Fluorouracil	3.62±0.52	120.94±12.65 [®]	3.21±1.58	99.17±6.24 [®]	2.63±0.37	100.44±8.92 [®]	6.87±0.46	148.31±6.56 [®]
Camptothecin	2.59±0.74	69.72±7.82 [®]	1.36±0.17	89.74±7.45 [®]	4.48±0.81	51.84±4.81 [®]	7.49±1.05	95.46±10.68 [®]

Each data point is represented as mean ± sem (n=4–5).

[®]P<0.001 Vs respective 2D groups.

Figure 3.24. Comparisons of IC₅₀ for anti-cancer drugs in 2D monolayer and 3D spheroid cultures *in vitro* of non-small cell lung cancer (NSCLC) cell lines H460, A549, H1650, and H1650 stem cells. Reproduced from [622] with minor changes.

Summarizing the information gained on the behaviour and effects of the therapeutic, diagnostic and research nanomaterials in 3D *in vitro* reconstructed tumor tissues, the following conclusion can be done. Every type of 3D *in vitro* culture and tissue engineering tumors contribute to the current understanding of the nano-bio interfaces at the tissue levels. This was almost impossible before the introduction of the 3D tumor model systems into the research practice. Multicellular spheroids represent the most developed instrument to study the interactions between the nanoparticles and solid tumor cellular masses. They provide an environment, where size- and charge-dependent limitations of the nanomaterials' transport can be modelled and even predicted by the mathematical analysis for further optimization of the particles' design. Hydrogel scaffolds facilitate cell aggregation and clustering, which results in formation of the systems like spheroids-in-the-gel. Many nanomaterials were shown to successfully diffuse through the gel scaffold, so that the diffusion limitations in these matrices are not critical (in a case of rational nanoparticles' choice and design). Despite the fact that the work with hydrogels is more rapid, the final barrier effects on the nanoparticles in hydrogel-based 3D *in vitro* tumor cultures are generally governed by cell-cell interactions rather than cell-matrix contacts. In contrast, the models of tumors based on solid scaffolds are the most complex and the closest to the real structure of the malignant foci. However, these models are still very rare. Exactly at this level of complexity the advantages of molecular targeting of the nanoparticles for the precise localization in the tumors may be demonstrated and can be developed. Finally, the functional tumor-specific barriers like increased IFP may be reconstructed *in vitro* with use of the microfluidic technology. Having being applied in a combination with various scaffolds, this approach looks very promising for further nanotheranostics research.

3.3. Conclusion

There is a significant gap in the current knowledge about the mechanisms of the effects of nanomaterials on human organism. The major attention is focused on the nanoparticles' effects at the cellular level, while the interactions of nanoagents with extracellular matrix, multiple cell types, humoral physiological mechanisms, tissues, organs and the body as a whole are largely ignored. The advancement in this field strongly depends on availability of the reliable and biomimetic methodology allowing modelling of the biological barriers, tissue- and organ-specific microenvironments in normal and pathological conditions for rational and ethical nanomedical research.

The novel approach to model normal and diseased tissues *in vitro* as 3D reconstructions has a great promise to improve and facilitate the development of the better NTAs. The solid-scaffold based engineered tissues provide the best level of biomimetics and the optimal conditions for the “reality-check” for the new nanostructures destined for biomedical applications. At the same time these approaches are still at the early stage of the development, and numerous methodological issues are waiting for the solutions (“easier said than done” [626]). First of all, the non-destroying observational and analytical methods, allowing to get the information about the state of the tissue construct as well as about the introduced nanomaterials. Next, the techniques to evaluate and optimize of the theranostics properties of the nanomaterials in 3D reconstructed cultures are expected to be in demand. In addition, the validation of the established models such as comparisons between *in vitro* and *in vivo* effects should be performed. On the other side, significant efforts should be also concentrated on the rational design of the NTAs. This is a challenging task, as the different biological barriers impose conflicting requirements regarding the size, surface charge and surface functionality of the nanoparticles. Finally, it seems reasonable to suggest that in order to translate the achievements of nanotheranostics research from bench to bedside, the future development of the 3D *in vitro* culture and tissue engineering modelling technologies should allow creation of dynamic systems, representing not only a single tissue/ tumor/ organ, but physiological systems of organs, while the counter stream from the nanotechnology filed should result in rational design of the NTAs, based on the understanding of the interaction of the nanomaterials with their real biological operational environment.

Cytotoxicity and non-specific cellular uptake of bare and surface-modified upconversion nanoparticles in human skin cells

4.1. Introduction

Upconversion nanoparticles (UCNPs) is promising photoluminescent nanotheranostics material under research highlight manifested by >12,000 publications over the past three years. Half of these are focused on biomedical applications of UCNPs, including background-free bioimaging, drug delivery, and light-controlled release of pharmaceuticals, photodynamic therapy and other bioassays. Clinical translation of these results requires systematic evaluation of biological safety of these nanomaterials.

It is generally held that UCNPs are non-toxic, however, thorough analysis of the literature shows that this claim is too strong for the currently presented evidence. In fact, significant variability of the tested concentrations of the particles, incubation times, compositions, sizes, shapes, charges, syntheses and surface modifications does not allow to make a final conclusion about the biocompatibility of UCNPs. In addition, the cell viability has been assessed primarily using cancer cell lines, which are usually more resilient to cytotoxic effects. The results on normal cells and tissues viability treated with UCNP are very limited, and, in particular, human skin tolerance to UCNPs remains unknown, despite the diagnostic and therapeutic potential of UCNPs for skin diseases, transdermal drug delivery and monitoring of the skin permeability. An essential question of the intrinsic cytotoxicity of upconverting nanocrystals remains largely unanswered due to the difficulties associated with the dispersion of naturally hydrophobic “bare” UCNPs in aqueous buffers or cell culture media. Correlation between the cellular uptake of UCNPs and cytotoxicity was also largely ignored, making it difficult to understand the mechanisms of the cytotoxic effects.

In this chapter, we report a systematic study of the cytotoxicity and non-specific cellular uptake of the most popular composition UCNPs in normal cells of human skin, such as epidermal keratinocytes and dermal fibroblasts cultured as monolayers *in vitro*. We also address the questions of the intrinsic cytotoxicity and relations between the uptake of UCNP and cell viability. In the addendum to the full paper I, we present our recent observations on the cytotoxicity and uptake of three types of surface-modified UCNPs tested in our original model of 3D reconstructed epidermis (unpublished data). The analysis of the biocompatibility of UCNPs with two representative types of normal skin cells as well as

CHAPTER 4

the comparison of the effects of this NTA in 2D and 3D *in vitro* cultures of keratinocytes has been performed for the first time to our knowledge.

4.2. The author's contribution to the paper I

The PhD candidate (Anna Guller) is the first author. She developed the main concept and design of the experiments, carried out most of the data analysis, prepared the figures and wrote the paper. She also performed some cell culture experiments and participated in the nanoparticles characterization and confocal microscopy imaging.

Dr. Alla Generalova conceptualized and experimentally realised the surface modification of UCNPs. The synthesis of UCNP nanocrystals was performed and optimized by Dr. Andrey Nechaev. Nanoparticle characterization by TEM, submicron particle analyser and Zetasizer, as well as photoluminescence spectroscopy were mainly performed by Drs. Annemarie Nadort and Ekaterina Grebenik. Dr. Elena Petersen, Ms. Inna Trusova and Mr. Nikolay Landyshev carried out the cytotoxicity tests. Microscopy studies of the cellular uptake of UCNPs were done by Dr. Annemarie Nadort and Ms. Anna Guller. Prof. Anatoly Shekhter and Prof. Sergey Deyev contributed to the development of the main concept of the paper and took part in the discussions and manuscript revision. A/Prof. Andrei Zvyagin (the corresponding author) contributed to the study concept, coordinated the project from conception to completion and took part in the paper structuring, drafting and refinement. All the co-authors revised and proofread the manuscript.

4.3. Author's contribution to the addendum paper I a

The Addendum entitled "Cytotoxicity and uptake of upconversion nanophosphors in 3D *in vitro* model of reconstructed human epidermis" represent a part of the manuscript "Skin-nanoparticles interactions: the model study with use of upconversion nanophosphors", which is to be submitted in a short time and authored by Z. Khabir, A. Guller, V. Rozova, L. Liang, E. Goldys, H. Hu, and A. Zvyagin. This study examines the permeability of human skin for nanoparticles with use of UCNPs as a model contrast nanomaterial and evaluates the biological effects associated with the possible interaction between UCNPs and viable keratinocytes in their biomimetic microenvironment with use of 3D *in vitro* reconstructed non-cornified epidermal equivalent.

The PhD candidate (Anna Guller) is the second author of this work. In fruitful discussions with A./Prof. Andrei Zvyagin, she first defined the significance of the dimensionality of the biological environment for the realistic evaluation of the effects of nanomaterials on living cells and tissues on the base of her experience as experimental pathologist and on the results of the literature research. Next, Ms. Anna Guller developed the protocols for the creation of acellular organ-specific scaffolds for biomimetic 3D reconstruction of the tissues *in vitro*. In this study, she developed an optimized protocol of decellularization (DCL) of chick embryo skin by testing three alternative ways to prepare the scaffold, as well as the protocols of seeding and culturing of the human keratinocytes on the DCL avian derma and testing of cytotoxicity and uptake of UCNPs in 3D *in vitro* culture of reconstructed epidermis. Ms.

CHAPTER 4

Anna Guller performed the analysis of the data on cytotoxicity and cellular uptake of UCNPs in 3D *in vitro* tissue engineering culture of HaCaT keratinocytes and wrote the part of the manuscript, included into the addendum.

Ms. Zahra Khabir performed the major part of the confocal microscopy study and participated in the cell culture and cytotoxicity experiments. Ms. Vlada Rozova developed the algorithms of digital image analysis to quantify the amount of UCNPs in the specified zones of the skin. Ms. Liuen Liang and Dr. Helen Hu synthesized, modified the surfaces and performed characterization of the UCNPs. Prof. Ewa Goldys supervised the experiments, discussed the data on the way and revised the manuscript. A./Prof. Andrei Zvyagin supervised the study in general, discussed the results of all the preliminary and finalized experiments and edited the manuscript.

4.4. Full paper I

Cytotoxicity and non-specific cellular uptake of bare and surface-modified upconversion nanoparticles in human skin cells

Anna E. Guller^{1,2}, Alla N. Generalova^{3,4}, Elena V. Petersen⁵, Andrey V. Nechaev^{4,6}, Inna A. Trusova⁵, Nikolay N. Landyshev⁵, Annemarie Nadort^{1,7}, Ekaterina A. Grebenik^{1,3,4}, Sergey M. Deyev^{3,4}, Anatoly B. Shekhter², and Andrei V. Zvyagin^{1,4,*}

¹Macquarie University, Australia;

²I.M. Sechenov First Moscow State Medical University, Russia;

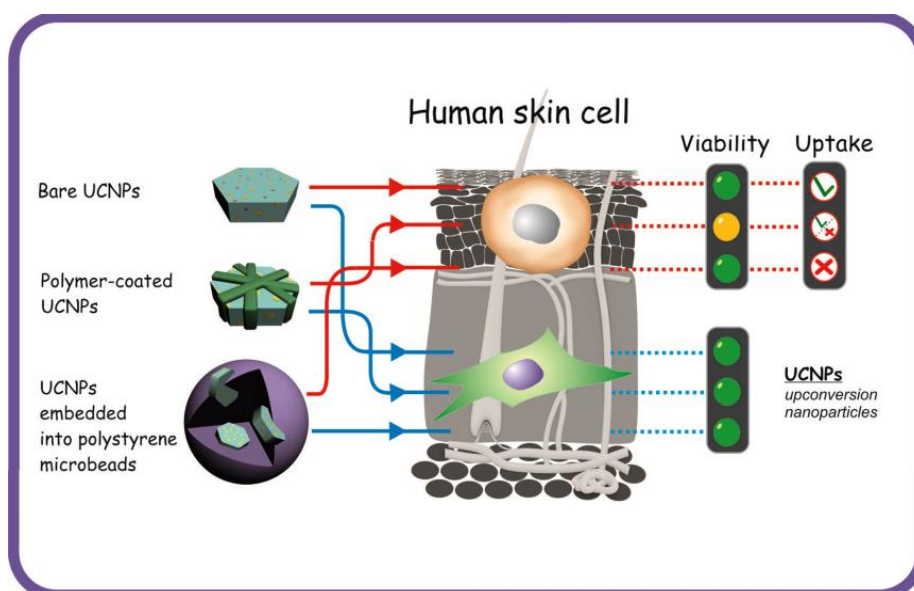
³Shemyakin-Ovchinnikov Institute of Bioorganic Chemistry, Russian Academy of Sciences, Russia;

⁴Nizhny Novgorod State University, Russia;

⁵Moscow Institute of Physics and Technology, Russia;

⁶Moscow State University of Fine Chemical Technologies, Russia;

⁷University of Amsterdam, The Netherlands.



Graphical abstract. Upconversion nanophosphors (UCNPs) NaYF₄:Er,Yb, induce different effects on viability of human skin cells depending on surface modification and the cell type. Hydrophilized bare UCNPs demonstrate acceptable level of cytotoxicity and the highest internalization rate among eight studied species of three types of surface-modified UCNPs.

Anna Guller, web-site: https://www.researchgate.net/profile/Anna_Guller

Andrei Zvyagin, web-site: <http://www.physics.mq.edu.au/research/obis>

Pages 101-125 of this thesis have been removed as they contain published material. Please refer to the following citation for details of the article contained in these pages:

Guller, A.E., Generalova, A.N., Petersen, E.V. *et al.* Cytotoxicity and non-specific cellular uptake of bare and surface-modified upconversion nanoparticles in human skin cells. *Nano Res.* 8, 1546–1562 (2015).
<https://doi.org/10.1007/s12274-014-0641-6>

4.5. Addendum

Cytotoxicity and uptake of upconversion nanophosphors in 3D in vitro model of reconstructed human epidermis

Background

Our next step in development of skin applications of UCNPs was focused on transcutaneous permeation of nanoparticles, where UCNPs were applied as a model nanomaterial with excellent contrasting properties. The resulting manuscript “Skin-nanoparticles interactions: the model study with use of upconversion nanophosphors” is under preparation now and is to be submitted in short time. Briefly, this paper demonstrates that UCNPs can permeate through the skin’s outermost layer and the main transport barrier, the stratum corneum (SC, see Chapter 3.1.3.5), into the epidermal and dermal layers located below it (Figure A1), and the penetration enhancers like ethanol and oleic acid as well as the surface modification of the particles can modulate the process. The data was obtained by the means of Franz diffusion cells technique and confocal microscopy on the frozen/thawed (nonviable) human skin samples.

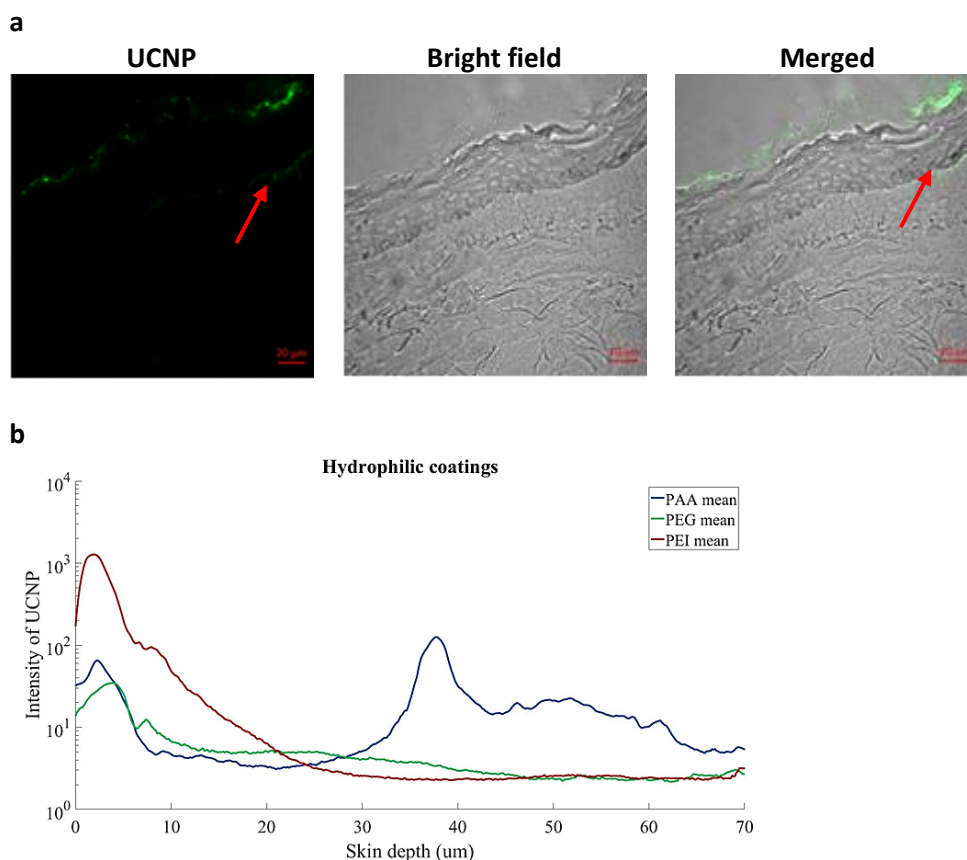


Figure A1. Illustration of the principal findings for the penetration of UCNPs into the depth of skin. (a) Representative confocal images of excised human skin with applied UCNPs (UCNP-PAA, 15 $\mu\text{g/mL}$ in 50% ethanol; 24 h); scale bars 20 μm ; (b) the distribution of UCNPs with different surface coatings in depth of excised human skin as measured by digital analysis of the confocal microscopy images. Note the deepest penetration of UNCP-PAA (red arrow), clearly visible underneath the epidermis in (a).

CHAPTER 4

Taking into account the potential cytotoxicity risks associated with the interactions between UCNPs and keratinocytes of the viable layers of epidermis, as it was reported in the full paper I, and the limitations of the nanotoxicity tests on monolayer cell cultures *in vitro* (see 1.1 and 3.1), we performed a study of the cytotoxicity and cellular uptake of UCNPs with different surface coatings in a 3D *in vitro* model of viable non-cornified epidermis created with use of the tissue engineering methodology developed during the current PhD project. We preferred to use a 3D reconstructed epidermis model without SC to make the exact dosing of the nanoparticles possible, as it could not be done on the established commercial epidermal *in vitro* equivalents (see 3.2.2). Three surface coatings of UCNPs were chosen for the study: the polyethylenimine (PEI), a positively charged polymer, as UCNP-PEI induced the highest cytotoxicity and uptake in 2D *in vitro* cultures of keratinocytes; negatively charged poly(acrylic acid) (PAA) and almost electrically neutral polyethylenglycol (PEG).

Materials and Methods

Synthesis of 6-phase NaYF₄:18% Yb, 2% Er upconversion nanoparticles, their surface modification with PAA, PEI, and PEG and the further characterization

β -phase NaYF₄:Yb,Er (18/2 mol %) nanocrystals as core nanoparticles were synthesized following a protocol developed in our group¹. For the surface modification all the starting materials were of analytical grades. All the chemicals including branched polyethylenimine (PEI-25,000), poly(acrylic acid) (PAA-130,000), N-(3-dimethylaminopropyl)-N'-ethylcarbodiimide hydrochloride (EDC·HCl), N-hydroxysulfosuccinimide sodium salt (Sulfo-NHS), nitrosyl tetrafluoroborate (NOBF₄, 95%), cyclohexane (99.5%), dichloromethane ($\geq 99\%$), dimethylformamide (DMF), and toluene ($\geq 99.5\%$) were purchased from Sigma-Aldrich (Australia) and Methoxy-poly(ethylene-glycol)-amine (PEG-NH₂) was received from Lyasan Bio (USA). A ligand-exchange approach was utilized for coating of UCNPs². 5 mg of oleic acid-capped UCNPs was dispersed in 5 mL of cyclohexane. Then 11.68 mg of NOBF₄ was mixed with 10 mL dichloromethane added to UCNPs' dispersion and the solution was kept under stirring over night at room temperature. This resulted to the formation of UCNPs capped with NOBF₄-capped UCNPs, which were centrifuged, washed with a toluene-cyclohexane mixture and dispersed in 5 mL of DMF.

To produce PAA-coated UCNPs, first 150 mg PAA was dissolved in 5 mL DMF. Then it was added to the NOBF₄-UCNP suspension, stirred, and heated at 80 °C for 3 h. The resultant PAA-UCNPs were collected by centrifuge, washed 3 times with ethanol and dispersed in water to be stored. To prepare PEI-coated UCNPs, first 25 mL of PEI-ethanol solution (4 mg/mL) was added to 5 mL of DMF, then the same protocol as the PAA-UCNP was followed except that instead of heating step, the mixture was stirred at room temperature for 24 h. For PEG-UCNP, PEG-NH₂ was conjugated to UCNP-PAA via the EDC/NHS coupling. First, 1 mg of PAA-UCNPs were dispersed in 1 mL distilled water at pH 5.5. To which, 0.4 mg of EDC·HCl and 1.1 mg sulfo-NHS were added in to activate the carboxylic groups of PAA. After incubation at room temperature for 30 min, UCNPs were centrifuged and washed with distilled water for 3 times and dispersed in 200 μ L of PBS (pH=7.4) through sonication under cold condition. Then 200 μ L of PBS containing 1.5 mg of PEG-NH₂, was added in and followed by incubation on a rotary shaker at 4 °C overnight. The unreacted PEG-NH₂ was removed by centrifugation and the UCNP-PEG particles were purified by washing with distilled water for three times. The particles were characterized by TEM, spectroscopy and DLS methods. The average size of as-synthesized UCNP nanocrystals was approximately 30 nm, accordingly to TEM, and did not significantly change after surface modification with PEI, PAA, and PEG (Figure A2, a). The average hydrodynamic size of all the surface modified UCNPs was as measured by DLS in

CHAPTER 4

PBS pH7.0, and the surface charge was 38.8 ± 3.0 mV for UCNP-PEI, -12.4 ± 1.0 mV for UCNP-PAA and -6.0 ± 0.5 mV for UCNP-PEG.

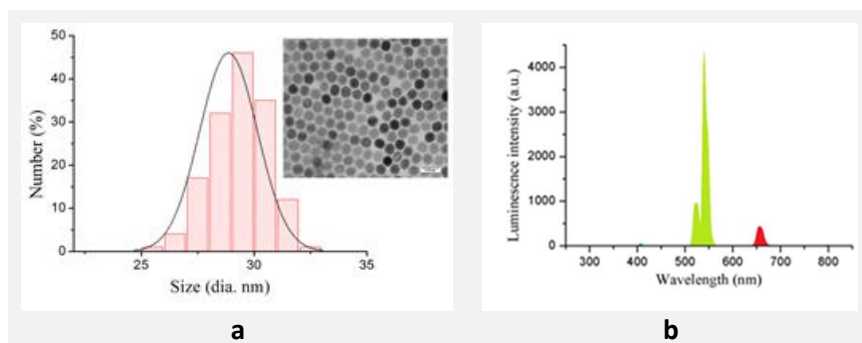


Figure A2. The size distribution of as-synthesized oleic acid-capped NaYF₄:Yb,Er nanoparticles by TEM (inset demonstrates the hexagonal morphology of the nanocrystals); (b) upconversion emission spectra of as-synthesized UCNPs.

Cell culture

Immortalized linear human epidermal keratinocytes (HaCaT) were kindly donated by a Prof. D. Damian (University of Sydney) and cultured as described in the paper I. The cells of 5-6 passage were used for creation of the 3D epidermal equivalents, cytotoxicity testing and uptake studies in 2D and 3D *in vitro* cultures. One passage before the beginning of the main experiment the cells were stained with a cell membrane tracer pkh26 (#Mini-26, Sigma-Aldrich) accordingly to the manufacturer's protocol for live imaging (the emission maximum of the fluorescent dye pkh26 is 567 nm).

3-D model of tissue engineered viable epidermal equivalent

The study was approved by animal ethics committee of Macquarie University (ARA 2015/006, 2015/006-2). Fertilized chicken eggs (embryo of *Gallus gallus domesticus*) were maintained as described in the full paper IV (Chapter 7). After euthanasia of the 18-day old embryos, the skin fragments were excised from back and washed with PBS. In a series of preliminary experiments (Figure A3) the optimal decellularization (DCL) protocol was defined as follows.

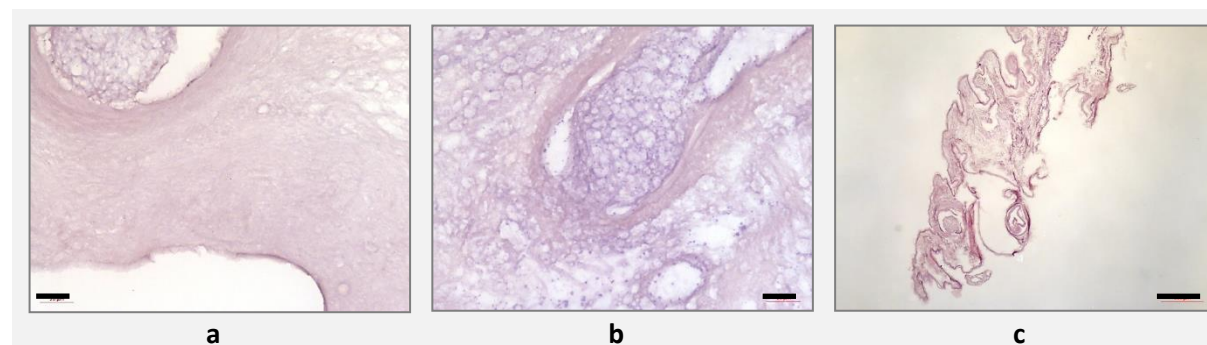


Figure A3. The effects of alternative immersion-agitation DCL protocols on chick embryo skin. (a) The protocol used in the study; note absence of cellular material, including epidermis, and homogenous structure of the DCL upper derma; (b) the protocol based on application of 1% sodium dodecyl sulphate; the abundant cellular debris is visible, the epidermis is partially kept; (c) the protocol based on application of 1% triton-X-100; sharp disorganization of the tissue, uneven density of the scaffold and cellular debris are notable. Scale bars: 20 μ m (a, b); 200 μ m (c).

The collected chick embryo skin fragments were placed in a falcon tube, containing 30 mL of sodium dodecyl sulphate (0.1% v/v) in phosphate buffer saline (PBS) for immersion-agitation DCL and processed as described in the full paper III (Chapter 6). The process of skin DCL usually took 2-4 days, depending on the embryos flock. Finally, the obtained DCL skin was destined to be used as tissue engineering scaffolds. They were washed with a

CHAPTER 4

solution of 1% v/v of antibiotic-antimycotic solution (AA, Sigma-Aldrich) in PBS on orbital shaker during 3-5 days with daily replacements of the washing media for the new portions of it. As a result of DCL epidermis and feather were removed, and the DCL derma of chick embryos was stored in the 1% AA solution in sterile PBS at 4°C until further use.

For recellularization and creation of 3D tissue engineering constructs (TECs), representing a living 3D reconstructed equivalent of non-cornified epidermis, the DCL skin fragments were cut into disks using biopsy punchers and seeded with HaCaT keratinocytes. Three alternative seeding protocols were tested before the beginning of the main experiments (data not shown). Following the chosen protocol, the scaffolds (diameter 4mm) were placed in a 24-well culture plates plate and sterilized with Millipore water containing 0.1 (v/v) peracetic acid and 4% (v/v) ethanol and incubated for 2 hours at room temperature. Then the sterilizing solution was removed and the scaffolds were washed 2-3 times with PBS and then left under UV for 45 min. Then 1 ml Dulbecco's modified Eagle Medium (DMEM, Sigma-Aldrich) supplemented with 10% fetal bovine serum and 1% penicillin-streptomycin was added to each well containing scaffold (next named "complete culture medium") and conditioned overnight at in tissue culture incubator. Afterwards, scaffolds were seeded with HaCaT keratinocytes (150,000 cells per sample) and grown in submerged static *in vitro* mode with culture media changes at every third day and without airlifting to avoid cornification of the cells. The structure of the developing TECs was controlled by histological methods (staining with hematoxylin and eosin (H&E) and toluidine blue, live imaging with nuclear staining with DAPI and live/dead staining with FDA/PI). After 3-4 weeks of *in vitro* culture the epidermal TECs were challenged with UCNP-PEI, UCNP-PAA and UCNP-PEG for cytotoxicity and uptake and benchmarked against the matching 2D *in vitro* cultures of HaCaT cells.

Cytotoxicity and cellular uptake assays

The cytotoxicity of UCNPs with different coatings was measured by a modified MTT test as described in full paper I (for 2D *in vitro* culture of keratinocytes) and in full paper IV, Chapter 7 (for 3d epidermal equivalents) after 24 h incubation of 2D and 3D cell cultures with the particles. The control 2D cultures of HaCaT cells were seeded in a 96-well plates (for cytotoxicity assay) and on 1cm diameter round cover slips placed in 24-well plates (for analysis of the uptake). The 3D TECs cultured *in vitro* for 21-28 days were used for cytotoxicity and uptake assays. Confocal microscopy of the samples of 2D and 3D *in vitro* culture of HaCaT cells have been performed as described in the full papers I (Chapter 4, see the methods related to excitation and detection of the emission of UCNPs) and IV (Chapter 7, for 2D and 3D cultures, stained with DAPI). UCNPs with different surface coatings were applied to the particles at the concentration 125 µg/mL.

Results and discussion

The general plan of skin structure of chick embryo was similar to the human one, excepting the presence of feather, which are the homologues of hairs. The total thickness of skin samples with resected subcutaneous fat was about 350-500 µm. As a result of DCL procedure almost 100% absence of cellular components was reached. The border of former epidermis was non-discernible, while two layers of former derma was notable. The ECM of upper two thirds of derma was relatively dense, and the deep portion of reticular derma had a distended organization. After seeding with HaCaT keratinocytes the entire multi-row epidermal lining was formed on the surface of DCL dermal scaffolds during 2-3 weeks. No signs of cornification of the surface rows of keratinocytes were found. The morphological features of the DCL dermal scaffold, 2D HaCaT cell culture and 3D epidermal equivalent are illustrated by Figure A4.

CHAPTER 4

Figure A5 demonstrates the results of MTT assay of cytotoxicity of UCNP with different surface coatings in 3D reconstructed epidermal TECs and in conventional 2D (monolayer) *in vitro* cultures of HaCaT keratinocytes. The most important finding was that no any type of the studied UCNP induced a statistically significant decrease of the keratinocytes' viability in 3D reconstructed epidermal equivalents, in contrast to the data obtained in monolayer cultures of HaCaT cells, where application of UCNP-PEI and UCNP-PAA resulted in notable cytotoxic effects. In 3D epidermal TECs, UCNP-PEI induced some growth of metabolic activity or increase of the cell number that may indicate the adaptation reaction. At the same time, UCNP-PEG were nontoxic in 2D and 3D cultures of keratinocytes.

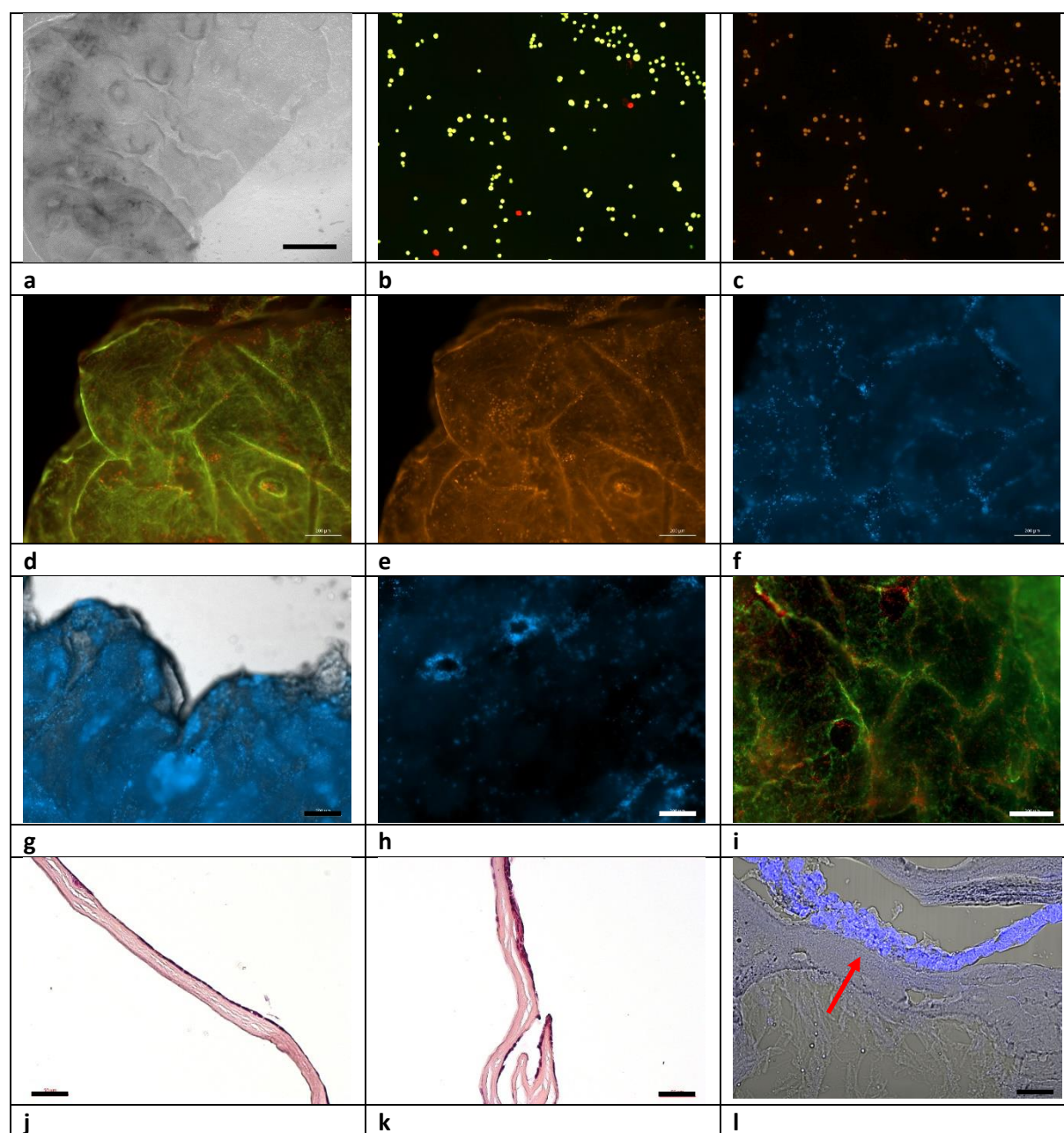


Figure A4. (a) A bright field image of the upper surface of DCL dermal scaffold before seeding with the cells; scale bar 400 μ m; (b, c) 2D culture of HaCaT keratinocytes, live imaging; (b) live/dead staining with FDA (green, live cells) and PI (red, dead cells), indicating the overall viability about 98% and (c) the same sample; staining with pH26 (yellow), which does not differentiate live and dead cells; (d, e, f) 3D epidermal TECs on DCL dermal scaffolds, 7 days of *in vitro* culture, live fluorescent microscopy imaging, view from the upper surface; (d) live/dead FDA/PI staining; (e) the same sample imaged by pH26 fluorescence; scale bars 200 μ m; (f) DAPI staining of cell nuclei; (g-i) 3D epidermal TECs on DCL dermal scaffolds, 21 days of *in vitro* culture, live

CHAPTER 4

fluorescent and bright field microscopy imaging, view from the upper surface; scale bars 200 μm ; (g) DAPI+bright field merged image, demonstrating almost total coverage of the scaffold by keratinocytes; (h) a detailed image of DAPI stained TEC, demonstrating the formation of multi-row cellular linings in the voids of the scaffold (former feather shafts); (i) live/dead FDA/PI (green/red) staining indicating that the viable cells comprise the majority of the cellular population of TEC; (j, k) H&E staining of paraffin sections of TECs on days 14 (j) and 21 (k) of *in vitro* culture; note increase of the number of cell rows in the growing reconstructed epidermis; scale bars 50 μm ; (l) confocal image of cryosection of TEC, 21 day in culture *in vitro*; merged bright field and DAPI staining. Red arrow indicates dense DCL upper dermal part of the scaffold, underlying the reconstructed non-cornified epidermis.

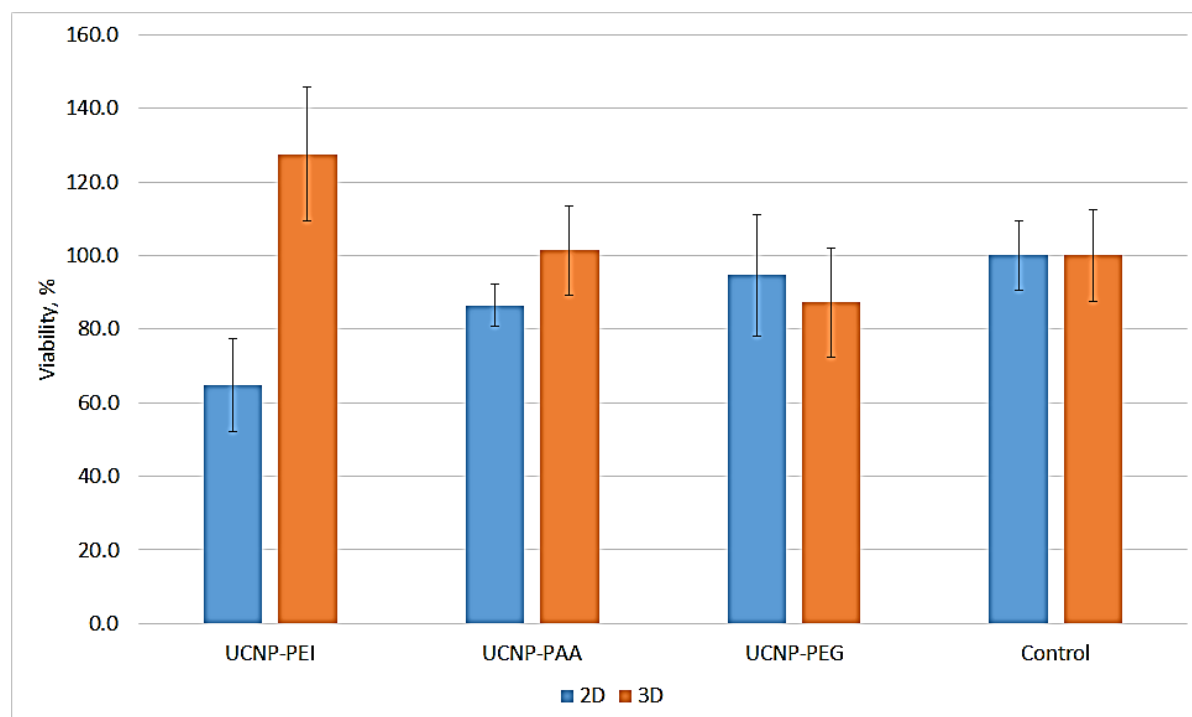


Figure A5. Cytotoxicity assay in 2D *in vitro* culture of HaCaT keratinocytes and 3D epidermal TECs. Effect of UCNPs with different surface coatings evaluated by MTT assay after 24 h exposure in 2D and 3D culture *in vitro*.

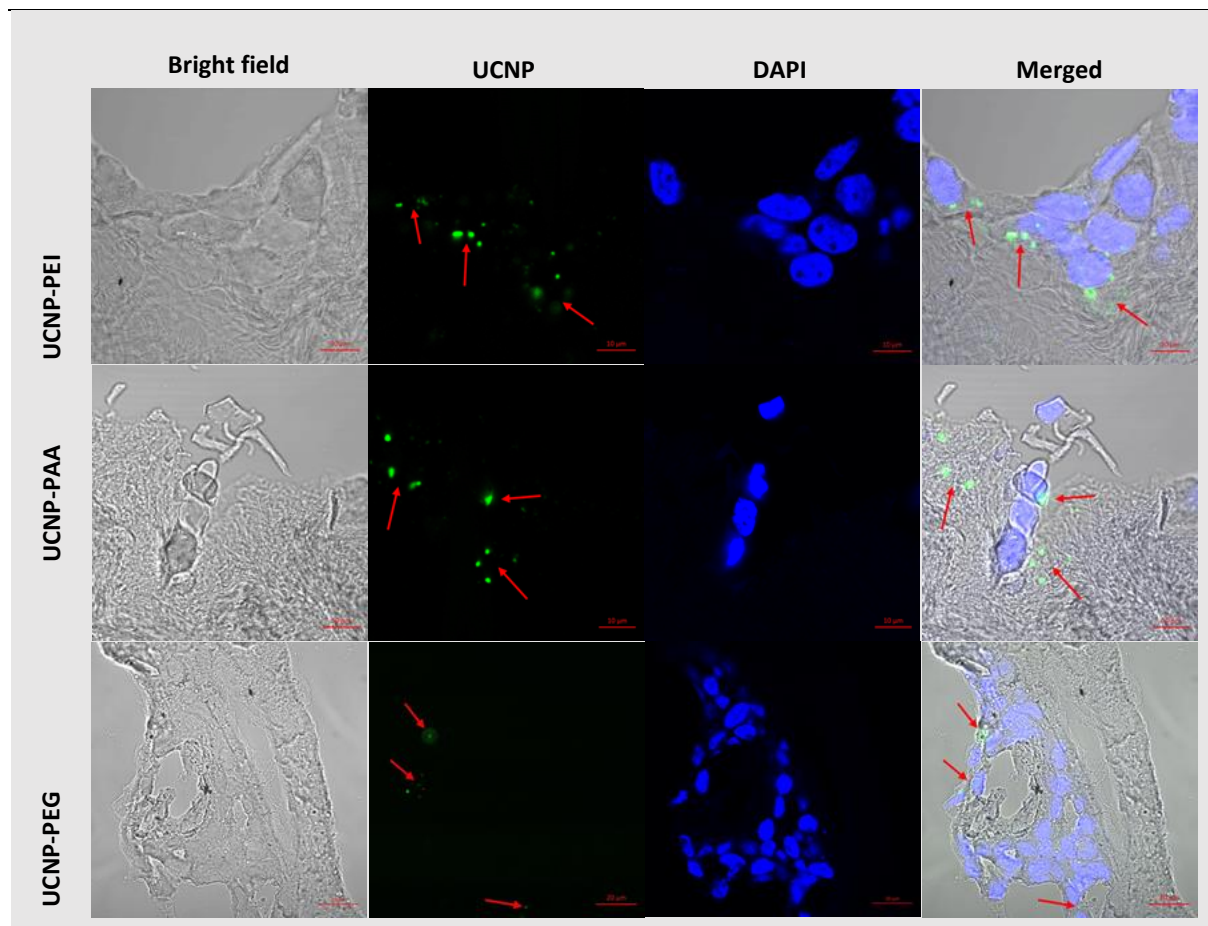


Figure A6. Cellular uptake of UCNPs with different surface coatings in 3D reconstructed epidermal TECs, confocal microscopy imaging of cryosections of TECs stained with DAPI for cell nuclei. Note the decrease of the amount of the internalized UCNPs in the row of $\text{UCNP-PEI} \geq \text{UCNP-PAA} > \text{UCNP-PEG}$. Red arrows indicate clusters of UCNPs. Scale bars: 20 μm .

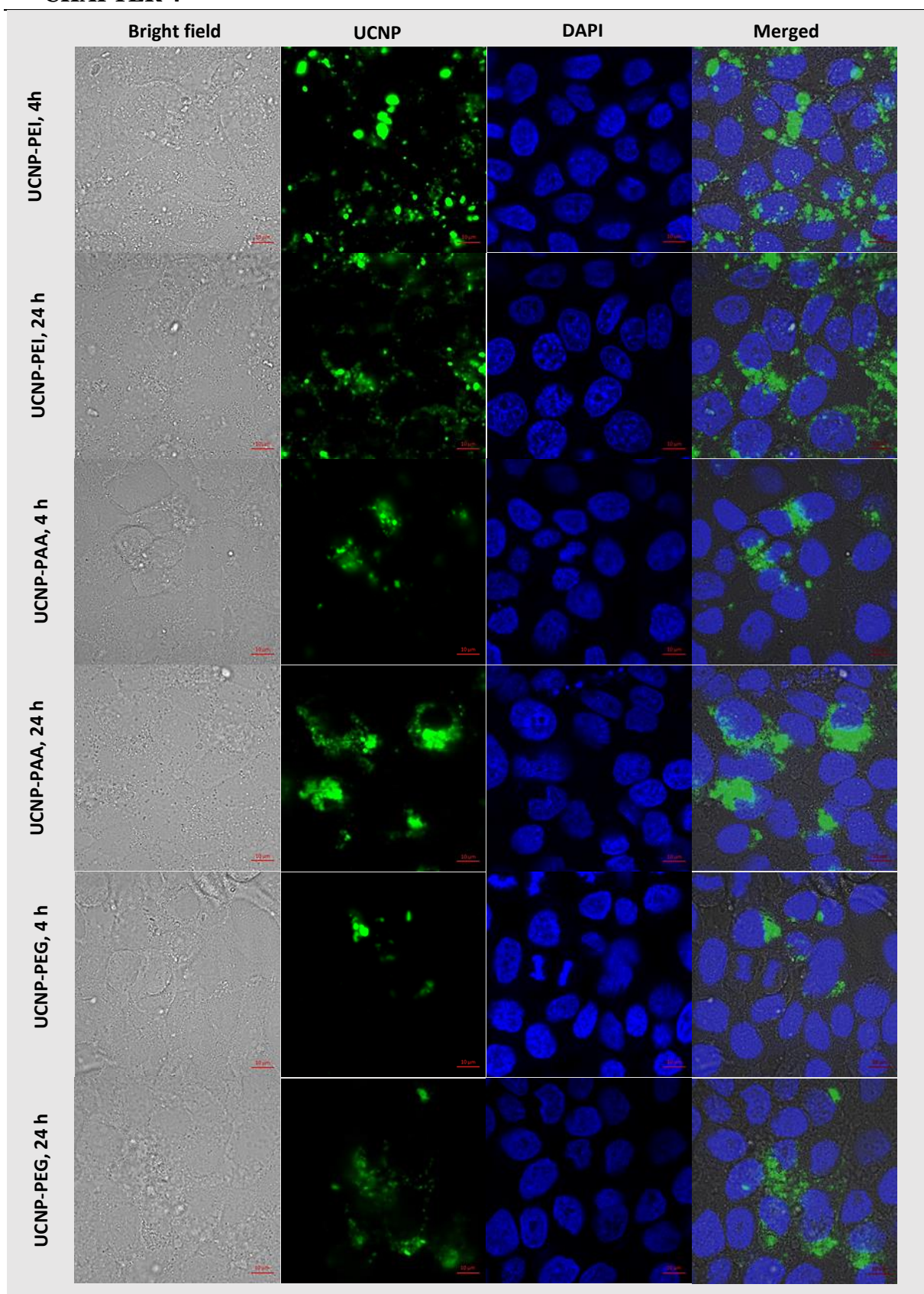


Figure A7. Cellular uptake of UCNPs with different surface coatings in 2D (monolayer) cultures of HaCaT keratinocytes, incubated with the particles during 4 h or 24 h. Cell nuclei stained with DAPI. Scale bars: 50 μm .

Figures A6 and A7 show the results of evaluation of the cellular uptake of surface modified UCNPs in 2D and 3D (epidermal TECs) *in vitro* cultures of HaCaT cells. It was found that all types of the studied UCNPs are internalized

CHAPTER 4

by keratinocytes in 3D reconstructed non-cornified epidermis, however, the amount of the particles visible inside the cells was much smaller, than in monolayer cultures, indicating that the factors of 3D epidermal microenvironment like cell-cell contacts and cell-matrix interactions affect the transport of UCNPs into the cells. The most notable intracellular accumulation was revealed in 3D TECs incubated with UCNP-PEI and UCNP-PAA, while UCNP-PAA and, especially, UCNP-PEG were less uptaken by the cells. This result indicate that non-neutral surface charge of UCNPs, probably, favours for the nanoparticles cellular internalization in 3D viable epidermal layers. The control uptake experiment in monolayer culture of HaCaT keratinocytes *in vitro* (see Figure A7) demonstrated more intensive accumulation of the UCNPs in the cells, that those observed in 3D TECs, implying the *in vitro* culture conditions had strong effect on interactions between the cells and the particles. In particular, it seems reasonable to suppose that the exposed surface of the cells growing in a monolayer is higher, that resulted in the increased uptake of UCNPs. The time-dependent pattern in accumulation of UCNPs with different surface coatings also was notable from this experiment. It has been found that UCNP-PEI can be internalized faster than UCNP-PAA and UCNP-PEG and, at the same time, having being less clustered than UCNP-PAA and PEG.

Conclusion

The results of the study, included into the Addendum, for the first time to our knowledge, demonstrate the interactions between UCNPs coated with PEI, PAA or PEG and human skin HaCaT keratinocytes growing *in vitro* as 3D multilayer, reconstructed by the methodology of tissue engineering as non-cornified viable epidermal equivalent. In contrast to our previous results, obtained in conventional monolayer cultures of the same cells, UCNP-PEI, which were found to be the most toxic and intensively internalized, do not induce cytotoxic effects in the keratinocytes forming the 3D reconstructed epidermis, while also can accumulate in the cells. UCNP-PAA in 3D epidermal culture *in vitro* also loss their cytotoxic potential, which can be observed in 2D models. UCNP-PEG were nontoxic to all the studied types of HaCaT cell cultures *in vitro*. The cellular internalization of UCNPs in 3D epidermal equivalents depends on the surface modification of the particles. UCNP-PEI and UCNP-PAA has similar cellular uptake profiles in 3D HaCaT cultures, and UCNP-PEI is less prone to be internalized. Finally, this data shows the significance of 3D tissue-like microenvironment for the cell reactions on the exposure to the UCNPs. The obtained data indicates that in a case of permeation of the studied types of UCNPs to the viable layers of human skin epidermis, the adverse toxic reactions on the particles are not of high probability (the particles may be considered as safe nanomaterials). The demonstrated internalization of UCNPs in keratinocytes in 3D reconstructed epidermis implies the possibility of the future applications of these particles as drug vehicles, contrast agents or combined nanotheranostic probes in human skin.

References for the Addendum

1. Liang, L., A. Care, R. Zhang, Y. Lu, N. H. Packer, A. Sunna, Y. Qian and A. V. Zvyagin (2016). "Facile Assembly of Functional Upconversion Nanoparticles for Targeted Cancer Imaging and Photodynamic Therapy." *ACS Appl Mater Interfaces* 8(19): 11945-11953.
2. Dong, A., X. Ye, J. Chen, Y. Kang, T. Gordon, J. M. Kikkawa and C. B. Murray (2011). "A generalized ligand-exchange strategy enabling sequential surface functionalization of colloidal nanocrystals." *J Am Chem Soc* 133(4): 998-1006.

5. Submicron polyacrolein particles in situ embedded with upconversion nanoparticles for bioassay

5.1. Introduction

In the previous chapter we considered the effects of surface modification on interactions between UCNPs and human skin cells grown *in vitro*. Among eight types of the examined nanophosphors, only two exhibited zero or negligible cytotoxic effect both on keratinocytes and fibroblasts in 2D cell cu, or even enhanced the cellular viability. These nanoparticles were prepared by embedding of UCNPs into the polystyrene beads (Lx-UCNP and Lx-MNP-UCNP) during the course of polymerization. In the core study of the current chapter, we focused our attention on the improved technology of embedding of UCNPs into polymer beads, its effect on photoluminescence of the resulting nanoparticles and feasibility of this approach for bioimaging in vivo.

Embedment of the contrasting nanoagents into polymer beads host is a promising methodology, allowing to deliver the contrast agents to the target sites without quenching of photoluminescence by the aqueous biological environment and, to the certain degree, preserving inorganic fillers from the immune attack. The major drawbacks of the existing schemes of the development of polymer particles impregnated with inorganic nanoparticles are the poor compatibility between the hydrophilic polymer chains and the hydrophobic surfaces of the fillers. This may result in leakage of the nanostructures from the host beads with following uncontrollable effects. In the presented paper we propose a novel approach of embedment of as-synthesized UCNPs into submicron polyacrolein beads *in situ*. In particular, a low-molecular weight phase transition agent tetramethylammonium hydroxide was employed to simultaneously hydrophilize of the UCNPs' surfaces and to induce polymerization of acrolein. This results in secure anchoring of UCNPs in the polymer host and shielding of the embedded nanoparticles from the deteriorating environmental effects. The optimal parameters of the reaction were found in order to keep the small size of the impregnated beads and strong photoluminescence. Next, it was confirmed that the *in vitro* cytotoxicity of the obtained submicron composites is low. Finally, we developed the imaging system to excite the photoluminescence and detect the emission signal from UCNPs and proved the feasibility of this complex approach in experiments on animals and *ex vivo*, on histological slices of the excised organs. As a preliminary result good biocompatibility of the UCNP-impregnated polyacrolein beads was proved in terms of absence of acute and subacute allergic and histotoxic

reactions, and the pattern of biodistribution of the studied biomaterial after intravenous injection was described.

This work demonstrates the feasibility of the proposed surface modification procedure for preparation of the biocompatible submicron photoluminescent beads for bioassays. It could be expected that the further development of this methodology may be useful for creation of drug delivery systems, contrast imaging agents and, probably, for 3D tissue culture on the traceable microcarriers.

5.2. The author's contribution to the paper II

The PhD candidate (Anna Guller) is a co-author of this paper. Her main contributions were made into the study of biological effects of polymer-embedded UCNPs, including the cytotoxicity evaluation *in vitro*, as well as observation and interpretation of the reactions of the animals on the tail vein injections of the particles, biodistribution of the injected nanomaterials, bioimaging and histopathological study of the exposed tissues. Ms. Anna Guller also took part in manuscript writing and editing.

The first author of the paper Dr. Alla N. Generalova developed the concept of UCNP embedment into polymer beads *in situ* and, in collaboration with Ms. Irina Kochneva, performed all the experiments for surface modification of the oleate-capped UCNPs as well as a significant part of the studies for the particles' characterization (see sections 3.2.1 -3.2.3 and 3.2.5 of the paper II). Dr. Andrey V. Nechaev optimized and performed synthesis of UCNPs and provided the characteristics of the nanocrystals. Dr. Evgeny V. Khaydukov and Dr. Vladimir A. Semchishen developed the optical imaging system, studied optical properties of UCNP-impregnated polymer particles, and analyzed the main photophysical results and FTIR data. Prof. Vitaly P. Zubov conceptualized and supervised all the polymer chemistry experiments and edited the manuscript. Prof. Anatoly Shekhter contributed to the design of biological experiments and to the histopathological data analysis. Prof. Sergey M. Deyev contributed to the discussion and the analysis of the results and edited the manuscript. A/Prof. Andrei V. Zvyagin (the corresponding author) coordinated the project and finalized the manuscript. All authors approved the manuscript.

5.3. Full paper II



Nanoscale

PAPER

View Article Online
View Journal | View Issue

Submicron polyacrolein particles *in situ* embedded with upconversion nanoparticles for bioassay

A. N. Generalova,^{a,b,c} I. K. Kochneva,^a E. V. Khaydukov,^b V. A. Semchishen,^b A. E. Guller,^{d,e} A. V. Nechaev,^f A. B. Shekhter,^d V. P. Zubov,^{a,b} A. V. Zvyagin^{*c,e} and S. M. Deyev^{a,c}

Cite this: *Nanoscale*,
2015, 7, 1709

We report a new surface modification approach of upconversion nanoparticles (UCNPs) structured as inorganic hosts NaYF₄ codoped with Yb³⁺ and Er³⁺ based on their encapsulation in a two-stage process of precipitation polymerization of acrolein under alkaline conditions in the presence of UCNPs. The use of tetramethylammonium hydroxide both as an initiator of acrolein polymerization and as an agent for UCNP hydrophilization made it possible to increase the polyacrolein yield up to 90%. This approach enabled the facile, lossless embedment of UCNPs into the polymer particles suitable for bioassay. These particles are readily dispersible in aqueous and physiological buffers, exhibiting excellent photoluminescence properties, chemical stability, and also allow the control of particle diameters. The feasibility of the as-produced photoluminescent polymer particles mean-sized 260 nm for *in vivo* optical whole animal imaging was also demonstrated using a home-built epifluorescence imaging system.

Received 8th October
2014,
Accepted 1st
December 2014
DOI:
10.1039/c4nr05908e
www.rsc.org/nanoscale

^aM.M. Shemyakin & Yu.A. Ovchinnikov Institute of Bioorganic Chemistry of the Russian Academy of Sciences, 117997 Moscow, Russia

^bInstitute on Laser and Information Technologies of the Russian Academy of Sciences, 140700 Shatura, Russia

^cN.I. Lobachevsky Nizhny Novgorod State University, 603950 Nizhny Novgorod, Russia

^dI.M. Sechenov First Moscow State Medical University, 119992 Moscow, Russia

^eMQ Biofocus Research Centre, Macquarie University, NSW 2109, Australia.

*E-mail: andrei.zvyagin@mq.edu.au

^fM.V. Lomonosov Moscow University of Fine Chemical Technology, 119571 Moscow, Russia

†Electronic supplementary information (ESI) available: SI 1, SI 2. See DOI: 10.1039/c4nr05908e

1. Introduction

The last decade has seen a productive confluence of life sciences and nanotechnology. In particular, photoluminescent (PL) nanomaterials, such as quantum dots,¹ gold nanoparticles,² metal–ligand complexes³ and fluorescent nanodiamonds⁴ provide a means for imaging biomolecular processes in a broad physiological context. The exceptional photophysical properties of these nanoparticles (NPs) push the sensitivity limit to a single biomolecule level, while the well-developed surface of these NPs represents a flexible platform, where various surface moieties can be attached, enabling targeting and/or therapeutic biomolecules to dock. These biomolecules and NPs are pieced together to form a targeting hybrid nanoassembly with diagnostic capabilities, whereas the attachment of the therapeutic cargo enables the treatment of these targeted cells or biological tissues.

Lanthanide-doped upconversion nanoparticles (UCNPs) represent one of the most promising types of these PL nanomaterials. UCNPs are characterised by sharp absorption and emission lines, high conversion efficiency,⁵ long lifetimes, low reported cytotoxicity,⁶ negligible photobleaching,⁷ and high spatial-temporal resolution during bioimaging.⁸ The efficient conversion of near-infrared (NIR) excitation at a wavelength of 980 nm into shorter-wavelength infrared and visible spectral range emission (known as “upconversion”) represents its most acclaimed property. The near-infrared excitation band of UCNPs entails two additional useful properties. Firstly, the excitation of the intrinsic tissue fluorescence, known as autofluorescence, is almost negligible;⁹ secondly, the excitation light penetration in the biological tissue is greater in comparison with visible light, up to one centimetre, because the excitation band falls into the so-called biological tissue transparency window.^{10,11}

In most cases, UCNP is composed of a host matrix doped with sensitizer and activator rear-earth ions. The most effective matrix for the NIR-to-visible or shorter-wavelength NIR upconversion has been reported¹² to be a hexagonal phase (β -phase) NaYF₄ crystal characterised by low phonon energy. The sensitizer (Yb³⁺) and activator (Er³⁺ and/or Tm³⁺) are doped in the host matrix in relatively low concentrations, usually 20 mol% and (2 and/or 0.5 mol%), respectively. Typically, these UCNPs are synthesized in organic solvents, resulting in UCNPs stabilized with hydrophobic oleate ligands. They are dispersible only in nonpolar organic solvents and aggregate in aqueous solutions and physiological buffers, which limits their scope of biomedical application. The surface hydrophilization of UCNPs, therefore, represents an essential pre-requisite for grafting the UCNP surface with reactive functional moieties suitable for conjugation with biomolecules.

A number of surface modification approaches have been reported, including: (i) ligand oxidation reaction;¹³ (ii) ligand exchange reaction;¹⁴ (iii) intercalation using amphiphilic polymers;¹⁵ (iv) cross-linked polymer coating;¹⁶ (v) layer-by-layer self-assembly;¹⁷ (vi) host–guest self-assembly;¹⁸ (vii) encapsulation of NPs in silica.¹⁹ As a result, the as-synthesized hydrophobic PL NPs are rendered dispersible in aqueous media, allowing further bioconjugation with biomolecules, while preserving their photoluminescence properties.²⁰ However, most of these approaches usually result in the formation of a

CHAPTER 5

loose protective shell around the UCNP, unable to shield the UCNP surface from the solvent molecules, including the ions of buffer salts, which can penetrate and damage the UCNP surface resulting in fluorescence quenching.²⁰

The embedment of the UCNPs into the polymer particles obtained by heterogeneous polymerization, while transferring them to aqueous media, represents a promising approach of tight shielding the UCNPs by the formation of a solid polymer shell impenetrable to the small solvent molecules. To the best of our knowledge, such an approach has not been reported for UCNPs. At the same time, polymer particle hosts have been employed for the encapsulation of such inorganic fillers as quantum dots,²¹ iron oxides,²² metal–ligand complexes,²³ etc. Usually, these fillers are encapsulated either into preformed polymer particles swelled in an appropriate solvent,²⁴ or in the course of the polymerization procedure.²⁵ Although the preformed polymers provide an adequate isolation to the inorganic fillers from the physiological environment, the fillers are not securely anchored and can escape from the polymer host, if its structural properties, e.g. porosity, change in response to the environmental changes.²⁴

In order to address the problem of filler retention in the polymer host, we propose the following new synthesis concept: the polymerization itself is initiated by the fillers, in our case, hydrophilized upconversion nanoparticles, which are introduced at the stage of polymerization. As a result, the UCNP forms bonds with the polymer matrix during its in situ formation, eventually yielding a hybrid water-dispersible submicron polymer particle containing UCNPs well secluded from the aqueous environment, but capable of interfacing with biomolecules. The challenge of in situ embedding of the UCNPs into a polymer matrix lies in the design of the method providing chemical compatibility between the UCNP and polymer chains while protecting the optical properties from quenching agents, photobleaching, and effects of solvent polarity, pH, and ionic strength.

Acrolein was the monomer, giving rise to polymer particles readily dispersible in water, with variable particle diameters and with aldehyde groups on the surface.²⁶ These groups easily form a Schiff's base with the primary amine groups of biomolecules under mild conditions. We have previously reported a two-stage precipitation polymerization of acrolein in aqueous media under alkaline conditions.²⁴ This reaction was modified aiming at the encapsulation of UCNPs into polyacrolein (PA) particles and the chemical compatibility between the UCNPs and polymer chains. This was realized by the hydrophilization of UCNPs using tetramethylammonium hydroxide (TMAH), which can promote the transfer from an organic to an aqueous medium.²⁷ The base strength of TMAH is close to an alkali and that makes it possible to use TMAH as an initiator of acrolein polymerization.

In this paper, we have reported a new synthesis of polymer particles embedded with UCNPs in the course of polymerization. The use of TMAH both as a hydrophilizing agent of UCNPs and as an initiator of acrolein polymerization in the presence of UCNPs resulted in the formation of uniform bright PL polymer particles whose diameters were controllable in the broad range. The PL properties of the UCNPs were protected from quenching agents of the environmental surroundings in a secluded polymer

matrix whose colloidal chemical properties were suitable for theranostic applications, one example of which was demonstrated by whole-animal imaging.

2. RESULTS AND DISCUSSION

2.1. Synthesis of upconversion nanoparticles

The UCNPs ($\text{NaYF}_4:\text{Yb}^{3+}, \text{Er}^{3+}$) were synthesized by a modified solvothermal method, as described in ref. ¹⁵ and imaged by TEM (see Fig. 1). The mean size of the as-synthesised UCNPs was evaluated to be 41 ± 3 nm, which was most favourable for the energy transfer upconversion process of the hexagonal crystal phase.²⁸

The as-synthesized UCNPs were capped with hydrophobic oleate ligands and hence were neither miscible with water, nor suitable for an immediate bioconjugation with biomolecules.

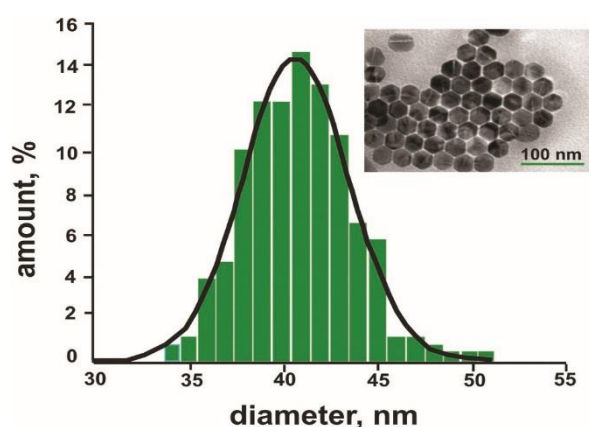


Fig. 1 Size distribution histogram and TEM image of the as-synthesised $\text{NaYF}_4:\text{Yb}^{3+}/\text{Er}^{3+}$ nanoparticles.

2.2. Synthesis of polymer particles embedded with UCNPs in the course of polymerization

2.2.1. Design of the polymerization method

Recently, we have reported the production and characterisation of preformed polyacrolein (PA) particles which served as a matrix for the encapsulation of the fillers, i.e. quantum dots.²⁴ Despite their promising colloidal and photoluminescence properties which are suitable for bioimaging, they showed a propensity for the desorption of quantum dots from the PA particles and a concomitant degradation of the PL efficiency. In order to avoid the desorption of the filler, we developed an approach which was realized by the introduction of the filler and upconversion nanoparticles, in the course of acrolein polymerization, as detailed in “Materials and methods”. The reaction scheme is presented in Fig. 2A.

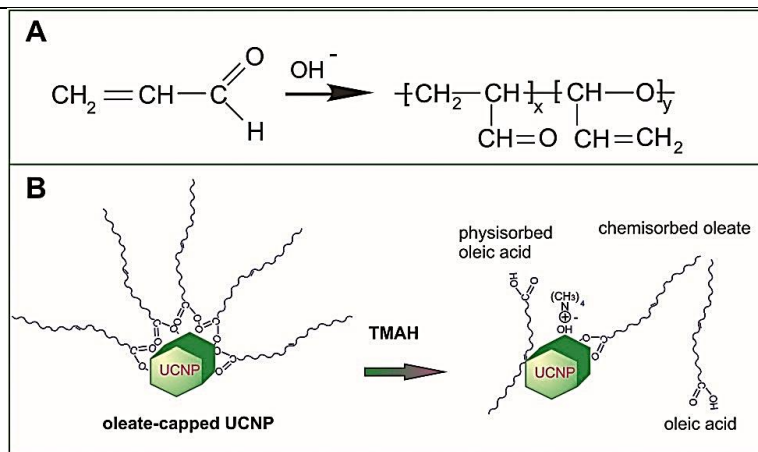


Fig. 2 Schematic formula for acrolein polymerization under alkaline conditions (A); schematic diagram of UCNP hydrophilization by the tetramethylammonium hydroxide (B).

In order to introduce the filler, i.e. the UCNPs, into the PA polymer at the 1st polymerization stage, it has to be sufficiently hydrophilic to facilitate its transport through the water phase from the monomer droplets to the growing seed particles. The surface of the as-synthesized UCNPs, however, is strongly hydrophobic due to the coordination with oleate ligands, which precludes its solubility in a variety of monomers and solvents. Our initial experiments proved that, indeed, the as synthesized UCNPs were not miscible with acrolein. We then developed a new approach, which satisfied both the conditions for the encapsulation of the UCNP into polyacrolein particles and the chemical compatibility between the UCNP and the polymer chains. To this end, UCNPs were hydrophilized by TMAH, making their transfer from an organic solvent to aqueous media possible,²⁷ whereby the oleate ligands were partially displaced from the UCNP surface. In addition, the base strength of TMAH was close to that of the alkali usually employed in the polymerization reaction that makes it possible to use TMAH as an initiator of acrolein polymerization.

The oleate ligands were chemically adsorbed on the UCNP through the coordination between the COO^- group and the lanthanide ions on the surface.²⁹ As reported in the literature,³⁰ the partial removal of oleate ligands from the UCNP surface (as demonstrated using magnetite NPs) reduced the hydrophobicity and made it possible to prepare the polymer particles with a controllable content of nanoparticles. In our case, we hydrophilized the oleate-capped UCNPs by applying a facile base reaction with TMAH,²⁹ which resulted in the partial release of oleic acid from the surface. In order to confirm the outcome of this reaction, we acquired and analysed Fourier transform infrared (FTIR) spectra of UCNPs, UCNPs hydrophilized with TMAH, followed by further purification with water (Fig. 3B), and with water–acrolein mixture (20 : 1 vol) (Fig. 3C). Water–acrolein mixture was used since oleic acid is almost insoluble in water and can remain in the samples after purification.

The spectra of UCNPs (Fig. 3A) and UCNPs + TMAH purified with water (Fig. 3B) are almost identical within the two bands: 1461 and 1550 cm^{-1} , which are attributed to the asymmetric (δ_s) and the symmetric $-\text{COO}-$ (δ_{as}) stretches of oleic acid, respectively.³¹ A strong stretching vibration of $-\text{C}=\text{O}$ assigned to oleic acid appears at 1737 cm^{-1} in the sample treated with TMAH and purified with water

CHAPTER 5

(Fig. 3B). However, this characteristic band of the C=O stretch practically disappears in the sample C spectrum (Fig. 3C), indicating the removal of the outer layer of oleic acid after purification with the water–acrolein mixture.³⁰ In addition, the removal of oleic acid is corroborated by the disappearance of a peak at 1550 cm^{-1} and a decrease of the stretching band at 1461 cm^{-1} .

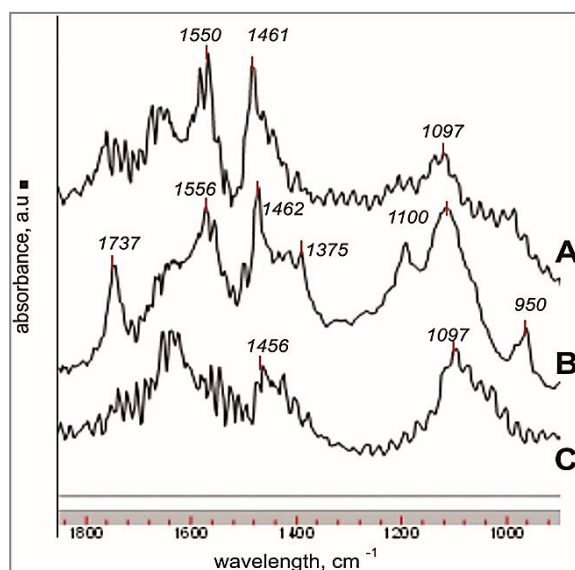


Fig. 3 FTIR-spectra of the UCNP sample: (A) in dry powder form; (B) hydrophilized with tetramethylammonium hydroxide, (C) purified with a water–acrolein (20 : 1 vol) mixture.

Based on this analysis, our interpretation of the TMAH based reaction is schematically presented in Fig. 2B. The oleic acid which was chemically adsorbed on the as-synthesised UCNP surface was partially displaced with TMAH, facilitating UCNP hydrophilization and its transfer to aqueous media. It was likely that the hydrophilized UCNPs still contained oleic acid moieties, which were physisorbed by intermolecular forces (van der Waals, hydrophobic, hydrogen bond formation) on the UCNP surface. These moieties were resilient to washing with water, but were removable with organic solvents.

We found that TMAH initiated acrolein polymerization in the absence of UCNPs with the polymer yield in excess of 90% (see Fig. 5) in comparison with that of the alkali measured as 45%.²⁴ TMAH seemed to cause the formation of a more effective carbanion of acrolein in the chain propagation reaction. In aqueous media, an $\text{N}^+(\text{CH}_3)_4$ ion can support the presence of free ions (these free ions promote polymerization unlike the contact pairs of ions, which inhibit polymerization³²), owing to steric hindrance, more efficiently than Na^+ in alkali, thus causing a higher monomer conversion, and subsequently a higher polymer yield.

Since TMAH was found to be capable of initiating the high yield polymerization reaction, it was anticipated that TMAH surface-modified UCNPs would efficiently initiate the polymerization reaction. In order to demonstrate this reaction mechanism, we synthesized the polyacrolein particles with the addition of UCNPs in the range of concentration (C_{UCNPs}) from 0.1 to 1.5 wt% calculated with respect to the monomer (Fig. 4A).

Indeed, TMAH as a part of the hydrophilized UCNPs resulted in high polymer yields for all the tested CUCNPs, as shown in Fig. 4A. The polymer yield was found to decrease versus an increase in the CUCNP. We speculate that TMAH displaced the oleate ligands from the UCNP surface and the increase of CUCNP caused the depletion of OH^- ions in the dispersion medium, which promoted the propagation of polymerization, so that the polymer yield was decreased as CUCNPs increased. In the FTIR spectrum of UCNP-TMAH (Fig. 3B), a single band at 950 cm^{-1} attributed to the asymmetric C–N stretch³³ is observable, in contrast to the dry UCNP powder spectrum (Fig. 3A). Moreover, a new peak at 1375 cm^{-1} and a 1100 cm^{-1} peak increase, which are characteristic for the deformation vibration of O–H,³⁴ suggest that TMAH adsorption on the UCNP surface causes a decrease in the polymer yield.

Thus, the proposed method assisted by the UCNPs provides a well-controlled synthesis of PA particles with a high polymer yield; these assemblies are hereafter abbreviated as PA-UCNP.

2.2.2. 2nd polymerization stage.

At the 2nd polymerization stage, the radical initiator ($\text{K}_2\text{S}_2\text{O}_8$) caused the polymerization of the residual double bonds of acrolein. Fig. 4 presents the FTIR spectra of polyacrolein particles after the 1st and 2nd polymerization stages in the presence of the hydrophilized UCNPs. The FTIR spectrum exhibited a change in the relative intensity of peaks at 1719 cm^{-1} attributed to the C=O bond of the aldehyde group and at 1678 cm^{-1} assigned to $\text{C}=\text{C}$.³⁵ The reduction of the peak at 1678 cm^{-1} indicated a decrease of the terminal double bond relative to the number of aldehyde groups. Besides, no vibration band at 3080 cm^{-1} attributed to $=\text{CH}_2$ ³⁵ was observable in the spectra of the sample after the second stage (Fig. 4B). It is to be noted that the crosslinking of the residual double bonds in polymerization caused an increase of the polymer yield and chemical stability. The polymer particles became practically insoluble in alcohol and the concentration of water-soluble oligomers as typical side products of acrolein polymerization formed during this synthesis decreased (Fig. 4C).

However, it is worth noting that the chemical stability of the resultant particles decreased versus the UCNP concentration, as shown in Fig. 4C. This effect was apparently related to the steric hindrance of the growing oligomer chain to access the active center (OH^-) partially adsorbed on the UCNP surface. It arrested the growth of the water-soluble short chain oligomers, leading to their diffusion into the dispersion medium. As a result, PA particles became loose, allowing infiltration of the alcohol molecules.

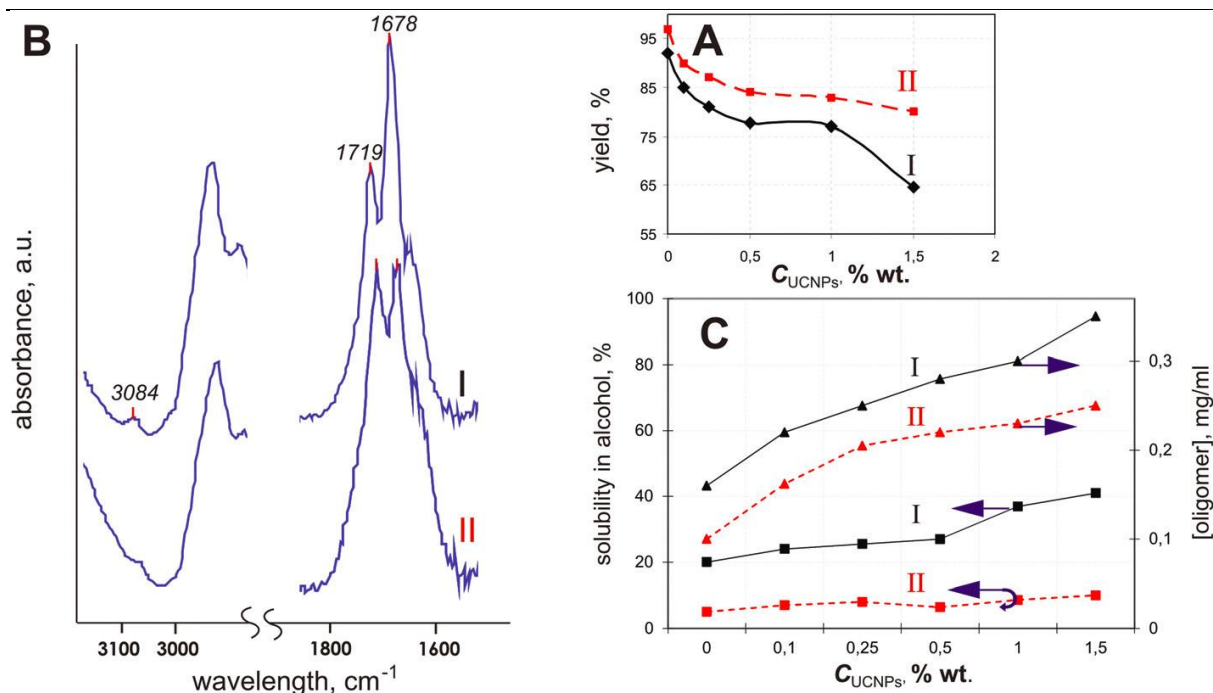


Fig. 4 Polyacrolein yield versus UCNPs concentrations in the course of polymerization (A); FTIR spectra of polyacrolein particles after the first and second stages of polymerization in the presence of UCNPs (B); solubility of polyacrolein particles in alcohol and oligomer concentrations versus the concentration of UCNPs (C). (I represents polymerization under alkaline conditions; II represents the radical cross-linking of the residual C=C bonds.)

2.3. Characterization of PA particles synthesized in the presence of UCNPs

The obtained particles remained colloidally stable for at least 6 months, and were unaffected by electrolytes (0.15 M NaCl and other physiological buffers).

It is important to note that the functional (aldehyde) groups of the hybrid PA particles are convenient for their coupling with biomolecules, paving the way for a broad range of imaging and targeted delivery applications. Owing to the nonporous character of the PA matrix,³⁶ only aldehyde groups on the PA particle surfaces participate in the immobilization of biologically active molecules. We found that the concentration of the surface aldehyde groups per g of the polymer particles increased versus CUCNPs after the 2nd polymerization stage, as shown in Fig. 5A.

2.3.1. Particle diameters.

The use of TMAH as the initiator of polymerization enabled the formation of pristine polymer particles with a diameter (d) larger (Fig. 5A) than that obtained in the course of the alkali-induced polymerization of acrolein ($d = 620$ nm), as reported previously in ref. ²⁴. This was explained by the fewer nucleation centers generated in the case of TMAH than those in the case of alkali, provided, the concentrations of TMAH and alkali were equal. We speculate that the early-stage initiation was accompanied by the salvation of counterion, which, probably, prevailed in the case of an alkali

CHAPTER 5

counterion Na^+ .³² The decrease of the nucleation centers gave rise to the increase of d , in the case of TMAH.

d of the PA-UCNP particles depended on the concentration of the inorganic NPs and varied from 500 to 260 nm, as it was measured by using a method of dynamic light scattering (Fig. 5A). It is noteworthy that the higher the concentration of UCNP in the polymerization initial mixture, the smaller the particles that are formed at the 1st polymerization stage. d remained practically unchanged at the 2nd polymerization stage (Fig. 5A). This observation can be explained in terms of PA particle stabilization in the course of polymerization. As described earlier, the short-chain oligomers prevented the aggregation of the PA particles. At the same time, their surface activity was insufficient to significantly decrease the diameter, since the reduction of the dynamic surface tension at the water–air interface by the oligomers was in excess of 60 mN m^{-1} , falling short of the value of 30 mN m^{-1} achievable with effective surfactants.³⁷ We refer to the ESI section 1 (SI-1†) for more details. Also, the oligomers were likely to desorb from the PA particle surface to the dispersion media. The decrease of d was also due to the influence of another surface active moiety, the oleate ligand, physisorbed on the UCNP surface after the hydrophilization treatment with TMAH. Being surfactants, oleate ligands can adsorb on the surface during the synthesis of PA particles thus reducing d . At a UCNP concentration greater than 0.5 wt%, the effect of oleic acid diminished, and the d variation halted.

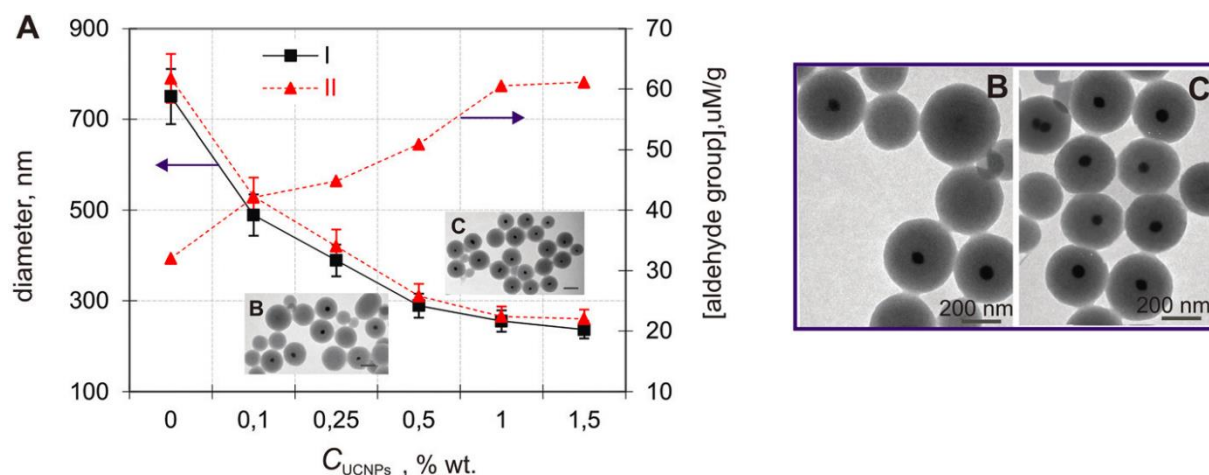


Fig. 5 Diameters of polyacrolein particles impregnated with UCNP versus UCNP concentration (A); TEM images of polyacrolein particles obtained in the presence of UCNP: 0.25 wt% mean-diameter, 400 nm (B); 1.5 wt% mean-diameter, 260 nm (C). Scale bar, 200 nm. (I represents polymerization under alkaline conditions; II represents the radical cross-linking of the residual C=C bonds.)

2.3.2. Structural and photoluminescence properties of hybrid PA-UCNPs.

The UCNP-assisted acrolein polymerization can be classified as a template polymerization, which is characterized by specific interactions between the template, i.e. UCNP, and the growing polymer chains. The oligomer complexation with the template occurs in solution via intermolecular forces, when the oligomers reach a critical length. Then the oligomers continue to propagate along the template by sourcing monomer molecules from the surrounding media.³⁸

CHAPTER 5

TEM images of the PA-UCNP particles synthesized in situ are shown in Fig. 5. UCNP were seen buried at the center of the polymer host, thus confirming the template role of UCNP, with a polymer shell formed around the UCNP core. Pristine coreless PA particles were also formed. The proportion of the PA-UCNP to pristine PA particles showed a clear tendency to grow versus the CUCNPs in the range from 0 to 1 wt%, as shown in Fig. 5C. This graph plateaus at 1 wt%; the proportion of the pristine PA particles remained constant, while the PA-UCNPs occasionally featured more than two UCNP cores. We speculate that both precipitation and template polymerization mechanisms participated in the formation of PA-UCNPs.

It is worth noting that all the UCNP appeared to be embedded in the PA particles, as suggested by two observations: (1) TEM imaging revealed no individual UCNP but only those embedded in the PA particles; (2) no photoluminescence of the supernatants after the centrifugation of PA-UCNP particles was detected, hence the supernatants contained no stand-alone UCNP.

Several comments on the PL properties of the hybrid PA-UCNP assemblies are now in order. The susceptibility of the UCNP to environmental effects is notorious and has been addressed in many reports.^{10–12} Oleic acid ligands coordinated to the UCNP surface were found to reduce this susceptibility and protect the UCNP emitting state from environmental surroundings, which ushered the UCNP uptake in life sciences.²⁸ The TMAH-mediated replacement of the oleic ligands with a PA polymer preserved the high PL efficiency of the oleic coordinated UCNP. In particular, an intensity ratio of the characteristic green and red spectral bands of NaYF₄:Yb,Er was reported to be a sensitive indicator of the PL emission state variation due to environmental effects.²⁹ As can be inferred from the PL spectra of the UCNP and PA-UCNP particles at the 1st and 2nd production stages (Fig. 6A), the green-to-red emission ratio calculated for all CUCNPs remained unaltered. Based on this result, we assume the passivation of the UCNP quenching surface defects by the polymer shell occupying the vacant coordinate sites on the UCNP surface.²⁸

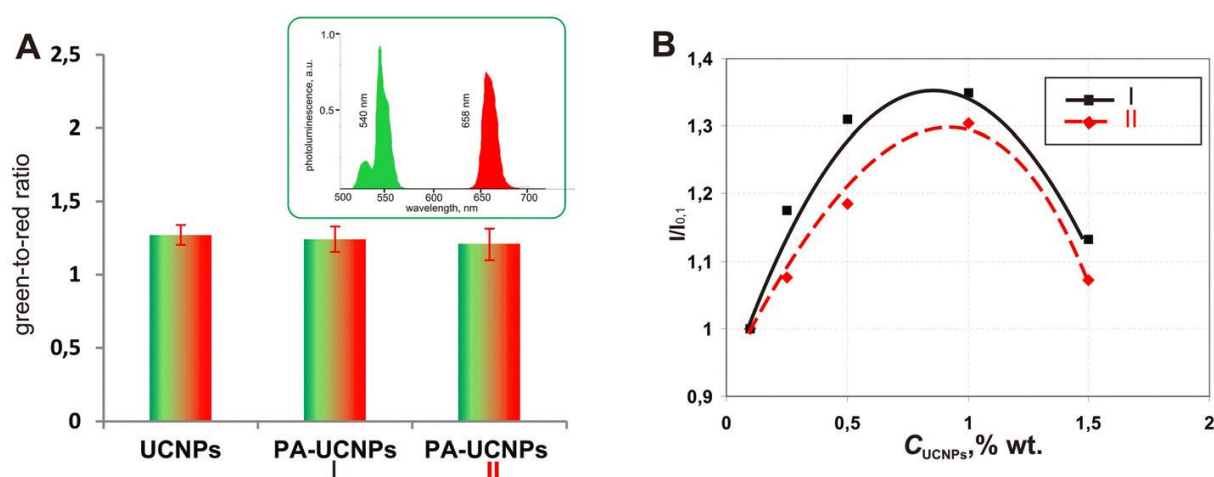


Fig. 6 The green-to-red emission ratio from the PL spectra of UCNP and polyacrolein particles impregnated with UCNP obtained under laser excitation at wavelength 975 nm. Excitation intensity, 10 W cm^{-2} (A); inset represents the PL spectrum of UCNP in chloroform. A plot of the PL intensity, I normalised to the reference intensity $I_{0.1}$

CHAPTER 5

versus the UCNP concentration. $I_{0.1}$ is defined as the PL intensity at 0.1 wt% UCNP (B). (I represents polymerization under alkaline conditions; II represents the radical cross-linking of the residual C=C bonds.)

In order to analyze the PL dependence on CUCNP in the polymerization initial mixture, we plotted the PL signal intensity at 545 nm versus CUCNP (Fig. 6B). The maximum PL efficiency occurred at CUCNP = 1 wt% with respect to the monomer. The PL decrease at 1 wt% < CUCNP < 1.5 wt% can be explained by the formation of UCNP aggregates inside the PA particles. In this case, a poor polymer shell was formed on the surface of UCNPs at their contact area, resulting in an insufficient surface passivation, and hence PL degradation.²⁸ As one can see from Fig. 6B, the PL signal changed slightly after the 2nd polymerization stage. The reason behind this variation is unclear and warrants further study.

2.4. Application of PA-UCNP particles in optical bioimaging

In order to demonstrate the feasibility of applications of photoluminescent polymer particles in theranostics, we carried out in vivo whole-animal imaging experiments using a PA-UCNP intravenous injection. A preliminary MTT assay for the evaluation of PA-UCNP and UCNP-TMAH cytotoxicity demonstrated low cytotoxic effects performed on linear keratinocytes HaCaT (see SI 2, Fig. S2†). We designed an epi-luminescence imaging system equipped with a raster-scanning laser excitation source to visualize PA-UCNP distribution in a live mouse (see Fig. 7A). The laser light was projected onto the animal surface and the emitted photoluminescence was collected from the same side with a camera lens (f-number 0.95).³⁹ Raster scanning was implemented with a collimated beam of a continuous-wave semiconductor laser operated at wavelength 975 nm, redirected off the fast galvanometer scanning mirror units (Miniscan-07, Raylase®, Germany). The elicited PL signal was recorded by an electron-multiplication(EM) CCD camera (Falcon, Raptor Photonics®, Ireland). The position of the camera was adjusted so as to make its matrix and the top surface of the mouse lie in optically conjugated planes. Rejection spectral filters were used to suppress the excitation signal in the detection path.

In order to demonstrate the visualization of the biodistribution of PA-UCNP particles in vivo, 0.5 mg of PA-UCNPs (CUCNP = 1 wt%) suspended in 0.1 mL of phosphate buffer saline was injected in the animal tail vein. No acute systemic toxicity and allergic reactions were observed. The following sequence of pharmacokinetic events was observed (see Fig. 7B). A rapidly vanishing signal at the venepuncture site was noticeable immediately after the injection. 5–10 min postinjection, a bright signal in the projection of the lungs (both from chest and back sides) was clearly detectable in 10 investigated animals. Then PL was redistributed towards the projections of the spleen and liver, reaching its maximum in 60–80 min, while it virtually disappeared in the lungs. Furthermore, a weak PL signal in the projection of the bowel and pelvic organs of the animals was observed 40–60 min postinjection. Apparently, no PL signal was detected in the animals injected with pristine PAs.

It was also possible to perform informative PL *ex vivo* imaging of organ tissue slices using our epi-luminescence imaging system. PA-UCNP particles were found immobilised in tissue sections of the liver, spleen, lungs and kidney (see SI-2, Table S2†), with a maximum accumulation observed in the

liver and spleen. In addition, PA-UCNPs were observed in the lungs with a trend of increasing local concentration in the areas of partial atelectasis. In the kidney, the PL clusters were hardly detectable localized mainly near the proximal convoluted renal tubules.

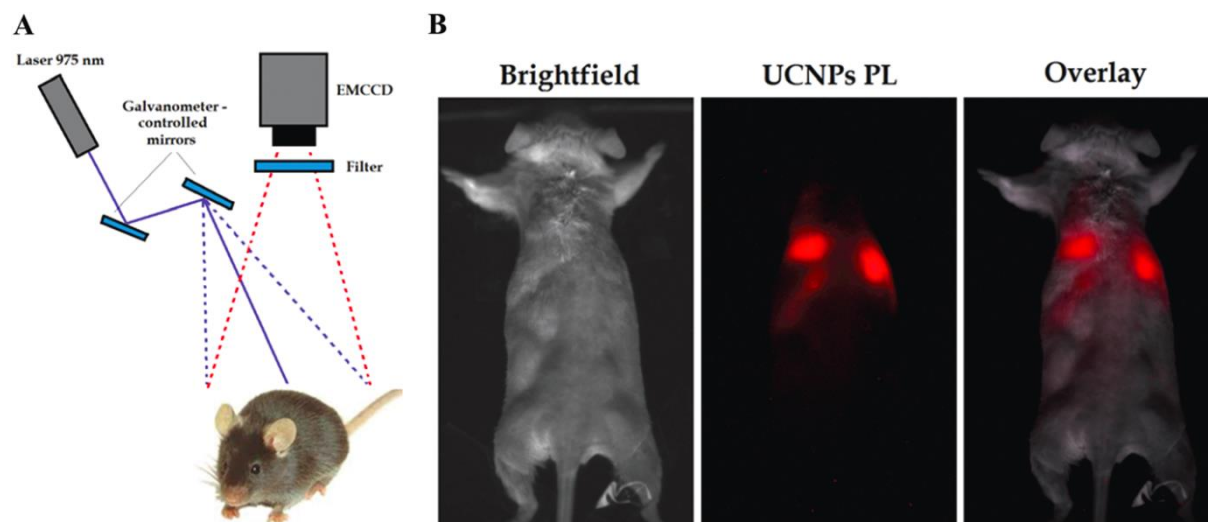


Fig. 7 Schematic rendering of the epi-luminescence imaging system (A). In vivo photoluminescence imaging of a live mouse, post 1-hour intravenous injection of PA-UCNPs. Left: a bright-field image; centre: PL image; right: an overlay of the bright-field and PL images (B).

According to the histological data of the organ tissue slices harvested and processed post-injection of PA-UCNPs, pathological changes were minor or absent. In particular, moderate blood congestion was revealed in the central and triad veins in the liver. In the lungs, small lymphocyte and macrophage infiltrates with individual neutrophils and plasma cells were found in the vicinity of the large bronchi and blood vessels. In the kidney and spleen, the tissue structure was found to be normal (see SI-2, Table S2[†]).

Thus, polyacrolein particles in situ embedded with upconversion nanoparticles have great potential as bioimaging probes well suited for fluorescence visualization in whole animals.

3. EXPERIMENTAL

3.1. Materials

Acrolein purchased from Fluka (Germany) was distilled three times at atmospheric pressure and a fraction of it with a boiling point of 56 °C, $\rho_{420} = 0.806 \text{ g cm}^{-3}$, $n_{D20} = 1.40$ was used. Polymer yield was measured gravimetrically.

The following materials were purchased from Sigma-Aldrich (USA), and used without further purification: potassium persulfate, sodium hydroxide, sodium chloride, phosphate buffered saline (PBS), sodium azide, tetramethylammonium hydroxide pentahydrate (TMAH), p-nitrophenylhydrazine. Ethanol, hexane and chloroform were of analytical grade and purchased from Sigma-Aldrich.

3.2. Methods

The size of particles was measured using a Coulter N4-MD submicron particle analyzer (Coultronics, France). Optical characteristics were measured using a Beckman DU-70 spectrophotometer (Beckman, Germany). Spectra of fluorescence were recorded by using a Fluorolog spectrofluorometer (Horiba Jobin Yvon, France). The photoluminescence spectra of histological sections were registered by using a fluorescence microscope, as reported previously in ref. ¹⁵.

3.2.1. Polymerization of acrolein in the presence of UCNPs.

The polymerization of acrolein was carried out, as reported previously in ref. ²⁴ with some modifications. In the beginning, dispersions with varying concentrations of UCNPs in TMAH were obtained: 10, 25, 50, 100 or 150 μl of UCNP dispersion (20 mg ml^{-1}) in chloroform was added dropwise to 1 ml of a 1% aqueous solution of TMAH and the two immiscible phases were thoroughly shaken and sonicated for 15 min. UCNPs were transferred from one phase to another, chloroform was evaporated. Then, freshly distilled acrolein 0.2 ml was placed in a three-necked reaction flask containing water (monomer–water = 1 : 20 v/v) under stirring. One of the aforementioned UCNP dispersions in TMAH was added dropwise under stirring. After 3 h of stirring at room temperature, water insoluble polymer particles were formed. Then, the reaction mixture was deoxygenated by purging with N_2 for 30 min and $\text{K}_2\text{S}_2\text{O}_8$ (2% wt in respect to monomer) was added to increase the chemical stability of the obtained polymer particles. The mixture was kept at 70 °C under N_2 and stirred for 3 h. The procedure was repeated for all the concentrations of UCNPs in TMAH.

3.2.2. Measurement of the aldehyde group concentration.

The aldehyde group concentration was measured by using p-nitrophenylhydrazine (NPH) in an alcohol/phosphate buffer pH 5.3 as we have reported previously in ref. ²⁴. The supernatants of the mixture containing 1 mL of NPH and 100 μL 5 wt% polymer particle dispersion after preparation and incubation for 8 h were collected and analyzed using a Beckman DU-70 spectrophotometer at wavelength 392 nm. The aldehyde group concentration was calculated as the concentration of NPH that has reacted with the aldehyde groups.

3.2.3. Measurement of the acrolein oligomer concentration.

Polyacrolein dispersion was centrifuged and the supernatant containing acrolein oligomers was measured using a Beckman DU-70 spectrophotometer at wavelength 273 nm, as we have reported previously in ref. ²⁴. The acrolein oligomer concentration was calculated using the calibration graph of optical absorption of the dry oligomer dissolved in water.

Transmission electron microscopy (TEM).

The UCNP and polyacrolein particles containing UCNPs were diluted by hexane and water, respectively, then sonicated and drop-casted onto thin bar 300-mesh copper TEM grids, coated with

CHAPTER 5

0.3% pioloform. After overnight drying in a desiccator at room temperature, the grids were imaged using a Philips CM10 TEM (Philips, Eindhoven, The Netherlands).

3.2.4. *Sample preparation of UCNPs in TMAH for FTIR spectroscopy.*

The UCNP dispersions in TMAH were prepared as described in 3.2.1. To remove an excess of TMAH, one sample of the aqueous UCNPs was purified three times with water (consecutive centrifugation at 13400 rpm for 10 min – redispersion steps). The pellet was air-dried. Another sample at the same concentration of UCNPs was purified three times in the same manner with a water–acrolein mixture (1 : 20, v/v) at 0 °C to avoid oligomer formation. The pellet was air-dried.

3.2.5. *Fourier-transform infrared (FTIR) spectroscopy.*

Pure UCNPs were thoroughly ground and then pressed with KBr to form a tablet. The air-dried samples of UCNP modified with TMAH: purified with water and with water–acrolein, as well as polymer particles were dried using a Savant SpeedVac Concentrator (France), then ground and pressed with KBr to form a tablet. FTIR spectra were recorded using an FTIR spectrophotometer (Varian 3100, USA).

3.2.6. *Mice for in vivo imaging, microscopy and morphological study.*

Preliminary animal imaging experiments were performed in male BALB/c mice weighing 20–25 g to examine the biodistribution of these particles after a single intravenous injection. The study was carried out with the permission of the Ethics Committee of I.M. Sechenov First Moscow State Medical University.

Anaesthesia was performed by using a mixture of Zoletil (5.0 mg kg⁻¹), and 10 µL of 2% Rometar solution. The anaesthetic cocktail was administered intraperitoneally in doses of 0.2–0.3 ml per animal for a minimum of 2 hours sleeping time. Anaesthesia was maintained to the end of the experiment with additional Zoletil (0.1 ml, i.p., 5.0 mg kg⁻¹), if necessary. Fur around the chest, abdomen and back areas of the animals was shaved to reduce scattering of the photoluminescence signal and localize it with maximal precision.

Then each mice was injected via a lateral tail vein with 100 µL 0.5 wt% PA-UCNPs/PA dispersion (1 mg kg⁻¹) (n = 10) in PBS, pH 7.2. Immediately after the injection, the animals were placed into the optical imaging system to evaluate the PA-UCNP PL signal distribution time evolution. The detection of PL was carried out either from the ventral or the back side of the animals.

Mice were sacrificed within 2 h after the injection of PA-UCNPs/PA by using the drug overdose method and necropsy was performed. The heart, lungs, liver, spleen, kidney were excised and fixed in 10% neutral buffered formalin for 48 h. After fixation, the excised organs were dehydrated in a graded series of alcohol, embedded in paraffin wax and cut into 5 µm matched serial sections for conventional light microscopy histological examination and photoluminescence microscopy examination, respectively. The slices for the histological study were stained with haematoxylin and eosin (H&E), following the conventional protocol, and examined using an upright light microscope Olympus BX51

CHAPTER 5

(Olympus Optical, Tokyo, Japan) equipped with an SDU-252 digital camera (Spetstelektika, Russia). The slices for PL measurements were left unstained. All the samples were embedded in the polystyrene-based mounting media and covered with cover slips.

4. CONCLUSIONS

A new in situ method for the synthesis of water-dispersible polymer particles impregnated with upconversion nanoparticles in the course of acrolein polymerization was designed and demonstrated. The obtained uniform polymer particles were size-controllable in the range of 260–650 nm. The photoluminescence efficiency was found comparable to that of the state-of-the-art as-synthesised UCNPs, and immune to aqueous and physiological environments. The use of tetramethylammonium hydroxide both as a hydrophilizing agent (by way of displacing capping oleic acids) and as an initiator of polymerization represented the key enabling step. The peculiarity of polymerization in the presence of UCNPs, consisted of precipitation and template methods for the formation of polymer particles, provided a deep burying of UCNPs into the polymer matrix. The feasibility of these polymer particles in biomedical applications was demonstrated with the example of the in vivo optical imaging of hybrid PA-UCNP particle distribution in a whole animal using a home-built epi-luminescence imaging system.

ACKNOWLEDGEMENTS

This work was supported by the Russian Science Foundation grant no. 14-13-01421 (in part of synthesis of polymer dispersions and their characterization), by the Government of the Russian Federation Contract no. 14.Z50.31.0022 (in part of optical bioimaging) and the Russian Foundation for Basic Research projects no. 13-04-40228-H and 12-04-01258 (in part of biosamples). The authors are grateful to Drs A.P. Popov, A.V. Bykov and L. Liang for carrying out the TEM imaging of our samples and T. Rudenko for his assistance in slice preparation for histology.

REFERENCES

1. U. Resch-Genger, M. Grabolle, S. Cavaliere-Jaricot, R. Nitschke and T. Nann, *Nat. Methods*, 2008, 5, 763.
2. S. Lee, E. J. Cha, K. Park, S. Y. Lee, J. K. Hong, I. C. Sun, S. Y. Kim, K. Choi and I. C. Kwon, *Angew. Chem., Int. Ed.*, 2008, 47, 2804.
3. Q. Zhao, M. X. Yu, L. X. Shi, S. J. Liu, C. Y. Li, M. Shi, Z. G. Zhou, C. H. Huang and F. Y. Li, *Organometallics*, 2010, 29, 1085.
4. J. Mona, J. S. Tu, T. Y. Kang, C. Y. Tsai, E. Perevedentseva and C. L. Cheng, *Diamond Relat. Mater.*, 2012, 24, 134.
5. A. Nadort, V. K. A. Sreenivasan, Z. Song, E. A. Grebenik, A. V. Nechaev, V. A. Semchishen, V. Y. Panchenko and A. V. Zvyagin, *PLoS One*, 2013, 8, e63292.
6. C. Bouzigues, T. Gacoin and A. Alexandrou, *ACS Nano*, 2011, 5, 8488.
7. F. Auzel, *Chem. Rev.*, 2004, 104, 139.
8. E. V. Khaydukov, V. A. Semchishen, V. N. Seminogov, A. V. Nechaev and A. V. Zvyagin, *Biomed. Opt. Express*, 2014, 5, 1952.
9. C. T. Xu, N. Svensson, J. Axelsson, P. Svenmarker and G. Somesfalean, *Appl. Phys. Lett.*, 2008, 93, 171103.
10. F. Wang and X. G. Liu, *Chem. Soc. Rev.*, 2009, 38, 976.
11. J. C. G. Bunzli, *Chem. Rev.*, 2010, 110, 2729.
12. M. Wang, G. Abbineni, A. Clevenger, C. Mao and S. Xu, *Nanomedicine*, 2011, 7, 710.
13. Z. Chen, H. Chen, H. Hu, M. Yu and F. Li, *J. Am. Chem. Soc.*, 2008, 130, 3023.
14. J. C. Boyer, M. P. Manseau, J. I. Murray and F. C. J. M. Veggel, *Langmuir*, 2010, 26, 1157.
15. E. A. Grebenik, A. Nadort, A. N. Generalova, A. V. Nechaev, V. K. A. Sreenivasan, E. V. Khaydukov, V. A. Semchishen, A. P. Popov, V. I. Sokolov, A. S. Akhmanov, V. P. Zubov, D. V. Klinov, V. Y. Panchenko, S. M. Deyev and A. V. Zvyagin, *J. Biomed. Opt.*, 2013, 18, 076004.
16. M. An, J. Cui, Q. He and L. Wang, *J. Mater. Chem. B*, 2013, 1, 1333.
17. H. Zhang, Y. Li, I. A. Ivanov, Y. Qu, Y. Huang and X. Duan, *Angew. Chem., Int. Ed.*, 2010, 49, 2865.
18. Q. Liu, M. Chen, Y. Sun, G. Chen, T. Yang, Y. Gao, X. Zhang and F. Li, *Biomaterials*, 2011, 32, 8243.
19. Z. Q. Li and Y. Zhang, *Angew. Chem., Int. Ed.*, 2006, 45, 7732.
20. A. Gnach and A. Bednarkiewicz, *Nano Today*, 2012, 7, 532.
21. M. Han, X. Gao, J. Z. Su and S. Nie, *Nat. Biotechnol.*, 2001, 19, 631.
22. F. Yan, J. Li, J. Zhang, F. Liu and W. Yang, *J. Nanopart. Res.*, 2009, 11, 289.
23. E. Dzunuzovic, K. Jeremica and J. M. Nedeljkovic, *Eur. Polym. J.*, 2007, 43, 3719.
24. A. N. Generalova, S. V. Sizova, T. A. Zdobnova, M. M. Zarifullina, M. V. Artemyev, A. V. Baranov, V. A. Oleinikov, V. P. Zubov and S. M. Deyev, *Nanomedicine*, 2011, 6, 195.
25. W. Sheng, S. Kim, J. Lee, S. W. Kim, K. Jensen and M. G. Bawendi, *Langmuir*, 2006, 22, 3782.
26. S. Margel and E. Wiesel, *J. Polym. Sci., Polym. Chem. Ed.*, 1984, 22, 145.
27. A. N. Generalova, M. M. Zarifullina, E. V. Lankina, S. V. Sizova, M. V. Artemyev, V. P. Zubov and V. A. Oleinikov, *J. Colloid Interface Sci.*, 2011, 357, 265.
28. G. Chen, H. Qiu, P. N. Prasad and X. Chen, *Chem. Rev.*, 2014, 114, 5161.
29. N. Bogdan, F. Vetrone, G. A. Ozin and J. A. Capobianco, *Nano Lett.*, 2011, 11, 835.
30. F. Yan, J. Li, J. Zhang, F. Liu and W. Yang, *J. Nanopart. Res.*, 2009, 11, 289.
31. A. L. Willis, N. J. Turro and S. O'Brien, *Chem. Mater.*, 2005, 17, 5970.
32. *Reactivity, Mechanism and Structure in Polymer Chemistry*, ed. A. D. Jenkins and A. Ledwith, J. Wiley & Sons, New York, 1974, p. 645.
33. A. Ouasri, A. Rhandour, M. C. Dhamelincourt, P. Dhamelincourt and A. Mazzah, *Spectrochim. Acta*, 2002, 58, 2779.
34. R. M. Silverstein and F. X. Webster, in *Spectrometric Identification of Organic Compounds*, John Wiley & Sons, New York, 6th edn, 1998, p. 655.
35. A. Rembaum, M. Chang and J. Richards, *J. Polym. Sci., Polym. Chem. Ed.*, 1984, 22, 609.
36. S. Slomkowski, *Prog. Polym. Sci.*, 1998, 23, 815.
37. *Surfactants and Polymers in Aqueous Solution*, ed. K. Holmberg, B. Jonsson, B. Kronberg and B. Lindman, J. Wiley & Sons, New York, 2nd edn, 2002, p. 547.
38. S. Polowinski, in *Encyclopedia of Polymer Science and Technology*, J. Wiley & Sons, New York, 2003, p. 151.
39. G. D. Luker and K. E. Luker, *J. Nucl. Med.*, 2008, 49, 1.

Supplementary Electronic Information

Submicron Polyacrolein Particles in situ Embedded with Upconversion Nanoparticles for Bioassay

A.N. Generalova,^{a,b,d} I.K. Kochneva,^a E.V. Khaydukov,^b V.A. Semchishen,^b A.E. Guller,^{c,f} A.V. Nechaev,^e
A.B. Shekhter,^c V.P. Zubov,^{a,b} A.V. Zvyagin*^{d,f} and S.M. Deyev^{a,d}

^aM.M. Shemyakin & Yu.A. Ovchinnikov Institute of Bioorganic Chemistry of the Russian Academy of Sciences, 117997, Moscow, Russia

^bInstitute on Laser and Information Technologies of the Russian Academy of Sciences, 140700, Shatura, Russia

^cI.M. Sechenov First Moscow State Medical University, 119992, Moscow, Russia;

^dN.I. Lobachevsky Nizhny Novgorod State University, 603950, Nizhny Novgorod, Russia;

^eM.V. Lomonosov Moscow University of Fine Chemical Technology, 119571 Moscow, Russia

^fMQ Biofocus Research Centre, Macquarie University, NSW 2109, Australia

*Corresponding author: Andrey Zvyagin, PhD, Associate Professor, e-mail: andrei.zvyagin@mq.edu.au

SUPPLEMENTARY INFORMATION 1

Surface tension of acrolein oligomers

Surface tension of acrolein oligomers was measured by using the instrument PAT1 (SINTERFACE Technologies, Germany) based on the drop profile analysis tensiometry. The main principle of this technique is to determine the surface tension of a liquid from the shape of a pendent drop.¹

Dry sample of oligomer was obtained from supernatant after centrifugation of polyacrolein dispersion with following desiccation. Pluronic F-168 is commonly used surfactant poly(ethylene oxide-propylene oxide), Mw 8.750, ratio 5/1, which was purchased from “Polyscience, Inc” (USA).

The surface tension of water was 71,2 mN/m. Concentration of oligomer as well as the concentration of pluronic F-168 in water was 10 mg/ml. After forming the drop of the solution via the syringe dosing system 5 min were required to ensure a stability of drop. We used water/air conditions. The experimental temperature was controlled at 22°C.

Figure S1 demonstrates that the acrolein oligomers have weak effect on the surface tension at the water/air interface (decreases to 60 mN/m) in comparison with pluronic F-168.

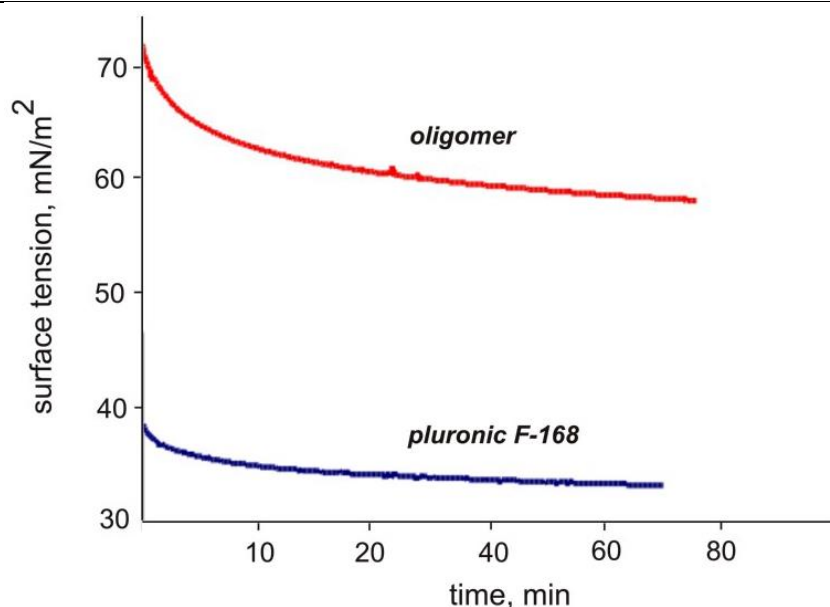


Figure S1. Dynamic surface tension of acrolein oligomers and pluronic F-168.

Supplementary Reference 1

1. A.V. Makievski, R. Miller, G. Czichocki and V.B. Fainerman, *Colloids Surfaces A*, 1998, 133, 313S.

SUPPLEMENTARY INFORMATION 2

MTT assay for evaluation of polyacrolein particle biocompatibility

To evaluate cytotoxicity of polyacrolein particles embedded with UCNP (PA-UCNPs) standard colorimetric MTT assay has been performed, as described in1 with minor modifications. The spontaneously immortalized human keratinocytes of HaCaT cell line were cultured under standard conditions (37° C, humidified, 5% CO₂: 95% air) on Dulbecco's Modification of Eagles Medium (DMEM/F12 medium, #11960044, Gibco, and #21765029, Gibco) containing 10 % FetalClone III serum (#SH3010903 Thermo Sci Hyclone) and 20 mg/l gentamicin. Cells were cultured until they reached a confluence of 80–90% and then trypsinized. Approximately 50,000 HaCaT keratinocytes per well were seeded onto 96-well plates. 25 µl of PA-UCNPs or UCNP-TMAH were diluted in 75 µl of culture media, sonicated and then added to the wells for the next 24 h or 120 h incubation. Cells incubated with the 100 µl of the culture medium were used as a control.

After incubation for 24 or 120 h, the medium with the particles as well as control growth medium were removed, then the cultures were washed triple with PBS, and, finally, the 3-[4,5dimethylthiazol-2-yl]-2,5-diphenyltetrazolium-bromide (MTT) reagent (Sigma-Aldrich) in cell culture medium (100 µl) was added to each well and incubated at 37 °C for 4 h to allow precipitation of insoluble purple formazan crystals by the action of mitochondrial succinate dehydrogenase of the viable cells. Then the supernatant was carefully collected and 100 µL of dimethyl sulfoxide was added to each well and left for 10 min in

CHAPTER 5

dark at room temperature. The absorbance of the resulted dye solution was evaluated in comparison with the control culture by measuring the optical density at 540 nm by a multiwell reader UNIPLAN (Pikon Ltd, Russia). Since the absorbance was proportional to the viable cell number, and survival value was calculated, as the percentage of the staining values normalized to that of the control cultures.

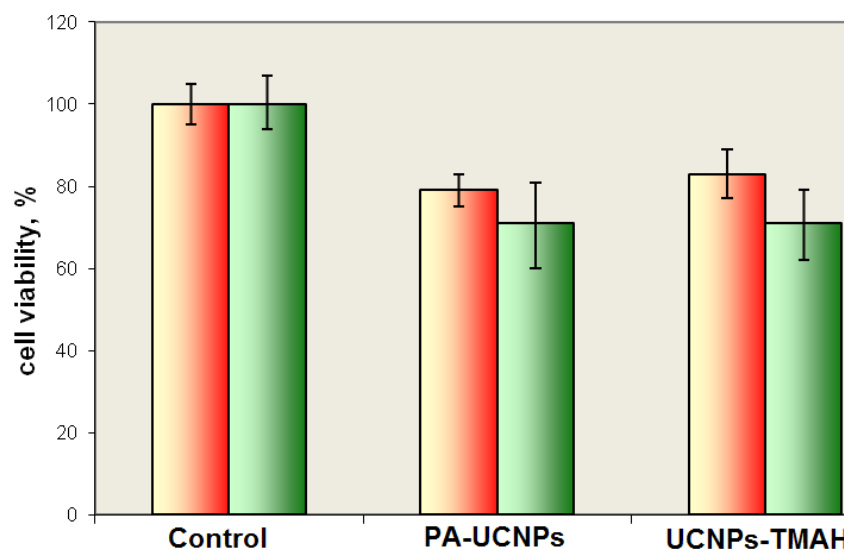


Figure S2. Mean viability (%) of human keratinocytes HaCaT co-cultured with polyacrolein particles (PA-UCNPs) and UCNPs modified with TMAH (UCNPs-TMAH) materials for 24 h (red bars) or 120 h (green bars).

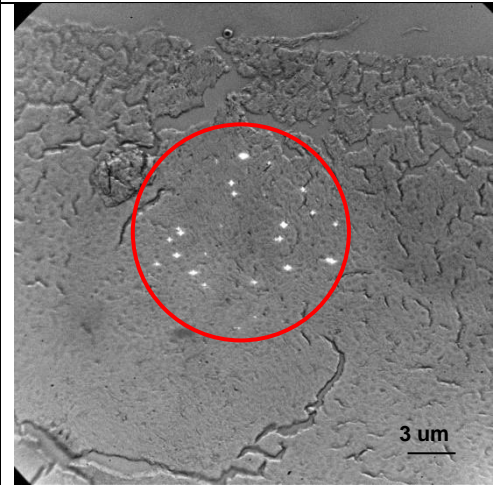
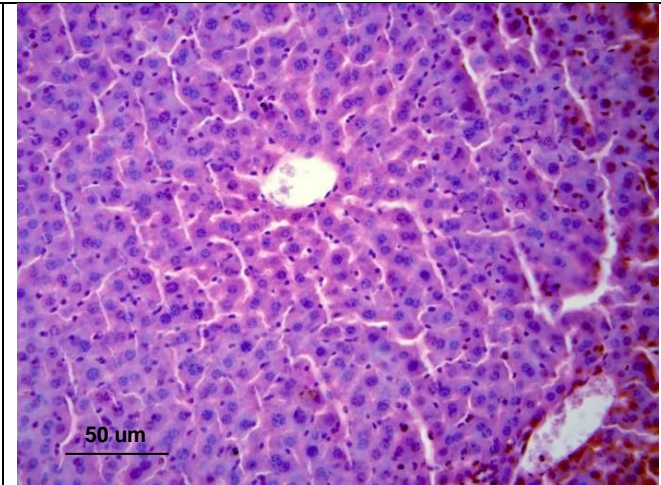
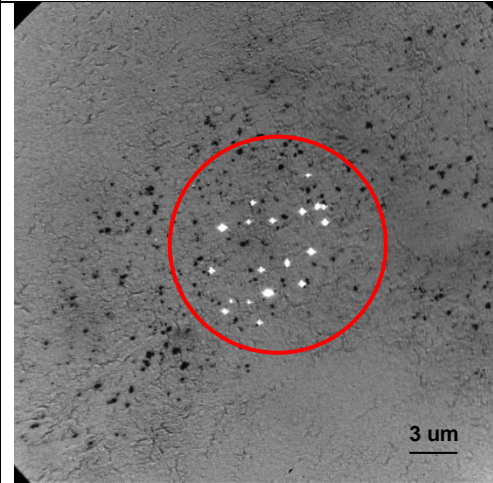
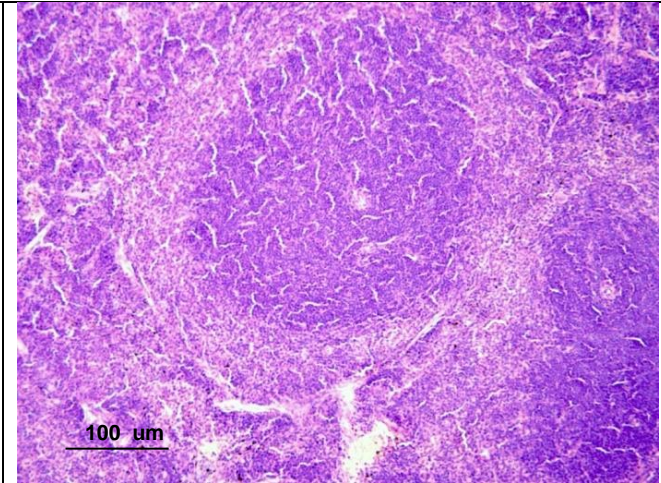
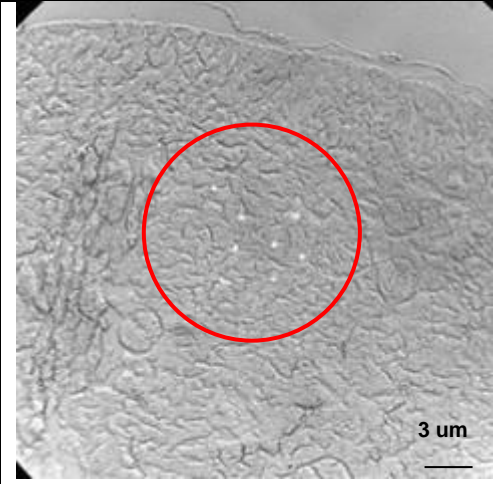
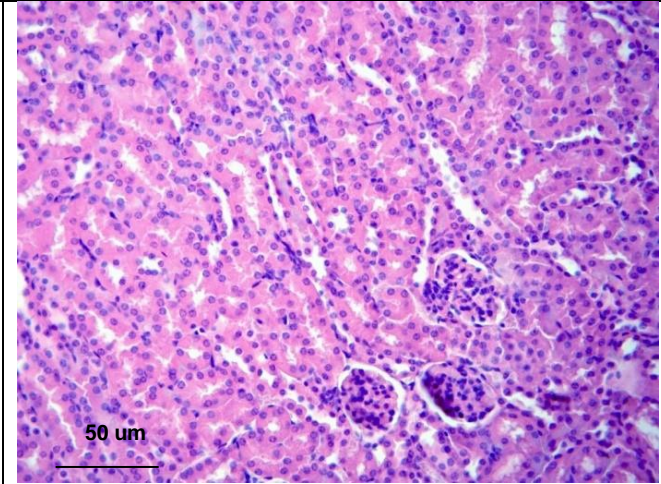
The exposure of HaCaT keratinocytes to PA-UCNPs caused, in average, 20% or 30% reduction of cell viability after 24 and 120 hours of incubation, respectively, as benchmarked against that of the control. The innate cytotoxicity of UCNPs hydrophilized with TMAH was also at the same levels, implying no significant changes in cell viability induced by embedding of these type of nanocrystals into the polymer particles.

Supplementary Reference 2

1. Mosmann T., J. Immunol Methods, 1983, 65, 55-63.

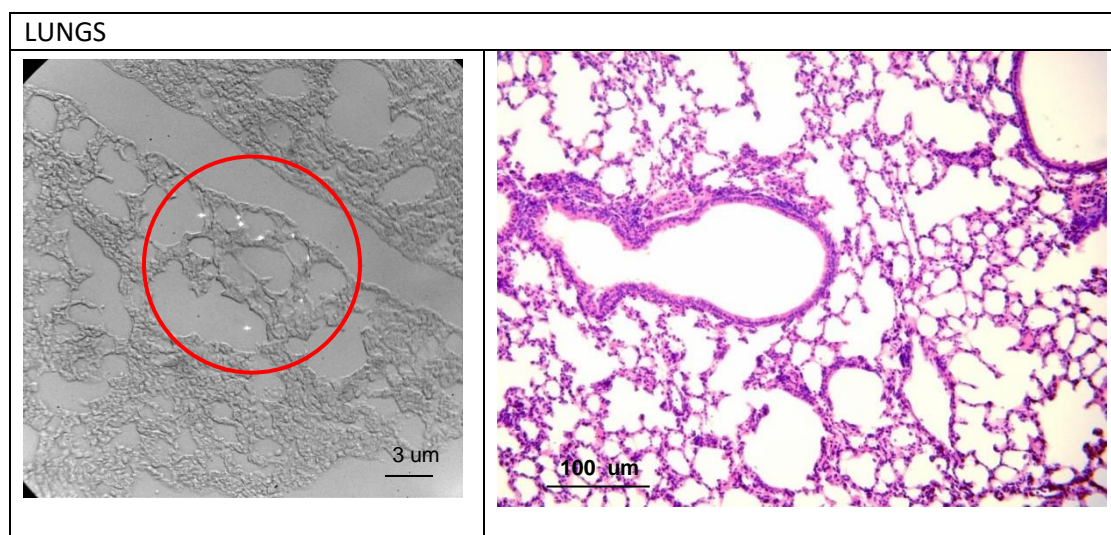
CHAPTER 5

Table S2. Epi-luminescent microscopy and histological examination of organ tissue slices

Epi-luminescent microscopy	Histological examination
LIVER	
	
SPLEEN	
	
KIDNEYS	
	

CHAPTER 5

Table S2. Epi-luminescent microscopy and histological examination of organ tissue slices (continue).



Note: red circle shows the field of microscope view.

Acellular organ scaffolds for tumor tissue engineering

6.1. Introduction

This chapter is focused on the first stage of the development of organ-specific 3D engineered tissue models, such as preparation of the scaffolds. Currently the greater part of the available scaffold-based *in vitro* 3D cell cultures are grown on the synthetic or natural surrogates of the natural extracellular matrix. This include various hydrogels and solid scaffolds obtained by different fabrication approaches like gelation, electrospinning, phase separation and rapid prototyping. Despite the numerous benefits, there is a significant limitation related to use of these biomaterials such as limited cell adhesion and viability on the artificial solid scaffolds and abnormal cellular behaviour in hydrogels (for the details see Chapter 3, section 3.2.1).

The alternative approach relies on use of decellularized (DCL) tissues and organs. This methodology, well-recognized in tissue engineering for regenerative medicine purposes for good biocompatibility and the cell guiding potential, just enter the field of *in vitro* 3D culture and modelling of normal and diseased tissues and organs for the research applications. The principal advantages of the DCL scaffolds are the reproduction of the major traits of the composition and architecture of the natural tissue- or organ-specific ECM, feasibility of implantation of the *ex vivo* grown tissue engineering constructs (TECs) and wide potential to use the TECs for drug development and testing, nanoresearch and general biomedical studies.

There are two ways of preparation of the DCL scaffolds, which are classified by the method of delivery of the decellularizing agent, the immersion and the perfusion, respectively. Immersion DCL implies destroying and removal of the cells from various tissues by submerging of the tissue fragments in the decellularizing solutions. The effect may be enhanced by shaking and other types of physical actions, however, the diffusion of the DCL agent through the processed tissue remains the main mechanism of this procedure. As a result the immersion DCL is mainly applied to the small volumes of the tissues. However, this method is very simple and affordable. On the other hand, the perfusion DCL is based on injection of the DCL solutions into the large blood vessels of whole organs with following perfusion. In this case the reagent is efficiently delivered even to the distant parts in depth of the tissue by the capillary networks. Whole-organ DCL allows to preserve the natural organ-specific ECM architecture as well as its composition. The most important limitation of this method is its applicability

only to certain types of organs (mainly heart, liver, pancreas, kidneys and lungs) and the requirement for absolute intactness of the vasculature, which is usually a practical problem as even a small accident cut results in discarding of the organ.

In this chapter we report a new technique of whole-organ immersion DCL, which shares the simplicity and universality of the immersion method and the advantages of the perfusion scheme, while avoiding the limitations of the last one. The efficiency of the whole-organ DCL performed by different protocols were compared. Then, the acellular organ-specific scaffolds (AOSS) were prepared by cutting of the DCL whole organs into small-size fragments. This allowed to obtain multiple organ-specific DCL solid scaffolds for further research, including high-throughput assays. Next, we tested the biocompatibility of the kidney-derived AOSS by seeding them with normal and cancer linear cells and *in vitro* culture of the TECs during four days with subsequent series of assays, performed to demonstrate several aspects of the interactions of the cells with the scaffolds. The results of this study are included into the paper III “Acellular organ scaffolds for tumor tissue engineering” published in *SPIE Proceedings* and provide a base for the next stages of the research presented in this PhD thesis.

6.2. The author’s contribution to the paper III

The PhD candidate (Anna Guller) is the first author of this paper. She performed all the preliminary data analysis, developed the concept of the whole study, experimental design and particular protocols of the DCL, performed surgery, macroscopic and histopathological analysis and wrote the manuscript. Ms. Inna Trusova and Dr. Elena Petersen carried out the main part of the cell culture experiments and participated in the development and execution of the DCL procedures. Ms. Alexander Kurkov took part in the histological studies and preparation of the figures. Prof. Anatoly Shekhter conceptualized the experimental applications of the DCL scaffolds, helped to analyse the histological data and edited the manuscript. Prof. Qian Yi advised the team with regard of the optimal DCL diffusion and perfusion conditions and revised the manuscript. A./Prof. Andrei Zvyagin performed the general supervision and coordination of the project, discussed and helped to analyse the results and edited the manuscript. All the co-authors revised and approved the manuscript.

6.3. Full paper III

Acellular organ scaffolds for tumor tissue engineering

Anna Guller^{*a, b, d}, Inna Trusova^c, Elena Petersen^c, Anatoly Shekhter^b, Alexander Kurkov^b, Yi Qian^d, Andrei Zvyagin^{a, e}

^aBiofocus Research Centre, Macquarie University, 2109, New South Wales, Australia; ^bSechenov First Moscow State Medical University, 8 Trubetskaya street, Moscow, 11992, Russia; ^cMoscow Institute of Physics and Technology, 9 Institutskiy per., Dolgoprudny, Moscow Region, 141700, Russia; ^dFaculty of Medicine and Health Science, Macquarie University, 2109, New South Wales, Australia; ^eNizhny Novgorod State University, Russia.

ABSTRACT

Rationale: Tissue engineering (TE) is an emerging alternative approach to create models of human malignant tumors for experimental oncology, personalized medicine and drug discovery studies. Being the bottom-up strategy, TE provides an opportunity to control and explore the role of every component of the model system, including cellular populations, supportive scaffolds and signalling molecules.

Objectives: As an initial step to create a new *ex vivo* TE model of cancer, we optimized protocols to obtain organ-specific acellular matrices and evaluated their potential as TE scaffolds for culture of normal and tumor cells.

Methods and results: Effective decellularization of animals' kidneys, ureter, lungs, heart, and liver has been achieved by detergent-based processing. The obtained scaffolds demonstrated biocompatibility and growth-supporting potential in combination with normal (Vero, MDCK) and tumor cell lines (C26, B16). Acellular scaffolds and TE constructs have been characterized and compared with morphological methods.

Conclusions: The proposed methodology allows creation of sustainable 3D tumor TE constructs to explore the role of organ-specific cell-matrix interaction in tumorigenesis.

Keywords: tumor, tissue engineering, scaffold, decellularization, 3D cell culture *in vitro*.

1. INTRODUCTION

Recent advances in 3D cell and tissue culture emphasize the role of spatial microenvironment cues in the development of malignant tumors. In particular, this means that the commonly assumed understanding of tumor behaviour mechanisms and pharmacological screens for anti-tumor drugs verified on conventional 2D substrates could be misleading. Indeed, the lack of progress in a 5-year survival rate for the most spread types of cancer during the recent 30 years¹ as well as current 95% chances of falls in clinical trials of anti-neoplastic medicines² indicate the growing demand of biomimetic tumor models.

* E-mail: anna.guller@mq.edu.au

Tissue engineering, being initially a part of regenerative medicine focused on reconstruction of healthy tissues and organs for reconstructive surgery, now attracts great attention of the experimental oncologists as a very promising approach to create a bottom-up models of various types of cancer to dissect the intrinsic mechanisms involved into growth, progression, invasion and metastasis³⁻⁹. Tissue engineering constructs of tumors include tumor cells, 3-dimensional scaffold and a “3rd components” (other cell types, signalling molecules, physical factors etc.), with the intention to simulate tumor development and behaviour in dependence of the constituents of the microenvironment.

The biomimetic models of human diseases like cancer are in high demand for the development of novel diagnostics and therapy methods. These bioartificial tissues are ideal models for experimental science: 1) they demonstrate far more realistic physiological responses than Petri-dish-cultured cells, offering unprecedented reproducibility and outcomes acceptable to industry and regulators; 2) they do not require ethical approvals, and reduce animal testing and costs.

The purpose of this study was to evaluate feasibility of different approaches to development of acellular organ-specific scaffolds for tissue engineering of malignant tumors.

2. MATERIALS AND METHODS

2.1. Surgery and tissue collection

The study was performed in accordance with the ethics committee protocol for animal experiments of I.M. Sechenov First Moscow State Medical University. Two Chinchilla male rabbits of $3,000 \pm 120$ g, being originally used for control observations in an unrelated surgical experiment, were anesthetized by injection of 40 mg/kg ketamine and 10 mg/kg xylazine intramuscularly (i/m) as a single dose and underwent bilateral nephrectomy with circumferential exposure and preservation of the adjacent parts of renal artery, renal vein and ureter (Fig. 1a). The excess perinephric fat was removed, and perihilum tissues were ligated. Intravenous catheter (26G, Flexicath, Apexmed, Netherlands) was inserted into the renal artery and secured with 6/0 Prolene suture to allow perfusion (Fig. 1 b). After that animals were euthanized by overdose i/m injection of ketamine. Prepared kidneys with inserted cannulas were extirpated, and the catheter was connected to a perfusion contour. Whole organ dissection of liver, lungs, heart and trachea was performed postmortem during 1 hour after the animal's death. The organs were immediately placed into cold sterile phosphate-buffered saline (PBS) (Gibco), containing 50 units/mL of sodium heparin (JSC “Synthet”, Russia) until further operations (about 30 min). All the surgical procedures were performed under aseptic conditions.

2.2. Decellularization

The protocol A of whole kidney perfusion decellularization was adapted from¹⁰. Briefly, the cannula previously inserted into the renal artery of a rabbit's left kidney was connected to a perfusion contour of ORCA Bioreactor complex (Harvard Apparatus, USA) (Fig. 1 c), and the kidney was freely placed

onto the bottom of the bioreactor organ chamber to allow continuous exposure to working solutions in closed fluid circulation setup (Fig. 1 d). The perfusion was initiated with PBS (Gibco), containing 50 units/mL of sodium heparin (JSC “Synthetiz”, Russia) for 90 min. Then 0.1% sodium dodecyl sulphate (SDS) dissolved in sterile PBS has been perfused through native kidney vasculature for 16 hours with periodic changes for new portions of the medium at 1, 3, 6 and 12 hours of processing. Afterward, 1% SDS in PBS has been delivered to the organ during next 4 days with total replacement of the washing solution for fresh portions at every 6 hours. Finally kidneys of rabbits were perfused with 6 portions of sterile PBS (Gibco), containing 1% of antibiotic-antimycotic solution (Sigma Aldrich) and 2 mg/ml of ciprofloxacin for 2 days. The flow rate of perfusion was set at 30 ml/min for the whole experiment.

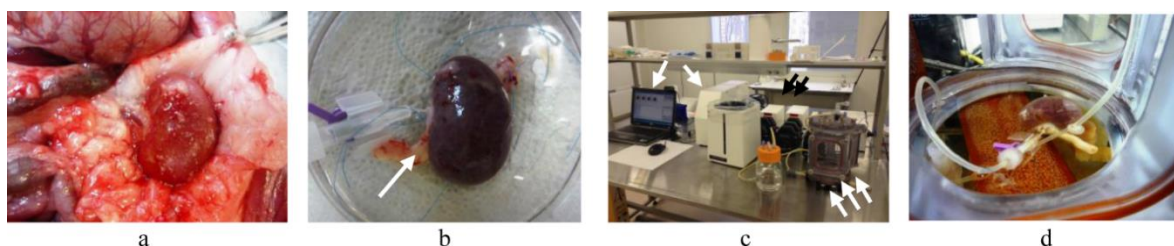
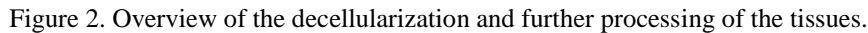


Figure 1. Preparation and start of decellularization of a rabbit left kidney (protocol A): (a) surgical approach; (b) cannula is secured in renal artery; arrow shows the ureter; (c) a view of ORCA bioreactor: a block of controller (single white arrows), a block of peristaltic pumps (double black arrows), and the organ chamber (triple white arrows); (d) a kidney in the organ chamber, the vasculature is connected to the perfusion contour.

The protocol B of immersion-agitation decellularization was applied to slices of rabbit right kidneys, fragments of livers, and to whole lungs, hearts and tracheas. Right kidneys first were perfused with heparinised PBS by a syringe. Fibrous capsules of right kidneys were carefully removed and the organs were cut transversely for disc slices of 3-6 mm in thickness. Each slice was immersed in an individual vial with 0.1% SDS solution in PBS. Livers were sectioned for fragments of the same thickness. Other dissected (but not cannulated) organs, including lungs, tracheas and hearts were transferred as a whole from heparinised PBS solution into individual containers with 0.1% SDS in PBS solution for further decellularization. The volume of the washing medium was approximately 10-20 times bigger than the volume of the samples. The organ containers were placed on digital speed control orbital shaker (OS-100, Joyfay International, China) and agitated at 120 revolutions per minute (rpm) for 12 hours. Then the concentration of SDS in the washing medium has been increased up to 1%, while the agitation rate was reduced to 90 rpm. Decellularization medium has been changed for fresh portions every 24 h until tissues became semi-transparent or transparent (3-6 days, depending on the organ). Following finishing of decellularization the organs and kidney slices were washed with sterile PBS (Gibco), containing 1% of antibiotic-antimycotic solution (Sigma Aldrich) and 2 mg/ml of ciprofloxacin for 2 days.

All the manipulations were performed at room temperature. During the decellularization the organs/organ sections were photographed and sampled for morphological study. The scheme of the decellularization protocols and distribution of organ samples is depicted at Figure 2.



Preparation of scaffolds for cell seeding. After finishing of decellularization and washing, the small fragments (approximately 3×5 mm) of decellularized whole organs and the same size sectors of right kidney and liver slices were cut by a scalpel blade and put into 12-well flat bottom tissue culture plates (Corning, USA). One milliliter of sterile PBS with 1% antibiotic-antimycotic solution (Sigma Aldrich) was added to every well, and after that the decellularized tissue fragments were sterilized by ultraviolet light in a tissue culture hood for 3 hours. Then the tissues were aseptically transferred into sterile 50 ml tubes (Falcon) filled with DMEM/F12 culture medium supplemented with 10% fetal bovine serum, 2 mM L-glutamine, 100 U/ml penicillin/streptomycin, and 2 mg/ml ciprofloxacin and conditioned in a tissue culture incubator on a vertical rotary stage at 37 °C/ 6 rpm for 24 hours. After that the tissue fragments were placed into the individual wells of 12-well plate for further cell seeding. To define the quality of decellularization, the scaffolds were stained for DNA with Hoechst 33342 (1.0 µg/mL), a fluorescent nuclear dye.

164

Cell seeding and culture of tissue engineering constructs. Every scaffold prepared as described above was seeded with approximately 1×10^5 cells in 30 μ l of DMEM/F12 supplemented with 10% fetal bovine serum, 2 mM L-glutamine, 100 U/ml penicillin/streptomycin. The cells were allowed to attach to the substrates for 1 hour in tissue culture incubator and then 2 ml of the culture medium was added to each well. Control scaffolds were left without cell seeding. Following that the tissue engineering constructs were cultured under standard conditions for 4 days. Growth medium was carefully changed once during this period without disturbing the constructs. A day after seeding and on a reference day 4 the constructs were imaged with phase contrast and fluorescence microscopy (for the last the samples were stained with Hoechst 33342 for DNA). After 4 days, control scaffolds and tissue engineering constructs were collected and fixed in 10% neutral buffered formalin for histological examination, in 70% ethanol for scanning electron microscopy and 2.5% buffered glutaraldehyde (at 4 °C) for semi-thin sectioning.

2.4. Morphology

2.4.1. Histological study

Formalin-fixed tissue samples were processed through alcohols of increasing concentrations and embedded in paraffin. Microtome slices of 5-6 μ m in thickness were stained with hematoxylin and eosin (H&E), toluidine blue (for acid glycosaminoglycans), picrofuchsin by Van-Gieson (for collagen). The samples fixed in glutaraldehyde were post-fixed with 1% OsO₄ in cacodylate buffer for 1 h, dehydrated in graded alcohols, embedded in epoxy resin and cut using an ultra-microtome (LKB, Sweden) into semi-thin sections of 1- μ m thickness, and then stained with methylene blue (azure II) basic fuchsin three chrome method (MAFT). Stained slides were mounted with Bio Mount HM mounting medium (Bio-Optica, Italy) and covered with cover slips. The H&E-stained and semi-thin histological preparations were examined by an upright light microscope Olympus BX51 using dry-air (4 \times /NA0.10; 10 \times /NA0.25; 20 \times /NA0.40) and oil-immersion (100 \times /NA1.25 oil) objectives (Olympus Optical, Japan) and photographed with a digital video camera SDU-252 (2048 \times 1536 , “Spetstelechnika”, Russia).

2.4.2. Scanning electron microscopy (SEM)

The samples fixed in 70% ethanol were further dehydrated in 70-100% alcohols and underwent critical point drying in Emitech K850 Critical Point Dryer (Emitech Ltd., UK). Afterwards, the samples were mounted on stabs with conductive carbon/graphite paint (ProSciTech, Australia) and coated with gold using an Emitech K550 gold sputter coater (Emitech Ltd., UK). Electron microscope images were taken using a JEOL JSM- 6480 LA under accelerating voltage 5 kV, work distance 20 mm and size point 30 by the secondary electron imaging mode.

3. RESULTS AND DISCUSSION

3.1. Macroscopic observations

Significant macroscopic changes of organs have been revealed during the process of decellularization (Fig. 3). Despite the differences of rate of decellularization of the studied organs, progressive loss of natural color up to total discoloration, as well as various degree of volume reduction and increase of tissue transparency were visible in all the samples, as it was observed by many other researches¹¹⁻¹⁴. Dense organs like heart and trachea show the slowest rate of these modifications.

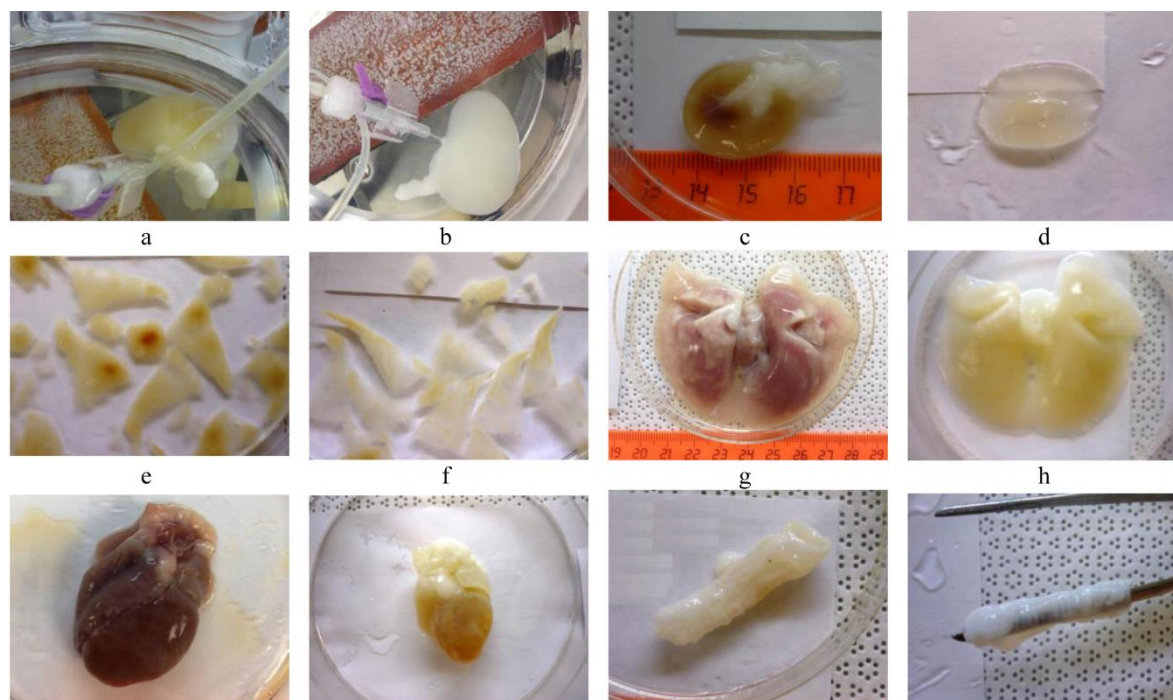


Figure 3. Effect of decellularization by protocols A (a, b) and B (c-l) on external appearance of organs and organ sections at certain time points of processing: (a, b) – left kidney, 12 h (a) and 3 days (b); (c, d) – a section of right kidney, 15 h (c) and 2 days (d); (e, f) – sections of liver, 15 h (e) and 24 h (f); (g, h) - whole lungs, 15 h (g) and 6 days (h); (i, j) - whole heart, 15 h and 6 days (j); (k, l) – whole trachea, 15 h (k) and 6 days (l). Note loss of natural color and increase of transparency.

In the samples of left kidneys processed by perfusion decellularization (the protocol A) the discoloration started from the hilum area and then spread to the rest part of the organ as marble-like pattern and later as diffuse semitransparency. The samples of whole lungs, processed by immersion-agitation (protocol B) demonstrated the spread of transparency from the outer margins to the central part of the organ. The same but less clear trend was notable in the samples of hearts and tracheas. The sections of liver and right kidneys became semitransparent faster than whole organs, but only the kidney matrix kept original shape of the slices, while the matrix of liver was significantly deformed and loosened.

3.2. Histological examination and SEM imaging of decellularized tissues

Histological examination and SEM imaging confirmed complete decellularization of kidney tissue by both studied protocols. The extracellular matrix of glomeruli as well as that of tubules generally preserved its spatial organization, but after immersion-agitation some deformation of tubules and flattening of the surfaces of glomeruli were visible (Fig. 4). Van-Gieson staining of decellularized kidneys signified that collagen carcass was not damaged, while toluidine blue staining indicated almost total loss of glycosaminoglycans. These observations are in accordance of the previously published results of detergent-based decellularization¹⁵.

Complete absence of cells as a result of immersion-agitation decellularization was also found in the samples of liver, lungs (including bronchial cartilage), ureters and renal arterial walls. In deep parts of heart tissue some basophilic material was visible implying the residual nuclear material, and in hyaline cartilage of trachea the areas containing well-shaped cell nuclei were revealed (Fig. 5). In contrast to notable decrease of metachromatic staining by toluidine blue indicating decrease in acid glycosaminoglycans, the spatial architecture and collagen content of the organ-specific extracellular matrix were kept in all the cases.

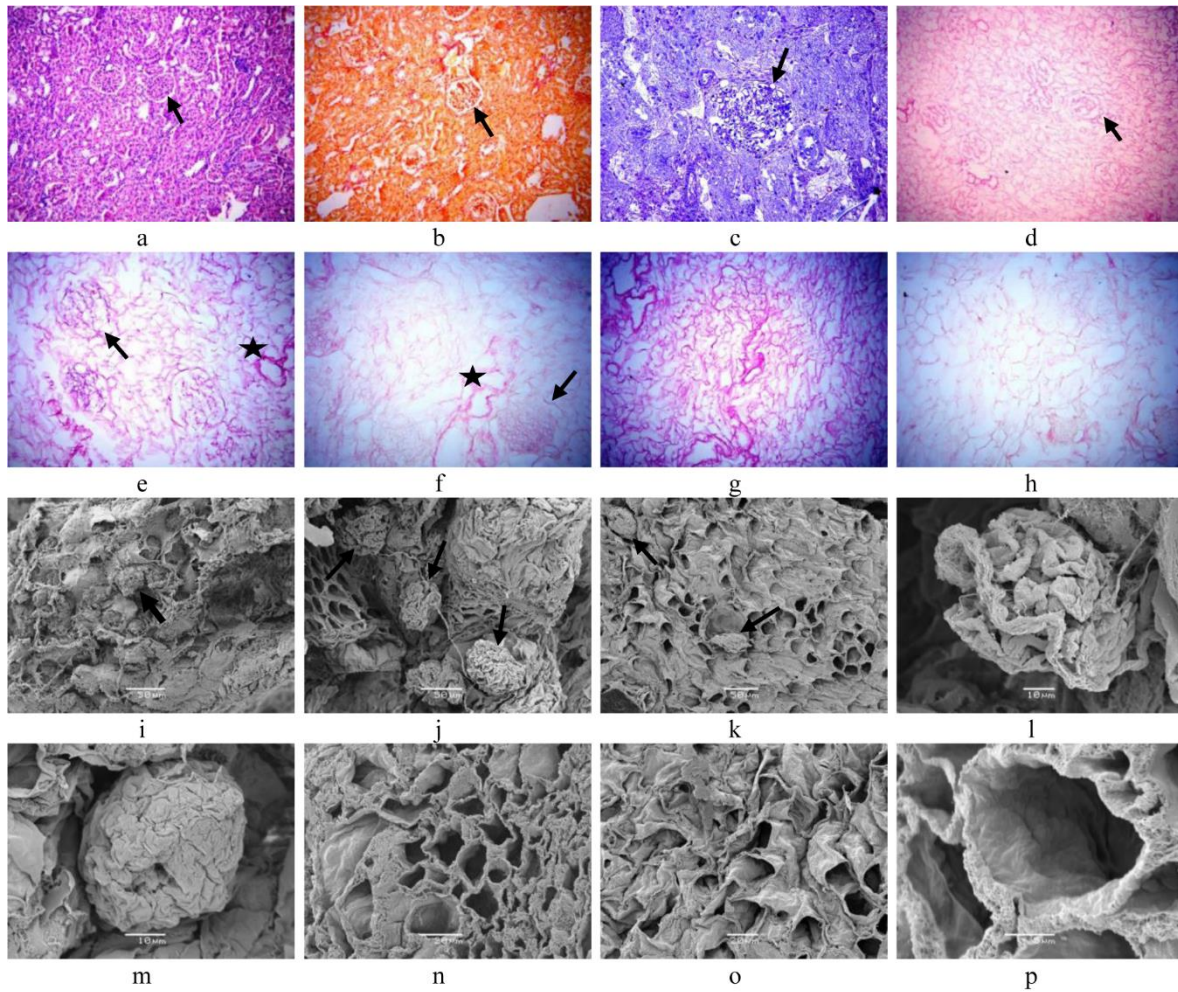


Figure 4. Effect of decellularization by the protocols A (d, e, g, j, l, and n) and B (f, h, k, m, o and p) on the kidney tissue: (a, b, c, i) – intact cortex of kidneys; note numerous glomeruli (arrows); (d-h) – histological images demonstrate absence of cells in kidney tissue after decellularization, well preserved stromal structure of glomeruli (arrows) and densification of perivascular matrix (stars) regardless the protocol; in addition, relative loosening of fibrous elements of stroma is visible in scaffolds treated by the protocol B, in comparison with the same components after the protocol A; (j-p) general stromal base of kidney cortex zone (j-m) with glomeruli (arrows) and medulla zone (n-p) is preserved after decellularization. The stromal structures after decellularization by the protocol B appear more flattened and deformed than after the protocol A treatment, but still preserve the key geometry features. Histological images, specimens stained with H&E (a, d-h), Van-Gieson's staining (b), c – semi-thin slice, MAFT. Original magnification: (a, b and d) - $\times 200$; (c, e-h) - $\times 400$. SEM images are presented at (i-p); scale bars: (i-k) – 50 μm ; (l, m) – 10 μm ; (n, o) – 20 μm ; (p) – 5 μm .

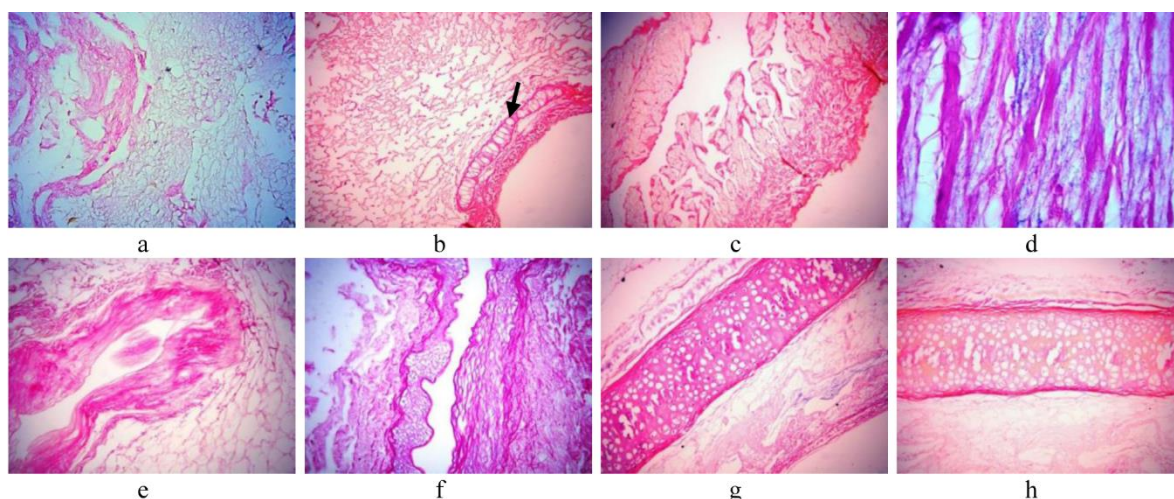


Figure 5. Effect of decellularization by the protocol B on the structure of (a) - liver sections; (b) – whole lungs; (c, d) whole heart (right atrium matrix is shown); (e) – ureter; (f) renal artery wall; (g, h) – whole trachea. Absence of any cellular material is notable in liver, lungs (including bronchial cartilage, arrow), ureter, and renal artery. Residual basophilic nuclear material is visible between fibrous bunds of myocardium (d) and numerous nuclei are revealed in trachea cartilage (g). Note also the well preserved fibrillary structure of collagen in perichondrium stained fuchsinophilic (h). Histological images, specimens stained with H&E (a, b, d-h) and Van-Gieson's stain (c, h). Original magnification: (a, f) - $\times 400$; (b, c, e-h) - $\times 200$; (d) - $\times 1000$.

3.3. Results of recellularization of acellular organ-specific scaffolds

All the types of developed acellular organ-specific scaffolds were successfully repopulated by Vero, MDCK, C26 and B16 cells. Effective cellular adhesion on the matrices was confirmed by phase contrast and fluorescence microscopy at 24 hours after seeding, indicating absence of contact cytotoxicity of all the scaffolds and acceptability of the studied protocols of decellularization for further development of 3D culture models. Normal kidney cells (Vero, MDCK), in general, demonstrated lower rate of growth, in comparison with the cells of cancer cell lines (C26 and B16).

Preliminary analysis of cellular distribution in 4-days tissue engineering constructs show differences in spreading and penetration depth between Vero, C26 and B16 cells, growing on kidney acellular scaffold obtained by perfusion decellularization (Fig. 6). The number of colon carcinoma C26 and melanoma B16 cells attached to the scaffold surfaces was higher, than in tissue engineering construct with normal Vero cells, which probably reflects the difference in rates of proliferation or/and motility between cancer and normal cells. In addition, colon cancer cells demonstrated strong preference to grow in folders, grooves and cavities (see Fig. 6, e-g), while melanoma cells were mainly found on and near relatively flat matrix surfaces and along the decellularized vascular conduits. At the same time, probably to the differences in diameters, the smaller Vero and B16 cells penetrated narrow tubules on nephrons more deep and extensively, than C26 cells. The last were found on the internal surfaces of Bowman's membrane and on the loops of basal membranes of glomeruli. Interestingly, that many of C26 cells formed own matrix adhesions *de novo* as well as membrane blebbing (see Fig. 6 k). Membrane blebs

are temporary plasma membrane protrusions, which are considered as functional response of a cell to reduced substrate adhesion¹⁶. This, in turn, emphasizes that acellular organ-specific scaffold provides a special type of 3D microenvironment, in contrast to conventional monolayer culture, where cells are gravity force-flattened and their contact substrate-contacting surface is much higher¹⁷. The observed blebbing, especially in single-sitting cells, can also be indirect evidence in favor of initiation of epithelial-mesenchymal transition, the key process for cancer invasion and metastasis¹⁸.

The structure of matrices during the observation period has not been changed significantly, however, it appeared more blurry on the day 4, than initially. This may be a result of direct physical or chemical transformation of the scaffolds under the culture conditions as well as the effect of cell-mediated matrix remodeling implying cancer niche formation¹⁹. Further studies are needed to understand this mechanism better.

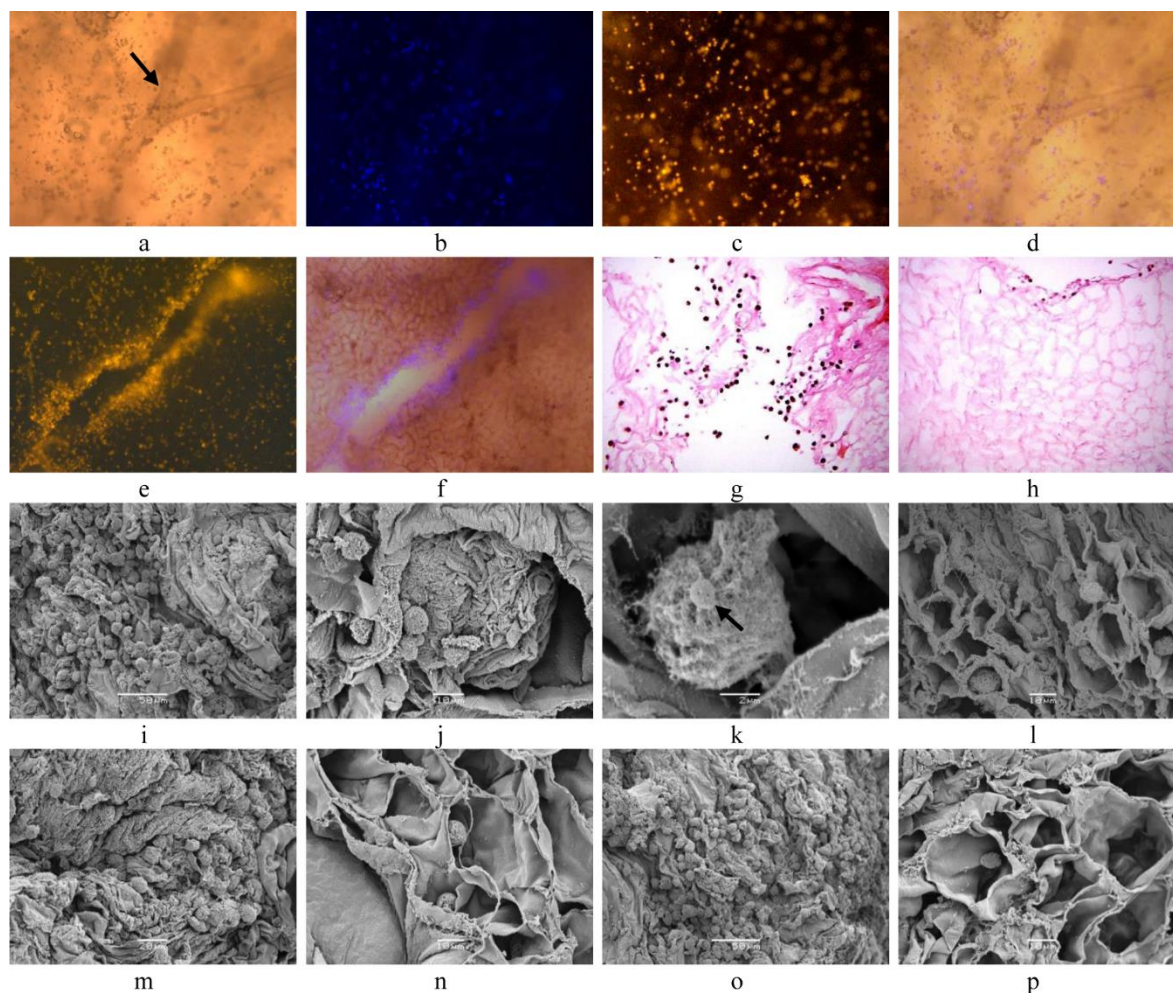


Figure 6. Recellularization of acellular kidney organ-specific matrix obtained by the protocol A: (a-d) - tissue engineering construct with Vero cells, $\times 10$; phase contrast image demonstrating preservation of native vasculature (arrow) in the scaffold (a); Hoechst staining of nuclei (b), membrane tracer staining (c), overlay of phase contrast and Hoechst stained images (d); (e, f) – tissue engineering construct with C26 cells, $\times 10$; membrane tracer staining of cells reveals dense cellular cluster, forming along a scaffold's groove (e), overlay of phase contrast and Hoechst

stained image of the same area shows preservation of matrix of kidney tubules and some penetration of the cells into the volume of the scaffold (f); (g, h) - histological H&E stained images of tissue engineering constructs with C26 (g) and B16 (h) cells; note the difference in cellular numbers and distribution between the constructs depending on the cell types; original magnification $\times 400$; (i-p) – SEM images of tissue engineering constructs with C26 (i-l), Vero (m, n) and B16 (o, p) cells. Cancer cells C26 and B16 demonstrate higher rate of the matrix surface repopulation (i, o), than normal kidney cells Vero (m). Penetration into renal tubules is relatively limited for large C26 cells (l), in contrast to Vero (n) and B16 (p) cells. Attachment of C26 cells to the Bowman's capsule matrix and a glomerulus surface (j); note blebbing of cell membrane (arrow) of a C26 cell and formation of cell-matrix adhesions (k). Scale bars in SEM images: (i, o) – 50 μm ; (j, l, n, and p) – 10 μm ; (k) – 2 μm ; (m) – 20 μm .

4. CONCLUSION

This study was purposed to analyze the methodological aspects, possibilities and limitations of three-dimensional tumor modelling on acellular organ-specific scaffolds obtained by using of two strategies of tissue decellularization.

Acellular organ-specific scaffolds of kidneys were prepared in parallel by perfusion of the SDS solution through native organ vasculature and by immersion-agitation at 90 -120 rpm in the same detergent. Our data indicate that the method of delivery for decellularization agent can be neglected if the further use of whole-organ scaffold with internal vascular conduits is not expected. It seems, therefore, warranted to conclude that the immersion-agitation method of decellularization can be considered as a relatively high throughput alternative for development of organ-specific natural scaffolds for tissue engineering. However, a second conclusion that can be derived from the present investigation is that immersion-agitation decellularization can mechanically damage the spatial organization of matrix if applied to dissected fragments of organs instead of whole organs. At the same time we did not note any effect of this deformation on viability and adhesion of cells seeded on the scaffolds resulted from perfusion or immersion-agitation during the period of observation.

The current work has also shown the possibility to get whole-organ scaffolds from rabbit lungs and heart without perfusion, but by immersion-agitation method. This result and the procedure, to our knowledge, have not been published yet and indicate that complete or almost complete decellularization of such a big organs may be reached by a simplified approach of immersion-agitation, instead of perfusion in a bioreactor. In particular, this shows a possibility to use discarded human and animal organs, lacking of well-preserved vascular trees, for preparation of complex tissue engineering scaffolds.

Analysis of the results of recellularization of acellular organ-specific scaffolds obtained from rabbit organs confirms biocompatibility of the matrices, absence of contact cytotoxicity as it follows from successful 4-days culture of tissue engineering constructs. Four cell lines, including two normal kidney types (Vero and MDCK) and two tumor ones (C26 and B16) were integrated into the constructs with

kidney, lungs, liver, trachea and heart matrices. Some signs of specific features of cancer behavior in colonization of matrices were revealed, like growth rate, preferable colonization sites, membrane blebbing associated with adhesions formation.

From the foregoing it seems reasonable to conclude that acellular organ-specific scaffolds can be produced from various types of organs and used for tumor tissue engineering. The immersion-agitation method of whole-organ decellularization can be considered a sustainable alternative to the perfusion decellularization for the purposes of 3D cell culture. The proposed approach may be used to develop novel biomimetic models to evaluate the effects of natural organ-specific microenvironment on cancer growth and progression.

ACKNOWLEDGEMENTS

Authors thank DRs Nicole Vella and Debra Birch (Macquarie University Microscopy Unit, Faculty of Science and Engineering) for their help with SEM, and Dr. Alexander Luzin (Sechenov First Moscow Medical University) for his guidance regarding the animal care procedures. The study was partially supported by the Russian Foundation for Basic Research (grants No 13-02-01363 and 13-04-12075) and by Grant of the Government of the Russian Federation for state support for scientific research under the guidance of leading scientists in Russian educational institutions of higher professional education, scientific establishments of the National Academy of Sciences and state research centers of the Russian Federation (Megagrant), No. 14.Z50.31.0022.

REFERENCES

1. Williams, S. A., Anderson, W. C., Santaguida, M. T., et al., "Patient-derived xenografts, the cancer stem cell paradigm, and cancer pathobiology in the 21st century," *Lab Invest*, 93(9), 970-82 (2013).
2. Hickman, J. A., Graeser, R., de Hoogt, R., et al., "Three-dimensional models of cancer for pharmacology and cancer cell biology: capturing tumor complexity *in vitro/ex vivo*," *Biotechnol J*, 9(9), 1115-28 (2014).
3. Ingber, D. E., "Can cancer be reversed by engineering the tumor microenvironment?," *Seminars in Cancer Biology*, 18(5), 356-364 (2008).
4. Hutmacher, D. W., Horch, R. E., Loessner, D., et al., "Translating tissue engineering technology platforms into cancer research," *Journal of cellular and molecular medicine*, 13(8a), 1417-1427 (2009).
5. Burdett, E., Kasper, F. K., Mikos, A. G., et al., "Engineering tumors: a tissue engineering perspective in cancer biology," *Tissue Eng Part B Rev*, 16(3), 351-9 (2010).
6. Ricci, C., Moroni, L., and Danti, S., "Cancer tissue engineering - new perspectives in understanding the biology of solid tumours - a critical review," *OA Tissue Engineering*, 1(1), 4 (2013).
7. Fong, E. L., Santoro, M., Farach-Carson M. C., et al., "Tissue Engineering Perfusable Cancer Models," *Curr Opin Chem Eng*, 3, 112-117 (2014).
8. Gill, B. J. and West, J. L., "Modeling the tumor extracellular matrix: Tissue engineering tools repurposed towards new frontiers in cancer biology," *J Biomech*, 47(9), 1969-78 (2014).
9. Seib, F. P., Berry, J. E., Shiozawa, Y., et al., "Tissue engineering a surrogate niche for metastatic cancer cells," *Biomaterials*, 51, 313-9 (2015).

10. Song, J. J., Guyette, J. P., Gilpin, S. E., et al., "Regeneration and experimental orthotopic transplantation of a bioengineered kidney," *Nat Med*, 19(5), 646-51 (2013).
11. Park, K. M. and Woo, H. M., "Systemic Decellularization for Multi-organ Scaffolds in Rats," *Transplantation Proceedings*, 44(4), 1151-1154 (2012).
12. Badylak, S. F., Weiss, D. J., Caplan, A., et al., "Engineered whole organs and complex tissues," *Lancet*, 379(9819), 943-52 (2012).
13. Crapo, P. M., Gilbert, T. W. and Badylak, S. F., "An overview of tissue and whole organ decellularization processes," *Biomaterials*, 32(12), 3233-43 (2011).
14. Maghsoudlou, P., Georgiades, F., Tyraskis A., et al., "Preservation of micro-architecture and angiogenic potential in a pulmonary acellular matrix obtained using intermittent intra-tracheal flow of detergent enzymatic treatment," *Biomaterials*, 34(28), 6638-48 (2013).
15. Gilbert, T. W., Sellaro, T. L., and Badylak, S. F., "Decellularization of tissues and organs," *Biomaterials*, 27(19), 3675-83 (2006).
16. Fackler, O. T., and Grosse, R., "Cell motility through plasma membrane blebbing," *J Cell Biol*, 181(6), 879-84 (2008).
17. Baker, B. M. and Chen, C. S., "Deconstructing the third dimension: how 3D culture microenvironments alter cellular cues," *J Cell Sci*, 125(Pt 13), 3015-24 (2012).
18. Kimlin, L. C., Casagrande, G., and Virador, V. M., "*In vitro* three-dimensional (3D) models in cancer research: an update," *Mol Carcinog*, 52(3), 167-82 (2013).
19. Lu, P., Weaver, V. M. and Werb, Z., "The extracellular matrix: a dynamic niche in cancer progression," *J Cell Biol*, 196(4), 395-406 (2012).

Triple negative breast cancer metastasis to the liver: a tissue engineering model shows the invasion patterns and predicts the effects of free and nanoformulated drugs

7.1. Introduction

This PhD thesis aims to develop 3D *in vitro* culture and tissue engineering models of normal and diseased tissues and evaluate their feasibility for nanotheranostics research. This chapter includes a manuscript entitled “Triple negative breast cancer metastasis to the liver: a tissue engineering model shows the invasion patterns and predicts the effects of free and nanoformulated drugs” and prepared for submission to “Biomaterials” journal.

Firstly, this manuscript describes the original methodology developed in the course of this PhD project aiming at the development of a biomimetic 3D tissue engineering model of the early stages of metastatic colonization of the liver by breast cancer cells. The validation and evaluation of this model feasibility for drug testing and nanotheranostics research is also addressed. Briefly, experimental breast cancer tumors were cultured and maintained for 4 weeks *in vitro* by employing the tissue engineering methodology. Acellular organ-specific scaffolds (AOSS) of chick embryo livers were prepared following the modified immersion DCL technique reported in Chapter 6. These scaffolds were seeded with MDA-MB-231 cells to model aggressive human mammary carcinoma, known as triple-negative breast cancer (TNBC) and characterized by a strong mortal trend to metastasize to the liver. My colleagues and I found strikingly different patterns of the breast cancer metastatic colonization of different compartments of the liver, where the extracellular matrix was the key determinant. We also demonstrated the biological validity of the model by *in vivo* angiogenic assay in chick embryos.

Due to the TNBC insensitivity to main targeted anti-cancer drugs, the treatment is resorted to chemotherapy with concomitant side effects, where nanoformulated drugs can ameliorate the clinical outcomes. To this aim, our tumor tissue engineering model was employed to investigate drug uptake and cytotoxicity effects in the close-to-real model of the breast cancer hepatic metastases.

The manuscript of this chapter contains ample of supplementary material, detailing the tissue engineering methodology, synthesis and characterization of the relevant nanomaterials. The supplementary material contains also the results of our pilot study of feasibility of the simplified 3D *in*

vitro breast cancer models grafted on chick embryo chorioallantoic membrane for real-time bioimaging of UCNPs injected into the blood stream.

7.2. The author's contribution to the paper IV

The PhD candidate (Anna Guller) is the first author on this paper. She developed the core concept, designed all experiments, which involved animals, organs, scaffolds, cell cultures and tissue engineering procedures; analysed the data and drafted the manuscript. The 2nd author, Ms. Inga Kuschnerus, performed synthesis of nanoformulated Dox (AMS-6-Dox) and control experiments using pristine AMS-6. She contributed to the cytotoxicity experiments on 2D and 3D TNBC *in vitro* models and angiogenic tests, developed algorithms of the digital image analysis of cancer colonization depth and took part in the data interpretation.

Ms. Zahra Khabir performed most of the confocal microscopy study of Dox and AMS-6-Dox uptake in the *in vitro* models of TNBC. She took part in the tissue engineering procedures, performed characterization of AMS-6 nanoparticles and contributed to the data analysis.

Dr. Alfonso Garcia-Bennett designed and demonstrated the synthesis of AMS-6s, performed their characterization by TEM, XRD and TGA, analyzed the pore size distribution by nitrogen adsorption/desorption isotherms and DFT-modelling, and developed 3D computer model of the nanoparticles structure. He also commented and edited the manuscript.

Dr. Annemarie Nadort carried out mathematical modelling of the cellular population dynamics and the cytotoxicity data. She contributed to development and optimization of the experiments on the chick embryo model, carried out imaging of the nanoparticle biodistribution *in vivo*.

Ms. Liuen Liang was involved in the tissue engineering procedures and helped adapting the uptake protocols and confocal microscopy imaging approaches for the study of 3D tissue engineering cancer models. She contributed to the preparation of the figures and experiments on chick embryo simplified tumor model challenged with UCNPs *in vivo*.

Prof. Ewa Goldys discussed the data on the way and contributed to the experimental design; and provided her interpretation of the results of the *in vitro* and *in vivo* study and nanoparticle effects in 2D and 3D conditions. She edited the manuscript.

A/Prof. Andrei Zvyagin (the corresponding author) coordinated this project, discussed and planned the experiments. His contribution to the manuscript preparation was essential.

All authors contributed to this manuscript write up.

Triple negative breast cancer metastasis to the liver: a tissue engineering model shows the invasion patterns and predicts the effects of free and nanoformulated drugs

Anna Guller^{1-3,5}, Inga Kushnerus^{2,4}, Zahra Khabir^{1,2}, Alfonso Garcia-Bennett^{2,4}, Annemarie Nadort^{1,2}, Liuen Liang^{1,2,5}, Yi Qian⁵, Ewa M. Goldys^{1,2}, Andrei V. Zvyagin^{1-3,6,}*

¹Department of Physics and Astronomy, Macquarie University, NSW 2109, Australia;

²Centre for Nanoscale Biophotonics, Macquarie University, NSW 2109, Australia;

³Institute for Regenerative Medicine, I.M. Sechenov First Moscow State Medical University, Moscow, 119992, Russia;

⁴Department of Chemistry and Biomolecular Science, Macquarie University, NSW 2109, Australia;

⁵Department of Biomedical Science, Faculty of Medicine and Health Sciences, Macquarie University, NSW 2109, Australia;

⁶Laboratory of Optical Theranostics, Nizhny Novgorod State University, Nizhny Novgorod, 603950, Russia.

*Corresponding author: Andrei Zvyagin, PhD, Associate Professor, Fax: +61 2 9850 811;

e-mail: andrei.zvyagin@mq.edu.au.

KEYWORDS

Tissue engineering; disease models *in vitro*, triple-negative breast cancer, metastasis, liver, chick embryo, antitumor drug screening assays, doxorubicin, mesoporous silica nanoparticles, nanotheranostics.

Abbreviations

2D – two-dimensional; 3D – three-dimensional; AMS-6 - anionic surfactant template mesoporous silica nanoparticles; AMS-6-Dox – the same nanoparticles loaded with 20% doxorubicin; AOSS – acellular organ-specific scaffold; DCL – decellularization or decellularized; Dox – doxorubicin hydrochloride; EC50 - 50% effectivity concentration; ED – embryonic day (an incubation term, in days); ECM – extracellular matrix; ER – estrogen receptor; HER2 - human epidermal growth factor receptor 2; IC50 – 50% inhibition concentration; TEC – tissue engineering construct; TNBC – triple-negative breast cancer; PR – progesterone receptor.

ABSTRACT

Background. Three-dimensional (3D) tumor tissue engineering models have numerous advantages as biomimetic and sustainable testbeds for experimental oncology. This work introduces a new tissue engineering model of early triple-negative breast cancer (TNBC) metastasis to the liver and evaluates its feasibility for cancer biology and drug testing.

Methods. 3D organ-specific scaffold derived from a decellularized chick embryo liver compounded with metastatic TNBC (MDA-MB-231) cells represented a tissue engineering construct (TEC). TECs were cultured *in vitro* for 4 weeks and examined by histological and MTT assays. The cytotoxicity and cellular uptake of anti-cancer drug doxorubicin (Dox) and mesoporous silica nanoparticles loaded with Dox (AMS-6-Dox) were assessed in 3D TECs and monolayer two-dimensional (2D) MDA-MB-231 *in vitro* cell cultures in the Dox concentration range of 0.1 – 10 $\mu\text{g/mL}$. In vivo assay on chick embryo chorioallantoic membrane was performed to examine the grafting and angiogenic potential of the reconstructed tumors.

Results. Cells demonstrated less adherence but more sustainable growth rate in 3D TECs than in 2D cultures, reaching stabilisation in 3 and 1 weeks, respectively. Cells progressively invaded the scaffolds up to $\sim 800\ \mu\text{m}$ in depth by employing adaptive attachment and migration strategies specific to the different compartments of the liver extracellular matrix (ECM). In particular, the “parenchymal compartment” comprised by the perisinusoidal ECM was invaded by discrete cells migrating diffusely in depth at a moderate rate. In contrast, in contact with the decellularized tissue of portal triads, interlobular septae and central veins termed “stromal compartment”, cells migrated collectively in clusters, relatively superficially and slowly for the first two weeks. During the last two weeks of observation, the liver ECM was remodelled and the compartments’ boundaries were blurred, followed by in-depth and rapid cancer invasion throughout the scaffolds. Drug tests showed that both free and nanoformulated Dox were efficiently internalized in the cell nuclei. Dox was observed to permeate the entire TECs inducing profound tumor decay in their deep parts. Cells were significantly more resilient to the cytotoxic effects of free Dox and AMS-6-Dox in the TECs than in the matching 2D cell cultures. The higher therapeutic efficacy of AMS-6-Dox in comparison with that of free Dox was predicted in 3D TEC based on the calculated IC₅₀. The ability of TECs to initiate growth of new blood vessels in the chick embryo host tissue *in vivo* confirmed the cancer behaviour relevance of the model.

Conclusion. We introduced an original tissue engineering model based on a sustainable and affordable chick embryo animal material. Using this model, liver ECM was found to be the key determinant of the colonization pattern employed by TNBC cells. Cells cultured in the 3D liver-specific matrix demonstrated an increased resilience to free and nanoformulated doxorubicin. The feasibility of the proposed approach holds promise for cancer biology, drug development and nanobiotechnology. We believe that the introduced model is extendable for modelling of other types of metastatic cancers and for the development of more complex tumor TECs.

Introduction

Metastatic cascade includes the dissemination of cancer cells from the primary tumor to the distant organs mainly through the blood and lymphatic vessels, their escape from the vasculature (extravasation), homing in a secondary organ and its colonization. The organ colonization begins with the formation of an avascular micrometastases, followed by transient tumor-induced blood vessels growth in the vicinity of the cancer cell colony (angiogenic switch)¹. This results in a transition from the dormant malignant hyperplasia to massive blood-perfused macrometastases²) and, finally, progressive development of secondary tumor foci³. The spontaneous metastatic spreading is widely addressed in the literature with a number of experimental models of the induction or distant metastases, mainly by direct injections of cancer cells into vasculature. At the same time, the studies of the post-extravasation events like colonization of secondary organs by malignant cells and specific organotropism of the certain types of tumors, known by Paget's "seed and soil" metaphor, are rare³ and the most experimentally challenging because of lack of reliable methodologies⁴, especially for breast cancer metastases to the liver⁵.

This problem is applicable to one of the most aggressive types of mammary carcinoma, the triple-negative breast cancer (TNBC), which lacks the key therapeutic cellular targets, including estrogen, progesterone and human epidermal growth factor receptors (ER-, PR-, and HER2-, respectively)^{6,7}. TNBC has a tripled risk of distant metastases and much poorer prognosis in contrast to the other breast cancer types^{8,9}. According to the autopsy data, up to 50% of distant recurrences of TNBC emerge in the liver^{6,10,11} and are associated with the excessive death rates from TNBC – 70% versus 44% for the other types of breast cancer⁸. Despite the dramatic significance of these observations, virtually nothing is known about causes of the excessive liver metastasis rate of TNBC. Due to the topographic anatomy of primary breast carcinomas, the drainage by hepatic portal vein is unlikely to be the main cause, as it is observed in the case of gastrointestinal cancers¹². At the same time, as the role of blood inflow in the development of the hepatic metastasis of various primary breast carcinomas is rather comparable, the local liver tissue-specific mechanisms are the major contributors to the colonization and subsequent development of hepatic macrometastases of TNBC¹³.

A special structural organization of the liver vasculature allows direct access of the circulating cancer cells to the intrinsic parts of the hepatic parenchyma¹³, because of discontinuous (fenestrated) endothelial lining and almost complete absence of basement membrane in the liver sinusoid capillaries^{14,15}. As a result, the escape of the circulating cancer cells from the blood stream is readily facilitated and occurs in the narrow ($\sim 1\text{-}2\ \mu\text{m}$) gap, known as a Disse's space, separating the endothelial cells of sinusoids and surrounding hepatocytes¹⁶⁻¹⁸. It is mainly filled with blood plasma, collagens types I, III, V, VI and VII, as well as with fibronectin, and tenascin¹⁹. Therefore, the extracellular matrix (ECM) of Disse's space makes the first representative environment of the liver for the incoming cancer cells^{16, 20,21}. It is known that the initial metastatic homing is extremely inefficient, as only 0.01% of

CHAPTER 7

circulating cancer cells can attach in the secondary organ microenvironment and start a new colony²². So, these are the interactions between the cancer cells and the liver-specific ECM that, probably, can perform as limiting factors defining the possibility of the organ colonization and, following that, require the detailed study.

In addition to the gradually recognised role of ECM in metastatic pathways²³, its influence on the drug transport is profound hampering small-molecule drugs spread throughout the tumor and trapping nanodrugs in ECM network²⁴. This is especially important in the case of TNBC, as the current options of treatment of this type of breast carcinoma are almost limited to cytostatic chemotherapy, causing devastating side effects²⁵⁻²⁷. And although the existing chemotherapeutic protocols are relatively efficient for the control of primary TNBC, they remain much less useful for the inhibition of metastatic foci of this cancer²⁸. In order to gain insight into the key mechanisms of TNBC metastatic progression and guide the development of new treatment modalities, reliable, reproducible and realistic cancer models are demanded.

The most popular approach to model different aspects of TNBC employs representative linear cells. Approximately 30 TNBC-related cell lines are currently available²⁹ and used for pharmacological, genetic and cancer biology research as *in vitro* cultures, or, less frequently, as cellular suspension-induced xenografts in mice. Among these lines, MDA-MB-231 is recognized as a triple-negative, mesenchymal-like invasive cell phenotype *in vitro*, which is also tumorigenic *in vivo*³⁰ and commonly favoured for simulations of the metastatic-related features of TNBC. For example, conventional *in vitro* MDA-MB-231 cultures were used to study the cell-ECM interactions^{31,32} and the role of physical parameters of the microenvironment in cancer progression^{33,34}. This cell line was also employed for testing of the anti-proliferative, pro-apoptotic and anti-invasion activity of the drugs³⁵⁻³⁸ and anti-cancer effects of some nanoparticles^{39,40}.

However, the multiple limitations of two-dimensional (2D) monolayer cell cultures *in vitro*, including, first of all, absence of cell-ECM interactions and artificial stiffness and geometry of the plastic cultural substrate, have been recognised as critical for cancer biology research and drug testing^{41,42}. At the same time, tumor tissue engineering, which relies on creation of 3D tissue engineering constructs (TECs) from the studied cells and solid scaffolds, emerges as the most advanced and promising 3D *in vitro* culture (plus, in some cases, *in vivo* grafting) approach for experimental oncology and cancer nanotheranostics⁴³⁻⁴⁵. Tumor tissue engineering fills the methodology and ideology gap between the conventional 2D cell cultures and expensive, cumbersome *in vivo* animal models^{24, 42, 46}. Most recently, tissue engineering applications for TNBC research have been reported, including models of MDA-MB-231 cell metastasis to bone tissue, which was mimicked by polycaprolactone⁴⁷ and silk⁴⁸ scaffolds and tested in murine hosts. Also, the mechanisms of metastatic invasion of TNBC cells into the lungs were analyzed using scaffolds obtained by whole-organ decellularization (DCL) of mouse lung-heart complexes⁴⁹.

CHAPTER 7

In current study we present a new tissue engineering model of early metastasis of TNBC to the liver, which includes MDA-MB-231 cells representative for TNBC, and DCL chick embryo liver scaffolds. Providing the liver-specific ECM microenvironment to MDA-MB-231 cells, the 3D tissue engineering constructs (TECs) introduced here are promising for fundamental cancer biology studies and for testing of the therapeutic efficacy and mechanisms of action of anti-cancer drugs. In particular, our research interests were focused on: 1) development and validation of the proposed tumor engineering model; 2) the study of the colonization strategies employed by TNBC cells in the liver organotypic ECM; and 3) evaluation of the feasibility of the developed 3D engineered tumor model for testing of small molecular weight and nanoformulated anti-cancer drugs.

The first two tasks were motivated because of lack of the *in vitro* models allowing to observe the dynamic interactions between the metastatic cancer cells and the 3D liver ECM at the beginning of the metastatic foci formation. The second goal was set in attempt to improve the predicting power of *in vitro* models of metastatic cancer in drug development and nanomedicine, as the evidence accumulates for dramatic discrepancy between the “optimistic” drug evaluation reports obtained in 2D *in vitro* cell cultures and the disappointing results of clinical trials of the same medications following the unexpected inefficiency or nonselective toxicity⁴⁶.

In a particular case of TNBC, the adjuvant and neoadjuvant chemotherapy remains the most used options of its nonsurgical treatment, while the nonspecific toxic action of these drugs, drug resistance of the cancer cells and non-optimal clinical outcomes are still problematic⁵⁰. The emerging nanoformulated drugs can offer more targeted delivery, better pharmacokinetics and pharmacodynamics of chemotherapeutic drugs^{51,52}. Mesoporous silica nanoparticles are particularly suitable for drug delivery⁵³ and theranostics applications⁵⁴ due to the high loading capacity, colloidal stability, biocompatibility and facile coupling of biomolecules. In our study we tested the therapeutic efficiency (as cytotoxicity towards the cancer cells) and cellular uptake of free Doxorubicin hydrochloride (Dox), a cytostatic drug widely used in chemotherapy of primary and metastatic TNBC, and original anionic surfactant template mesoporous silica nanoparticles (AMS-6), loaded with Dox (AMS-6-Dox) in our 3D engineered model of metastatic TNBC in the liver and in conventional 2D *in vitro* cultures of MDA-MB-231 cells.

Materials and methods

2.1. Design of the experiment

The study included the experiments performed *in vitro/ ex vivo* and schematically illustrated in Figure 1, and a series of *in vivo* experiments, which were also carried out with use of chick embryo experimental platform.

The development of the 3D tissue engineering tumor model and study of metastatic colonization of liver ECM by TNBC. The chick embryos (Figure 1, 1) were incubated in a standard laboratory egg incubator until embryonic day 18 (ED18), when the major organs have formed, while the pain sensitivity

CHAPTER 7

is not fully developed. The embryos were extracted from the shells through small openings and immediately euthanized by decapitation. The liver (Figure 1, 2) of each embryo was extracted and decellularized (DCL, Figure 1, 3) by original whole-organ immersion-agitation procedure reported by us recently⁵⁵. The decellularized liver was sectioned (Figure 1, 4) for fragments of approximately 3-4 mm in size (Figure 1, A), sterilized and conditioned in the cultural medium in order to serve as acellular organ-specific scaffolds (AOSSes) (Figure 1, 4A). Then 3D tissue engineering constructs (TECs) were formed (Figure 1, 5) by seeding of the AOSSes with high-density suspension of MDA-MB-231 cells (Figure 1, 6). The TECs were grown in static *in vitro* culture (A+) up to 4 weeks (Figure 1, 7), demonstrating increased number of cells and invasion depths (Figure 1, 8). The TECs were sampled histological analysis and for the cellularity assay (MTT) on the days 1, 7, 14, 21 and 28 of the culture (blue dotted arrow from 8 in Figure 1). Matching 2D *in vitro* cell cultures of the same cells (not shown on the figure) were prepared and studied in parallel with the TECs by the same methods.

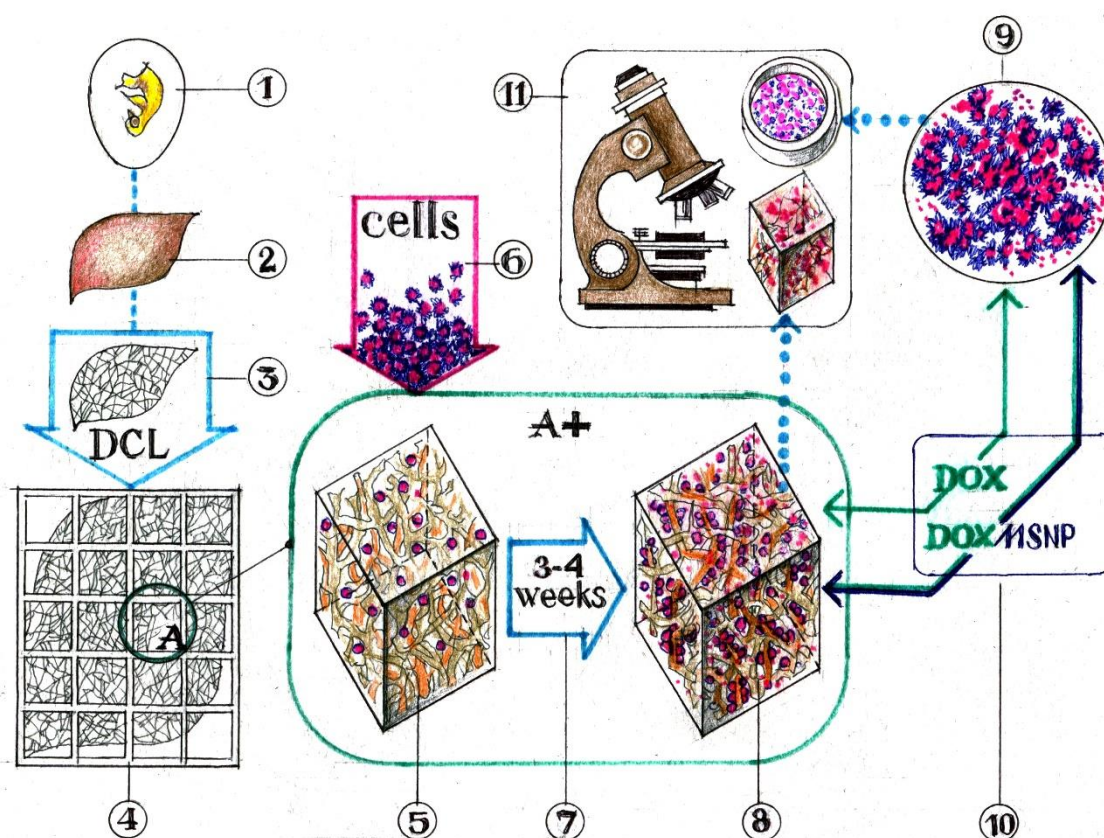


Figure 1. A schematic illustration of the experimental design of the first stage of development and validation of a chick embryo-based tissue engineering model of the early TNBC metastasis to the liver. The *in vitro/ ex vivo* experiments are shown. See the explanation in the main text. Abbreviations: DCL – decellularization; DOX – doxorubicin; DOX-MSNP – mesoporous silica nanoparticles loaded with 20% doxorubicin (AMS-6-Dox). The scheme does not show the *in vivo* experiments, included into the current study.

Evaluation of the effects of free and nanoformulated Dox. Testing of feasibility of 3D *in vitro* tumor models for nanotheranostic research. The TECs with well-developed cell colonies formed after 3 weeks of *in vitro* culture (Figure 1, 8) were used for evaluation of the cytotoxicity and cellular uptake (Figure 1, 9) of Dox and original anionic surfactant template (AMS-6) mesoporous silica nanoparticles loaded

CHAPTER 7

with Dox (Figure 1, 10). The parallel tests were performed in the matching 2D monolayer cultures of MDA-MB-231 cells (blue dotted arrow from 9 in Figure 1). The data obtained in the 2D and 3D (TECs) *in vitro* cultures was compared with analytic methods (MTT assay, mathematical modelling of drug effects, microscopy and statistical analysis). In addition, we performed a pilot study with use of simplified 3D *in vitro* TNBC model grafted on chick embryo chorioallantoic membrane (CAM) and upconversion nanoparticles (UCNPs) to examine the feasibility of the 3D *in vitro* tumor models for nanotheranostic bioimaging *in vivo* (See Supplementary Information, SI 8).

Evaluation of angiogenic potential of TECs in vivo. The preliminary qualitative chick embryo chorioallantoic membrane (CAM) assay⁵⁶ was applied to prove the biological relevance the TNBC-liver ECM TECs *in vivo*. The angiogenic potential of the engineered tumors was examined as the ability to induce growth of blood vessels in the host tissue is a critical cancer hallmark⁵⁷, especially significant for metastatic tumors' progression¹⁻³.

2.2. Cell culture

MDA-MB-231 (ECACC 92020424) cells were expanded by culture in complete culture medium prepared from Dulbecco's Modified Eagle's Medium (DMEM/F12/Ham medium, #D8437, Sigma-Aldrich) supplemented with 10% fetal bovine serum (FBS, #12003C, Sigma Aldrich) and 1% Penicillin-Streptomycin (PS, 10,000 U/mL; #15140122, Gibco) under standard conditions (37 °C, humidified, 5% CO₂ gas atmosphere) during 7-10 days prior use in further experiments to reach the 4th-6th passage. Culture medium was changed every two days and the cellular growth was controlled by using a phase-contrast microscope and cell counting. According to the cell counting data, the average population doubling time of MDA-MB-231 cells (passages 4 to 6) was approximately 34 h, with the average viability ~98%. The same culture medium was used for all *in vitro* experiments, unless otherwise specified.

2.3. Development of *in vitro* 3D TEC model of early metastasis of TNBC IN the liver

2.3.1. CHICK EMBRYO INCUBATION AND ORGAN COLLECTION

The study was approved by animal ethics committee protocol of Macquarie University (ARA 2015/006). Fertilized chicken (*Gallus gallus domesticus*, the strain of White Leghorn) eggs were delivered from a local hatchery, allowed to rest for 3-4 h at room temperature and then incubated in a standard cradle-type laboratory poultry incubator (R Com MARU Max 190, Autoelex Co., LTD, South Korea) at 37.5 °C, 65-70% humidity with hourly turn over until the embryonic day 18 (ED18), 3 days before natural hatching. This period was sufficient for the development of the organ structure and main physiological systems of a chick, excepting the central nervous system. The pain sensitivity was immature at this stage, and it was permissible to extract an embryo from the egg for research purposes in accordance with the Australian code of animal research. Egg shells were opened by a cut on the blunt ends of eggs, and the embryo with embryonic membranes were extracted using forceps and immediately

CHAPTER 7

decapitated. Then feathers were removed from the abdominal wall and thorax, and the liver was carefully extracted through the wide central section (for details see Supplementary Information, SI 1, Figure S1).

2.3.2. DECELLULARIZATION

The extracted livers were washed in sterile PBS and placed in 50-mL Falcone tubes, 5 livers/ per tube filled with 30 mL of 0.1% solution of sodium dodecyl sulphate (SDS) in phosphate buffer saline (PBS), then closed tightly and fixed horizontally on the platform of an orbital shaker. Then the organs underwent shaking at the speed of 90-150 rotations per minute (rpm) with periodic aseptic changes of washing media for a fresh portion every 3 h during first 12 h, and then every 6 h during the next 12 h. Afterwards, the solution was changed daily until the organs became translucent and the liquid media turned colourless and transparent. The total processing time ranged from 14 to 21 days depending on the embryo flock. Next, the processed organs were aseptically placed in sterile containers and washed with 1% of antibiotic-antimycotic solution (A-A) (#A5955, Sigma-Aldrich) in PBS (pH 7.0) for 3-5 days under shaking (30 – 90 rpm) periodically changing A-A/PBS with fresh portions, until the washing media is transparent, colourless, with no observable tissue components and foam. The processing was performed at room temperature. As-obtained scaffolds were stored in fresh sterile 1% A-A/PBS solution in a fridge (+4 °C) until further use.

2.3.3. RECELLULARIZATION OF ACELLULAR CHICK EMBRYO LIVER SCAFFOLDS WITH MDA-MB-231 CELLS

2.3.3.1. Preparation of scaffolds (AOSSes) for cell seeding.

Small fragments (approximately, 3 × 4 mm) of decellularized livers were cut by a scalpel blade and put into 24-well flat bottom tissue culture plates (Costar, Corning, #3524). 1 mL of 0.1% peracetic acid solution (#77240, Sigma-Aldrich) in 4% ethanol was added to every well and placed onto an orbital shaker platform for 2 h at 50 rpm. Then this solution was replaced with sterile PBS (0.4 mL per well) and decellularized liver AOSSes were sterilized by ultraviolet light in a tissue culture hood for 45 min. Next, PBS was removed and each well was refilled with 1 mL of complete culture medium. Following that, the plates with the AOSSes were placed into a tissue culture incubator and conditioned overnight under humidified atmosphere with 5% CO₂ at 37 °C.

2.3.3.2. Seeding cells on liver AOSS to prepare liver-specific tissue engineering constructs (TECs).

MDA-MB-231 cells (1×10^5 cells in a 30- μ L drop of complete culture media) were seeded on as-obtained AOSSes, one TEC per a well of 24-well culture plate. Control scaffolds were left unseeded. Next, the cells were allowed to attach to the substrates for 2 h in a tissue culture incubator, then added with 1 mL of complete culture media per well and cultured for 1-28 days. Medium in these growing cultures was carefully changed twice a week. On days 1, 7, 14, 21 and 28 after seeding, TECs were

sampled for imaging using a fluorescence microscope, performing viability assay and histological analysis.

2.4. *In vitro/ex vivo* experimental studies on TECs and control 2D *in vitro* cell cultures

In order to characterize and validate the proposed TE model of interaction between the MDA-MB-231 cells and the liver-specific ECM, the structural transformations of TECs during cancer cell colonization were investigated during a 4-week period by histological methods and live fluorescence microscopy, and MTT test was carried out to quantify the evolution of the cell populations in TECs versus the established in parallel control 2D *in vitro* cell cultures. On Day 28, TECs were treated for 36 h with two types of chemotherapeutic drugs: free-molecule and nanoformulated doxorubicin (termed Dox and AMS-6-Dox, respectively) followed by cytotoxicity tests. The cellular uptake of Dox and AMS-6-Dox in 3D TEC and in the matching 2D *in vitro* cell cultures was imaged and analysed by a fluorescence laser-scanning confocal microscope after 24 h exposure of the cultures to the drugs.

2.4.1. MORPHOLOGICAL STUDY OF IN VITRO STRUCTURAL EVOLUTION OF TECs

AOSSes were sampled and investigated after the DCL procedure (see 2.3.2) to examine their structural integrity and sterility and as-developed TECs were also sampled for morphological study after 1, 2, 3 and 4 week incubation with cancer cells (see 2.3.3). The samples were fixed in 10% neutral buffered formalin, dehydrated in a graded series of alcohols, embedded in paraffin wax and cut into serial sections of 5 μm in thickness by a rotary microtome. After thorough deparaffination, slices were stained with haematoxylin and eosin (H&E), van Gieson's picrofuchsin, Masson's trichrome and toluidine blue, following conventional protocols. In addition, unfixed TECs were stained with 4',6-diamidine-2'-phenylindole dihydrochloride (DAPI) to highlight the cell nuclei. Staining with fluorescein diacetate (FDA) and propidium iodide (PI) was used to label and discriminate live and dead cells, respectively. Stained histological preparations were examined using an upright research microscope Axio Imager Z2 (Zeiss, Germany) equipped with dry-air EC Plan-Neofluar (5 \times /NA0.16; 10 \times /NA0.30; 20 \times /NA0.50 Ph) and oil-immersion α Plan Apochromat (100 \times /NA1.46 oil) objectives (Zeiss, Germany). Fluorescence microscopy was performed within 30 min after collection and staining of the samples with the use of the filter settings for DAPI, and FITC (for FDA) and PI on the same microscope. Images were recorded using a preinstalled microscope digital video camera AxioCam (1388 \times 1040, Zeiss, Germany) in a single-frame and stitching modes, and analyzed using Zen 2012 proprietary software.

2.4.2. MTT ASSAY FOR EVALUATION OF THE POPULATION EVOLUTION OF MDA-MB-231 CELLS IN 2D AND 3D TECs

MDA-MB-231 cell viability was tested in 3D TECs and in matching 2D cell cultures using a modified MTT colorimetric assay. This assay relies on the reduction and conversion of yellow 3-(4,5-dimethylthiazol-2-yl)-2,5-diphenyltetrazolium-bromide (MTT) reagent (#M2128, Sigma-Aldrich) into purple formazan salt, where the optical absorbance of formazan crystals dissolved in dimethyl sulfoxide

CHAPTER 7

(DMSO) represents the activity measure of cellular mitochondrial dehydrogenase⁵⁸. The tested cultures were grown in complete culture medium in a humidified atmosphere under 5% CO₂ at 37°C.

The following procedure ensured equal-footing comparison between 2D and 3D TEC cultures. The 5th passage MDA-MB-231 cells were seeded on a chick embryo liver AOSSes, as described earlier (see 2.3.3), while the same amount of the cells (1×10^5 in a 30-μL drop of complete culture media) was deposited in the middle of 24-well culture plate (Costar) wells to perform high-density seeding. Next, cells in both cultures were allowed to attach to the substrates for 2 h in a tissue culture incubator in a humidified atmosphere under 5% CO₂ at 37°C, and then filled with 1 mL of complete culture media per well and cultured for 1 day.

After 24 h, the media was removed, and the samples were washed twice with PBS to eliminate unattached cells. Next, 3D TECs were aseptically transferred to new 24-well culture plates to get rid of the cells adhered to the plastic and not to the scaffolds in the original cultures, then filled with fresh complete culture media (1 mL per well) and cultured for 4 weeks. At the same time, 2D cell cultures after washing with PBS, were filled with complete culture media, and cultured for 4 week, without splitting in the same way as 3D TECs. The media was changed twice a week in both types of cultures.

MTT assays were carried out on days 1, 7, 14, 21 and 28 after seeding (day 1 and weeks 1, 2, 3 and 4, respectively). For each assay, 3 samples of TECs were randomly selected and transferred to a separate 24-well plate for testing, while 3 wells of cells growing in 2D culture were used as the internal control. After double washing with PBS, 500 μL of MTT reagent (0.5 mg/mL in the phenol red free cell culture medium; DMEM/F12; #D6434, Sigma-Aldrich), was added to each well. Then the samples were incubated at 37 °C in a tissue culture incubator for 1 h to allow precipitation of insoluble formazan crystals. After that, the supernatant was carefully collected and 500 μL of DMSO was added to the wells and left for 10 min in the dark on a rocking platform at room temperature to dissolve purple formazan crystals. Next, four portions of 100 μL of the dissolved MTT product was taken from each well, transferred to separate wells of a clear 96-well culture plate (#3585, Costar, Corning) and used for absorbance measurements. The samples' absorbance was measured in a spectral band centred at 570 nm by a PHERAstar multiplate reader (BMG Labtech, Germany), with empty wells used as blank controls. Each reading was repeated twice, the results were corrected for the blank controls by MARS Data Analysis software (BMG Labtech, Germany) and averaged. Since the absorbance is proportional to a number of viable cells, relative changes of the cell population number can be calculated as the sample absorbance normalised to that of the seeding sample. The percent change of the viable cell number per week termed “weekly increment” was calculated as:

$$v = \left(\frac{(OD_X - OD_{X-1})}{OD_X} \right) \times 100\%, \quad (1)$$

where OD_X stands for the absorbance sampled in Week X.

The number of viable cells in 2D cell culture on Day 1 (24 h after seeding) N_s was calculated by taking into account the population doubling time in 2D cell culture *in vitro*, seeded number of cells, and

CHAPTER 7

the observed average cell viability, and resulted in $N_s = 1.43 \times 10^5$ viable cells per well. Then number of viable cells in each sample was calculated as:

$$N_x = \frac{OD_x}{OD_s} N_s, \quad (2)$$

where OD_s is the average absorbance of the control sample in 2D control cell culture on Day 1.

2.4.3. EVALUATION OF THE CYTOTOXICITY AND CELLULAR UPTAKE OF DOXORUBICIN (DOX) AND MESOPOROUS SILICA NANOPARTICLES LOADED WITH DOX IN 3D TECs AND 2D CULTURES

2.4.3.1. Preparation of mesoporous silica nanoparticles and their loading with Dox.

Anionic surfactant-templated mesoporous silica nanoparticles (AMS-6) have been reported by us in Refs^{59,60}. Nanoparticles were synthesized in-house following a protocol described elsewhere⁶¹. Briefly, N-lauroyl-L-alanine was used as surfactant, APES was applied as a co-structure directing agent to achieve connected pores in TEOS-sourced silica nanomaterial. The sample was calcinated at $\sim 550^\circ\text{C}$ using the temperature gradient of $1.5^\circ\text{C}/\text{min}$ to remove surfactant. Next, as-synthesised mesoporous silica nanoparticles (AMS-6) were loaded with 20% Dox (Doxorubicin hydrochloride, #D1515, Sigma-Aldrich). Dox diluted in 100% ethanol was added to AMS-6 nanoparticles in a round bottom flask mounted on a rotary evaporator, and ethanol was evaporated at 40°C under vacuum with slow rotation. The collected sample was air dried overnight.

2.4.3.2. Characterization of mesoporous silica nanoparticles.

As-synthesized AMS-6 and Dox-loaded AMS-6 (AMS-6-Dox) were characterized using transmission electron microscopy (TEM), X-ray diffraction (XRD), thermogravimetric analysis (TGA) and dynamic light scattering (DLS). Nitrogen adsorption/desorption isotherm measurements were carried out to evaluate the effective surface area of the AMS-6 and AMS-6-Dox samples.

For TEM sample preparation, a small amount of dry AMS-6 or AMS-6-Dox was thoroughly crushed in a mortar and then diluted in ethanol. A drop of the suspension was placed on a copper grid and dried. Next, the grid was placed in a sample holder of JEOL 3000F TEM (Peabody, USA) and imaged at 300 kV with the resolution of 1.6 \AA . Images were obtained using Gatan SC1000 11-megapixel CCD camera (Pleasanton, USA), with a 1024×1024 pixel Gatan image filter (Pleasanton, USA). XRD measurements of 20 mg of the dried MSNP sample were carried out using XRD instrument Bruker D8 Discover equipped with VÅNTEC-500 detector featuring a 140 mm diameter window (Billerica, USA). XRD patterns were recorded using Cu $K\alpha$ anode ($\lambda = 0.1542 \text{ nm}$), operating at 40 kV and 30 mA. TGA measurements were performed using 1-mg sample placed in an aluminium crucible (TA Instruments TGA2050, New Castle, USA) and heated from 25 to 850°C at $10^\circ\text{C}/\text{min}$ under air flow at 10 mL/min. Nitrogen adsorption/desorption isotherms were acquired at a temperature of -196°C using liquid nitrogen with a TriStar II by Micromeritics® instrument (Norcross, USA), following the MSNPs sample degassing under vacuum using VacPrep™ 061 by Micromeritics® instrument (Norcross, USA) for ~ 10

CHAPTER 7

h at 120°C. The surface area was calculated using BET equation. Hydrodynamic diameters and the zeta-potentials of colloidal MSNPs and MSNP-Dox were measured in PBS and complete culture media (1 mg/mL) by Zetasizer Nano ZS (Malvern, UK) in three runs followed by averaging.

2.4.3.3. MTT viability assay of 2D and 3D TEC cell cultures treated with free and nanoformulated Dox.

Experimental part. TECs were cultured for 3 weeks as described above (see 2.3.3). For control 2D *in vitro* culture MDA-MB-231 cells were seeded in 96-well plates (Costar, Corning, #3599) at the density of 2×10^4 cells per well and incubated in complete culture medium for 24 h before the test. Then culture medium was removed from all the cultures, TECs were aseptically transferred to new 24-well culture plates and all the cultures were washed 3 times with PBS. Free Dox of the concentrations ranging from 0.1 to 10 $\mu\text{g/mL}$, AMS-6 (50 $\mu\text{g/mL}$) and AMS-6-Dox of the concentrations ranging from 0.5 to 50 $\mu\text{g/mL}$ (Dox-equivalent, 0.1 – 10 $\mu\text{g/mL}$) were diluted in complete culture media and sonicated immediately before the test. Each concentration of each type of the tested compounds was applied in a total volume of 100 μL to 8 parallel wells of 96-well plates for challenging of 2D culture of MDA-MB-231 cells. At the same time 2 parallel TECs growing in 24-well plates were used for testing of the each concentration of each tested compound, and the added volume of the dispersions was 400 μL per a well. The 2D and 3D cultures treated with complete culture medium were used as a control. The exposure time was 36 h. Then MTT tests were performed, as described above (see 2.4.2) with minor changes. In particular, after removal of culture media and washing with PBS, the TECs and cells were incubated in MTT solution in phenol red free culture media (0.5mg/mL) for a longer period of 3 h. Then the supernatant was removed and 100 μL or 400 μL of DMSO was added to the wells of 96-well plates (2D cultures) and 24-well plates (3D TECs), respectively. The solution of formazan in DMSO from the TECs was transferred to the new 96-well plate (100 μL per a well; 3 samples per a TEC), and the optical absorption of the tested cultures were carried out with following analysis of cellular viability as described above (see 2.4.2).

Mathematical modelling. In order to translate the experimental data on the free Dox and the AMS-6-Dox efficacy in the monolayer and 3D *in vitro* cultures of MDA-MB-231 cells to the general population (i.e. make a prediction), the IC₅₀ and EC₅₀ values were calculated with use of mathematical modelling. IC₅₀ (inhibition concentration) was considered as the drug/nanoformulated drug concentration at which inhibition (death) of 50% of the cell numbers occurs, in comparison with that of the control sample (100% average viability), while EC₅₀ (effectivity concentration) was termed as the concentration, where 50% of the maximum actually observed effect was obtained⁶².

The experimental data was fitted to the following sigmoidal equation:

$$\text{Cell death} = A / (1 + 10^{(EC_{50} - \text{dose}) * s}), \quad (3)$$

where A is the maximum effect (%), EC_{50} is the drug concentration at half effect, and s is the Hillslope. The fit was performed using a weighted unconstrained nonlinear curve fit (Matlab r2016b)

CHAPTER 7

with the inverse error as the weight, and the dose values were first logarithmically transformed. The 0% cell death (100% viability) at 0 $\mu\text{g/mL}$ in control, presented as 0.01 $\mu\text{g/mL}$ for visibility on the logarithmic scale, was given a high weight as the data was normalized to this value and the model is expected to approach this intercept closely. The percent of dead cells (frequency of cell death) was considered as a response measure. The goodness of fit was high for all assays ($r^2 = 0.99$ for free Dox in 2D culture (termed below as Dox, 2D), $r^2 = 0.97$ for free Dox in TECs (termed as Dox, 3D), $r^2 = 0.99$ for AMS-6-Dox nanoparticles in 2D cultures (termed AMS-6-Dox, 2D) and $r^2 = 0.98$ for AMS-6-Dox nanoparticles in TECs (termed AMS-6-Dox, 3D).

2.4.3.4. Confocal microscopy study of the uptake of free and nanoformulated Dox in 3D TEC and 2D cultures.

As produced TECs were cultured for 4 weeks (see 2.3.3). Control 2D *in vitro* cultures of MDA-MB-231 cells were seeded onto sterile coverslips placed into wells of a 24-well plate (Costar) at the density of 5×10^4 cells/well, and incubated under standard conditions in 1 mL of complete culture media during 24 h prior to the observation. Dox solution (10 $\mu\text{g/mL}$), AMS-6 nanoparticles (50 $\mu\text{g/mL}$), and AMS-6-Dox nanoparticles (50 $\mu\text{g/mL}$; Dox-equivalent, 10 $\mu\text{g/mL}$) dispersions were prepared as described above (see 2.4.3.3). Next, after removal of the culture media and triple washing with PBS the tested compounds were added to the wells with 2D and 3D cultures in a total single volume of 0.5 mL per well. The wells added with complete culture media without Dox or nanoparticles were used as controls. The prepared 2D and 3D cultures were incubated for 24 h in tissue culture incubator at 37 °C and 5% CO_2 , and, next, following thorough rinsing with PBS 3 times to remove free Dox and nanoparticles, they fixed with 10% neutral buffered formalin at room temperature.

After 24-h fixation process and another washing with PBS, the fixed samples were stained with DAPI solution in PBS (#D9542, Sigma-Aldrich) for 20 min at 37 °C. Next, the staining solution was removed, the coverslips were washed twice with PBS to eliminate unbound DAPI. Finally, the samples were mounted on glass slides with Dako anti-fade mounting media and sealed with nail polish.

Dox and AMS-6-Dox cellular uptake was imaged by an inverted Zeiss LSM 880 laser-scanning confocal microscope (Zeiss, Germany), using a Plan-Apochromat 10 \times /0.45 N.A. M27 and Plan-Apochromat 40 \times /1.3 N.A. oil DIC UV-IR M27 objectives. Dox fluorescence was observed using 488-nm excitation and emission 535-673 nm; DAPI fluorescence was observed using 405-nm excitation and emission 411-528 nm.

2.4.4. ANALYSIS OF ANGIOGENIC POTENTIAL OF TECs AND AOSSes IN VIVO

The detailed description of the used procedures of angiogenic assay on chick embryo chorioallantoic membrane (CAM) can be found in Supplementary Information (SI 7, Figures S19, S20). Briefly, the angiogenic effect of TECs, liver AOSSes and cell suspensions of MDA-MB-231 cells grafted on CAM was evaluated by stereomicroscopy imaging performed on the day of grafting (embryonic day 8, ED8) and on ED12, in comparison to natural growth of blood vessels of CAM

CHAPTER 7

occurring during the same period of chick embryo development. TECs, AOSSes or cell suspensions were grafted on CAM separately, one sample of each material type per egg. Before grafting TECs were cultured *in vitro* for 12 day as described above (2.3.3). The liver AOSSes were kept in complete culture media for 24 h before grafting on CAM. The MDA-MB-231 cell suspensions containing 3.3×10^6 cells per mL of complete culture media were prepared by trypsinization of the *in vitro* monolayer cultures of 5th - 6th passages (see 2.2.2).

2.4.5. STATISTICAL ANALYSIS

The data were expressed as means \pm standard deviations (SD), and the 95% confidence intervals (CI_{95%}) for the means were calculated. The statistical significance of the inter-groups differences between the average values of the variables were evaluated by nonparametric U Manna-Whitney test because of non-Gaussian data distribution. The critical level of the statistical significance was set at $p < 0.05$ and 2-side tests were used in all cases. The data were analyzed using SPSS 13.0 / 22.0 (IBM SPSS, USA) and Excel 2010 (Microsoft Office).

Results

3.1. Macroscopic observations and histological study of *in vitro* development of TECs

3.1.1. NATIVE STRUCTURE OF THE CHICK EMBRYO LIVER AND THE EFFECT OF DCL

A chick embryo liver at the ED18 had less differentiated lobular microstructure, than in normal human liver tissue, which nevertheless, could be recognized by reference vascular and biliary elements (Figure 2 (a, b)). The portal triads had typical structure and contained interlobular portal veins, branches of hepatic arteries and portal bile ducts. At the same time the interlobular connective tissue sheaths were discernible only by special staining (see Figure 2 (b)). The liver was coated with a connective tissue capsule, and the subcapsular vascular elements were enlarged and well differentiated (see Figure S2 (a) in SI 2). More details of the observed histological structure of the native chick embryo liver can be found in Figure S2 (b, c) in SI 2. An artistic representation of the histoanatomical features of the liver and the effect of DCL on it is presented in Figure S3 (in SI 2); and the organization of the Disse's space is shown schematically in Figure S4 in SI 2.

The macroscopic observations of the effects of immersion-agitation whole-organ DCL on the native chick embryo liver are illustrated by Figure S5 in SI 2. Briefly, the whole-organ immersion-agitation DCL decellularization process (as described in 2.3.2) resulted in a loss of the natural organ colouration up to a translucent state. While the volume of the DCL liver was significantly decreased, the former right (larger), left and medial left liver (macro) lobules were preserved.

In DCL liver tissue cells and cellular debris were no longer observable by histological methods (Figure 2 (c, d)). Hepatic parenchyma transformed into loose, fine mesh-like matrix, formed mainly by the residuals of perisinusoidal ECM of Disse's spaces (see Figures S3 and S4 in SI 2). The former septal

CHAPTER 7

connective tissue and portal elements as well as acellular walls of the former central veins were represented by denser ECM structures and were clearly distinguished from the DCL parenchyma by the architectonics and tinctorial properties. We describe these distinctive types of structures as two compartments of liver ECM as they had clear histoanatomical associations with hepatic parenchyma and with the dense liver stroma, respectively. For the study purposes, the first compartment comprising the mesh-like ECM of former parenchyma is further termed as “parenchymal” and the other one, which includes the DCL portal vasculature, interlobular septal stroma and central veins is further termed “stromal” (see Figure S3 (g) in SI 2).

3.1.2. HISTOLOGICAL OBSERVATION OF THE CELL GROWTH PATTERNS IN TECs

The following main trends of the TEC evolution were revealed as a result of the histological observation and analysis.

Firstly, distinctive patterns of the initial cellular attachment and following metastatic colonization behaviour occurred in the parenchymal and stromal ECM compartments (Figure 3). The detailed comparison is given in the Table 1.

In particular, significantly less cells attached initially to the ECM of parenchymal compartment, than to the ECM of stromal origin (Figure 2 (a, b)). The cells colonizing parenchymal compartment preserved epithelioid morphology during first 2 weeks of observation. After 3 weeks in culture the subpopulations of cells with different morphology (epithelioid, mesenchymal and intermediate) emerged for short time (Figure 2 (e)), and then the epithelioid phenotype predominated till the end of the study. In addition, the parenchymal compartment was mainly colonized by diffuse invasion of discrete cells. At the same time, the mesenchymal-like morphology of cells was mainly observed in association with ECM of stromal compartment, with transitory changes to intermediate mesenchymal-epithelioid shape. The general trends observed in the stromal compartment, included formation of multicellular clusters both on the scaffold surfaces (as linings and bumps) and in the depth of the matrix. The invasion by clusters occurred mainly along the voids and clefts of the ECM, and resulting depth of the invasion was smaller, than the observed in the parenchymal compartment. Notable spongy-like remodelling of ECM was also a feature of the stromal compartment, which resulted in partial blurring the demarcation between the matrix of parenchymal and stromal origin. Cooperatively, cancer cells invaded liver-derived scaffolds almost completely in 4 weeks.

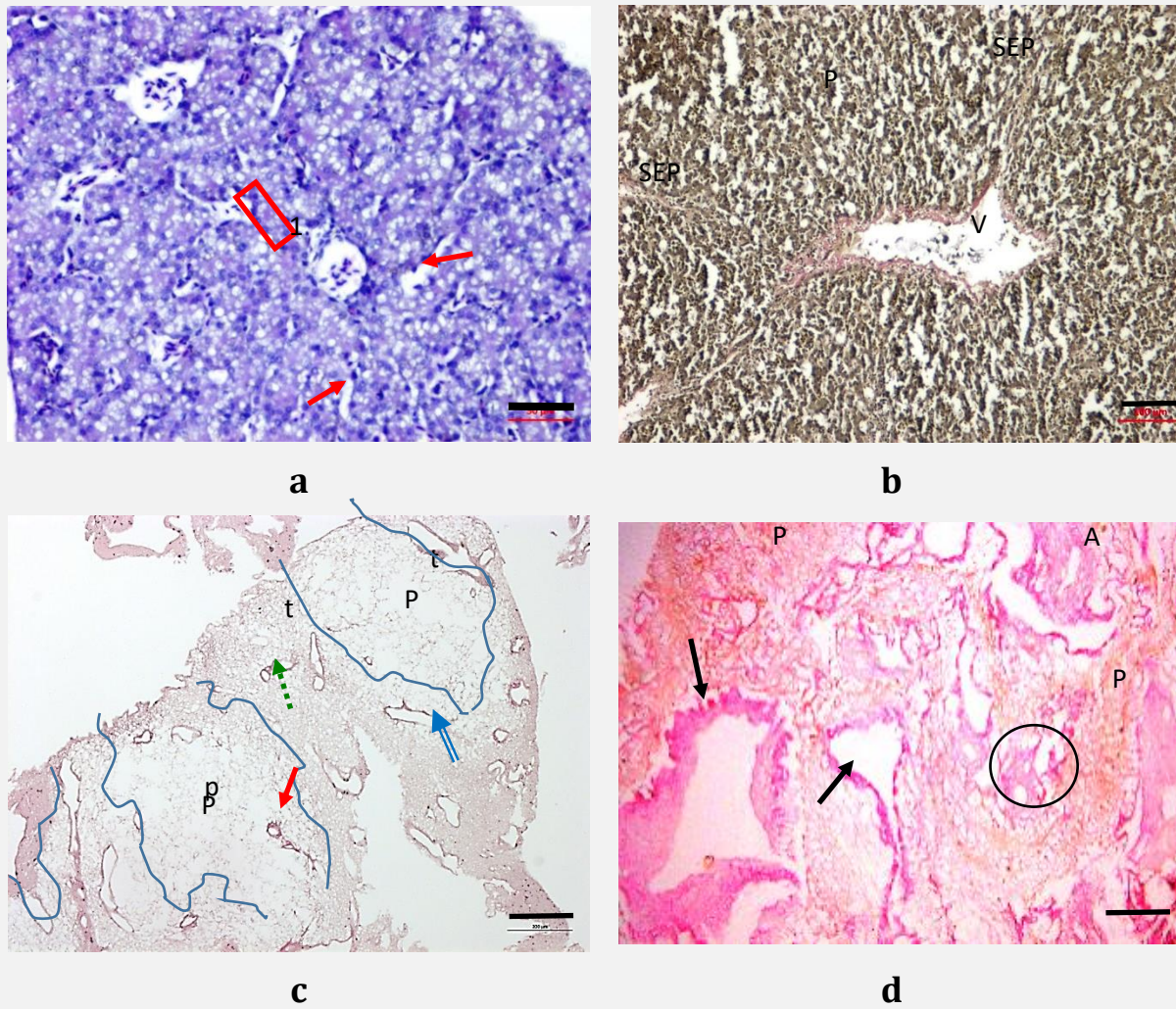
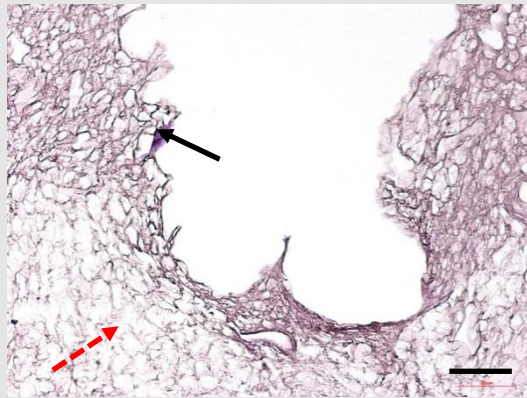


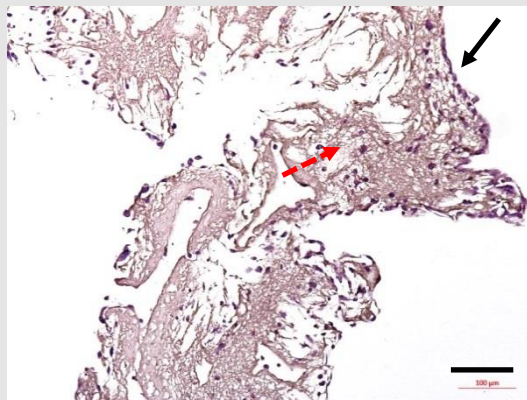
Figure 2. Intact chick embryo liver and effect of DCL on it. (a) The cords of hepatocytes (red box) are separated by narrow voids of sinusoids (red arrows), which have clear visible discontinuous endothelial linings, and arranged around the central vein (1). (b) Lobular structure of the intact liver revealed by elastica-Van Gieson's staining. Red: collagen of the interlobular vein (V) and radially arranged interlobular septae (SEP); yellow-brown: hepatic parenchyma lacking of mature fibrillar collagen. (c) General view of a section of DCL chick embryo liver. Pale-stained, loose ECM of the former parenchyma (P) and the denser structures of portal triads (green dotted arrow), interlobular veins (blue double arrow) and arteries (red arrow) are visible. Note intermittent loose and dense matrix areas (conditionally demarcated by blue lines) which can be attributed to the parenchymal and stromal compartments, respectively. (d) Van-Gieson's staining of DCL liver. Red-magenta staining (fuchsinophilia) of DCL walls of large blood vessels and connective tissue sheaths indicate that fibrillar collagen is mainly preserved (arrows). Yellow-orange coloured (picrinophilic) DCL parenchyma (P) lacks mature fibrillar collagen. An encircled area indicates a small DCL portal triad (large lumen of former vein, and small lumens of former arteria and bile duct). *Scale bars*: 50 μm (a); 100 μm (b, d); 200 μm (c).

Compartments

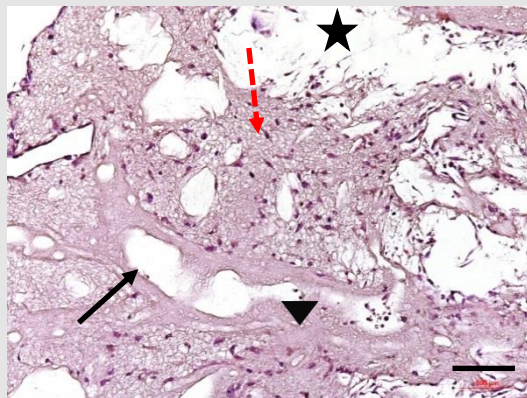
Parenchymal and mixed



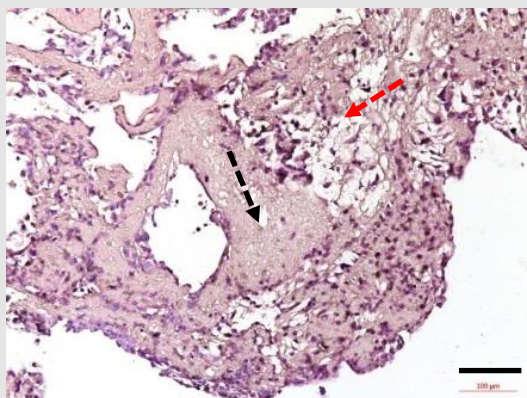
a



c

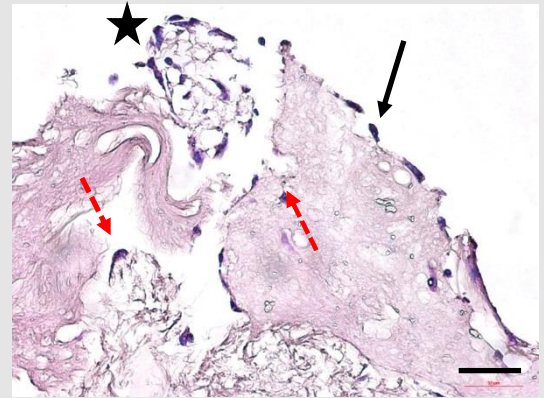


e

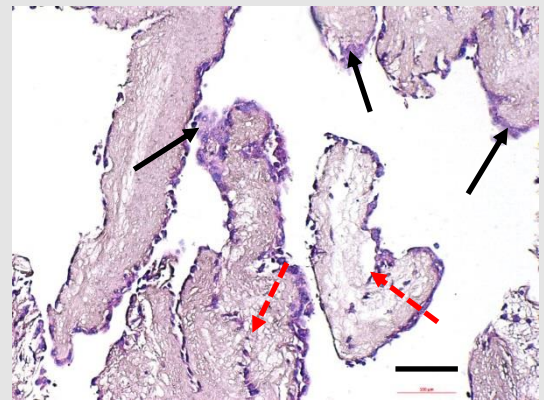


g

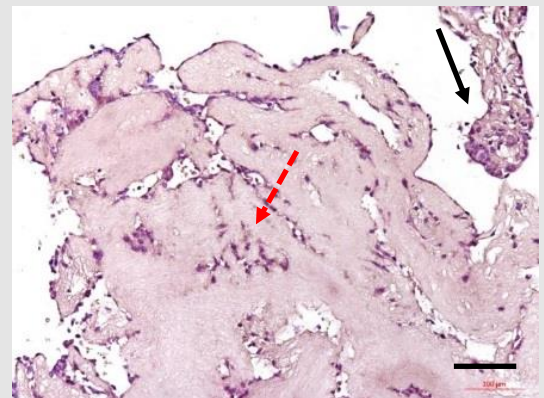
Stromal



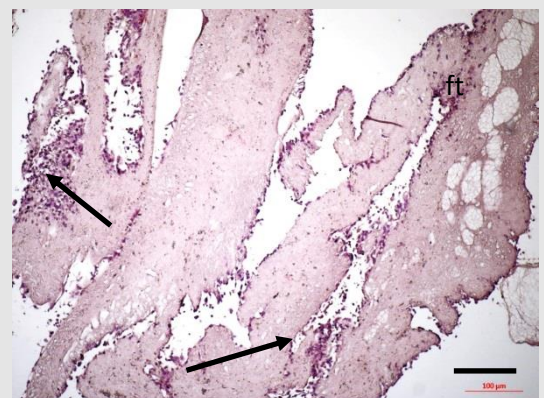
b



d



f



h

CHAPTER 7

Figure 3. Structural evolution of the breast cancer/ liver ECM 3D TECs during 4 weeks of *in vitro* culture. (a, b) Week 1. Notable difference in the ECM structure and the attachment efficiency, numbers, shapes and distribution of cells between 2 compartments of the liver ECM. Only a single cell (black arrow) of epithelioid morphology is attached to the very loose spongy-like ECM of parenchymal compartment (red dashed arrow) (a), in contrast to the formation of discontinuous surface lining (black arrow) formed by a single row of cells of mesenchymal morphology; and migration of single cells into the voids of the scaffold (red arrows) in the dense ECM of stromal compartment (b). Diffuse cellular infiltration of a small isolated fragment of ECM (b, star). (c, d) Week 2. Diffuse cellular invasion (in the parenchymal compartment) versus clustering and formation of multi-row cellular linings of the surface of the scaffold (in the stromal compartment). (c) Mixed type ECM. Discontinuous single-row cell lining on the surface of the loose parenchymal ECM (black arrow), with penetration of discrete cells in depth (red dashed arrow). (d) ECM of the stromal compartment. Continuous multilayer cell lining on the ECM surfaces and cell cluster formation in sites with acute curvatures (black arrows). Cell permeation through a void in ECM and formation of cellular cord (red dashed arrows). (e, f) Week 3. Deep diffuse invasion in parenchymal compartment, cell clusters in the depth and spongy-like remodelling in stromal compartment; transformational changes of cellular morphology in both compartments. (e) Cells of the mixed epithelioid-mesenchymal phenotype diffusely invade parenchymal compartment of ECM (red dashed arrow). A DCL vascular element is surrounded by spongy-like matrix (black arrow), indicating massive remodelling of stromal ECM. Cell permeation through a void in the residual of stromal ECM, formation of a cellular cord (arrowhead). An acellular zone featuring tissue decay (secondary necrosis) (star). (f) Big fragment of stromal ECM. Surface cell linings were degrading, while cells increasingly penetrated ECM in depth, forming the clusters (red dashed arrow). An isolated ECM fragment was colonised by cells (black arrow). (g, h) Week 4. Massive diffuse colonization of the parenchymal compartment and in remodelled ECM of stromal compartment, fragmentation of dense residuals if stromal compartment ECM by large cellular clusters. (g) Massive invasion of polymorph cancer cells throughout the ECM. Remaining acellular remodelled ECM of stromal origin (black arrow). Paranecrotic area with disorganized loose ECM and a few cells (red dashed arrow). (h) Several fragments preserving dense structure of the stromal ECM were separated by cell clusters (arrows). No signs of cellular invasion in the fragment of decellularized fat tissue (ft). *Hematoxylin and eosin staining*. Scale bars: (a, b) 50 μm ; (c-h) 100 μm .

CHAPTER 7

Table 1. Morphological features of *in vitro* evolution of TEC.

Weeks	Morphological features	Parenchymal compartment	Stromal compartment
1	Cell number	Very low , ~1-2 cells per field of view at $\times 200$ magnification	Low, ~50 cells per field of view at $\times 200$ magnification
	Cell morphology	Epithelioid (cells have roundish shape) or intermediate mesenchymal-epithelioid (cells have voluminous spindle shape without cytoplasm protrusions)	Mesenchymal (cells acquire elongated shape; form cytoplasm protrusions and bridges)
	Cell distribution	Individual cells on the surface	Discontinuous single-cell linings on the surfaces
	Cell invasion	Discrete cells invade scaffolds for ≤ 50 μm in depth	Cells permeate into depth of the scaffolds through defects, cell-by-cell, ≤ 50 μm in depth, formation of small clusters in cul-de-sac areas
	ECM	As produced	Spongy-like matrix around cellular clusters
2	Total number of cells	Moderate, but lower than in the stromal compartment	Moderate to high
	Cell morphology	Epithelioid	Intermediate mesenchymal-epithelioid
	Cell distribution	Discontinuous surface cellular linings; absence of clusters	Continuous multi-row cellular linings on the exposed surfaces; Cell clusters on the curved surfaces
	Cell invasion	Diffuse invasion of individual cells into the depth of the scaffolds increases and reaches 150-200 μm	Discrete cells diffusely invade the ECM < 50 μm in depth, including DCL walls of large blood vessels; Cells penetrated to < 400 μm in depth through ECM voids
	ECM	Very light condensation	ECM loosening with no cells in the remodelled zones
3	Cell number	High	High
	Cell morphology	Epithelioid, mesenchymal and intermediate	Mesenchymal and intermediate mesenchymal-epithelioid
	Cell distribution	Single-cell surface linings; A network of spindle-like cells at the depth of 150-200 μm ; Relatively homogenous cell distribution	Degradation of surface linings into spotted-cell coatings; The deepest zones remain acellular; Small isolated fragments are totally colonized by dense cellular infiltrates; large cell clusters in ECM voids
	Cell invasion	Diffuse invasion depth > 800 μm	The surface zones are densely invaded by the cells up to 20-50 μm ; Clusters in the defects at the depth of 200-300 μm
	ECM	Very light condensation; formation of decay zones	Spongy-like transformation of 85% of dense vascular and septal stroma with blurring of the demarcation between the matrix types; formation of decay zones
4	Cell number	Very high	Very high
	Cell morphology	Predominantly epithelioid, highly polymorph, dedifferentiated	Intermediate mesenchymal-epithelioid and epithelioid
	Cell distribution	Dense cellular infiltrate throughout ECM; surface linings and clusters; 10% acellular zones	Surface linings and clusters; large clusters in the depth; 25% acellular zones
	Cell invasion	Entire ECM	Surfaces and < 400 μm in depth
	ECM	Very loose structure; zones of ECM decay around the clusters of cells	Spongy-like transformation of ECM, with remnants of muscular arterial walls: decay zones centred at cell clusters.

3.2. Dynamics of the cell growth in 3D TECs and 2D cultures of MDA-MB-231 cells *in vitro*

The main results of MTT assay performed for comparative analysis of cell growth in 2D and 3D *in vitro* cultures are summarised in Figure 4; the reference live microscopy observations of TECs and monolayer cultures of MDA-MB-231 cells are shown in Figure S6 in SI 3 and the detailed numerical results of MTT assay is included into Table S1 in SI 3. As it can be seen from the Figure 4 (a), in both types of the experimental settings the cellularity increased until the 3rd week of *in vitro* culture, and later, between 21st and 28th days it decreased in monolayer culture for approximately 20% (up to 2.1×10^6 cells per a sample) and for 9% in TECs (up to 3.7×10^5 cells per a sample). The differences between the numbers of the viable cells in 2D and 3D cultures were highly statistically significant at each observational time point during the whole experimental period ($p < 0.001$).

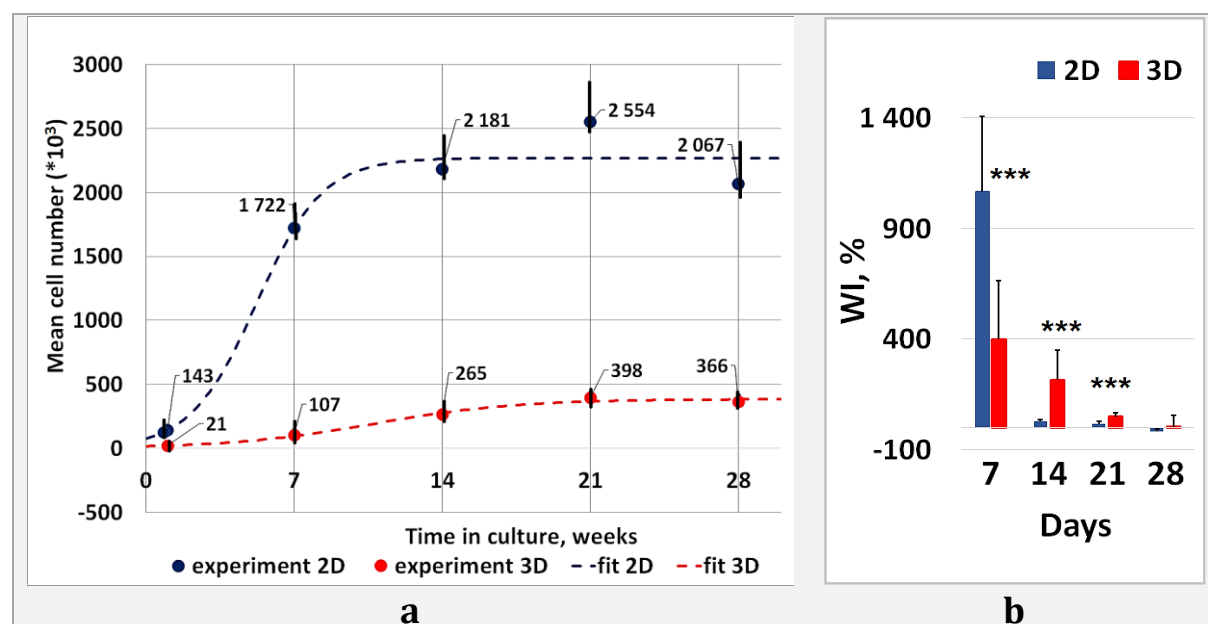


Figure 4. Cell growth in matching 2D and 3D *in vitro* cultures of MDA-MB-231 cells evaluated by MTT assay. (a) The numbers of cells obtained by normalization of the experimental values of the optical densities (OD) (labelled as “experiment 2D” and “experiment 3D”) and the well corresponding with them growth curves (fit 2D and fit 3D), reflecting the logistic fit of the data. (b) Weekly increment (WI) of cell numbers, normalized to 100%. Note that the growth in 3D culture conditions during 2nd and 3rd weeks is faster, than in the cell monolayer *in vitro* culture. Statistical significant differences between WIs in the matching 2D and 3D cultures were examined with U Manna-Whitney test and labelled as following: *** - $p < 0.001$. Error bars indicate CI_{95%} for the mean values on each graph.

Accordingly to the comparison of the absorbance values on the experimental day 1, the number of viable cells, successfully attached to the surface of chick embryo liver AOSSES, was equal to 14-16% of the population of the live cells in the matching 2D culture. After that the cells in 2D cell culture and in the TECs demonstrated strikingly different growth behaviour. During the first week of *in vitro* culture, the cells placed into 2D conditions exhibited the bursting growth, which was much faster than in 3D counterparts. However, during the next 2 weeks, the weekly increment of cellularity in the 3D TECs was much higher, than in 2D *in vitro* culture (Figure 4 (b)). These difference were of high statistical significance as well. Finally, the growth rates of cell populations were decreased, in comparison to the

CHAPTER 7

previous week, in the both types of the culture. The descending was less prominent in TECs, than in the monolayer model, but the difference was below the accepted critical level of statistical significance ($p > 0.05$).

In order to reveal the major trends in cell population dynamics in the matching 2D and 3D *in vitro* cultures of MDA-MB-231 cells, a number of conventional fitting models were tested. As a result, it was founded that a logistic growth model fits to the experimental data in the best way as it is shown by dashed lines in Figure 4 (a). In particular, a general logistic growth model with the following 3 parameters was applied to the data:

Cell density = $A/(1 + Be^{-Ct})$, where the time t was taken in days⁶³. The A represents the maximum cell density, and B and C define the growth rate. The model-based calculations also show that both the maximum cell density and the overall average growth rate were higher in the 2D cell culture compared to the 3D environment. The goodness of the fit was high ($r^2 = 0.99$ for both 2D and 3D experimental conditions), therefore a logistic growth model represents the cell growth accurately.

3.3. Cytotoxicity and cellular uptake of Dox and AMS-6-Dox in 3D TECs and 2D *in vitro* cultures of MDA-MB-231 cells

3.3.1. CHARACTERIZATION OF NANOPARTICLES

As-synthesised AMS-6 mesoporous silica nanoparticles were characterised by TEM and XRD, with detailed results presented in SI 4 (Figures S7, S9). The particle diameters ranged from 50 nm to 150 nm. They featured 3D-interconnected uniformly distributed cylindrical pores and ordered (Figure S8 in SI). Drug loading was confirmed by XRD and nitrogen adsorption/desorption isotherms (Figures S9-S11 in SI). Main peaks of the pore size of pristine AMS-6 and AMS-6-Dox samples were both centred at 3.81 nm (Figure S10 in SI 4), whereas the maximum pore volumes were measured 0.007 cm³/g and 0.002 cm³/g, respectively. No organic compounds were found by TGA measurements, which ruled out a possibility of the pore clogging with covalently bound propyl amine groups (Figure S12 in SI 4). The hydrodynamic diameters and zeta-potentials of the calcinated colloidal sample varied broadly from 90 to 400 nm in PBS and complete culture medium, respectively, as measured by DLS and presented in Table 2. A plot in Figure S13 in SI 4 shows the size distribution of pristine and drug-loaded AMS-6 nanoparticles. A considerable degree of aggregation was found in PBS and explained by the reduced repulsive surface potential of nanoparticles in ionic PBS solution, which was captured by the low values of the zeta-potentials. We speculate that the same conditions caused less aggregation in complete culture medium, because swiftly formed protein corona prevented the aggregation of pristine AMS-6 and drug-loaded AMS-6-Dox nanoparticles.

CHAPTER 7

Table 2. Results of DLS measurements of the samples of AMS-6 and AMS-6-Dox nanoparticles at 25 °C.

Sample	pH	DLS size, nm	Polydispersity index, $(D_w/D_m)^2$	Zeta-potential, mV
AMS-6 in PBS	7.2	396	0.544	-10.9
AMS-6-Dox in PBS	7.4	342	0.685	- 8.3
AMS-6 in CCM	7.2	142	1.000	-11.2
AMS-6-Dox in CCM	7.4	91	1.000	- 8.8

*CCM – complete culture medium; PBS – phosphate buffer saline.

3.3.2. RESULTS OF MTT ASSAY: CYTOTOXICITY OF DOX AND AMS-6-DOX IN 3D

TECs AND 2D IN VITRO CULTURES OF MDA-MB-231 CELLS

No cytotoxicity was found for the pristine AMS-6 nanoparticles in the concentration range from 0 to 250 µg/mL in 3D TECs and 2D cultures. The results of MTT assay performed in 2D and 3D TEC cultures incubated during 36 h in presence of molecular and nanoformulated Dox are shown in Figure 5, and details are provided in Figures S14-S17 in SI 5.

The cells appeared to be considerably more resilient to both molecular and nanoformulated Dox in 3D TEC cultures in comparison with 2D cultures, as it is shown in Figure 5 (a, b). The result was statistically significant for the concentration range 0.1 µg/mL to 10 µg/mL. At the same time, the experimental data did not show clear difference in the cellular response in dependence of drug delivery system such as Free Dox versus AMS-6-Dox nanoparticles in both 2D and 3D *in vitro* cultures (Figures S14, 15, and S17 in SI 5).

In order to predict to what extent the experimental data can be extrapolated to the general population, the IC₅₀ and EC₅₀ values were calculated using Eq. (3) (see 2.4.3.3). As it follows from the graph (Figure 5 (c)), the predicted values of the maximal effects were close to the experimental observations. EC₅₀ was found to be increased in 3D TECs treated with AMS-6-Dox, in comparison with the other groups. The IC₅₀ value of AMS-6-Dox was marginally greater than that of Dox in 2D cell cultures. IC₅₀ for the molecular Dox in 3D TECs was poorly predicted (Table S2 in SI 5). We speculate the cell developed drug resistance at the applied concentrations of Dox > 9 µg/mL, as it was observed experimentally by the decreased ratio of dead cells in 2D and 3D *in vitro* cultures after reaching of the higher cell death rates at the lower concentrations. Taken together, the fitted values of EC₅₀ and IC₅₀, for the first time, showed an unambiguous difference between the cell sensitivity to drugs in 2D and 3D biomimetic liver-specific 3D microenvironments.

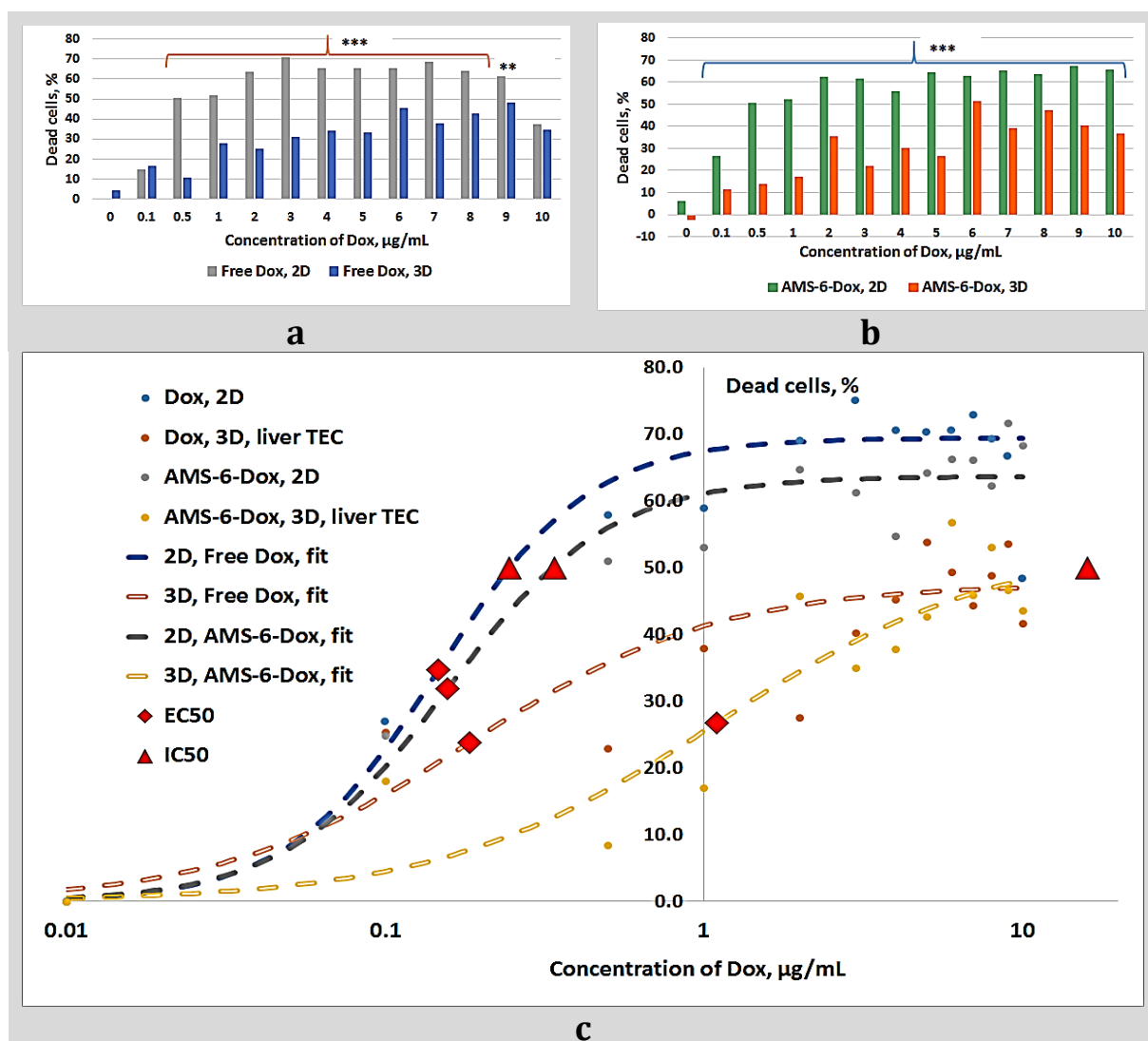


Figure 5. (a) Effect of free Dox on MDA-MB-231 cells in 2D (monolayer) and 3D (liver-specific TEC) *in vitro* cultures. (b) Effect of AMS-6-Dox on MDA-MB-231 cells in 2D (monolayer) and 3D (liver-specific TEC) *in vitro* cultures. The exposure time was 36 h for (a) and (b). (c) Fitting of the cytotoxicity data using Eq. (3).

3.4. Cellular uptake of Dox and AMS-6-Dox in 3D TECs and 2D *in vitro* cultures of MDA-MB-231 cells

The results of the evaluation of the cell and tissue uptake of Dox and AMS-6-Dox in 2D monolayer and 3D TEC cultures performed using laser-scanning confocal microscopy, are shown in Figure 6 and Figure S18 of SI 6 (for the control samples without Dox). In 2D cultures of MDA-MB-231 cells the fluorescent signal of free Dox and Dox originated from AMS-6-Dox nanoparticles was found in the cellular nuclei in strong association with chromatin structures. In contrast, in 3D *in vitro* cultures, free and nanoformulated Dox exhibited fluorescence distributed between the cell nuclei, the cytoplasm of the cells and ECM of TECs. Free Dox in 3D TECs induced a notable leakage from cell nuclei, resulting in the diffuse mixed DAPI and Dox fluorescence of ECM of the tissue samples. A number of well preserved, but swollen, cellular nuclei containing Dox applied as a molecular drug, were visible in depth of TECs. At the same time, the signal from Dox introduced into 3D cell cultures in the form of AMS-6-

CHAPTER 7

Dox nanoparticles, was mainly detected in the nuclei of the cells located at the surface of TEC, while in depth parts of the reconstructed tumors (> 50 μm in depth) only diffuse DAPI staining (i.e. leakage of nucleic acids from destroyed nuclei) in combination with very small Dox-positive cell debris fragments were found, indicating the destruction of the tumor. This allows us to conclude that the distribution and the cytotoxic effects of free and nanoformulated Dox are strongly influenced by liver-specific ECM microenvironment, and the method of Dox delivery in 3D engineered tumors modulates the therapeutic response in terms of the zone and the volume of the affected tissue.

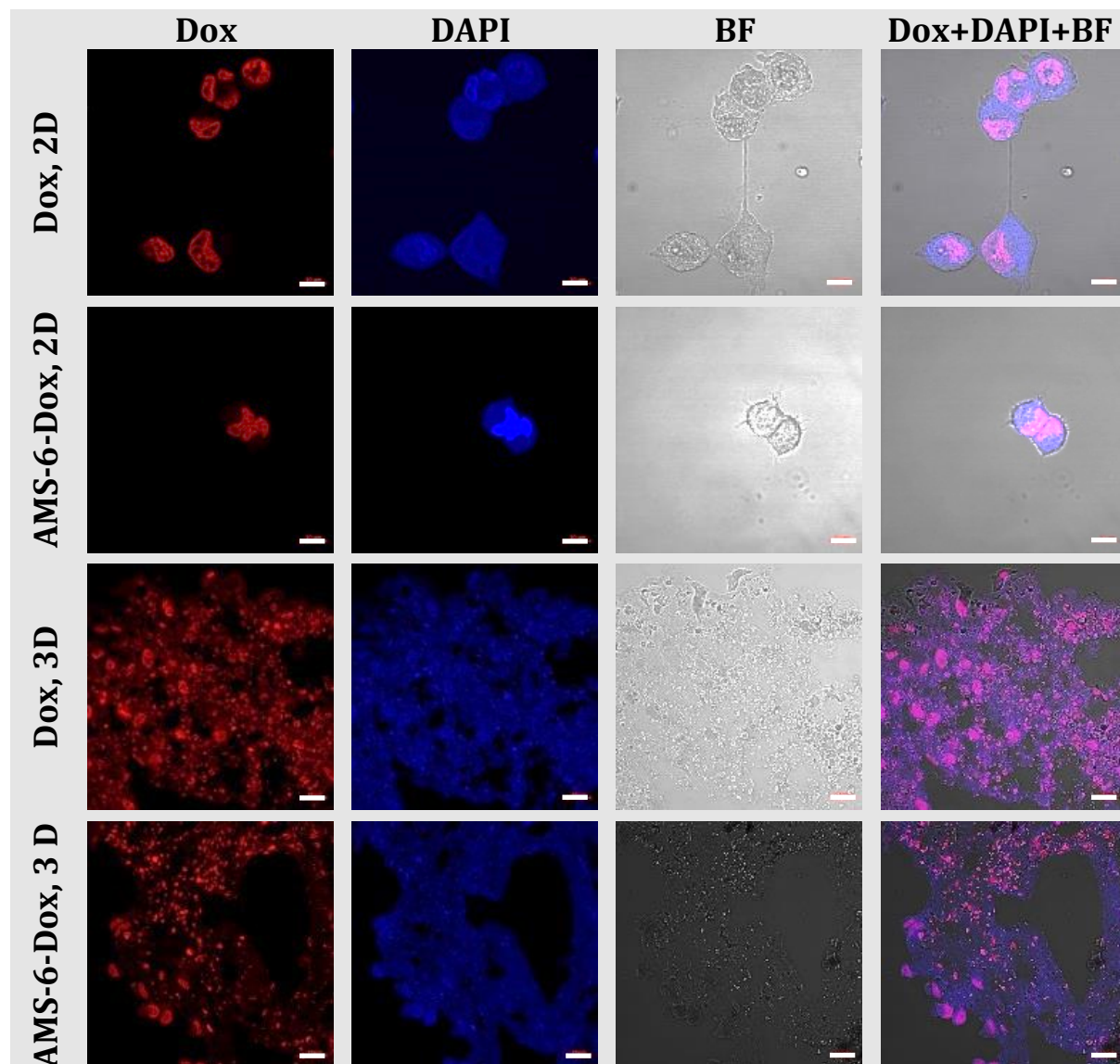


Figure 6. Confocal microscopy images 2D and 3D TECs *in vitro* cultures of MDA-MB-231 cells incubated with free Dox and AMS-6-Dox nanoparticles for 24 h. The intrinsic Dox fluorescence was registered in the red channel (Dox), the fluorescence staining of nuclei was done by DAPI (blue channel, DAPI). The control bright field (BF) images were taken for visualization of the tissue structures, and the combination of the mentioned types of images is used for colocalization of the signals of Dox and DAPI on the background of BF. 2D and 3D stand for 2D and 3D TEC *in vitro* cultures of MDA-MB-231 cells respectively. Note the absence of preserved cell nuclei in the depth of TEC treated with AMS-6-Dox nanoparticles, in comparison to TEC treated with free Dox. The applied concentration of Dox was 10 $\mu\text{g/mL}$. Scale bars: 10 μm (Dox, 2D; AMS-6-Dox, 2D); 20 μm (Dox, 3D; AMS-6-Dox, 3D).

3.5. Angiogenic potential of TECs and liver AOSSes in vivo

The results of CAM assay of angiogenic potential of 3D TECs, chick embryo-derived DCL liver AOSSes and MDA-MB-231 cells suspension xenografts are shown in Figure 7; and additional details can be also found in Figures S21 and S22 in SI 7. The most pronounced increase in the vascular density, branching and the spatial disorganization of blood vessels was observed on ED12 in CAMs grafted with TECs, in comparison to other groups. Convergence on the host blood vessels towards the graft (“spoke-wheel” pattern) was most visible in CAMs grafted with AOSSes and, to the a less degree, in CAMs grafted with TECs, but it was absent in other groups. Cellular xenografts initiated spatially irregular branching of the small diameter vessels, while in the native CAM the parallel large calibre blood vessels in combination with regularly arranged capillary meshes prevailed.

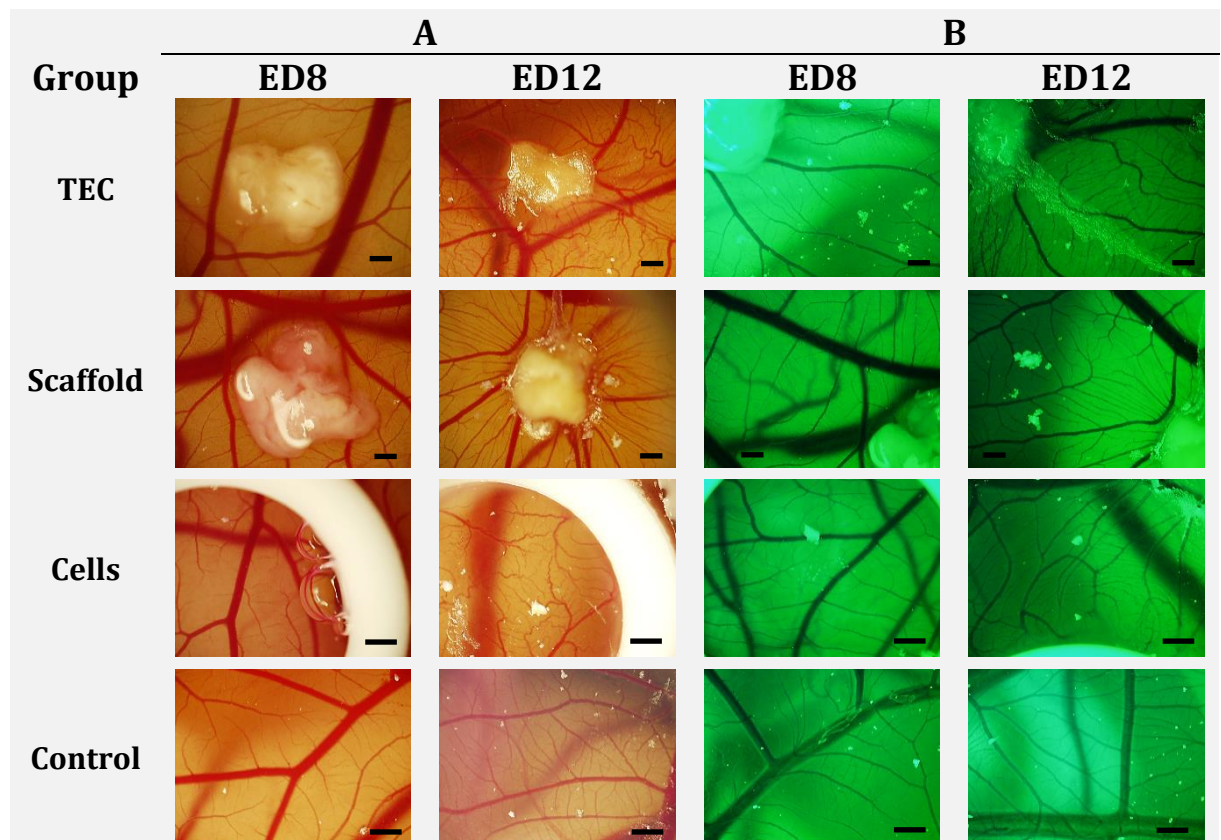


Figure 7. Angiogenic effects induced by 3D engineered tumors (*TEC*), liver AOSS (*Scaffold*), and suspension of MDA-MB-231 cells (*Cells*), grafted on chick embryo CAM, in comparison to the natural embryonic development of CAM vasculature (*Control*) during the period between ED8 and ED12. The images of CAM were obtained by a stereomicroscopy technique (see SI 7 for the details). (A) Unfiltered images of grafted areas of CAM in TEC, Scaffold and Cells groups, and a central part of control CAM obtained on ED8 and ED12. Cellular suspension (*Cells*) was placed inside the white rubber ring to avoid leakage. (B) The images of the areas located in vicinity to the grafted materials and at a periphery of the control CAM taken with blue light illumination and filtering from the same eggs as in (A). (A, B): The following changes of vascularization of CAM were observed on ED12 in comparison to ED8 in the studied groups: In TEC: sharply increased branching and vascular convergence pattern emerged around the grafted 3D model tumor; In Scaffold: a spoke-wheel pattern of blood vessels around the liver AOSS with less vessels' branching was found; In Cells: irregular spatial pattern on blood vessels with increased branching; In Control: development of regular pattern of parallel blood vessels of large diameter and branched small diameter vessels filling the gaps between them. Note that the blood vessels' pattern in TEC group resembled a combination of the spatial structures of the vasculature in Scaffold and Cell, indication possible cumulative effect of the cell and ECM-derived factors of TEC on angiogenesis in CAM.

Discussion

In this study, we demonstrated a new model of early metastasis of TNBC to the liver, created by tissue engineering methodology as *in vitro* 3D culture combining MDA-MB-231 cells and the acellular solid scaffolds, prepared from the whole livers of chick embryos by our original non-perfusion DCL method⁵⁵. As it is shown in the paper, the proposed model fills the gap between conventional cell culture *in vitro* and experimental oncology research in animals. It allows not only to maintain the engineered 3D tumors *in vitro* for long periods of time (at least 1 month), but also may be transferred *in vivo*, creating an unique possibility to observe intrinsic mechanisms of metastatic cancer outside and inside the body, and providing an affordable and sustainable platform for drug development and nanotheranostic research.

The scaffolding technique used in this model, as a DCL approach in general, provides a way for preservation of the organ-specific spatial structure and the major molecular components of ECM^{64,65}. Following this, we preferred to use the DCL liver scaffold assuming that DCL tissues may have notable advantages in biomimetic experimental reproduction of the hepatic microenvironment, in comparison to the scaffolds manufactured artificially from a few defined natural or synthetic materials. Indeed, the DCL methodology used in the current study allowed us to keep the principal components of the liver lobular ECM histoanatomy such as the parenchymal and stromal compartments. This resulted in a possibility to reveal the two distinct and earlier unknown strategies of TNBC metastatic colonization of the liver.

In general, the cells of TNBC demonstrated preferred initial attachment to the denser ECM of the stromal compartment and ~50-times less frequent adhesion to the ECM of the parenchymal compartment. Next, the cells associated with parenchymal compartment, exhibited mostly individual but very “efficient” invasion to the deeper parts of the scaffolds without histological signs of the significant remodelling of the matrix. At the same time, the cells spatially linked to the stromal compartment demonstrated a strong trend to formation of multicellular clusters, collective migration along the voids of the scaffold and overall smaller invasion depth. It was combined with sharp remodelling (loosening) of the dense ECM of former vascular walls and interlobular connective tissue sheaths. These observations testify in favour of the following hypothesis: *TNBC cells adopt a variable migration strategy when interacting with the liver ECM, where the ECM histoanatomical origin and density represent the key determinants.*

The features of the invasive behaviour of TNBC cells in parenchymal compartment may be attributed to so called amoeboid and, at the later stages, mesenchymal, *single-cell migration*⁶⁶. It is occurred via cell permeation through the small ECM voids, while inducing negligible proteolysis of ECM at the leading edge of the migrating cells. Then, it can be concluded that ECM of parenchymal compartment facilitated migration more than proliferation, at least for 2-3 weeks after the attachment of the first cells. The number of cells in the parenchymal compartment increased gradually. In contrast, the

CHAPTER 7

ECM of stromal compartment limited the cell penetration, while the proliferation rate was kept higher, in comparison to the cells in parenchymal zone, until the remodelling of the ECM after approximately 2-3 weeks in culture. The stromal compartment of the liver ECM initially was invaded by the cohorts of cancer cells⁶⁶, therefore, indicating *collective cell migration* as the early mechanism of colonization within this type of ECM. Later, after significant remodelling of the ECM of stromal compartment resulted in decrease of its density, the cells associated with the both compartments exhibited the fluctuating changes of their morphology and behaviour between the epithelioid and mesenchymal phenotypes and demonstrated similar proliferation rates. Earlier it was confirmed, that the link between the amoeboid and collective migratory modes and the characteristic molecular markers and cellular morphology implies reversible transitions between mesenchymal and epithelial phenotypes⁶⁷. We anticipate that the mesenchymal-epithelial transition (MET) took place in the stromal compartment of the liver ECM following the matrix remodelling and result in change of the migratory strategy from the collective to the single-cell mode. These observations are in concert with the results, showing that the epithelial-mesenchymal transition of MDA-MB-231 cells co-cultured with hepatocytes was arrested and reversed to the MET⁶⁸. This led us to the conclusion that *the single-cell invasion mechanism and not the collective migrations, is a predominant resulting strategy defining the metastatic colonization of the entire liver ECM*, despite the fact that the initial distribution of the cancer cells attachment and numbers is shifter towards the cellular clusters and linings formed in the association with the stromal compartment.

It is important to emphasize that the parenchymal compartment of the DCL liver scaffolds, following the organ-specific histology (see SI 2), can be formed only by the residuals of Disse's space, which is known as a place of primary contact between the liver tissue and extravasating cancer cells^{16, 20, 21}. Our observations of the leading role of the cells attached and invading the parenchymal compartment of the DCL liver in development of the metastatic colony are in a good logical agreement with this fact. At the same time, taking into account our results indicating that these cells move individually, and the migratory activity prevails over the proliferation, it could be reasonable to consider adding of the cytostatic chemotherapeutic strategies against secondary TNBC in the liver with the methods specifically controlling the motility of the cells. This idea is indirectly supported by the recent data indicating that MDA-MB-231 cells are able to acquire the drug resistance by employing the cellular migration along the concentration gradient of doxorubicin and surviving more at the higher local dose of the drug⁶⁹. In contrast, the inhibition of proliferation may be more significant to tame the cancer aggression within the stromal compartment of the liver ECM. This may be significant also in terms of the metastatic triggering effect of surgical treatment⁷⁰ of the secondary TNBC in the liver, which normally results in a trauma of the structures related to the stromal compartment. Therefore, the surgery may create an additional access window for the circulating cancer cells to the liver and initiate the massive proliferation of the TNBC cells approaching the stromal compartment. So, it is reasonable to

CHAPTER 7

suppose that the operative treatment of TNBC metastases to the liver may require a kind of local cytostatic chemotherapy support.

The current study of the liver colonization by TNBC cells has some obvious limitations. Firstly, we have not yet examined the biochemical and biophysical signalling cues contributing to the colonization in different compartments of the liver ECM. However, taking into account the distribution of the ECM components between the parenchymal and stromal compartments, we can suppose that the most possible candidatures to be a differentiating ligands are the basement membranes (laminin) and two glycoproteins, such as fibronectin and tenascin. Fibronectin is abundant along the Disse's spaces, while laminin and tenascin are almost absent there¹⁹. In addition, it has been recently shown that in 3D matrices, in contrast to the monolayer cultures, cancer cells prefer to migrate towards the less stiffer and more porous substrates, when the other parameters like the ECM ligand densities are equal⁷¹. This can explain the more efficient colonization of the parenchymal compartment of the liver ECM. Despite the another limitation, stemming from the fact that the presented tissue engineering model does not include any hepatic cells, comprises only a single phenotype of the breast cancer cells, and not perfused by blood, we believe, that it may be considered as an initial step in reconstruction of the puzzling process of the secondary organ metastatic colonization.

Several important facts and concepts emerged as a result of comparisons of TNBC cells' behaviour and responses between 2D and 3D (TEC) *in vitro* cultures of MDA-MB-231 cells. In particular, using a modified MTT assay we revealed the different cell population dynamics in the two studied types of the *in vitro* culture systems. The cells in monolayer cultures attached to the plastic substrate much more efficiently, than to the DCL liver scaffolds. However, after first week burst of growth, the cell population in 2D *in vitro* cultures was stagnated and even decreased until the end of the one-month observation, while in 3D TECs the growth of cell density was steadily increasing during the first 3 weeks and later did not change significantly. The logistic nature of the cell population growth in both types of the TNBC cell cultures was confirmed in this study by mathematical modelling, being consistent with the growth model of breast carcinomas revealed by the analysis of the large database of real clinical cases⁷². The logistic growth implies the cells to experience lack of some resources at the certain time points⁷³. The 2D cell cultures almost stopped growing after 1 week *in vitro*. This is, probably, not because of any metabolic deficiencies as the cultural media was regularly changed, but due to reaching the maximal cell attachment capacity of the wells (accordingly to the manufacturer protocol, the normal cell yield of each well of these plates is about 1.9×10^5 cells, which should be reached by the tested culture on the day 2 or 3 of the experiment); next the cells start to form dense overpopulated layer and multicellular aggregates on the bottom of the well (see SI 3, Figure S6 (b)). Lack of the attachment sites could not be the case for the TECs because of the initially smaller numbers of the attached cells, and because of the availability of a large surface area in the porous ECM scaffold, which also can be additionally remodelled. Then, some inhibition of cell growth, observed after 3 weeks of *in vitro* culture of TECs, is most probably due to metabolic conditions. Hypoxia is the most expectable factor to limit the growth of

CHAPTER 7

cells in 3D *in vitro* cultures⁷⁴. This idea is in agreement with our histological observations of secondary necrotic areas forming at the late stages of the TECs *in vitro* development, which are similar to the formation of the necrotic core in typical 3D multicellular spheroid cultures.

Another interesting finding resulted from this study is that the sensitivity of TNBC cells to chemotherapeutic drug doxorubicin in free and nanoformulated forms is strongly compromised by the liver-specific ECM in TECs. This observation is in agreement with the data published earlier and indicating that the additional signalling inputs from 3D microenvironment and ECM ligands can lead to decreased responses to the chemotherapeutic challenges⁴⁴. Experimentally, we did not find any significant therapeutic advantage of free Dox or AMS-6-Dox nanoparticles, comparing their effects both in 2D and 3D cell cultures within the applied Dox concentration range up to 10 µg/mL. However, our mathematical modelling of the drug-dose-effect relationship indicated on the possible better therapeutic efficiency of the nanoformulated Dox in 3D TECs mimicking the real tumor conditions, in comparison to free Dox, as only application of the Dox-loaded nanoparticles predicts reaching the IC50 level at the concentration of loaded Dox of ~16 µg/mL, while free Dox curve never touches this limit. We would prefer to do not consider the obtained results regarding the therapeutic efficiency of AMS-6-Dox nanoparticles against TNBC hepatic metastases as a direct indications of the needed doses etc., because the particles might require additional studies (first of the analysis of the Dox release kinetics) and optimization (like development of the nanovehicles with controllable drug release). To our opinion, this results rather demonstrate the feasibility of the proposed tumor engineering model for nanomedical research. This is also supported by the results of the evaluation of the uptake of free and nanoformulated Dox in 2D and 3D TNBC *in vitro* models, which allowed us to prove that the studies on 3D tumor TECs may be added with bioimaging experiments, which are especially important for the development of nanotheranostics. In current study, particularly, the differential effect of the drug delivery method (the free drug versus drug-loaded mesoporous silica nanoparticles) was observed in 2D *in vitro* cell cultures and in TECs. While in monolayer models of TNBC the uptake and intracellular distribution of free and nanoformulated was very similar, in 3D model tumors AMS-6-Dox nanoparticles killed cells in the depth of TECs almost totally, in contrast to the free drug, which accumulated in the cell nuclei but did not induce the tumor decay. We believe that this difference may occur because of the potentiation of the cytotoxic effect of Dox in depth of TECs by hypoxia in combination with a somehow changes kinetics of drug release from the nanoparticles.

Finally, we validated the proposed tumor engineering model *in vivo* by angiogenic assay on chick embryo CAM basing on the generally accepted understanding of angiogenic switch as a key limiting process in transition between micro- and macrometastatic states. It was shown that the grafted TECs induce the strongest angiogenic response in CAM, in comparison to the natural embryonic development and the reactions induced solely by the TECs' components such as MDA-MB-231 cells and liver AOSSes applied in the equivalent amounts. In contrast to natural embryonic angiogenesis, which occurs within the studied incubation age mainly by intussusceptive microvascular growth (i.e. splitting of the

CHAPTER 7

existing capillaries along the blood vessel axis)⁷⁵, the grafted tumors stimulated extensive branching of the host blood vessels, indicating that sprouting angiogenesis was taking place. As the sprouting angiogenesis is known as the main mechanism involved in angiogenic switch in metastatic progression^{1,76}, it seems trustable to say that the presented in the study engineered models of early TNBC metastases to the liver behave in a relevant way and demonstrate an important hallmark of a metastatic cancer. In addition, we demonstrated the feasibility of the same in vivo experimental approach for real-time observation of the interactions between the 3D TNBC models grafted on CAM and such a promising nanotheranostic agent as upconversion nanoparticles (see SI 8).

In conclusion, it's worth to mention, that the presented study shows some practical experimental advances. It is known that DCL tissues of the same organ have negligible cross-species differences in terms of their structure and composition, which makes it possible to use them even as xenotransplants for the purposes of regenerative medicine⁷⁷. This gave us a chance to use the chick embryo liver for scaffolds preparation, having in mind a number of benefits related to this organ source. Chick embryo, or poultry experimental platform allows more affordable costs and the simplicity of the animal care conditions, high level of standardization and the relative ease of animal ethics clearance, in comparison to the mammalian models. The proposed simplified immersion-agitation whole-organ DCL technique facilitates obtaining the whole-organ scaffolds without use of cumbersome perfusion bioreactor setups. The whole-organ DCL scaffolds may be cut for the smaller fragments, still preserving the organ specificity of spatial and chemical organization of the ECM, but allowing high-throughput assays. In our pilot experiments we confirmed that this methodology is highly universal and may be applied to a variety of the chick embryo organs and cell lines (the unpublished data). We also considering the idea that some possible other advantages may originate from the use of embryonic and not mature tissues and organs for tissue engineering tasks. However, this require further investigations.

Conclusion

We introduced an original tissue engineering model of early TNBC metastasis to the liver, based on sustainable and affordable chick embryo experimental platform. Using this model, liver ECM was found to be the key determinant of the colonization pattern employed by TNBC cells. Cells cultured in the 3D liver-specific matrix demonstrated an increased resilience to free and nanoformulated doxorubicin. The biological relevance of the model was proved in vivo as an ability of the engineered tumors to induce angiogenic switch in the host tissue. The feasibility of the proposed approach holds promise for cancer biology, drug development and nanobiotechnology. We believe that the introduced model is extendable for modelling of other types of metastatic cancers and for the development of more complex tumor TECs.

Acknowledgements

Many useful discussions, help with the early stages of this work and critical reviewing of the histological results by Professor Anatoly Shekhter (I.M. Sechenov First Moscow State Medical University) are gratefully acknowledged. We are thankful to Ms. Larisa Grivans for her excellent help with scientific illustrations. The gift of fertilized chicken eggs from Baiada Poultry PTY Ltd is thankfully appreciated. We would like to express our gratitude to the ARC Centre of Nanoscale Biophotonics (CNBP) for funding of the part of research expenses of the study. Ms. Anna Guller thanks to Macquarie University for providing her iMQRes scholarship.

References

1. D. Hanahan, J. Folkman, Patterns and emerging mechanisms of the angiogenic switch during tumorigenesis, *Cell* 86(3) (1996) 353-64.
2. V. Baeriswyl, G. Christofori, The angiogenic switch in carcinogenesis, *Semin Cancer Biol* 19(5) (2009) 329-37.
3. D.X. Nguyen, P.D. Bos, J. Massague, Metastasis: from dissemination to organ-specific colonization, *Nature Reviews Cancer* 9(4) (2009) 274-U65.
4. A.W. Lambert, D.R. Pattabiraman, R.A. Weinberg, Emerging Biological Principles of Metastasis, *Cell* 168(4) (2017) 670-691.
6. W.D. Foulkes, I.E. Smith, J.S. Reis-Filho, Triple-negative breast cancer, *N Engl J Med* 363(20) (2010) 1938-48.
7. L. Carey, E. Winer, G. Viale, D. Cameron, L. Gianni, Triple-negative breast cancer: disease entity or title of convenience?, *Nat Rev Clin Oncol* 7(12) (2010) 683-92.
8. R. Dent, M. Trudeau, K.I. Pritchard, W.M. Hanna, H.K. Kahn, C.A. Sawka, L.A. Lickley, E. Rawlinson, P. Sun, S.A. Narod, Triple-negative breast cancer: clinical features and patterns of recurrence, *Clin Cancer Res* 13(15 Pt 1) (2007) 4429-34.
9. G. Lorusso, C. Ruegg, New insights into the mechanisms of organ-specific breast cancer metastasis, *Semin Cancer Biol* 22(3) (2012) 226-33.
10. N.U. Lin, E. Claus, J. Sohl, A.R. Razzak, A. Arnaout, E.P. Winer, Sites of distant recurrence and clinical outcomes in patients with metastatic triple-negative breast cancer: high incidence of central nervous system metastases, *Cancer* 113(10) (2008) 2638-45.
11. R. Dent, W.M. Hanna, M. Trudeau, E. Rawlinson, P. Sun, S.A. Narod, Pattern of metastatic spread in triple-negative breast cancer, *Breast Cancer Res Treat* 115(2) (2009) 423-8.
12. K. Jin, W. Gao, Y. Lu, H. Lan, L. Teng, F. Cao, Mechanisms regulating colorectal cancer cell metastasis into liver (Review), *Oncology letters* 3(1) (2012) 11-15.
13. R. Ma, Y. Feng, S. Lin, J. Chen, H. Lin, X. Liang, H. Zheng, X. Cai, Mechanisms involved in breast cancer liver metastasis, *Journal of Translational Medicine* 13 (2015) 64.
14. L.M. Reid, A.S. Fiorino, S.H. Sigal, S. Brill, P.A. Holst, Extracellular matrix gradients in the space of Disse: relevance to liver biology, *Hepatology* 15(6) (1992) 1198-203.
15. R. McClelland, E. Wauthier, J. Uronis, L. Reid, Gradients in the liver's extracellular matrix chemistry from periportal to pericentral zones: influence on human hepatic progenitors, *Tissue engineering. Part A* 14(1) (2008) 59-70.
16. F. Rosenow, R. Ossig, D. Thormeyer, P. Gasmann, K. Schlüter, G. Brunner, J. Haier, J.A. Eble, Integrins as Antimetastatic Targets of RGD-Independent Snake Venom Components in Liver Metastasis, *Neoplasia (New York, N.Y.)* 10(2) (2008) 168-176.
17. J. Haier, An Intravital Model to Monitor Steps of Metastatic Tumor Cell Adhesion Within the Hepatic Microcirculation, *Journal of Gastrointestinal Surgery* 7(4) (2003) 507-515.
18. E. Roos, K.P. Dingemans, I.V. Van de Pavert, M.A. Van den Bergh-Weerman, Mammary-carcinoma cells in mouse liver: infiltration of liver tissue and interaction with Kupffer cells, *British journal of cancer* 38(1) (1978) 88-99.

CHAPTER 7

19. A. Martinez-Hernandez, P.S. Amenta, The extracellular matrix in hepatic regeneration, *FASEB journal : official publication of the Federation of American Societies for Experimental Biology* 9(14) (1995) 1401-10.
20. S. Tabaries, Z. Dong, M. Annis, A. Omeroglu, F. Pepin, V. Ouellet, C. Russo, M. Hassanain, P. Metrakos, Z. Diaz, Claudin-2 is selectively enriched in and promotes the formation of breast cancer liver metastases through engagement of integrin complexes, *Oncogene* 30(11) (2011) 1318-1328.
21. S. Ishii, T. Mizoi, K. Kawano, O. Cay, P. Thomas, A. Nachman, R. Ford, Y. Shoji, J.B. Kruskal, G. Steele, J.M. Jessup, Implantation of human colorectal carcinoma cells in the liver studied by in vivo fluorescence videomicroscopy, *Clinical & experimental metastasis* 14(2) (1996) 153-164.
22. I.J. Fidler, The pathogenesis of cancer metastasis: the 'seed and soil' hypothesis revisited, *Nat Rev Cancer* 3(6) (2003) 453-8.
23. D. Barkan, J.E. Green, A.F. Chambers, Extracellular matrix: a gatekeeper in the transition from dormancy to metastatic growth, *Eur J Cancer* 46(7) (2010) 1181-8.
24. B.R. Seo, P. Delnero, C. Fischbach, *In vitro* models of tumor vessels and matrix: engineering approaches to investigate transport limitations and drug delivery in cancer, *Adv Drug Deliv Rev* 69-70 (2014) 205-16.
25. B.P. Schneider, E.P. Winer, W.D. Foulkes, J. Garber, C.M. Perou, A. Richardson, G.W. Sledge, L.A. Carey, Triple-negative breast cancer: risk factors to potential targets, *Clin Cancer Res* 14(24) (2008) 8010-8.
26. S.L. Davis, S.G. Eckhardt, J.J. Tentler, J.R. Diamond, Triple-negative breast cancer: bridging the gap from cancer genomics to predictive biomarkers, *Ther Adv Med Oncol* 6(3) (2014) 88-100.
27. E.A. Rakha, S. Chan, Metastatic triple-negative breast cancer, *Clin Oncol (R Coll Radiol)* 23(9) (2011) 587-600.
28. F. Kassam, K. Enright, R. Dent, G. Dranitsaris, J. Myers, C. Flynn, M. Fralick, R. Kumar, M. Clemons, Survival Outcomes for Patients with Metastatic Triple-Negative Breast Cancer: Implications for Clinical Practice and Trial Design, *Clinical Breast Cancer* 9(1) (2009) 29-33.
29. B.D. Lehmann, J.A. Bauer, X. Chen, M.E. Sanders, A.B. Chakravarthy, Y. Shyr, J.A. Pietersen, Identification of human triple-negative breast cancer subtypes and preclinical models for selection of targeted therapies, *J Clin Invest* 121(7) (2011) 2750-67.
30. D.L. Holliday, V. Speirs, Choosing the right cell line for breast cancer research, *Breast Cancer Res* 13(4) (2011) 215.
31. C.P. Huang, J. Lu, H. Seon, A.P. Lee, L.A. Flanagan, H.Y. Kim, A.J. Putnam, N.L. Jeon, Engineering microscale cellular niches for three-dimensional multicellular co-cultures, *Lab Chip* 9(12) (2009) 1740-8.
32. K. Wolf, P. Friedl, Mapping proteolytic cancer cell-extracellular matrix interfaces, *Clinical & experimental metastasis* 26(4) (2009) 289-98.
33. W.J. Polacheck, J.L. Charest, R.D. Kamm, Interstitial flow influences direction of tumor cell migration through competing mechanisms, *Proceedings of the National Academy of Sciences of the United States of America* 108(27) (2011) 11115-20.
34. A. Guzman, M.J. Ziperstein, L.J. Kaufman, The effect of fibrillar matrix architecture on tumor cell invasion of physically challenging environments, *Biomaterials* 35(25) (2014) 6954-63.
35. E. Caldas-Lopes, L. Cerchietti, J.H. Ahn, C.C. Clement, A.I. Robles, A. Rodina, K. Moulick, T. Taldone, A. Gozman, Y. Guo, N. Wu, E. de Stanchina, J. White, S.S. Gross, Y. Ma, L. Varticovski, A. Melnick, G. Chiosis, Hsp90 inhibitor PU-H71, a multimodal inhibitor of malignancy, induces complete responses in triple-negative breast cancer models, *Proc Natl Acad Sci U S A* 106(20) (2009) 8368-73.
36. S. Aroui, N. Ram, F. Appaix, M. Ronjat, A. Kenani, F. Pirollet, M. De Waard, Maurocalcine as a non toxic drug carrier overcomes doxorubicin resistance in the cancer cell line MDA-MB 231, *Pharm Res* 26(4) (2009) 836-45.
37. E.M. Goldblatt, E.R. Gentry, M.J. Fox, S.M. Gryaznov, C. Shen, B.S. Herbert, The telomerase template antagonist GRN163L alters MDA-MB-231 breast cancer cell morphology, inhibits growth, and augments the effects of paclitaxel, *Mol Cancer Ther* 8(7) (2009) 2027-35.
38. H. Zhou, B. Zhang, J. Zheng, M. Yu, T. Zhou, K. Zhao, Y. Jia, X. Gao, C. Chen, T. Wei, The inhibition of migration and invasion of cancer cells by graphene via the impairment of mitochondrial respiration, *Biomaterials* 35(5) (2014) 1597-607.
39. H. Meng, G. Xing, E. Blanco, Y. Song, L. Zhao, B. Sun, X. Li, P.C. Wang, A. Korotcov, W. Li, X.J. Liang, C. Chen, H. Yuan, F. Zhao, Z. Chen, T. Sun, Z. Chai, M. Ferrari, Y. Zhao, Gadolinium metallofullerenol nanoparticles inhibit cancer metastasis through matrix metalloproteinase inhibition: imprisoning instead of poisoning cancer cells, *Nanomedicine* 8(2) (2012) 136-46.

CHAPTER 7

40. B.A. Othman, C. Greenwood, A.F. Abuelela, A.A. Bharath, S. Chen, I. Theodorou, T. Douglas, M. Uchida, M. Ryan, J.S. Merzaban, A.E. Porter, Correlative Light-Electron Microscopy Shows RGD-Targeted ZnO Nanoparticles Dissolve in the Intracellular Environment of Triple Negative Breast Cancer Cells and Cause Apoptosis with Intratumor Heterogeneity, *Advanced healthcare materials* (2016) n/a-n/a.
41. K.M. Yamada, E. Cukierman, Modeling tissue morphogenesis and cancer in 3D, *Cell* 130(4) (2007) 601-10.
42. M.C. Cox, L.M. Reese, L.R. Bickford, S.S. Verbridge, Toward the Broad Adoption of 3D Tumor Models in the Cancer Drug Pipeline, *ACS Biomaterials Science & Engineering* 1(10) (2015) 877-894.
43. D.W. Hutmacher, R.E. Horch, D. Loessner, S. Rizzi, S. Sieh, J.C. Reichert, J.A. Clements, J.P. Beier, A. Arkudas, O. Bleiziffer, Translating tissue engineering technology platforms into cancer research, *Journal of cellular and molecular medicine* 13(8a) (2009) 1417-1427.
44. C. Fischbach, R. Chen, T. Matsumoto, T. Schmelzle, J.S. Brugge, P.J. Polverini, D.J. Mooney, Engineering tumors with 3D scaffolds, *Nat Methods* 4(10) (2007) 855-60.
45. C.Y. Tay, M.S. Muthu, S.L. Chia, K.T. Nguyen, S.-S. Feng, D.T. Leong, Reality Check for Nanomaterial-Mediated Therapy with 3D Biomimetic Culture Systems, *Advanced Functional Materials* 26(23) (2016) 4046-4065.
46. J.A. Hickman, R. Graeser, R. de Hoogt, S. Vidic, C. Brito, M. Gutekunst, H. van der Kuip, I.P. Consortium, Three-dimensional models of cancer for pharmacology and cancer cell biology: capturing tumor complexity *in vitro/ex vivo*, *Biotechnol J* 9(9) (2014) 1115-28.
47. L. Thibaudau, A.V. Taubenberger, B.M. Holzapfel, V.M. Quent, T. Fuehrmann, P. Hesami, T.D. Brown, P.D. Dalton, C.A. Power, B.G. Hollier, D.W. Hutmacher, A tissue-engineered humanized xenograft model of human breast cancer metastasis to bone, *Dis Model Mech* 7(2) (2014) 299-309.
48. F.P. Seib, J.E. Berry, Y. Shiozawa, R.S. Taichman, D.L. Kaplan, Tissue engineering a surrogate niche for metastatic cancer cells, *Biomaterials* 51 (2015) 313-9.
49. G. Xiong, T.J. Flynn, J. Chen, C. Trinkle, R. Xu, Development of an *ex vivo* breast cancer lung colonization model utilizing a decellularized lung matrix, *Integrative biology : quantitative biosciences from nano to macro* 7(12) (2015) 1518-25.
50. D.S. Tan, C. Marchio, R.L. Jones, K. Savage, I.E. Smith, M. Dowsett, J.S. Reis-Filho, Triple negative breast cancer: molecular profiling and prognostic impact in adjuvant anthracycline-treated patients, *Breast Cancer Res Treat* 111(1) (2008) 27-44.
51. S. Nie, Y. Xing, G.J. Kim, J.W. Simons, Nanotechnology applications in cancer, *Annual review of biomedical engineering* 9(1) (2007) 257-88.
52. D.A. Scheinberg, C.H. Villa, F.E. Escorcía, M.R. McDevitt, Conscripts of the infinite armada: systemic cancer therapy using nanomaterials, *Nat Rev Clin Oncol* 7(5) (2010) 266-276.
53. C. Argyo, V. Weiss, C. Bräuchle, T. Bein, Multifunctional Mesoporous Silica Nanoparticles as a Universal Platform for Drug Delivery, *Chemistry of Materials* 26(1) (2014) 435-451.
54. J.E. Lee, N. Lee, T. Kim, J. Kim, T. Hyeon, Multifunctional mesoporous silica nanocomposite nanoparticles for theranostic applications, *Accounts of chemical research* 44(10) (2011) 893-902.
55. A. Guller, I. Trusova, E. Petersen, A. Shekhter, A. Kurkov, Y. Qian, A. Zvyagin, Acellular organ scaffolds for tumor tissue engineering, *SPIE Micro+Nano Materials, Devices, and Systems* 9668 (2015) 96684G-96684G-9.
56. D. Ribatti, M.T. Conconi, B. Nico, S. Baiguera, P. Corsi, P.P. Parnigotto, G.G. Nussdorfer, Angiogenic response induced by acellular brain scaffolds grafted onto the chick embryo chorioallantoic membrane, *Brain research* 989(1) (2003) 9-15.
57. Hanahan, D. and R. A. Weinberg (2011). "Hallmarks of cancer: the next generation." *Cell* 144(5): 646-674.
58. T. Mosmann, Rapid colorimetric assay for cellular growth and survival: application to proliferation and cytotoxicity assays, *Journal of immunological methods* 65(1-2) (1983) 55-63.
59. A.E. Garcia-Bennett, K. Miyasaka, O. Terasaki, S. Che, Structural Solution of Mesocaged Material AMS-8, *Chemistry of Materials* 16(19) (2004) 3597-3605.
60. A.E. Garcia-Bennett, O. Terasaki, S. Che, T. Tatsumi, Structural Investigations of AMS-n Mesoporous Materials by Transmission Electron Microscopy, *Chemistry of Materials* 16(5) (2004) 813-821.
61. S. Che, A.E. Garcia-Bennett, T. Yokoi, K. Sakamoto, H. Kunieda, O. Terasaki, T. Tatsumi, A novel anionic surfactant templating route for synthesizing mesoporous silica with unique structure, *Nat Mater* 2(12) (2003) 801-5.

CHAPTER 7

62. J. Haycock, 3D cell culture: Methods and Protocols, in: J.W. Haycock (Ed.) *Methods in Molecular Biology* 695, Humana Press, New York, 2011, p. 343.
63. C.T. Goudar, K. Joeris, K.B. Konstantinov, J.M. Piret, Logistic equations effectively model Mammalian cell batch and fed-batch kinetics by logically constraining the fit, *Biotechnol Prog* 21(4) (2005) 1109-18.
64. P.M. Crapo, T.W. Gilbert, S.F. Badylak, An overview of tissue and whole organ decellularization processes, *Biomaterials* 32(12) (2011) 3233-43.
65. D.M. Faulk, J.D. Wildemann, S.F. Badylak, Decellularization and cell seeding of whole liver biologic scaffolds composed of extracellular matrix, *J Clin Exp Hepatol* 5(1) (2015) 69-80.
66. P. Friedl, K. Wolf, Tumour-cell invasion and migration: diversity and escape mechanisms, *Nat Rev Cancer* 3(5) (2003) 362-74.
67. P. Friedl, Prespecification and plasticity: shifting mechanisms of cell migration, *Curr Opin Cell Biol* 16(1) (2004) 14-23.
68. Y.L. Chao, C.R. Shepard, A. Wells, Breast carcinoma cells re-express E-cadherin during mesenchymal to epithelial reverting transition, *Molecular cancer* 9(1) (2010) 179.
69. A. Wu, K. Loughback, G. Lambert, L. Estevez-Salmeron, T.D. Tlsty, R.H. Austin, J.C. Sturm, Cell motility and drug gradients in the emergence of resistance to chemotherapy, *Proceedings of the National Academy of Sciences of the United States of America* 110(40) (2013) 16103-8.
70. S. Tohme, R.L. Simmons, A. Tsung, Surgery for Cancer: A Trigger for Metastases, *Cancer Res* 77(7) (2017) 1548-1552.
71. M.H. Zaman, L.M. Trapani, A.L. Sieminski, D. Mackellar, H. Gong, R.D. Kamm, A. Wells, D.A. Lauffenburger, P. Matsudaira, Migration of tumor cells in 3D matrices is governed by matrix stiffness along with cell-matrix adhesion and proteolysis, *Proceedings of the National Academy of Sciences of the United States of America* 103(29) (2006) 10889-94.
72. J.A. Spratt, D. von Fournier, J.S. Spratt, E.E. Weber, Decelerating growth and human breast cancer, *Cancer* 71(6) (1993) 2013-9.
73. A. Tsoularis, J. Wallace, Analysis of logistic growth models, *Math Biosci* 179(1) (2002) 21-55.
74. M. Singh, S. Mukundan, M. Jaramillo, S. Oesterreich, S. Sant, Three-Dimensional Breast Cancer Models Mimic Hallmarks of Size-Induced Tumor Progression, *Cancer Res* 76(13) (2016) 3732-43.
75. P. Schlatter, M.F. Konig, L.M. Karlsson, P.H. Burri, Quantitative study of intussusceptive capillary growth in the chorioallantoic membrane (CAM) of the chicken embryo, *Microvascular research* 54(1) (1997) 65-73.
76. F. Hillen, A.W. Griffioen, Tumour vascularization: sprouting angiogenesis and beyond, *Cancer Metastasis Rev* 26(3-4) (2007) 489-502.
77. S.F. Badylak, Decellularized allogeneic and xenogeneic tissue as a bioscaffold for regenerative medicine: factors that influence the host response, *Ann Biomed Eng* 42(7) (2014) 1517-27.

SUPPLEMENTARY INFORMATION (SI) FOR THE MANUSCRIPT

entitled “Triple negative breast cancer metastasis to the liver: a tissue engineering model shows the invasion patterns and predicts the effects of free and nanoformulated drugs”

By Anna Guller, Inga Kushnerus, Zahra Khabir, Alfonso Garcia-Bennett, Annemarie Nadort,
Liu Liang, Yi Qian, Ewa M. Goldys, Andrei V. Zvyagin

SI 1. Chick embryo incubation and organ collection

Figure S1 illustrates the sectioning of chick embryo on ED18.

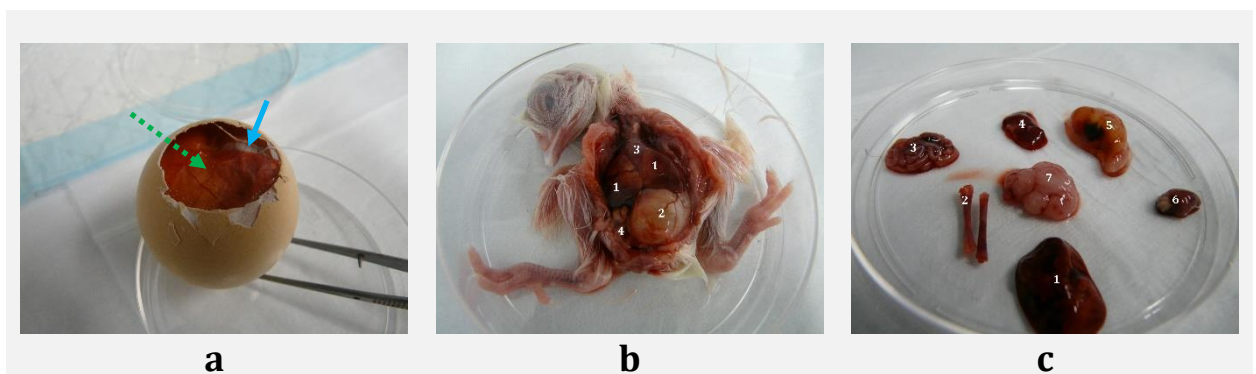


Figure S1. Sectioning of chick embryos on ED18. (a) The blunt end of the shell was removed. The embryo (blue arrow) resides underneath the chorioallantoic membrane (CAM), which is visible as a vascularized semi-transparent film on the top (green dotted arrow). (b) The body of decapitated chick embryo extracted from the egg, after removal of extraembryonic membranes and prolapsing part of the yolk sack. Note that the general anatomy of the embryo is similar to the hatching chick as the major body parts and organs have been formed already. Wide central sectioning of the body is performed for organs extraction. The localization of the visceral and thoracic organs is shown: 1- lobules of the liver; 2 – the ventriculus (stomach); 3 – the heart and lungs complex (partially covered by the liver); 4 – loops of the intestine (behind the ventriculus). (c) The extracted organs of ED18 chick embryo in a standard Petri dish (100 mm): 1 – liver, 2- femoral bones, 3 – small intestine, 4 – lungs, 5 – stomach, 6 – heart, 7 – brain.

SI 2. Native structure of the chick embryo liver and the effect of DCL

The Figure S2 shows the details of histological structure of intact and DCL chick embryo liver on ED18. Figure S3 presents the schematic explanation of the effect of DCL on histoanatomical structure of the liver. Figure S4 illustrates the structure and composition of the Disse's space, the components of which make the bulk of the “parenchymal” compartment of the DCL liver.

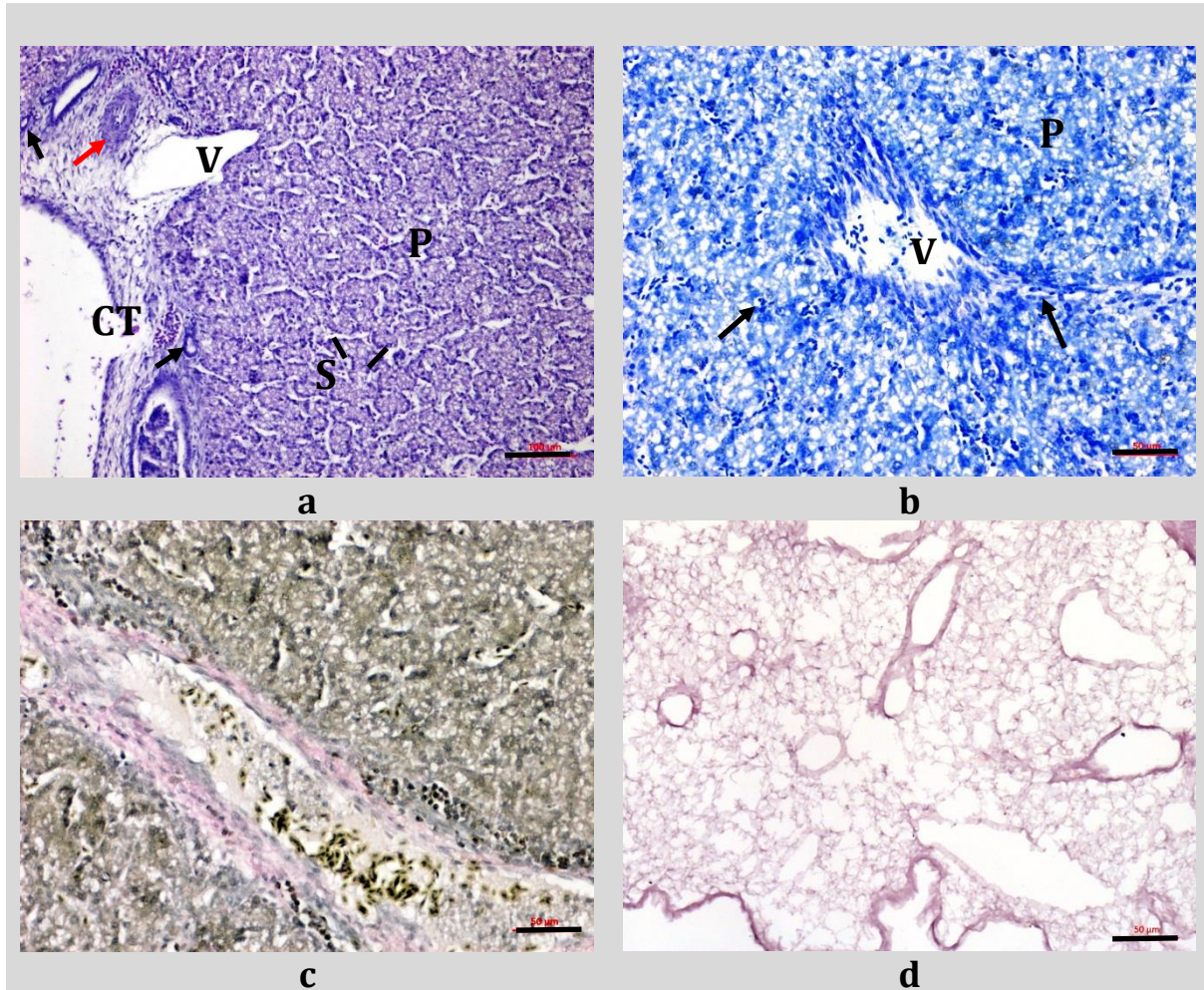


Figure S2. Details of histological structure of intact chick embryo liver extracted on ED18 (a-c) and DCL liver (d). (a) Subcapsular area of the liver. Note fibrous connective tissue (CT) of the liver capsule. Veins (V) are recognizable by wide open lumens of irregular shape and thin walls. The sections of arteries (red arrow) are discernible by smaller diameter of the lumen and thick walls with circularly arranged smooth muscle cells. The portal bile ducts also have small diameter, their wall contains only one row of cubic epithelial internal lining (black arrows). Hepatic parenchyma (P) is formed by cords of hepatocytes separated by sinusoids (S with indicating lines). H&E staining. (b) Liver tissue stained with toluidine blue is totally orthochromatic, indicating low concentration of acid glycosaminoglycans at this development stage. Note sinusoids containing dark stained nucleated ellipsoid erythrocytes (arrows), which are transported towards the vein (V) through the parenchyma (P). (c) Liver tissue stained by elastica-Van Gieson's method. Hepatocytes of parenchyma and erythrocytes are yellow-brown. Note pink staining of collagen in media and adventitia of a large vein. (d) DCL liver tissue. Note combination of dense ECM of former blood vessels and loose ECM of former parenchyma. H&E staining. Scale bars: 100 μm (a); 50 μm (b, c, d).

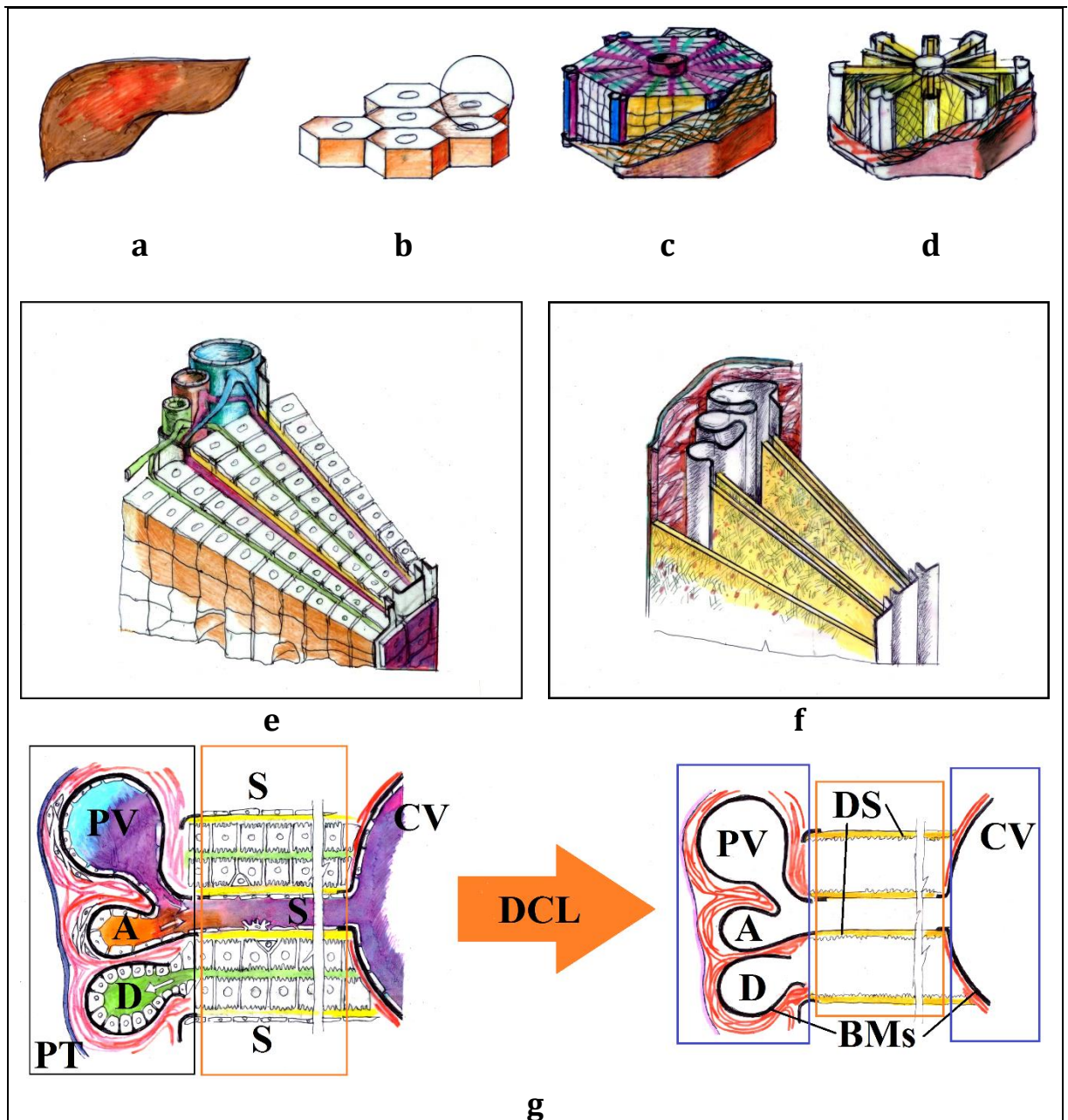


Figure S3. Artistic scheme of the histoanatomical hierarchy of the liver structure and the effect of DCL on its constituents. The liver (a) is formed by the lobules (b). Each lobule (c) has a central vein in the middle and radially arranged cords of hepatocytes separated by sinusoids (radial violet lines) and bile canaliculi (radial green lines). The border of each lobule consists of loose connective tissue sheaths (red coating), which contains portal triads and interlobular vasculature branches in the corners of each lobule's "hexagon". As a result of DCL (labelled as DCL lobule, (d)) all the cellular elements are removed. (e) Detailed view of the sector of a single lobule. Each cord of hepatocytes contains two rows of the polarized cells. One side of the cell row contacts with a sinusoid blood vessel (purple) through the space of Disse (yellow), while other one contacts a bile canaliculus (green) directly. The cells of sinusoids and other cells of parenchyma, excepting hepatocytes, are not shown for simplicity. The blood from portal vein (large blue blood vessel) and hepatic artery (smaller red blood vessel) is mixed in capillaries and transported through the liver parenchyma towards central vein in the middle of lobule. Bile is transported to the portal bile duct in opposite direction. Portal vein, artery and bile duct make a portal triad. (f) 3D view of the effect of DCL on the sector of a single lobule, shown at (e). Note absence of cellular elements and preservation of collagenous stroma of interlobular septae and connective tissue sheaths of large blood vessels (red), basement membranes of large blood vessels and portal bile ducts (grey) and the ECM of Disse's space (yellow). (g) The 2D detailed schematic view of a segment of a lobule before (left) and after (right) DCL. Note a portal triad (PT), containing portal vein (PV), hepatic artery (A) and interlobular bile duct (D); sinusoids (S) with discontinuous endothelial lining separated from hepatocytes by Disse's space (yellow). Narrow bile canaliculi (green) are visible between the rows of hepatocytes inside the cords. Bile canaliculi do not have own cell linings. Central vein (CV) has the entire endothelial lining, basement membrane (BM) and collagenous sheath (red lines)

CHAPTER 7

around it. The structure of portal blood vessels is similar to the CV, but the layer of smooth muscle cells is thicker (it exists only before DCL). Red colour indicates collagen fibres. Black lines indicate basement membranes (BM). “Parenchymal” compartment is shown by orange boxes, and the “stromal” one is indicated by blue boxes.

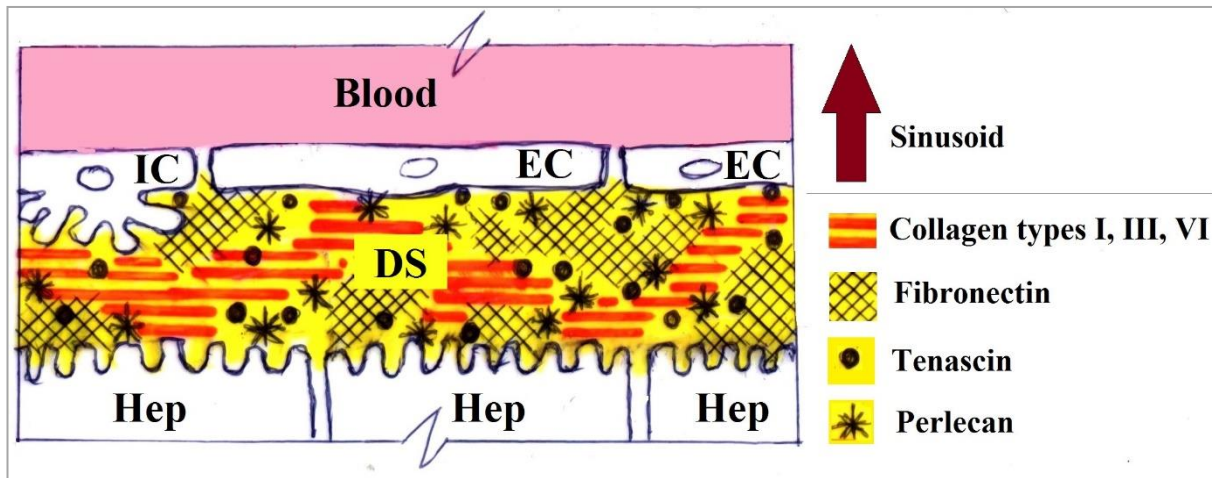


Figure S4. Schematic view of the relationship between sinusoids, Disse's space and hepatocytes. Note the wall of a sinusoid formed by discontinuous layer of endothelial cells (EC) and absence of basement membrane underneath the EC. The Disse's space (DS, yellow) separates the endothelial cells of sinusoids from hepatocytes (Hep) and stellate cells of Ito (IC). The concentration of fibronectin increases along the sinusoids towards the central veins. Tenascin is relatively rare component. Perlecan is predominantly associated with basement membranes. Laminin is almost absent along the sinusoids in Disse's space, excepting the area near the portal triads. The scheme is based on the literature data¹⁻⁴.

CHAPTER 7

The Figure S5 demonstrates macroscopic changes of chick embryonic livers during the process of immersion-agitation whole-organ DCL.

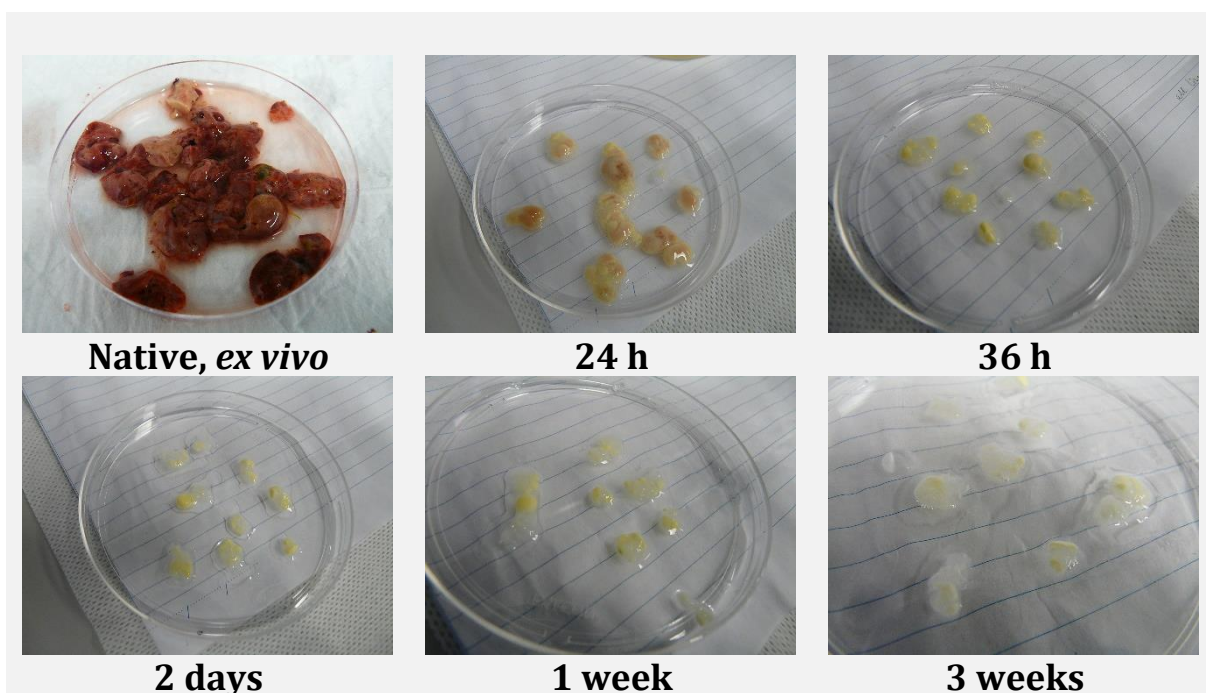


Figure S5. Effect of whole-organ immersion-agitation DCL on native chick embryo liver. Native chick embryo livers collected on ED18 after initial washing in PBS and the macroscopic changes of them during the labelled periods of DCL. Note discoloration and 30% decrease of the organ's volume, comparing to the native state after 24 h of DCL; whitening and decrease of organ's volume to the 20% of original after 36 h of DCL; additional down-sizing and emergence of translucent parts after 2 days of DCL; followed by progression of these changes up to the end of the 1st week of DCL. Finally decellularized livers (3 weeks of DCL) have milky-white translucent appearance and slightly increased volume because of swelling of the loosened tissue.

SI 3. Dynamics of the cell growth in 3D TECs and 2D cultures of MDA-MB-231 cells *in vitro*

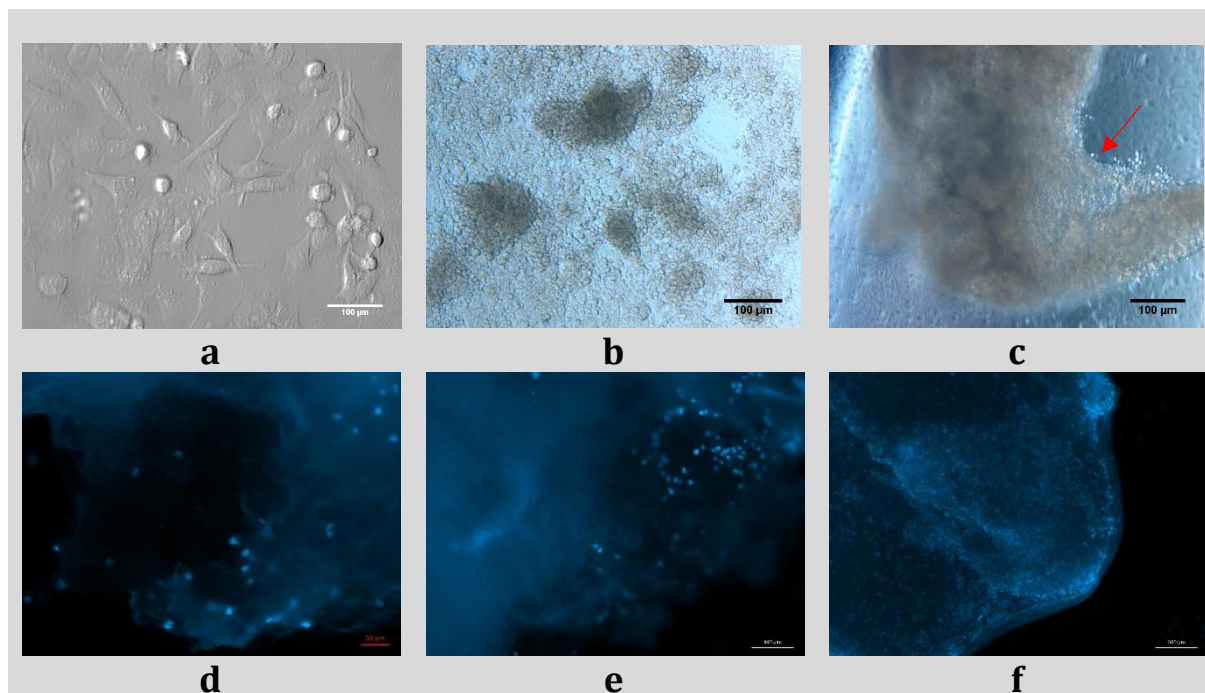


Figure S6. Morphological features of the MDA-MB-231 cells growing in 2D and 3D (TEC) cultures *in vitro*. (a) Typical appearance of MDA-MB-231 cells in a monolayer 2D culture *in vitro*. The spindle-like shape cells with long protrusions are spread and flattened when growing on the surface of plastic culture dish. Differential interferential contrast (DIC) image. Scale bar 100 μm . (b) Aggregates of the cells in overgrowing monolayer culture on 14th day of the experiment. Note that the cells are smaller, less flattened and more round-shaped than in the normal monolayer culture; cytoplasmic protrusions are absent. DIC image. (c) A TEC in a culture plate. 14th days after seeding. Note the cells on the surfaces of the scaffold (arrow), which have almost spherical shape. DIC image. (d-f) Distribution of the cells in TECs on the 1st (d), 7th (e) and 21st (f) days after seeding. Note progression of cellular invasion into depth of the scaffold and increasing cell numbers during the period of observation. Initial attachment of the cells to the scaffold's surface (d); a cellular cluster formation in the cavity, connected by a narrow channel to the surface of the scaffold; and total colonization of the scaffold by cells (f). Live fluorescence microscopy imaging, cell nuclei stained with DAPI. Scale bars: 50 μm . The contrast of the images (d-f) was enhanced for better discernibility of the cells on the scattering background of the liver AOSS. Scale bars 50 μm (d), 100 μm (e) and 200 μm (f).

CHAPTER 7

Table S1. The results of MTT test of viability of MDA-MB-231 cells in 2D and 3D *in vitro* cultures.

Time in culture, days	Calculated number of cells, 10 ⁶					
	2D			3D		
	Mean	CI _{95%} for Mean		Mean	CI _{95%} for Mean	
		Lower border	Upper border		Lower border	Upper border
1	0.143	0.130	0.156	0.02	0.019	0.022
7	1.722	1.695	1.927	0.107	0.082	0.144
14	2.181	2.108	2.485	0.265	0.246	0.284
21	2.554	2.488	2.888	0.398	0.361	0.435
28	2.067	1.983	2.372	0.366	0.318	0.415

SI 4. Characterization of nanoparticles

The Figures S7 – S13 demonstrate the results of the characterization of AMS-6 and AMS-6-Dox nanoparticles.

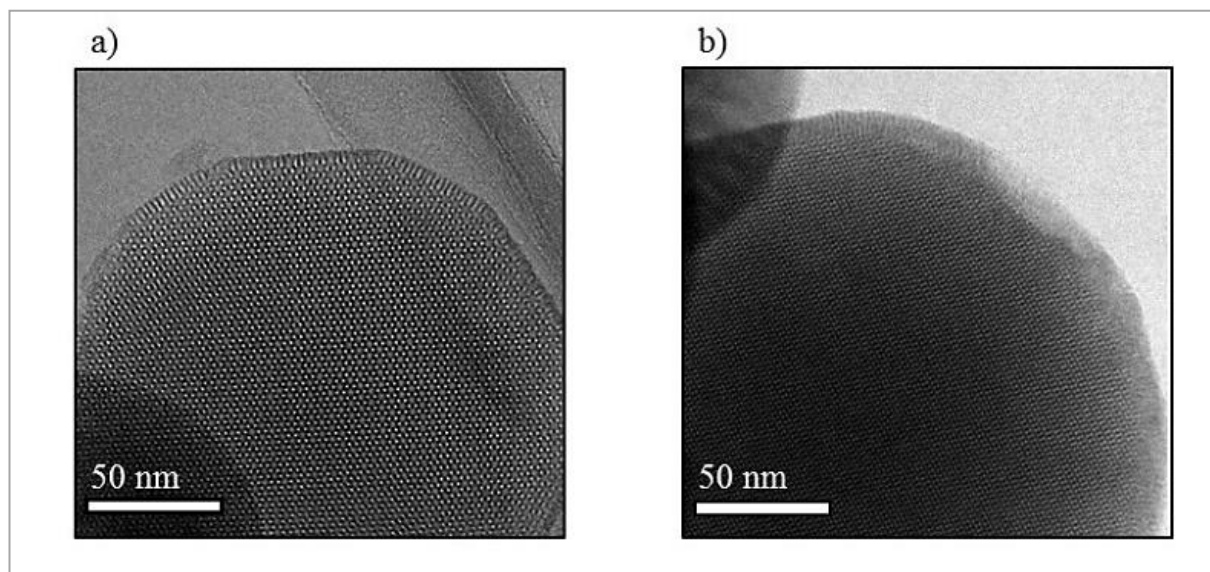


Figure S7. Image of the AMS-6 NPs. (a) and (b) represent a typical TEM images of calcined AMS-6 mesoporous material showing a high degree of mesoporous order.

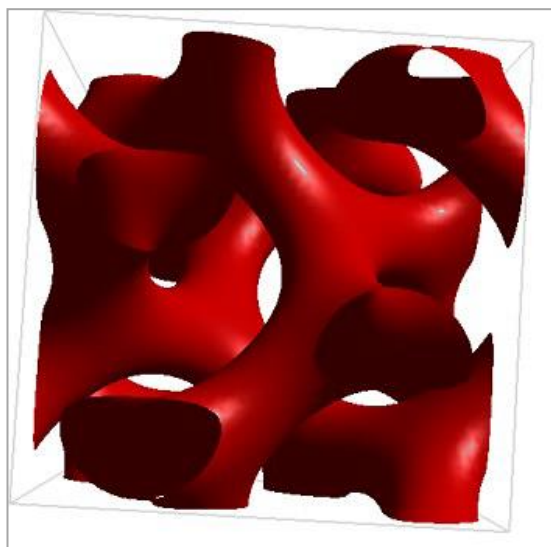


Figure S8. Scheme of AMS-6 structure. 3D model.

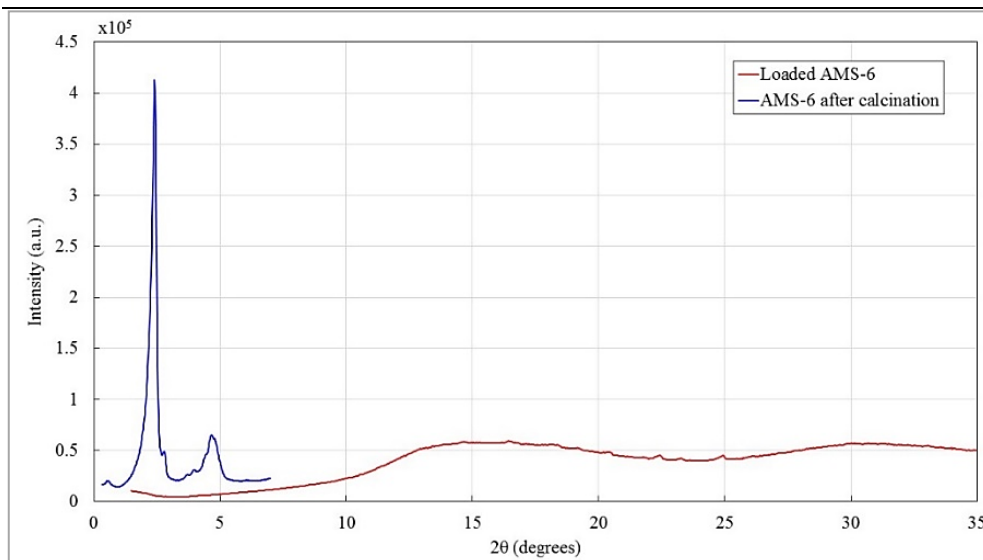


Figure S9. XRD pattern of pure calcined AMS-6 mesoporous nanoparticles (blue) and the loaded AMS-6-Dox nanoparticles (red). The measurements of the pure calcined AMS-6 NPs reveal a highly ordered mesostructure with peaks of scatter in-between the pores of the nanoparticles. The typical XRD pattern of the pure sample display peaks at low angles of 2.4 and 4.8° with an intensity of $4.12 \cdot 10^5$ and $0.6 \cdot 10^5$ a.u., respectively. The loaded AMS-6-Dox sample curve shows small peaks at high angles of approximately 15 and 30° with intensities below $0.75 \cdot 10^5$ a.u., which are most likely the scattering patterns of crystallized Dox outside of the pores. The pores of the AMS-6-Dox still seem to be filled with DOX since the pattern does not show any peaks at low angles which would indicate scatterings between the pore walls of the nanoparticles.

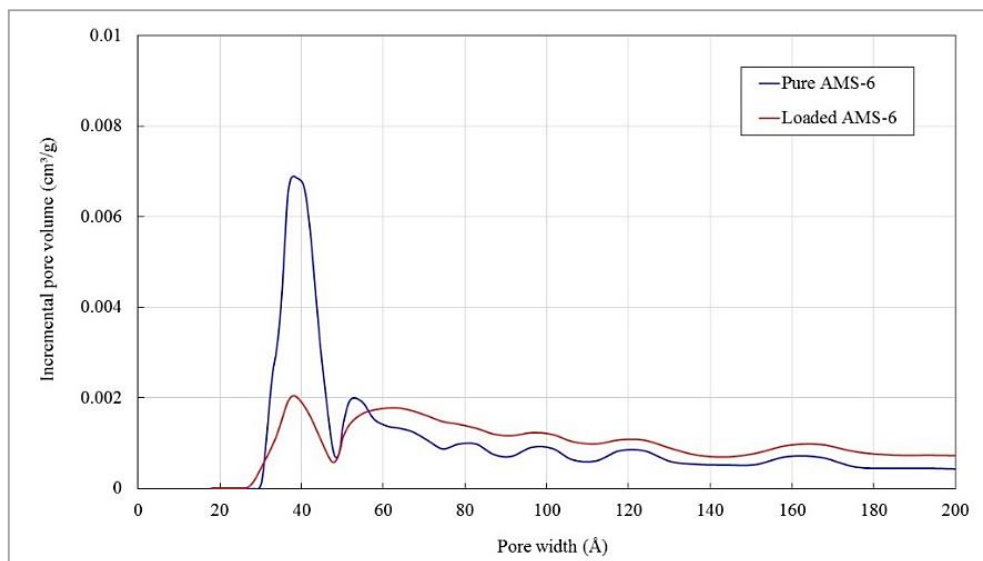


Figure S10. DFT pore size analysis. The pore width of pure AMS-6 and loaded AMS-6-Dox nanoparticles is in a range of 30 to 50 Å.

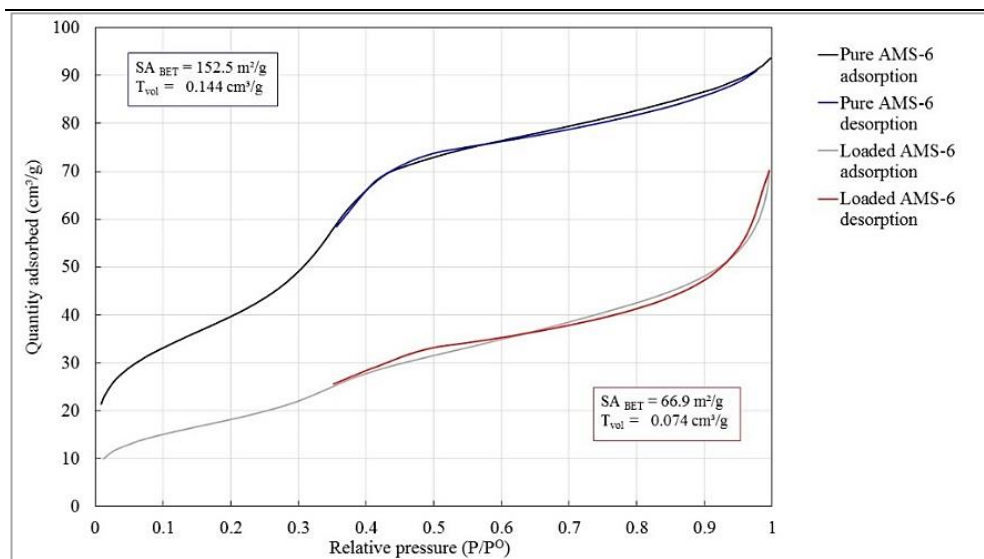


Figure S11. The nitrogen adsorption/desorption isotherm curves of pure AMS-6 and loaded AMS-6-Dox nanoparticles. A very narrow hysteresis loop where the plotted adsorption and desorption curves are close together results from the fact that the pore width of 3.81 nm is very small.

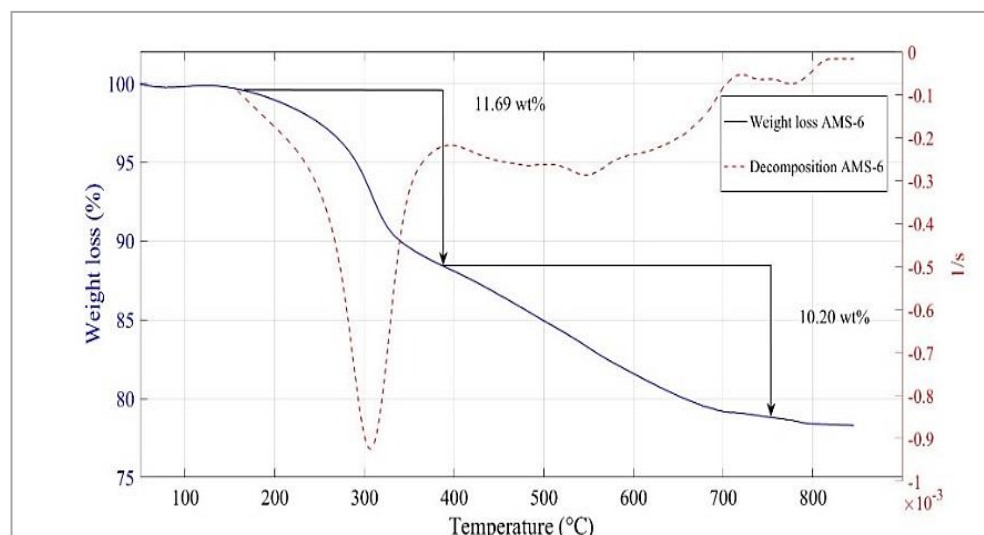


Figure S12. TGA of the unloaded AMS-6 nanoparticles sample. The thick blue line corresponds to the weight loss versus the temperature, and the dashed red line represents the first derivative from the thermogravimetric analysis (DTG) curve. The latter shows characteristic decomposition peaks, e.g. at 380°C. The measurement was performed on the pure AMS-6 to confirm the absence of any organic compounds that could block the pores, which were supposed to contain the loaded drug later. The peak of DTG at approximately 310 °C corresponds to the loss (decomposition) of propyl amine functionalized groups. The analysis also revealed the incorporation of approximately 11.69 wt% of covalently bound propyl amine groups in the pores of the NPs. However, with 11.69 wt% the presence of amine groups was slightly elevated. A higher value would indicate a high amount of remaining amino groups, which would mean a blockage of the NPs pores. The remaining weight loss above 400°C was due to evaporating water (also known as extra framework water) caused by condensation of silanol groups.

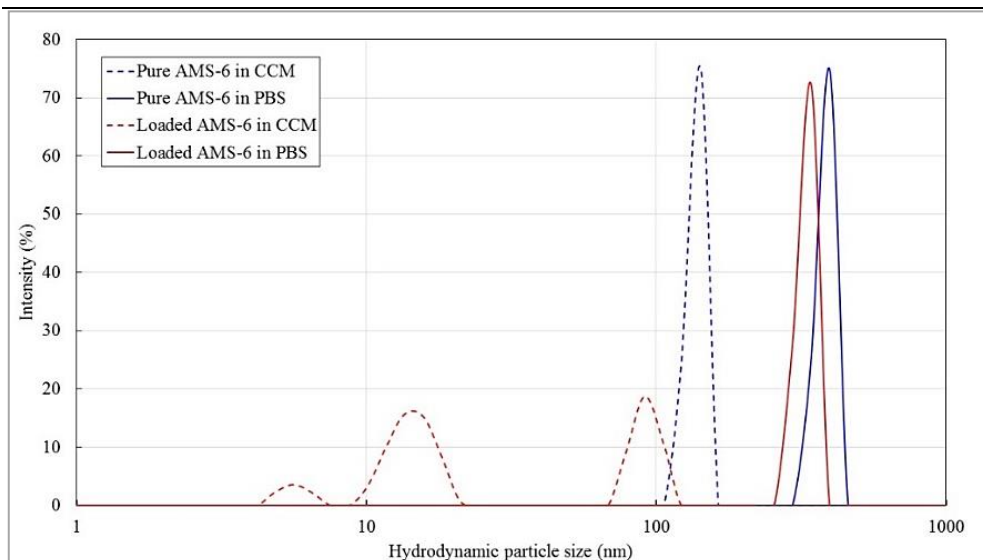


Figure S13. Hydrodynamic size distribution of pure and loaded AMS-6 NPs in complete culture medium (CCM) and in PBS. Note the variation of the particles' size distribution depending on the used dilution medium.

SI 5. Results of MTT assay: Cytotoxicity of Dox and AMS-6-Dox in 3D TECs and 2D *in vitro* cultures of MDA-MB-231 cells

Figures S14 and S15 demonstrate the comparisons between the effect of free and nanoformulated Dox in 2D and 3D (the role of drug delivery method) *in vitro* cultures of MDA-MB-231 cells. No obvious trends were found, however, the statistical significance of the difference between the number of dead cells in Dox and AMS-6-Dox treated cultures was observed at several concentrations in 2D and 3D *in vitro* culture conditions.

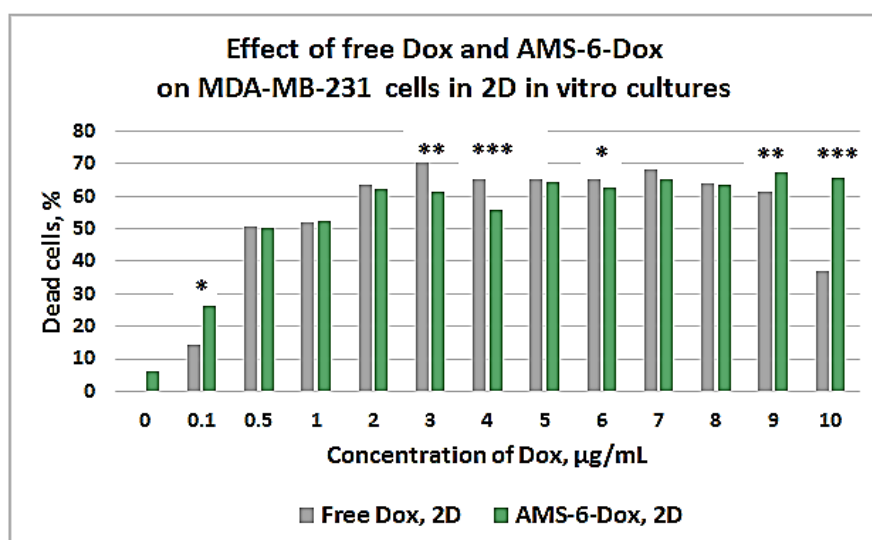


Figure S14. Effect of drug delivery method (free Dox versus MSNP-Dox nanoparticles) in 2D *in vitro* cultures of MDA-MB-231 cells. The level of statistical significance was calculated with use of U Mann-Whitney test and labelled as following: * - $p \leq 0.05$; ** - $p \leq 0.01$; *** - $p \leq 0.001$.

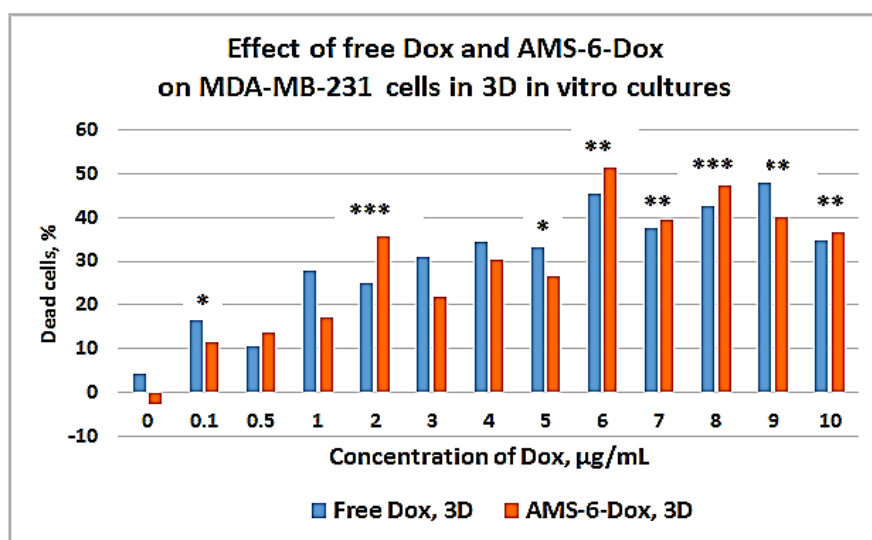


Figure S15. Effect of drug delivery method (free Dox versus MSNP-Dox nanoparticles) in 3D liver-specific TEC *in vitro* cultures of MDA-MB-231 cells. The level of statistical significance was calculated with use of U Mann-Whitney test and labelled as following: * - $p \leq 0.05$; ** - $p \leq 0.01$; *** - $p \leq 0.001$.

CHAPTER 7

Figure S16 shows the detailed experimental data on the cytotoxicity effects of free and nanoformulated Dox in 2D and 3D cultures of MDA-MB-231 cells.

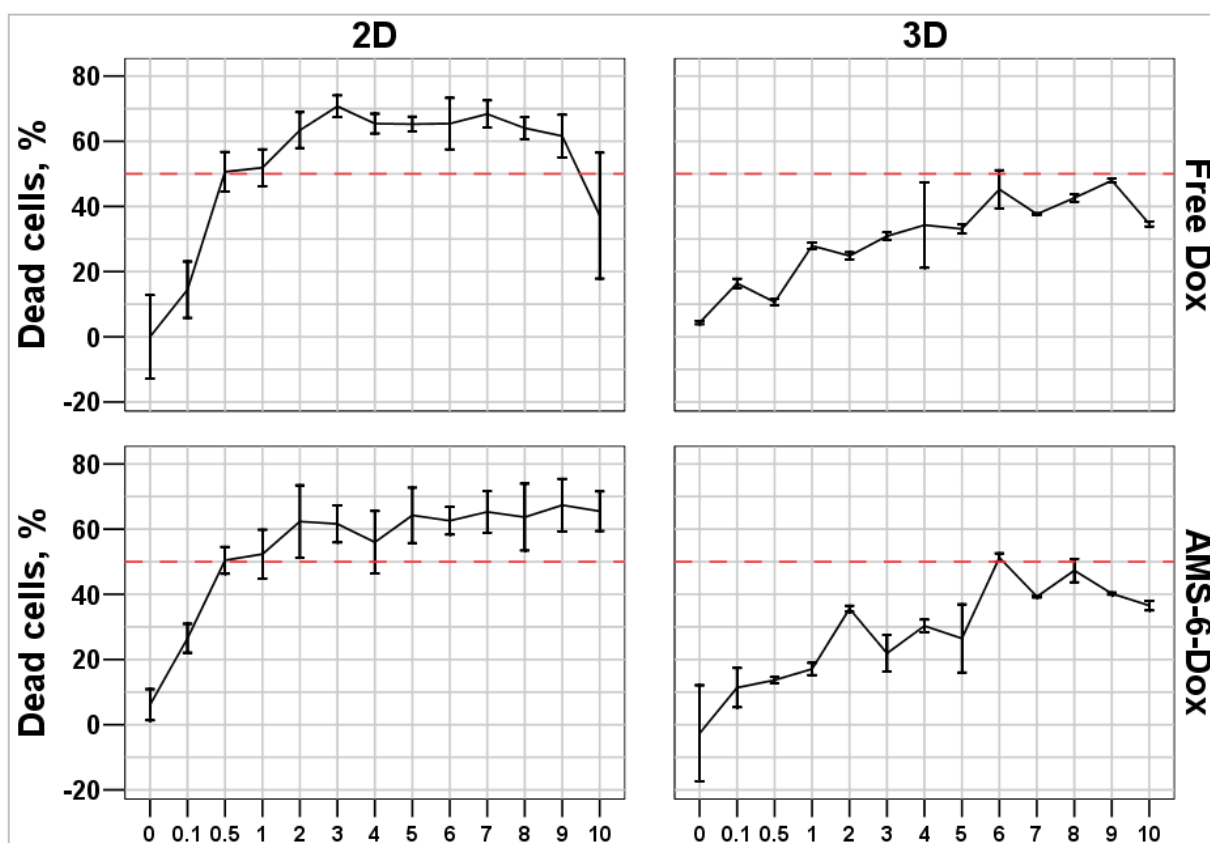


Figure S16. The response of MDA-MB-231 cells on free Dox and AMS-6-Dox under 36 h exposure in 2D and 3D (liver-specific TEC) *in vitro* cultures. Experimental data. The X axis indicates the applied concentration of Dox, µg/mL. Error bars: CI_{95%} for mean percent of dead cells. Red dashed line shows the level of 50% cell death (experimental IC₅₀).

CHAPTER 7

Figure S17 allows paired comparisons of the studied groups and conditions at each applied concentration of Dox.

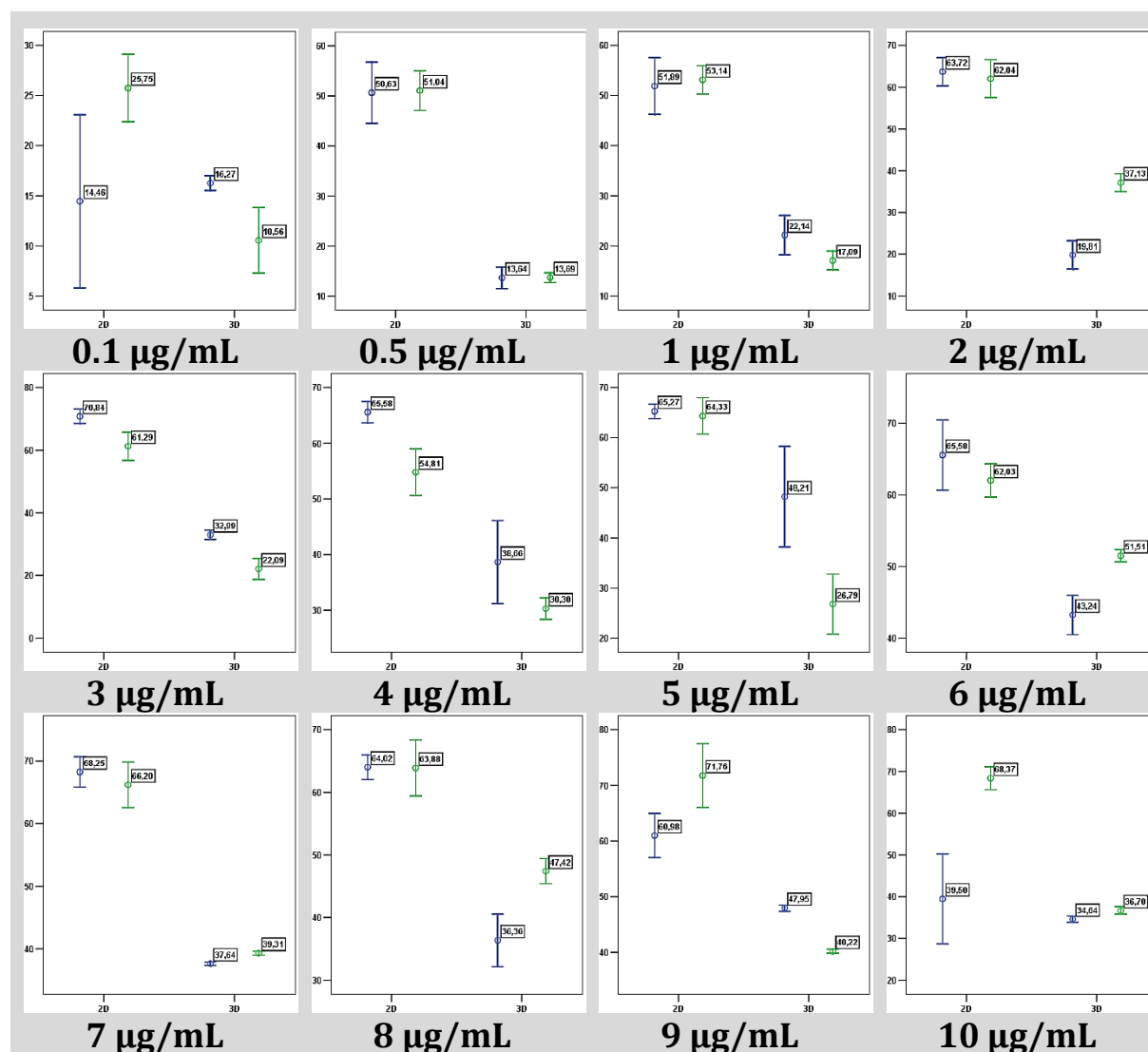


Figure S17. Summary of the data obtained by MTT assay in 2D and 3D *in vitro* cultures of MDA-MB-231 cells exposed to free Dox and AMS-6-Dox nanoparticles during 36 h. Blue and green dots represent the mean ratio of dead cells after application of free Dox and AMS-6-Dox, respectively. Mean ratio of dead cells, % is plotted on Y axis. Experimental conditions, 2D (left) and 3D (right), respectively, are shown by the X axis. Numbers under the graphs indicate the nominal concentration of applied Dox. Error bars show the CI_{95%} for mean percent of dead cells and color coded in the same manner as the dots standing for the experimental data points. Data labels on the graphs also indicate the mean % of dead cells in the group.

Table S2. Quantitative parameters of the free and nanoformulated Dox efficacy for monolayer and 3D cell culture as obtained from a nonlinear fitting model.

Parameters	Groups	Dose of Dox (µg/mL)		Effect (Dead cells, %)	
		2D	3D	2D	3D
Max. effect	Free Dox	N/A		69	48
	AMS-6-Dox			64	54
EC50	Free Dox	0.15	0.18	35	24
	AMS-6-Dox	0.16	1.10	30	27
IC50	Free Dox	0.25	infinity	50	
	AMS-6-Dox	0.34	16.02		

SI 6. Cellular uptake of Dox and AMS-6-Dox in 3D TECs and 2D *in vitro* cultures of MDA-MB-231 cells

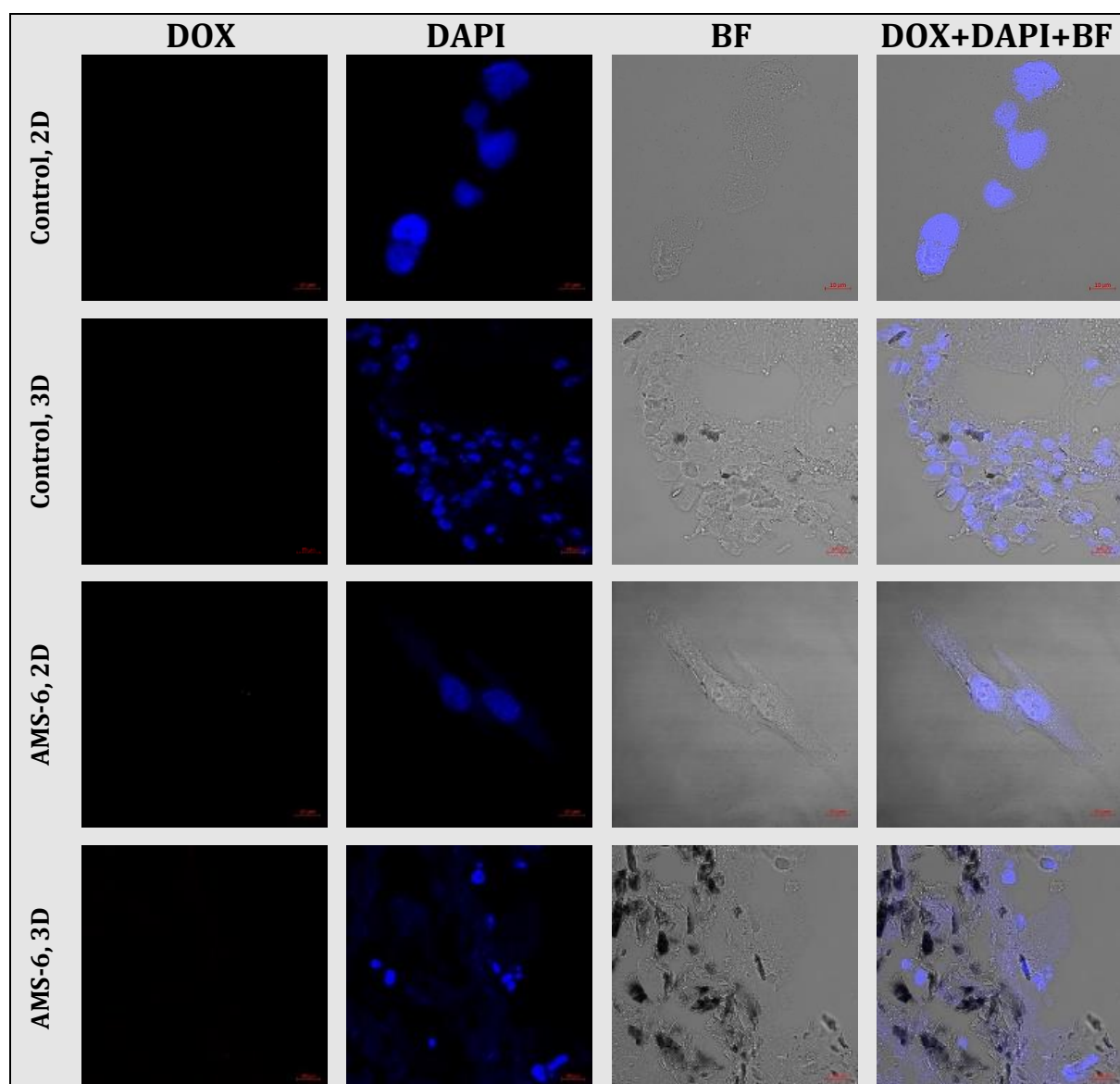


Figure S18. Confocal microscopy images 2D and 3D TECs *in vitro* cultures of MDA-MB-231 cells incubated with complete culture medium (control 2D and 3D) and pure AMS-6 nanoparticles for 24 h. Note absence of the Dox fluorescence in the red channel (Dox), the clear association of DAPI fluorescence staining with cell nuclei (blue channel, DAPI). The control bright field (BF) images were taken for visualization of the tissue structures, and the combination of the mentioned types of images is used for colocalization of the fluorescence signals on the background of BF. The concentration of AMS-6 was 50 µg/mL.

SI 7. Analysis of angiogenic potential of TECs and AOSSes *in vivo*

The eggs preparation and the grafting procedure

The experiment was approved by the Animal Ethics Committee of Macquarie University (ARA 2015/006; 2015/006-2). The fertilized White Leghorn chicken eggs were incubated as described in the section 2.3.1 of this paper for 72 h, until embryonic day 3 (ED3). Then the eggs were placed in a horizontal position and left in the incubator for the next 30 min for repositioning of the embryos. Afterwards, the tops of the blunt ends of the shells were wiped with 70% ethanol, and 3-4 mL of the egg white was extracted from the bottom part of the egg by puncturing of the blunt end of the shell with a syringe needle (18G) at the angle of $\sim 45^\circ$ (Figure S19 (a) in SI 7). The albumin extraction resulted in decrease of the total volume of the egg and dropping of the chorioallantoic membrane (CAM), which were necessary for the further grafting procedure. After the extraction the stab holes were sealed with a sticky tape and the eggs were returned to the incubator until ED8. On ED8 the egg shells were cut on the blunt end to create a lid and expose the CAM. Following this, the grafting procedure was performed.

All the embryos were divided into 5 groups, with 10 eggs per a group. The group 1 was used as a control (labelled “Control”) and left ungrafted in order to evaluate the parameters of natural angiogenesis occurred in chick embryos during the period between ED8 and ED12. In other groups the following materials were aseptically implanted onto CAM under sterile conditions: 1) filter paper soaked in sterile PBS (labelled “PBS”); 2) chick embryo liver AOSS soaked in complete culture media following the pre-seeding protocol described in the Section 2.3.3 (labelled “Scaffold”) for 24 h; 3) cell suspension of MDA-MB-231 cells, 2×10^5 cells in 60 μL of complete culture media (labelled “Cells”) and 4) the TECs, prepared as described above (see Section 2.3.3) and cultured *in vitro* for 12 days prior grafting (labelled “TEC”). This time period of preliminary culture of TECs *in vitro* was chosen to obtain the engineered tumor samples containing the similar number of cells ($\sim 2 \times 10^5$ cells per sample) in the compared TECs and cell suspension xenografts. This period was also preferred to obtain the TECs with actively grown cell populations. The filter paper was sterilized by soaking in ethanol, followed by drying on air in sterile environment and UV sterilization in tissue culture hood for 45 min. The other materials were prepared as described above (see sections 2.2. and 2.3 of the paper for the details). The workflow of the grafting procedure is shown on Figure S19.

Following this, the images of the CAM were taken with a stereomicroscope. Then the eggs were sealed and returned back to the incubator and maintained under standard conditions with excluded rotation. Afterwards, on ED12 the eggshells were re-opened, and the imaging was repeated under the same conditions as on ED8. After the imaging session on ED12 the chick embryos were euthanized by quick decapitation. The CAM with grafter materials and control samples of ungrafted CAM were dissected, washed in PBS and studied by histological methods as described elsewhere (see 2.4.1).

CHAPTER 7

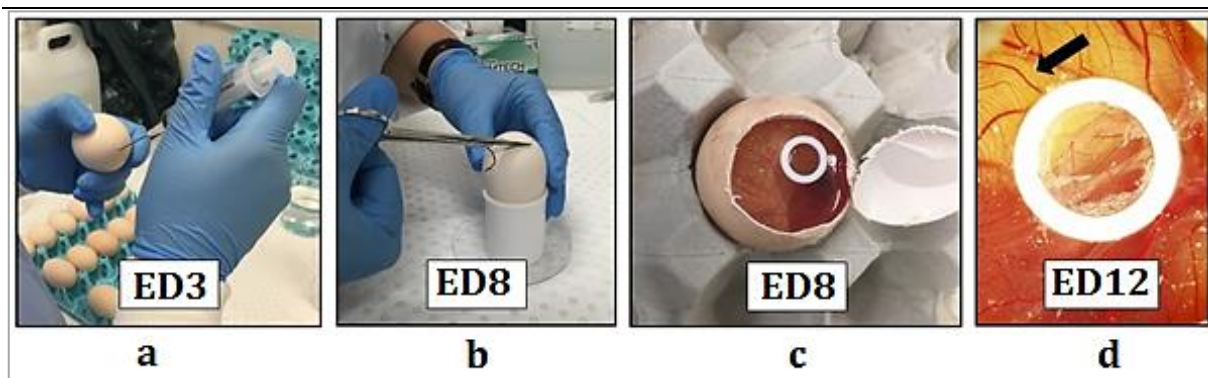


Figure S19. Summarized grafting protocol. (a) Extraction of the egg white. (b) Opening of the egg. (c) Implantation on the CAM. The cell suspension grafting is shown; a sterile white rubber ring taken from a 1 mL cryovial is used to prevent leakage of the suspension. (d) The image of the same egg on ED12. The arrow shows a bifurcation of a blood vessel as a preferential grafting site.

Imaging of CAM in vivo

The CAM of the eggs with open shell lids were imaged *in vivo* using the Olympus MVX10 (Olympus, Japan) stereomicroscope equipped with an eyepiece magnification ranging between 0.63 \times to 6.3 \times , a fixed focus and two objective lenses, 1 \times /0.25 N.A. and 2 \times /0.5 N.A. The microscope featured long working distance (20 to 87 mm), adjustable field-of-view (FOV, 1.7 to 55mm in diameter). In order to maintain the healthy state of the chick embryos the heating stage ThermoPlate by (Tokai Hit, Shizuoka-ken, Japan) was used during *in vivo* inspection of CAM. The objective 1 \times /0.25 N.A. was applied for the rough focusing and the lens magnification of 2 \times was used for the detailed imaging. The samples were illuminated from above by a 100 W mercury lamp. In order to achieve a higher contrast of the red color of the blood, a filter cube with blue illumination light was used. This filter cube contained one single-edge short pass dichroic beam splitter (Semrock, USA) with transmission of the wavelengths above 750 nm and a single-band bandpass (510-570 nm) filter as the emission filter by (Semrock, USA) (Figure S20). The microscope was coupled with a motorized Z focus ProZ Stand (Prior Scientific, USA), which provided seamless zooming from 40 to 1250 \times magnification (used for the focusing and study purposes).

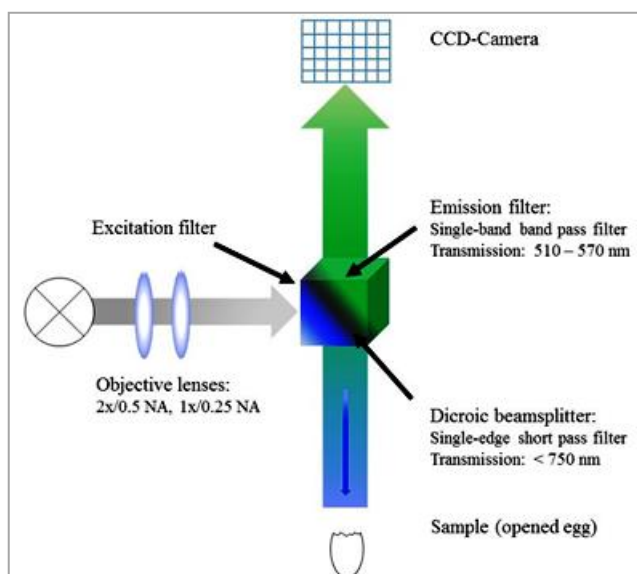


Figure S20. Schematic diagram of a stereomicroscope used for CAM imaging.

Results

Figure S20 shows the macroscopic view of the grafted CAM in the studied group. The group PBS is not shown as there no any notable effect on angiogenesis in comparison to the control.

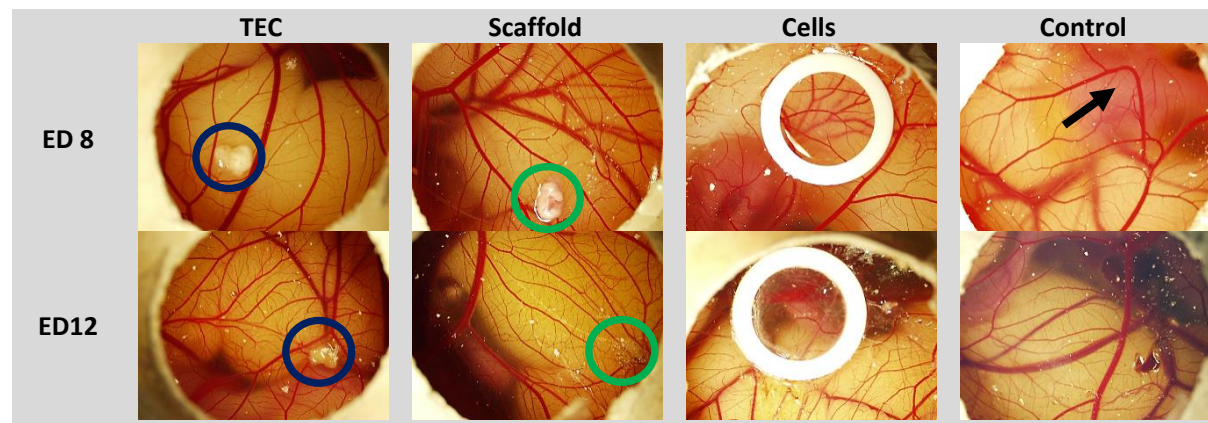


Figure S21. Low magnification ($\times 0.63$) view of control and grafted CAM on ED 8 and ED12 obtained with bright field settings. Angiogenic effects induced by 3D engineered tumors (*TEC*, the grafts are labelled with blue circles), liver AOSSes (*Scaffold*; the grafts are labelled with green circles), and suspension of MDA-MB-231 cells (*Cells*; the xenograft suspension is placed into a chamber formed by white rubber ring) grafted on chick embryo CAM, in comparison to the natural embryonic development of CAM vasculature (*Control*) during the period between ED8 and ED12. Note that the degree of vascularization of CAM on ED8 is naturally varying between the embryos; then the representative images of the same eggs on ED8 and ED12 were used for analysis and shown there for each group. The equal volume samples of the grafted TECs and AOSSes were used. The number of cells in the cellular xenograft and TECs was similar to each other ($\sim 2 \times 10^5$ - cells). The arrow on the image of Control CAM, ED8, indicates the chick embryo residing underneath the CAM. White dust on the surface of CAM are the small fragments of eggshell dropped on the CAM following the shell windowing.

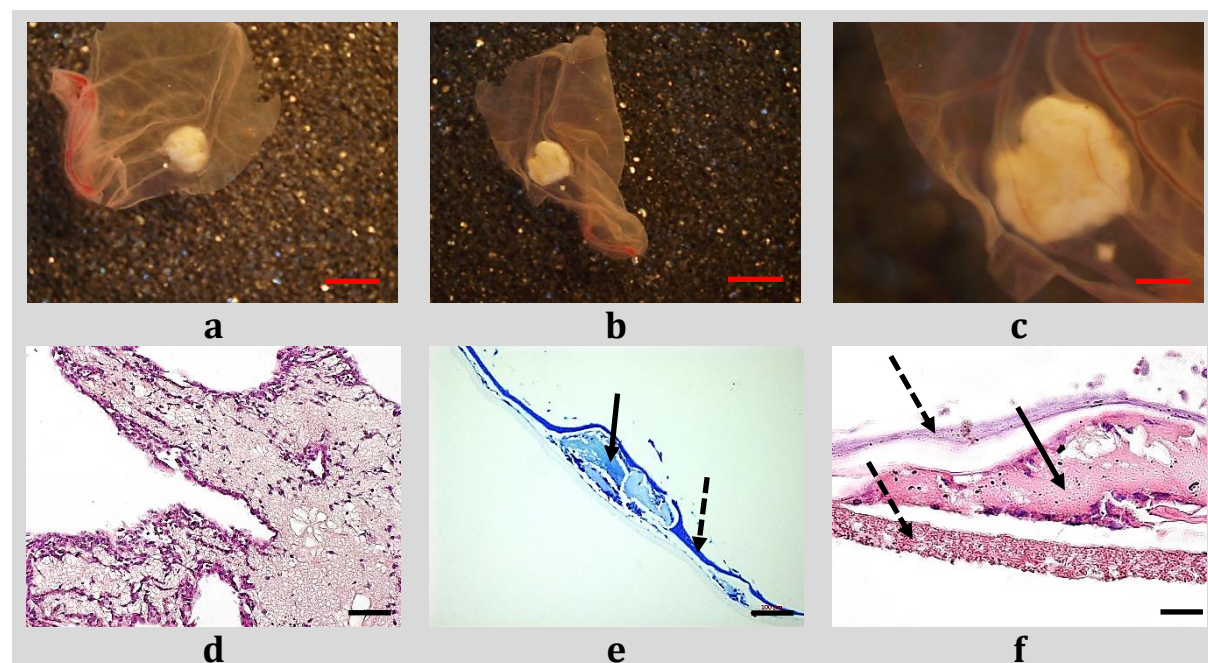


Figure S22. Excised fragments of CAM with grafted TEC (a-c) and the structural relationship between the TECs and CAM (d-f). (a) A view from the top of CAM; (b) a view from the bottom of CAM; (c) higher magnification view from the bottom of CAM; the large blood vessels supplying the graft are visible. (d) A histological section of TEC on 12th day of *in vitro* culture (before grafting). H&E staining. Note the compartmentalized distribution of cancer cells. (e, f) The sections of grafted TECs (arrow) engulfed by a double-layered CAM (dashed arrow). Histological image, toluidine blue staining (e), H&E (f). Scale bars: (a, b) - 5 mm; (c) - 2.5 mm; (d, e) - 100 μ m; (f) - 20 μ m.

SI 8. In vivo imaging of grafted 3D model of TNBC tissue on the chick embryo chorioallantoic membrane using upconversion nanoparticles

Background

Early diagnosis and treatment of cancer is essential for improved patient survival. To detect early stage small tumors, photoluminescence imaging using upconversion nanoparticles (UCNPs) has gained considerable attention. UCNPs possess unique optical properties that promise in vivo biomedical imaging with high sensitivity⁵. This is mainly attributed to anti-Stokes, long-lifetime photoluminescence emission after near-infrared excitation of UCNPs, allowing for background-free deep tissue imaging⁶. In addition, small-sized nanoparticles are suggested to accumulate in the tumor due to the so-called EPR (Enhanced Permeability and Retention) effect⁷. In order to study the in vivo labelling of small tumors by UCNPs through the EPR effect, we designed a chick embryo chorioallantoic membrane (CAM) tumor model. The chick embryo CAM is a naturally immunodeficient (up to embryonic day 12) and highly vascularized tissue, that can be employed as an ideal in vivo platform for tumor grafting. By incubating the chick embryo using the “*ex ovo*” method^{8,9} (Figure S23), the CAM is easily accessible for manipulations, including tumor growth monitoring, injection of drugs and contrast agents, and (microscopic) photoluminescence imaging of the grafts. Here, we describe the development of an *ex ovo* CAM tumor model and the imaging of small vascularized tumors using intravenously injected UCNPs.

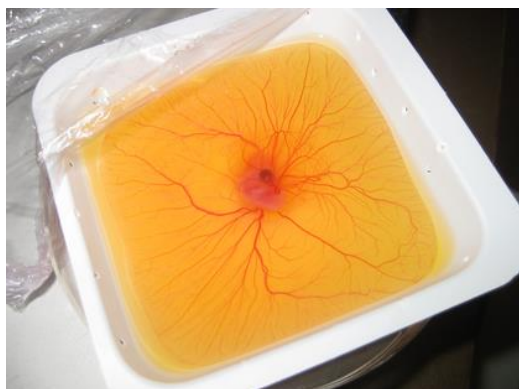


Figure S23. *Ex ovo* chick embryo culturing, showing the vascularized CAM suitable for experimental intervention (tumor grafting, injection of contrast agents, etc.).

Methods

Preparation of Polyacrylic acid modified UCNPs (PAA-UCNPs)

UCNPs (NaYF₄:18%Yb,2%Er) were prepared using the well-developed solvothermal decomposition method¹⁰. The as-synthesized nanoparticles were hydrophobic due to surface capping oleate ligands being hydrophobic. Therefore, further surface modification was conducted to confer the nanoparticle with hydrophilicity for use in biological environments. Poly(acrylic acid) (PAA) was adopted to modify UCNP via the ligand exchange method, resulting in UCNP bound with PAA molecules and yielding a hydrophilic surface¹¹.

Preparation of a simplified 3D model of TNBC tumors and their grafting on CAM

The experiment was approved by the Animal Ethics Committee of Macquarie University (ARA 2013/007-4). Fresh fertilized chicken eggs were incubated as described in the methods (see 2.3.1) until ED3, when the eggs were taken out of the incubator, the shells were opened and the contents was carefully transferred to plastic weighing boats and covered by a breathable plastic film to create *ex ovo* incubation system (see Figure S23). The eggs were then

CHAPTER 7

returned to the incubator for further incubation. The simplified 3D models of TNBC was created by pre-soaked of sterile gelatine sponge ($1\text{--}3\text{ mm}^3$) in $5\text{ }\mu\text{L}$ suspension of MDA-MB-231 cells in PBS that contained 2.5×10^4 cells for 2 h. On ED8 the cell-gelatine sponge constructs were implanted onto the CAM without rupturing the membrane as described elsewhere¹².

Injection of UCNPs into CAM vessels

When neovascularization of implanted tumors was observed on/after ED14, PAA-UCNPs were injected intravenously. The injections were conducted using micro-needles that were pulled from glass capillaries with $\sim 50\text{ nm}$ tip. Before injection, the glass needles were sterilized by perfusion with 70% ethanol and sterile PBS. $100\text{ }\mu\text{L}$ of PAA-UCNP PBS suspension (3.5 mg/mL) was then injected into the vessel that was far away from the tumor site.

Imaging of UCNPs deposited in 3D model tumors

After another 24 h of incubation, the imaging of UCNPs was performed with our in-house-built microscope that consisted of an Olympus MVX10 upright stereo microscope with a long working distance objective (Olympus PLAPO $0.63\times\text{NA}0.15$) in conjunction with an EMCCD camera (Andor, iXon) at the top. In UCNP-imaging mode, the fiber coupled 980 nm excitation beam was focused onto the sample from the side to excite UCNPs. The excitation light was long-pass filtered (850 nm , Edmund Optics) and the emitted signal entered the objective and passed through a 842 nm short pass filter (Semrock) and an extra colour glass band pass filter ($330\text{--}665\text{ nm}$ pass) to block the leaking scattered excitation light. The laser emitted 1 W of 980 nm light, the power density was $\sim 60\text{ W/cm}^2$ on the excitation spot. The UCNP signal was recorded using these two emission filters in the range of $330\text{--}665\text{ nm}$ by the linear EMCCD camera, where the pixel values represent the photoluminescence signal of the UCNPs.

Results

The physical size of the as-prepared PAA-UCNPs were determined by transmission electron microscope (TEM) (Figure S22 (a)) as $25.35 \pm 1.28\text{ nm}$ in diameter. The hydrodynamic diameter of PAA-UCNPs in aqueous suspension was measured to be $76.46 \pm 43.51\text{ nm}$, which is a favourable size for the particles' accumulation in a tumor via the EPR effect¹³. Under NIR excitation, UCNPs display two characteristic emissions peaks centred at $\sim 545\text{ nm}$ and $\sim 655\text{ nm}$ respectively (Figure S24 (b)). The nanocrystal matrix and doping Ln^{3+} concentrations of the UCNPs used in this study ($\text{NaYF}_4\text{:}18\%\text{Yb}, 2\%\text{Er}$) is reported as the brightest composition¹⁴, demonstrating promising utility in animal imaging¹⁵ as well as targeted labelling of tumors¹⁶, showing highly desirable merits for application in CAM tumor imaging.

After placing the gelatine sponge soaked in tumor cells suspension on the CAM for six days, the well-vascularized tumors were observed (Figure S24 (c), bright field). The implanted gelatine sponge provided a 3D biocompatible matrix for MDA-MB-231 cells to grow and eventually form a vascularised tumor through angiogenesis on the CAM. When UCNPs were injected into a small blood vessel of CAM, the particles circulated rapidly throughout the embryonic vasculature and reached the tumor site. Using the modified fluorescence microscope, UCNPs located within the tumor area were visualized under NIR excitation (Figure S24 (c), UCNP). As can be seen, UCNP signal was detected in and around the grafter model tumor (Figure 24 (c), Merged). The UCNP concentration was higher in the tumor area, compared to the surrounding blood vessels, but, a significant UCNP

CHAPTER 7

signal was present at the vasculature as well. The undesirable labelling of the blood vessels will be addressed in our future work where different coatings will be tested against their blood vessel labelling tendency.

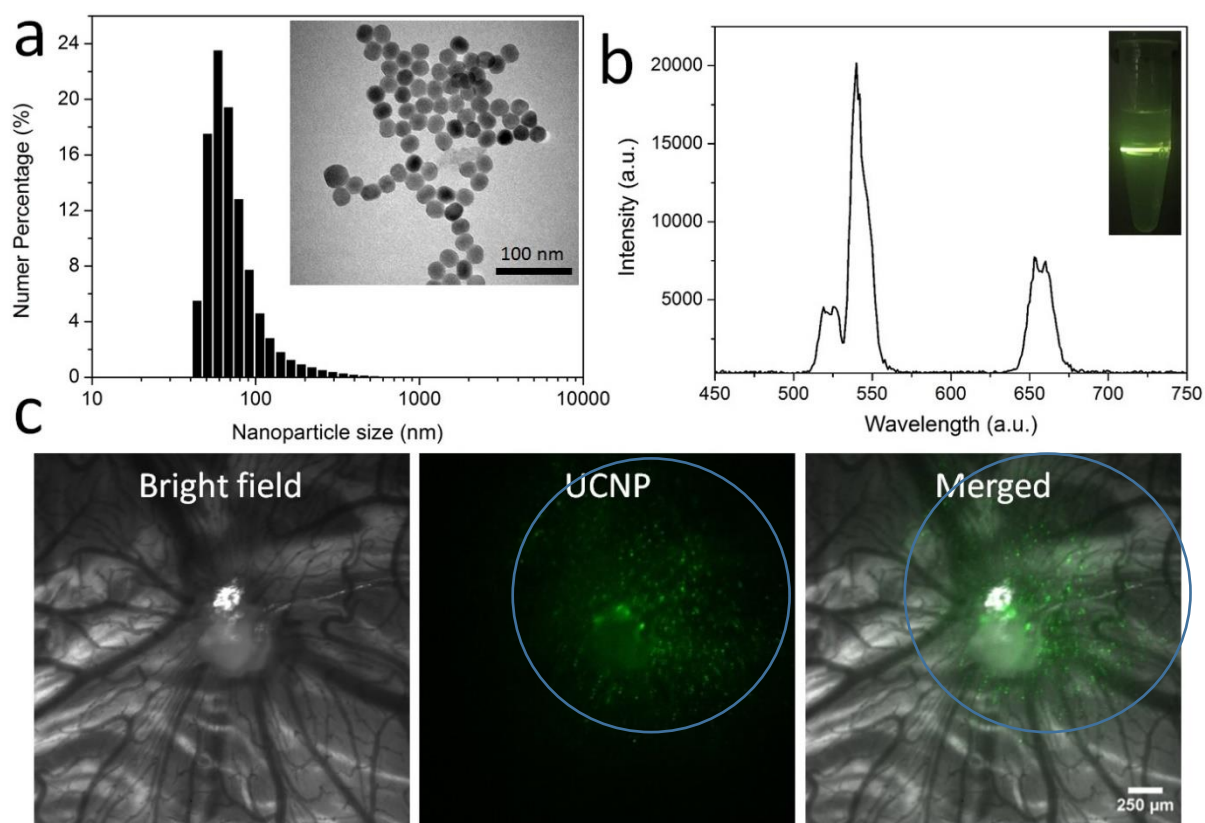


Figure S24. (a) Size distribution of PAA-UCNP measured with Dynamic Light Scattering. Inset is a transmission electron microscope image of PAA-UCNPs. (b) Upconversion luminescence spectrum of PAA-UCNPs under 980 nm excitation. Inset is a photograph of PAA-UCNPs dispersed in water and illuminated with a 980 nm laser. (c) Bright field, photoluminescent and overlay images of MDA-MB-231 cells/gelatine sponge tumor labelled with intravenous injected PAA-UCNPs. The concentration of UCNPs is highest in the tumor, however, the surrounding blood vessels' labeling by UCNPs is also visible. The blue circle represents the laser illumination spot.

Conclusion

This study demonstrated the feasibility of creating vascularized tumors on chick embryonic CAM by implanting cancer cell enriched gelatine sponges to develop an *in vivo* tumor model for studying nanoparticle delivery to tumors. Our results suggest that UCNPs are well suited for *in vivo* imaging of tumors. Although further quantitative assessment is required for in-depth understanding of tumor labelling by UCNPs via the EPR effect, this study exemplifies a practical high-throughput *in vivo* model for real-time monitoring of nanoparticle accumulation in tumors.

SI. References

1. Martinez-Hernandez A, Amenta PS. The extracellular matrix in hepatic regeneration. *FASEB J* 1995; 9: 1401-1410.
2. McClelland R, Wauthier E, Uronis J, Reid L. Gradients in the liver's extracellular matrix chemistry from periportal to pericentral zones: influence on human hepatic progenitors. *Tissue Eng Part A* 2008; 14: 59-70.
3. Reid LM, Fiorino AS, Sigal SH et al. Extracellular matrix gradients in the space of Disse: relevance to liver biology. *Hepatology* 1992; 15: 1198-1203.
4. Mak KM, Png CY, Lee DJ. Type V Collagen in Health, Disease, and Fibrosis. *Anat Rec (Hoboken)* 2016; 299: 613-629.

CHAPTER 7

5. Heer S, Kömpe K, Güdel HU, Haase M. Highly efficient multicolour upconversion emission in transparent colloids of lanthanide-doped NaYF₄ nanocrystals. *Advanced Materials* 2004; 16: 2102-2105.
6. Nadort A, Zhao J, Goldys EM. Lanthanide upconversion luminescence at a nanoscale: fundamentals and optical properties. *Nanoscale* 2016.
7. Matsumura Y, Maeda H. A new concept for macromolecular therapeutics in cancer chemotherapy: mechanism of tumortropic accumulation of proteins and the antitumor agent smancs. *Cancer Res* 1986; 46: 6387-6392.
8. Dohle DS, Pasa SD, Gustmann S et al. Chick *ex ovo* culture and *ex ovo* CAM assay: how it really works. *JoVE (Journal of Visualized Experiments)* 2009; e1620-e1620.
9. Yalcin HC, Shekhar A, Rane AA, Butcher JT. An ex-ovo chicken embryo culture system suitable for imaging and microsurgery applications. *J Vis Exp* 2010; e2154-e2154.
10. Zhao J, Lu Z, Yin Y et al. Upconversion luminescence with tunable lifetime in NaYF₄: Yb, Er nanocrystals: role of nanocrystal size. *Nanoscale* 2013; 5: 944-952.
11. Xiong L, Yang T, Yang Y et al. Long-term in vivo biodistribution imaging and toxicity of polyacrylic acid-coated upconversion nanophosphors. *Biomaterials* 2010; 31: 7078-7085.
12. Ribatti D, Nico B, Vacca A, Presta M. The gelatin sponge-chorioallantoic membrane assay. *Nat Protoc* 2006; 1: 85-91.
13. Blanco E, Shen H, Ferrari M. Principles of nanoparticle design for overcoming biological barriers to drug delivery. *Nature biotechnology* 2015; 33: 941-951.
14. Suyver J, Aebischer A, Biner D et al. Novel materials doped with trivalent lanthanides and transition metal ions showing near-infrared to visible photon upconversion. *Optical Materials* 2005; 27: 1111-1130.
15. Zhou J, Liu Z, Li F. Upconversion nanophosphors for small-animal imaging. *Chemical Society Reviews* 2012; 41: 1323-1349.
16. Cheng L, Yang K, Li Y et al. Facile Preparation of Multifunctional Upconversion Nanoprobes for Multimodal Imaging and Dual-Targeted Photothermal Therapy. *Angewandte Chemie* 2011; 123: 7523-7528.

Conclusions and final remarks

8.1. Motivation

This PhD project was focused on the development and experimental approbation of the new research tools and methodology, which are in demand to bring together, amalgamate and provide the mutual reality verification for the state-of-the-art nanotheranostic materials and the novel biomimetic 3D *in vitro* engineered models of normal and diseased tissues. The idea of the study stemmed from the analysis of the three principal facts.

First, it is generally accepted that the rapid evolution of the nanotechnology holds great promises for the biological research and clinical applications. At the same time, it introduces a number of safety risks associated with intentional or accidental exposure of the human body to the nanomaterials. Then, our primary and strong motivation was ignited by the need of coupling of the studies concentrated on the creation of new nanoparticles with the parallel nanotoxicological tests.

Second, the surface characteristics and size of the nanoparticles play a critical role in defining of the effects of the nanomaterials on the living matter and vice versa. It is especially important for the photoluminescent nanotheranostic agents, as the treatment and diagnostic functionality of these particles is strongly influenced by their biological operational environment. This concept mobilized us to put the efforts into the detailed studies of the strategies of surface modifications of upconversion nanoparticles (UCNPs) in line with the biological significance of these particles' adaptations and their influence on the feasibility of bioimaging applications.

Third, in order to provide reliable information on the nano-bio interactions, this environment should be thoroughly and responsibly reproduced in experimental conditions. The current strategies used for evaluation of the biological effects of nanomaterials are mainly borrowed from pharmacology and toxicology. In particular, the large part of the preliminary tests is performed on laboratory animals and on the monolayer (2D) cell cultures *in vitro*. This methodology is thought to be reasonable in a case of the conventional drugs with low molecular weight and defined chemical structure, where, roughly, under otherwise equal conditions, only two additional factors such as the dose and the exposure time determine the final biological response. At the same time, the fine tunability of the core and surface properties of the nanoparticles usually results in numerous work versions of every single material. Then, as the

CHAPTER 8

outcome of the nano-bio contact can be influenced by multiple parameters, the required number of experimental groups, as well as the samples' size, are increasing tremendously. It makes the preliminary nanobiological experiments on animals unacceptable in terms of research ethics. In addition, as it was discussed in Chapter 3, the effects of nanoparticles on the living matter are highly dependent on their ability to overcome various human body biological barriers as well as numerous physicochemical changes. Therefore, placement of the nanoparticles into a Petri dish with the growing cells *in vitro* in order to evaluate the biological activity of the nanoagent is a contract oversimplification of the complex processes involved into nano-bio interactions. Three-dimensional cell culture *in vitro*, as well as the reconstruction of normal and diseased body structures by the means of tissue engineering, could provide the reliable alternative to bridge the gap between 2D cell culture *in vitro* and animal studies in nanoresearch. It also allows modelling human tissues directly, avoiding the problem of the respective extrapolation of the data from the animal-based research. However, this approach is neither well-known nor fully entered the field of nanotechnology and requires practical checks of feasibility and methodological advances. Thuswise, finally, we adventured to create some original 3D tissue models and test the properties of two types of nanotheranostic materials such as UCNPs and mesoporous silica nanoparticles loaded with fluorescent anti-cancer drug doxorubicin (MSNP-Dox) on them.

8.2. Summary and relevance of the study

There are several research outcomes of the presented work, which are the most important, to my opinion.

First of all, my collaborators and I revealed that UCNPs are not absolutely “innocuous” nanoparticles as it was generally held. This nanomaterial can induce notable undesirable effects emerged as decreased viability in the certain types of normal human cells. Several factors contribute to the final response of the sensitive cells, such as (at least) the way of surface modification (the chemical composition and charge, as well as the method of the coating) and concentration of the particles. This indicates that the safety risks for all the types of cells and tissues, which potentially could be exposed to the nanotheranostic agents, should be examined every time in separate experiments without extrapolation of the data from one study to another. In addition, there was also no direct correlation between the cytotoxic action and the cellular uptake of UCNPs, implying the possible negative potential of deposition of these materials in the interstitial space of the tissues or the absorption on the extracellular matrix should be taken into account. The significance of this finding is emphasized by our most recent observation, which was not included into the thesis [627], indicating the decrease of the cellular viability under longer exposure to the UCNPs as well as the another latest data published elsewhere [247] showing the dissolution of the lanthanide-doped nanophosphors in aqueous environments with the ions leakage.

However, the notable adverse reactions on UCNPs were only observed in 2D monolayer cell cultures of the human epidermal keratinocytes and were not revealed *in vivo* and in the 3D reconstructed

CHAPTER 8

viable epidermis. Following this, it is reasonable to conclude that 3D engineered tissues demonstrate the biological responses on the nanomaterials exposure more similar to the living tissues and organs than the 2D *in vitro* cell cultures.

The next significant result of this PhD project is the creation of the methodology of whole organ immersion decellularization (DCL) for the preparation of acellular organ specific scaffolds (AOSS) for 3D *in vitro* cell culture and tissue engineering. While the thesis itself includes only the data on two types of the AOSSes applied for the 3D *in vitro* reconstruction of normal viable human epidermis and breast cancer metastasis to the liver, in general, we created and tested the protocols for preparation of 10 types of AOSSes from different organs of chick embryo. I suggest that this outcome is an especially valuable as the limited availability of biomimetic and highly biocompatible solid scaffolds remains one of the most important obstacles for the advancement in the field of experimental tissue engineering.

It also may be emphasized that the proposed methodology is realized on the base of affordable and sustainable chick embryo experimental platform (which may be generalized to the term such as poultry embryo platform). This approach has a number of advantages. For example, there is no need in specialized animal facilities to work with the avian eggs (as only laboratory egg incubator and biosafety cabinets are critically needed for the typical manipulations), as well as no special animal keeping expenditures. The platform provides a source of sterile, structurally and functionally matching organs, harvested from the avian embryos of the same age. It worth mentioning that chick embryo model allows to perform various experiments *in vivo* more efficiently, because, accordingly to the “Australian code of practice for the care and use of animals for scientific purposes”, there is no need in a special ethical clearance until certain stage of embryonic development (for the chicks this period is equal to 12 days from the beginning of incubation). For instance, it is relatively easy to carry out grafting of the cells, tissues or biomaterials on the embryonic chorioallantoic membrane (CAM), inject the nanoparticles into blood stream etc. as all these procedures rely on use immature embryos (up to 12 days of embryonic age). Some of these approaches were verified in our preliminary experiments, which are briefly reported in the thesis such as the study of angiogenic potential of the AOSSes and engineered tumors and the accumulation of UCNPs in vicinity of the grafted on CAM tumor spheroids, as well as in a separate nano-pharmacokinetics test [628].

Further progress of this work was translated into the creation of the 3D engineered tissue models of skin and metastatic breast cancer. After the initial stage of the development and optimization of 3D organospecific scaffold-based cell culture protocols for HaCaT keratinocytes and MDA-MB-231 breast cancer cells, respectively, the examination of the feasibility of the reconstructed tissues for nanoresearch became our primary task. This, in particular, required adaptation of the existing methodology used for evaluation of the nanotoxicity and cellular internalization of the nanoparticles to the voluminous *in vitro* cultures as there were no commonly accepted or standard procedures for doing this. Next, we found that both normal and cancer cells grown in 3D tissue engineered cultures were less sensitive to the cytotoxic challenges such as exposure to UCNPs with different surface coatings and mesoporous silica

CHAPTER 8

nanoparticles loaded with doxorubicin and free doxorubicin drug, than their counterparts cultured in conventional monolayers. The obtained result emphasizes the regulating role of microenvironment in the cellular responses on the nanoparticles, as well as importance of the prevalidation of the effective/toxic doses of nanotherapeutics/ nanoprobe with use of 3D cell cultures before the transition to the animal models and clinical trials.

We also successfully demonstrated feasibility of various approaches to visualization and quantitative bioimaging of nanotheranostic materials in the cells cultured *in vitro* in 2D and 3D conditions (for both UCNPs and AMS-6-Dox) as well as in animal experiments *in vivo* and *ex vivo* (for UCNPs only). The methodology developed and provided as a result of these studies may be helpful for further research applications involving photoluminescent and fluorescent nanomaterials in the major available experimental settings (*in vitro* monolayers, reconstructed tissues, live animals and *ex vivo* organs).

Finally, the current project resulted in interesting findings in cancer biology obtained with use of our 3D engineered model of breast cancer metastasis to the liver. We believe that the proposed model made possible the direct *in vitro* observation of the metastatic colonization of a secondary organ by cancer cells for the first time. The advantageous technique applied for the DCL of chick embryo liver allowed to preserve the structure of ECM of different compartments of the organ such as former sinusoid capillaries associated with the hepatic parenchyma and the “stromal” structures including decellularized vasculature and connective tissue of the interlobular septae. Following high-density seeding of the liver scaffolds with breast cancer cells we found that the efficiency of initial cellular adhesion to the AOSSes comprises approximately 15% of the number of cells attached under the matching conditions to the cultural plastic, which is in accordance with the modern understanding of the critical role of the initial attachment of the circulating cancer cells to the host organ structures after the vasculature escape (which is very low) for initiation of the metastasis in general [629]. After that different dynamics of cell populations was also observed in 2D and 3D *in vitro* cultures during 4 weeks. The data testified in favour of the hypothesis that in conventional 2D monolayer cultures *in vitro* the cells demonstrate a kind of artificial proliferation and metabolic activity. This implies that the drug- and nanotesting results obtained with use of 2D cell cultures *in vitro* should be treated with caution. Finally, a result, which as we believe, has a particular significance for the understanding of the metastatic cancer machinery is the demonstration of possible co-existence of two alternative niches in the liver ECM, able to govern and switch the colonization behaviour programs of the cancer cells. This observation, in addition to its theoretical value, may be used to improve the application schemes of therapeutic agents and for more reasonable interpretation of the diagnostic data, evaluation of the metastatic cancer status and progression.

8.3. Future perspectives

I believe that this work has contributed to the understanding of the effects of the nanoparticles' design on nano-bio interactions and emphasized the importance of the validation of the theranostic potential of the nanoagents in the experimental settings, mimicking the actually existing tissue and body context. I also hope that this project revealed several compelling arguments in favour to shift the current nanotechnology testing paradigm from simple, well-known and easy-to-get-a-result 2D *in vitro* cell culture techniques towards the challenging, unpredictable and risky territory of discoveries, opening for the applications of 3D experimental tissue engineering in nanoresearch. I can see the current study as one of the initial steps in this direction, as a number of limitations of this research are obvious, but, expectably, can be approached in future.

In order to get closer to the more realistic reproduction of the normal and diseased tissues, the two issues should be addressed first such as 1) the diversity of the cell types/phenotypes/maturity stages or malignancy degrees simultaneously included into the models and 2) the oxygen/nutrients/metabolites transport systems able to replace or reconstruct the blood and lymphatic circulation. For example, with regard to the first challenge, the further development of the model of the metastasis of breast cancer to the liver, may involve the population of the liver AOSS with hepatocytes, endothelial cells and fibroblasts. To improve the model of reconstructed viable epidermis other types of epidermal cells such as dendritic cells, melanocytes and the cells of inflammatory infiltrates may be added to the basic keratinocytes culture, while the AOSS part, representing the dermis, may be seeded with dermal fibroblasts and coated with Matrigel or another surrogate of basement membrane for restoration of the full-thickness skin structure. This complexity is important, because, as it follows from our current results, different cell types may have a distinctive reaction on nanoparticles, so the cumulative response of the tissue on the exposure to various nanomaterials may vary dependently on the construct composition. In addition, we can expect that new types of *in vitro* models of diseases will be in high demand in short time for the nanoresearch applications. For instance, the methods to model pathogenesis of the inflammatory conditions and infections in 3D cell cultures *in vitro* or by tissue engineering look as an attractive alternative to the animal studies. This point is significant because the recent reports indicate that the nano-bio interactions are altered not only in cancer foci but also in the inflamed tissues [630]. In particular, many types of nanomaterials can induce inflammation [351, 488, 631-633], or, in contrast, can help to control this pathological process, as it has been demonstrated in our study, which was not included into the thesis [634], and several other reports [635, 636]. At the same time, the inert nanotheranostic materials like MSNPs loaded with contrast agents may be used for bioimaging of the inflammation sites [637]. In addition, I envisage that the 3D engineered models of healthy and diseased tissues may be adapted in order to provide reproducible and affordable testbeds for high-throughput pharmacological drug evaluation after the development of the procedures of massive production of the AOSSes.

CHAPTER 8

The second problem, which is vascularization of engineered tissues, is important not only to make it possible to increase the volume of the reconstructed tissues maintained *in vitro* (i.e. avoid central necrosis in the constructs), but also to model the transport of nanoagents through the vasculature, their extravasation into the interstitial space and interaction with the interstitial fluid flows, shear and solid stresses. This may be approached by the sophisticated DCL methods [638, 639]. An alternative strategy may rely on the development of the bioreactor systems. In particular, our analysis of the field of bioreactor-based tumor tissue engineering, which was not included into the thesis [502], testifies for the greatest potential of microfluidic methodologies like organ-on-a-chip, system-of-organs-on-a-chip and tumor-on-a-chip to contribute towards novel breakthroughs in the field.

Following the literature analysis [11, 640] and our observations, another trend, promising for notable outcomes for the development of nanotheranostics, such as *in silico* modelling of nano-bio interactions under complex bioenvironmental conditions, could be envisaged. In a future perspective *in silico* modelling can replace a significant part of nanotesting on living subjects, however, currently the formation of the background databases is needed [640], and 3D engineered tissues and 3D *in vitro* cell cultures may be used for this.

Finally, I would suppose that the nanotheranostic materials and associated methods, in turn, may promote the advances in the 3D *in vitro* culture and tissue engineering in general. A challenging problem of non-invasive data collection from the growing *in vitro* or implanted *in vivo* engineered tissues is now emerging because of the specific volume, density and non-transparency of 3D reconstructed tissues. Labelling of the cells and equipping of the scaffolds with the contrasting nanotheranostic agents may help to make these structures more “readable” for the endpoint assays. Moreover, the concept of nanocomposite smart-scaffolds, containing interactive nanocomponents, like, for example, light-triggerable UCNPs, potentially allow overcoming a number of barriers normally existing for drug delivery, distant control of the tissues development and various research applications.

References

1. Bleeker, E.A., et al., *Considerations on the EU definition of a nanomaterial: science to support policy making*. Regul Toxicol Pharmacol, 2013. **65**(1): p. 119-25.
2. *Comission recomendation of 18 October 2011 on the definition of nanomaterial*. Official Journal of the European Union, 2011. **686**/EU.
3. *Nanoscale Materials in Targeted Drug Delivery, Theragnosis and Tissue Regeneration / edited by Sudesh Kumar Yadav*, ed. S.K. Yadav, et al. 2016: Singapore : Springer Singapore : Imprint: Springer.
4. Cedervall, T., et al., *Understanding the nanoparticle-protein corona using methods to quantify exchange rates and affinities of proteins for nanoparticles*. Proc Natl Acad Sci U S A, 2007. **104**(7): p. 2050-5.
5. Porter, A.L. and J. Youtie, *Where does nanotechnology belong in the map of science?* Nat Nano, 2009. **4**(9): p. 534-536.
6. Cui, H. and J. Wang, *Progress in the Development of Nanotheranostic Systems*. Theranostics, 2016. **6**(7): p. 915-917.
7. *Advances in Nanotheranostics I*. Springer Series in Biomaterials Science and Engineering ed. M. Wang. 2016.
8. Mura, S. and P. Couvreur, *Nanotheranostics for personalized medicine*. Advanced Drug Delivery Reviews, 2012. **64**(13): p. 1394-1416.
9. Muthu, M.S., et al., *Nanotheranostics - application and further development of nanomedicine strategies for advanced theranostics*. Theranostics, 2014. **4**(6): p. 660-77.
10. Kathawala, M.H., et al., *Emerging in vitro models for safety screening of high-volume production nanomaterials under environmentally relevant exposure conditions*. Small, 2013. **9**(9-10): p. 1504-20.
11. Tay, C.Y., et al., *Reality Check for Nanomaterial-Mediated Therapy with 3D Biomimetic Culture Systems*. Advanced Functional Materials, 2016. **26**(23): p. 4046-4065.
12. Leong, D.T. and K.W. Ng, *Probing the relevance of 3D cancer models in nanomedicine research*. Adv Drug Deliv Rev, 2014. **79-80**(0): p. 95-106.
13. Baker, B.M. and C.S. Chen, *Deconstructing the third dimension: how 3D culture microenvironments alter cellular cues*. J Cell Sci, 2012. **125**(Pt 13): p. 3015-24.
14. Ingber, D.E., *Mechanical control of tissue growth: Function follows form*. Proceedings of the National Academy of Sciences of the United States of America, 2005. **102**(33): p. 11571-11572.
15. Huttmacher, D.W., et al., *Can tissue engineering concepts advance tumor biology research?* Trends Biotechnol, 2010. **28**(3): p. 125-33.
16. Ricci, C., L. Moroni, and S. Danti, *Cancer tissue engineering - new perspectives in understanding the biology of solid tumours - a critical review*. OA Tissue Engineering, 2013. **1**(1): p. 4.
17. Ho, D.N. and S. Sun, *The gap between cell and animal models: nanoparticle drug-delivery development and characterization using microtissue models*. Therapeutic Delivery, 2012. **3**(8): p. 915-917.
18. Damour, O., C. Augustin, and A.F. Black, *Applications of reconstructed skin models in pharmacotoxicological trials*. Med Biol Eng Comput, 1998. **36**(6): p. 825-32.
19. Schanz, J., et al., *Vascularised human tissue models: a new approach for the refinement of biomedical research*. J Biotechnol, 2010. **148**(1): p. 56-63.
20. Mazzoleni, G., D. Di Lorenzo, and N. Steimberg, *Modelling tissues in 3D: the next future of pharmacotoxicology and food research?* Genes Nutr, 2009. **4**(1): p. 13-22.
21. Xu, X., M.C. Farach-Carson, and X. Jia, *Three-dimensional in vitro tumor models for cancer research and drug evaluation*. Biotechnol Adv, 2014. **32**(7): p. 1256-68.
22. Gibbons, M.C., M.A. Foley, and K.O. Cardinal, *Thinking inside the box: keeping tissue-engineered constructs in vitro for use as preclinical models*. Tissue Eng Part B Rev, 2013. **19**(1): p. 14-30.
23. Wang, L.S., M.C. Chuang, and J.A. Ho, *Nanotheranostics--a review of recent publications*. Int J Nanomedicine, 2012. **7**: p. 4679-95.
24. Zhang, P., et al., *Recent Progress in Light-Triggered Nanotheranostics for Cancer Treatment*. Theranostics, 2016. **6**(7): p. 948-68.
25. Peer, D., et al., *Nanocarriers as an emerging platform for cancer therapy*. Nat Nano, 2007. **2**(12): p. 751-760.
26. Tan, H.L., et al., *Surface modification: how nanoparticles assemble to molecular imaging probes*. Journal of Nanoparticle Research, 2013. **15**(12): p. 1-16.
27. Petros, R.A. and J.M. DeSimone, *Strategies in the design of nanoparticles for therapeutic applications*. Nat Rev Drug Discov, 2010. **9**(8): p. 615-27.
28. Janib, S.M., A.S. Moses, and J.A. MacKay, *Imaging and drug delivery using theranostic nanoparticles*. Advanced drug delivery reviews, 2010. **62**(11): p. 1052-1063.

REFERENCES

29. Xie, J., S. Lee, and X. Chen, *Nanoparticle-based theranostic agents*. Advanced drug delivery reviews, 2010. **62**(11): p. 1064-1079.
30. Hahn, M.A., et al., *Nanoparticles as contrast agents for in-vivo bioimaging: current status and future perspectives*. Anal Bioanal Chem, 2011. **399**(1): p. 3-27.
31. Gupta, A.K. and M. Gupta, *Synthesis and surface engineering of iron oxide nanoparticles for biomedical applications*. Biomaterials, 2005. **26**(18): p. 3995-4021.
32. Bulte, J.W. and D.L. Kraitchman, *Iron oxide MR contrast agents for molecular and cellular imaging*. NMR Biomed, 2004. **17**(7): p. 484-99.
33. Gupta, B.K., et al., *Highly luminescent-paramagnetic nanophosphor probes for in vitro high-contrast imaging of human breast cancer cells*. Small, 2012. **8**(19): p. 3028-34.
34. Kievit, F.M. and M. Zhang, *Cancer Nanotheranostics: Improving Imaging and Therapy by Targeted Delivery Across Biological Barriers*. Advanced Materials, 2011. **23**(36): p. H217-H247.
35. He, F., et al., *Enhanced up/down-conversion luminescence and heat: Simultaneously achieving in one single core-shell structure for multimodal imaging guided therapy*. Biomaterials, 2016. **105**: p. 77-88.
36. Wang, S., et al., *Core/shell quantum dots with high relaxivity and photoluminescence for multimodality imaging*. J Am Chem Soc, 2007. **129**(13): p. 3848-56.
37. Zhou, T., B. Wu, and D. Xing, *Bio-modified Fe₃O₄core/Au shell nanoparticles for targeting and multimodal imaging of cancer cells*. J. Mater. Chem., 2012. **22**(2): p. 470-477.
38. Liu, H., et al., *Size-controlled synthesis of dendrimer-stabilized silver nanoparticles for X-ray computed tomography imaging applications*. Polymer Chemistry, 2010. **1**(10): p. 1677.
39. Talanov, V.S., et al., *Dendrimer-based nanoprobe for dual modality magnetic resonance and fluorescence imaging*. Nano Lett, 2006. **6**(7): p. 1459-63.
40. Hu, J., et al., *Drug-loaded and superparamagnetic iron oxide nanoparticle surface-embedded amphiphilic block copolymer micelles for integrated chemotherapeutic drug delivery and MR imaging*. Langmuir, 2011. **28**(4): p. 2073-2082.
41. Mitchell, N., et al., *Incorporation of paramagnetic, fluorescent and PET/SPECT contrast agents into liposomes for multimodal imaging*. Biomaterials, 2013. **34**(4): p. 1179-1192.
42. Hemmer, E., et al., *Exploiting the biological windows: current perspectives on fluorescent bioprobes emitting above 1000 nm*. Nanoscale Horizons, 2016. **1**(3): p. 168-184.
43. Haglund, E., M.M. Seale-Goldsmith, and J.F. Leary, *Design of multifunctional nanomedical systems*. Ann Biomed Eng, 2009. **37**(10): p. 2048-63.
44. Wicki, A., et al., *Nanomedicine in cancer therapy: challenges, opportunities, and clinical applications*. J Control Release, 2015. **200**: p. 138-57.
45. Herranz-Blanco, B., et al., *pH-Switch Nanoprecipitation of Polymeric Nanoparticles for Multimodal Cancer Targeting and Intracellular Triggered Delivery of Doxorubicin*. Adv Healthc Mater, 2016. **5**(15): p. 1904-16.
46. Dani, R.K., et al., *Temperature-Tunable Iron Oxide Nanoparticles for Remote-Controlled Drug Release*. AAPS PharmSciTech, 2014.
47. Lee, S.F., et al., *Ultrasound, pH, and magnetically responsive crown-ether-coated core/shell nanoparticles as drug encapsulation and release systems*. ACS Appl Mater Interfaces, 2013. **5**(5): p. 1566-74.
48. Shinde, K.N., et al., *Basic Mechanisms of Photoluminescence*, in *Phosphate Phosphors for Solid-State Lighting*. 2012, Springer Berlin Heidelberg: Berlin, Heidelberg. p. 41-59.
49. König, K., *Multiphoton microscopy in life sciences*. J Microsc, 2000. **200**(Pt 2): p. 83-104.
50. Jamieson, T., et al., *Biological applications of quantum dots*. Biomaterials, 2007. **28**(31): p. 4717-32.
51. Zhang, H., D. Yee, and C. Wang, *Quantum dots for cancer diagnosis and therapy: biological and clinical perspectives*. Nanomedicine, 2008. **3**(1): p. 83-91.
52. Hui, Y.Y., C.-L. Cheng, and H.-C. Chang, *Nanodiamonds for optical bioimaging*. Journal of Physics D: Applied Physics, 2010. **43**(37): p. 374021.
53. Hsiao, W.W., et al., *Fluorescent Nanodiamond: A Versatile Tool for Long-Term Cell Tracking, Super-Resolution Imaging, and Nanoscale Temperature Sensing*. Acc Chem Res, 2016. **49**(3): p. 400-7.
54. Edmonds, A.M., et al., *Nano-Ruby: A Promising Fluorescent Probe for Background-Free Cellular Imaging*. Particle & Particle Systems Characterization, 2013. **30**(6): p. 506-513.
55. Razali, W.A., et al., *Wide-field time-gated photoluminescence microscopy for fast ultrahigh-sensitivity imaging of photoluminescent probes*. J Biophotonics, 2016. **9**(8): p. 848-58.
56. Liu, Z. and X.J. Liang, *Nano-carbons as theranostics*. Theranostics, 2012. **2**(3): p. 235-7.
57. Liu, Z., et al., *Carbon Nanotubes in Biology and Medicine: In vitro and in vivo Detection, Imaging and Drug Delivery*. Nano Res, 2009. **2**(2): p. 85-120.
58. Conde, J., G. Doria, and P. Baptista, *Noble metal nanoparticles applications in cancer*. J Drug Deliv, 2012. **2012**: p. 751075.

REFERENCES

59. Chen, J., et al., *Gold nanocages: bioconjugation and their potential use as optical imaging contrast agents*. Nano letters, 2005. **5**(3): p. 473-477.
60. Boisselier, E. and D. Astruc, *Gold nanoparticles in nanomedicine: preparations, imaging, diagnostics, therapies and toxicity*. Chem Soc Rev, 2009. **38**(6): p. 1759-82.
61. Lu, J., et al., *Biocompatibility, biodistribution, and drug-delivery efficiency of mesoporous silica nanoparticles for cancer therapy in animals*. Small, 2010. **6**(16): p. 1794-805.
62. Wang, Z., G. Niu, and X. Chen, *Polymeric materials for theranostic applications*. Pharm Res, 2014. **31**(6): p. 1358-76.
63. Wu, S., et al., *Non-blinking and photostable upconverted luminescence from single lanthanide-doped nanocrystals*. Proc Natl Acad Sci U S A, 2009. **106**(27): p. 10917-21.
64. Razali, W.A., *A nanoruby-based photoluminescent probe towards bioimaging applications*, in *Faculty of Science and Engineering*. 2016, Macquarie University: Sydney. p. 203.
65. Zhou, J., et al., *Upconversion luminescent materials: advances and applications*. Chem Rev, 2015. **115**(1): p. 395-465.
66. Haase, M. and H. Schafer, *Upconverting nanoparticles*. Angew Chem Int Ed Engl, 2011. **50**(26): p. 5808-29.
67. Nadort, A., J. Zhao, and E.M. Goldys, *Lanthanide upconversion luminescence at a nanoscale: fundamentals and optical properties*. Nanoscale, 2016.
68. Xu, C.T., et al., *Upconverting nanoparticles for pre-clinical diffuse optical imaging, microscopy and sensing: Current trends and future challenges*. Laser & Photonics Reviews, 2013. **7**(5): p. 663-697.
69. Hemmer, E., et al., *Upconverting and NIR emitting rare earth based nanostructures for NIR-bioimaging*. Nanoscale, 2013. **5**(23): p. 11339-61.
70. Wang, F. and X. Liu, *Recent advances in the chemistry of lanthanide-doped upconversion nanocrystals*. Chem Soc Rev, 2009. **38**(4): p. 976-89.
71. Zhou, B., et al., *Controlling upconversion nanocrystals for emerging applications*. Nat Nanotechnol, 2015. **10**(11): p. 924-36.
72. Wang, F., et al., *Upconversion nanoparticles in biological labeling, imaging, and therapy*. Analyst, 2010. **135**(8): p. 1839-54.
73. Min, Y., et al., *Recent Advance of Biological Molecular Imaging Based on Lanthanide-Doped Upconversion-Luminescent Nanomaterials*. Nanomaterials, 2014. **4**(1): p. 129-154.
74. Suyver, J.F., et al., *Upconversion spectroscopy and properties of NaYF₄ doped with , and/or*. Journal of Luminescence, 2006. **117**(1): p. 1-12.
75. Wang, F., et al., *Simultaneous phase and size control of upconversion nanocrystals through lanthanide doping*. Nature, 2010. **463**(7284): p. 1061-5.
76. Ye, X., et al., *Morphologically controlled synthesis of colloidal upconversion nanophosphors and their shape-directed self-assembly*. Proc Natl Acad Sci U S A, 2010. **107**(52): p. 22430-5.
77. Wilhelm, S., et al., *Water dispersible upconverting nanoparticles: effects of surface modification on their luminescence and colloidal stability*. Nanoscale, 2015. **7**(4): p. 1403-10.
78. Wang, F., J. Wang, and X. Liu, *Direct evidence of a surface quenching effect on size-dependent luminescence of upconversion nanoparticles*. Angew Chem Int Ed Engl, 2010. **49**(41): p. 7456-60.
79. Feng, W., X. Zhu, and F. Li, *Recent advances in the optimization and functionalization of upconversion nanomaterials for in vivo bioapplications*. NPG Asia Materials, 2013. **5**: p. e75.
80. Shang, Y., et al., *Synthesis of Upconversion β -NaYF₄:Nd³⁺/Yb³⁺/Er³⁺ Particles with Enhanced Luminescent Intensity through Control of Morphology and Phase*. Nanomaterials, 2015. **5**(1): p. 218-232.
81. Chen, G., C. Yang, and P.N. Prasad, *Nanophotonics and nanochemistry: controlling the excitation dynamics for frequency up- and down-conversion in lanthanide-doped nanoparticles*. Acc Chem Res, 2013. **46**(7): p. 1474-86.
82. Pokhrel, M., et al., *Stokes emission in GdF(3):Nd(3)(+) nanoparticles for bioimaging probes*. Nanoscale, 2014. **6**(3): p. 1667-74.
83. Gorris, H.H. and O.S. Wolfbeis, *Photon-upconverting nanoparticles for optical encoding and multiplexing of cells, biomolecules, and microspheres*. Angew Chem Int Ed Engl, 2013. **52**(13): p. 3584-600.
84. Wang, F. and X. Liu, *Upconversion multicolor fine-tuning: visible to near-infrared emission from lanthanide-doped NaYF₄ nanoparticles*. J Am Chem Soc, 2008. **130**(17): p. 5642-3.
85. Zhang, F., et al., *Fluorescence upconversion microbarcodes for multiplexed biological detection: nucleic acid encoding*. Advanced Materials, 2011. **23**(33): p. 3775-3779.
86. Mahalingam, V., et al., *Colloidal Tm³⁺/Yb³⁺-Doped LiYF₄ Nanocrystals: Multiple Luminescence Spanning the UV to NIR Regions via Low-Energy Excitation*. Adv. Mater., 2009. **21**: p. 4025.
87. Song, Z., et al., *Background free imaging of upconversion nanoparticle distribution in human skin*. J Biomed Opt, 2013. **18**(6): p. 061215.

REFERENCES

88. Chen, G., et al., *Upconversion nanoparticles: design, nanochemistry, and applications in theranostics*. Chem Rev, 2014. **114**(10): p. 5161-214.
89. Nadort, A., et al., *Quantitative imaging of single upconversion nanoparticles in biological tissue*. PLoS One, 2013. **8**(5): p. e63292.
90. Yang, T., et al., *Cubic sub-20 nm NaLuF₄-based upconversion nanophosphors for high-contrast bioimaging in different animal species*. Biomaterials, 2012. **33**(14): p. 3733-42.
91. Chen, G., et al., *(alpha-NaYbF₄:Tm(3+))/CaF₂ core/shell nanoparticles with efficient near-infrared to near-infrared upconversion for high-contrast deep tissue bioimaging*. ACS Nano, 2012. **6**(9): p. 8280-7.
92. Tuchin, V.V., et al., *Light propagation in tissues with controlled optical properties*. J Biomed Opt, 1997. **2**(4): p. 401-17.
93. Idris, N.M., et al., *Upconversion nanoparticles as versatile light nanotransducers for photoactivation applications*. Chem Soc Rev, 2015. **44**(6): p. 1449-78.
94. Zheng, X., et al., *High-Contrast Visualization of Upconversion Luminescence in Mice Using Time-Gating Approach*. Anal Chem, 2016. **88**(7): p. 3449-54.
95. Zvyagin, A.V., et al., *Luminescent Nanomaterials for Molecular-Specific Cellular Imaging*, in *Handbook of Nano-Optics and Nanophotonics*, M. Ohtsu, Editor. 2013, Springer Berlin Heidelberg: Berlin, Heidelberg. p. 563-596.
96. Lu, Y., et al., *Tunable lifetime multiplexing using luminescent nanocrystals*. Nat Photon, 2014. **8**(1): p. 32-36.
97. Hilderbrand, S.A., et al., *Upconverting luminescent nanomaterials: application to in vivo bioimaging*. Chem Commun (Camb), 2009(28): p. 4188-90.
98. Lim, S.F., et al., *In vivo and scanning electron microscopy imaging of up-converting nanophosphors in Caenorhabditis elegans*. Nano Lett, 2006. **6**(2): p. 169-74.
99. Werts, M.H., *Making sense of lanthanide luminescence*. Science progress, 2005. **88**(2): p. 101-131.
100. Na, H., et al., *Rational morphology control of beta-NaYF₄:Yb,Er/Tm upconversion nanophosphors using a ligand, an additive, and lanthanide doping*. Nanoscale, 2013. **5**(10): p. 4242-51.
101. Liu, D., et al., *Three-dimensional controlled growth of monodisperse sub-50 nm heterogeneous nanocrystals*. Nat Commun, 2016. **7**: p. 10254.
102. Zhao, L., et al., *Stem cell labeling using polyethylenimine conjugated (alpha-NaYbF₄:Tm³⁺)/CaF₂ upconversion nanoparticles*. Theranostics, 2013. **3**(4): p. 249-57.
103. Liu, K., et al., *Targeted labeling of an early-stage tumor spheroid in a chorioallantoic membrane model with upconversion nanoparticles*. Nanoscale, 2015. **7**(5): p. 1596-600.
104. Jiang, G., et al., *An effective polymer cross-linking strategy to obtain stable dispersions of upconverting NaYF₄ nanoparticles in buffers and biological growth media for biolabeling applications*. Langmuir, 2012. **28**(6): p. 3239-47.
105. Gargas, D.J., et al., *Engineering bright sub-10-nm upconverting nanocrystals for single-molecule imaging*. Nat Nanotechnol, 2014. **9**(4): p. 300-5.
106. Bagheri, A., et al., *Lanthanide-Doped Upconversion Nanoparticles: Emerging Intelligent Light-Activated Drug Delivery Systems*. Advanced Science, 2016: p. n/a-n/a.
107. Liu, J., et al., *NIR-triggered anticancer drug delivery by upconverting nanoparticles with integrated azobenzene-modified mesoporous silica*. Angew Chem Int Ed Engl, 2013. **52**(16): p. 4375-9.
108. Li, C., et al., *Multifunctional upconversion mesoporous silica nanostructures for dual modal imaging and in vivo drug delivery*. Small, 2013. **9**(24): p. 4150-9.
109. Wang, C., L. Cheng, and Z. Liu, *Drug delivery with upconversion nanoparticles for multi-functional targeted cancer cell imaging and therapy*. Biomaterials, 2011. **32**(4): p. 1110-20.
110. Wang, C., et al., *Near-infrared light induced in vivo photodynamic therapy of cancer based on upconversion nanoparticles*. Biomaterials, 2011. **32**(26): p. 6145-54.
111. Chatterjee, D.K. and Z. Yong, *Upconverting nanoparticles as nanotransducers for photodynamic therapy in cancer cells*. Nanomedicine (Lond), 2008. **3**(1): p. 73-82.
112. Liang, L., et al., *Facile Assembly of Functional Upconversion Nanoparticles for Targeted Cancer Imaging and Photodynamic Therapy*. ACS Appl Mater Interfaces, 2016. **8**(19): p. 11945-53.
113. Achatz, D.E., et al., *Luminescent sensing of oxygen using a quenchable probe and upconverting nanoparticles*. Angewandte Chemie International Edition, 2011. **50**(1): p. 260-263.
114. María, G.-B. and P.-P. Julia, *Upconversion luminescent nanoparticles in physical sensing and in monitoring physical processes in biological samples*. Methods and Applications in Fluorescence, 2015. **3**(4): p. 042002.
115. Chatterjee, D.K., M.K. Gnanasammandhan, and Y. Zhang, *Small upconverting fluorescent nanoparticles for biomedical applications*. Small, 2010. **6**(24): p. 2781-95.
116. Bogdan, N., et al., *Synthesis of ligand-free colloiddally stable water dispersible brightly luminescent lanthanide-doped upconverting nanoparticles*. Nano Lett, 2011. **11**(2): p. 835-40.

REFERENCES

117. Du, H., W. Zhang, and J. Sun, *Structure and upconversion luminescence properties of BaYF₅:Yb³⁺, Er³⁺ nanoparticles prepared by different methods*. Journal of Alloys and Compounds, 2011. **509**(7): p. 3413-3418.
118. Lin, M., et al., *Recent advances in synthesis and surface modification of lanthanide-doped upconversion nanoparticles for biomedical applications*. Biotechnol Adv, 2012. **30**(6): p. 1551-61.
119. Liu, H., et al., *Balancing power density based quantum yield characterization of upconverting nanoparticles for arbitrary excitation intensities*. Nanoscale, 2013. **5**(11): p. 4770-5.
120. Xu, C.T., et al., *Upconverting nanoparticles for pre-clinical diffuse optical imaging, microscopy and sensing: Current trends and future challenges*. Laser & Photonics Reviews, 2013. **7**(5): p. 663-697.
121. Sedlmeier, A. and H.H. Gorris, *Surface modification and characterization of photon-upconverting nanoparticles for bioanalytical applications*. Chem Soc Rev, 2015. **44**(6): p. 1526-60.
122. Bischof, C., et al., *Quantification of C-H quenching in near-IR luminescent ytterbium and neodymium cryptates*. J Am Chem Soc, 2010. **132**(41): p. 14334-5.
123. Yi, G., et al., *Synthesis, characterization, and biological application of size-controlled nanocrystalline NaYF₄: Yb, Er infrared-to-visible up-conversion phosphors*. Nano Letters, 2004. **4**(11): p. 2191-2196.
124. Heer, S., et al., *Highly Efficient Multicolour Upconversion Emission in Transparent Colloids of Lanthanide-Doped NaYF₄ Nanocrystals*. Advanced Materials, 2004. **16**(23-24): p. 2102-2105.
125. Li, Z. and Y. Zhang, *Monodisperse silica-coated polyvinylpyrrolidone/NaYF₄(4) nanocrystals with multicolor upconversion fluorescence emission*. Angew Chem Int Ed Engl, 2006. **45**(46): p. 7732-5.
126. Zhang, Y.W., et al., *Single-crystalline and monodisperse LaF₃ triangular nanoplates from a single-source precursor*. J Am Chem Soc, 2005. **127**(10): p. 3260-1.
127. Mai, H.X., et al., *High-quality sodium rare-earth fluoride nanocrystals: controlled synthesis and optical properties*. J Am Chem Soc, 2006. **128**(19): p. 6426-36.
128. Li, Z. and Y. Zhang, *An efficient and user-friendly method for the synthesis of hexagonal-phase NaYF₄:Yb, Er/Tm nanocrystals with controllable shape and upconversion fluorescence*. Nanotechnology, 2008. **19**(34): p. 345606.
129. Sun, L.D., et al., *Upconversion of rare Earth nanomaterials*. Annu Rev Phys Chem, 2015. **66**: p. 619-42.
130. Yi, G.S. and G.M. Chow, *Synthesis of Hexagonal-Phase NaYF₄:Yb,Er and NaYF₄:Yb,Tm Nanocrystals with Efficient Up-Conversion Fluorescence*. Advanced Functional Materials, 2006. **16**(18): p. 2324-2329.
131. Liu, Y., et al., *Tri-color upconversion luminescence of Rare earth doped BaTiO₃ nanocrystals and lowered color separation*. Optics Express, 2009. **17**(11): p. 9089.
132. Patra, A., et al., *Upconversion in Er³⁺:ZrO₂ Nanocrystals*. The Journal of Physical Chemistry B, 2002. **106**(8): p. 1909-1912.
133. Li, C., et al., *Shape-Controllable Synthesis and Upconversion Properties of Lutetium Fluoride (Doped with Yb³⁺/Er³⁺) Microcrystals by Hydrothermal Process*. The Journal of Physical Chemistry C, 2008. **112**(35): p. 13395-13404.
134. Patra, A., et al., *Fluorescence Upconversion Properties of Er³⁺-Doped TiO₂ and BaTiO₃ Nanocrystallites*. Chemistry of Materials, 2003. **15**(19): p. 3650-3655.
135. Quan, Z., et al., *Multicolor tuning of manganese-doped ZnS colloidal nanocrystals*. Langmuir, 2009. **25**(17): p. 10259-62.
136. Hanahan, D. and R.A. Weinberg, *Hallmarks of cancer: the next generation*. Cell, 2011. **144**(5): p. 646-74.
137. Wang, X., et al., *A general strategy for nanocrystal synthesis*. Nature, 2005. **437**(7055): p. 121-4.
138. Wang, F., et al., *Synthesis of polyethylenimine/NaYF₄ nanoparticles with upconversion fluorescence*. Nanotechnology, 2006. **17**(23): p. 5786.
139. Zhang, F., et al., *Uniform Nanostructured Arrays of Sodium Rare-Earth Fluorides for Highly Efficient Multicolor Upconversion Luminescence*. Angewandte Chemie International Edition, 2007. **46**(42): p. 7976-7979.
140. Chuai, X., et al., *Synthesis and characterization of Yb³⁺, Tm³⁺:Ba₂YF₇ nanocrystalline with efficient upconversion fluorescence*. Materials Letters, 2011. **65**(15-16): p. 2368-2370.
141. Feng, S. and R. Xu, *New materials in hydrothermal synthesis*. Acc Chem Res, 2001. **34**(3): p. 239-47.
142. Huang, P., D. Chen, and Y. Wang, *Host-sensitized multicolor tunable luminescence of lanthanide ion doped one-dimensional YVO₄ nano-crystals*. Journal of Alloys and Compounds, 2011. **509**(7): p. 3375-3381.
143. Hai, G., et al., *Seed-mediated synthesis of NaYF₄:Yb, Er / NaGdF₄ nanocrystals with improved upconversion fluorescence and MR relaxivity*. Nanotechnology, 2010. **21**(12): p. 125602.
144. Niu, W., et al., *Multicolor output and shape controlled synthesis of lanthanide-ion doped fluorides upconversion nanoparticles*. Dalton Trans, 2011. **40**(13): p. 3305-14.

REFERENCES

145. Yan, Z.-G. and C.-H. Yan, *Controlled synthesis of rare earth nanostructures*. Journal of Materials Chemistry, 2008. **18**(42): p. 5046.
146. Zhang, F., et al., *Shape, size, and phase-controlled rare-Earth fluoride nanocrystals with optical up-conversion properties*. Chemistry, 2009. **15**(41): p. 11010-9.
147. Wang, L., Y. Zhang, and Y. Zhu, *One-pot synthesis and strong near-infrared upconversion luminescence of poly(acrylic acid)-functionalized YF₃:Yb³⁺/Er³⁺ nanocrystals*. Nano Research, 2010. **3**(5): p. 317-325.
148. Su, J., et al., *Phase transition, structure and luminescence of Eu:YAG nanophosphors by co-precipitation method*. Journal of Alloys and Compounds, 2009. **470**(1-2): p. 306-310.
149. Xu, Z., et al., *Uniform Ln(OH)₃ and Ln₂O₃ (Ln = Eu, Sm) Submicrospindles: Facile Synthesis and Characterization*. Crystal Growth & Design, 2009. **9**(9): p. 4127-4135.
150. Lim, S.F., et al., *Upconverting nanophosphors for bioimaging*. Nanotechnology, 2009. **20**(40): p. 405701.
151. Mahalingam, V., et al., *Sensitized Ce(3+) and Gd(3+) ultraviolet emissions by Tm(3+) in colloidal LiYF₄ nanocrystals*. Chemistry, 2009. **15**(38): p. 9660-3.
152. Wang, F., et al., *Synthesis of polyethylenimine/NaYF₄ nanoparticles with upconversion fluorescence*. Nanotechnology, 2006. **17**(23): p. 5786-5791.
153. Gallini, S., J.R. Jurado, and M.T. Colomer, *Combustion Synthesis of Nanometric Powders of LaPO₄ and Sr-Substituted LaPO₄*. Chemistry of Materials, 2005. **17**(16): p. 4154-4161.
154. Shan, J. and Y. Ju, *A single-step synthesis and the kinetic mechanism for monodisperse and hexagonal-phase NaYF₄:Yb, Er upconversion nanophosphors*. Nanotechnology, 2009. **20**(27): p. 275603.
155. Vu, N., et al., *Photoluminescence and cathodoluminescence properties of Y₂O₃:Eu nanophosphors prepared by combustion synthesis*. Journal of Luminescence, 2007. **122-123**: p. 776-779.
156. Abdul Jalil, R. and Y. Zhang, *Biocompatibility of silica coated NaYF₄ upconversion fluorescent nanocrystals*. Biomaterials, 2008. **29**(30): p. 4122-8.
157. Su Kim, J., et al., *Optical and structural properties of ZnGa₂O₄: Eu³⁺ nanophosphor by hydrothermal method*. Journal of Luminescence, 2007. **122-123**: p. 851-854.
158. Venkatramu, V., et al., *Synthesis and luminescence properties of Er³⁺-doped Lu₃Ga₅O₁₂ nanocrystals*. Journal of Luminescence, 2008. **128**(5-6): p. 811-813.
159. Chen, X., et al., *Photon upconversion in core-shell nanoparticles*. Chem Soc Rev, 2015. **44**(6): p. 1318-30.
160. Wang, Z.L., et al., *A Facile Synthesis and Photoluminescent Properties of Redispersible CeF₃, CeF₃:Tb³⁺, and CeF₃:Tb³⁺/LaF₃(Core/Shell) Nanoparticles*. Chemistry of Materials, 2006. **18**(8): p. 2030-2037.
161. Mai, H.-X., et al., *Highly Efficient Multicolor Up-Conversion Emissions and Their Mechanisms of Monodisperse NaYF₄:Yb,Er Core and Core/Shell-Structured Nanocrystals*. The Journal of Physical Chemistry C, 2007. **111**(37): p. 13721-13729.
162. Vetrone, F., et al., *The Active-Core/Active-Shell Approach: A Strategy to Enhance the Upconversion Luminescence in Lanthanide-Doped Nanoparticles*. Advanced Functional Materials, 2009. **19**(18): p. 2924-2929.
163. Qian, H.S. and Y. Zhang, *Synthesis of hexagonal-phase core-shell NaYF₄ nanocrystals with tunable upconversion fluorescence*. Langmuir, 2008. **24**(21): p. 12123-5.
164. Yan, C., et al., *Near-IR photoresponse in new up-converting CdSe/NaYF₄:Yb,Er nanoheterostructures*. J Am Chem Soc, 2010. **132**(26): p. 8868-9.
165. Zhang, H., et al., *Plasmonic Modulation of the Upconversion Fluorescence in NaYF₄:Yb/Tm Hexaplate Nanocrystals Using Gold Nanoparticles or Nanoshells*. Angewandte Chemie, 2010. **122**(16): p. 2927-2930.
166. Zou, W., et al., *Broadband dye-sensitized upconversion of near-infrared light*. Nature Photonics, 2012. **6**(8): p. 560-564.
167. Stöber, W., A. Fink, and E. Bohn, *Controlled growth of monodisperse silica spheres in the micron size range*. Journal of colloid and interface science, 1968. **26**(1): p. 62-69.
168. Li, Z., Y. Zhang, and S. Jiang, *Multicolor Core/Shell-Structured Upconversion Fluorescent Nanoparticles*. Advanced Materials, 2008. **20**(24): p. 4765-4769.
169. Li, Z., et al., *Modification of NaYF₄:Yb,Er@SiO₂ Nanoparticles with Gold Nanocrystals for Tunable Green-to-Red Upconversion Emissions*. The Journal of Physical Chemistry C, 2011. **115**(8): p. 3291-3296.
170. Liu, R., et al., *Controlled synthesis and optical spectroscopy of lanthanide-doped KLaF₄ nanocrystals*. Nanoscale, 2012. **4**(15): p. 4485-91.
171. Liu, C., et al., *Monodisperse, size-tunable and highly efficient β-NaYF₄:Yb,Er(Tm) up-conversion luminescent nanospheres: controllable synthesis and their surface modifications*. Journal of Materials Chemistry, 2009. **19**(21): p. 3546.

REFERENCES

172. Wang, F., et al., *Tuning upconversion through energy migration in core-shell nanoparticles*. Nat Mater, 2011. **10**(12): p. 968-73.
173. Zhang, F., *Surface Modification and Bioconjugation of Upconversion Nanoparticles*, in *Photon Upconversion Nanomaterials*. 2015, Springer Berlin Heidelberg: Berlin, Heidelberg. p. 159-185.
174. Zhou, J., et al., *A versatile fabrication of upconversion nanophosphors with functional-surface tunable ligands*. Journal of Materials Chemistry, 2010. **20**(37): p. 8078-8085.
175. Li, X., et al., *Successive Layer-by-Layer Strategy for Multi-Shell Epitaxial Growth: Shell Thickness and Doping Position Dependence in Upconverting Optical Properties*. Chemistry of Materials, 2013. **25**(1): p. 106-112.
176. Wang, L., et al., *Fluorescence resonant energy transfer biosensor based on upconversion-luminescent nanoparticles*. Angew Chem Int Ed Engl, 2005. **44**(37): p. 6054-7.
177. Liu, Y., et al., *Lanthanide-doped luminescent nanoprobes: controlled synthesis, optical spectroscopy, and bioapplications*. Chem Soc Rev, 2013. **42**(16): p. 6924-58.
178. Wang, M., et al., *Two-phase solvothermal synthesis of rare-earth doped NaYF₄ upconversion fluorescent nanocrystals*. Materials Letters, 2009. **63**(2): p. 325-327.
179. Dong, A., et al., *A generalized ligand-exchange strategy enabling sequential surface functionalization of colloidal nanocrystals*. J Am Chem Soc, 2011. **133**(4): p. 998-1006.
180. Xiong, L., et al., *Long-term in vivo biodistribution imaging and toxicity of polyacrylic acid-coated upconversion nanophosphors*. Biomaterials, 2010. **31**(27): p. 7078-85.
181. Naccache, R., et al., *Controlled Synthesis and Water Dispersibility of Hexagonal Phase NaGdF₄:Ho³⁺/Yb³⁺ Nanoparticles*. Chemistry of Materials, 2009. **21**(4): p. 717-723.
182. Zhang, T., et al., *A general approach for transferring hydrophobic nanocrystals into water*. Nano Lett, 2007. **7**(10): p. 3203-7.
183. Wong, H.-T., et al., *Water dispersible ultra-small multifunctional KGdF₄: Tm³⁺, Yb³⁺ nanoparticles with near-infrared to near-infrared upconversion*. Journal of Materials Chemistry, 2011. **21**(41): p. 16589-16596.
184. Shen, J., et al., *Superparamagnetic and upconversion emitting Fe₃O₄/NaYF₄:Yb,Er hetero-nanoparticles via a crosslinker anchoring strategy*. Chem Commun (Camb), 2010. **46**(31): p. 5731-3.
185. Zhang, Q., et al., *Hexanedioic acid mediated surface-ligand-exchange process for transferring NaYF₄:Yb/Er (or Yb/Tm) up-converting nanoparticles from hydrophobic to hydrophilic*. J Colloid Interface Sci, 2009. **336**(1): p. 171-5.
186. Kumar, R., et al., *Combined Optical and MR Bioimaging Using Rare Earth Ion Doped NaYF₄ Nanocrystals*. Advanced Functional Materials, 2009. **19**(6): p. 853-859.
187. Zhan, Q., et al., *Using 915 nm laser excited Tm(3)+/Er(3)+/Ho(3)+-doped NaYbF₄ upconversion nanoparticles for in vitro and deeper in vivo bioimaging without overheating irradiation*. ACS Nano, 2011. **5**(5): p. 3744-57.
188. Bogdan, N., et al., *Carbohydrate-coated lanthanide-doped upconverting nanoparticles for lectin recognition*. Journal of Materials Chemistry, 2010. **20**(35): p. 7543.
189. Bao, Y., et al., *Layer-by-layer assembly of freestanding thin films with homogeneously distributed upconversion nanocrystals*. Journal of Materials Chemistry, 2010. **20**(38): p. 8356.
190. Liu, Q., et al., *Sub-10 nm hexagonal lanthanide-doped NaLuF₄ upconversion nanocrystals for sensitive bioimaging in vivo*. J Am Chem Soc, 2011. **133**(43): p. 17122-5.
191. Chen, Z., et al., *Versatile synthesis strategy for carboxylic acid-functionalized upconverting nanophosphors as biological labels*. J Am Chem Soc, 2008. **130**(10): p. 3023-9.
192. Zhou, H.-P., et al., *Clean and Flexible Modification Strategy for Carboxyl/Aldehyde-Functionalized Upconversion Nanoparticles and Their Optical Applications*. Advanced Functional Materials, 2009. **19**(24): p. 3892-3900.
193. Budijono, S.J., et al., *Synthesis of stable block-copolymer-protected NaYF₄: Yb³⁺, Er³⁺ up-converting phosphor nanoparticles*. Chemistry of Materials, 2009. **22**(2): p. 311-318.
194. Jiang, G., et al., *An effective polymer cross-linking strategy to obtain stable dispersions of upconverting NaYF₄ nanoparticles in buffers and biological growth media for biolabeling applications*. Langmuir, 2012. **28**(6): p. 3239-3247.
195. Cheng, L., et al., *Highly-sensitive multiplexed in vivo imaging using PEGylated upconversion nanoparticles*. Nano research, 2010. **3**(10): p. 722-732.
196. Liang, S., et al., *Decoration of up-converting NaYF₄: Yb, Er (Tm) nanoparticles with surfactant bilayer. A versatile strategy to perform oil-to-water phase transfer and subsequently surface silication*. CrystEngComm, 2012. **14**(10): p. 3484-3489.
197. Li, L.L., et al., *Biomimetic Surface Engineering of Lanthanide-Doped Upconversion Nanoparticles as Versatile Bioprobes*. Angewandte Chemie International Edition, 2012. **51**(25): p. 6121-6125.
198. Nichkova, M., et al., *Microarray immunoassay for phenoxybenzoic acid using polymer encapsulated Eu:Gd₂O₃ nanoparticles as fluorescent labels*. Anal Chem, 2005. **77**(21): p. 6864-73.

REFERENCES

199. Cao, T., et al., *High-quality water-soluble and surface-functionalized upconversion nanocrystals as luminescent probes for bioimaging*. Biomaterials, 2011. **32**(11): p. 2959-68.
200. Yi, G.-S. and G.-M. Chow, *Water-Soluble NaYF₄:Yb,Er(Tm)/NaYF₄/Polymer Core/Shell/Shell Nanoparticles with Significant Enhancement of Upconversion Fluorescence*. Chemistry of Materials, 2007. **19**(3): p. 341-343.
201. Decher, G., *Fuzzy Nanoassemblies: Toward Layered Polymeric Multicomposites*. Science, 1997. **277**(5330): p. 1232-1237.
202. Bao, Y., et al., *Upconversion polymeric nanofibers containing lanthanide-doped nanoparticles via electrospinning*. Nanoscale, 2012. **4**(23): p. 7369-75.
203. Wang, C., et al., *Imaging-Guided pH-Sensitive Photodynamic Therapy Using Charge Reversible Upconversion Nanoparticles under Near-Infrared Light*. Advanced Functional Materials, 2013. **23**(24): p. 3077-3086.
204. Wang, F., et al., *Synthesis of polyethylenimine/NaYF₄ nanoparticles with upconversion fluorescence*. Nanotechnology, 2006. **17**(23): p. 5786-5791.
205. Xiong, L.Q., et al., *Synthesis, characterization, and in vivo targeted imaging of amine-functionalized rare-earth up-converting nanophosphors*. Biomaterials, 2009. **30**(29): p. 5592-600.
206. Yang, J., et al., *One-step hydrothermal synthesis of carboxyl-functionalized upconversion phosphors for bioapplications*. Chemistry, 2012. **18**(43): p. 13642-50.
207. Liu, Q., et al., *18F-labeled magnetic-upconversion nanophosphors via rare-earth cation-assisted ligand assembly*. Acs Nano, 2011. **5**(4): p. 3146-3157.
208. Kamimura, M., et al., *Design of poly (ethylene glycol)/streptavidin coimmobilized upconversion nanophosphors and their application to fluorescence biolabeling*. Langmuir, 2008. **24**(16): p. 8864-8870.
209. Zhou, J., Z. Liu, and F. Li, *Upconversion nanophosphors for small-animal imaging*. Chem Soc Rev, 2012. **41**(3): p. 1323-49.
210. Yi, G., Y. Peng, and Z. Gao, *Strong red-emitting near-infrared-to-visible upconversion fluorescent nanoparticles*. Chemistry of Materials, 2011. **23**(11): p. 2729-2734.
211. Chatterjee, D.K. and Z. Yong, *Upconverting nanoparticles as nanotransducers for photodynamic therapy in cancer cells*. Nanomedicine, 2008. **3**(1): p. 73-82.
212. Wang, C., L. Cheng, and Z. Liu, *Drug delivery with upconversion nanoparticles for multi-functional targeted cancer cell imaging and therapy*. Biomaterials, 2011. **32**(4): p. 1110-1120.
213. Cheng, L., et al., *Facile Preparation of Multifunctional Upconversion Nanoprobes for Multimodal Imaging and Dual-Targeted Photothermal Therapy*. Angewandte Chemie, 2011. **123**(32): p. 7523-7528.
214. Li, Z., et al., *Modification of NaYF₄: Yb, Er@ SiO₂ nanoparticles with gold nanocrystals for tunable green-to-red upconversion emissions*. The Journal of Physical Chemistry C, 2011. **115**(8): p. 3291-3296.
215. Wang, M., et al., *Immunolabeling and NIR-excited fluorescent imaging of HeLa cells by using NaYF₄: Yb, Er upconversion nanoparticles*. ACS nano, 2009. **3**(6): p. 1580-1586.
216. Xiong, L., et al., *High contrast upconversion luminescence targeted imaging in vivo using peptide-labeled nanophosphors*. Anal Chem, 2009. **81**(21): p. 8687-94.
217. Zako, T., et al., *Cyclic RGD peptide-labeled upconversion nanophosphors for tumor cell-targeted imaging*. Biochem Biophys Res Commun, 2009. **381**(1): p. 54-8.
218. Chen, F., et al., *A Uniform Sub-50 nm-Sized Magnetic/Upconversion Fluorescent Bimodal Imaging Agent Capable of Generating Singlet Oxygen by Using a 980 nm Laser*. Chemistry—A European Journal, 2012. **18**(23): p. 7082-7090.
219. Sun, Y., et al., *The biosafety of lanthanide upconversion nanomaterials*. Chem Soc Rev, 2015. **44**(6): p. 1509-25.
220. Gnach, A., et al., *Upconverting nanoparticles: assessing the toxicity*. Chem Soc Rev, 2015. **44**(6): p. 1561-84.
221. Vedunova, M.V., et al., *Cytotoxic effects of upconversion nanoparticles in primary hippocampal cultures*. Rsc Advances, 2016. **6**(40): p. 33656-33665.
222. Wysokinska, E., et al., *Cytotoxic interactions of bare and coated NaGdF₄:Yb(3+):Er(3+) nanoparticles with macrophage and fibroblast cells*. Toxicol In Vitro, 2016. **32**: p. 16-25.
223. Das, G.K., D.T. Stark, and I.M. Kennedy, *Potential toxicity of up-converting nanoparticles encapsulated with a bilayer formed by ligand attraction*. Langmuir, 2014. **30**(27): p. 8167-76.
224. Atabaev, T., et al., *Cytotoxicity and cell imaging potentials of submicron color-tunable yttria particles*. J Biomed Mater Res A, 2012. **100**(9): p. 2287-94.
225. Wang, C., et al., *Towards whole-body imaging at the single cell level using ultra-sensitive stem cell labeling with oligo-arginine modified upconversion nanoparticles*. Biomaterials, 2012. **33**(19): p. 4872-81.

REFERENCES

226. Chatterjee, D.K., A.J. Rufaihah, and Y. Zhang, *Upconversion fluorescence imaging of cells and small animals using lanthanide doped nanocrystals*. Biomaterials, 2008. **29**(7): p. 937-43.
227. Guo, H., et al., *Upconversion nanoparticles modified with aminosilanes as carriers of DNA vaccine for foot-and-mouth disease*. Appl Microbiol Biotechnol, 2012. **95**(5): p. 1253-63.
228. Yang, D., et al., *One-step synthesis of small-sized and water-soluble NaREF₄ upconversion nanoparticles for in vitro cell imaging and drug delivery*. Chemistry, 2013. **19**(8): p. 2685-94.
229. Yang, D., et al., *Ultra-small BaGdF₅-based upconversion nanoparticles as drug carriers and multimodal imaging probes*. Biomaterials, 2014. **35**(6): p. 2011-23.
230. Xia, A., et al., *Gd³⁺ complex-modified NaLuF₄-based upconversion nanophosphors for trimodality imaging of NIR-to-NIR upconversion luminescence, X-Ray computed tomography and magnetic resonance*. Biomaterials, 2012. **33**(21): p. 5394-405.
231. Gao, G., et al., *One-pot hydrothermal synthesis of lanthanide ions doped one-dimensional upconversion submicrocrystals and their potential application in vivo CT imaging*. Nanoscale, 2013. **5**(1): p. 351-62.
232. Ma, J., et al., *Folic acid-conjugated LaF₃:Yb,Tm@SiO₂ nanoprobes for targeting dual-modality imaging of upconversion luminescence and X-ray computed tomography*. J Phys Chem B, 2012. **116**(48): p. 14062-70.
233. Zhou, N., et al., *Shape-controllable synthesis of hydrophilic NaLuF₄:Yb,Er nanocrystals by a surfactant-assistant two-phase system*. Nanoscale Res Lett, 2013. **8**(1): p. 518.
234. Sikora, B., et al., *Transport of NaYF₄:Er³⁺, Yb³⁺ up-converting nanoparticles into HeLa cells*. Nanotechnology, 2013. **24**(23): p. 235702.
235. Bae, Y.M., et al., *Endocytosis, intracellular transport, and exocytosis of lanthanide-doped upconverting nanoparticles in single living cells*. Biomaterials, 2012. **33**(35): p. 9080-6.
236. Zhou, J.C., et al., *Bioimaging and toxicity assessments of near-infrared upconversion luminescent NaYF₄:Yb,Tm nanocrystals*. Biomaterials, 2011. **32**(34): p. 9059-67.
237. Chen, J., et al., *Controllable synthesis of NaYF₄:Yb,Er upconversion nanophosphors and their application to in vivo imaging of Caenorhabditis elegans*. J Mater Chem, 2011. **21**(8): p. 2632.
238. Gu, Z., et al., *Recent advances in design and fabrication of upconversion nanoparticles and their safe theranostic applications*. Adv Mater, 2013. **25**(28): p. 3758-79.
239. Liu, Z., et al., *Long-circulating Gd(2)O(3):Yb(3+), Er(3+) up-conversion nanoprobes as high-performance contrast agents for multi-modality imaging*. Biomaterials, 2013. **34**(6): p. 1712-21.
240. Zhou, J., et al., *Dual-modality in vivo imaging using rare-earth nanocrystals with near-infrared to near-infrared (NIR-to-NIR) upconversion luminescence and magnetic resonance properties*. Biomaterials, 2010. **31**(12): p. 3287-95.
241. Cheng, L., et al., *In vivo pharmacokinetics, long-term biodistribution and toxicology study of functionalized upconversion nanoparticles in mice*. Nanomedicine (Lond), 2011. **6**(8): p. 1327-40.
242. Xing, H., et al., *A NaYbF₄:Tm³⁺ nanoprobe for CT and NIR-to-NIR fluorescent bimodal imaging*. Biomaterials, 2012. **33**(21): p. 5384-93.
243. Yang, Y., et al., *Hydrothermal synthesis of NaLuF₄:153Sm,Yb,Tm nanoparticles and their application in dual-modality upconversion luminescence and SPECT bioimaging*. Biomaterials, 2013. **34**(3): p. 774-83.
244. Cao, T., et al., *Biodistribution of sub-10 nm PEG-modified radioactive/upconversion nanoparticles*. Biomaterials, 2013. **34**(29): p. 7127-34.
245. Liu, Q., et al., *Multifunctional rare-earth self-assembled nanosystem for tri-modal upconversion luminescence /fluorescence /positron emission tomography imaging*. Biomaterials, 2011. **32**(32): p. 8243-53.
246. Li, R., et al., *Surface interactions with compartmentalized cellular phosphates explain rare earth oxide nanoparticle hazard and provide opportunities for safer design*. ACS Nano, 2014. **8**(2): p. 1771-83.
247. Lahtinen, S., et al., *Disintegration of Hexagonal NaYF₄:Yb³⁺,Er³⁺ Upconverting Nanoparticles in Aqueous Media: The Role of Fluoride in Solubility Equilibrium*. The Journal of Physical Chemistry C, 2016.
248. Hirano, S. and K.T. Suzuki, *Exposure, metabolism, and toxicity of rare earths and related compounds*. Environ Health Perspect, 1996. **104** Suppl 1: p. 85-95.
249. Marciniak, M., Z. Baltrukiewicz, and J. Chas, *The effect of toxic doses of lanthanum and cerium on the placental barrier and the blood/organ barrier in mice after intravenous injection of these elements*. Acta Physiol Pol, 1988. **39**(4): p. 294-9.
250. Sarkander, H.I. and W.P. Brade, *On the mechanism of lanthanide-induced liver toxicity*. Arch Toxicol, 1976. **36**(1): p. 1-17.
251. Ghosh, N., D. Chattopadhyay, and G.C. Chatterjee, *Chicken erythrocyte membrane: lipid profile and enzymatic activity under lanthanum chloride and neodymium chloride administration*. Indian J Exp Biol, 1991. **29**(3): p. 226-9.

REFERENCES

252. Liu, H., et al., *La³⁺, Gd³⁺ and Yb³⁺ induced changes in mitochondrial structure, membrane permeability, cytochrome c release and intracellular ROS level*. *Chemico-Biological Interactions*, 2003. **146**(1): p. 27-37.
253. Wang, K., et al., *Lanthanides—the future drugs?* *Coordination Chemistry Reviews*, 1999. **190-192**: p. 297-308.
254. Canada, R.G., et al., *The effects of terbium on the accumulation of cisplatin in human ovarian cancer cells*. *Biochim Biophys Acta*, 1995. **1267**(1): p. 25-30.
255. Heffeter, P., et al., *Anticancer activity of the lanthanum compound [tris(1,10-phenanthroline)lanthanum(III)]trithiocyanate (KP772; FFC24)*. *Biochem Pharmacol*, 2006. **71**(4): p. 426-40.
256. Kostova, I., N. Trendafilova, and G. Momekov, *Theoretical, spectral characterization and antineoplastic activity of new lanthanide complexes*. *J Trace Elem Med Biol*, 2008. **22**(2): p. 100-11.
257. Kostova, I., et al., *Antineoplastic activity of new lanthanide (cerium, lanthanum and neodymium) complex compounds*. *J Trace Elem Med Biol*, 2005. **18**(3): p. 219-26.
258. DaCosta, M.V., et al., *Lanthanide upconversion nanoparticles and applications in bioassays and bioimaging: A review*. *Analytica Chimica Acta*, 2014. **832**: p. 1-33.
259. Xu, H., et al., *Polymer encapsulated upconversion nanoparticle/iron oxide nanocomposites for multimodal imaging and magnetic targeted drug delivery*. *Biomaterials*, 2011. **32**(35): p. 9364-73.
260. Liu, J.N., et al., *Simultaneous nuclear imaging and intranuclear drug delivery by nuclear-targeted multifunctional upconversion nanoprobe*. *Biomaterials*, 2012. **33**(29): p. 7282-90.
261. Jiang, S. and Y. Zhang, *Upconversion nanoparticle-based FRET system for study of siRNA in live cells*. *Langmuir*, 2010. **26**(9): p. 6689-94.
262. Li, K., et al., *Ratiometric Monitoring of Intracellular Drug Release by an Upconversion Drug Delivery Nanosystem*. *ACS Appl Mater Interfaces*, 2015. **7**(22): p. 12278-86.
263. Tian, G., et al., *Facile Fabrication of Rare-Earth-Doped Gd₂O₃ Hollow Spheres with Upconversion Luminescence, Magnetic Resonance, and Drug Delivery Properties*. *Journal of Physical Chemistry C*, 2011. **115**(48): p. 23790-23796.
264. Zhang, F., et al., *Mesoporous multifunctional upconversion luminescent and magnetic "nanorattle" materials for targeted chemotherapy*. *Nano Lett*, 2012. **12**(1): p. 61-7.
265. Carling, C.J., J.C. Boyer, and N.R. Branda, *J. Am. Chem. Soc.*, 2009. **131**: p. 10838.
266. Boyer, J.C., et al., *J. Am. Chem. Soc.*, 2010. **132**: p. 15766.
267. Carling, C.J., et al., *Remote-Control Photorelease of Caged Compounds Using Near-Infrared Light and Upconverting Nanoparticles*. *Angewandte Chemie-International Edition*, 2010. **49**(22): p. 3782-3785.
268. Yan, B., et al., *Near-infrared light-triggered dissociation of block copolymer micelles using upconverting nanoparticles*. *J Am Chem Soc*, 2011. **133**(49): p. 19714-7.
269. Yang, Y., et al., *In vitro and in vivo uncaging and bioluminescence imaging by using photocaged upconversion nanoparticles*. *Angew Chem Int Ed Engl*, 2012. **51**(13): p. 3125-9.
270. Yang, Y., et al., *NIR light controlled photorelease of siRNA and its targeted intracellular delivery based on upconversion nanoparticles*. *Nanoscale*, 2013. **5**(1): p. 231-8.
271. Garcia, J.V., et al., *NIR-triggered release of caged nitric oxide using upconverting nanostructured materials*. *Small*, 2012. **8**(24): p. 3800-5.
272. Fan, N.C., et al., *Photocontrolled targeted drug delivery: photocaged biologically active folic acid as a light-responsive tumor-targeting molecule*. *Angew Chem Int Ed Engl*, 2012. **51**(35): p. 8806-10.
273. Jayakumar, M.K., N.M. Idris, and Y. Zhang, *Remote activation of biomolecules in deep tissues using near-infrared-to-UV upconversion nanotransducers*. *Proc Natl Acad Sci U S A*, 2012. **109**(22): p. 8483-8.
274. Zhao, L., et al., *Near-Infrared Photoregulated Drug Release in Living Tumor Tissue via Yolk-Shell Upconversion Nanocages*. *Advanced Functional Materials*, 2014. **24**(3): p. 363-371.
275. Yan, B., et al., *Near infrared light triggered release of biomacromolecules from hydrogels loaded with upconversion nanoparticles*. *J Am Chem Soc*, 2012. **134**(40): p. 16558-61.
276. Dolmans, D.E., D. Fukumura, and R.K. Jain, *Photodynamic therapy for cancer*. *Nat Rev Cancer*, 2003. **3**(5): p. 380-7.
277. Hamblin, M.R. and T. Hasan, *Photodynamic therapy: a new antimicrobial approach to infectious disease?* *Photochem Photobiol Sci*, 2004. **3**(5): p. 436-50.
278. Lambrechts, S.A., et al., *Photodynamic therapy for Staphylococcus aureus infected burn wounds in mice*. *Photochem Photobiol Sci*, 2005. **4**(7): p. 503-9.
279. Juarranz, A., et al., *Photodynamic therapy of cancer. Basic principles and applications*. *Clin Transl Oncol*, 2008. **10**(3): p. 148-54.
280. Zhang, P., et al., *Versatile photosensitizers for photodynamic therapy at infrared excitation*. *Journal of the American Chemical Society*, 2007. **129**(15): p. 4526-+.

REFERENCES

281. Park, Y.I., et al., *Theranostic probe based on lanthanide-doped nanoparticles for simultaneous in vivo dual-modal imaging and photodynamic therapy*. Adv Mater, 2012. **24**(42): p. 5755-61.
282. Qian, H.S., et al., *Mesoporous-Silica-coated up-conversion fluorescent nanoparticles for photodynamic therapy*. Small, 2009. **5**(20): p. 2285-2290.
283. Wang, Y., et al., *Graphene oxide covalently grafted upconversion nanoparticles for combined NIR mediated imaging and photothermal/photodynamic cancer therapy*. Biomaterials, 2013. **34**(31): p. 7715-7724.
284. Wang, A., et al., *Drug delivery function of carboxymethyl- β -cyclodextrin modified upconversion nanoparticles for adamantine phthalocyanine and their NIR-triggered cancer treatment*. Dalton Transactions, 2016. **45**(9): p. 3853-3862.
285. Cui, S., et al., *In vivo targeted deep-tissue photodynamic therapy based on near-infrared light triggered upconversion nanoconstruct*. ACS Nano, 2012. **7**(1): p. 676-688.
286. Xia, L., et al., *An upconversion nanoparticle-zinc phthalocyanine based nanophotosensitizer for photodynamic therapy*. Biomaterials, 2014. **35**(13): p. 4146-4156.
287. Gao, W., et al., *Photodynamic Therapy Induced Enhancement of Tumor Vasculature Permeability Using an Upconversion Nanoconstruct for Improved Intratumoral Nanoparticle Delivery in Deep Tissues*. Theranostics, 2016. **6**(8): p. 1131.
288. Dou, Q., et al., *Effective near-infrared photodynamic therapy assisted by upconversion nanoparticles conjugated with photosensitizers*. Int. J. Nanomed, 2015. **10**: p. 419-432.
289. Wang, C., et al., *Near-infrared light induced in vivo photodynamic therapy of cancer based on upconversion nanoparticles*. Biomaterials, 2011. **32**(26): p. 6145-6154.
290. Park, Y.I., et al., *Theranostic Probe Based on Lanthanide-Doped Nanoparticles for Simultaneous In Vivo Dual-Modal Imaging and Photodynamic Therapy*. Advanced Materials, 2012. **24**(42): p. 5755-5761.
291. Zeng, L., et al., *808 nm-excited upconversion nanoprobe with low heating effect for targeted magnetic resonance imaging and high-efficacy photodynamic therapy in HER2-overexpressed breast cancer*. Biomaterials, 2016. **103**: p. 116-127.
292. Zhou, L., et al., *One-step nucleotide-programmed growth of porous upconversion nanoparticles: application to cell labeling and drug delivery*. Nanoscale, 2014. **6**(3): p. 1445-1452.
293. Wang, H., et al., *Design and Synthesis of Core-Shell-Shell Upconversion Nanoparticles for NIR-Induced Drug Release, Photodynamic Therapy, and Cell Imaging*. ACS applied materials & interfaces, 2016. **8**(7): p. 4416-4423.
294. Liu, K., et al., *Covalently assembled NIR nanoplatfor for simultaneous fluorescence imaging and photodynamic therapy of cancer cells*. ACS Nano, 2012. **6**(5): p. 4054-4062.
295. Lu, F., et al., *Highly Emissive Nd³⁺-Sensitized Multilayered Upconversion Nanoparticles for Efficient 795 nm Operated Photodynamic Therapy*. Advanced Functional Materials, 2016.
296. Chen, Q., et al., *Protein modified upconversion nanoparticles for imaging-guided combined photothermal and photodynamic therapy*. Biomaterials, 2014. **35**(9): p. 2915-2923.
297. Dou, Q.Q., et al., *Core-shell upconversion nanoparticle-semiconductor heterostructures for photodynamic therapy*. Scientific Reports, 2015. **5**.
298. Lucky, S.S., et al., *Titania coated upconversion nanoparticles for near-infrared light triggered photodynamic therapy*. ACS nano, 2015. **9**(1): p. 191-205.
299. Zhang, L.e., et al., *Inorganic photosensitizer coupled Gd-based upconversion luminescent nanocomposites for in vivo magnetic resonance imaging and near-infrared-responsive photodynamic therapy in cancers*. Biomaterials, 2015. **44**: p. 82-90.
300. Wang, X., et al., *A dual-targeting upconversion nanoplatfor for two-color fluorescence imaging-guided photodynamic therapy*. Analytical Chemistry, 2014. **86**(7): p. 3263-3267.
301. Idris, N.M., et al., *In vivo photodynamic therapy using upconversion nanoparticles as remote-controlled nanotransducers*. Nat Med, 2012. **18**(10): p. 1580-5.
302. Lim, M.E., et al., *Photodynamic inactivation of viruses using upconversion nanoparticles*. Biomaterials, 2012. **33**(6): p. 1912-20.
303. Shan, J., et al., *Pegylated Composite Nanoparticles Containing Upconverting Phosphors and meso-Tetraphenyl porphine (TPP) for Photodynamic Therapy*. Advanced Functional Materials, 2011. **21**(13): p. 2488-2495.
304. Liu, K., et al., *Covalently assembled NIR nanoplatfor for simultaneous fluorescence imaging and photodynamic therapy of cancer cells*. ACS Nano, 2012. **6**(5): p. 4054-62.
305. Qian, H.S., et al., *Mesoporous-silica-coated up-conversion fluorescent nanoparticles for photodynamic therapy*. Small, 2009. **5**(20): p. 2285-90.
306. Guo, H., et al., *Singlet oxygen-induced apoptosis of cancer cells using upconversion fluorescent nanoparticles as a carrier of photosensitizer*. Nanomedicine, 2010. **6**(3): p. 486-95.

REFERENCES

307. Liu, X.H., et al., *Mesoporous silica-coated NaYF₄ nanocrystals: facile synthesis, in vitro bioimaging and photodynamic therapy of cancer cells*. Rsc Advances, 2012. **2**(32): p. 12263-12268.
308. Qiao, X.F., et al., *Triple-functional core-shell structured upconversion luminescent nanoparticles covalently grafted with photosensitizer for luminescent, magnetic resonance imaging and photodynamic therapy in vitro*. Nanoscale, 2012. **4**(15): p. 4611-23.
309. Fan, W., et al., *A smart upconversion-based mesoporous silica nanotheranostic system for synergetic chemo-/radio-/photodynamic therapy and simultaneous MR/UCL imaging*. Biomaterials, 2014. **35**(32): p. 8992-9002.
310. Tian, G., et al., *Red-emitting upconverting nanoparticles for photodynamic therapy in cancer cells under near-infrared excitation*. Small, 2013. **9**(11): p. 1929-38, 1928.
311. Cui, S., et al., *In vivo targeted deep-tissue photodynamic therapy based on near-infrared light triggered upconversion nanoconstruct*. ACS Nano, 2013. **7**(1): p. 676-88.
312. Ai, F., et al., *An upconversion nanoplatfrom for simultaneous photodynamic therapy and Pt chemotherapy to combat cisplatin resistance*. Dalton Trans, 2016. **45**(33): p. 13052-60.
313. Kresge, C.T., et al., *Ordered mesoporous molecular sieves synthesized by a liquid-crystal template mechanism*. Nature, 1992. **359**(6397): p. 710-712.
314. Slowing, I.I., et al., *Mesoporous silica nanoparticles for drug delivery and biosensing applications*. Advanced Functional Materials, 2007. **17**(8): p. 1225-1236.
315. Baeza, A., M. Colilla, and M. Vallet-Regi, *Advances in mesoporous silica nanoparticles for targeted stimuli-responsive drug delivery*. Expert Opin Drug Deliv, 2015. **12**(2): p. 319-37.
316. Trewyn, B.G., et al., *Biocompatible mesoporous silica nanoparticles with different morphologies for animal cell membrane, penetration*. Chemical Engineering Journal, 2008. **137**(1): p. 23-29.
317. M. Rosenholm, J., C. Sahlgren, and M. Linden, *Multifunctional Mesoporous Silica Nanoparticles for Combined Therapeutic, Diagnostic and Targeted Action in Cancer Treatment*. Current Drug Targets, 2011. **12**(8): p. 1166-1186.
318. Tang, F., L. Li, and D. Chen, *Mesoporous silica nanoparticles: synthesis, biocompatibility and drug delivery*. Adv Mater, 2012. **24**(12): p. 1504-34.
319. Mamaeva, V., C. Sahlgren, and M. Linden, *Mesoporous silica nanoparticles in medicine--recent advances*. Adv Drug Deliv Rev, 2013. **65**(5): p. 689-702.
320. Rosenholm, J.M., et al., *Mesoporous silica nanoparticles in tissue engineering--a perspective*. Nanomedicine (Lond), 2016. **11**(4): p. 391-402.
321. Song, Y., et al., *Mesoporous silica nanoparticles for stimuli-responsive controlled drug delivery: advances, challenges, and outlook*. Int J Nanomedicine, 2017. **12**: p. 87-110.
322. Tarn, D., et al., *Mesoporous silica nanoparticle nanocarriers: biofunctionality and biocompatibility*. Acc Chem Res, 2013. **46**(3): p. 792-801.
323. Wan, Y. and D. Zhao, *On the controllable soft-templating approach to mesoporous silicates*. Chem Rev, 2007. **107**(7): p. 2821-60.
324. Zhao, D., et al., *Triblock copolymer syntheses of mesoporous silica with periodic 50 to 300 angstrom pores*. Science, 1998. **279**(5350): p. 548-52.
325. Li, Z., et al., *Mesoporous silica nanoparticles in biomedical applications*. Chem Soc Rev, 2012. **41**(7): p. 2590-605.
326. Corma, A., *From Microporous to Mesoporous Molecular Sieve Materials and Their Use in Catalysis*. Chemical Reviews, 1997. **97**(6): p. 2373-2420.
327. Ying, J.Y., C.P. Mehnert, and M.S. Wong, *Synthesis and Applications of Supramolecular-Templated Mesoporous Materials*. Angewandte Chemie International Edition, 1999. **38**(1-2): p. 56-77.
328. Huh, S., et al., *Organic functionalization and morphology control of mesoporous silicas via a co-condensation synthesis method*. Chemistry of Materials, 2003. **15**(22): p. 4247-4256.
329. Lim, M.H. and A. Stein, *Comparative Studies of Grafting and Direct Syntheses of Inorganic–Organic Hybrid Mesoporous Materials*. Chemistry of Materials, 1999. **11**(11): p. 3285-3295.
330. Martín, A., et al., *Polyethyleneimine-functionalized large pore ordered silica materials for poorly water-soluble drug delivery*. Journal of Materials Science, 2013. **49**(3): p. 1437-1447.
331. Xia, T., et al., *Polyethyleneimine coating enhances the cellular uptake of mesoporous silica nanoparticles and allows safe delivery of siRNA and DNA constructs*. ACS Nano, 2009. **3**(10): p. 3273-86.
332. Andersson, J., et al., *Influences of material characteristics on ibuprofen drug loading and release profiles from ordered micro-and mesoporous silica matrices*. Chemistry of Materials, 2004. **16**(21): p. 4160-4167.
333. Lu, J., et al., *Mesoporous silica nanoparticles as a delivery system for hydrophobic anticancer drugs*. Small, 2007. **3**(8): p. 1341-6.
334. Muhammad, F., et al., *pH-Triggered controlled drug release from mesoporous silica nanoparticles via intracellular dissolution of ZnO nanolids*. J Am Chem Soc, 2011. **133**(23): p. 8778-81.

REFERENCES

335. Meng, H., et al., *Autonomous in Vitro Anticancer Drug Release from Mesoporous Silica Nanoparticles by pH-Sensitive Nanovalves*. Journal of the American Chemical Society, 2010. **132**(36): p. 12690-12697.
336. Colilla, M., B. González, and M. Vallet-Regí, *Mesoporous silica nanoparticles for the design of smart delivery nanodevices*. Biomater. Sci., 2013. **1**(2): p. 114-134.
337. Ambrogio, M.W., et al., *Mechanized silica nanoparticles: a new frontier in theranostic nanomedicine*. Acc Chem Res, 2011. **44**(10): p. 903-13.
338. Sun, Q., et al., *A photoresponsive and rod-shape nanocarrier: Single wavelength of light triggered photothermal and photodynamic therapy based on AuNRs-capped & Ce6-doped mesoporous silica nanorods*. Biomaterials, 2017. **122**: p. 188-200.
339. Zhang, Z., et al., *Mesoporous Silica-Coated Gold Nanorods as a Light-Mediated Multifunctional Theranostic Platform for Cancer Treatment*. Advanced Materials, 2012. **24**(11): p. 1418-1423.
340. He, Q., et al., *A pH-responsive mesoporous silica nanoparticles-based multi-drug delivery system for overcoming multi-drug resistance*. Biomaterials, 2011. **32**(30): p. 7711-20.
341. Thomas, C.R., et al., *Noninvasive remote-controlled release of drug molecules in vitro using magnetic actuation of mechanized nanoparticles*. Journal of the American Chemical Society, 2010. **132**(31): p. 10623-10625.
342. Lee, J.E., et al., *Multifunctional mesoporous silica nanocomposite nanoparticles for theranostic applications*. Acc Chem Res, 2011. **44**(10): p. 893-902.
343. He, Q., et al., *Mesoporous carbon@silicon-silica nanotheranostics for synchronous delivery of insoluble drugs and luminescence imaging*. Biomaterials, 2012. **33**(17): p. 4392-402.
344. Chen, W.H., et al., *Rational design of multifunctional magnetic mesoporous silica nanoparticle for tumor-targeted magnetic resonance imaging and precise therapy*. Biomaterials, 2016. **76**: p. 87-101.
345. Wang, X., et al., *Au-nanoparticle coated mesoporous silica nanocapsule-based multifunctional platform for ultrasound mediated imaging, cytolysis and tumor ablation*. Biomaterials, 2013. **34**(8): p. 2057-68.
346. Chen, Y., et al., *Manganese oxide-based multifunctionalized mesoporous silica nanoparticles for pH-responsive MRI, ultrasonography and circumvention of MDR in cancer cells*. Biomaterials, 2012. **33**(29): p. 7126-37.
347. Croissant, J.G., et al., *Protein-gold clusters-capped mesoporous silica nanoparticles for high drug loading, autonomous gemcitabine/doxorubicin co-delivery, and in-vivo tumor imaging*. J Control Release, 2016. **229**: p. 183-91.
348. Shahabi, S., et al., *Enhancing Cellular Uptake and Doxorubicin Delivery of Mesoporous Silica Nanoparticles via Surface Functionalization: Effects of Serum*. ACS Appl Mater Interfaces, 2015. **7**(48): p. 26880-91.
349. Mas, N., et al., *Towards the Development of Smart 3D "gated scaffolds" for on-command delivery*. Small, 2014. **10**(23): p. 4859-64.
350. Shang, L., K. Nienhaus, and G.U. Nienhaus, *Engineered nanoparticles interacting with cells: size matters*. J Nanobiotechnology, 2014. **12**: p. 5.
351. Chen, X., et al., *Renal interstitial fibrosis induced by high-dose mesoporous silica nanoparticles via the NF-kappaB signaling pathway*. Int J Nanomedicine, 2015. **10**: p. 1-22.
352. Nel, A.E., et al., *Understanding biophysicochemical interactions at the nano-bio interface*. Nature Materials, 2009. **8**(7): p. 543-557.
353. Laurent, S., et al., *Crucial ignored parameters on nanotoxicology: the importance of toxicity assay modifications and "cell vision"*. PLoS One, 2012. **7**(1): p. e29997.
354. Bozec, L., G. van der Heijden, and M. Horton, *Collagen fibrils: nanoscale ropes*. Biophys J, 2007. **92**(1): p. 70-5.
355. Kirillin, M., et al., *Contrasting properties of gold nanoshells and titanium dioxide nanoparticles for optical coherence tomography imaging of skin: Monte Carlo simulations and in vivo study*. J Biomed Opt, 2009. **14**(2): p. 021017.
356. Verma, A. and F. Stellacci, *Effect of surface properties on nanoparticle-cell interactions*. Small, 2010. **6**(1): p. 12-21.
357. Parhamifar, L., et al., *Polycation cytotoxicity: a delicate matter for nucleic acid therapy—focus on polyethylenimine*. Soft Matter, 2010. **6**(17): p. 4001-4009.
358. Conner, S.D. and S.L. Schmid, *Regulated portals of entry into the cell*. Nature, 2003. **422**(6927): p. 37-44.
359. Zaki, N.M. and N. Tirelli, *Gateways for the intracellular access of nanocarriers: a review of receptor-mediated endocytosis mechanisms and of strategies in receptor targeting*. Expert Opin Drug Deliv, 2010. **7**(8): p. 895-913.
360. Martens, T.F., et al., *Intracellular delivery of nanomaterials: How to catch endosomal escape in the act*. Nano Today, 2014. **9**(3): p. 344-364.

REFERENCES

361. Oh, N. and J.H. Park, *Endocytosis and exocytosis of nanoparticles in mammalian cells*. Int J Nanomedicine, 2014. **9 Suppl 1**(Suppl 1): p. 51-63.
362. Rejman, J., et al., *Size-dependent internalization of particles via the pathways of clathrin- and caveolae-mediated endocytosis*. Biochem J, 2004. **377**(Pt 1): p. 159-69.
363. Chithrani, B.D. and W.C. Chan, *Elucidating the mechanism of cellular uptake and removal of protein-coated gold nanoparticles of different sizes and shapes*. Nano Lett, 2007. **7**(6): p. 1542-50.
364. Chithrani, B.D., A.A. Ghazani, and W.C.W. Chan, *Determining the size and shape dependence of gold nanoparticle uptake into mammalian cells*. Nano Letters, 2006. **6**(4): p. 662-668.
365. Panyam, J. and V. Labhasetwar, *Biodegradable nanoparticles for drug and gene delivery to cells and tissue*. Adv Drug Deliv Rev, 2003. **55**(3): p. 329-47.
366. Clift, M.J., et al., *The impact of different nanoparticle surface chemistry and size on uptake and toxicity in a murine macrophage cell line*. Toxicol Appl Pharmacol, 2008. **232**(3): p. 418-27.
367. Doiron, A.L., B. Clark, and K.D. Rinker, *Endothelial nanoparticle binding kinetics are matrix and size dependent*. Biotechnol Bioeng, 2011. **108**(12): p. 2988-98.
368. Zhang, S., et al., *Size-Dependent Endocytosis of Nanoparticles*. Adv Mater, 2009. **21**(4): p. 419-424.
369. He, C., et al., *Effects of particle size and surface charge on cellular uptake and biodistribution of polymeric nanoparticles*. Biomaterials, 2010. **31**(13): p. 3657-66.
370. Cho, E.C., et al., *The effects of size, shape, and surface functional group of gold nanostructures on their adsorption and internalization by cells*. Small, 2010. **6**(4): p. 517-22.
371. Huang, K., et al., *Size-dependent localization and penetration of ultrasmall gold nanoparticles in cancer cells, multicellular spheroids, and tumors in vivo*. ACS Nano, 2012. **6**(5): p. 4483-93.
372. Kelf, T.A., et al., *Non-specific cellular uptake of surface-functionalized quantum dots*. Nanotechnology, 2010. **21**(28): p. 285105.
373. Albanese, A. and W.C. Chan, *Effect of gold nanoparticle aggregation on cell uptake and toxicity*. ACS Nano, 2011. **5**(7): p. 5478-89.
374. Slomberg, D.L., et al., *Role of size and shape on biofilm eradication for nitric oxide-releasing silica nanoparticles*. ACS Appl Mater Interfaces, 2013. **5**(19): p. 9322-9.
375. Napierska, D., et al., *Size-dependent cytotoxicity of monodisperse silica nanoparticles in human endothelial cells*. Small, 2009. **5**(7): p. 846-53.
376. Xiong, S., et al., *Size influences the cytotoxicity of poly (lactic-co-glycolic acid) (PLGA) and titanium dioxide (TiO₂) nanoparticles*. Archives of Toxicology, 2012. **87**(6): p. 1075-1086.
377. Fan, M.M., et al., *Evaluation of Rod-Shaped Nanoparticles as Carriers for Gene Delivery*. Particle & Particle Systems Characterization, 2014. **31**(9): p. 994-1000.
378. Huang, X., et al., *The effect of the shape of mesoporous silica nanoparticles on cellular uptake and cell function*. Biomaterials, 2010. **31**(3): p. 438-48.
379. Champion, J.A. and S. Mitragotri, *Shape induced inhibition of phagocytosis of polymer particles*. Pharm Res, 2009. **26**(1): p. 244-9.
380. Truong, N.P., et al., *The importance of nanoparticle shape in cancer drug delivery*. Expert Opin Drug Deliv, 2015. **12**(1): p. 129-42.
381. Ayala, V., et al., *Effect of surface charge on the colloidal stability and in vitro uptake of carboxymethyl dextran-coated iron oxide nanoparticles*. J Nanopart Res, 2013. **15**(8): p. 1874.
382. Patil, S., et al., *Protein adsorption and cellular uptake of cerium oxide nanoparticles as a function of zeta potential*. Biomaterials, 2007. **28**(31): p. 4600-7.
383. Sokolova, V., et al., *An outer shell of positively charged poly(ethyleneimine) strongly increases the transfection efficiency of calcium phosphate/DNA nanoparticles*. Journal of Materials Science, 2010. **45**(18): p. 4952-4957.
384. Jin, J., et al., *Polymer-coated NaYF₄:Yb(3+), Er(3+) upconversion nanoparticles for charge-dependent cellular imaging*. ACS Nano, 2011. **5**(10): p. 7838-47.
385. Sharifi, S., et al., *Toxicity of nanomaterials*. Chem Soc Rev, 2012. **41**(6): p. 2323-43.
386. Xiao, K., et al., *The effect of surface charge on in vivo biodistribution of PEG-oligocholic acid based micellar nanoparticles*. Biomaterials, 2011. **32**(13): p. 3435-46.
387. Frohlich, E., *The role of surface charge in cellular uptake and cytotoxicity of medical nanoparticles*. Int J Nanomedicine, 2012. **7**: p. 5577-91.
388. Mahmoudi, M., et al., *Cell "vision": complementary factor of protein corona in nanotoxicology*. Nanoscale, 2012. **4**(17): p. 5461-8.
389. Carroll, S.B., *Chance and necessity: the evolution of morphological complexity and diversity*. Nature, 2001. **409**(6823): p. 1102-1109.
390. Anderson, J.M., A. Rodriguez, and D.T. Chang, *Foreign body reaction to biomaterials*. Semin Immunol, 2008. **20**(2): p. 86-100.
391. Alili, L., et al., *Combined cytotoxic and anti-invasive properties of redox-active nanoparticles in tumor-stroma interactions*. Biomaterials, 2011. **32**(11): p. 2918-29.

REFERENCES

392. Tang, W., et al., *Differential cytotoxicity and particle action of hydroxyapatite nanoparticles in human cancer cells*. Nanomedicine (Lond), 2014. **9**(3): p. 397-412.
393. Othman, B.A., et al., *Correlative Light-Electron Microscopy Shows RGD-Targeted ZnO Nanoparticles Dissolve in the Intracellular Environment of Triple Negative Breast Cancer Cells and Cause Apoptosis with Intratumor Heterogeneity*. Adv Healthc Mater, 2016: p. n/a-n/a.
394. Lunov, O., et al., *Differential uptake of functionalized polystyrene nanoparticles by human macrophages and a monocytic cell line*. ACS Nano, 2011. **5**(3): p. 1657-69.
395. Orłowski, P., et al., *Assessment of in vitro cellular responses of monocytes and keratinocytes to tannic acid modified silver nanoparticles*. Toxicology in Vitro, 2013. **27**(6): p. 1798-1808.
396. Joris, F., et al., *Assessing nanoparticle toxicity in cell-based assays: influence of cell culture parameters and optimized models for bridging the in vitro-in vivo gap*. Chem Soc Rev, 2013. **42**(21): p. 8339-59.
397. O'Donnell, K.A., et al., *Activation of transferrin receptor 1 by c-Myc enhances cellular proliferation and tumorigenesis*. Mol Cell Biol, 2006. **26**(6): p. 2373-86.
398. Roberts, R.L., R.E. Fine, and A. Sandra, *Receptor-Mediated Endocytosis of Transferrin at the Blood-Brain-Barrier*. Journal of Cell Science, 1993. **104**(2): p. 521-532.
399. Rao, P.N., et al., *Elevation of serum riboflavin carrier protein in breast cancer*. Cancer Epidemiol Biomarkers Prev, 1999. **8**(11): p. 985-90.
400. De Deyne, P.G., et al., *The vitronectin receptor associates with clathrin-coated membrane domains via the cytoplasmic domain of its beta5 subunit*. J Cell Sci, 1998. **111** (Pt 18)(18): p. 2729-40.
401. Upla, P., et al., *Clustering induces a lateral redistribution of alpha 2 beta 1 integrin from membrane rafts to caveolae and subsequent protein kinase C-dependent internalization*. Mol Biol Cell, 2004. **15**(2): p. 625-36.
402. Schiffelers, R.M., et al., *Anti-tumor efficacy of tumor vasculature-targeted liposomal doxorubicin*. J Control Release, 2003. **91**(1-2): p. 115-22.
403. Jiang, X., et al., *Integrin-facilitated transcytosis for enhanced penetration of advanced gliomas by poly(trimethylene carbonate)-based nanoparticles encapsulating paclitaxel*. Biomaterials, 2013. **34**(12): p. 2969-79.
404. Kim, W.J., et al., *Soluble Flt-1 gene delivery using PEI-g-PEG-RGD conjugate for anti-angiogenesis*. J Control Release, 2005. **106**(1-2): p. 224-34.
405. Torchilin, V.P., *Tat peptide-mediated intracellular delivery of pharmaceutical nanocarriers*. Adv Drug Deliv Rev, 2008. **60**(4-5): p. 548-58.
406. Khalil, I.A., et al., *High density of octaarginine stimulates macropinocytosis leading to efficient intracellular trafficking for gene expression*. J Biol Chem, 2006. **281**(6): p. 3544-51.
407. Lewinski, N., V. Colvin, and R. Drezek, *Cytotoxicity of nanoparticles*. Small, 2008. **4**(1): p. 26-49.
408. Nel, A., et al., *Toxic potential of materials at the nanolevel*. Science, 2006. **311**(5761): p. 622-7.
409. Marano, F., et al., *Nanoparticles: molecular targets and cell signalling*. Arch Toxicol, 2011. **85**(7): p. 733-41.
410. Soenen, S.J., et al., *Cellular toxicity of inorganic nanoparticles: Common aspects and guidelines for improved nanotoxicity evaluation*. Nano Today, 2011. **6**(5): p. 446-465.
411. Monopoli, M.P., et al., *Physical-chemical aspects of protein corona: relevance to in vitro and in vivo biological impacts of nanoparticles*. J Am Chem Soc, 2011. **133**(8): p. 2525-34.
412. Vippola, M., et al., *Preparation of nanoparticle dispersions for in-vitro toxicity testing*. Hum Exp Toxicol, 2009. **28**(6-7): p. 377-85.
413. Bakand, S. and A. Hayes, *Toxicological Considerations, Toxicity Assessment, and Risk Management of Inhaled Nanoparticles*. Int J Mol Sci, 2016. **17**(6).
414. Blanco, E., H. Shen, and M. Ferrari, *Principles of nanoparticle design for overcoming biological barriers to drug delivery*. Nat Biotechnol, 2015. **33**(9): p. 941-51.
415. Schroeder, A., et al., *Treating metastatic cancer with nanotechnology*. Nature Reviews Cancer, 2012. **12**(1): p. 39-50.
416. Maeda, H., H. Nakamura, and J. Fang, *The EPR effect for macromolecular drug delivery to solid tumors: Improvement of tumor uptake, lowering of systemic toxicity, and distinct tumor imaging in vivo*. Adv Drug Deliv Rev, 2013. **65**(1): p. 71-9.
417. Yoo, J.-W., E. Chambers, and S. Mitragotri, *Factors that Control the Circulation Time of Nanoparticles in Blood: Challenges, Solutions and Future Prospects*. Current Pharmaceutical Design, 2010. **16**(21): p. 2298-2307.
418. Owens, D.E., 3rd and N.A. Peppas, *Opsonization, biodistribution, and pharmacokinetics of polymeric nanoparticles*. Int J Pharm, 2006. **307**(1): p. 93-102.
419. Vonarbourg, A., et al., *Parameters influencing the stealthiness of colloidal drug delivery systems*. Biomaterials, 2006. **27**(24): p. 4356-73.
420. Salvati, A., et al., *Transferrin-functionalized nanoparticles lose their targeting capabilities when a biomolecule corona adsorbs on the surface*. Nature nanotechnology, 2013. **8**(2): p. 137-143.

REFERENCES

421. Anselmo, A.C. and S. Mitragotri, *Cell-mediated delivery of nanoparticles: Taking advantage of circulatory cells to target nanoparticles*. Journal of Controlled Release, 2014. **190**: p. 531-541.
422. Hynes, R.O., *The extracellular matrix: not just pretty fibrils*. Science, 2009. **326**(5957): p. 1216-9.
423. Meredith, J.E., B. Fazeli, and M.A. Schwartz, *The extracellular matrix as a cell survival factor*. Molecular Biology of the Cell, 1993. **4**(9): p. 953-961.
424. Scott, J.E., *Extracellular matrix, supramolecular organisation and shape*. J Anat, 1995. **187** (Pt 2)(Pt 2): p. 259-69.
425. Boudreau, N. and M.J. Bissell, *Extracellular matrix signaling: integration of form and function in normal and malignant cells*. Curr Opin Cell Biol, 1998. **10**(5): p. 640-6.
426. Netti, P.A., et al., *Role of extracellular matrix assembly in interstitial transport in solid tumors*. Cancer Res, 2000. **60**(9): p. 2497-503.
427. Kleinman, H.K., D. Philp, and M.P. Hoffman, *Role of the extracellular matrix in morphogenesis*. Curr Opin Biotechnol, 2003. **14**(5): p. 526-32.
428. Theocharis, A.D., et al., *Extracellular matrix structure*. Adv Drug Deliv Rev, 2016. **97**: p. 4-27.
429. Timpl, R., *Structure and biological activity of basement membrane proteins*. Eur J Biochem, 1989. **180**(3): p. 487-502.
430. Ingber, D.E., *Can cancer be reversed by engineering the tumor microenvironment?* Seminars in Cancer Biology, 2008. **18**(5): p. 356-364.
431. Mueller, M.M. and N.E. Fusenig, *Friends or foes - bipolar effects of the tumour stroma in cancer*. Nat Rev Cancer, 2004. **4**(11): p. 839-49.
432. Stylianopoulos, T., et al., *Diffusion of particles in the extracellular matrix: the effect of repulsive electrostatic interactions*. Biophys J, 2010. **99**(5): p. 1342-9.
433. Rosenow, F., et al., *Integrins as Antimetastatic Targets of RGD-Independent Snake Venom Components in Liver Metastasis*. Neoplasia (New York, N.Y.), 2008. **10**(2): p. 168-176.
434. Zaman, M.H., et al., *Migration of tumor cells in 3D matrices is governed by matrix stiffness along with cell-matrix adhesion and proteolysis*. Proc Natl Acad Sci U S A, 2006. **103**(29): p. 10889-94.
435. Tomasetti, L., et al., *Influence of PEGylation on nanoparticle mobility in different models of the extracellular matrix*. Eur J Pharm Biopharm, 2016. **108**: p. 145-155.
436. Mair, L.O. and R. Superfine, *Single particle tracking reveals biphasic transport during nanorod magnetophoresis through extracellular matrix*. Soft Matter, 2014. **10**(23): p. 4118-25.
437. Wang, D., et al., *Effects of nanoparticle size and charge on interactions with self-assembled collagen*. J Colloid Interface Sci, 2014. **417**: p. 244-9.
438. Florence, A.T., *"Targeting" nanoparticles: The constraints of physical laws and physical barriers*. Journal of Controlled Release, 2012. **164**(2): p. 115-124.
439. Han, Y., et al., *Brownian motion of an ellipsoid*. Science, 2006. **314**(5799): p. 626-30.
440. Hubbard, J.B. and J.F. Douglas, *Hydrodynamic friction of arbitrarily shaped Brownian particles*. Phys Rev E Stat Phys Plasmas Fluids Relat Interdiscip Topics, 1993. **47**(5): p. R2983-R2986.
441. Kuhn, S.J., D.E. Hallahan, and T.D. Giorgio, *Characterization of superparamagnetic nanoparticle interactions with extracellular matrix in an in vitro system*. Ann Biomed Eng, 2006. **34**(1): p. 51-8.
442. Neeves, K.B., et al., *Dilation and degradation of the brain extracellular matrix enhances penetration of infused polymer nanoparticles*. Brain Res, 2007. **1180**: p. 121-32.
443. Fan, D., E.E. Creemers, and Z. Kassiri, *Matrix as an interstitial transport system*. Circ Res, 2014. **114**(5): p. 889-902.
444. Arppe, R., et al., *Quenching of the upconversion luminescence of NaYF₄:Yb(3)(+),Er(3)(+) and NaYF₄:Yb(3)(+),Tm(3)(+) nanophosphors by water: the role of the sensitizer Yb(3)(+) in non-radiative relaxation*. Nanoscale, 2015. **7**(27): p. 11746-57.
445. Arifler, D., et al., *Light scattering from collagen fiber networks: micro-optical properties of normal and neoplastic stroma*. Biophys J, 2007. **92**(9): p. 3260-74.
446. Netti, P.A., et al., *Time-dependent behavior of interstitial fluid pressure in solid tumors: implications for drug delivery*. Cancer Res, 1995. **55**(22): p. 5451-8.
447. Stylianopoulos, T., et al., *Causes, consequences, and remedies for growth-induced solid stress in murine and human tumors*. Proc Natl Acad Sci U S A, 2012. **109**(38): p. 15101-8.
448. Wong, C., et al., *Multistage nanoparticle delivery system for deep penetration into tumor tissue*. Proc Natl Acad Sci U S A, 2011. **108**(6): p. 2426-31.
449. Fukumura, D. and R.K. Jain, *Tumor microvasculature and microenvironment: targets for anti-angiogenesis and normalization*. Microvasc Res, 2007. **74**(2-3): p. 72-84.
450. Levental, K.R., et al., *Matrix crosslinking forces tumor progression by enhancing integrin signaling*. Cell, 2009. **139**(5): p. 891-906.
451. Insua-Rodriguez, J. and T. Oskarsson, *The extracellular matrix in breast cancer*. Adv Drug Deliv Rev, 2016. **97**: p. 41-55.

REFERENCES

452. Jain, R.K., *Transport of molecules, particles, and cells in solid tumors*. Annu Rev Biomed Eng, 1999. **1**(1): p. 241-63.
453. Carmeliet, P. and R.K. Jain, *Principles and mechanisms of vessel normalization for cancer and other angiogenic diseases*. Nat Rev Drug Discov, 2011. **10**(6): p. 417-27.
454. Seo, B.R., P. Delnero, and C. Fischbach, *In vitro models of tumor vessels and matrix: engineering approaches to investigate transport limitations and drug delivery in cancer*. Adv Drug Deliv Rev, 2014. **69-70**: p. 205-16.
455. Pickup, M.W., J.K. Mouw, and V.M. Weaver, *The extracellular matrix modulates the hallmarks of cancer*. EMBO Rep, 2014. **15**(12): p. 1243-53.
456. Faurobert, E., A.P. Bouin, and C. Albiges-Rizo, *Microenvironment, tumor cell plasticity, and cancer*. Curr Opin Oncol, 2015. **27**(1): p. 64-70.
457. Huang, S. and D.E. Ingber, *Cell tension, matrix mechanics, and cancer development*. Cancer Cell, 2005. **8**(3): p. 175-176.
458. Lu, P., V.M. Weaver, and Z. Werb, *The extracellular matrix: a dynamic niche in cancer progression*. J Cell Biol, 2012. **196**(4): p. 395-406.
459. Dvorak, H.F., *Tumors: wounds that do not heal: similarities between tumor stroma generation and wound healing*. The New England journal of medicine, 1986. **315**(26): p. 1650-1659.
460. Kalluri, R. and M. Zeisberg, *Fibroblasts in cancer*. Nat Rev Cancer, 2006. **6**(5): p. 392-401.
461. Potenta, S., E. Zeisberg, and R. Kalluri, *The role of endothelial-to-mesenchymal transition in cancer progression*. Br J Cancer, 2008. **99**(9): p. 1375-9.
462. Kalluri, R. and V.P. Sukhatme, *Fibrosis and angiogenesis*. Curr Opin Nephrol Hypertens, 2000. **9**(4): p. 413-8.
463. Radisky, D.C., P.A. Kenny, and M.J. Bissell, *Fibrosis and cancer: do myofibroblasts come also from epithelial cells via EMT?* J Cell Biochem, 2007. **101**(4): p. 830-9.
464. Gilkes, D.M., G.L. Semenza, and D. Wirtz, *Hypoxia and the extracellular matrix: drivers of tumour metastasis*. Nat Rev Cancer, 2014. **14**(6): p. 430-9.
465. Pietroiusti, A., L. Campagnolo, and B. Fadeel, *Interactions of engineered nanoparticles with organs protected by internal biological barriers*. Small, 2013. **9**(9-10): p. 1557-72.
466. Barua, S. and S. Mitragotri, *Challenges associated with Penetration of Nanoparticles across Cell and Tissue Barriers: A Review of Current Status and Future Prospects*. Nano Today, 2014. **9**(2): p. 223-243.
467. Braakhuis, H.M., et al., *Progress and future of in vitro models to study translocation of nanoparticles*. Arch Toxicol, 2015. **89**(9): p. 1469-95.
468. Jepps, O.G., et al., *Modeling the human skin barrier--towards a better understanding of dermal absorption*. Adv Drug Deliv Rev, 2013. **65**(2): p. 152-68.
469. Cevc, G. and U. Vierl, *Nanotechnology and the transdermal route: A state of the art review and critical appraisal*. Journal of Controlled Release, 2010. **141**(3): p. 277-299.
470. Darlenski, R., et al., *Non-invasive in vivo methods for investigation of the skin barrier physical properties*. European Journal of Pharmaceutics and Biopharmaceutics, 2009. **72**(2): p. 295-303.
471. van Smeden, J., et al., *The important role of stratum corneum lipids for the cutaneous barrier function*. Biochimica et Biophysica Acta (BBA) - Molecular and Cell Biology of Lipids, 2014. **1841**(3): p. 295-313.
472. Moser, K., et al., *Passive skin penetration enhancement and its quantification in vitro*. Eur J Pharm Biopharm, 2001. **52**(2): p. 103-12.
473. Baroni, A., et al., *Structure and function of the epidermis related to barrier properties*. Clinics in Dermatology, 2012. **30**(3): p. 257-262.
474. Lane, M.E., *Skin penetration enhancers*. Int J Pharm, 2013. **447**(1-2): p. 12-21.
475. Barry, B.W., *Lipid-Protein-Partitioning theory of skin penetration enhancement*. Journal of Controlled Release, 1991. **15**(3): p. 237-248.
476. Marjukka Suhonen, T., J.A. Bouwstra, and A. Urtti, *Chemical enhancement of percutaneous absorption in relation to stratum corneum structural alterations*. J Control Release, 1999. **59**(2): p. 149-61.
477. Barry, B.W., *Mode of action of penetration enhancers in human skin*. Journal of Controlled Release, 1987. **6**(1): p. 85-97.
478. Holmes, A.M., et al., *Relative Penetration of Zinc Oxide and Zinc Ions into Human Skin after Application of Different Zinc Oxide Formulations*. ACS Nano, 2016.
479. Alnasif, N., et al., *Penetration of normal, damaged and diseased skin--an in vitro study on dendritic core-multishell nanotransporters*. J Control Release, 2014. **185**: p. 45-50.
480. Liang, X.W., et al., *Penetration of nanoparticles into human skin*. Curr Pharm Des, 2013. **19**(35): p. 6353-66.
481. Prow, T.W., et al., *Quantum dot penetration into viable human skin*. Nanotoxicology, 2012. **6**(2): p. 173-85.

REFERENCES

482. Larese Filon, F., et al., *Nanoparticles skin absorption: New aspects for a safety profile evaluation*. Regul Toxicol Pharmacol, 2015. **72**(2): p. 310-22.
483. Kamali, T., et al., *Assessment of transcutaneous vaccine delivery by optical coherence tomography*. Laser Physics Letters, 2012. **9**(8): p. 607-610.
484. Rattanapak, T., et al., *Transcutaneous immunization using microneedles and cubosomes: Mechanistic investigations using Optical Coherence Tomography and Two-Photon Microscopy*. Journal of Controlled Release, 2013. **172**(3): p. 894-903.
485. Lemelle, A., et al., *Application of gold nanoparticles as contrast agents in confocal laser scanning microscopy*. Laser Physics Letters, 2008. **6**(1): p. 71.
486. Labouta, H.I. and M. Schneider, *Interaction of inorganic nanoparticles with the skin barrier: current status and critical review*. Nanomedicine: Nanotechnology, Biology and Medicine, 2013. **9**(1): p. 39-54.
487. Samberg, M.E., S.J. Oldenburg, and N.A. Monteiro-Riviere, *Evaluation of silver nanoparticle toxicity in skin in vivo and keratinocytes in vitro*. Environ Health Perspect, 2010. **118**(3): p. 407-13.
488. Zhang, L.W., et al., *Biological interactions of quantum dot nanoparticles in skin and in human epidermal keratinocytes*. Toxicol Appl Pharmacol, 2008. **228**(2): p. 200-11.
489. Reichelt, J., *Mechanotransduction of keratinocytes in culture and in the epidermis*. Eur J Cell Biol, 2007. **86**(11-12): p. 807-16.
490. Niepel, M.S., et al., *Nanoscaled surface patterns influence adhesion and growth of human dermal fibroblasts*. Langmuir, 2013. **29**(43): p. 13278-90.
491. Katsuta, Y., et al., *Function of oleic acid on epidermal barrier and calcium influx into keratinocytes is associated with N-methyl D-aspartate-type glutamate receptors*. Br J Dermatol, 2009. **160**(1): p. 69-74.
492. Wagner, H., et al., *Drug distribution in human skin using two different in vitro test systems: comparison with in vivo data*. Pharmaceutical research, 2000. **17**(12): p. 1475-1481.
493. Nohynek, G.J., et al., *Safety assessment of personal care products/cosmetics and their ingredients*. Toxicology and Applied Pharmacology, 2010. **243**(2): p. 239-259.
494. Gordon, S., et al., *Non-animal models of epithelial barriers (skin, intestine and lung) in research, industrial applications and regulatory toxicology*. ALTEX, 2015. **32**(4): p. 327-78.
495. Verma, V., N. Singh, and R. Singh, *An introduction to the transdermal delivery of antiretrovirals*. Advances in Biology & BioMedicine, 2014(BIO14 06): p. 1-32.
496. Astashkina, A.I., et al., *Nanoparticle toxicity assessment using an in vitro 3-D kidney organoid culture model*. Biomaterials, 2014. **35**(24): p. 6323-31.
497. Pampaloni, F., E.G. Reynaud, and E.H. Stelzer, *The third dimension bridges the gap between cell culture and live tissue*. Nat Rev Mol Cell Biol, 2007. **8**(10): p. 839-45.
498. Knight, E. and S. Przyborski, *Advances in 3D cell culture technologies enabling tissue-like structures to be created in vitro*. J Anat, 2015. **227**(6): p. 746-56.
499. Haycock, J., ed. *3D cell culture: Methods and Protocols*. Methods in Molecular Biology 695, ed. J.W. Haycock. 2011, Humana Press: New York. 343.
500. Tsang, V.L. and S.N. Bhatia, *Three-dimensional tissue fabrication*. Adv Drug Deliv Rev, 2004. **56**(11): p. 1635-47.
501. Martin, Y. and P. Vermette, *Bioreactors for tissue mass culture: design, characterization, and recent advances*. Biomaterials, 2005. **26**(35): p. 7481-503.
502. Guller, A.E., et al., *Bioreactors in tumor tissue engineering*. Acta Naturae, 2016. **8**(3 (30)): p. 44-58.
503. Portner, R., et al., *Bioreactor design for tissue engineering*. J Biosci Bioeng, 2005. **100**(3): p. 235-45.
504. Sutherland, R.M., J.A. McCredie, and W.R. Inch, *Growth of Multicell Spheroids in Tissue Culture as a Model of Nodular Carcinomas*<xref ref-type="fn" rid="FN2">2</xref>. JNCI: Journal of the National Cancer Institute, 1971. **46**(1): p. 113-120.
505. Benton, G., et al., *Matrigel: from discovery and ECM mimicry to assays and models for cancer research*. Adv Drug Deliv Rev, 2014. **79-80**(0): p. 3-18.
506. May, J.E., et al., *Development of a novel, physiologically relevant cytotoxicity model: application to the study of chemotherapeutic damage to mesenchymal stromal cells*. Toxicol Appl Pharmacol, 2012. **263**(3): p. 374-89.
507. Patra, B., et al., *Migration and vascular lumen formation of endothelial cells in cancer cell spheroids of various sizes*. Biomicrofluidics, 2014. **8**(5): p. 052109.
508. Friedrich, J., et al., *Spheroid-based drug screen: considerations and practical approach*. Nat Protoc, 2009. **4**(3): p. 309-24.
509. Kelm, J.M. and M. Fussenegger, *Microscale tissue engineering using gravity-enforced cell assembly*. Trends Biotechnol, 2004. **22**(4): p. 195-202.
510. Kunz-Schughart, L.A., et al., *The use of 3-D cultures for high-throughput screening: the multicellular spheroid model*. J Biomol Screen, 2004. **9**(4): p. 273-85.

REFERENCES

511. Tung, Y.C., et al., *High-throughput 3D spheroid culture and drug testing using a 384 hanging drop array*. Analyst, 2011. **136**(3): p. 473-478.
512. Horman, S.R., et al., *High-content analysis of three-dimensional tumor spheroids: investigating signaling pathways using small hairpin RNA*. Nat Meth, 2013. **10**(10).
513. Hirschhaeuser, F., et al., *Multicellular tumor spheroids: an underestimated tool is catching up again*. J Biotechnol, 2010. **148**(1): p. 3-15.
514. Thoma, C.R., et al., *3D cell culture systems modeling tumor growth determinants in cancer target discovery*. Adv Drug Deliv Rev, 2014. **69-70**(0): p. 29-41.
515. Goodman, T.T., P.L. Olive, and S.H. Pun, *Increased nanoparticle penetration in collagenase-treated multicellular spheroids*. Int J Nanomedicine, 2007. **2**(2): p. 265-74.
516. Londono, R. and S.F. Badylak, *Biologic Scaffolds for Regenerative Medicine: Mechanisms of In vivo Remodeling*. Ann Biomed Eng, 2014: p. 1-16.
517. Lee, J., M.J. Cuddihy, and N.A. Kotov, *Three-dimensional cell culture matrices: state of the art*. Tissue Eng Part B Rev, 2008. **14**(1): p. 61-86.
518. Gilbert, T.W., T.L. Sellaro, and S.F. Badylak, *Decellularization of tissues and organs*. Biomaterials, 2006. **27**(19): p. 3675-83.
519. Hodde, J., *Naturally occurring scaffolds for soft tissue repair and regeneration*. Tissue Eng, 2002. **8**(2): p. 295-308.
520. Crapo, P.M., T.W. Gilbert, and S.F. Badylak, *An overview of tissue and whole organ decellularization processes*. Biomaterials, 2011. **32**(12): p. 3233-43.
521. Badylak, S.F., D. Taylor, and K. Uygun, *Whole-organ tissue engineering: decellularization and recellularization of three-dimensional matrix scaffolds*. Annu Rev Biomed Eng, 2011. **13**: p. 27-53.
522. Ott, H. and D. Taylor, *Decellularization and recellularization of organs and tissues*. 2013, Google Patents.
523. Guyette, J.P., et al., *Perfusion decellularization of whole organs*. Nat Protoc, 2014. **9**(6): p. 1451-68.
524. Barnes, C.A., et al., *The surface molecular functionality of decellularized extracellular matrices*. Biomaterials, 2011. **32**(1): p. 137-43.
525. Moran, E.C., et al., *Whole-organ bioengineering: current tales of modern alchemy*. Transl Res, 2014. **163**(4): p. 259-67.
526. Lutolf, M.P. and J.A. Hubbell, *Synthetic biomaterials as instructive extracellular microenvironments for morphogenesis in tissue engineering*. Nature Biotechnology, 2005. **23**(1): p. 47-55.
527. Gill, B.J. and J.L. West, *Modeling the tumor extracellular matrix: Tissue engineering tools repurposed towards new frontiers in cancer biology*. J Biomech, 2014. **47**(9): p. 1969-78.
528. Nair, L.S. and C.T. Laurencin, *Biodegradable polymers as biomaterials*. Progress in Polymer Science, 2007. **32**(8-9): p. 762-798.
529. Tibbitt, M.W. and K.S. Anseth, *Hydrogels as extracellular matrix mimics for 3D cell culture*. Biotechnol Bioeng, 2009. **103**(4): p. 655-63.
530. Peppas, N.A., et al., *Hydrogels in Biology and Medicine: From Molecular Principles to Bionanotechnology*. Advanced Materials, 2006. **18**(11): p. 1345-1360.
531. Sawkins, M.J., et al., *Hydrogels derived from demineralized and decellularized bone extracellular matrix*. Acta Biomater, 2013. **9**(8): p. 7865-73.
532. DeQuach, J.A., et al., *Decellularized porcine brain matrix for cell culture and tissue engineering scaffolds*. Tissue Eng Part A, 2011. **17**(21-22): p. 2583-92.
533. Phillip, L., et al., *Liver-derived decellularized extracellular matrix gels induce complex branching and bile ductule network formation of cholangiocytes in vitro*. Frontiers in Bioengineering and Biotechnology, 2016. **4**.
534. Zhu, N. and X. Che, *Biofabrication of Tissue Scaffolds*, in *Advances in Biomaterials Science and Biomedical Applications*, R. Pignatello, Editor. 2013, InTech.
535. Janik, H. and M. Marzec, *A review: fabrication of porous polyurethane scaffolds*. Mater Sci Eng C Mater Biol Appl, 2015. **48**: p. 586-91.
536. Mohanty, S., et al., *Fabrication of scalable and structured tissue engineering scaffolds using water dissolvable sacrificial 3D printed moulds*. Materials Science and Engineering: C, 2015. **55**: p. 569-578.
537. Mohanty, S., et al., *Fabrication of scalable tissue engineering scaffolds with dual-pore microarchitecture by combining 3D printing and particle leaching*. Mater Sci Eng C Mater Biol Appl, 2016. **61**: p. 180-9.
538. Ayres, C.E., et al., *Nanotechnology in the design of soft tissue scaffolds: innovations in structure and function*. Wiley Interdiscip Rev Nanomed Nanobiotechnol, 2010. **2**(1): p. 20-34.
539. Giannitelli, S.M., et al., *Combined additive manufacturing approaches in tissue engineering*. Acta Biomater, 2015. **24**: p. 1-11.
540. Yeong, W.Y., et al., *Rapid prototyping in tissue engineering: challenges and potential*. Trends Biotechnol, 2004. **22**(12): p. 643-52.

REFERENCES

541. Sobral, J.M., et al., *Three-dimensional plotted scaffolds with controlled pore size gradients: Effect of scaffold geometry on mechanical performance and cell seeding efficiency*. Acta Biomater, 2011. **7**(3): p. 1009-18.
542. Landers, R., et al., *Fabrication of soft tissue engineering scaffolds by means of rapid prototyping techniques*. Journal of Materials Science, 2002. **37**(15): p. 3107-3116.
543. Pfister, A., et al., *Biofunctional rapid prototyping for tissue-engineering applications: 3D bioplotting versus 3D printing*. Journal of Polymer Science Part A: Polymer Chemistry, 2004. **42**(3): p. 624-638.
544. Li, W.J., et al., *Electrospun nanofibrous structure: a novel scaffold for tissue engineering*. J Biomed Mater Res, 2002. **60**(4): p. 613-21.
545. Buttafoco, L., et al., *Electrospinning of collagen and elastin for tissue engineering applications*. Biomaterials, 2006. **27**(5): p. 724-34.
546. Ji, Y., et al., *Electrospun three-dimensional hyaluronic acid nanofibrous scaffolds*. Biomaterials, 2006. **27**(20): p. 3782-92.
547. He, X., et al., *Electrospun collagen/poly(L-lactic acid-co-epsilon-caprolactone) hybrid nanofibrous membranes combining with sandwich construction model for cartilage tissue engineering*. J Nanosci Nanotechnol, 2013. **13**(6): p. 3818-25.
548. Moroni, L., et al., *Fiber diameter and texture of electrospun PEOT/PBT scaffolds influence human mesenchymal stem cell proliferation and morphology, and the release of incorporated compounds*. Biomaterials, 2006. **27**(28): p. 4911-22.
549. Xu, W., et al., *Controllable dual protein delivery through electrospun fibrous scaffolds with different hydrophilicities*. Biomed Mater, 2013. **8**(1): p. 014104.
550. Hou, Z., et al., *Electrospun upconversion composite fibers as dual drugs delivery system with individual release properties*. Langmuir, 2013. **29**(30): p. 9473-82.
551. Zhao, C., et al., *Nanomaterial scaffolds for stem cell proliferation and differentiation in tissue engineering*. Biotechnol Adv, 2013. **31**(5): p. 654-68.
552. Hosseinkhani, H., et al., *DNA nanoparticles encapsulated in 3D tissue-engineered scaffolds enhance osteogenic differentiation of mesenchymal stem cells*. J Biomed Mater Res A, 2008. **85**(1): p. 47-60.
553. Hirata, E., et al., *3D collagen scaffolds coated with multiwalled carbon nanotubes: initial cell attachment to internal surface*. J Biomed Mater Res B Appl Biomater, 2010. **93**(2): p. 544-50.
554. Roohani-Esfahani, S.I., et al., *The influence hydroxyapatite nanoparticle shape and size on the properties of biphasic calcium phosphate scaffolds coated with hydroxyapatite-PCL composites*. Biomaterials, 2010. **31**(21): p. 5498-509.
555. Roohani-Esfahani, S.I., et al., *Effects of bioactive glass nanoparticles on the mechanical and biological behavior of composite coated scaffolds*. Acta Biomater, 2011. **7**(3): p. 1307-18.
556. Chahine, N.O., et al., *Nanocomposite scaffold for chondrocyte growth and cartilage tissue engineering: effects of carbon nanotube surface functionalization*. Tissue Eng Part A, 2014. **20**(17-18): p. 2305-15.
557. Sharma, Y., et al., *Fabrication of conducting electrospun nanofibers scaffold for three-dimensional cells culture*. Int J Biol Macromol, 2012. **51**(4): p. 627-31.
558. Tan, Q., et al., *Controlled release of chitosan/heparin nanoparticle-delivered VEGF enhances regeneration of decellularized tissue-engineered scaffolds*. Int J Nanomedicine, 2011. **6**: p. 929-42.
559. Liu, X., et al., *Delivery of growth factors using a smart porous nanocomposite scaffold to repair a mandibular bone defect*. Biomacromolecules, 2014. **15**(3): p. 1019-30.
560. Izadifar, M., et al., *Rate-programming of nano-particulate delivery systems for smart bioactive scaffolds in tissue engineering*. Nanotechnology, 2015. **26**(1): p. 012001.
561. Mohiti-Asli, M., et al., *Ibuprofen loaded PLA nanofibrous scaffolds increase proliferation of human skin cells in vitro and promote healing of full thickness incision wounds in vivo*. J Biomed Mater Res B Appl Biomater, 2015.
562. Haisler, W.L., et al., *Three-dimensional cell culturing by magnetic levitation*. Nat Protoc, 2013. **8**(10): p. 1940-9.
563. Daquinag, A.C., G.R. Souza, and M.G. Kolonin, *Adipose tissue engineering in three-dimensional levitation tissue culture system based on magnetic nanoparticles*. Tissue Eng Part C Methods, 2013. **19**(5): p. 336-44.
564. Souza, G.R., et al., *Three-dimensional tissue culture based on magnetic cell levitation*. Nat Nanotechnol, 2010. **5**(4): p. 291-6.
565. Ito, A., et al., *Construction and delivery of tissue-engineered human retinal pigment epithelial cell sheets, using magnetite nanoparticles and magnetic force*. Tissue Eng, 2005. **11**(3-4): p. 489-96.
566. Sidgwick, G.P., D. McGeorge, and A. Bayat, *Functional testing of topical skin formulations using an optimised ex vivo skin organ culture model*. Arch Dermatol Res, 2016. **308**(5): p. 297-308.
567. Kojima, H., *The use of 3-D models as alternatives to animal testing*. Altern Lab Anim, 2015. **43**(4): p. P40-3.

REFERENCES

568. Jung, M.H., S.M. Jung, and H.S. Shin, *Co-stimulation of HaCaT keratinization with mechanical stress and air-exposure using a novel 3D culture device*. Sci Rep, 2016. **6**: p. 33889.
569. Parenteau, N.L., et al., *Epidermis generated in vitro: practical considerations and applications*. J Cell Biochem, 1991. **45**(3): p. 245-51.
570. Chen, C.-S.J., et al., *Use of a Serum-Free Epidermal Culture Model to Show Deleterious Effects of Epidermal Growth Factor on Morphogenesis and Differentiation*. Journal of Investigative Dermatology, 1995. **104**(1): p. 107-112.
571. Roguet, R., et al., *Episkin, a reconstituted human epidermis for assessing in vitro the irritancy of topically applied compounds*. Toxicology in Vitro, 1994. **8**(2): p. 283-291.
572. Schmook, F.P., J.G. Meingassner, and A. Billich, *Comparison of human skin or epidermis models with human and animal skin in in-vitro percutaneous absorption*. International Journal of Pharmaceutics, 2001. **215**(1-2): p. 51-56.
573. Netzlaff, F., et al., *The human epidermis models EpiSkin®, SkinEthic® and EpiDerm®: An evaluation of morphology and their suitability for testing phototoxicity, irritancy, corrosivity, and substance transport*. European Journal of Pharmaceutics and Biopharmaceutics, 2005. **60**(2): p. 167-178.
574. Schafer-Korting, M., et al., *Reconstructed human epidermis for skin absorption testing: results of the German prevalidation study*. Altern Lab Anim, 2006. **34**(3): p. 283-94.
575. Tornier, C., M. Rosdy, and H.I. Maibach, *In vitro skin irritation testing on reconstituted human epidermis: reproducibility for 50 chemicals tested with two protocols*. Toxicol In Vitro, 2006. **20**(4): p. 401-16.
576. Netzlaff, F., et al., *Permeability of the reconstructed human epidermis model Episkin in comparison to various human skin preparations*. Eur J Pharm Biopharm, 2007. **66**(1): p. 127-34.
577. Spielmann, H., et al., *The ECVAM international validation study on in vitro tests for acute skin irritation: report on the validity of the EPISKIN and EpiDerm assays and on the Skin Integrity Function Test*. Altern Lab Anim, 2007. **35**(6): p. 559-601.
578. Alepee, N., et al., *A catch-up validation study on reconstructed human epidermis (SkinEthic RHE) for full replacement of the Draize skin irritation test*. Toxicol In Vitro, 2010. **24**(1): p. 257-66.
579. Katoh, M., et al., *Assessment of the human epidermal model LabCyte EPI-MODEL for In vitro skin corrosion testing according to the OECD test guideline 431*. J Toxicol Sci, 2010. **35**(3): p. 411-7.
580. Boelsma, E., et al., *Characterization and comparison of reconstructed skin models: morphological and immunohistochemical evaluation*. Acta Derm Venereol, 2000. **80**(2): p. 82-8.
581. Ponec, M., *Skin constructs for replacement of skin tissues for in vitro testing*. Advanced Drug Delivery Reviews, 2002. **54**, **Supplement**: p. S19-S30.
582. Kidd, D.A., M. Johnson, and J. Clements, *Development of an in vitro corrosion/irritation prediction assay using the EpiDerm skin model*. Toxicol In Vitro, 2007. **21**(7): p. 1292-7.
583. Ackermann, K., et al., *The Phenion full-thickness skin model for percutaneous absorption testing*. Skin Pharmacol Physiol, 2010. **23**(2): p. 105-12.
584. Kuchler, S., et al., *Hallmarks of atopic skin mimicked in vitro by means of a skin disease model based on FLG knock-down*. Altern Lab Anim, 2011. **39**(5): p. 471-80.
585. Engelhart, K., et al., *In vitro reproduction of clinical hallmarks of eczematous dermatitis in organotypic skin models*. Arch Dermatol Res, 2005. **297**(1): p. 1-9.
586. Barker, C.L., et al., *The development and characterization of an in vitro model of psoriasis*. J Invest Dermatol, 2004. **123**(5): p. 892-901.
587. Hill, D.S., et al., *A Novel Fully Humanized 3D Skin Equivalent to Model Early Melanoma Invasion*. Mol Cancer Ther, 2015. **14**(11): p. 2665-73.
588. Meier, F., et al., *Human melanoma progression in skin reconstructs : biological significance of bFGF*. Am J Pathol, 2000. **156**(1): p. 193-200.
589. MacNeil, S., *Progress and opportunities for tissue-engineered skin*. Nature, 2007. **445**(7130): p. 874-80.
590. Labouta, H.I., S. Thude, and M. Schneider, *Setup for investigating gold nanoparticle penetration through reconstructed skin and comparison to published human skin data*. J Biomed Opt, 2013. **18**(6): p. 061218.
591. Alepee, N., et al., *State-of-the-art of 3D cultures (organs-on-a-chip) in safety testing and pathophysiology*. Altex, 2014. **31**(4): p. 441-77.
592. Jeong, S.H., et al., *Assessment of penetration of quantum dots through in vitro and in vivo human skin using the human skin equivalent model and the tape stripping method*. Biochem Biophys Res Commun, 2010. **394**(3): p. 612-5.
593. Lee, O., et al., *A quantitative study of nanoparticle skin penetration with interactive segmentation*. Med Biol Eng Comput, 2015: p. 1-11.

REFERENCES

594. Park, B., et al., *Initial in vitro screening approach to investigate the potential health and environmental hazards of Enviroxtrade mark - a nanoparticulate cerium oxide diesel fuel additive*. Part Fibre Toxicol, 2007. **4**(1): p. 12.
595. Park, Y.H., et al., *Assessment of dermal toxicity of nanosilica using cultured keratinocytes, a human skin equivalent model and an in vivo model*. Toxicology, 2010. **267**(1-3): p. 178-81.
596. Kuchler, S., et al., *3D-wound healing model: influence of morphine and solid lipid nanoparticles*. J Biotechnol, 2010. **148**(1): p. 24-30.
597. Mahajan, S., et al., *Innovative nanotherapy for the treatment of the chronic skin condition, rosacea (P3259)*. The Journal of immunology, 2013. **190** (1 Supplement): p. 192.
598. Faller, C. and M. Bracher, *Reconstructed skin kits: reproducibility of cutaneous irritancy testing*. Skin Pharmacol Appl Skin Physiol, 2002. **15 Suppl 1**(Suppl. 1): p. 74-91.
599. Netzlaff, F., et al., *The human epidermis models EpiSkin, SkinEthic and EpiDerm: an evaluation of morphology and their suitability for testing phototoxicity, irritancy, corrosivity, and substance transport*. Eur J Pharm Biopharm, 2005. **60**(2): p. 167-78.
600. Hayden, P.J., et al., *Microvesicating effects of sulfur mustard on an in vitro human skin model*. Toxicol In Vitro, 2009. **23**(7): p. 1396-405.
601. Faller, C., et al., *Predictive ability of reconstructed human epidermis equivalents for the assessment of skin irritation of cosmetics*. Toxicol In Vitro, 2002. **16**(5): p. 557-72.
602. Mewes, K.R., et al., *Elastin expression in a newly developed full-thickness skin equivalent*. Skin Pharmacol Physiol, 2007. **20**(2): p. 85-95.
603. Kanapathipillai, M., A. Brock, and D.E. Ingber, *Nanoparticle targeting of anti-cancer drugs that alter intracellular signaling or influence the tumor microenvironment*. Adv Drug Deliv Rev, 2014. **79-80**(0): p. 107-18.
604. Niu, W., W. Shi, and D. Weng, *Nanoparticle drug delivery systems and three-dimensional cell cultures in cancer treatments and research*. Cancer Translational Medicine, 2016. **2**(5): p. 154.
605. Goodman, T.T., C.P. Ng, and S.H. Pun, *3-D tissue culture systems for the evaluation and optimization of nanoparticle-based drug carriers*. Bioconjug Chem, 2008. **19**(10): p. 1951-9.
606. da Rocha, E.L., L.M. Porto, and C.R. Rambo, *Nanotechnology meets 3D in vitro models: tissue engineered tumors and cancer therapies*. Mater Sci Eng C Mater Biol Appl, 2014. **34**: p. 270-9.
607. Yang, Y., et al., *Evaluation of photodynamic therapy efficiency using an in vitro three-dimensional microfluidic breast cancer tissue model*. Lab Chip, 2015. **15**(3): p. 735-44.
608. Goodman, T.T., et al., *Spatio-temporal modeling of nanoparticle delivery to multicellular tumor spheroids*. Biotechnol Bioeng, 2008. **101**(2): p. 388-99.
609. Gao, Y., et al., *Predictive models of diffusive nanoparticle transport in 3-dimensional tumor cell spheroids*. Aaps j, 2013. **15**(3): p. 816-31.
610. Du, A.W., H. Lu, and M.H. Stenzel, *Core-Cross-Linking Accelerates Antitumor Activities of Paclitaxel-Conjugate Micelles to Prostate Multicellular Tumor Spheroids: A Comparison of 2D and 3D Models*. Biomacromolecules, 2015. **16**(5): p. 1470-9.
611. Ma, H., et al., *Multicellular tumor spheroids as an in vivo-like tumor model for three-dimensional imaging of chemotherapeutic and nano material cellular penetration*. Molecular imaging, 2012. **11**(6): p. 487.
612. Jiang, X., et al., *Solid tumor penetration by integrin-mediated pegylated poly(trimethylene carbonate) nanoparticles loaded with paclitaxel*. Biomaterials, 2013. **34**(6): p. 1739-46.
613. Wang, X., et al., *Doxorubicin delivery to 3D multicellular spheroids and tumors based on boronic acid-rich chitosan nanoparticles*. Biomaterials, 2013. **34**(19): p. 4667-79.
614. Chia, S.L., et al., *Biomimicry 3D gastrointestinal spheroid platform for the assessment of toxicity and inflammatory effects of zinc oxide nanoparticles*. Small, 2015. **11**(6): p. 702-12.
615. Xu, X., et al., *A hydrogel-based tumor model for the evaluation of nanoparticle-based cancer therapeutics*. Biomaterials, 2014. **35**(10): p. 3319-30.
616. Lee, J., et al., *In vitro toxicity testing of nanoparticles in 3D cell culture*. Small, 2009. **5**(10): p. 1213-21.
617. Charoen, K.M., et al., *Embedded multicellular spheroids as a biomimetic 3D cancer model for evaluating drug and drug-device combinations*. Biomaterials, 2014. **35**(7): p. 2264-71.
618. Biondi, M., et al., *Sub-100 nm biodegradable nanoparticles: in vitro release features and toxicity testing in 2D and 3D cell cultures*. Nanotechnology, 2013. **24**(4): p. 15.
619. Shi, W.B., et al., *Overcoming multidrug resistance in 2D and 3D culture models by controlled drug chitosan-graft poly(caprolactone)-based nanoparticles*. J Pharm Sci, 2014. **103**(4): p. 1064-74.
620. Wang, K., et al., *3D Porous Chitosan-Alginate Scaffolds as an In Vitro Model for Evaluating Nanoparticle-Mediated Tumor Targeting and Gene Delivery to Prostate Cancer*. Biomacromolecules, 2015. **16**(10): p. 3362-72.

REFERENCES

621. Godugu, C. and M. Singh, *AlgiMatrix-Based 3D Cell Culture System as an In Vitro Tumor Model: An Important Tool in Cancer Research*. Methods Mol Biol, 2016. **1379**: p. 117-28.
622. Godugu, C., et al., *AlgiMatrix based 3D cell culture system as an in-vitro tumor model for anticancer studies*. PLoS One, 2013. **8**(1): p. e53708.
623. Kwak, B., K. Park, and B. Han, *Tumor-on-chip: simulation of complex transport around tumor*, in *ASME 2013 2nd Global Congress on NanoEngineering for Medicine and Biology*. 2013, American Society of Mechanical Engineers. p. V001T02A006-V001T02A006.
624. Meng, H., et al., *Gadolinium metallofullerenol nanoparticles inhibit cancer metastasis through matrix metalloproteinase inhibition: imprisoning instead of poisoning cancer cells*. Nanomedicine, 2012. **8**(2): p. 136-46.
625. Mitra, M., et al., *A novel in vitro three-dimensional retinoblastoma model for evaluating chemotherapeutic drugs*. Mol Vis, 2012. **18**: p. 1361-78.
626. Comley, D., *3D cell culture: easier said than done! (2013)*. Drug Discovery World, 2013. **Winter**(4).
627. Guller, A., et al., *Onion-like surface design of upconverting nanophosphors modified with polyethylenimine: shielding toxicity versus keeping brightness?* SPIE Biophotonics Australasia 2016, 2016. **10013**: p. 100132Q-100132Q-5.
628. Nadort, A., et al., *Systematic assessment of blood circulation time of functionalized upconversion nanoparticles in the chick embryo*, in *SPIE Micro+ Nano Materials, Devices, and Applications*. 2015, International Society for Optics and Photonics: Sydney, New South Wales, Australia. p. 96683Y-96683Y-7.
629. Fidler, I.J., *The pathogenesis of cancer metastasis: the 'seed and soil' hypothesis revisited*. Nat Rev Cancer, 2003. **3**(6): p. 453-8.
630. Sussewind, J., et al., *A 3D co-culture of three human cell lines to model the inflamed intestinal mucosa for safety testing of nanomaterials*. Nanotoxicology, 2015: p. 1-10.
631. Hussain, S., et al., *Oxidative stress and proinflammatory effects of carbon black and titanium dioxide nanoparticles: role of particle surface area and internalized amount*. Toxicology, 2009. **260**(1-3): p. 142-9.
632. Song, Y., X. Li, and X. Du, *Exposure to nanoparticles is related to pleural effusion, pulmonary fibrosis and granuloma*. Eur Respir J, 2009. **34**(3): p. 559-67.
633. Kedmi, R., N. Ben-Arie, and D. Peer, *The systemic toxicity of positively charged lipid nanoparticles and the role of Toll-like receptor 4 in immune activation*. Biomaterials, 2010. **31**(26): p. 6867-75.
634. Kost, O.A., et al., *Superoxide Dismutase 1 Nanozyme for Treatment of Eye Inflammation*. Oxid Med Cell Longev, 2015. **2015**: p. 5194239.
635. Li, W., et al., *Pharmacokinetic and anti-inflammatory effects of sanguinarine solid lipid nanoparticles*. Inflammation, 2014. **37**(2): p. 632-8.
636. Blecher, K., et al., *Nitric oxide-releasing nanoparticles accelerate wound healing in NOD-SCID mice*. Nanomedicine, 2012. **8**(8): p. 1364-71.
637. Pascual, L., et al., *Mesoporous silica as multiple nanoparticles systems for inflammation imaging as nano-radiopharmaceuticals*. Microporous and Mesoporous Materials, 2017. **239**: p. 426-431.
638. Mishra, D.K., et al., *Human lung cancer cells grown on acellular rat lung matrix create perfusable tumor nodules*. Ann Thorac Surg, 2012. **93**(4): p. 1075-81.
639. Mishra, D.K., et al., *Human Lung Fibroblasts Inhibit Non-Small Cell Lung Cancer Metastasis in Ex Vivo 4D Model*. Ann Thorac Surg, 2015. **100**(4): p. 1167-74; discussion 1174.
640. Henriksen-Lacey, M., S. Carregal-Romero, and L.M. Liz-Marzan, *Current Challenges toward In Vitro Cellular Validation of Inorganic Nanoparticles*. Bioconjug Chem, 2017. **28**(1): p. 212-221.

List of abbreviations

2D	Two-dimensional
3D	Three-dimensional
A-A	Antibiotic-antimycotic
ADAMs	Family name for metalloendopeptidases
ADAMTs	Family of multidomain extracellular protease enzymes
AMS-6	Anionic surfactant template mesoporous silica nanoparticles (type 6)
AMS-6-Dox	AMS-6 loaded with doxorubicin
AOSS	Acellular organ specific scaffold
ATP	Adenosine triphosphate
ATPase	Adenosine triphosphatase
BET	Brunauer–Emmett–Teller (theory)
BM	Basement membrane
BSA	Bovine serum albumin
CCD	Charge-coupled device
CCK-8	Cell counting kit-8
CEST	Chemical exchange saturation transfer
CNS	Central nervous system
CPE	Chemical penetration enhancer
CT	Computer tomography
CTAB	Cetyltrimethylammonium bromide
DAPI	4',6-diamidine-2'-phenylindole dihydrochloride
DCL	Decellularization; decellularized
DFT	Density functional theory
DLS	Dynamic light scattering
DMEM	Dulbecco's Modification of Eagles Medium
DMF	dimethylformamide
DMSO	Dimethyl sulfoxide
DNA	Deoxyribonucleic acid
Dox or DOX	Doxorubicin
DSL	Deeper skin layers (subepidermal)
DSS	Dextran sulphate sodium salt

APPENDICES

Dtxl	Docetaxel
EC	Endothelial cells
EC ₅₀	50% effectivity concentration
ECM	Extracellular matrix
ED	Embryonic day
EDC-HCl	N-(3-dimethylaminopropyl)-N'-ethylcarbodiimide hydrochloride
EDTA	Ethylenediaminetetraacetic acid
EGFR	Epidermal growth factor receptor
EMT	Epithelial-mesenchymal transition
EPR	Enhanced permeability and retention
ESI	Electronic supplementary information (for the full paper in Chapter 5)
ESM	Electronic supplementary material (for full paper in the Chapter 4)
FBS	Fetal bovine serum
FDA	Fluorescein diacetate (in the context of staining); Food and Drug Administration (in the context of legal regulations)
FDA/PI	Combined staining with fluorescein diacetate (FDA) and propidium iodide (PI)
FDM	Fused deposition modelling
FITC	Fluorescein isothiocyanate
FR	Folic acid receptor
FRET	Fluorescence energy transfer mechanism
FT	Full-thickness
FTIR	Fourier transform infrared
Gem	Gemcitabine
GFP	Green fluorescent protein
GI	Gastrointestinal
HEEDA	N-(2-hydroxyethyl)ethyl-enediamine
HER2	Human epidermal growth factor receptor 2
HP	Hematoporphyrin
HSE	Human skin equivalents
IC	Stellate cells of Ito
IC ₅₀	50% inhibitory concentration
ICG	Indocyanine green
ICP	Ion coupled plasma
IFP	Interstitial fluid pressure
IL	Interleukin

APPENDICES

IONPs	Iron oxide nanoparticles
IV	Intravenous
LD ₅₀	50% lethal dose
Ln ³⁺	Trivalent lanthanide ions
LSE	Living skin equivalents
Lx	Polystyrene
MB	Methylene blue
MCM	Mobile Crystalline Materials
MDR	Multidrug resistance
MET	Mesenchymal-epithelial transition
MMPs	Metalloproteinases
MNP	Magnetic nanoparticles
MPS	Mononuclear phagocyte system
MRI	Magnetic resonance imaging
MS	Micellar delivery system
MSNP	Mesoporous silica nanoparticle
MTS	3-[4,5-dimethylthiazol-2-yl]-5-(3-carboxymethoxyphenyl)-2-(4-sulfophenyl)-2H-tetrazolium
MTT	3-[4,5-dimethylthiazol-2-yl]-2,5-diphenyltetrazolium-bromide
NAD(P)H	Reduced form of nicotinamide adenine dinucleotide phosphate (NADP)
NADH	Reduced form of nicotinamide adenine dinucleotide (NAD)
NIR	Near infrared radiation
NIRF	Near-infrared fluorescence
NO	Nitric oxide
NPH	p-nitrophenylhydrazine
NP	Nanoparticle
NSCLC	Non-small cell lung cancer
NTA	Nanotheranostic agent
OA	Oleic acid
OA-PAA-PEG	Octylamine-poly(acrylic acid)-poly(ethylene glycol)
OECD	Organisation for Economic Cooperation and Development
ORS	Outer root sheath of hair follicle
P/S, PS	Penicillin-Streptomycin mixed solution
PA	Polyacrylamide (in Chapter 3) and polyacrolein (in Chapter 5)
PAA	Polyacrylic acid

APPENDICES

PAH	Poly(allylamine hydrochloride)
PAI	Photoacoustic imaging
PAMAM	Poly(amidoamine)
PBS	Phosphate buffer saline
PDT	Photodynamic therapy
PEG	Polyethyleneglycol
PEG-b-PCL	Poly(ethylene glycol)- <i>block</i> -poly(caprolactone)
PEG-b-PLA	Poly((ethylene glycol)- <i>block</i> -lactic acid)
PEG-b-PLGA	Poly(ethylene glycol)- <i>block</i> -poly(lactic- <i>co</i> -glycolic acid)
PEI	Polyethylenimine
PET	Positron emission tomography
PI	Propidium iodide
PL	Photoluminescence
PLA	Poly(lactic acid)
PLGA	Poly(lactic- <i>co</i> -glycolic acid)
PMAO	Poly(maleic anhydride- <i>alt</i> -1-octadecene)
PNS	Peripheral nervous system
PR	Progesterone receptor
PS	Photosensitizer
PSS	Poly(styrene sulfonate)
PTT	Photothermal therapy
PTX	Paclitaxel
PVP	Polyvinylpyrrolidone
QDs	Quantum dots
RB	Rose Bengal
RFP	Red fluorescent protein
RGD	Arginine-glycine-aspartic acid (amino acid sequence)
RHE	Reconstructed human epidermis
RNA	Ribonucleic acid
ROS	Reactive oxygen species
SBA	Santa Barbara Amorphous
SC	Stratum corneum
SD	Standard deviation
SDS	Sodium dodecyl sulphate

APPENDICES

SEM	Scanning electron microscopy
SI	Supplementary information (for the full paper in Chapter 7)
siRNA	Small interfering RNA
SLA	Stereolithography
SLS	Selective laser sintering
SPECT	Single photon emission tomography
SPION	Superparamagnetic iron oxide nanoparticles
Sulfo-NHS	N-hydroxysulfosuccinimide sodium salt
SWNTs	Single-walled carbon nanotubes
TAT	Trans-activating transcriptional activator
TEC	Tissue engineering construct
TEM	Transmission electron microscopy
TGA	Thermogravimetric analysis
TL	Therapeutic load
TMAH	Tetramethylammonium hydroxide
TNBC	Triple-negative breast cancer
TNF	Tumor necrosis factor
UCL	Upconversion luminescence
UCNP	Upconverting nanoparticles
US	Ultrasound imaging
UV	Ultraviolet
XRD	X-ray powder diffraction

Animal ethics approvals



MACQUARIE
University

ANIMAL RESEARCH AUTHORITY (ARA)

AEC Reference No.: 2015/006

Date of Expiry: 16 May 2016

Full Approval Duration: 16 May 2015 to 16 May 2018 (36 months)

This ARA remains in force until the Date of Expiry (unless suspended, cancelled or surrendered) and will only be renewed upon receipt of a satisfactory Progress Report before expiry (see Approval email for submission details).

Principal Investigator:

Dr Andrei Zvyagin
Department of Physics and Astronomy
Macquarie University, NSW 2109
andrei.zvyagin@mq.edu.au
0451 925 116

Associate Investigators:

Anna Guller 0450 124 218
Annemarie Nadort 0405 036690

In case of emergency, please contact:
the Principal Investigator / Associate Investigator named above
Or Manager, CAF: 9850 7780 / 0428 861 163 and Animal Welfare
Officer: 9850 7758 / 0439 497 383

The above-named are authorised by MACQUARIE UNIVERSITY ANIMAL ETHICS COMMITTEE to conduct the following research:

Title of the project: Optical imaging and sensing for tissue engineering applications: study on chicken embryos

Purpose: 5 - Research: Human or Animal Health and Welfare

Aims: 1) To develop new protocols of Decellularisation (DCL) of organs of chick embryo. 2) To determine the effects of different DCL conditions on the amount of residual cellular material and integrity of extracellular matrix in kidneys, liver, lungs and heart tissues to find optimal conditions of organ processing and reseeded. 3) To develop methods of non-destructive control of the quality of DCL based on monitoring of optical properties of the solutions used for tissue processing instead of cutting the organ for histology.

Surgical Procedures category: 3 - Minor Conscious Intervention

All procedures must be performed as per the AEC-approved protocol, unless stated otherwise by the AEC and/or AWO.

Maximum numbers approved (For the Full Approval Duration):

Species	Strain	Age/Weight/Sex	Total	Supplier/Source
13 Poultry	chick embryo	Day 3- 18/ any/any	306	http://www.countrycacklers.net
			306	

Location of research:

Location	Full street address
School of Advanced Medicine	Level 1, F10A, 2 Technology Place, Macquarie University, NSW 2109
Other Facilities	Physics and Astronomy Department of FSE: Macquarie University, Building E7B, PC1 lab 109, 2109 N.S.W. Australia; Physics and Astronomy Department of FSE: Macquarie University, Building F7B, rooms 004 -006 (optical labs), 2109 N.S.W. Australia; Microscopy Unit of CBMS: Macquarie University, Building E8A, rooms 010 -016A, 2109 N.S.W. Australia.

Amendments approved by the AEC since initial approval: N/A

Conditions of Approval: N/A

Being animal research carried out in accordance with the Code of Practice for a recognised research purpose and in connection with animals (other than exempt animals) that have been obtained from the holder of an animal suppliers licence.

Professor Mark Connor (Chair, Animal Ethics Committee)

Approval Date: 14 May 2015



MACQUARIE
University

ANIMAL RESEARCH AUTHORITY (ARA)

AEC Reference No.: 2015/U06-2

Date of Expiry: 16 May 2017

Full Approval Duration: 16 May 2015 to 16 May 2018 (36 months)

This ARA remains in force until the Date of Expiry (unless suspended, cancelled or surrendered) and will only be renewed upon receipt of a satisfactory Progress Report before expiry (see Approval email for submission details).

Principal Investigator:

Dr Andrei Zvyagin
Department of Physics and Astronomy
Macquarie University, NSW 2109
andrei.zvyagin@mq.edu.au
0451 925 116

Associate Investigators:

Anna Guller 0450 124 218
Annemarie Nadort 0405 036 690

In case of emergency, please contact:
the Principal Investigator / Associate Investigator named above
Or Manager, CAF: 9850 7780 / 0428 861 163 and Animal Welfare
Officer: 9850 7758 / 0439 497 383

The above-named are authorised by MACQUARIE UNIVERSITY ANIMAL ETHICS COMMITTEE to conduct the following research:

Title of the project: Optical imaging and sensing for tissue engineering applications: study on chicken embryos

Purpose: 5 - Research: Human or Animal Health and Welfare

Aims: 1) To develop new protocols of Decellularisation (DCL) of organs of chick embryo. 2) To determine the effects of different DCL conditions on the amount of residual cellular material and integrity of extracellular matrix in kidneys, liver, lungs and heart tissues to find optimal conditions of organ processing and reseeded. 3) To develop methods of non-destructive control of the quality of DCL based on monitoring of optical properties of the solutions used for tissue processing instead of cutting the organ for histology.

Surgical Procedures category: 3 - Minor Conscious Intervention

All procedures must be performed as per the AEC-approved protocol, unless stated otherwise by the AEC and/or AWO.

Maximum numbers approved (For the Full Approval Duration):

Species	Strain	Age/Weight/Sex	Total	Supplier/Source
13 Poultry	chick embryo	Day 3- 18/ any/any	306	http://www.countrycacklers.net
			306	

Location of research:

Location	Full street address
School of Advanced Medicine	Level 1, F10A, 2 Technology Place, Macquarie University, NSW 2109
Other Facilities	Physics and Astronomy Department of FSE: Macquarie University, Building E7B, PC1 lab 109, 2109 N.S.W. Australia; Physics and Astronomy Department of FSE: Macquarie University, Building F7B, rooms 004-006 (optical labs), 2109 N.S.W. Australia; Microscopy Unit of CBMS: Macquarie University, Building E8A, rooms 010 -016A, 2109 N.S.W. Australia.

Amendments approved by the AEC since initial approval: N/A

Conditions of Approval: N/A

Being animal research carried out in accordance with the Code of Practice for a recognised research purpose and in connection with animals (other than exempt animals) that have been obtained from the holder of an animal suppliers licence.

Assoc. Professor Jennifer Cornish (Chair, Animal Ethics Committee)

Approval Date: 14 April 2016

Adapted from Form C (issued under part IV of the Animal Research Act, 1985)

Ethics Approval



ANIMAL RESEARCH AUTHORITY (ARA)

AEC Reference No.: 2013/007-4

Date of Expiry: 31 March 2016

Full Approval Duration: 1 April 2013 to 31 March 2016 (24 Months+12 months)

This ARA remains in force until the Date of Expiry (unless suspended, cancelled or surrendered) and will only be renewed upon receipt of a satisfactory Progress Report before expiry (see Approval email for submission details).

Principal Investigator:

Dr Andrei Zvyagin
Physics and Astronomy
Macquarie University, NSW 2109
andrei.zvyagin@mq.edu.au
0451 925 116

Associate Investigators:

Mark Connor 0413 202 762
Annemarie Nadort 0405 036 690
Luen Liang 0451 976 934
Anna Guller 0450 124 218

In case of emergency, please contact:
the Principal Investigator / Associate Investigator named above
Animal Welfare Officer - 9850 7758 / 0439 497 383,

The above-named are authorised by MACQUARIE UNIVERSITY ANIMAL ETHICS COMMITTEE to conduct the following research:

Title of the project: High-sensitivity targeted imaging of tumours on the chick embryo chorio-allantoic membrane

Purpose: 4 - Research: Human or Animal Biology

Aims: 1. To assess methods to detect tumours, based on labeling tumours with luminescent nanoparticle-antibody complexes that adhere to the tumour;
2. To graft small tumours on the chick embryo chorio-allantoic membrane
3. To develop nanoparticles that can attach to tumours and also have therapeutic effects

Surgical Procedures category: 3 - Minor Conscious Intervention

All procedures must be performed as per the AEC-approved protocol, unless stated otherwise by the AEC and/or AWO.

Maximum numbers approved (for the Full Approval Duration):

Species	Strain	Age/Sex/Weight	Total	Supplier/Source
13	-	Day 11-17	100+160	Country Cacklers
		TOTAL	260	

Location of research:

Location	Full street address
MQ	Macquarie University, Building E78, PC1 lab 109, NSW 2109
ASAM	Level 1, F10A, 2 Technology Place, Macquarie University, NSW 2109

Amendments approved by the AEC since initial approval:

1. Experimental design, technique or procedure, number of animals and extension of approval duration (Approved 20 March 2014).
2. Amendment # 2 - Removal of Ekaterina A Ivukina as Associate Investigator (Approved AEC 17 July 2014).
3. Amendment # 3 - Addition of Luen Liang as Associate Investigator (Exec approved 25 June 2014, ratified at AEC 17 July 2014).
4. Amendment #4 - Addition of Anna Guller as Associate Investigator - (Exec approved & ratified by AEC 16 April 2015)
5. Amendment #5 - Request of extension of 12 months (approved by AEC 16 April 2015)

Conditions of Approval: N/A

Being animal research carried out in accordance with the Code of Practice for a recognised research purpose and in connection with animals (other than exempt animals) that have been obtained from the holder of an animal suppliers licence.

Dr Simon McMullan (Acting Chair, Animal Ethics Committee)

Approval Date: 16 April 2015

APPENDICES

Перевод с русского языка на английский язык
Translation from Russian into English



Ministry of Healthcare of the Russian Federation
Federal State-Funded Educational Institution
of Higher Vocational Education
—I.M. SECHENOV FIRST MOSCOW STATE MEDICAL UNIVERSITY

LOCAL ETHICS COMMITTEE

119991, 8, Trubetskaya str., Moscow, Russia

Ph.: +7(495)622-97-06, fax: +7(495)622-97-56

E-mail: IEC@mma.ru

Extract from the protocol number 11-16 of Local Ethics Committee meeting of 14.12.2016.

Attendees:

The Chair of the Local Ethics Committee – Balalykin D.A.;
Vice-Chairman of the Local Ethics Committee – Rebrova E.L.;
Members of the Local Ethics Committee - Ermolayeva I.I., Borisova N.I., Volkova E.A., Grigoryan V.A., Dubogray E.V., Subbotina O.A.
A quorum is present, so that the meeting is duly constituted to transact the action for which it had been convened.

The meeting has taken place at: 8, Trubetskaya Str., Moscow, Russia at 6 pm.

Meeting Agenda: Review of whether to approve the scientific research project entitled "The Study of Biocompatibility and Biological Effects of the Materials for Tissue Engineering and Nanomedicine", conducted under grant support provided by The Russian Foundation For Basic Research (grants numbers are the following: 13-04-12075-ofi, 13-02-00934, 13-02-01363-a and 12-04-01258); carried out on the base of the Laboratory of Experimental Morphology, Centre of Bioimaging, Institute For Regenerative Medicine of Federal State-Funded Educational Institution of Higher Vocational Education I.M. Sechenov First Moscow State Medical University; 119991, Building 8-2, Trubetskaya street, Moscow.

The investigator – Guller A.E.

The documents provided by the Applicant:

1. Application for the LEC expertise by Ms. A.E. Guller.
2. Annotation of the research project.
3. Curriculum Vitae of the investigators, involved into the project.

Hereby it has been resolved that: The materials of the scientific research project entitled "The Study of Biocompatibility and Biological Effects of the Materials for Tissue Engineering and Nanomedicine", conducted under grant support provided by The Russian Foundation For Basic Research (grants numbers are the following: 13-04-12075-ofi, 13-02-00934, 13-02-01363-a and 12-04-01258) carried out on the base of the Laboratory of Experimental Morphology, Centre of Bioimaging, Institute For Regenerative Medicine of Federal State-Funded Educational Institution of Higher Vocational Education I.M. Sechenov First Moscow State Medical University; 119991, Building 8-2, Trubetskaya street, Moscow, are to be acknowledged in terms of compliance to the ethical requirements.

Certified to be a true and correct extract.

Executive Secretary of LEC

signature

I. I. Ermolayeva

22.12.2016

Stamp: Local Ethics Committee

Federal State-Funded Educational Institution of Higher Vocational Education I.M. Sechenov First Moscow State Medical University of Ministry of Healthcare of the Russian Federation
Ph.: +7(495)622-97-06

I confirm an accurate translation of the original document

Translation Office of
IE Karnaukhov E.S.

City of Moscow, Leninskiy Ave., 86

(495) 505-25-39, 8 (499) 131-28-29

TRANSLATION OFFICE

MOSCOW, LENINSKIY AVE.

495 505 25 39/499 131 28

TRANSLATOR KUZNETSOVA IRINA

Irina Kuznetsova



Translated by Kuznetsova Irina
Vitalievna,
December 30, 2016